LIQUEFACTION INDUCED BY CYCLIC LOADING

March 1, 1982

Submitted to

National Science Foundation
Washington, D. C.

By

Geotechnical Engineers Inc.
1017 Main Street
Winchester, Massachusetts 01890
617/729-1625

Project 80696

John L. Enos
Engineer

Steve J. Poulos
Principal

John W. France
Assistant Project Manager

Gonzalo Castro
Principal-in-Charge

50272-101

REPORT DOCUMENTATION PAGE	1. REPORT NO. NSF/CEE-82018	2.	3. Recipient's Accession No. PB82 235508
4. Title and Subtitle: Liquefaction Induced by Cyclic Loading			5. Report Date: March 1982
			6.
7. Author(s): G. Castro, J.L. Enos, J.W. France, S.J. Poulos			8. Performing Organization Rept. No.
9. Performing Organization Name and Address: Geotechnical Engineers, Inc., 1017 Main Street, Winchester, MA 01890			10. Project/Task/Work Unit No. 80696
			11. Contract(C) or Grant(G) No. (C) (G) PFR7924731
12. Sponsoring Organization Name and Address: Directorate for Engineering (ENG), National Science Foundation, 1800 G Street, N.W., Washington, DC 20550			13. Type of Report & Period Covered
			14.

15. Supplementary Notes: Submitted by: Communications Program (OPRM), National Science Foundation, Washington, DC 20550

16. Abstract (Limit: 200 words)

The results of a study of liquefaction induced by cyclic loading are presented. Liquefaction and cyclic mobility are defined and compared with published definitions. The steady state of deformation is described and its relationship to liquefaction is discussed. The results of comprehensive laboratory triaxial testing programs on two sands are supplied. The test data demonstrate that, for a given soil, the steady state line is independent of stress history, and the magnitude of cyclic loading required to trigger liquefaction is a function of static shear stress and number of load cycles. The steady state lines for the two sands tested are compared to steady state lines for a variety of other sands. General trends are recorded for variation of steady state lines in grain size distribution and in grain angularity. A procedure for practical application of steady state concepts to geotechnical engineering is recommended.

17. Document Analysis a. Descriptors

Liquefaction
Sand
Loads (forces)
Cyclic loads
Steady state
Deformation
Soils
Grain size
Grain shape
Earthquakes
Stresses
Shear stress

b. Identifiers/Open-Ended Terms

Cyclic mobility
G. Castro, /PI

c. COSATI Field/Group

18. Availability Statement: NTIS	19. Security Class (This Report)	21. No. of Pages
	20. Security Class (This Page)	22. Price

(See ANSI-Z39.18) See Instructions on Reverse

OPTIONAL FORM 272 (4-77) (Formerly NTIS-35) Department of Commerce

This material is based upon work supported by the National Science Foundation under Grant No. PFR-7924731.

Any opinions, findings, and conclusions or recommendations expressed in this publication are those of the writer(s) and do not necessarily reflect the views of the National Science Foundation.

TABLE OF CONTENTS

TABLE OF CONTENTS
(continued)

TABLE OF CONTENTS
(continued)

TABLE OF CONTENTS
(concluded)

LIST OF TABLES

LIST OF FIGURES

LIST OF FIGURES
(continued)

Chapter 5

LIST OF FIGURES
(continued)

Chapter 6

Chapter 7

LIST OF FIGURES
(concluded)

LIST OF APPENDICES

LIST OF NOTATIONS

The following symbols are used in this report:

B = Skempton's pore pressure parameter

CSR = cyclic stress ratio = $\frac{\tau_{cy}}{\bar{\sigma}_{3c}}$

C_{ss} = slope of the steady state line in semi-logarithic plot

C_u = coefficient of uniformity = D_{60}/D_{10}

D_{10} = grain size for which 10% of sample by weight is smaller

D_{60} = grain size for which 60% of sample by weight is smaller

D_r = relative density = $\frac{e_{max} - e}{e_{max} - e_{min}} = \frac{\gamma_{max}}{\gamma} \frac{\gamma - \gamma_{min}}{\gamma_{max} - \gamma_{min}}$

D_{rc} = relative density after consolidation

D_{ro} = initial relative density before consolidation

e = void ratio

e_c = void ratio after consolidation

e_i = void ratio after application of vacuum to triaxial specimen during setup

e_m = void ratio of specimen as compacted in mold

e_{max} = maximum void ratio according to particular method specified

e_{min} = minimum void ratio according to particular method specified

e_{ss} = void ratio on the steady state line, corresponding to $\bar{\sigma}_3 = 1.00$ kg/cm^2

G = specific gravity of solids

K_c = consolidation stress ratio = $\bar{\sigma}_{1c}/\bar{\sigma}_{3c}$

P = percent compaction = percent of maximum density determined according to ASTM D1557

SSL = steady state line

LIST OF NOTATIONS
(continued)

S_d = drained shear strength

S_{dp} = peak drained shear strength

S_{ds} = drained shear strength at steady state

S_u = undrained shear strength

S_{up} = peak undrained shear strength

S_{us} = undrained shear strength at steady state

u = pore water pressure

u_c = pore water pressure at completion of consolidation (same as back pressure)

δ = deformation

δ_e = cumulative deformation induced by earthquake

γ_d = dry unit weight (dry density)

$\gamma_{d_{max}}$ = maximum dry unit weight

$\gamma_{d_{min}}$ = minimum dry unit weight

$\bar{\sigma}_1$ = effective major principal stress

σ_1 = total major principal stress

$\bar{\sigma}_2$ = effective intermediate principal stress

σ_2 = total intermediate principal stress

$\bar{\sigma}_3$ = effective minor principal stress

$\bar{\sigma}_{3i}$ = effective minor principal stress prior to shearing

σ_3 = total minor principal stress

$\bar{\sigma}_H$ = effective horizontal stress

$\bar{\sigma}_v$ = effective vertical stress

$(\sigma_1-\sigma_3)/2$ = maximum shear stress in triaxial test

$(\sigma_1-\sigma_3)_{cy}$ = cyclic deviator stress

LIST OF NOTATIONS
(concluded)

τ = shear stress

τ_d = driving shear stress

τ_e = earthquake shear stress

τ_{cy} = cyclic shear stress [$\left(\frac{\sigma_1-\sigma_3}{2}\right)_{cy}$ in triaxial test]

Subscripts

c = refers to consolidation state

e = refers to earthquake stresses and deformations

s or ss = refers to steady state

Test Designations*

$\bar{R}$ = isotropically consolidated-undrained axial compression test with pore pressure measurement (CIU)

$A\bar{R}$ = anisotropically consolidated-undrained axial compression test with pore pressure measurement (CK_oU)

$CA\bar{R}$ = anisotropically consolidated-undrained cyclic axial compression test with pore pressure measurement (Cyclic CK_oU)

$CA\bar{R}$-$\bar{R}$ = $CA\bar{R}$ test followed by an $\bar{R}$ test.

*MIT system test designation is given in parentheses.

ABSTRACT

This report presents the results of a study of liquefaction induced by cyclic loading. The study was based on steady state concepts. Definitions of "liquefaction" and "cyclic mobility" are presented and compared with other published definitions. The steady state of deformation is described and its relationship to liquefation is discussed.

The results of comprehensive laboratory triaxial testing programs on two sands are presented. The test data demonstrate that, for a given soil, the steady state line (locus of steady states of deformation) is independent of stress history.

Liquefaction can develop when the static shear stresses exceed the undrained steady state strength. The magnitude of cyclic loading required to trigger liquefaction was found to be a function of static shear stress and number of load cycles.

The steady state lines for the two sands tested in this study were compared to steady state lines for a variety of other sands. General trends were observed for the variation of steady state lines with changes in grain size distribution and in grain angularity.

Finally, a recommended procedure for practical application of steady state concepts to geotechnical engineering is presented.

1.0 INTRODUCTION

1.1 Statement of the Problem

The term "liquefaction," as used in this report, is defined as follows:

> Liquefaction - is a phenomenon wherein a mass of soil loses a large percentage of its shear resistance, when subjected to undrained monotonic, cyclic or shock loading, and flows in a manner resembling a liquid until the shear stresses acting on the mass are as low as the reduced shear resistance.

The loss in shear resistance is due to the conversion of the mass from a practically drained condition, at which it can sustain the in situ shear stresses, to a practically undrained condition of shear.

Liquefaction can occur in saturated sands, silts, and quick clays and can also occur in very large masses of sands or silts that are dry and loose enough so that the air cannot escape from the voids fast enough to prevent undrained shear. This report deals only with liquefaction of saturated sands.

If a slope or embankment composed of saturated sand or silt fails by liquefaction, the soil mass comes to rest only after the slope has been reduced to a few degrees and the shear stresses have consequently been reduced to the mobilized shear resistance. Because of the rapid movement, very large displacement and the fluid-like appearance of the soil associated with these types of slope failures, the term "flow slide" has been used to describe them.

Similarly, if saturated sands supporting a structure fail by liquefaction, the structure floats or sinks, and tilts until the shear stresses applied to the soil are less than or equal to its mobilized shear resistance.

Historically, failures of the type described above have been associated principally with loose sand and silt deposits.

It has been postulated that soils sheared to large strains eventually reach the steady state of deformation. Poulos (1971, 1981) has presented the following definition of the steady state of deformation:

> The steady state of deformation for any mass of particles is that state in which the mass is continuously deforming at constant volume, constant normal effective stress, constant shear stress, and constant velocity. The steady state of deformation is achieved only after all particle orientation has reached a statistically steady-state condition and after all particle breakage, if any, is complete, so that the shear stress needed to continue deformation and the velocity of deformation remain constant.

It is hypothesized that, for a given soil, there is a unique relationship between void ratio, effective normal stress and shear stress at the steady state, and that this relationship is independent of stress history or stress path prior to reaching the steady state of deformation, so long as grain breakage is not significant.

Liquefaction, as defined above, involves large unidirectional shear deformations, and thus one would expect that during liquefaction failures the soil will tend towards the steady state of deformation. If the shear strength at the steady state is lower than the applied shear stress in the ground, then, in principle, it is possible for liquefaction to occur. Conversely, if the steady state shear strength is greater than the shear stress in the ground, then liquefaction cannot occur because the associated large unidirectional deformations are not possible.

Investigations of liquefaction of saturated cohesionless soils based on steady state concepts have been presented by Castro, 1969; Casagrande, 1975; Castro, 1975; Castro and Poulos, 1977; Sangrey et al, 1978. To date there have been no comprehensive investigations of the effects of parameters such as stress history, static shear stresses, soil compressibility, and type of sand on the development of liquefaction induced by cyclic loading.

A large number of studies (e.g., Finn et al, 1970, Finn et al, 1971; Ishihara, 1975; Lee and Seed, 1967, Nos. 1 and 2; Ross et al, 1969; Seed and Lee, 1966) have been reported in the literature as investigations of liquefaction due to cyclic loading. However, these studies have not addressed the phenomenon of liquefaction as defined above. Rather they have addressed a different phenomenon involving high pore pressures and large accumulated cyclic deformations. Various authors have called this phenomenon cyclic mobility, initial liquefaction, partial liquefaction, initial liquefaction with limited strain potential, cyclic liquefaction, cyclic strain softening, and peak cyclic pore pressure ratio of 100% with limited strain potential. In

this report the term "cyclic mobility," as defined below, will be used to distinguish it from liquefaction, as defined above:

> Cyclic Mobility is the progressive softening of a saturated sand when subjected to cyclic loading at constant void ratio. The softening is accompanied by high pore pressures, increasing cyclic deformation, and in some cases, permanent deformations, but it does not lead to loss in shear strength nor to continuous deformation, both of which are essential aspects of liquefaction.

Cyclic mobility has been observed in the laboratory in loose and in dense sands.

A detailed discussion of terminology is presented in Section 2.

The principal subject of the study reported herein is liquefaction caused by cyclic loading. Cyclic mobility will be considered only when it is useful in understanding the factors affecting liquefaction.

1.2 Purpose and Scope of the Investigation

The two purposes of the investigation reported herein were as follows:

1) To evaluate the validity of the application of steady state concepts to the problem of liquefaction of saturated sands induced by cyclic loading.

2) To determine how these concepts may be applied in the engineering solution of problems involving liquefaction induced by cyclic loading.

The investigation consisted of a laboratory triaxial testing program on five sands with extensive testing programs on two of the sands.

The data obtained from the testing program were used to evaluate:

1. The effects of the initial state of the soil with respect to the steady state line on the response to cyclic loading.

2. The effects of stress history and loading stress path on the steady state of deformation.

3. The effects of static shear stresses (anisotropic consolidations) on liquefaction caused by cyclic loading.

4. The effects of cyclic loading on subsequent stress-strain behavior.

5. The effects of grain angularity and grain size distribution on the steady state of deformation.

A method is presented for the application of steady state concepts to the practice of geotechnical earthquake engineering.

2.0 BACKGROUND INFORMATION

2.1 The Distinction Between Liquefaction and Cyclic Mobility

2.1.1 Definitions for this Report

During the past 15 years there has been considerable confusion in the literature concerning the phenomenon of "liquefaction." Consequently, it is necessary to present the following two definitions, which are basically those previously advanced by two of the present writers (Castro and Poulos, 1977), and which will be adhered to in this report:

> Liquefaction is a phenomenon wherein a mass of soil loses a large percentage of its shear resistance, when subjected to undrained monotonic, cyclic or shock loading, and flows in a manner resembling a liquid until the shear stresses acting on the mass are as low as the reduced shear resistance.

The loss in shear resistance is due to the conversion of the mass from a practically drained condition, at which it can sustain the in situ shear stresses, to a practically undrained condition of shear.

Upon liquefaction, the soil flows in a manner that resembles a liquid; however, its shear resistance is of a frictional nature rather than of a viscous nature, as in a true liquid. During flow the shear strength is a function of the effective stresses, and it is not zero, except in special cases.

Liquefaction can occur in saturated sands, silts, and quick clays and can also occur in very large masses of sands or silts that are dry and loose enough so that the air cannot escape from the voids fast enough to prevent undrained shear.

> Cyclic Mobility is the progressive softening of a saturated soil when subjected to cyclic loading at constant void ratio. The softening is accompanied by high pore pressures, increasing cyclic deformations, and in some cases, permanent deformations, but it does not lead to loss in shear strength nor to con-

tinuous deformation, both of which are essential aspects of liquefaction.

The shear strength referred to in the above definition is the strength at large strains, which later in this report is designated as steady state strength (see Section 2.2.). If the soil exhibits a peak strength, with a reduction in strength upon subsequent straining, the peak strength can be reduced as a result of cyclic mobility, but the strength at large strains would not be reduced.

Various other authors have referred to the second phenomenon, "cyclic mobility," as initial liquefaction (Lee and Seed, 1967), partial liquefaction (Seed and Lee, 1966), initial liquefaction with limited strain potential (Seed, 1976), cyclic liquefaction (Casagrande, 1975), peak cyclic pore pressure ratio of 100% with limited strain potential (Seed, 1979), and simply, liquefaction (e.g., Isihara, 1977; Finn et al, 1978).

The distinction between liquefaction and cyclic mobility, as defined above, would be relatively unimportant if it were not for the fact that the two phenomena are significantly different with respect to the physical laws that govern them and the practical consequences of their occurrence in situ. It has been shown (Castro and Poulos, 1977) that different parameters (e.g. soil type, confining stress, initial shear stress) influence liquefaction and cyclic mobility differently, and thus many conclusions drawn from studies of cyclic mobility are not applicable to liquefaction.

A careful examination of the definition of liquefaction stated above indicates the following two implicit conditions:

1. Liquefaction involves large, unidirectional shear deformations, which usually occur at a relatively rapid rate when failures occur in situ so that it appears to be flowing.

2. Liquefaction requires the presence of "driving" shear stresses significantly greater than the shear strength of the soil after the loss of shear resistance. These driving shear stresses supply the driving force which produces the large and rapid, continuous deformation.

Driving Shear Stresses

Consider the embankment dam illustrated in Fig. 2-1a, which is stable under static conditions. Since the slope is stable, the drained shear strength, S_d, for a representative soil element on a potential slip surface, such as element "A," is greater than the "driving" shear stress, τ_d, applied to the element. This "driving" shear stress is the shear stress resulting from the geometry of and the loading on the soil (i.e., the shear stress which one would calculate in a stability analysis). It is not that shear stress which would result from placement of the soil (i.e., the shear stress in an element of soil beneath level ground, which results from the deposition of the material with an at-rest lateral pressure coefficient different from one).

In a stability analysis, one determines the minimum shear stresses that are necessary for equilibrium of the soil mass above a potential failure surface. If one performs a stability analysis of a soil mass with a level surface, the analysis will indicate zero shear stresses along the full length of any potential failure surface. However, if one assumes an at rest earth pressure coefficient different from one (usually smaller than one), there are shear stresses in all planes at each point, except for the vertical and horizontal planes. These shear stresses are not "driving" shear stresses because they are not needed for equilibrium. Only those shear stresses that are needed for equilibrium, as given by a conventional stability analysis, are considered driving shear stresses, in the sense that they can "drive" large deformations of a mass of soil if, at any time, they exceed the available shear resistance.

If an earthquake or other disturbance affects the dam so rapidly that the conditions are essentially undrained, then the strength that controls stability will be the undrained shear strength, S_u. If S_u is greater than the driving shear stress, τ_d, loss of stability will not occur. If s_u is only slightly less than τ_d, then a relatively small slope failure or slumping, as illustrated in Fig. 2-1b, will occur to reduce the applied shear stresses to less than S_u. Such a failure would not be referred to as a liquefaction failure. If, however, S_u is much less than the driving shear stresses, τ_d, then large changes in the slope geometry would be required to reduce the shear stresses to S_u, and a large amount of potential energy would be available to produce a flow slide failure, as illustrated in Fig. 2-1c. This type of failure would be recognized as a liquefaction

failure. Note that large, unidirectional deformations are associated with this liquefaction failure.

An example of the type of failure illustrated in Fig. 2-1 is the failure of the Lower San Fernando Dam, illustrated in Fig. 2-2, which failed as a result of the 1971 San Fernando earthquake due to liquefaction of a large zone of the hydraulic fill sand. The sand that liquefied was identified by the extreme degree of deformation of the original stratification of the hydraulic fill as observed in borehole samples and in the walls of a transverse trench excavated in the zone of failure (Seed, Lee, et al, 1975). The zone that liquefied is identified in the cross sections before and after the failure in Fig. 2-2. Note the large, unidirectional motions of the soil and the relatively flat surface after the failure.

A similar example could be developed for the case of soils supporting a structure. In this case, a liquefaction failure would cause the structure to sink or float until the applied shear stresses are reduced to the available shear resistance. Two examples of liquefaction of foundation soils which occurred during the 1964 Niigata, Japan earthquake are illustrated in the photographs in Fig. 2-3. In the first example, apartment buildings sank and tilted (as much as 80°) as a result of liquefaction, and consequent loss of bearing capacity of the fine sands on which they were founded. In the second example, an underground sewerage treatment tank rose to the surface when the surrounding fine sands failed by liquefaction. In both cases there were apparent large unidirectional strains in the sand under and around the structures.

From the above discussion, it can be seen that the loss of shear resistance referred to in the definition of liquefaction is the change in available shear resistance from the previously available drained shear strength, S_d, to a lower undrained shear strength, S_u. A schematic representation of the stress-strain curve during an earthquake induced liquefaction failure is given in Fig. 2-6e, which will be discussed in detail in a subsequent section.

2.1.2 Definitions by Others

To the writers' knowledge the term "liquefaction" originally developed from a paper by Hazen (1920) in which the term "liquefies" was used in the description of the flow slide failure of the hydraulic fill sands in Calaveras Dam

in California. As further research has been done, the understanding of the phenomenon of liquefaction has changed and definitions of the term have evolved. At times, the definition has been the subject of much controversy. In this section some of the definitions or explanations of liquefaction that have been advanced by others during the past six years are presented and are compared to the definitions presented by the writers in Section 2.1.1.

Casagrande, 1975, presented the following definitions:

1. Actual Liquefaction = what was simply called "liquefaction" before the development of cyclic laboratory tests. It is the response of loose, saturated sand when subjected to strains or shocks that results in substantial loss of strength and in extreme cases leads to flow slides.

2. Cyclic Liquefaction = the response of a test specimen of dilative sand to cyclic loading in a triaxial test when the peak pore pressure rises momentarily in each cycle to the confining pressure.

These two definitions are seen to be essentially the same as the definitions of liquefaction and cyclic mobility, respectively, presented in Section 2.1.1. In fact, Casagrande was the first to propose the use of the term "cyclic mobility" (Casagrande, 1971).

Seed, 1979 presented the following definitions:

1. "Liquefaction": denotes a condition where a soil will undergo continued deformation at a constant low residual stress or with low residual resistance, due to the buildup and maintenance of high pore water pressures, which reduce the effective confining pressure to a very low value; pore pressure buildup leading to liquefaction may be due either to static or cyclic stress applications and the possibility of its occurrence will depend on the void ratio or relative density of a sand and the confining pressure; it may also be caused by a critical hydraulic gradient during an upward flow of water in a sand deposit.

2. "Peak Cyclic Pore Pressure Ratio of 100%": denotes a condition where, during the course of cyclic stress applications, the residual Pore water pressure on completion of any full stress cycle becomes equal to the applied confining pressure; the development of a peak cyclic pore pressure ratio of 100% has no implications concerning the magnitude of the deformations that the soil might subsequently undergo; however, it defines a condition that is a useful basis for assessing various possible forms of subsequent soil behavior.

3. "Peak Cyclic Pore Pressure Ratio of 100% with Limited Strain Potential" or "Cyclic Mobility": denotes a condition in which cyclic stress applications develop a peak cyclic pore pressure ratio of 100% and subsequent cyclic stress applications cause limited strains to develop either because of the remaining resistance of the soil to deformation or because the soil dilates, the pore pressure drops, and the soil stabilizes under the applied loads. Cyclic mobility may also be used in a broader sense to describe the cyclic straining that may occur even with pore pressure ratios less than 100% in which case the actual peak value of pore pressure ratio may simply be stated.

Again it is seen that these definitions of liquefaction (1) and cyclic mobility (3) are very similar to those presented in Section 2.1.1. As Seed, 1979 states, the term "peak cyclic pore pressure ratio of 100%' had previously been referred to as "initial liquefaction" (Seed and Lee, 1966; Lee and Seed, 1967) and the term "cyclic mobility" had previously been referred to as "cyclic liquefaction" (Casagrande, 1975) and "initial liquefaction with limited strain potential" (Seed, et al, 1975; Seed, 1976).

The above definitions proposed by Seed, 1979 have not been universally accepted, and some investigators still use the earlier terms and in some cases simply use the term "liquefaction" for cyclic mobility. Consequently, when reading papers in the literature on the topic of "liquefaction," one must be careful to distinguish which of the two phenomenon is being discussed.

Some published papers (e.g., Ishihara, 1977; Finn, et al, 1978, Dobry et al, 1980) indicate that some investigators are implicitly using the definition that liquefaction due to cyclic loading occurs when the pore water pressure increases to a value equal to the overburden pressure and the effective overburden pressue is consequently equal to zero. This condition is interpreted to indicate that the soil has zero shear strength. Except for the assertion of zero shear strength, which will be discussed later, this condition is seen to correspond to "peak cyclic pore pressure ratio of 100%."

Hence there is still confusion in the literature regarding a definition for liquefaction. For the purposes of this report, the definitions in Section 2.1.1 will be used.

2.1.3 Examples of Stress-Strain Curves for Liquefaction and Cyclic Mobility

Examples of stress-strain curves during liquefaction caused by undrained monotonic loading of three anisotropically consolidated triaxial specimens are presented in Fig. 2-4a. In each test, after anisotropic consolidation, the axial load was increased monotonically in increments using load control. For about the first 1% axial strain in each test, the shear stress and the pore pressure both increased. Then the pore pressure suddenly increased, the resistance decreased, and the specimen deformed from 1 percent to 26 percent axial strain in 0.15 to 0.25 sec.* During this rapid deformation, the specimens appeared to flow "in a manner resembling a liquid," and the shear strength decreased significantly, i.e., they liquefied. In none of the three cases did the effective stress or the shear strength decrease to zero; in fact, the minimum shear strength was about 0.25 kg/cm^2.

An example of liquefaction due to undrained cyclic loading of an anisotropically consolidated triaxial specimen is illustrated in Fig. 2-4b. The stress-strain curve is seen to be similar except that the strength reduction was triggered by cyclic rather than monotonic loading. It should be noted that in the test shown in Fig. 2-4b, the rapid deformation actually started 28 seconds after the cyclic loading stopped. Consequently, although the cyclic loading triggered the liquefaction, the additional shear stress of the cyclic load was not required to drive the large deformations.

*The applied load remained constant; although the load felt by the specimen dropped significantly, the difference betweeen applied and specimen-supported loads caused an acceleration of the loading mechanism.

For sands and silts, liquefaction, as defined in Section 2.1.1 and as illustrated in Fig. 2-4, has been observed in situ and in the laboratory only when the soils are in a loose condition.

Cyclic mobility is illustrated in Fig. 2-5a by the results of an undrained cyclic triaxial test, reported by Seed and Lee, 1966, in which a cyclic deviator stress, of equal magnitude in compression and extension, was applied to an isotropically consolidated specimen. The following observations can be made from these results:

1. Up to a certain number of cycles the strains that develop during each cycle are very small (less than 1%), but the pore pressure shows a cumulative increase.

2. A point is reached after which the value of the pore pressure at zero deviator stress is momentarily equal to the confining pressure, which means the effective stresses momentarily drop to zero.

3. The strains during each subsequent cycle become progressively larger as more cycles of load are applied. During the last load cycle applied during the test, double amplitude strain was equal to about 10%. During each cycle, the pore pressure becomes equal to the confining pressure when the deviator stress is zero but drops substantially when either the axial extension or axial compression load is applied.

In Fig. 2.5b, data are presented for undrained monotonic compression loading of the same specimen, after cyclic loading. It is seen that the pore-water pressure decreased, the effective stress increased, and the specimen had an undrained strength more than 15 times greater than the cyclic shear stress.

Since the cyclic loading resulted in a condition of zero effective stress, momentarily, during each cycle, the sample was said to have achieved initial liquefaction, according to the original Seed and Lee 1966 terminology (see Section 2.1.2.). However, as demonstrated by the increase in effective stress (decrease in pore pressure) within each half cycle of load and by the subsequent monotonic loading,

the specimen had not experienced a reduction in shear strength to less than the cyclic shear stress, and any tendency for large, unidirectional deformations was resisted by the decrease pore pressure and consequent stiffening of the specimen. This behavior should be contrasted with that illustrated in Fig. 2-4b, where it is seen that the specimens lost shear strength and underwent large, unidirectional strains with no subsequent increase in resistance. As discussed in Section 2.1.2, terms such as "initial liquefaction" and "cyclic liquefaction" were introduced for description of the behavior illustrated in Fig. 2-5b, and the terms "liquefaction" or "true liquefaction" were used for the behavior illustrated in Fig. 2-5.

Two other observations regarding cyclic mobility should be noted. First, unlike liquefaction, cyclic mobility has been observed in the laboratory in sands covering the full range of densities from loose to dense. Second, the momentary condition of zero effective stress has only been observed in laboratory tests in which reversal of direction of the shear stress and a momentary isotropic stress state occurs. For anisotropically consolidated specimen loaded with a cyclic shear stresses less than the consolidation shear stress, no such momentary condition of zero effective stress has been observed.

On the basis of the above discussion, the following points should be emphasized:

First, as shown by laboratory research (Casagrande, 1938; Castro, 1969; Castro 1975), the pore pressure need not be equal to the overburden pressure (i.e., the effective stresses need not be equal to zero) for the development of liquefaction.

Second, shear strength losses are not associated with cyclic mobility. It has been shown in the literature that cyclic mobility does not produce losses in shear strength (Castro and Christian, 1976; Sangrey et al, 1978), as illustrated above.

Third, liquefaction does not occur exclusively as a result of cyclic loading, but also occurs as a result of monotonic loading, as shown by many cases cited in the literature, e.g. Koppejan et al, 1948; Casagrande, 1936; Geuze, 1948; WES, 1956; WES, 1967; Casagrande, 1965; COE, 1939, Middlebrooks, 1942; Hazen, 1920; Terzaghi, 1925 and Terzaghi, 1956.

2.1.4 Stability and Deformation Considerations in Earthquake Engineering

Stability and deformation considerations have been well recognized in the design of foundations for static loads as bearing capacity and settlement, respectively. Foundations are routinely designed against bearing capacity failures, in which the foundation would punch into the underlying soil if the applied shear stresses exceeded the available shear resistances. A bearing capacity failure might be preceded by only small settlements. These same foundations are also routinely designed to limit settlements to acceptable values. These settlements occur due to compression of underlying soils and may be very large, even though the applied shear stresses are much less than the available shear resistance.

Consideration of both problems is important, and inadequate design in either case results in an engineering failure of the structure, i.e., the structure does not or cannot function as specified. However, it is recognized that the mechanics of the two problems are different and, consequently, different analytical techniques are used to evaluate them.

The distinction between stability problems and deformation problems is the crux of the practical difference between liquefaction and cyclic mobility, as can be illustrated by the following example.

Consider the elements of soil illustrated in Fig. 2-6a and b, which are representative of soils in an embankment (Fig. 2-6a) and in the foundation soils under a storage tank (Fig. 2-6b). Under static loading these elements are subjected to a state of stress consisting of effective normal stresses and shear stresses. The shear stresses include some "driving" shear stresses, which were not produced by consolidation or placement of the soil, but rather are the result of the loads imposed by the weight of the embankment (Fig. 2-6a) or the loads imposed by the weight of structure (Fig. 2-6b). These "driving" shear stresses will continue to act on the soil until the geometry of the embankment or the effective structural loads change. In other words, the driving shear stresses are the minimal shear stresses required for equilibrium of the soil mass. During deposition of a sand while the surface of the sand mass remains horizontal, shear stresses are generated in the sand which are a function of the "at-rest" lateral pressure

coefficient K_o (the ratio of effective horizontal to vertical normal stresses). These shear stresses are not considered driving shear stresses because they are not needed for the overall equilibrium of the mass. In fact, laboratory experiments have shown (Silver et al, 1980) that in a sand mass with a level surface, vibrations will cause a gradual increase in K_o towards a value of one. When K_o becomes equal to one, the shear stresses in the sand mass become zero.

If the soil is a loose sand its strength and deformation characteristics may be schematically represented by the plots in Fig. 2.6c and 2.6e. Under slowly applied loads, the soil is stable because the applied driving shear stress, τ_d, is less than the available drained shear strength, S_{ds}. However, if an earthquake loading represented by $\pm \tau_e$ is applied to the soil, the pore pressure increases, the shear resistance decreases to the post peak undrained shear strength, S_{us}, which is less than τ_d and the soil mass experiences large unidirectional deformation (i.e., liquefaction occurs). The soil loses its stability, the slope experiences a flow slide or the structure sinks or floats, and deformations continue until the driving shear stresses are reduced to the available strength, S_{us}, or until subsequent drainage increases the available strength to greater than the applied stresses. When failure occurs rapidly, inertia forces may increase the driving forces during the fast failure. The explanation of the flow slide failure illustrated in Fig. 2.6a, c and e is essentially the same as that offered by Casagrande in 1938, as illustrated in Fig. 2-7. Note that in Casagrande's figure, the shear strength during flow is assumed to be independent of the normal stress prior to flow, and that for initial normal stresses higher than a certain value the strength during flow is smaller than the strength before flow (drained strength), but it is not equal to zero.

In contrast, if the soil is the same sand but in a sufficiently denser state, its strength and deformation characteristics may be schematically represented by the plots in Fig. 2-6d and 2-6f. Under slowly applied loads, this soil is also stable because the applied driving shear stress, τ_d, is less than both the peak and post peak drained shear strengths, S_{dp} and S_{ds}. However, during the same earthquake loading, $\pm \tau_e$, the soil builds up pore pressure and accumulates deformation, δ_e, but any tendency for large unidirectional deformation is resisted by a stiffening of the soil and an increase in shear stress because the applied

shear stresses are less than the undrained post peak shear strength, S_{us}. The accumulated strains may be large enough that unacceptable crest settlements or cracking of the dam (possibly resulting in overtopping or piping) or damage to the structure may result; however, the failures are not the result of liquefaction, but rather of accumulated deformations due to cyclic loading of the soil and their effects on the embankment or the structure. The term cyclic mobility describes the case in which cyclic loading produces severe softening or large accumulation of deformation.

Consequently, it is seen that liquefaction is a problem related to loss of stability of the soil and cyclic mobility is a problem involving deformation of the soil, in the same manner that bearing capacity is a stability problem and settlement is a deformation problem.

It should be noted that in the above examples for loose sands, the undrained shear strength that was compared to the driving shear stresses was the undrained shear strength at large strains, S_{us}, and not the peak shear strength, S_{up}. This is appropriate because, as previously discussed, liquefaction is a phenomenon involving large unidirectional deformations, and hence any peak strength at small strain (which would be a function of loading path and soil structure) will be destroyed during the liquefaction failure, leaving only the remaining post peak strength at large strains.

Data supporting the particular shapes of the stress-strain curves presented in Fig. 2-4 will be presented in subsequent sections of this report.

2.2 The Steady State of Deformation and Its Relationship to Liquefaction

2.2.1 The Steady State of Deformation

The concept of the steady state(*) of deformation is an extension of Casagrande's concept of "critical void ratio" (Casagrande, 1936; Casagrande, 1938). Poulos (Poulos, 1971, 1981) has described the concept as follows:

> "The steady state of deformation for any mass of particles is that state in which the mass is continuously deforming at constant volume, constant normal effective stress, constant shear stress, and constant velocity. The

*The term "state" refers to the description of the effective stress (shear stress and normal stress) and void ratio (or density) state of the soil.

> steady state of deformation is achieved only after all particle orientation has reached a statistically steady-state condition and after all particle breakage, if any, is complete, so that the shear stress needed to continue deformation and the velocity of deformation remain constant."

The laboratory test results shown in Fig. 2-4 illustrate that the steady state of deformation can be achieved by monotonic or cyclic loading. Between 10% and 20% to 25% axial strain, for each of these tests, the shear stress, the effective confining stress and the volume (undrained conditions) remain constant and the specimens are deforming continuously at essentially constant velocity.

The following three points regarding the steady state of deformation are important to the understanding of liquefaction:

1. The steady state is <u>not</u> a static state of a soil, but rather occurs only during continuous deformation at constant velocity (Poulos, 1971). If the parameters of the state of the soil are equal to those at steady state, but the soil is static, not deforming, subsequent deformation may cause changes in the state parameters (e.g., volume or pore pressure). Only after sufficient deformation has taken place and the soil is deforming continuously at constant effective stresses, volume and velocity, has the steady state of deformation been reached.

2. A special structure of the soil exists at the steady state which allows the soil to deform continuously at its minimum shearing resistance with no tendency for stress or volume changes. For cohesionless soils this structure has been postulated by Casagrande to be a "flow structure" (Castro, 1969; Casagrande, 1975; Poulos, 1981) in which "the particles become oriented such that the shear stress needed to continue deformation eventually reaches a constant value." Casagrande, 1976, suggested that for bulky grained cohesionless soils, the flow structure consists of a structure in which "each grain is constantly

rotating in relation to all surrounding grains so as to offer a minimum of frictional resistance." Once deformation stops, the soil changes into a structure other than the flow structure, and shear stresses in excess of the steady state strength are needed to reform the flow structure.

3. The flow structure, and hence the steady state, can only be achieved after all grain orientation and grain breakage, if any, are complete. Large strains are normally required to achieve this condition (Poulos, 1971, 1981).

Based on laboratory test data, it has been suggested that for a given sand, (1) the stresses in the steady state of deformation are dependent only on the void ratio and are independent of stress history and (2) at steady state a friction angle, about equal to the friction angle determined in drained tests in contractive specimens at large strains, is mobilized (Castro and Poulos, 1977; Poulos, 1981; Sangrey, et al 1978). Tests were performed in this investigation to verify the validity of these hypotheses, see Section 5.2.

2.2.2 Relationship to Liquefaction

From the previous discussions, it is seen that (1) liquefaction is a physical phenomenon involving large, unidirectional deformations of soil masses and (2) the steady state of deformation is the final stage of shear during large, unidirectional continuous deformations of a soil. Consequently, it has been suggested (Castro, 1969, 1975; Casagrande, 1936, 1976; Castro and Poulos, 1977; Sangrey et al, 1978; Poulos, 1971, 1981) that the shear strength which is appropriate for analysis of liquefaction is the undrained, steady state shear strength, S_{us}.

Liquefaction of a saturated sand is then perceived as the physical process in which a previously stable mass of sand experiences large, unidirectional deformation (e.g., a flow-slide type failure) as the result of the following sequence of events:

1. The sand is deposited in a loose state and is fully saturated.

2. Driving shear stresses develop under drained conditions due, for example, to loading produced by buildings or embankments, such that the driving shear stresses are lower than the drained strength, S_{ds}, but higher than S_{us}.

3. A relatively rapid disturbance (e.g., an earthquake, rapid erosion at the toe of a slope, a rapid increase in dead load, a rapid change in seepage pressure) is applied to the soil, which results in conversion of the mass of soil from a practically drained condition of shear to a practically undrained condition of shear.

4. A resultant shear deformation which reduces the mobilized shear resistance from the previously available drained shear strength, S_{ds}, to a lower, undrained shear strength. As deformation continues, the available strength tends to the undrained steady state shear strength, S_{us}, which is significantly less than the applied driving shear stresses.

5. A resultant large deformation (flow) ensues, usually rapid, which continues until the applied shear stresses are reduced to the undrained steady state shear strength, S_{us}. For rapid deformations, inertia forces can drive the soil mass beyond the position in which the mass achieves static equilibrium with S_{us}.

2.2.3 Steady State Lines

Research (Casagrande, 1938; Watson, 1940; Roscoe and Schofield, 1958; Bishop, et al, 1965; Castro, 1969) has demonstrated that, for a given soil, as the void ratio decreases, the shear stresses and effective normal stresses at the steady state of deformation increase. To apply steady state concepts to practical engineering problems, it has been helpful to consider the steady state line which is a graphical representation of the locus of all steady states of deformation for a particular soil. Since the full description of the state of a soil consists of three elements (an effective normal stress, a shear stress, and a void ratio or density), the complete graphical representation is a three dimensional plot. However, any line in a

three dimensional space can be accurately and conveniently represented by a pair of two dimensional plots, with one common axis.

Two such sets of steady state line plots are shown in Fig. 2-8.

For a soil to be in the steady state of deformation all of the following criteria must be met:

1. The void ratio vs effective normal stress point must be on the steady state line (SSL) in that plot.

2. The void ratio vs shear stress point must be on the SSL in that plot.

3. The deformation (strain) must have been sufficient so that the soil is deforming continuously, with no tendency for changes in stresses, volume, or velocity.

For example, a soil at state "A" in Fig. 2-8 could not be in the steady state of deformation because, even though it is on the SSL in the void ratio vs effective normal stress plot, the shear stress is less than the shear stress at the steady state. A soil at state "B" may be in the steady state of deformation, but only if the flow structure has formed and the soil is deforming continuously with no changes in stresses, volume, or velocity. Thus, in addition to the position of the state in the plot in Fig. 2-8, one needs to know the stress strain behavior to determine whether the soil is in a steady state of deformation.

The the void ratio vs effective normal stress and void ratio vs shear stress SSL's are hypothesized to be uniquely related, see Sections 2.2.1 and 5.2. Consequently, for a given void ratio, the steady state shear strength and steady state effective normal stress are related by functions of the friction angle at the steady state.

In general, any effective normal stress parameter [e.g., the effective minor principal stress, $\bar{\sigma}_3$; the effective major principal stress, $\bar{\sigma}_1$; the effective octahedral normal stress, $1/3(\bar{\sigma}_1+\bar{\sigma}_2+\bar{\sigma}_3)$; the effective normal stress, $1/2(\bar{\sigma}_1+\bar{\sigma}_3)$, and any shear stress parameter [e.g., maximum shear stress, $1/2(\sigma_1-\sigma_3)$; the principal stress difference, $\sigma_1-\sigma_3$; the octahedral shear stress $1/3[(\sigma_1-\sigma_3)^2 + (\sigma_1-\sigma_2)^2 +$

$(\sigma_2-\sigma_3)^2]^{1/2}$ may be used for the plots illustrated in Fig. 2-4. In this report, plots of void ratio vs effective minor principal, $\bar{\sigma}_3$, and void ratio vs the maximum shear stress in the specimen, $1/2(\sigma_1-\sigma_3)$, will generally be used.

2.2.4 Relationship Between Steady State and Critical State

There are similarities in the concept of the steady state of deformation, as described above, and the concept of critical state as described by Schofield and Wroth, 1968. Poulos, 1981, has reviewed these two concepts and has summarized his evaluation of the principal differences between them as follows (information in brackets added by the writers):

> "In general, the concept of steady state deformation has been embodied in the previously quoted writings (Casagrande 1936, Schofield and Wroth 1968, Rowe 1965, Castro 1969). However, it has not generally been recognized that continuous deformation is a necessary condition of the steady state. Nor has it been recognized clearly that a flow structure develops at the steady state in all soils--clays or sands--and for both drained and undrained conditions." (Poulos, 1981).

That there is a difference between the current use of the term critical state and the steady state of deformation, at least for clays, is illustrated by the results of direct shear tests on a stiff clay by Skempton, see Fig. 2-9, reproduced from Schofield and Wroth 1968. The steady state corresponds to the residual strength rather than to the critical state as given in Fig. 2-9.

3. LABORATORY TESTING PROGRAM

3.1 General

A total of five different sands were used in the laboratory testing program; however, most of the testing was performed on two of these sands.

The laboratory testing included triaxial tests, one-dimensional consolidation tests, and a variety of index tests.

The sands tested and a brief description of the triaxial testing program are given in this section.

Results of individual triaxial tests are tabulated and plotted in Appendix A. The triaxial testing procedures and apparatus are described in Appendix C.

The results of the triaxial tests are discussed in Sections 4 and 5.

3.2 Description and Properties of Sands Tested

3.2.1 Banding Sands

Banding sand is the trade name for a type of sand produced and sold by the Ottawa Silica Co., Ottawa, Illinois. It is derived from the St. Peter sandstone through a washing and screening process that produces a clean, uniform, fine quartz sand with subrounded grains. The specific gravity of the grains is 2.66. Scanning electron microphotographs are shown in Fig. 3-1. Commercial uses of the sand include glass making and molds for metal castings.

For this investigation, four different gradations of Banding sand were tested. These gradations were the result of different mixtures of two shipments of Banding sand which were received a few years apart. These mixtures were designated as BS #1, BS #5, BS #6 and BS #9. Grain size curves for the four Banding sands are shown in Fig. 3-2 and the gradation data are summarized in Table 3-1. Gradation data is also presented for "Sand B," tested by Castro (Castro, 1969), which was from another, still earlier shipment of Banding sand.

The steady state line was determined for each of the Banding sand mixtures; however, extensive testing was done on Banding Sand #6 because, of the four Banding sand mixtures, it has the highest densities at the steady state of deformation.

In the following sections, references to Banding sand without numerical designations (e.g., #1, #5 or #9) refer to Banding Sand #6.

Maximum void ratio determinations were made on all four gradations by pouring oven dried sand through a funnel into a 4-in.-diameter by 4.58-in.-high mold as specified in ASTM-2049. The funnel was kept approximately 1 in. from the surface of the sand and a spiral motion was made with the funnel. Three determinations were made and the average taken. Results for all four banding sands are given in Table 3-2.

Minimum void ratio determinations were also made according to ASTM D-2049 - Vibratory Table Method. After no measurable difference was found for Sand #1 between the wet and dry methods, the other sands were tested by the dry method only. Results for all four banding sands are presented in Table 3-2.

Compaction tests were performed using ASTM D1557, Method A. The maximum dry densities and minimum void ratios determined in the compaction test are given in Table 3-2, and the individual compaction test results are presented in Appendix B. The maximum densities were obtained for the dry sand. The densities decreased to a minimum for water contents of about 10% to 17%. For higher water contents, the specimen "bled," i.e., water flowed from the sample, during compaction and the water contents shown are those after compaction.

Minimum and maximum void ratios were also determined by the following procedures suggested by A. Casagrande, and which will be referred to herein as the Casagrande Method.

The Casagrande maximum void ratio was determined by pouring oven-dried sand through a funnel to which was attached 0.5 cm below its tip a horizontal piece of cardboard from which the sand spilled into a 7.3 cm diameter and 10.1 cm high mold. The cardboard was kept at a distance of not more than 3 mm over the surface of the sand in the mold, and a spiral motion was described with the funnel in order

to keep the surface of the sand approximately level at all times. Results for all four Banding sands are listed in Table 3-2.

The Casagrande minimum void ratio was determined on oven dried sand, using the same mold as above, by hammering forcefully the sides of the mold and also over a plate on top of every one of three layers until measuring no further settlement of the surface of each layer. Results for all four Banding sands are listed in Table 3-2. A plot of minimum void ratio according to the Casagrade method vs uniformity coefficient ($c_u = D_{60}/D_{10}$) is presented in Fig. 3-3 for all four Banding sands tested in this study and for Sand B (Castro, 1969). It is seen that the minimum void ratio decreases nearly linearly with increasing c_u.

For the Banding sands the maximum densities, from the compaction tests in accordance with ASTM 1557, were lower than those from either ASTM 2049 or the Casagrande Method.

A summary of the index test data from Banding Sand #6 is presented in Table 3-3 for comparison with similar data from the mine tailings sand discussed below.

Two one-dimensional consolidation tests were performed on Banding Sand #6. The results are shown in Fig. 3-4. Specimens were consolidated in Teflon™ rings, loads were doubled every 24 hours, and the deformation was measured by DCDT's connected to an automatic data acquisition system.

3.2.2 Mine Tailings Sand

Approximately 300 pounds of tailings sand from a copper mining operation in Highland Valley, British Columbia were obtained for testing in this investigation. The tailings sand is a uniform, fine sand, almost entirely quartz, with angular grains. Specific gravity of the grains is 2.68. Scanning electron microphotographs are shown in Fig. 3-1.

The tailings sand was received in a moist condition. After oven drying, the sand was mixed and stored in 5-gallon plastic containers. Grain size analyses on each pail showed a fairly constant gradation. Two pails, having nearly identical grain size curves, were selected for the investigation and were thoroughly mixed prior to testing. The grain size

curve for the tailings sand is shown in Fig. 3-2 and summarized in Table 3-1.

The same maximum and minimum void ratio tests performed on the Banding sands were performed on the mine tailings sand and the results are presented in Table 3-2 and in Appendix B. For the tailings sand, the compaction tests yielded a maximum density which was equal to that from the Casagrande method and was higher than that from ASTM 2049. This relationship between the compaction test result and the ASTM 2049 result is opposite to that observed for Banding sand.

A summary of the index test data from the mine tailings is presented in Table 3-3 for comparison with similar results from Banding Sand #6.

Two, one-dimensional consolidation tests were performed on the mine tailings. The results are shown in Fig. 3-5. Specimens were consolidated in Teflon™ rings, loads were doubled every 24 hours, and the deformation was measured by DCDT's connected to an automatic data acquisition system. It should be noted that, at pressures greater than approximately 16 kg/cm^2, the denser specimen, C-1002, actually consolidated to void ratios below the minimum void ratio determined by the index tests.

3.3 Triaxial Testing Program

Four types of triaxial tests were performed on the Banding sands and on the mine tailings, as follows:

1. $\bar{R}$-Tests - Isotropically Consolidated-Undrained Triaxial Compression Tests

2. A$\bar{R}$-Tests - Anisotropically Consolidated-Undrained Triaxial Compression Tests

3. CA$\bar{R}$-Tests - Anisotropically Consolidated-Undrained Cyclic Triaxial Compression Tests

4. CA$\bar{R}$-$\bar{R}$-Tests - Anisotropically Consolidated-Undrained Cyclic Followed by Monotonic Triaxial Compression Tests

The procedures and equipment used for the tests are described in detail in Appendix C.

The numbers of tests performed on the different sands are given in Table 3-4. In addition to the wide variety of tests performed on Banding Sand #6 and on Mine Tailings, a limited number of R-tests were performed on Banding Sands #1, #5, and #9.

All tests were performed on compacted and saturated specimens, and all shear stages were performed maintaining undrained conditions and measuring pore water pressures. For all except eight tests, low friction lubricated end platens were used. For all except three tests, shear stresses were applied by load control methods. For all except four tests, 3.6-cm-diameter test specimens were used. Electronic load, pressure and displacement transducers were used to measure axial load, pore water pressure and axial deformation, respectively. The transducers were monitored on a strip chart recorder, so that accurate data could be obtained during rapid deformations.

Individual triaxial test results are presented in Appendix A, and details of the test procedures and equipment are presented in Appendix C. The significant results of the testing program are discussed in the next two sections of this report.

4. STRESS-STRAIN CURVES

4.1 General

A total of seven distinct types of stress-strain curves were observed in the triaxial testing program. The type of stress-strain curves observed for a particular test was found to be a function of the soil type and the position of the initial state relative to the steady state line.

In this section, each type of observed stress-strain curve is discussed and example test results are presented. In the tables presented in Appendix A, the results of each test are classified according to the type of stress-strain curve observed (Type A through Type H). In some cases the stress-strain curves were intermediate between two types and were so classified (i.e., Type A-B).

4.2 Type A: Contractive Behavior with a Peak Shear Stress Prior to Steady State Deformation

The results of Test R-603, presented in Fig. 4-1, are typical of Type A stress-strain curves. In this test, the pore pressure and shear stress both increased gradually, as axial load increments were added over a period of 18 minutes. At about one percent axial strain, the pore pressure suddenly increased, the effective stresses and the shear stress decreased, and the specimen deformed from 1 percent to greater than 20 percent axial strain in 0.08 seconds. The rapid deformations were the result of the use of load control for axial loading. At strains greater than about 10 percent, the shear stress, the effective stresses, and the volume (undrained conditions) were essentially constant. Hence the steady state of deformation had been achieved. Castro, 1969, referred to this type of stress-strain behavior as "liquefaction failure."

Type A stress-strain curves were observed for all isotropically and anisotropically consolidated undrained triaxial compression ($\bar{R}$ and $A\bar{R}$) tests on specimens of Banding sands which were consolidated to states significantly above and to the right of the steady state line (SSL) in the void ratio vs effective minor principal stress (e vs $\bar{\sigma}_3$ plot), Fig. 4-13. For $\bar{R}$ and $A\bar{R}$ tests on Banding sand specimens with consolidation states only slightly above and to the right of the SSL in the e vs $\bar{\sigma}_3$ plot, Castro, 1969, observed that the initial stress-strain behavior was similar to the Type A curve, as shown in Fig. 4-2, but subsequent straining resulted in behavior similar to Type E

described in Section 4.6. This latter type of stress-strain curve which Castro, 1969, referred to as "limited liquefaction," would be designated Type A-E. No type A-E curves were observed in the course of this investigation.

For $\bar{R}$ and $A\bar{R}$ tests on mine tailings specimens, Type A stress-strain curves were observed for consolidation states to the right of the SSL in the e vs $\bar{\sigma}_3$ plot and with void ratios (after consolidation) greater than about 0.96.

4.3 Type B: Contractive Behavior with No Peak Shear Stress Prior to Steady State Deformation

The results of Test $\bar{R}$-1015, presented in Fig. 4-3, are typical of Type B stress-strain curves. In this test, the pore pressure and shear stress both increased during the first 2 percent strain, as axial load was slowly added over a period of 11 minutes. Then the specimen deformed from 2 percent to about 20 percent axial strain in 106 seconds, while the shear stress, the effective stresses, and the volume (undrained conditions) were essentially constant. Hence the steady state of deformation had been achieved.

The principal differences between Type A and Type B stress-strain curves are that in the Type B curves no peak shear stress and subsequent decrease in shear stress was observed prior to steady state deformation, and as a result, no driving shear stress greater than the steady shear strength was present to drive a very rapid deformation. Consequently, the velocity of steady state deformation observed in the Type B curves was slower than that in the Type A curves.

No Type B stress-strain curves were observed for Banding sand specimens. In Test $\bar{R}$-618 on a specimen of Banding sand consolidated to a state slightly above and to the right of the SSL in the e vs $\bar{\sigma}_3$ plot, the stress-strain curve was initially like a Type B curve, (see Fig. 4-4); however, under subsequent straining the specimen exhibited a behavior similar to a Type E curve (described in Section 4.6). Consequently, this behavior was designated as Type B-E.

As shown in Fig. 4-14, Type B stress-strain curves were observed for $\bar{R}$-tests on two mine tailings specimens consolidated to the right of the SSL in the e vs $\bar{\sigma}_3$ plot and to void ratios less than about 0.96 and higher than 0.90. For $\bar{R}$-tests on all but one other mine tailings specimen consolidated to a state to the right of the SSL and to void ratios less than about 0.90, an intermediate behavior between Type A and Type B was observed.

This intermediate Type A-B stress-strain curve was characterized by a relatively small drop in shear stress from the peak to the steady state and consequent relatively slow velocities during steady state deformation, as illustrated in Fig. 4-5. For one specimen of mine tailings consolidated to a state to the right of the SSL in the e vs $\bar{\sigma}_3$ plot and to a void ratio of 0.832 (<0.90), the $\bar{R}$-test resulted in a Type A stress-strain curve.

4.4 Type C: Dilative Behavior with a Peak Shear Stress Prior to Steady State Deformation

The results of Test $\bar{R}$-619, presented in Fig. 4-6, are typical of Type C stress-strain curves. In this test, after one initial increase in pore pressure with increasing shear stress, the pore pressures decreased with increasing shear stress and strain. The pore pressure decrease continued to about 15 percent axial strain, by which point a substantial negative induced pore pressure had been measured. The loading to 15 percent strain occurred over an interval of about 100 minutes. Then, the pore pressure suddenly increased (became less negative), the effective stresses and the shear stress decreased, and the specimen deformed from 15 percent to about 20 percent strain in 5.3 seconds. During this relatively rapid deformation, the steady state of deformation was achieved towards the end of the test. It should be noted that the induced pore pressure was still negative during steady state deformation. Stress-strain behavior of this type was first reported by Poulos, 1981.

Type C stress-strain curves were observed in two $\bar{R}$-tests on specimens of Banding sand consolidated to states slightly below and to the left of the SSL in the e vs $\bar{\sigma}_3$ plot, Fig. 4-13.

No Type C stress-strain curves were observed in tests on the mine tailings specimens.

4.5 Type D: Dilative Behavior with No Peak Shear Stress Prior to Steady State Deformation

The results of Test $\bar{R}$-1026, presented in Fig. 4-7, are typical of Type D stress-strain curves. In this test, after an initial increase in pore pressure with increasing shear stress, the specimen began to dilate. The dilation continued up to 25 percent axial strain, and from about 25 to 30 percent strain the pore pressure, the effective stresses, the shear stress and the volume (undrained conditions) were nearly constant. Hence, the steady state of deformation had been practically achieved.

The principal difference between Type C and Type D stress strain curves is that in the Type D curve, no peak shear stress

and subsequent decrease in shear stress was observed prior to steady state deformation.

Type D stress-strain curves were observed in two R-tests on mine tailings specimens consolidated to states slightly below and to the left of the SSL in the e vs $\bar{\sigma}_3$ plot, Fig. 4-14.

No Type D stress-strain curves were observed in tests on Banding sand.

4.6 Type E: Dilative Behavior with Tests Terminated Prior to Steady State Deformation

The results of Test $\bar{R}$-617, presented in Fig. 4-8, are typical of Type E stress-strain curves. Type E curves do not represent a fundamentally distinct stress-strain behavior but rather are the result of test limitations. From Fig. 4-8, it is seen that after an initial increase in pore pressure with increasing shear stress, the specimen began to dilate and was still dilating when the test had to be terminated because the axial load exceeded the load cell capacity. All tests with Type E stress-strain curves were still dilating when the tests were terminated because of either load or axial strain limitations. It is believed that if these tests could have been continued to the steady state of deformation, either Type C or Type D stress-strain curves would have been observed. Castro, 1969, referred to Type E stress-strain curves as "dilative response."

Type E stress-strain curves were observed in four $\bar{R}$-tests on Banding sand specimens consolidated to states below and to the left of the SSL in the e vs $\bar{\sigma}_3$ plot.

No Type E stress-strain curves were observed in tests on mine tailings; however, no tests were performed on mine tailings specimens consolidated to states significantly below and to the left of the SSL in the e vs $\bar{\sigma}_3$ plot, Fig. 4-13.

4.7 Type F: Cyclic Loading Leading to Steady State Deformation

The results of Test CA$\bar{R}$-608, presented in Fig. 4-9, are typical of Type F stress-strain curves. The specimen was anisotropically consolidated. During the first eight cycles of undrained cyclic loading, the pore pressures in the specimen increased to nearly 50 percent of the effective minor principal stress of the end of consolidation, $\bar{\sigma}_{3c}$; however, less than 1 percent axial strain accumulated. These eight cycles were applied to the specimen at a frequency of 0.25 Hz over a period of time of about 30 sec. On the first half of the ninth cycle,

the pore pressures suddenly increased, the shear stress decreased and the specimen deformed from 1 percent to greater than 20 percent axial strain in 1.2 seconds. From 10 percent strain to greater than 25 percent strain, the effective stresses, the shear stresses, and the volume (undrained conditions) were essentially constant, i.e., the steady state of deformation had been achieved. Note that the steady state shear strength is less than the shear stress during anisotropic consolidation.

Type F stress-strain curves were observed in 19 CAR̄-tests on specimens of Banding sand consolidated to states significantly above and to the right of the SSL in the e vs $\bar{\sigma}_3$ plot and e vs $(\sigma_1-\sigma_3)/2$ plots, Fig. 4-15. The number of cycles prior to steady state deformation ranged from 2 to 1,393.

Type F stress-strain curves were observed in one CAR-test on a specimen of mine tailings consolidated to a state above and to the right of the SSL in the e vs $\bar{\sigma}_3$ and e vs $(\sigma_1-\sigma_3)/2$ plots, Fig. 4-16.

4.8 Type G: Cyclic Loading Leading to Significant Strain Accumulation But Not Resulting in Steady State Deformation

The results of Test CAR̄-1007B, presented in Fig. 4-10, are typical of Type G stress-strain curves. In this test, the pore pressures and strains continued to accumulate with each cycle so that by the 52nd cycle the accumulated axial strain was greater than 25 percent and the accumulated pore pressures were about 70 percent of the effective minor principal stress at the end of consolidation. However, at no point was there a sudden increase in pore pressure and decrease in shear stress leading to large unidirectional strains, as observed in Type F stress-strain curves. Castro, 1975; Casagrande, 1976; and Castro and Poulos, 1977 referred to Type G stress-strain curves as "cyclic mobility."

Type G stress-strain curves were observed for four specimens of Banding sand consolidated to states below and to the left of the SSL in the e vs $\bar{\sigma}_3$ and e vs $(\sigma_1-\sigma_3)/2$ plots, Fig. 4-15.

Type G stress-strain curves were observed for five specimens of mine tailings consolidated to states above and to the right of the SSL in the e vs $\bar{\sigma}_3$ plot, but below and to the left of the SSL in the e vs $(\sigma_1-\sigma_3)/2$ plot, Fig. 4-16.

4.9 Type H: Cyclic Loading with No Significant Strain Accumulation

The results of Test CAR̄-1067, presented in Fig. 4-11, are typical of Type H stress-strain curves. In this test, after 214 cycles of loading, less than 2 percent strain had accumulated and the induced pore pressure was less than 40 percent of the effective minor principal effective stress during consolidation, $\bar{\sigma}_{3c}$. For all Type H stress-strain curves, the accumulated strain at the end of the cyclic loading was less than 5 percent and the number of cycles varied from 98 to 214.

Type H stress-strain curves were observed for Banding sand in two tests on specimens consolidated to states above and to the right of the SSL in the e vs $\bar{\sigma}_3$ plot and in three tests on specimens consolidated to states below and to the left of the SSL in the e vs $\bar{\sigma}_3$ plot.

Type H stress-strain curves were observed for mine tailings in two tests on specimens consolidated to states above and to the right of the SSL in the e vs $\bar{\sigma}_3$ plot but below and to the left of the SSL in the e vs $(\sigma_1-\sigma_3)/2$ plot.

4.10 Summary of Observed Stress-Strain Curves

The eight different types of stress-strain curves discussed above are illustrated schematically in Fig. 4-12. This figure is also reproduced in Appendix A for reference to the classifications of stress-strain curves presented in the tables in that appendix.

Some general trends regarding expected stress-strain curves can be observed by plotting the consolidation states for the laboratory tests and noting the type of stress-strain curves observed for each test.

In Fig. 4-13, the consolidation states for all monotonically loaded, isotropically consolidated (R̄) and anisotropically consolidated (AR̄) undrained triaxial compression tests on specimens of Banding Sand #6 are plotted, and the different types of stress-strain curves observed are noted. The average steady state lines (SSL's) for Banding Sand #6 are also shown in this figure. Determination of these SSL's are discussed in sections of this report. As illustrated in this figure the following observations can be made:

1. Type A stress strain curves were observed for all specimens with consolidation states signifi-

cantly above and to the right of the SSL in the e vs log $\bar{\sigma}_3$ plot.

2. For specimens with consolidation states below and to the left of the SSL in the e vs log $\bar{\sigma}_3$ plot, Type C and Type E stress-strain curves were observed.

3. For one specimen with a consolidation state slightly above the SSL line in the e vs $\bar{\sigma}_3$ plot, an intermediate behavior, Type B-E, was observed. (For similar states, Castro 1969 also observed Type A-E stress-strain curves).

In Fig. 4-14, similar plots are presented for $\bar{R}$ and $A\bar{R}$ tests on mine tailings and the following observations can be made:

1. Type A stress-strain curves were observed for all specimens consolidated to states above and to the right of the SSL in the e vs log $\bar{\sigma}_3$ plot and with void ratios greater than 0.96.

2. Except for Test $A\bar{R}$-1001, Type A-B stress-strain curves were observed for all specimens consolidated to states above and to the right of the SSL in the e vs log $\bar{\sigma}_3$ plot and with void ratios less than 0.90.

3. Test $A\bar{R}$-1001, which exhibited Type A stress-strain curves, was consolidated to a state above and to the right of the SSL's in both the e vs log $\bar{\sigma}_3$ and the e vs log $(\sigma_1-\sigma_3)/2$ plots.

4. Types A, B, and A-B stress-strain curves were observed for the five specimens consolidated to states above and to the right of the SSL in the e vs log $\bar{\sigma}_3$ plot and with void ratios between 0.90 and 0.96. However, the two specimens with Type A stress-strain curves were for Tests $A\bar{R}$-1002 and 1003 which had consolidation states similar to that for $A\bar{R}$-1001 (see observation 3, above).

5. For two specimens consolidated to states slightly below and to the left of the SSL in the e vs log $\bar{\sigma}_3$ plot, Type D stress-strain curves were observed.

These data suggest that for monotonically loaded specimens the location of the consolidation state relative to the SSL (principally in terms of $\bar{\sigma}_3$) can be used as a predictive tool for expected stress-strain curves, which is in agreement with earlier studies (e.g., Castro, 1969; Poulos, 1971; Castro, 1975; Castro and Poulos, 1977; Sangrey, et al, 1978). The types of stress-strain curves expected will vary with different soil types, as can be demonstrated by comparing the results for Banding Sand #6 (subrounded particles) and for mine tailings (angular particles). For Banding Sand #6, over the full range of $\bar{\sigma}_{3c}$ from 1 kg/cm^2 to 40 kg/cm^2, Type A stress-strain curves were observed for all specimens consolidated to states above and to the right of the SSL in the e vs log $\bar{\sigma}_3$ plot. However, for mine tailings, over the same range of stresses, Types A, B, and A-B curves were observed for specimens consolidated to states above and to the right of the SSL in the e vs log $\bar{\sigma}_3$ plot. The type of stress-strain curves for a particular mine tailings specimen appeared to also be a function of the consolidation shear stress. For Banding Sand #6, two specimens consolidated to states slightly below and to the left of the SSL in the e vs $\bar{\sigma}_3$ plot resulted in Type C stress-strain curves; while two specimens of mine tailings consolidated to similar states resulted in Type D stress-strain curves, again illustrated differences in stress-strain curves attributable to variation in soil type.

In Fig. 4-15, the types of stress-strain curves observed for different consolidation states are presented for all anisotropically consolidated, cyclicly loaded, undrained triaxial ($CA\bar{R}$) tests on Banding Sand #6. The following observations can be made:

1. Type F stress-strain curves were observed for all specimens consolidated to states above and to the right of the SSL's in both the e vs log $\bar{\sigma}_3$ and the e vs log $(\sigma_1-\sigma_3)/2$ plots.

2. Both Type G and H stress-strain curves were observed for specimens consolidated to states below and to the left of the SSL's in both the e vs log $\bar{\sigma}_3$ and the e vs log $(\sigma_1-\sigma_3)/2$ plots. Whether Type G or H behavior develops is a function of the magnitude of cyclic load applied and cannot be predicted solely on the basis of the consolidated states, as will be discussed in a later section of this report.

In Fig. 4-16, similar plots are presented for $CA\bar{R}$-Tests on mine tailings and the following observations can be made:

1. Type F stress-strain curves were only observed in the one test in which the specimen was consolidated to a state above and to the right of the SSL's in both the e vs log σ_3 and the e vs log $(\sigma_1-\sigma_3)/2$ plots.

2. For the other four specimen, all of which were consolidated to states above and to the right of the SSL in the e vs log σ_3 plot but below the SSL in the e vs log $(\sigma_1-\sigma_3)/2$ plot, both Types G and H stress-strain curves were observed.

From this data, it appears that consolidation shear stresses greater than the steady state shear strength are necessary to produce Type F stress-strain curves. When the consolidation shear stresses are less than the steady state shear strength, either Type G or Type H stress-strain curves may result. These two observations will be discussed in more detail in a later section of this report.

Based on the foregoing data, the type of stress-strain curve resulting from monotonic loading is principally a function of the position of the consolidation state with respect to the SSL in terms of effective normal stress (σ_3) and that the consolidation shear stress with respect to the SSL has a secondary effect. However, for cyclic loading the consolidation shear stresses relative to the SSL are the principal factors in determining the type of stress-strain curves that will result. The reasons for this distinction between monotonic and cyclic loading is discussed in Section 5.3.

5. APPLICABILITY OF STEADY STATE CONCEPTS TO CYCLIC LOADING OF SANDS

5.1 General

As discussed in detail in Section 2.2 of this report, it is the writers' opinion that liquefaction failures in situ result from the reduction of the mobilized shear strength of a soil deposit to the undrained, steady state shear strength, when the latter is significantly less than the applied driving shear stresses. Prior to the liquefaction failure, these driving shear stresses are safely resisted by the drained strength of the soil.

In this chapter, it will be shown that in order to investigate liquefaction due to cyclic loading, one must determine how large the static driving shear stresses are compared with the undrained steady state shear strength.

5.2 Effects of Stress History and Loading Path on the Steady State Line (SSL)

5.2.1 Method of Investigation

As discussed in Section 2.2, it has been suggested that, for a particular soil, there is one unique steady state line (SSL) which is independent of stress history and loading path. The validity of this assertion is essential to the applicability of steady state concepts to cyclic loading; otherwise, different steady state lines would be expected to apply to different magnitudes of cyclic loads, to different numbers and frequencies of load cycle applications, and to different initial conditions.

To test this hypothesis assertion for Banding Sand #6 and for mine tailings, reference steady state lines (SSL's) were first determined from monotonically loaded $\bar{R}$-tests on highly contractive specimens (i.e., with Types A, B or A-B stress-strain curves). In these types of tests, the steady state of deformation develops for a significant range of strains. Thus the determination of steady state parameters is more definitive than in other types of tests. Subsequently, steady state points were determined from the following types of tests and compared to the reference SSL's:

1. $\bar{R}$-tests on initially dilative specimens (i.e., with Type C and D stress-strain curves).

2. $A\bar{R}$-tests on dilative and contractive specimens. Anisotropically consolidated undrained triaxial compression ($A\bar{R}$) tests.

3. $CA\bar{R}$-tests - Anisotropically consolidated undrained cyclic triaxial compression ($CA\bar{R}$) tests.

4. $CA\bar{R}$-$\bar{R}$-tests - Anisotropically consolidated undrained cyclic followed by monotonic triaxial compression ($CA\bar{R}$-$\bar{R}$) tests.

5.2.2 Results for Banding Sand #6

For Banding Sand #6, the steady state of deformation was achieved in 16 $\bar{R}$-tests on contractive specimens (i.e., with Type A stress-strain curves) and the steady state points are plotted in Fig. 5-1. The consolidation states are presented in Fig. 5-1a to illustrate the range of consolidation states used. Based on the results of these $\bar{R}$-tests, average SSL's in the e vs log $\bar{\sigma}_3$ and the e vs log $(\sigma_1-\sigma_3/2)$ plots were determined by least square fits to the data and are shown in Fig. 5-1. Lines parallel to the average SSL's were then constructed through the extreme data points to define the bands of SSL's shown in Fig. 5-1. The maximum deviation in void ratio from the average SSL's is 0.011 (which represents a dry density difference of about 0.7 pcf).

Six $A\bar{R}$-tests were performed on contractive specimens (i.e., Type A stress-strain curves), and the resultant steady state points are plotted in Fig. 5-2, along with the bands of SSL's defined in Fig. 5-1. All of the $A\bar{R}$-test specimens were consolidated to $\bar{\sigma}_{3c} = 4.00$ kg/cm^2. Three of the tests were consolidated to $K_c = \bar{\sigma}_{1c}/\bar{\sigma}_{3c} = 2.0$ and the other three were consolidated to $K_c = 1.5$. All of the steady state points from the $A\bar{R}$-tests plot in the lower half or slightly below the bands from Fig. 5-1, with a maximum deviation in void ratio of 0.01 from the average SSL's.

The steady state of deformation was achieved in two $\bar{R}$-tests on specimens which were dilative prior to reaching the steady state (i.e., Type C stress-strain curves). The steady state points from these two tests are plotted in Fig. 5-3, along with the bands from Fig. 5-1. Both points plot slightly below the bands, with a maximum deviation in void ratio of .018 from the average SSL's.

The steady state of deformation was achieved in 20 $CA\bar{R}$-tests and 2 $CA\bar{R}$-$\bar{R}$-tests on specimens of Banding sand, and the steady state points are plotted in Fig. 5-4, along with the bands from Fig. 5-1. These tests were consolidated to $\bar{\sigma}_{3c} = 4.00$ kg/cm^2 and to K_c values of 2.0 and 1.5, as shown in Fig. 5-3. For all except one test, the steady state points plot in the lower half or slightly below the bands from Fig. 5-1, with a maximum deviation in void ratio of 0.021 from the average SSL's. The one exception is a data point near the upper limits of the bands of SSL's.

From Figs. 5-1 through 5-4, it is seen that the steady state points from $\bar{R}$-tests with Type C stress-strain curves, $A\bar{R}$-tests with Type A stress-strain curves, $CA\bar{R}$-tests and $CA\bar{R}$-$\bar{R}$-tests deviate no more than 0.021 in void ratio (1.2 pcf in dry density) from the average SSL's determined from $\bar{R}$-tests with Type A stress-strain curves. This should be compared to the range of 0.30 from minimum to maximum void ratio for Banding Sand #6 (See Table 3-3). However, almost all of the steady state points from the former four types of tests lie in the lower half of or slightly below the bands of steady state lines from the $\bar{R}$-tests with Type A stress strain curves. A possible explanation for this systematic variation is discussed in Section 5.2.5.2.

5.2.3 Results for Mine Tailings

For mine tailings, the steady state of deformation was achieved in 20 $\bar{R}$-tests on contractive specimens (i.e., with Types A, B, and A-B stress-strain curves) and the steady state points are plotted in Figs. 5-5 and 5-6. The consolidation states are also plotted in Fig. 5-5.

Based on the results of these $\bar{R}$-tests, average SSL's in the e vs log $\bar{\sigma}_3$ and the e vs log $(\sigma_1-\sigma_3/2)$ plots were determined by the best visual fit to the data, as shown in Fig. 5-5 and 5-6. Lines approximately parallel to the average SSL's were then constructed through the extreme data points to define the bands of SSL's shown in Figs. 5-5 and 5-6. The maximum deviation in void ratio from the average SSL was 0.05.

The steady state of deformation was achieved in four $A\bar{R}$-tests with Type A stress-strain curves, two $\bar{R}$-tests with Type D stress-strain curves and one CAR-test, and the resultant steady state points are presented in Figs. 5-7 and 5-8 along with the bands of SSL's defined in Figs. 5-5 and 5-6. All seven steady state points lie within the bands of

SSL's from the $\bar{R}$-tests with Type A, B or A-B stress-strain curves. No trend toward the lower half of the bands (as observed for Banding sand) was evident for the mine tailings.

Hence, for all steady state points determined for the mine tailings, the maximum deviation in void ratio from the average SSL was 0.05. This should be compared to the range of 0.40 from minimum to maximum void ratio for the mine tailings (see Table 3-3).

5.2.4 Conclusions

The variations in steady state points among the different types of tests performed is relatively small and for all practical purposes the steady state line is unique for a given soil and is independent of stress history and loading path.

For each of the soils, some small variations were observed in the steady state line among the results from one particular type of test (e.g. $\bar{R}$-tests with Type A stress-strain curves). To account for this variation in practical applications of steady state concepts, it may be more reasonable to use steady state bands (as shown in Figs. 5-1, 5-5 and 5-6) rather than steady state lines.

For Banding sand, some systematic variations in steady state points among results from different types of tests were observed.

Some possible reasons for variations of individual steady state points from the average steady state line are discussed in the next section.

5.2.5 Variations from the Average Steady State Line

5.2.5.1 Variations Among Results from the Same Type of Test

For $\bar{R}$-tests with Type A, B or A-B stress-strain curves, the steady state points had maximum variations in void ratio from the average SSL of 0.011 and 0.05 for Banding sand and mine tailings, respectively. If the SSL is unique for a given soil, as the data suggest, the five principal reasons for these observed variations are:

1. Variations in grain size distributions among the specimens (i.e., minor differences among the soils being tested).

2. Inaccuracies in the measurements of void ratio.

3. Inaccuracies in the measurements of shear stress.

4. Inaccuracies in the measurements of effective minor principal stress.

5. Strain limitations in the triaxial test.

Variations in grain size distributions among the specimens could result from either: 1) differences among individual specimens taken from the batch sample or 2) grain breakage during the tests. Differences among individual specimens were minimized by thoroughly mixing the batch sample prior to the testing program and periodically remixing the batch sample during the course of the program to minimize segregation of particle sizes. If grain breakage was a significant factor, an increasing deviation from the average SSL with increasing consolidation stress would be expected. This trend was not observed for either Banding sand or mine tailings. For these reasons, it is probable that grain breakage was not a significant factor in this testing program. In addition, several grain size analyses were performed on Banding sand and mine tailings specimens which had been tested at high confining pressures and no discernible changes in grain size distribution were observed.

Inaccuracies in the measurements of void ratio could result from either: 1) uncertainties in measurements of initial specimen dimensions and dry weight and subsequent volume changes or 2) nonuniformities within the specimen. Uncertainties in measurements constitute an error in void ratio of no more than 0.005. The uniformity of the void ratios of the compacted specimens of Banding sand was investigated as described in Appendix D, and it was determined that the void ratio varied no more than

0.011 for relatively loose specimens and no more than 0.008 for relatively dense specimens. The possible variations in the SSL for Banding sand resulting from those variations in void ratio are illustrated in Fig. 5-9. The possible variation in the SSL for mine tailings due to nonuniformity of individual specimens was not measured but might be expected to be similar on a percentage variation basis.

Inaccuracies in the determination of shear stress would be principally the result of errors in measurement of axial loads. The estimated range in SSL for Banding sand due to errors in axial load measurement are illustrated in Fig. 5-10. This range includes the cummulative effects of nonlinearity in the force transducer and of drift and reading errors in the strip chart recorder. The errors in terms of shear stresses would be expected to be similar for the mine tailings; however they would result in larger variation in terms of void ratio because of the generally steeper SSL for the tailings.

Inaccuracies in effective minor principal stress would be principally due to errors in pore water pressure measurement. The estimated range in SSL for Banding sand due to errors in pore water pressure measurement are illustrated in Fig. 5-11. This range includes the cummulative effects of nonlinearity in the pressure transducer and of drift and reading errors in the strip chart recorder. Again, a similar range in effective stress errors and a resultant larger range in void ratio errors would be expected in the mine tailings due to the steeper SSL.

Variation in the SSL due to strain limitations in the triaxial test is difficult to evaluate quantitatively; however, for the two soils tested, it appears to be a significant factor. In concept, the steady state of deformation is achieved only when continuous deformation occurs at constant effective stresses and volume. This implies very large deformations relative to the sizes of the individual particles (i.e., strains that are large enough so that a triaxial specimen would be essentially squashed flat). However, in the triaxial test at strains greater than about 10 to 15 percent, the accuracy of the measurements becomes questionable due to nonuniformity of the stresses and deformations within the

specimen. Consequently, if the tests could be continued to very large strains without the problems of nonuniformity, there may be subsequent changes from the apparent steady state values which were measured. This problem was particularly evident in the mine tailings where the shear stresses were still decreasing at large strains in several tests. In this case, the conditions at 30 percent strain were used as the best estimate of the steady state conditions, since the stresses were not changing greatly at that strain.

The writers believe that strain limitations are responsible for a significant amount of the variation observed in SSL's. For example, consider the steady state points for Tests $\bar{R}$-1004, 1006, 1011, 1023 and 1025, as shown in Figs. 5-5 and 5-6. These five tests were all consolidated to $\bar{\sigma}_{3c}$ = 40 kg/cm^2 but to different void ratios. With increasing void ratio, the resultant steady points were higher in the band of SSL's. The same trends were observed for several other similar sets of $\bar{R}$-tests on mine tailings and on Banding sand. The writers believe that each of these tests would require a different amount of strain to achieve the steady state of deformation and that the differences in steady state points are the result.

The cummulative variations due to the five factors discussed above reasonably explain the ranges in SSL's observed in the results of the $\bar{R}$-tests with Type A, B, or A-B stress-strain curves.

5.2.5.2 Variations Among Results of Different Types of Tests

As noted in Section 5.2.2 for Banding sand, the steady state points from all types of tests other than $\bar{R}$-tests on contractive specimens tended to plot either in the lower half of or below the bands of SSL's determined from the $\bar{R}$-tests on contractive specimens. It is the writers' opinion that this systematic variation is due to zonation of the specimens.

The measured void ratio of a specimen is the average void ratio for the entire specimen. If the void ratio within the specimen varies from the average and the specimen is tested in undrained

compression, it would be expected that the looser zones would reach the steady state of deformation at lower axial loads than would the denser zones. Hence, in a specimen with significant variation in void ratio, the measured steady state stresses would be expected to be determined by the loosest sections of the specimen. If the steady state point is then plotted based on the measured stresses and the average void ratio, which is lower than that in the loosest zone, the point would tend to plot lower in the e vs log $\bar{\sigma}_3$ and e vs log $(\sigma_1-\sigma_3/2)$ plots than the actual steady state point, as illustrated in Fig. 5-12. The higher the degree of zonation (i.e., variation from average void ratio), the greater would be the variation of the apparent steady state point from the actual steady state point.

If all of the specimens have about the same degree of variation after compaction, it is not unreasonable that anisotropic consolidation and cyclic loading produce greater variation in void ratio within the specimen than do isotropic consolidation and monotonic loading. Hence the variation observed for the $\bar{AR}$ and $\bar{CAR}$-tests can be reasonably explained by zonation. For the $\bar{R}$-tests with Type C stress-strain curves in Banding sand, the strains prior to steady state deformation were about 12 percent and 18 percent compared to 5 percent to 10 percent for $\bar{R}$-tests with Type A stress-strain. It is reasonable that these higher strains produce greater variation in void ratio resulting in larger deviation from the average SSL.

The fact that similar variations from the average SSL's were not observed for mine tailings may be explained by the lower sensitivity of the mine tailings specimens to variations in void ratio because of the relative steepness of the SSL's.

5.3 Effects of Driving Shear Stresses on Steady State Deformation Caused by Cyclic Loading

5.3.1 General

As discussed in Section 4.10, the analysis of stress-strain curves observed in the testing program indicates that the magnitudes of the static shear stresses are critical to determining whether or not steady state deformation results

magnitudes of cyclic shear stress, $\pm [(\sigma_1-\sigma_3)/2]_{cy} = \tau_{cy}$, were applied to the individual specimens and cyclic loading was continued at a frequency of 0.25 Hz until steady state deformation occurred. Cyclic shear stress, as used herein, means the maximum change in shear stress, both plus and minus, from the consolidation (driving) shear stress (i.e. during a full cycle of load the shear stress varies from $\tau_d = \tau_c = [(\sigma_1-\sigma_3)/2]_c$ to $\tau_d + \tau_{cy}$ to $\tau_d - \tau_{cy}$ to τ_d). In all cases $\tau_d = \tau_c$ was greater than τ_{cy}, so no shear stress reversal occurred.

The results of both series of tests are presented in Fig. 5-13 in terms of cyclic shear stress versus the number of cycles required to cause steady state deformation. For reference, the peak additional shear stresses (undrained shear stress increments) from six monotonically loaded AR test, three with $K_c = 1.5$ and three with $K_c = 2.0$, are plotted at 1 cycle in Fig. 5-13.

It is important to note that, once a sufficient number of cycles of load have been applied to trigger steady state deformation, continuation of cyclic loading is not required for the deformation to continue (see Figs. 2-4 and 4-9 for examples).

It is clear from Fig. 5-13 that as the magnitude of the cyclic shear stress increases, the number of cycles required to cause steady state deformation decreases. It is interesting to note that a line drawn through the data for the CAR tests with $K_c = 1.5$ projects to the average of the data for the $A\bar{R}$ tests with $K_c = 1.5$. However, the projection of a similar line for the $CA\bar{R}$ tests with $K_c = 2.0$ gives a value at 1 cycle which is higher than any of the results from the $A\bar{R}$ tests with $K_c = 2.0$. This would indicate that a load greater than the peak monotonic load in an $A\bar{R}$ test would be required to cause steady state deformation in 1 cycle of a $CA\bar{R}$ test. This is not unreasonable, since in the $A\bar{R}$ tests the load was applied slowly over a period of time so that strain can accumulate gradually while in the $CA\bar{R}$ tests the peak load is applied in about 1 sec. Consequently, it may take a load larger than the peak load in an AR test to produce sufficent strain to cause steady state deformation in the first cycle of a $CA\bar{R}$ tests.

For the CAR-tests summarized in Fig. 5-13, the driving shear stresses, τ_d, were 1.00 kg/cm^2 and 2.00 kg/cm^2 for K_c's of 1.5 and 2.0, respectively. The measured, undrained, steady state shear strengths, S_{us}, for these specimens

from cyclic loading. In all cases when driving shear stresses, τ_d, were higher than the undrained, steady state shear strength, S_{us}, cyclic loading eventually led to steady state deformation (Type F stress-strain curves). However, in all cases when driving shear stresses were less than S_{us}, cyclic loading did not result in steady state deformation, but rather cyclic mobility occurred as on in Type G or Type H stress-strain curves.* In the laboratory tests, the driving shear stresses, τ_d, are simply the shear stress after consolidation, τ_c.

The above observation is reasonable when considered in light of the fact that full development of steady state deformation requires continuous, unidirectional deformation. A sustained, applied shear stress greater than S_{us} would be necessary to drive this large, unidirectional deformation. If the shear stress on a specimen was cycled about a driving consolidation shear stress which was less than S_{us}, the specimen would have a tendency for large, unidirectional deformation only if the combined cyclic plus consolidation shear stress was greater than S_{us}, and even then, this tendency would be present only when the shear stress was at its peak or decreasing but still above the steady state strength and would disappear when the shear stress was reduced below the steady state strength. Consequently, it is reasonable that such specimens would not experience steady state deformation.

In this section, the effects of driving shear stresses are evaluated in more detail with the use of specific examples from the results of the laboratory study. The cases of 1) driving (static) shear stresses greater than S_{us} and 2) driving (static) shear stresses less than S_{us} are considered separately.

5.3.2 Driving Shear Stress, τ_d, Greater than the Undrained, Steady State Shear Strength, S_{us}

For Banding sand, two series of $C\bar{A}\bar{R}$-tests with S_{us} greater than S_{us} where performed to investigate the relationship between cyclic stress level and the number of cycles of loading required to cause steady state deformation. All specimens for both series of tests were consolidated to a void ratio of 0.760 ± 0.015 and to an effective minor principal stress, $\bar{\sigma}_{3c}$ of 4.00 kg/cm^2. Both series were anisotropically consolidated: one with K_c ($= \bar{\sigma}_{1c}/\bar{\sigma}_{3c}$) = 1.5 and the other with K_c = 2.0. Different

*In this discussion the maximum shear stress, $\tau_{max} = \sigma_1 - \sigma_3/2$, which occurs on the 45° plane in the triaxial test will be used rather than the shear stress on the "failure plane." However, the two shear stresses are related by a function of the friction angle, ϕ.

varied from 0.2 kg/cm^2 to 0.8 kg/cm^2. With driving shear stresses this much larger than S_{us}, it is surprising and important in practice to note that more than 100 cycles of load were required to produce steady state deformation with cyclic stresses equal to about half the maximum additional shear stress in the $\bar{AR}$-tests (see Fig. 5-13).

The magnitude of these cyclic loads can be more clearly understood by replotting Fig. 5-13 in terms of cyclic stress ratio, defined as CSR = $(\sigma_1-\sigma_3)/2\bar{\sigma}_{3c}$ = $\tau_{cy}/\bar{\sigma}_{3c}$. From this plot (see Fig. 5-14), it is seen that for both sets of cyclic tests performed on Banding sand, the CSR required to produce steady state deformation (i.e., to cause liquefaction) in 10 cycles varied from 0.05 to 0.08. These cyclic stress ratios correspond to earthquake motions with maximum ground accelerations of about 0.10g or less.

It is also important to note that, for a given number of cycles, as the driving shear stress increases (K_c increases) the magnitude of cyclic load required to cause steady state deformation decreases. Consequently, the higher the driving shear stress on a soil, the weaker is the earthquake motion required to cause a reduction in strength to the undrained steady state shear strength.

In all of the test on Banding sand in which steady state deformation occurred, the specimens were observed to "creep" just prior to failure. That is, when the last load increment was applied, the specimen began to strain slowly, and then with time the rate of deformation increased until the rapid deformations noted previously occurred. Consequently, it was hypothesized that the shape of plots such as those in Figs. 5-13 and 5-14 may be functions of load cycle, shape, and frequency. For example, if, after the next to last cycle in any of the $\bar{CAR}$ tests, the cycling, had been stopped (the driving shear stress still being on the specimen) the specimen may have continued to strain and may have reached the steady state deformation. This possibility was checked by performing a test ($\bar{CAR}$-618) in which 13 cycles of load were applied to the specimen and then the cyclic loading was stopped for 40 minutes. No significant increases in strain or pore pressure were observed during this period. A 14th cycle of load was then applied and steady state deformation occurred. As illustrated in Fig. 5-13, the results are consistent with those of the other $\bar{CAR}$-tests. Consequently, the creep does not appear to significantly affect the results of the cyclic load tests for Banding sand.

For other soils or loading conditions this may not be the case. For example, consider the test result in Fig. 5-15, which was previously presented by Castro, 1978. In this triaxial test on an anisotropically consolidated specimen of Banding sand, a simulated blast loading was applied. The vibrations due to the load damped out after about 0.5 sec and about 0.3 percent strain. The specimen continued to creep and after an additional 28 sec. steady state deformation occurred. In this test creep was clearly a significant factor.

An extensive program of $CA\bar{R}$-tests on specimens with τ_d greater than S_{us} was not performed for mine tailings; however, one demonstration test was performed to verify that the observed stress-strain behavior was similar to that for Banding sand.

Test $CA\bar{R}$-1001 was consolidated to a state with a void ratio of 0.831, $\bar{\sigma}_{3c}$ = 10 kg/cm^2 and $K_{c\_}$ = 2.0; essentially the same consolidation state as Test $A\bar{R}$-1001. A cyclic shear stress of $\pm$ 0.42 kg/cm^2 (about 76 percent of the maximum additional shear stress in Test $A\bar{R}$-1001) was applied at a frequency of 0.25 Hz and steady state deformation resulted after 786 cycles. Again the large number of cycles required to cause steady state deformation was surprising, considering that the cyclic load was a large percentage of the maximum monotonic load. However, as for Banding sand, the cyclic stress ratio was relatively small (0.042 in this case).

In performing the triaxial tests on specimens with τ_d greater than S_{us}, an interesting, and perhaps important, difference between Banding sand and mine tailings was observed. It was relatively easy to consolidate Banding sand specimens to states with τ_d much greater than S_{us} (See Figs. 4-13 and 4-15) because of the relatively flat slopes of the compression curves relative to that of the steady state lines. This was not true for mine tailings.

Figure 5-16 contains two sets of anisotropic consolidation curves for mine tailings in terms of e vs $(\sigma_1-\sigma_3)/2$: one set for an initial void ratio of 1.04 (10% relative density) and one set for an initial void ratio of 0.945 (34% relative density). Each set contains curves for three different K_c values. It is clear that, for K_c = 1.5, it is practically impossible to consolidate a specimen of mine tailings to states with τ_d greater than S_{us}. For K_c = 2.0 or 2.5, it is possible to consolidate specimens to sta-

tes with τ_d greater than S_{us}; however, there appears to be an upper limit for the ratio τ_d/S_{us} because all of the consolidation curves apear to become parallel to the SSL as the consolidation stresses increase.

On first examination, this appears to indicate that soils with steady state properties similar to Banding sand would be more susceptible to be found in a condition such that the steady state of deformation could be caused by cyclic loading. However, this is not true in all cases. For example, consider the hypothetical case of two dams, one constructed of Banding sand and the other of mine tailings. Further assume that both soils are placed with initial relative densities of 35% (a reasonable value for hydraulic fill placement), which correspond to void ratios of 0.715 and 0.940 for Banding sand and mine tailings, respectively. If these soils followed consolidation curves for $K_c = 2.0$ as the dam was constructed, the Banding sand would not reach states with τ_d greater than S_{us} even for vertical stresses greater than 40 kg/cm^2, as shown in Fig. 5-17a; however, the mine tailings would reach τ_d greater than S_{us} when the vertical stresses exceeded about 12kg/cm^2, as shown in Fig. 5-17b. Stresses of greater than 12 kg/cm^2 would be expected in high embankments, such as high tailings dams, which are often substantially comprised of hydraulic fill soils. Of course, the actual relative densities and stresses will vary for other soils; however, the above example illustrates the type of analysis that should be made for determining potential susceptibility of a soil to liquefaction. Similar results are obtained if the comparison made for the two sands being placed with the same initial percent compaction. For some practical applications, the appropriate comparison to be made is one based on the sands being deposited with the same procedure (say hydraulically) which may not lead to the same initial relative density nor to the same initial percent compaction for different sands.

5.3.3 Driving Shear Stress, τ_d Less than the Undrained, Steady State Shear Strength, S_{us}

5.3.3.1 General

For cyclic loading of specimens with τ_d less than S_{us}, two cases must be considered: 1) the driving plus the cyclic shear stress ($\tau_d + \tau_{cy}$) is greater than S_{us} and 2) the driving plus cyclic shear stress is less than S_{us}.

5.3.3.2 Results for Mine Tailings

Seven CAR̄-tests were performed on mine tailing specimens to examine the stress-strain behavior in both of the cases described in the previous section. Pertinent parameters from the tests are summarized in Table 5-1, and plots of axial compressive strain at the end of a cycle vs cycle number for all seven tests are presented in Fig. 5-18. The ratio of the cyclic plus driving shear stress to the undrained steady state shear strength from the average SSL $[(\tau_d + \tau_{cy})/(S_{us})avg]$ for the tests are also presented in Fig. 5-18. All seven tests had consolidation states above and to the right of the average SSL in the e vs log $\bar{\sigma}_3$ plot and slightly below and to the left of the average SSL in the e vs log $(\sigma_1-\sigma_3)/2$ plot, as shown in Fig. 5-19.

In Tests CAR̄-1003 and CAR̄-1005, which had $(\tau_d + \tau_{cy})/(S_{us})avg$ ratios much greater than 1.0, the accumulated strain increased from less than 5 percent to greater than 20 percent in two consecutive cycles, and in both cases this occurred in less than 10 cycles. This behavior can be understood by an examination of the stress-strain curves from Test CAR̄-1005, as presented in Fig. 5-20. During the first four cycles, some pore pressure accumulated; however, the accumulated strain was relatively small. During the compressive half of the fifth cycle, further pore pressure increase occurred and the rate of strain began to increase significantly. On the extension half of the fifth cycle the pore pressure increased further. On the compression half of the sixth cycle, the pore pressure started to decrease and then appeared to approach a constant value as the specimen strained from about 5 percent to 17 percent strain. It appears as though the specimen was tending toward the steady state of deformation; however, this process was interrupted by unloading during the extension half of the sixth cycle, during which the pore pressures again increased. The stress-strain behavior during the seventh cycle was similar to that of the sixth. Consequently, it appears that after a sufficient number of cycles of load have been applied, the specimen tends toward steady state deformation whenever the maximum compressive load is applied $[(\tau_d + \tau_{cy}) > S_{us}]$; however, before the steady state of deformation can be fully achieved,

the axial load is reduced and the deformation stop. As this tendency towards steady state deformation continues to recur on successive cycles, large strains accumulate very quickly, as illustrated in Fig. 5-18; however, continuous, unidirectional deformations do not occur.

Such tendencies toward steady state deformation were not observed in any of the other five tests including three tests (CAR̄-1004, CAR̄-10006 and CAR̄-1007B) which had $(\tau_d + \tau_{cy})/(S_{us})$avg ratios between 1.1 and 1.2. The discrepancy in these three tests is probably attributable to either 1) variation in s_{us} from the average value or 2) decreases in applied shear stresses due to area increases during cyclic loading. The second explanation is illustrated by the results of Test CAR̄-1007B, presented in Fig. 5-21. During the first several cycles, the maximum shear stress actually exceeded (S_{us})avg; however, as axial strain began to accumulate, the cross sectional area of the specimen increased (total volume remains constant in an undrained test). Since the cyclic axial load was constant, the maximum shear stress decreased and in the later cycles was actually less than (S_{us})avg. It appears that the number of cycles with peak shear stresses greater than S_{us} was not sufficient to cause the tendency to steady state deformation to develop.

For the tests in which the tendency to steady deformation did not develop, the specimens accumulated strains progressively over many cycles (developed cyclic mobility), as illustrated in Fig. 5-18, in a manner similar to that observed in cyclic load tests on soils in states below and to the left of the steady state line in the e vs $\bar{\sigma}_3$ plot. (Castro and Poulos, 1977, Sangrey et al, 1978).

In general, for all seven of the CAR̄-tests, the rate at which strain accumulated increased with increasing $(\tau_d + \tau_{cy})/(S_{us})$avg, as can be seen from Fig. 5-18. There are some exceptions to this trend, but they are most probably attributable to inaccuracies in the measurements of void ratio and variations in (S_{us})avg.

For constant values of void ratio and consolidation shear stresses, the number of cycles

required to accumulate a given axial strain decreases with increasing cyclic stress ratio, as illustrated in Fig. 5-22 for the case of 5 percent compressive strain. The shapes of these curves are similar to those which have been observed for medium dense sands with consolidation states below and to the left of the SSL in the e vs $\bar{\sigma}_3$ plot.

5.3.3.3 Results for Banding Sand

Six CA$\bar{R}$-tests were performed on Banding Sand #6 specimens with τ_d less than S_{us}. Pertinent parameters from the tests are summarized in Table 5-2, and plots of axial compressive strain at end of a cycle vs cycle number for all six tests are presented in Fig. 5-23. In all of the tests, the sum of the driving plus cyclic shear stress was less than S_{us}, as illustrated in Table 5-2. All six tests had consolidated states below and to the left of the SSL in the e vs log $\bar{\sigma}_3$ plot and below and to the left of the SSL in the e vs log $(\sigma_1-\sigma_3)/2$ plot, as shown in Fig. 5-24.

With the exception of Test CA$\bar{R}$-626, all of the tests show gradual accumulation of strain over many cycles, in a manner similar to that observed in the mine tailings specimens with $\tau_d + \tau_{cy}$ less than S_{us}. In general, as the void ratio increased, the rate of strain accumulation increased, all other parameters being equal. Comparing Tests CA$\bar{R}$-629 and CA$\bar{R}$-630, it is seen that as the cyclic stress ratio increased, the rate of strain accumulation increased, all other parameters being equal.

Test CA$\bar{R}$-626, which is the only test which did not fit in the general trends described above, exhibited an unusual strain accumulation pattern. Relatively small strains accumulated during the first three cycles, then the strains rapidly increased to about 11 percent in the fourth and fifth cycles. Subsequently, strains accumulated more slowly over the next 107 cycles. The behavior during the first 5 cycles was similar to that observed for mine tailings specimens with $\tau_d + \tau_{cy}$ greater than S_{us}. However, while the latter specimens continued to strain to greater than 20 percent on subsequent cycles, the rate of strain accumulation in Test CA$\bar{R}$-626 suddenly

decreased after the fifth cycle. A possible cause for this behavior is nonuniformity of void ratio within the specimen. If the specimen was nonuniform after compaction and consolidation it would have had some zones denser and some zones looser than the average void ratio of 0.722. The first 3 cycles of load may have caused some further redistribution within the specimen creating even looser and denser zones, i.e., greater density variations. As a result, there may have been a zone within the specimen which was loose enough so that its S_{us} was less than $\tau_d + \tau_{cy}$. On the fourth and fifth cycles this zone would have tended toward steady state deformation and accumulated larger strains. However, as the specimen tended toward large deformations, the denser zones would have dilated and drawn pore water from the looser zones. As a result, the loose zone may have densified sufficiently so that S_{us} was now greater than $\tau_d + \tau_{cy}$ and subsequently strains accumulated more slowly. This specimen was consolidated only slightly below the SSL's and if the maximum void ratio in the specimen had been 0.745 (compared to the average of 0.722), S_{us} would have been about 2.00 kg/cm^2, which is less than $\tau_d + \tau_{cy} = 2.60$ kg/cm^2.

As note in Chapter 4, intermediate stress-strain behaviors (Type A-E and Type B-E), probably attributable to void ratio nonuniformity, were observed in monotonic loading of Banding sand specimens which were consolidated to states close to the SSL in the e vs log $\bar{\sigma}_3$ plot. Hence, the behavior observed in Test CAR-626 is not entirely unexpected. Nonuniformities of void ratio are not as significant a factor for the mine tailings because large void ratio changes are necessary to significantly change S_{us}, because of the relatively steep SSL's.

5.3.4 Summary of the Effects of Driving Shear Stresses

The significant observations from the foregoing discussions may be summarized as follows:

1. The presence of driving shear stresses, τ_d, greater than the undrained, steady state shear strength, S_{us}, is a necessary condition for cyclic loading to produce steady state deformation. With this condition, once sufficient

cyclic loading has been applied to trigger steady state deformation; continuous, unidirectional deformations occur, regardless of whether or not the cyclic loading is continued. This case is representative of earthquake-induced liquefaction failures in the field.

2. When τ_d is greater than S_{us}, the number of cycles of load required to cause steady state deformation decreases as the magnitude of the cyclic load increases.

3. When τ_d is greater than S_{us}, the magnitude of the cyclic stress required to cause steady state deformation in a given number of cycles, all other parameters being equal, decreases with increasing consolidation stress ratio, $K_c = \sigma_{1c}/\sigma_{3c}$. Consequently, the higher the initial driving shear stress, the more susceptible the soil is to steady state deformation (liquefaction) caused by cyclic loading, all other parameters being equal.

4. When τ_d is greater than S_{us}, the strain at which the drop in strength (liquefaction) starts to develop ranged between 0.19% and 1.50% for the Banding sand specimens.

5. The practical range of stresses and initial placement densities over which a condition of τ_d greater than S_{us} can be achieved appear to be a function of the compressibility of the soil and the location of its steady state line in the state diagram.

6. Steady state deformation and hence liquefaction cannot be fully developed by cyclic loading of soils with τ_d less than S_{us}.

7. For the case of τ_d less than S_{us} and the sum of driving plus cyclic shear stress, $\tau_d + \tau_{cy}$, greater than S_{us}, a tendency toward steady state deformation may develop during peak shear stress application. However, full development of steady state deformation is prevented by subsequent reduction of shear stress to less than S_{us}. The tendency toward

steady state deformation may recur on subsequent cycles and a large accumulation of deformation may result. However, continuous, unidirectional deformation, without additional cyclic loading (as observed for τ_d greater than S_{us}) cannot occur.

8. For the case of τ_d less than S_{us} and $\tau_d + \tau_{cy}$ less than S_{us}, no tendency toward steady state deformation occurs during cyclic loading. Rather strains accumulate over a large number of cycles and the rate of strain accumulation increases with increasing magnitude of cyclic load. This case is the one defined as cyclic mobility in this report.

5.4 Effects of Cyclic Loading on Subsequent Stress-Strain Behavior

It has been suggested (Klohn, et al, 1978) that, for analyzing seismic stability of embankments, cyclic triaxial tests should be performed to determine the magnitude of pore pressures and the corresponding reductions in effective stresses which will result from earthquake loading, and that these reduced effective stresses should be used in conjunction with traditional Mohr-Coulomb strength envelopes to determine strengths to be used in a seismic stability analysis. This suggestion is based on the misconception that large (plastic) deformations occur when the Coulomb strength envelope is reached. Such is not necessarily the case, as illustrated in the example below. However, while the cyclic loading and pore pressure generation may produce significant deformations, they do not substantially affect the ultimate stress-strain properties of the soil (Castro and Christian, 1976; Castro and Poulos, 1977; Sangrey et al, 1978). The shape of the stress-strain curve at low strains may be influenced by cyclic loading; however, the steady state strength will be unaffected.

This point is clearly illustrated by the results of Tests $C\bar{A}\bar{R}$-$\bar{R}$-631, 632, and 633, which are presented in Figs. 5-25, 5-26, and 5-27, respectively. All three tests were consolidated to σ_{3c} = 4.00 kg/cm^2 and K_c = 1.5. The void ratios after consolidation were 0.752, 0.734 and 0.701 for Tests $C\bar{A}\bar{R}$-$\bar{R}$-631, 632, and 633, respectively; which correspond to consolidation states significantly above, approximately on, and significantly below the SSL in the e vs log σ_3 plot. A cyclic shear stress of about

$\pm$ 0.30 kg/cm^2 (cyclic stress ratio of 0.075) was applied to each specimen until an induced pore pressure of about 1 kg/cm^2 had accumulated, at which point cyclic loading was stopped.

At the end of cyclic loading, all three specimens had practically the same effective stress state. Hence, if a conventional Mohr-Coulomb failure envelope were used to determine a "strength" based on the effective stress at the end of cycling, all three specimens would be said to have practically the same strength.

This is clearly not the case, as was demonstrated in the subsequent undrained monotonic loadings, which were performed immediately after cyclic loading without allowing dissipation of the pore pressure generated during cyclic loading. In Test CA$\bar{R}$-$\bar{R}$-631, a Type A stress-strain curve with a steady state strength of 0.50 kg/cm^2 resulted. In Test CA$\bar{R}$-$\bar{R}$-632, the stress-strain curve was Type C with a steady state strength of 2.60 kg/cm^2. In Test CA$\bar{R}$-$\bar{R}$-633, the resultant stress-strain curve was Type E and a steady state strength could not be determined because the specimen was still dilating when the test had to be terminated (because of load limitations at a shear stress of greater than 4.00 kg/cm^2. The stress paths of the two dilative specimens reached the strength envelope at strains on the order of one percent and moved along the envelope as the shear stress increased, i.e., plastic failure did not occur when the stress path first reached the envelope. The two steady state points determined in these tests are in reasonable agreement with the steady state bands determined from other types of loading (see Section 5.2). It should be further noted that the three specimens behaved very differently, even though their void ratio only ranged from 0.701 to 0.752, i.e., a total range of 0.051 as compared with a range of maximum to minimum void ratios of 0.3 (see Table 3-3).

Consequently, it is clear that a cyclic loading history does not affect the steady state strength and that pore pressures accumulated during cyclic loading cannot be used as a predictor of shear strength after cyclic loading.

6. APPLICATION OF STEADY STATE CONCEPTS TO EARTHQUAKE ENGINEERING

6.1 General

As explained in Section 2.2.2, the writers suggest that liquefaction of sand is a phenomenon resulting from the following sequence of events:

1. Deposition and saturation of sand in a loose state.

2. Application of driving shear stresses under drained conditions, such that the driving shear stresses are lower than the drained shear strength but higher than the undrained steady state shear strength.

3. Application of a disturbance in such a manner that the loading conditions of the soil are converted from a practically drained condition of shear to a practically undrained condition of shear.

4. Resultant shear deformations which reduce the available shear strength of the soil from the previously available drained shear strength to a lower, undrained shear strength. As deformation continues, the available strength tends to the undrained, steady state shear strength, which is significantly less than the applied, driving shear stresses.

5. Resultant large, unidirectional deformations, which continue until the applied shear stresses are reduced to the available undrained steady state shear strength.

The remainder of this section of the report contains: 1) a comparison of the data available from several in situ liquefaction failures with the sequence of events suggested above and 2) a discussion of a proposed method of analysis of soils subjected to earthquakes based on steady state concepts.

6.2 Comparison of In situ Liquefaction Failures with the Proposed Mechanism of Liquefaction

6.2.1 Lower San Fernando Dam

The Lower San Fernando Dam failed as a result of the San Fernando, California earthquake of 1971. The failure of the dam was extensively studied and reported by Seed et al, 1975. Cross sections of the dam before and after the failure are presented in Fig. 6-1. Large (on the order of 100 ft), unidirectional deformations of some sections of the dam are evident from the figure.

Based on identification of various sections of the dam from test pits and borings, Seed et al, 1971 reconstructed the mechanics of the failure and concluded that a significant section of the hydraulically placed sand in the dam liquefied and flowed beneath and through the other elements of the dam, as illustrated in Fig. 6-1. This reconstruction of the failure combined with the relatively flat (6.5° average) slope of the slide debris indicate that the available shear strength in the liquefied zone was very low.

It is interesting to note that the available data indicate that the failure of the dam occurred after the earthquake motion had ended. This suggests that, although the earthquake triggered the failure, the presence of seismically-induced shear stresses was not required to drive the large deformations.

6.2.2 Sheffield Dam

The Sheffield Dam failed during the 1925, Santa Barbara, California earthquake. Available records show that a large mass of the dam moved about 100 ft downstream (Seed, et al, 1969). Photographs (Seed et al, 1969) indicate that the inclination of the debris after the failure was very flat, suggesting a very low mobilized shear strength during the failure.

6.2.3 Alaska, 1969

During the 1964 Alaska earthquake, several slope failures occurred in sand and gravel delta deposits in Valdez and in Kenai Lake (Seed, 1968). The soils involved in these failures flowed downstream distances varying from 600 ft to 5,000 ft. The initial slopes were inclined between 10° and 25° from the horizontal, while the landslide

debris was inclined between 0° and 5°, indicating substantial decreases in shear strength.

6.2.4 Chilean Tailings Dams

Eleven tailings dams in Chile failed during an earthquake in 1965 (Dobry and Alvarez, 1967). The debris from the failures reportedly traveled as far as 7 miles from the dams.

6.2.5 Niigata Bearing Capacity Failures

During the Niigata earthquake of 1964, several apartment buildings settled more than 3 ft and tilted through angles of as much as 80° (Seed and Idriss, 1967). Large, unidirectional deformations and significant reductions in shear strength in the foundation sands are indicated by these failures.

The reduction in shear strength was further evidenced by the fact that several underground structures "floated" to the surface during the earthquake (Seed and Idriss, 1967).

6.2.6 Fort Peck Dam Failure

The Fort Peck Dam failure is the only example of liquefaction included in this report which was not caused by earthquake loading. Other examples of liquefaction due to static loading, such as Calaveras Dam (Hazen, 1920), slides in Zeeland Province, Holland (Koppejan et al, 1948) and slides along the Mississippi River (WES, 1967), are readily available in the literature.

There is not universal agreement in the geotechnical engineering profession regarding the cause of the failure of the Fort Peck Dam. The writers concur with the explanation presented by Casagrande, 1965, that, although the failure may have been triggered by movements in the underlying clay shales, the massive proportions of the failure can only be explained by a liquefaction of the soils comprising the dam.

The Fort Peck Dam was constructed of river sands and silts, using the hydraulic-fill method. On September 22, 1938, as the dam neared completion and the reservoir was partially filled, a slope failure occurred involving a 10 million cubic yard portion of the upstream shell. Cross sections through the dam before and after failure are shown in Fig. 6-2.

Some sections of the dam flowed as far as 1,500 ft upstream in less than 10 minutes. The slope prior to the failure was about 14° and the average slope of the slide debris was less than 3°, indicating a substantial reduction of shear strength.

6.2.7 Comments

All of the above examples are believed by the writers to have involved liquefaction (not cyclic mobility) of saturated sandy soils. All six examples involved the failure, by loss of stability, of large masses of soil which were stable prior to the application of an external disturbance (earthquake loading in the first five cases and slippage in the underlying clay shales in the case of the Fort Peck Dam). In all six cases, unidirectional deformations of the soil many times greater than the sizes of the soil particles occurred during the failures. The large reductions in slope angles in five of the cases and the loss of bearing capacity in the Niigata case indicate significant losses of shear strength from that which was available prior to the disturbance. The facts that 1) the Lower San Fernando Dam failure occurred after the earthquake motion had stopped and 2) the Fort Peck Dam failure continued to deform large distances after the initial triggering, suggest that, at least for these cases, the static shear stresses acting prior to the failure (not including the shear stresses that triggered the failure) were the driving forces that caused the large deformations.

All of these observations are consistent with the explanation of liquefaction given in Section 6.1.

Note that the very large deformations involved in the liquefaction failures involve strains that are infinite for all practical purposes, compared to the 20 percent to 30 percent axial strain which can be measured in conventional triaxial tests. Consequently, to be consistent with the observed liquefaction failures, the stress-strain behavior observed in the laboratory must predict potential for essentially unlimited unidirectional deformation, not potential for limited deformation of say 20 percent. Laboratory tests resulting in steady state deformation do predict such unlimited deformation. However, laboratory tests resulting in cyclic mobility do not. Consider the example of cyclic mobility illustrated in Fig. 2.6. This test exhibits the potential for accumulation of 5 to 10% strain during cyclic loading; however, upon subsequent monotonic loading, as the

strain increased, the specimen tried to dilate and provided shear resistances much greater than the cyclic shear stresses. Consequently, any tendency toward large, unidirectional deformation greater than 10 percent or 20 percent strain would be resisted by increasing shear resistance.

6.3 Proposed Earthquake Engineering Analysis Procedure

6.3.1 General Considerations

On the basis of the mechanism of liquefaction described in Section 6.1, a methodology for analyzing the stability and deformations of sand masses, during and immediately after seismic loading, is presented in the flow chart in Fig. 6.3. In principle, the method is based on the determination of answers to the following two questions:

1. Will the earthquake loading trigger large unidirectional deformations (i.e., liquefaction failures)?

2. If liquefaction failures will not occur, will the earthquake loading produce accumulated deformations which are unacceptably large?

Answering the first question involves determation of the undrained, steady state shear strengths of the sands and comparing them with the applied driving shear stresses. If the driving shear stresses are significantly higher than the steady state strengths in a sufficiently large mass of soil, then large, unidirectional deformation (liquefaction failure) can occur. If this is the case, consideration of accumulated deformations is moot, unless something is done to remedy the liquefaction problem.

If, however, the driving shear stresses are less than undrained, steady state strength, a liquefaction failure cannot occur and the magnitude of accumulated deformations must be evaluated. This can be done by performing laboratory cyclic load tests to evaluate deformations caused by cyclic loads (not the cyclic load strength). The evaluation of accumulated deformations must include consideration of both shear deformations during cyclic loading (which is normally undrained loading but could be drained loading) and densification due to subsequent dissipation of accumulated pore water pressure if the cyclic loading was undrained.

As can be seen, the method considers both: 1) soil instability (i.e., liquefaction) and 2) accumulated soil deformation, but considers them separately by different analytical methods, in a manner analogous to the considerations of bearing capacity and settlement in conventional, static foundation design (see Section 2.1.3).

The flow chart presented in Fig. 6-3 is generalized and contains all the steps that might be involved in an earthquake engineering analysis. The following is a detailed discussion of use of the flow chart.

6.3.2 Empirical Criteria

For an in situ deposit (e.g. foundation soils, existing earth dams), the analysis begins with a field investigation of the soil with borings and/or test pits. The first data which are generally available from the field investigation are some form of penetration resistances (e.g. standard penetration test blowcounts, cone penetration resistances).

These penetration resistances should be evaluated to determine whether there are any factors that render them inaccurate. For example, a high gravel content in the soil could lead to erroneously high penetration resistances or, on the other hand, incorrect field procedures could lead to erroneously low penetration resistances. If there is doubt about the accuracy of the penetration resistances, methods must be developed to correct the data or additional field investigations must be performed to obtain more reliable data. Once reliable penetration resistances are available, the first step is to compare them to available empirical correlations.

Empirical correlations have been developed for sands relating earthquake-induced failure in level ground and some forms of penetration resistances. The most common of these correlations use the standard penetration test blowcount (Seed and Idriss, 1971; Whitman, 1971; Castro, 1975; Kishida, 1966; Koizumi, 1966; Ohsaki, 1966). Most correlations have been developed for clean sands; however, recently, Seed and Idriss (1981) have presented a correlation for silty sands. The correlation proposed by Castro, 1975 is shown in Fig. 6-4. This correlation was developed from data on sand deposits which had been subjected to strong earthquake shaking. For all cases when N'_1 (corrected blowcount) was greater than the line designated N_u, no

ground failure was observed. For all cases when N' was less than the line designated N'_L, ground failure was observed. For N' values between N'_L and N'_U, both cases of failure and cases of nonfailure were observed.

Cases denoted as "failure" in the empirical correlations correspond to unsatisfactory behavior of structures on level ground or to observations of sand boils, or other manifestations of high pore pressure, at the surface of a sand deposit. Some of the failure cases, e.g., Niigata, correspond to liquefaction, while others may correspond to accumulation of deformations which were excessive in the sense of leading to "failure" of a structure. On the other hand, some nonfailure cases may have involved deformations that were too small to cause "failure" of the particular structures at that site. Manifestations of high pore pressures at level sites with no structures do not necessarily indicate liquefaction nor that a structure at the site would have settled excessively; however, it is reasonably conservative to classify such cases as "failures."

The penetration resistance criteria should be viewed as a tool to provide a preliminary, crude evaluation of the expected stress-strain behavior of the sands, which is the information that the engineer seeks to determine. If all of the blowcounts are significantly greater than N'_U, then for most structures only Type H stress-strain curves (accumulation of small cyclic deformations) would be expected. On the other hand, if all of the blowcounts are much less than N'_L, then Types F or G stress-strain curves (steady state deformation or accumulation of large cyclic deformations) would be likely. For intermediate blowcounts, the correlations are not sensitive enough to clearly distinguish between the three types of stress-strain curves.

With plots such as that in Fig. 6-4, the penetration resistance data for sands from a site can be evaluated.

If nearly all of the blowcounts are significantly higher than N'_U, the earthquake engineering analysis may be complete for most conventional structures, since the cyclic deformations would be expected to be small. For particularly sensitive structures, such as nuclear power plants, it may be necessary to make an evaluation of the magnitude of expected deformations, even for soils with very high penetration resistances.

If most of the blowcounts are less than N_L, in some cases, it may be reasonable and practical to conclude that liquefaction is likely, and to take remedial action, such as densifying the soil in situ, removing and replacing the soil, modifying the foundation design or abandoning the site. If in situ densification is chosen for remedial action, additional field investigations must be performed to demonstrate the sufficiency of the remedial action. There are some cases when, even though most of the blowcounts are less than N'_L, it is reasonable and practical to obtain undisturbed samples for laboratory testing to determine steady state properties. For example, if the soils are intensely stratified sands with silts and clays, the empirical correlations, which were developed for clean sands, do not strictly apply, and hence, further investigation would be warranted. Or if the possible cost savings to the project justify the additional expense, further investigation may be reasonable.

If the blowcounts are generally between N'_U and N'_L, it is difficult to draw conclusions from the penetration resistance data. The liquefaction will then be based on the determination of the steady state of the soil.

6.3.3 Liquefaction Analysis Based on Steady State

For in situ soils, undisturbed samples should be taken, and the steady state line or band of steady state lines should be determined for the soil. Methods for determination of steady state lines will be discussed in more detail later in this section of the report.

If the sand in question is not yet in place (e.g., a proposed earth dam, embankment or tailings dam), the earthquake engineering analysis should actually begin with the determination of the steady state line(s), to estimate the minimum density at which the sand should be placed.

After the steady state lines have been determined for the soil, the in situ void ratio and the statically applied "driving" shear stresses should be evaluated. For in situ soils, the void ratios can be estimated based on the tube samples. For soils to be placed in the future, void ratio changes due to stress increases after placement should be estimated (e.g., void ratio decreases resulting from stress increases during construction of a dam).

The "driving" shear stresses are not the shear stresses resulting from placement or consolidation of the

soil, but rather are the minimum shear stresses which are necessary to maintain equilibrium of the soil mass under external loads (e.g., static foundation loads). These shear stresses are those that one would calculate in a stability analysis. In the consideration of liquefaction, the shear stresses that should be compared to the steady state shear strength are shear stresses which will continue to be applied to the soil as very large deformations occur.

Consider the "locked-in" shear stress that results from anisotropic consolidation of a soil element beneath level ground, as illustrated in Fig. 6-5. As an earthquake shakes this element, shear deformations may occur due to the "locked-in" shear stress. However, with relatively small shear deformation, the stresses would be redistributed and the "locked-in" shear stresses would disappear. Simple shear test results demonstrating this have been presented by Silver et al, 1980.

Now consider the shear stress applied to a similar soil element beneath the corner of a large oil tank, due solely to the weight of the oil tank. As an earthquake shakes this element, shear deformations may occur due to the applied shear stress, and the shear stresses will be continually applied until the tank either sinks or tilts enough to reduce the shear stress. The applied shear stress in this case is a "driving" shear stress, in the sense that it can "drive" very large shear deformations before it is relieved.

The calculated driving shear stresses, τ_d, are compared with the estimated undrained steady state shear strengths, S_{us}, at the estimated in situ void ratios. If τ_d is greater than S_{us}, the possibility of steady state deformation triggered by cyclic loading exists. If τ_d is less than S_{us}, a judgment must be made as to whether the margin of safety is sufficient, considering the uncertainties in τ_d, S_{us}, and e. The writers believe that the margin of safety should be expressed in terms of void ratio, since it is generally the parameter with the greatest uncertainty. In other words, instead of expressing a factor of safety in terms of the ratio of S_{us} to τ_d, use a margin of safety in terms of how much higher the void ratio would have to be for τ_d to be greater than S_{us}. If the margin of safety is judged to be insufficient, the possibility of steady state deformation must be considered.

To determine whether liquefaction is likely, stability analyses should be performed to calculate τ_d. This

value should be compared with undrained steady state shear strength for all potentially critical failure surfaces. For example, consider the hypothetical dam shown in Fig. 6-6, for which it has been determined that in the shaded area it is likely that τ_d is greater than S_{us}. Further, assume that drained shear strength parameters apply to the remainder of the dam. If stability analyses using S_{us} in the shaded zone, give factors of safety lower than 1.0, it is likely that a liquefaction failure will occur (i.e. a failure consisting of large unidirectional deformations and extreme flattening of slopes).

It should be noted that in the analytical evaluation of liquefaction, the magnitude of the cyclic loading was not considered. This is based on the observation (as discussed in Section 5.3) that when τ_d is greater than S_{us}, it appears that any moderately strong earthquake shaking will trigger steady state deformation in less than 10 cycles. As more data become available, it may be found that for some soils this is not the case and in fact the magnitude of cyclic loading is an important consideration. The writers believe that until such data are available, it is prudent to assume that steady state deformation will result from any moderately strong earthquake motion when τ_d is greater than S_{us}. Note that in the CAR-tests on Banding sand which resulted in liquefaction, the failures were preceded by only small strains. Thus a cyclic test might indicate small deformations, even though in terms of stability, the soil is at the verge of a liquefaction failure.

If it is determined that either: 1) τ_d is sufficiently less than S_{us} or 2) even with the undrained, steady state shear strength in the zone with τ_d greater than S_{us}, no instability problems result, then it is concluded that a liquefaction failure is unlikely. The accumulated deformations due to cyclic loading must then be evaluated.

6.3.4 Evaluation of Earthquake-Induced Deformation

Detailed procedures for the evaluation of accumulated deformations are beyond the scope of this report. These procedures involve the use of laboratory cyclic loading test results in conjunction with shear stresses calculated from one-dimensional or two-dimensional dynamic analyses. The laboratory tests provide data regarding accumulated deformations due to a magnitude of cyclic loading, which is estimated from the dynamic analysis (Seed, et al,1975). Methods based on yield accelerations and displacements along

possible slip surfaces have been presented by others and are well documented in the literature (Newmark, 1965; Makdisi and Seed, 1978).

If the deformations are judged to be unacceptably large, remedial measures are again required. If the deformations are judged to be acceptable, the analysis is complete.

6.4 Considerations for Determination of Steady State Lines

6.4.1 General

In theory, any type of test can be used to determine the steady state line, because it is independent of stress history, as demonstrated in Section 5.2. The test loading does not have to model the anticipated field loading (e.g, cyclic loading does not have to be used to determine steady state lines for use in earthquake engineering).

The test actually used should provide the best possible definition of the steady state of deformation, i.e., the most constant values of effective stress and shear stress for the largest range of strain with the best estimate of the void ratio in the failure zone.

The writers' experience has indicated that isotropically consolidated, monotonically loaded, undrained triaxial compression ($\bar{R}$-test) on contractive specimens provide the best estimate of the void ratio in the failure zone and a relatively large range of stressing over which the steady state is observed. Initial states near or below the steady state line in terms of $\bar{\sigma}_3$ do not result in a well defined steady state within the strain limitation of the triaxial test.

For soils such as Banding sand, $\bar{R}$-tests on contractive specimens result in Type A stress-strain curves with pronounced post-peak shear strength reductions. In such a case, load control results in very fast deformations. It has been reported, Casagrade, 1975, that load control results in steady state shear strengths that are lower than those from strain controlled tests on specimens with the same void ratio. Limited data, discussed in Section 7.3.3 of this report, indicate that such a difference in steady state lines for load and strain control was not observed for Banding Sand No. 6, for mine tailings, or for Sand No. 19 (see Table 6-1). Thus, at the present time, it is recom-

mended that either load control be used on the soils with stress strain properties like those of Banding sand, or that initially comparable load and strain controlled tests be performed to determine whether there is a significant difference in steady state lines. If no such difference is found, it is more convenient to perform strain control tests.

For soils such as the mine tailings, in which $\bar{R}$-tests on contractive specimens often have little or no pronounced shear stress peak (Type B or A-B curves), the usefulness of load control is not apparent. With these types of curves, the stresses are generally not constant for a large range of strain. For these soils, it may be more appropriate to perform strain controlled $\bar{R}$-tests or modified load controlled $\bar{R}$-tests in which additional loads are added to compensate for the area increases and to maintain a nearly constant velocity of deformation once steady state deformation has begun. More research is required regarding this topic, as discussed in Section 7.

At this time, the available data are not sufficient to develop quantitative relationships between steady state lines and other soil properties (e.g. compressibility, grain size distribution, angularity, percent compaction). However, some general trends have been observed and are summarized in the following section.

6.4.2 Effects of Grain Size Distribution and Grain Angularity on Steady State Characteristics

6.4.2.1 Effects of Grain Size Distribution

In this study, steady state data were obtained for four different gradations of Banding sand (Nos. 1, 5, 6 and 9). In addition, data were available from Castro, 1969, for another gradation of Banding sand. The grain size distributions for the different gradations were presented in Table 3-1 and in Fig. 3-2, and the index properties are summarized in Table 3-2.

The steady state lines (in the e vs log $\bar{\sigma}_3$ plot) for all five gradations are presented in Fig. 6-7. It was demonstrated in Fig. 3-3, that for these five gradations of Banding sand, the minimum void ratios decreased with increasing uniformity coefficient, C_u. In Fig. 6-7, the uniformity co-

efficients are also given, and it is seen that the five steady state lines are nearly parallel but plot at lower void ratios as C_u increases. Since void ratio is not a measure of degree of density, steady state plots were prepared for relative density, Fig. 6-8, and percent of the maximum density determined with ASTM D2049 and referred to herein as percent compaction, Fig. 6-9. The maximum density obtained with ASTM D2049 was used because the ASTM 1557 densities were available only for two sands, and the test results were somewhat erratic. In the relative density and percent compaction plots, the steady state lines are still different for the different sands, and they exhibit the same trend with C_u as in the void ratio plot except for Banding Sand No. 5.

Based on the results of the steady state lines for the five different gradations of Banding sand, it can be concluded that relatively small differences in grain size distribution can produce significant differences in the position of the steady state line, regardless of the density parameterused (i.e. void ratio, relative density, or percent compaction).

Including this study, the writers have determined steady state lines for the 16 different sands whose index properties are summarized in Table 6-1. Steady state lines for these sands are plotted in terms of void ratio vs log $\bar{\sigma}_3$, relative density vs log $\bar{\sigma}_3$ and percent compaction vs log $\bar{\sigma}_3$ in Figs. 6-10, 6-11 and 6-12, respectively. Note that all three forms of the data are not available for all of the sands. Wide variations in the locations of the steady state lines are apparent in all plots; however, the following two general observations can be made:

1. With the exception of Sand 16, all of the steady state lines plot at less than 60 percent relative density at $\bar{\sigma}_3$ values less than 1 kg/cm^2.

2. Although percent compaction data are available only for five sands, none of the five sands for which percent compaction data are available have steady state lines

plotting at percent compactions greater than 88% for $\bar{\sigma}_3$ values less than 1 kg/cm^2.

They are consistent with the fact that liquefaction failures in situ have only been observed in relatively loose soil deposits.

Another general trend in the steady state line data is illustrated in Fig. 6-13, in a plot e_{ss}, vs e_{min}, where e_{ss} is the void ratio on the steady state line at an effective minor principal stress, $\bar{\sigma}_3$, of 1 kg/cm^2 and e_{min} is the minimum void ratio determined using ASTM D2049 or from the Casagrande method (see Section 3.2). A stress of 1 kg/cm^2 was selected because steady state data are available for all except three of the sands at this stress level. From Fig. 6-13, it is seen that all of the data plot in a relatively narrow band, approximately parallel to the $e_{ss} = e_{min}$ line. This means that for all of the data, there is a relatively small variation in the difference between e_{ss} and e_{min}.

The previously discussed relationship between uniformity coefficient and steady state line position for Banding sands is also clear in Fig. 6-13, in that all of the Banding sand points plot nearly in a straight line, varying consistently with changes in uniformity coefficient. Soils Nos. 14 and 18 are similar to each other, differing only in that the fraction finer than the #200 sieve had been removed in the case of No. 14, substantially reducing the uniformity coefficient. These two soils exhibit a similar relationship to that observed for the Banding sands.

6.4.2.2 Effects of Grain Angularity

In Table 6-1 and in Figs. 6-10 through 6-13, the grain shapes for the various soils are given.

From Figs. 6-10 through 6-12, it is seen that all of the subrounded and subrounded to subangular sands have nearly linear and relatively flat steady state lines. The two subangular sands (Nos. 14, and 18) have slightly nonlinear and generally steeper steady state lines, and with two exceptions, the angular to subangular and angular sands have significantly nonlinear and generally much

steeper steady state lines. The steady state lines for the more angular sands generally vary from relatively flat at low stresses to relatively steep at higher stresses. For the only two exceptions to the general trends for the angular soils, no steady state data are available for $\bar{\sigma}_3$ values greater than 2 kg/cm^2.

The differences in slopes of the steady state lines can be clearly seen in Fig. 6-14 where C_{ss}, the tangent slope ($\Delta e/\Delta \log \bar{\sigma}_3$) of the steady state lines, are plotted vs $\bar{\sigma}_3$ for all of the available data. The trends discussed above are clear, and it is further seen that for the angular soils, the slopes, C_s, become constant at relatively high stress values.

An examination of Fig. 6-13 indicates that, in general, as the particle shape changes from subrounded to subangular, both e_{ss} and e_{min} increase; however, the difference between the two does not appear to change significantly.

Banding Sand #6 and the mine tailings sand, which were extensively tested in this study, have similar grain size distributions but differ in that the Banding sand particles are subrounded while the mine tailings particles are angular (see Table 3-3). In addition to the differences between rounded and angular sands noted above, the following differences were observed between the mine tailings and the Banding sand; as have been discussed in earlier sections of this report:

1. Generally the difference between the peak shear strength prior to steady state deformation and the steady state shear strength was smaller for mine tailings than for Banding sand (except for high void ratios in the mine tailings).

2. The velocity of deformation at steady state was generally lower for mine tailings than for Banding sand.

Although extensive data are available only for these two sands, the writers believe that the two differences observed are attributable to the difference in

grain angularity. Some of the more limited data from the other sands listed in Table 6-1 support this opinion.

6.4.3 Summary of Effects of Grain Size Distribution and Grain Angularity

Both grain size distribution and grain angularity appear to significantly affect the steady state line. Based on the data available, quantitative relationships between steady state parameters and grain size and grain shape parameters cannot be developed. However, the following qualitative trends have been observed:

1. Relatively small differences in grain size distribution appear to significantly affect the position (in terms of void ratio, relative density or percent compaction) but not the shape and slope of the steady state line. The data from the Banding sands suggest that the position in terms of void ratio is directly related to the uniformity coefficient.

2. In general, there is a wide variation in the positions of the steady state lines with respect to void ratio, relative density or percent compaction; however, for the data available, the variation in the difference between e_{ss} (the void ratio on the steady state line with $\bar{\sigma}_3$ = 1 kg/cm^2) and e_{min} appears to be relatively small. The values of (e_{ss} - e_{min}) range from 0.13 to 0.27 with most of the values in the range from 0.21 to 0.27.

3. As the angularity of the particles change from subrounded to angular, the shape of the steady state line changes from nearly linear (in the semi-log plot) and relatively flat to non-linear and relatively steep.

4. As the angularity of the particles increases both e_{ss} and e_{min} increase; however, the difference between them does not change greatly.

5. Except for high void ratios, the more angular soils tend to have smaller differences between peak shear strength and steady state shear strength than do the more rounded soils.

6. The velocity of deformation at steady state is generally lower for angular soils than for subrounded soils if load control is used.

6.5 Recommended Methods for Determination of Steady State Lines

6.5.1 For Soils to be Used in Constructed Fills

Steady state lines for soils to be used for in constructed fills can most readily be determined by R-tests on compacted specimens of borrow samples. Load controlled tests may be most appropriate for soils with large decreases from peak to steady state shear strengths (Type A stress-strain curves), see Section 6.4.1. Strain controlled or modified load controlled methods may be more appropriate for soils with small peak to steady state decreases (Types A-B or B stress-strain curves), as discussed in Section 6.4.1. If load controlled methods are used, the deformations and stress changes may be very rapid, and it is important that load, deformation, and pore pressure be measured with electronic transducers and that the load transducer be located so that it accurately senses the load actually on the specimen (see Appendix C for discussion of the equipment used in this study).

Since the position of the steady state line appears to vary significantly with small changes in gradation, it is recommended that steady state line determinatons be performed on several different borrow samples to account for variations of the borrow source. Grain size analyses should then be done periodically during fill placement to determine whether the fill is within the grain size limits tested. If not, some additional steady state determinations may be required.

6.5.2 For In situ Soils

Steady state lines for in situ soils can best be determined by R-tests on undisturbed tube samples of the soils.

Undisturbed tube samples can be obtained, even in relatively clean sands. The procedures which the writers have used successfully include:

1. Using a fixed-piston tube sampler.

2. Using a mudded and cased borehole.

3. Using a perforated packer to seal the bottom of the tube, after recovering the sample, so that some drainage can occur to produce capillary stresses and provide resistance to densification due to vibrations.

4. Using careful packing and padding methods for transporation and maintaining the sample in the vertical position at all times.

It is important that careful measurements be made of the length of tube penetration, the length of gross recovery and the changes in sample length during transportation so that one can estimate density changes from the field to the triaxial cell.

Careful procedures must also be used in the laboratory to minimize density changes in the soils. The writers have had good success with the following procedures:

1. Cutting the tubes into 6-in.- to 8-in.-long sections with a tube cutter, while the tube is held vertically in a pipe vise; applying a slight vacuum if necessary to minimize densification during cutting.

2. Extruding the specimen directly into a triaxial membrane using a close-tolerance membrane stretcher and a vertically oriented extrusion jack.

3. Placing the specimen in the triaxial cell and applying a vacuum to support the specimen until the cell pressure is applied.

Even using these very careful methods, the writers have found that for very loose specimens, density changes can occur during sampling, transportation and extrusion. In some cases, even when the density has changed by less than 0.5 pcf from the field to the initial setup in the triaxial cell, the dry density changes which occur during triaxial consolidation have been very large (5 to 10 pcf). Consequently, the tests would be performed on specimens with void ratios less than those in the field and the resultant stress-strain curves would not be representative of those anticipated in the field. Hence a procedure is needed to make corrections for these density changes.

The writers have used a procedure based on the observation that for similar soils with slightly different gradations, the locations of the steady state lines vary; however, the slopes are essentially the same. The procedure consists of: 1) performing $\bar{R}$-tests on the undisturbed samples at stresses high enough so that the specimens are contractive and 2) performing a series of $\bar{R}$-tests on compacted specimens from a batch sample composed of soil from the tube samples. The slope and shape of the steady state line are obtained from the tests on the compacted specimens, and parallel lines are constructed through the steady state points from the undisturbed tube samples to estimate the band of steady state lines for the in situ samples, as illustrated in Fig. 6-15.

It is important to note that, for in situ soils, determination of the steady state line solely on the basis of tests on compacted specimens is not recommended, because although the shape of the steady state line would be correctly determined in this manner, the position would not, as is clearly illustrated in Fig. 6-15.

7. RECOMMENDATIONS FOR FURTHER RESEARCH

7.1 Introduction

During the course of this investigation, several questions have arisen which are beyond the scope of this work but which would be fruitful topics for further study. These questions are discussed briefly below.

7.2 Effects of Grain Size Distribution and Grain Angularity on the Steady State Line

The work reported herein has indicated that grain size distribution and grain angularity significantly influence both the angularity and position of the steady state line no matter what type of density parameter is used (i.e., void ratio, relative density or percent compaction). Furthermore, it has been shown that relatively small changes in grain size distribution (grain angularity being constant) result in significant changes in the position but not the slope of the steady state lines.

Based on the limited steady state data that are available, some general relationships between steady state lines and grain size distribution and grain angularity have been observed. Investigations on more soils should be performed to further investigate, and possibly to quantify, these relationships. It is very important that the relationships among steady state lines of soils with similar grain angularity but slightly different grain size distributions be further investigated, since it is the basis for the procedure for correcting for density changes during sampling and laboratory testing as discussed in Section 6.5.2.

7.3 Influence of Initial Void Ratio and Consolidation History on Position of State Relative to the Steady State Line

As discussed in Section 5.3.2, the susceptibility of a soil to be deposited in a liquefaction susceptible state in constructed fills (e.g., a tailings dam) cannot be evaluated solely on the basis of the initial placement void ratio (density) and the position of the steady state line. But rather the initial void ratio combined with the state path which will be followed during subsequent consolidation must be used to estimate the in-place state, which is then compared to the steady state lines.

As shown by the example illustrated in Fig. 5-17, the relative slopes of the compression lines and the steady state lines

may be significantly different for angular particles (such as the mine tailings) than for rounded particles (such as Banding sand).

Investigations should be performed on a variety of sands to determine whether there are any general relationships for angularity, grain size distribution, compressibility, and shape of steady state line, which could be used to guide engineers' studies of liquefaction susceptiblity of constructed fills.

7.4 Development of Alternate Testing Procedures for Steady State Line Determination

As mentioned a number of times in this report, the strain limitations of the triaxial test presents a significant problem in the determination of steady state lines. Strains in the triaxial test are limited to on the order of 20 to 30 percent, while the strains during steady state deformation and field liquefaction failures are very much larger.

Investigation of alternate testing procedures which allow larger strains could be very fruitful. The use of some type of rotation shear device is one possible alternative.

7.5 Effects of Test Details

7.5.1 General

Some of the testing procedures used in this study are not conventional procedures which are commonly in use in most geotechnical laboratories. Further studies of these test details should be performed to determine whether modifications of conventional procedures will be required for practical determinations of steady state lines.

7.5.2 Specimen End Restraint

In all except eight of the tests in this study, lubricated end platens were used to reduce the lateral restraints on the ends of the triaxial specimens.

Three different types of lubricated ends were used in this study. Initially, ends consisting of a 0.01-in.-thick rubber membrane over a 0.01 in. thick layer of Dow Corning high vacuum grease (similar to those used by Castro, 1969) were used. However, it was discovered that with these ends significant amounts of the grease were extruding into the drainage ports during isotropic and anisotropic consolida-

tion, resulting in inaccurate void ratio measurements. This problem became particularly acute at high stresses.

Two alternate types of lubricated ends were tested. The first type had the same thicknesses of rubber and grease as noted above; however, the grease was 20% Dow Corning 7 and 80% Molykote III, plus 10% by weight DuPont Teflon powder, which was similar to mixes used by Arthur and Dalili, 1979 in a plane strain device. It was hoped that the higher viscosity of the grease would eliminate the extrusion problem while the addition of the Teflon powder would still reduce end restraint. Tests of this type of lubricated end indicated grease extrusion between 20% and 35% of that for the initial type of lubricated end; however, even this amount of extrusion was sufficient to produce unacceptable inaccuracies in the void ratio measurements.

The second alternate type of lubricated ends consisted of a 0.02-in.-thick rubber membrane over a thin smear of grease. The extrusion problem was completely eliminated, and based on visual observation of the deformed shapes of the specimens, these alternative ends appeared to perform as well as the initial type of ends in reducing end restraints. This latter observation was confirmed by the fact that tests with the second alternate type of lubricated ends resulted in stress-strain properties (both at peak shear stress and at steady state) which were not significantly different than those with the initial type of ends. The second alternate type of lubricated ends were used in the remainder of the tests with lubricated end platens.

Lubricated end platens are not normally used in triaxial testing. To provide some preliminary information regarding the effects of the lubricated end platens, five R-tests on Banding Sand No. 6 and three R-tests on mine tailings were performed using conventional triaxial end platens. In Figs. 7-1 and 7-2, the steady state points from these tests are compared to the bands of SSL's determined with lubricated end platens.

From Fig. 7-1, it is seen that for Banding Sand No. 6, three of the five tests with conventional ends resulted in steady state points within the previously determined band of SSL's, while the other two tests resulted in steady state points below the band. Consequently, it appears that for Banding sand with conventional ends there is more scatter in the steady state data than for lubricated ends, and the average steady state line is lower.

From Fig. 7-2, it is seen that, for mine tailings, the results of tests with conventional ends agree well with the SSL determined from tests with lubricated ends.

Further studies should be performed to evaluate the effects of lubricated end platens and to determine whether lubricated end platens should be routinely used in triaxial tests to determine steady state properties.

7.5.3 Method of Loading

All except three of the tests in this study were performed using load-controlled triaxial compression. Two $\bar{R}$-tests on Banding Sand No. 6 and one $\bar{R}$-test on mine tailings were performed using strain-controlled axial compression to provide some preliminary data regarding the effects of method of loading.

In Figs. 7-3 and 7-4, it is seen that the steady state points resulting from the strain-controlled tests are in good agreement with the data from the load-controlled tests. Similar data are available for Sand No. 19 (see Table 6-1), as presented in Fig. 7-5, which also indicate no significant difference between results from load-controlled and strain-controlled tests.

Further studies should be made to evaluate the effects of the method of loading, and in particular, these studies should address the effects of the rate of loading in strain-contolled tests. It will be particularly valuable if it can be demonstrated that satisfactory steady state data can be obtained from strain-controlled tests, since most laboratories are equipped to employ this procedure. This also may alleviate some of the problems in interpreting load controlled test on angular soils (such as the mine tailings), in which the steady state of deformation is sometimes not well defined, as discussed earlier in this report.

7.5.4 Specimen Size

All except four of the tests reported in this study were performed on 3.6 cm diameter specimens. Two $\bar{R}$-tests on Banding Sand No. 1 and two $\bar{R}$-tests on Banding Sand No. 6 were performed on 7.1 cm diameter specimens to provide preliminary data regarding the effects of specimen size.

As can be seen in Fig. 7-6, the results from the 7.1 cm diameter specimens tend to plot on or above the SSL's from comparable tests on 3.6 cm diameter specimens. This trend is the opposite of that observed for Sand No. 19 (See Table 6-1), as illustrated in Fig. 7-7. This contradiction in data is significant, since the trend observed in the Banding sand indicates that smaller samples give more conservative (i.e. lower) values of the steady state line, while the data from Sand No. 19 indicate the opposite.

Further studies should be performed to clarify the effects of specimen size and to provide guidance regarding the appropriate size specimen to be used in practical steady state determinations.

7.6 Specimen Uniformity and Zonation

As stated previously, the writers believe that initial specimen nonuniformities and exaggeration and expansion of these uniformities (zonation) during testing have a significant effect on the calculated steady state parameters.

Further studies, possibly by freezing or X-raying specimens at various stages of testing, should be performed to evaluate the effects of variations of void ratio within the specimen.

ACKNOWLEDGEMENTS

We gratefully acknowledge the assistance of Dr. Robert Lo of Klohn-Leonoff Consultants, Ltd. in obtaining the Lornex mine tailings sample used in the testing program.

We thank Dr. William F. Marcuson and Mr. Victor F. Torrey of the Waterways Experiment Station, Vicksburg, Mississippi for reviewing the draft and providing comments.

REFERENCES

American Society for Testing and Materials, 1981, Annual Book of ASTM Standards, Part 19, Philadephia, PA

Arthur, J. R. F. and Dalili, A., 1979, "On the Lubrication of Rubber Surfaces," Geotechnique, London, England, Vol. 29, No. 1, pp. 96-98.

Bishop, A. W., Webb, D., and Skinner, A. E., 1965, "Triaxial Tests on Soils at Elevated Cell Pressures," Proceedings 6th ICSMFE, Vol. 1, pp. 170-174, Montreal.

Casagrande, A., 1936, "Characteristics of Cohesionless Soils Affecting the Stability of Slopes and Earth Fills," Boston Society of Civil Engineers, Oct. 1940. Originally published in the Journal of the Boston Society of Civil Engineers, Jan. 1936.

Casagrande, A., 1938, "The Shearing Resistance of Soils and its Relation to the Stability of Earth Dams," Proceedings, Soils and Foundation Conference of the U.S. Engineer Department.

Casagrande, A., 1965, "The Role of the 'Calculated Risk' in Earthwork and Foundation Engineering," Journal, Soil Mechanics and Foundations Division, ASCE, Vol. 91, No. SM4, pp. 1-40, Proc. Paper 4390.

Casagrande, A., 1975, "Liquefaction and Cyclic Deformation of Sands, A Critical Review," Proceedings, 5th Panamerican Conference on Soil Mechanics and Foundation Engineering, Vol. 5, pp. 79-133, Buenos Aires, Argentina.

Castro, G., 1969, "Liquefaction of Sands," PhD Thesis, Harvard Soil Mechanics Series, No. 81, Pierce Hall, Harvard University.

Castro, G., 1975, "Liquefaction and Cyclic Mobility of Saturated Sands," Journal of the Geotechnical Engineering Division, ASCE, Vol. 101, No. GT6, pp. 551-569.

Castro, G. and Christian, J. T., 1976, "Shear Strength of Soils and Cyclic Loading," Journal of the Geotechnical Engineering Division, ASCE, Vol. 102, No. GT9, pp. 887-894.

Castro, G. and Poulos, S. J., 1977, "Factors Affecting Liquefaction and Cyclic Mobility," Journal of the Geotechnical Engineering Division, ASCE, Vol. 103, No. GT6, pp. 501-516.

REFERENCE

Castro, G., 1978, "Comments on the Definition of Liquefaction and on Laboratory Experiments of Liquefaction Induced by Blasting," Transcripts of the International Workshop on Blast-Induced Liquefaction, sponsored by the U.S. Dept. of the Air Force, Maidenhead, UK.

Corps of Engineers, U.S. Dept. of the Army, 1939, "Report on the Slide of a Portion of the Upstream Face at Fort Peck Dam." U.S. Government Printing Office, Washington, D.C.

Dobry, R. and Alvarez, L., 1967, "Seismic Failures of Chilean Tailings Dams," Journal of the Soil Mechanics and Foundations Division, ASCE, Vol. 93, No. SM6, pp. 237-260.

Dobry, R.; Powell, D. S.; Yokel, F.Y; and Ladd, R. S., 1981, "Liquefaction Potential of Saturated Sand - The Stiffness Method," Seventh World Conference on Earthquake Engineering, Istanbul, Turkey.

Ferguson, P. A. S. and Green, P. A., 1971, "On Liquefaction Phenomena, by Professor A. Casagrande: Report of Lecture," Geotechnique, London, England, Vol. 21, No. 3, pp. 197-202.

Finn, W. D. L., Bransby, P. L. and Pickering, D. J., 1970, "Effect of Strain History on Liquefaction of Sand," Journal of the Soil Mechanics and Foundations Division, ASCE, Vol. 96, No. SM6, pp. 1917-1934.

Finn, W. D. L.; Pickering, D. J. and Bransby, P. L., 1971, "Sand Liquefaction in Triaxial and Simple Shear Tests," Journal of the Soil Mechanics and Foundations Division, ASCE, Vol. 97, No. SM4, pp. 639-659.

Finn, W. D. L.; Lee, K. W.; Maartman, C. H. and Lo, R., 1978, "Cyclic Pore Pressures under Anisotropic Conditions," Proceedings of Spec. Conference on Earthquake Engineering and Soil Dynamics, ASCE, Vol. 1, pp. 457-471, Pasadena, California.

Gueze, E., 1948, "Critical Density of Some Dutch Sands," Proceedings, 2nd ICSMFE, Vol. 3, pp. 125-130, Rotterdam.

Hazen, A., 1920, "Hydraulic Fill Dams," ASCE Transactions, Vol. 83, pp. 1713-1745.

Idriss, I. M. and Seed, H. B., 1981, "Evaluation of Liquefaction Potential of Sand Deposits Based on Observations of Performance in Previous Earthquakes," Proceedings of Session on In situ Testing to Evaluate Liquefaction Susceptibility, ASCE Convention, St. Louis, Missouri.

REFERENCES

Ishihara, K.; Tatsuaka, F. and Yasuda, S., 1975," Undrained Deformation and Liquefaction of Sand under Cyclic Stresses," Soils and Foundations, Tokyo, Japan, Vol. 15, No. 1, pp. 29-44.

Ishihara, K., 1977, "Pore Water Pressure Response and Liquefaction of Sand Deposits During Earthquakes," Proceedings of DMSR77, Vol. 2, pp. 161-193, Karlsruhe.

Kishida, H., 1966, "Damage to Reinforced Concrete Buildings in Niigata City with Special Reference to Foundation Engineering," Soils and Foundation, Tokyo, Japan, Vol. 7, No. 1.

Klohn, E. J.; Maartman, C. H.; Lo, R. C. Y. and Finn, W. D. L., 1978, "Simplified Seismic Analysis for Tailings Dams," Proceedings of Spec. Conference on Earthquake Engineering and Soil Dynamics, ASCE, pp. 540-556, Pasadena, California.

Koizumi, Y., 1966, "Change in Density of Sand Subsoil Caused by the Niigata Earthquake," Soils and Foundations, Tokyo, Japan, Vol. 8, No. 2, pp. 38-44.

Koppejan, A. W.; Wamelen, B. M. and Weinberg, L. J., 1948, "Coastal Flow Slides in the Dutch Providence of Zeeland," Proceedings, 2nd ICSMFE, Vol. 5, pp. 89-96, Rotterdam.

Lee, K. L. and Seed, H. B., 1967, "Cyclic Stress Conditions Causing Liquefaction of Sand," Journal of the Soil Mechanics and Foundations Division, ASCE, Vol. 93, No. SM1, pp. 47-70.

Lee, K. L. and Seed, H. B., 1967, "Dynamic Strength of Anisotropically Consolidated Sand," Journal of the Soil Mechanics and Foundations Division, ASCE, Vol. 93, No. SM5, p. 169-190.

Makdisi, F. I. and Seed, H. B., 1978, "Simplified Procedure for Estimating Dam and Embankment Earthquake-Induced Deformations," Journal of the Geotechnical Engineering Division, ASCE, Vol. 104, No. GT7, pp. 849-867.

Middlebrooks, T. A., 1942, "Fort Peck Slide," ASCE Transactions, Vol. 107, pp. 723-764.

Newmark, N. M. 1965, "Effects of Earthquakes on Dams and Embankments," Fifth Rankine Lecture, Geotechnique, London, England, Vol. 15, No. 2, pp. 139-159.

REFERENCES

Ohsaki, Y., 1966, "Niigata Earthquakes, 1964, Building Damage and Soil Conditions," Soils and Foundation, Tokyo, Japan, Vol. 6, No. 2, pp. 14-37.

Poulos, S. J., 1971, The Stress-Strain Curves of Soils, Geotechnical Engineers Inc., Winchester, Mass., pp. 1-80.

Poulos, S. J., 1981, "The Steady State of Deformation," Journal of the Geotechnical Engineering Division, ASCE, Vol. 107, No. GT5, pp. 553-562.

Roscoe, K. H. and Schofield, A. N., 1958, "On the Yielding of Soils," Geotechnique, Vol. VII, pp. 25-53.

Ross, G. A.; Seed, H. B and Migliaccio, R. R., 1969, "Bridge Foundation Behavior in Alaska Earthquake," Journal of the Soil Mechanics and Foundations Division, ASCE, Vol. 95, No. SM4, pp. 1007-1036.

Sangrey, D. A.; Castro, G.; Poulos, S. J. and France, J. W., 1978, "Cyclic Loadings of Sands, Silt and Clays," Proceedings of Spec. Conference on Earthquake Engineering and Soil Dynamics, ASCE, Vol. 2, pp. 836-851, Pasadena, California

Schofield, A. and Wroth, P., 1968, Critical State Soil Mechanics, McGraw-Hill Book Co. Ltd, U.K.

Seed, H. B. and Lee, K. L., 1966, "Liquefaction of Saturated Sands During Cyclic Loading," Journal of the Soil Mechanics and Foundations Division, ASCE, Vol. 92, No. SM6, pp. 105-134.

Seed, H. B. and Idriss, I. M., 1967, "Analysis of Soil Liquefaction: Niigata Earthquake," Journal of the Soil Mechanics and Foundations Division, ASCE, Vol. 93, No. SM3, pp. 83-108.

Seed, H. B. 1968, "Landslides During Earthquakes Due to Soil Liquefaction," Journal of the Soil Mechanics and Foundations Division, ASCE, Vol. 94, No. SM5, pp. 1055-1122.

Seed, H. B.; Lee, K. L. and Idriss, I. M, 1969, "Analysis of Sheffield Dam Failure," Journal of the Soil Mechanics and Foundations Division, ASCE, Vol. 95, No. SM6, pp. 1453-1490.

Seed, H. B. and Idriss, I. M., 1971, "Simplified Procedure for Evaluating Soil Liquefaction Potential," Journal of the Soil Mechanics and Foundations Division, ASCE, Vol. 97, No. SM9, pp. 1249-1273.

REFERENCES

Seed, H. B.; Lee, K. L.; Idriss, I. M. and Makdisi, F. I., 1975, "The Slides in the San Fernando Dams During the Earthquake of February 9, 1971," Journal of the Geotechnical Engineering Division, ASCE, Vol. 101, No. SM7, pp. 651-688.

Seed, H. B.; Martin, P. P. and Lysmer, J., 1975, "The Generation and Dissipation of Pore Water Pressures During Soil Liquefaction," Report No. EERC 75-26, Earthquake Engineering Research Center, University of California, Berkeley, California.

Seed, H. B., 1976, "Some Aspects of Sand Liquefaction Under Cyclic Loading," Proceedings, Conference on Behavior of Off-Shore Structures, The Norwegian Institute of Technology, Norway.

Seed, H. B., 1979, "Soil Liquefaction and Cyclic Mobility Evaluation for Level Ground During Earthquakes," Journal of the Geotechnical Engineering Division, Vol. 105, No. GT2, pp. 201-255.

Silver, M. L.; Tatsuoka, F.; Phukunhaphan, A. and Anestis, A., 1980, "Cyclic Undrained Strength of Sand by Triaxial Test and Simple Shear Test," Proceedings of the 7th World Conference on Earthquake Engineering, Turkey.

Terzaghi, K., 1925, Erdbaumechanik auf Bodenphysikalischer Grundlage," Vienna, Deuticke.

Terzaghi, K., 1956, "Varieties of Submarine Slope Failures," Proceedings 8th Texas Conference on Soil Mechanics and Foundation Engineering, Harvard Soil Mechanics Series No. 52.

Waterways Experiment Station, 1956, U.S. Corps of Engineers, Report 12-5, "A Review of the Soils Studies," Potamology Investigations, Vicksburg, Mississippi.

Waterways Experiment Station, 1967, U.S Corps of Engineers, Report 12-18, "Verification of Empirical Method for Determining Riverbank Stability, 1965 Data," Potamology Investigations, Vicksburg, Mississippi.

Watson, J. D., 1940, "Stress Deformation Charateristics of Cohesionless Soils from Triaxial Compression Tests," ScD. Thesis, Pierce Hall, Harvard University.

Whitman, R. V., 1971, "Resistance to Soil Liquefaction and Settlement," Soils and Foundations, Tokyo, Japan, Vol. 11, No. 4, pp. 59-67.

TABLES

TABLE 3-1 - SUMMARY OF GRAIN SIZE ANALYSES

Sand	Percent Passing Sieve No.							D_{10} mm	D_{50} mm	D_{60} mm	C_u
	30	40	50	70	100	140	200				
BS[1] #1	100	99.8	97.0	80.4	27.3	3.4	0.3	0.122	0.178	0.187	1.53
BS[1] #5	100	100	100	100	96.4	31.8	1.4	0.088	0.114	0.119	1.35
BS[1] #6	100	99.8	97.8	85.4	44.0	13.5	0.2	0.099	0.157	0.168	1.70
BS[1] #9	100	99.9	98.5	89.0	58.0	15.7	0.1	0.097	0.142	0.154	1.59
Sand B (#4) (Castro, 1969)	100	99.0	97.0	80.0	40.0	14.0	0.5	0.097	0.16	0.175	1.80
Mine Tailings	99.5 2)	91.2	63.6	37.4	17.4	10.3	6.5	0.107	0.256	0.290	2.71

Notes:

1) "BS" indicates Banding sand

2) 100% passing #16 sieve

TABLE 3-2 - MAXIMUM AND MINIMUM DENSITIES FOR FIVE DIFFERENT GRADATIONS OF BANDING SAND AND FOR MINE TAILINGS SAND

	Min-Max Densities According to ASTM 2049				Max Density According to ASTM D1557 (Compaction Test)		Min-Max Densities According to Casagrande Method(4)			
	e_{max} pcf	$\gamma_{d_{min}}$ pcf	e_{min} pcf	$\gamma_{d_{max}}$ pcf	e_{min} pcf	$\gamma_{d_{max}}$ pcf	e_{max} pcf	$\gamma_{d_{min}}$ pcf	e_{min} pcf	$\gamma_{d_{max}}$ pcf
Banding Sand #1	0.82	91.2	0.54	107.8	0.58	104.8 (1)	0.84	90.2	0.54	107.8
Banding Sand #5	0.87	88.8	0.55	107.1	(5)		0.89	87.8	0.58	105.0
Banding Sand #6	0.82	91.2	0.52	109.2	0.55	107.2 (3)	0.83	90.7	0.52	109.2
Banding Sand #9	0.80	92.2	0.53	108.5	(5)		0.84	90.2	0.53	108.5
Sand B (#4) (Castro, 1969)	(2)	(2)	(2)	(2)	(2)	(2)	0.84	90.2	0.50	110.6
Mine Tailings	1.08	80.4	0.68	99.5	0.65	101.5	1.15	77.8	0.65	101.4

Notes: (1) Maximum density determined from a eight-point compaction test.
(2) Not performed.
(3) Maximum density determined from a six-point compaction test.
(4) See text for description of procedure.
(5) Only one compaction point performed; insufficient data to determine maximum density.

TABLE 3-3 - COMPARISON OF INDEX PROPERTIES FOR BANDING SAND #6 AND FOR MINE TAILINGS SAND

	Banding Sand #6	Mine Tailings
D_{50}	0.157 mm	0.256 mm
Uniformity Coefficient, $C_u = D_{60}/D_{10}$	1.70	2.71
Minimum Density by ASTM 2049 e_{max} / $\gamma_{d_{min}}$	0.82 / 91.2 pcf	1.08 / 80.4 pcf
Maximum Density by ASTM 2049 e_{min} / $\gamma_{d_{max}}$	0.52 / 109.2 pcf	0.62 / 99.5 pcf
Maximum Density by ASTM D1557 (Compaction Test) e_{min} / $\gamma_{d_{max}}$	0.55 / 107.2 pcf	0.65 / 101.5 pcf
Specific Gravity of Solids	2.66	2.68
Grain Shape	Subrounded	Angular

TABLE 3-4 - SUMMARY OF TRIAXIAL TESTING PROGRAM

SAND	QUANTITY OF TESTS PERFORMED(1)			
	$\bar{R}$	$A\bar{R}$	$CA\bar{R}$	$CA\bar{R}-\bar{R}$
Banding Sand #1	5	-	-	-
Banding Sand #5	4	-	-	-
Banding Sand #6	32	6	22	7
Banding Sand #9	2	-	-	-
Mine Tailings	26	4	8	-

Notes:

(1) Types of tests are described in Section 3.3 of the text and in Appendix C.

(2) Individual test results presented in Appendix A. A discussion of test results is presented in Sections 4 and 5 of the text.

TABLE 5-1 - SUMMARY OF $CA\bar{R}$ TESTS ON MINE TAILINGS WITH DRIVING SHEAR STRESSES LESS THAN UNDRAINED STEADY STATE SHEAR STRENGTH[1]

Test No.	Effective Minor Principal Stress at Consolidation $\bar{\sigma}_{3c}$ kg/cm^2	$K_c = \bar{\sigma}_{1c}/\bar{\sigma}_{3c}$	Void Ratio after Consolidation e_c	Driving (Consolidation) Shear Stress τ_d kg/cm^2	Cyclic Shear Stress $\pm \tau_{cy}$ kg/cm^2	$\tau_d+\tau_{cy}$ kg/cm^2	Undrained Steady State Shear Strength, S_{us} kg/cm^2		$\tau_d + \tau_{cy}$ $(S_{us})_{avg}$
							(2) Range	(2) Average	
$CA\bar{R}$-1002	3	2.0	0.887	1.50	0.48	1.98	1.9-3.0	2.2	0.90
$CA\bar{R}$-1003	3	2.0	0.911	1.50	1.05	2.55	1.6-2.4	1.5	1.70
$CA\bar{R}$-1006	3	2.0	0.895	1.50	0.77	2.27	1.8-2.8	2.0	1.14
$CA\bar{R}$-1007	3	2.0	0.899	1.50	0.31	1.81	1.7-2.7	1.9	0.95
$CA\bar{R}$-1007B	3	2.0	0.891	1.50	0.84	2.34	1.9-2.9	2.1	1.12
$CA\bar{R}$-1004	8	1.38	0.914	1.50	0.50	2.00	1.4-2.3	1.7	1.18
$CA\bar{R}$-1005	8	1.38	0.910	1.50	1.33	2.83	1.6-2.4	1.7	1.66

Notes:

(1) More detailed information regarding individual tests is presented in Appendix A.

(2) Determined from Fig. 5-6.

TABLE 5-2 - SUMMARY OF $C\bar{A}\bar{R}$ TESTS ON BANDING SAND #6 WITH DRIVING SHEAR STRESSES LESS THAN UNDRAINED STEADY STATE SHEAR STRENGTH[1]

Test No.	Effective Minor Principal Stress at Consolidation σ_{3c} kg cm^2	$K_c = \bar{\sigma}_{1c}/\bar{\sigma}_{3c}$	Void Ratio after Consolidation e_c	Driving (Consolidation) Shear Stress τ_d kg/cm^2	Cyclic Shear Stress $\pm \tau_{cy}$ kg/cm^2	$\tau_d + \tau_{cy}$ kg/cm^2	Undrained Steady State Shear Strength, S_{us} kg/cm^2	
							Range[2]	Average[2]
$C\bar{A}\bar{R}$-625	4	2.0	0.642	2.0	0.60	2.60	-	>30
$C\bar{A}\bar{R}$-626	4	2.0	0.722	2.0	0.60	2.60	6 to 20	9
$C\bar{A}\bar{R}$-627	4	2.0	0.725	2.0	0.61	2.61	5 to 15	7
$C\bar{A}\bar{R}$-628	4	2.0	0.713	2.0	0.59	2.59	10 to 32	14
$C\bar{A}\bar{R}$-629	4	2.0	0.690	2.0	0.59	2.59	-	>30
$C\bar{A}\bar{R}$-630	4	2.0	0.691	2.0	1.09	3.09	-	>30

Notes:

(1) More detailed information regarding individual tests is presented in Appendix A.

(2) Determined from Fig. 5-1.

TABLE 6-1 - INDEX PROPERTIES OF VARIOUS SANDS FOR WHICH THE STEADY STATE LINE HAS BEEN DETERMINED

Sand No.	Designation(1)	D_{60}	C_u	Finer than 200 mesh Sieve, %	Grain Shape	Specific Gravity	ASTM D-2049		ASTM D-1557
							e_{max}	e_{min}	e_{min} 2)
1	Banding Sand No. 1	0.19	1.53	0.2	Subrounded	2.66	0.82	0.54	0.58
4	B(Banding Sand No.4)	0.17	1.8	0	Subrounded	2.65	0.84(3)	0.50(3)	(3)
5	Banding Sand No. 5	0.12	1.35	1.4	Subrounded	2.66	0.87	0.55	(5)
6	Banding Sand No. 6	0.17	1.70	0.2	Subrounded	2.66	0.82	0.52	0.55
9	Banding Sand No. 9	0.15	1.59	0.1	Subrounded	2.66	0.80	0.53	(5)
10	Mine Tailings	0.30	2.50	7	Angular to Subangular	2.68	1.08	0.68	0.65
12	A	0.40	3.1	5	Subangular to Angular	2.72	1.04(3)	0.55(3)	(4)
13	C	0.33	2.3	1	Angular	2.87	0.99(3)	0.66(3)	(4)
14	D	0.90	5.6	0	Subangular	2.71	0.77(3)	0.49(3)	(4)
15	E	0.17	2.1	8	Angular	2.87	1.26(3)	0.77(3)	(4)
16	F	0.23	2.0	0	Angular	2.50	1.88(3)	1.23(3)	(4)
17	G	0.15	-	26	Angular	2.79	1.45(3)	0.72(3)	(4)
18	H	0.85	17	13	Subangular	2.71	0.73(3)	0.37	(4)
19	-	0.14	2.98	18	Subangular to Angular	2.65	1.17	0.67	0.62
20	-	0.27	1.59	1	Subrounded to Subangular	2.67	0.88	0.56	0.60
21	-	0.22	3.3	10	Angular	2.70	(5)	(5)	(4)

Notes: (1) Designations A through H refer to designations used in Castro and Poulos, 1977
Sand B (Banding Sand No. 4) is the same as Sand B in Castro, 1969.
(2) e_{min} corresponding to γ_{dmax} from ASTM D-1557 Modified Compaction.
(3) Casagrande Method, see text for description of procedure.
(4) ASTM D-1557 not performed.
(5) Insufficient data to determine e_{min}.
(6) Max-min density tests not performed.

FIGURES

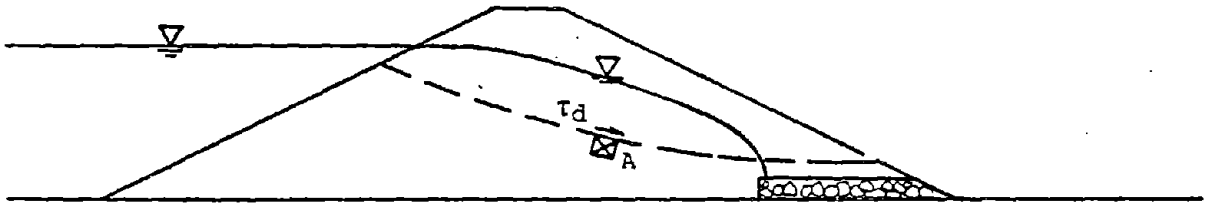

a) Embankment Dam, Drained Condition

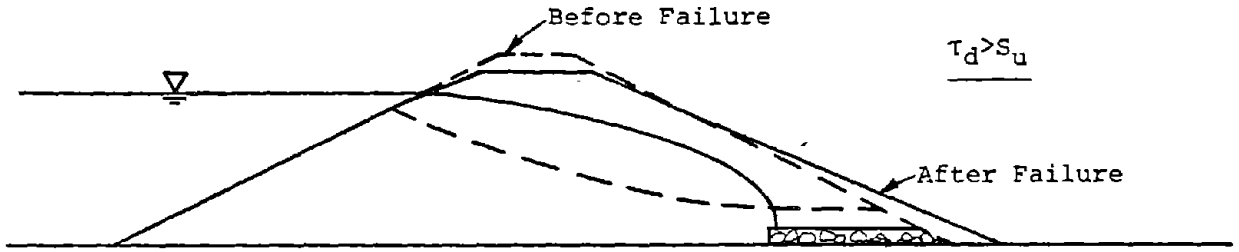

b) Embankment Dam, Undrained Slope
Failure of Limited Extent

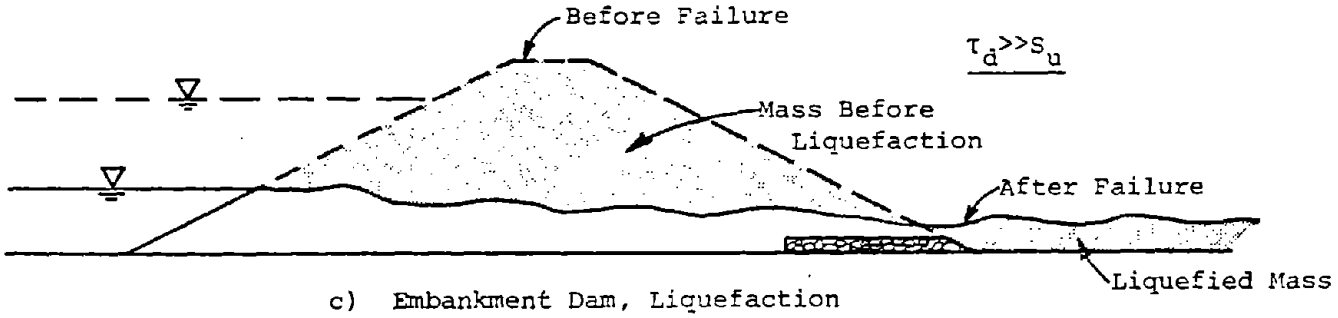

c) Embankment Dam, Liquefaction
Failure

Fig. 2-1: Examples of Two Types of Undrained Failure of Soil in an Embankment Dam

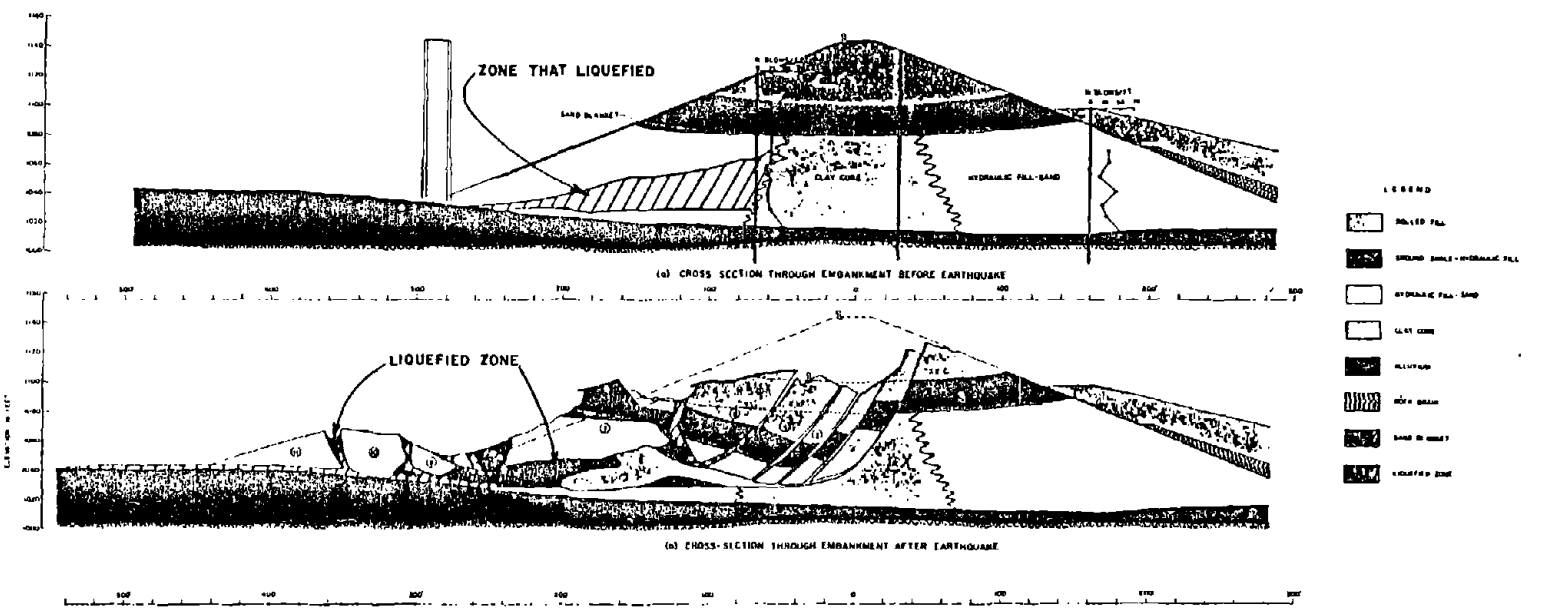

Fig. 2-2: Failure of Lower San Fernando Dam
(from Seed et al, 1975)

a) Buildings

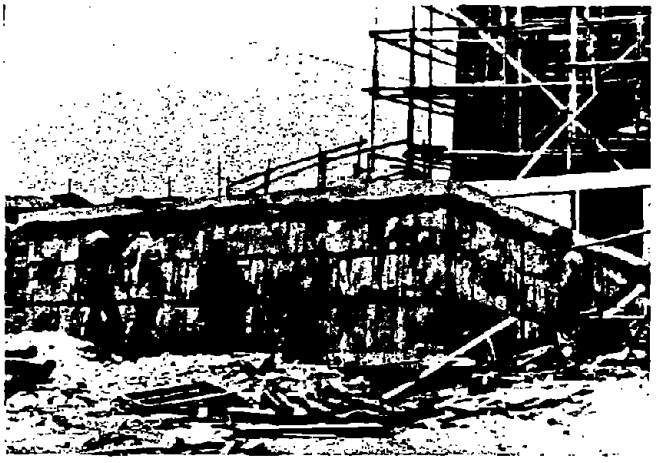

b) Sewerage Tanks

Fig. 2-3: Liquefaction Failures in Niigata, Japan, 1964, From Seed & Idriss, 1967.

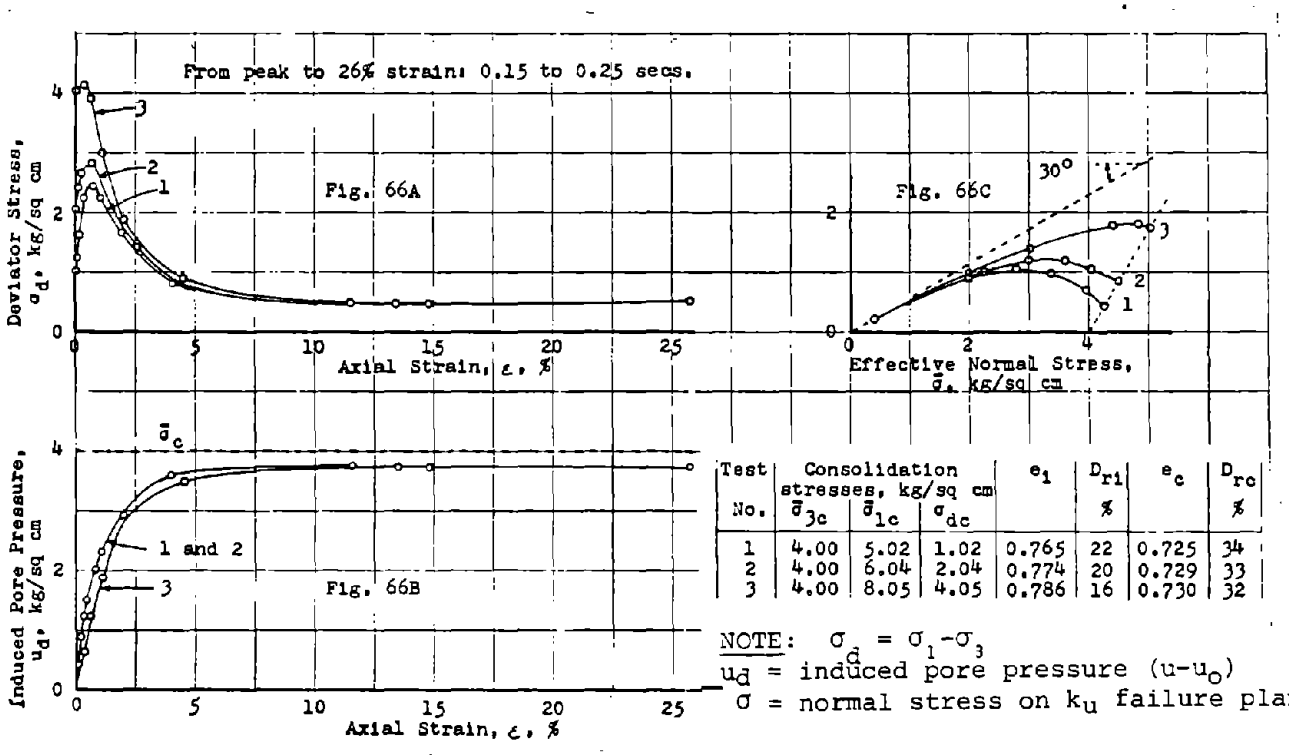

Test No.	Consolidation stresses, kg/sq cm $\bar{\sigma}_{3c}$	$\bar{\sigma}_{1c}$	σ_{dc}	e_1	D_{ri} %	e_c	D_{rc} %
1	4.00	5.02	1.02	0.765	22	0.725	34
2	4.00	6.04	2.04	0.774	20	0.729	33
3	4.00	8.05	4.05	0.786	16	0.730	32

NOTE: $\sigma_d = \sigma_1 - \sigma_3$
u_d = induced pore pressure ($u - u_o$)
σ = normal stress on k_u failure plane

a) Monotomically loaded, anisotropically consolidated Triaxial Test (From Castro, 1969)

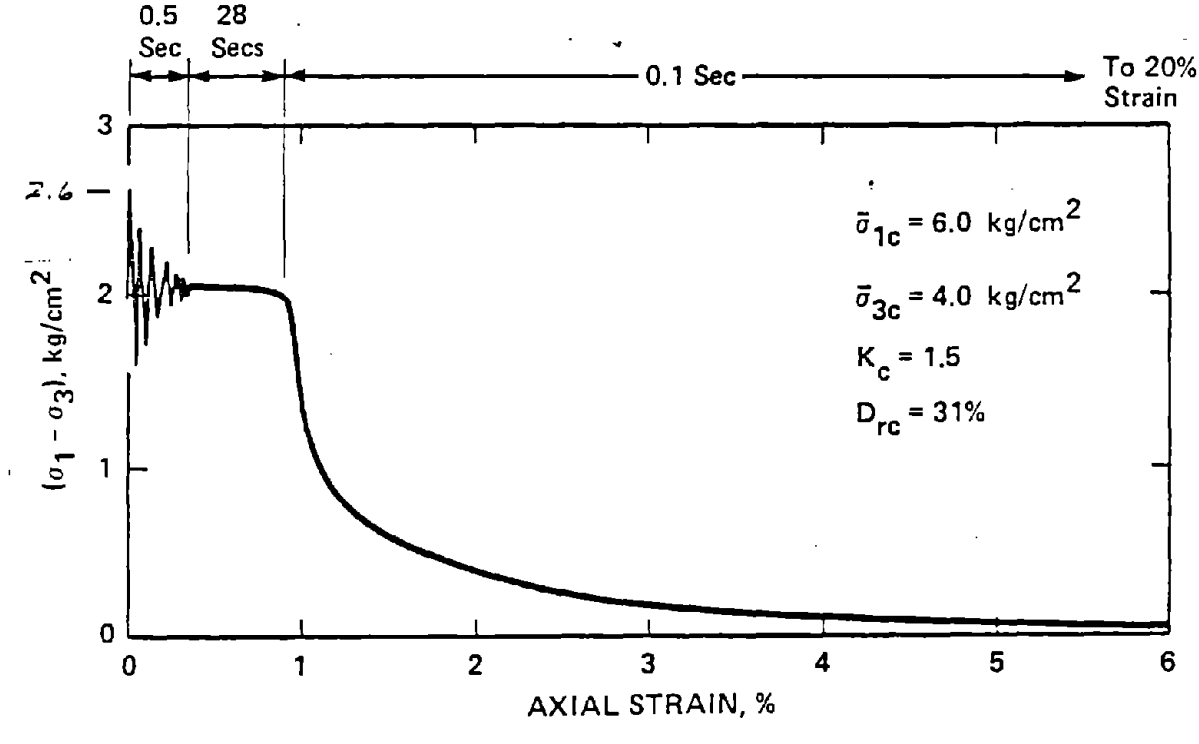

b) Cyclically loaded, anisotropically consolidated Triaxial Test (From Castro, 1978)

Fig. 2-4: Examples of Stress-Strain Curves During Liquefaction

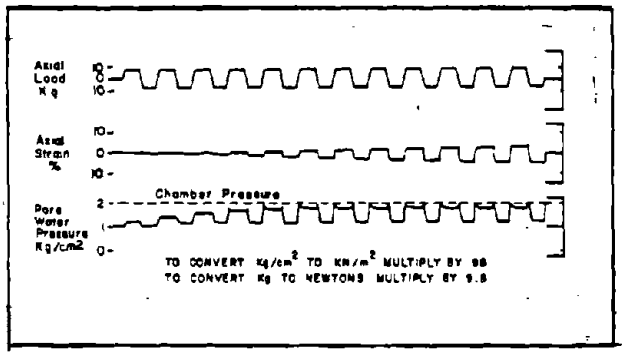

NOTE: Expanded Record

a) Undrained Cyclic Loading

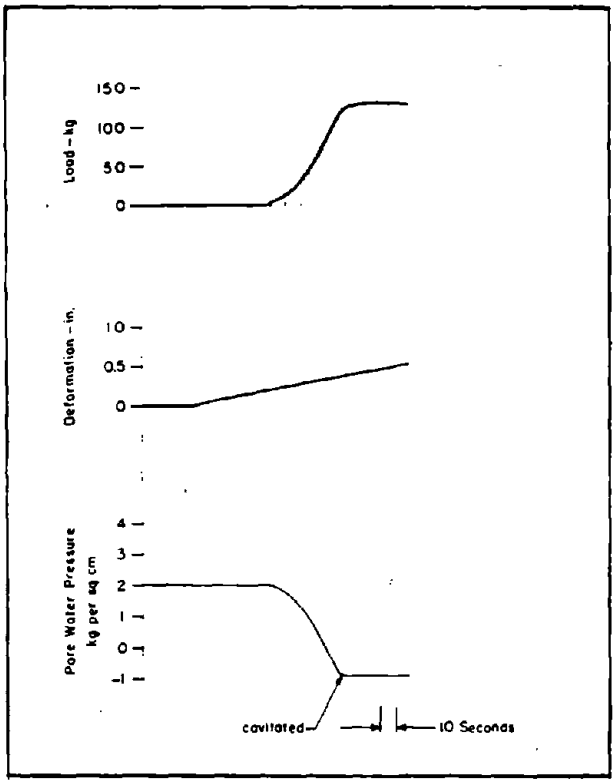

b) Undrained Monotonic Compression Loading After Cyclic Loading (a)

Fig. 2-5 Results of Undrained Cyclic Triaxial Test Illustrating Cyclic Mobility (After Seed and Lee, 1966)

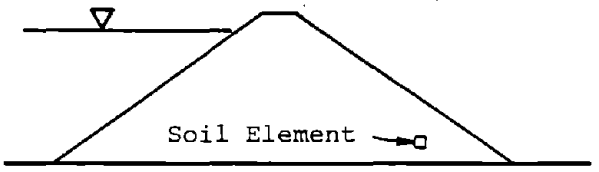

a) Representative soil element in an embankment

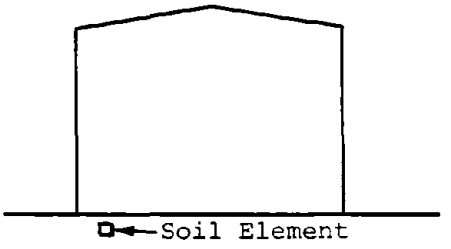

b) Representative soil element beneath a storage tank

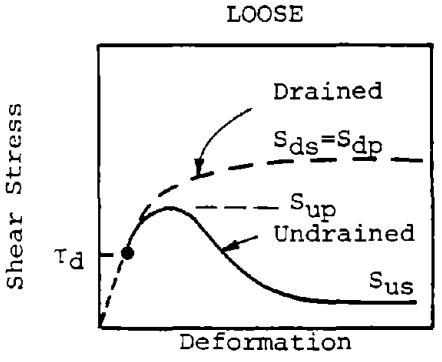

c) Loose soil, monotonic loading

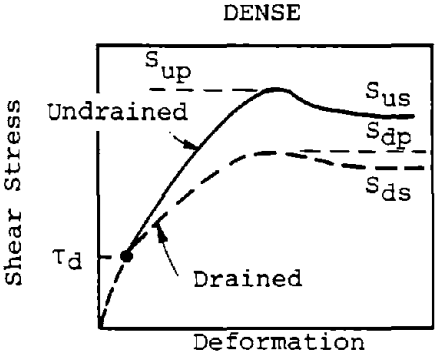

d) Dense soil, monotonic loading

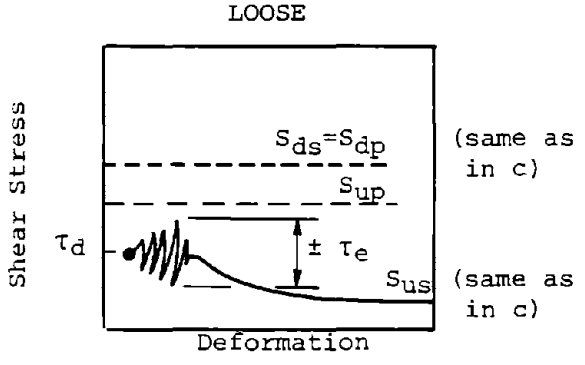

e) Loose soil, cyclic loading (Liquefaction)

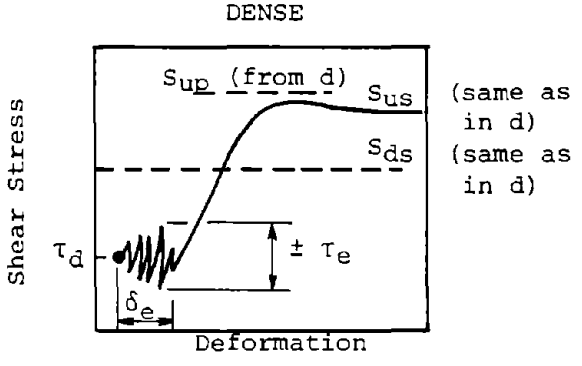

f) Dense soil, cyclic loading followed by monotonic loading (Cyclic Mobility)

Fig. 2-6 Illustration of the Practical Distinction Between Liquefaction Caused by Cyclic Loading and Cyclic Mobility.

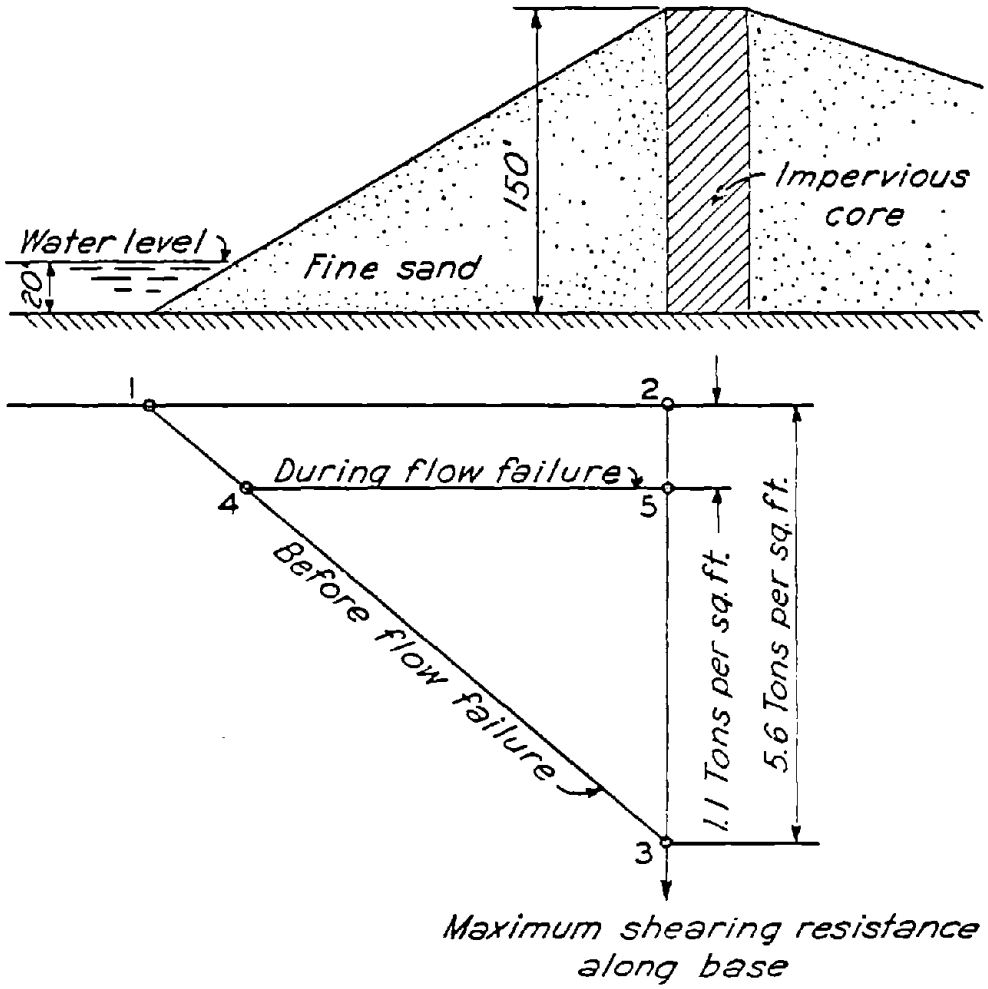

Fig. 2-7 Decrease in Shear Resistance During Undrained Loading of a Sand Above the Critical Void Ratio (After Casagrande, 1938)

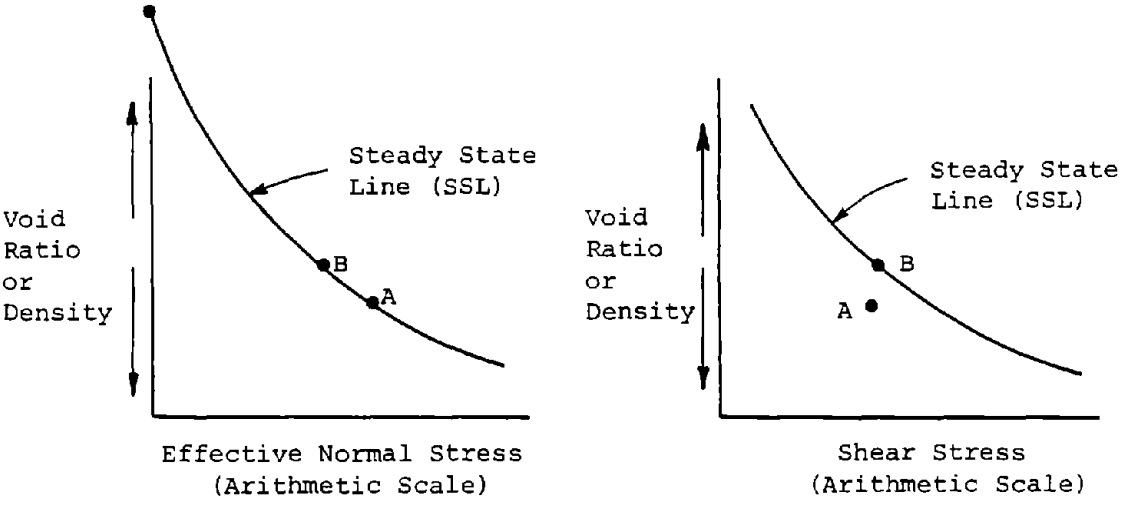

a) Steady State Lines in Arithmetic Plots

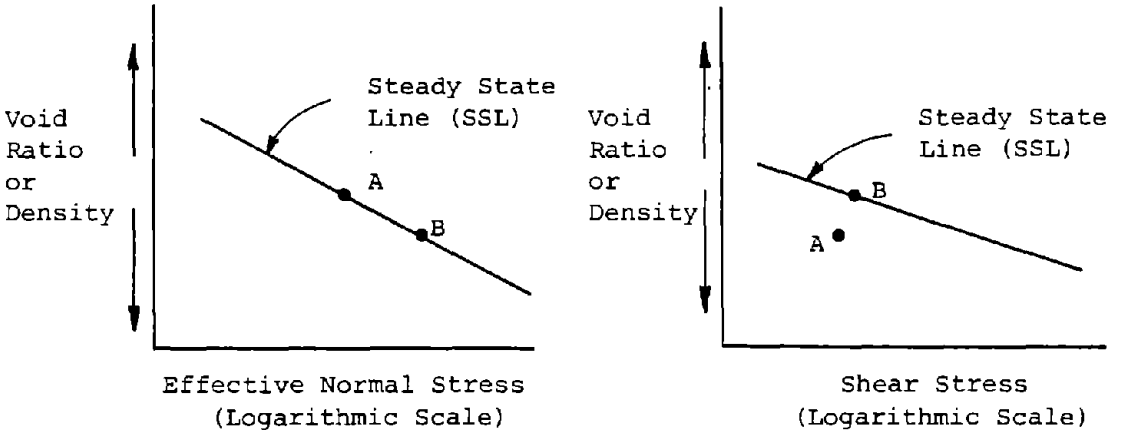

b) Steady State Lines in Semi-Logarithmic Plots

Fig. 2-8 Examples of Steady State Line Plots

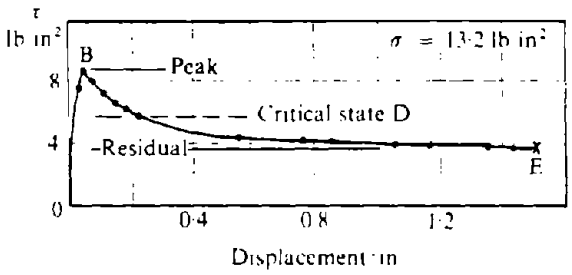

Fig. 2-9: Relationship between Critical State and Residual Strength of Clay (after Skempton) Schofield & Wroth, 1968

BANDING SAND

0.10 mm

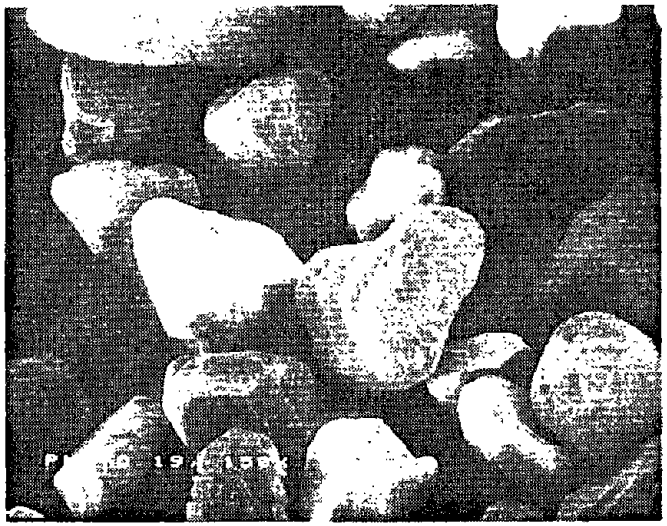

BANDING SAND

0.10 mm

MINE TAILINGS

0.10 mm

MINE TAILINGS

0.10 mm

FIG. 3-1: SCANNING ELECTRON MICROPHOTOGRAPHS

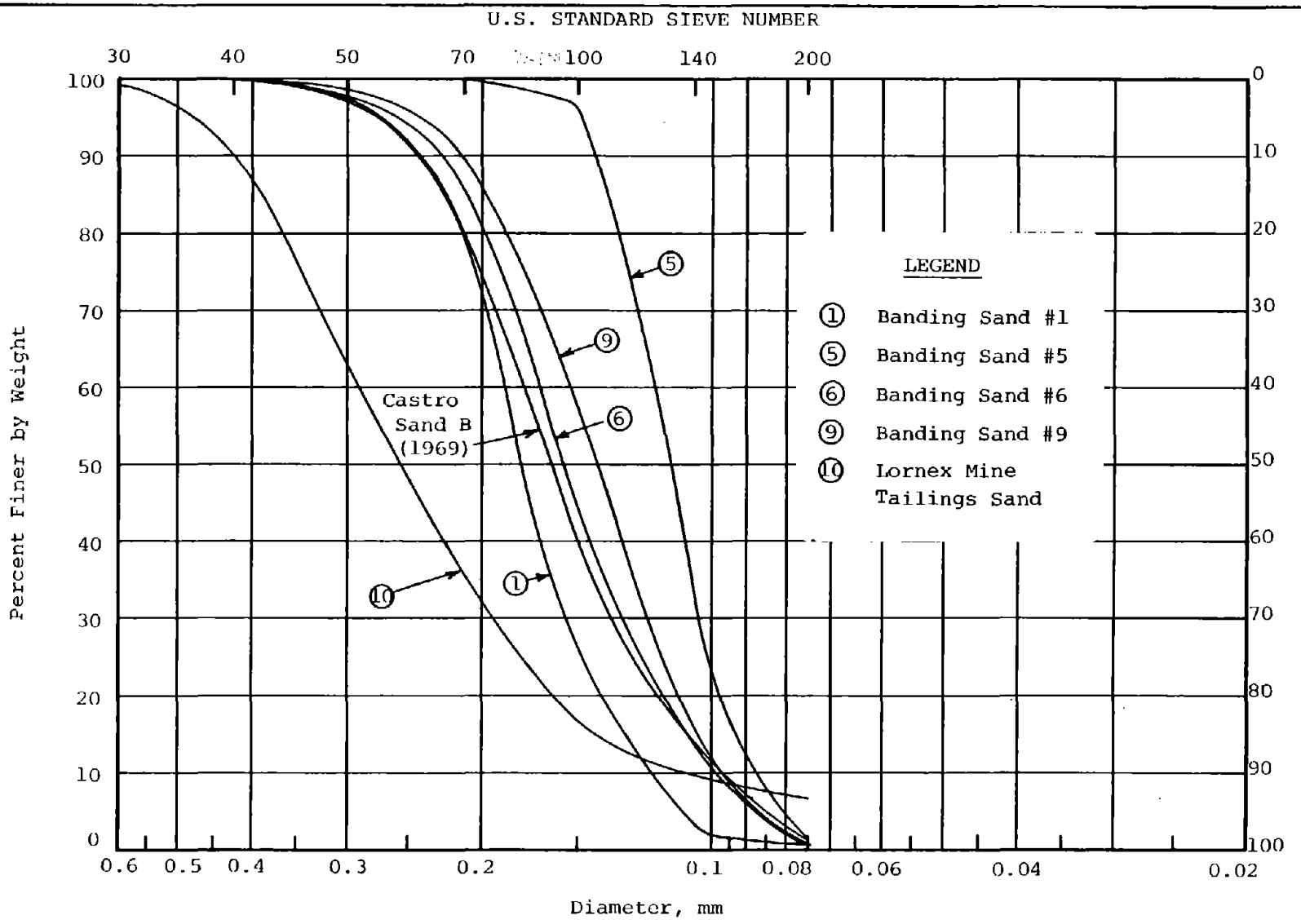

Fig. 3-2 Grain Size Curves for Banding Sands and Mine Tailings

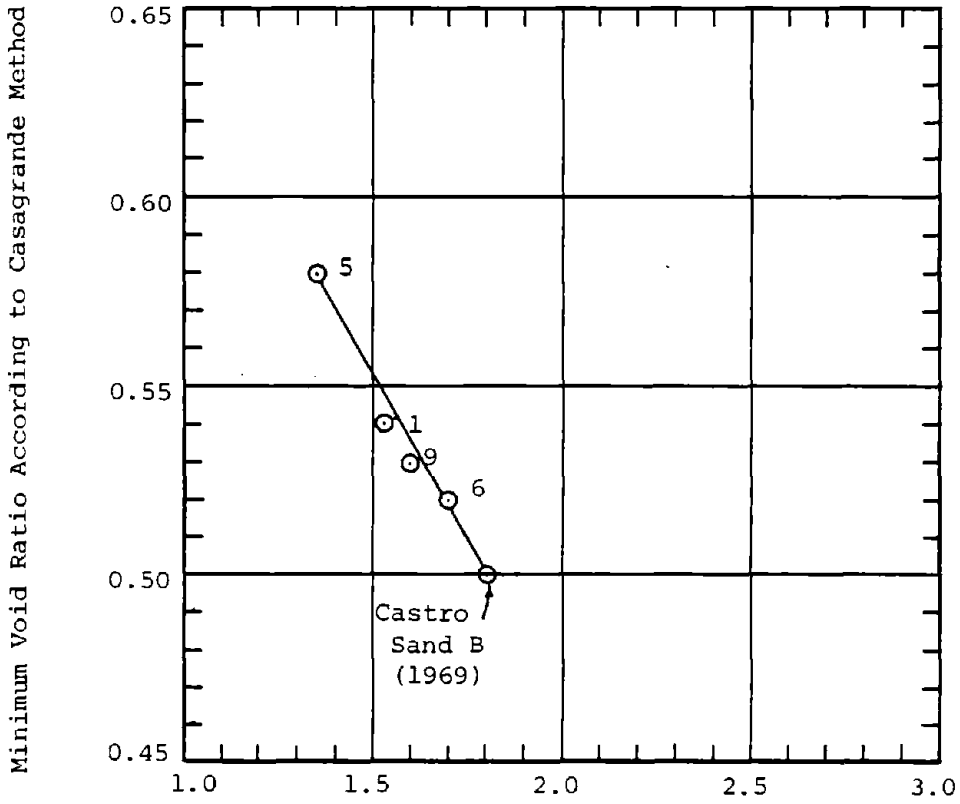

NOTE:

Minimum void ration for Sand B was from Casagrande method, because ASTM D-2049 was not performed. For other Banding Sands there was good agreement between minimum void ratio from the two methods.

Fig. 3-3 Minimum Void Ratio According to Casagrande Method versus Uniformity Coefficient.

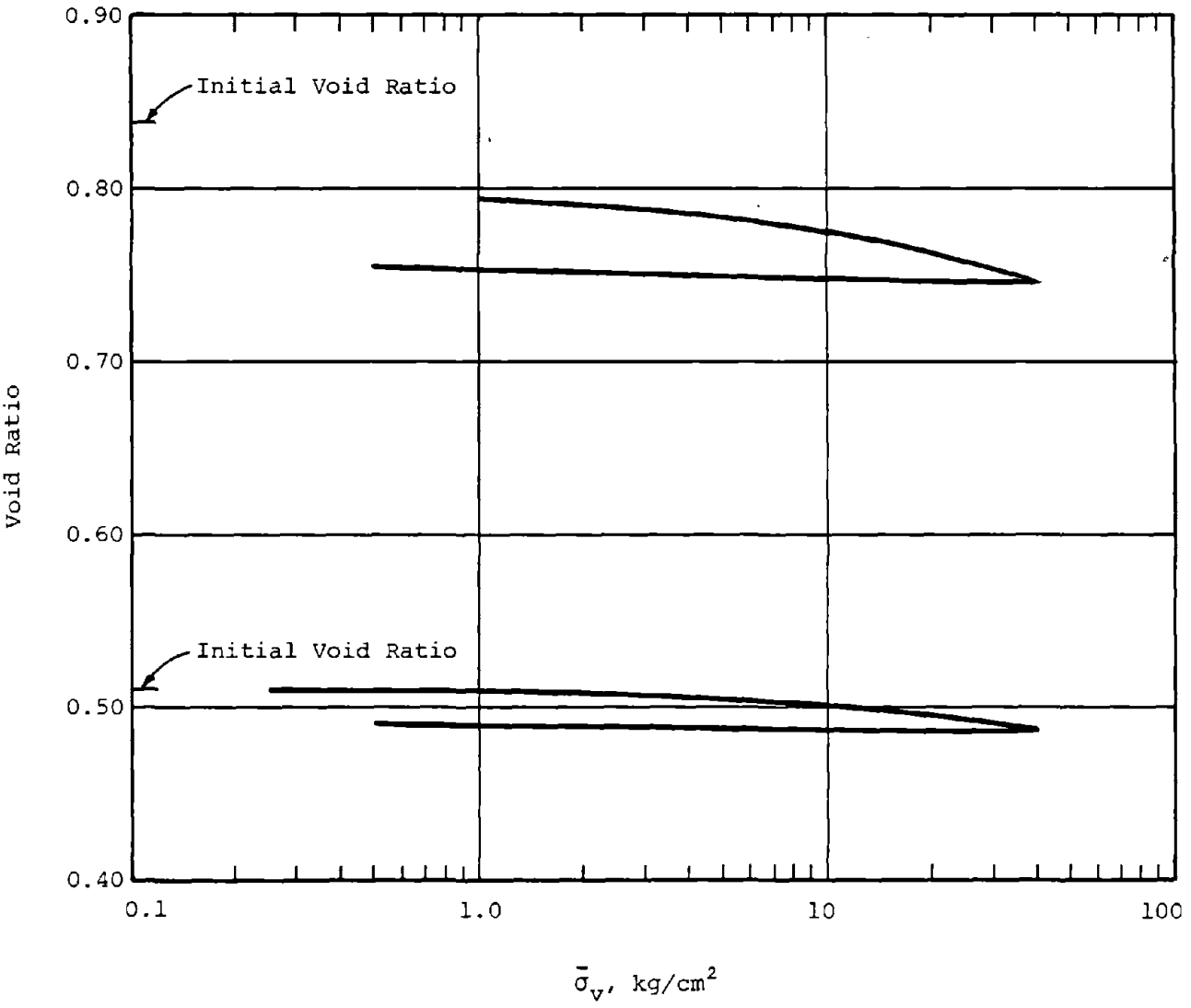

Fig. 3-4 One-Dimentional Consolidation Curves, Banding Sand #6

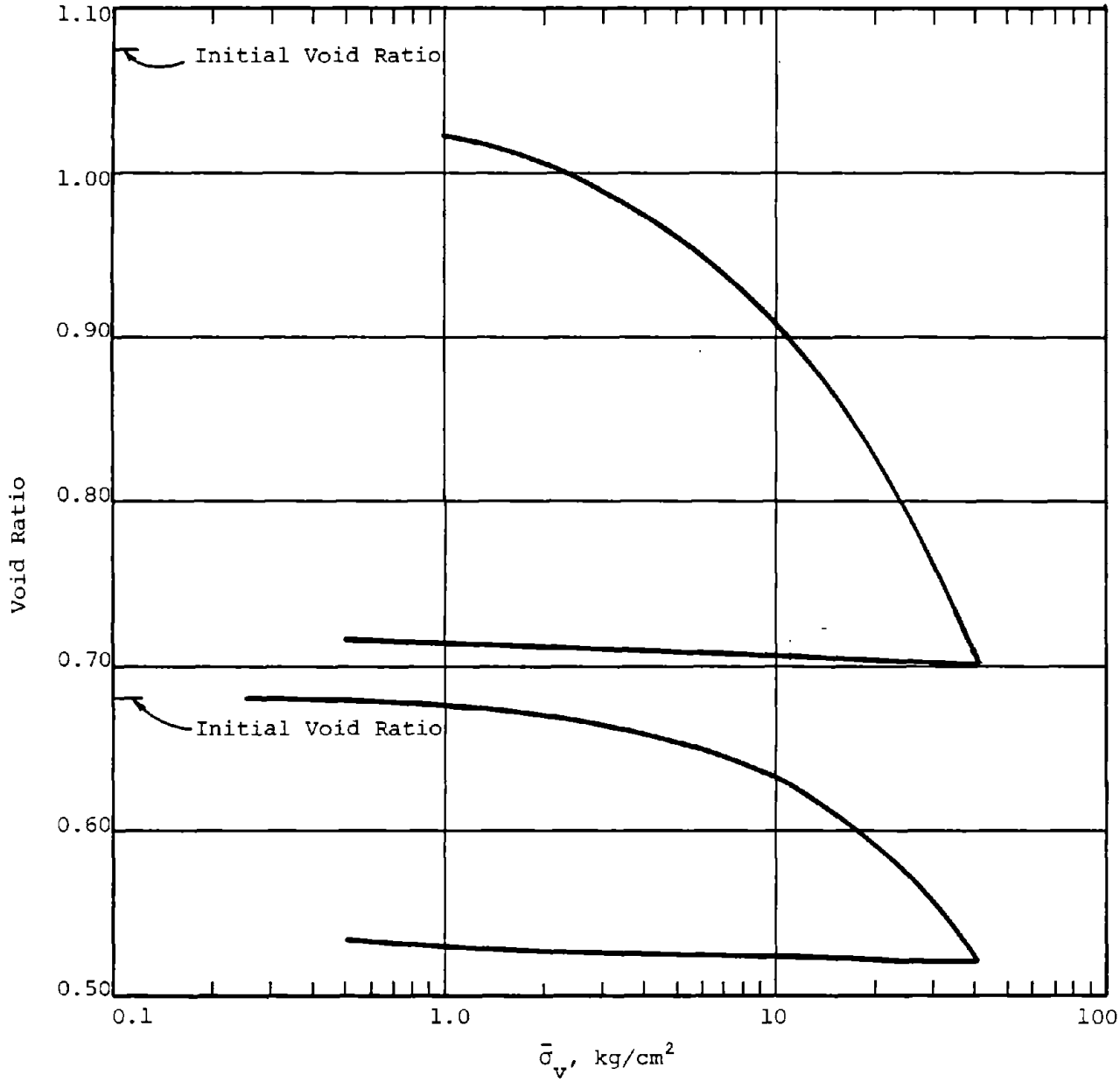

Fig. 3-5 One-Dimentional Consolidation Curves, Mine Tailings

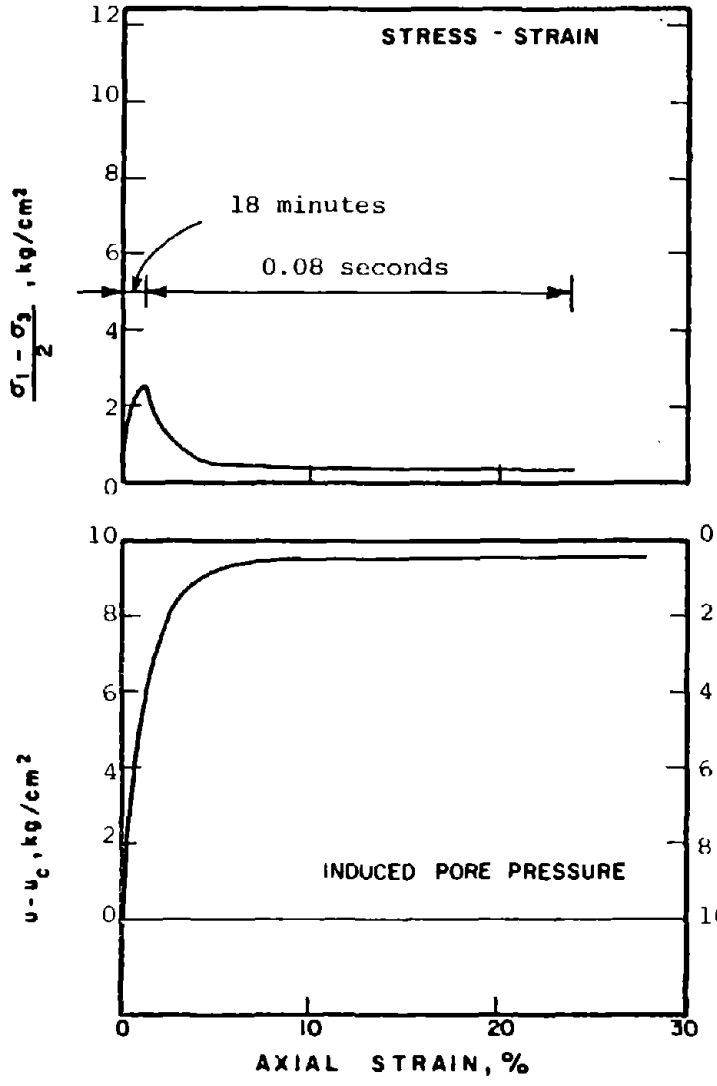

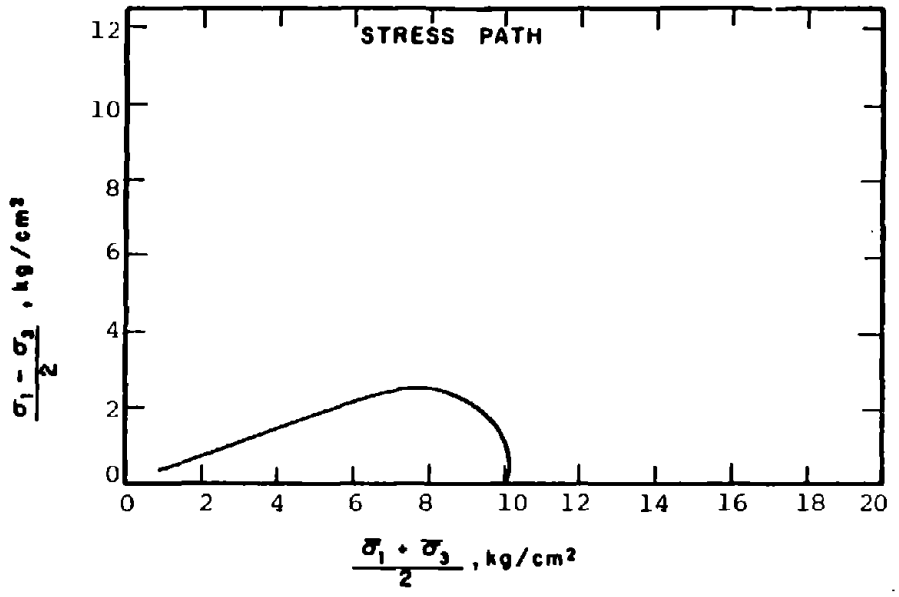

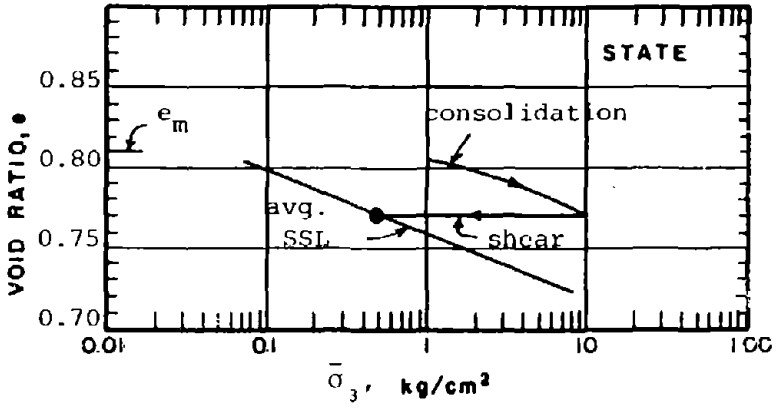

R-603

SOIL : Banding Sand #6

STRUCTURE : Compacted Moist

STATE AFTER CONSOLIDATION: $\bar{\sigma}_{3c} = 10.00 \text{ kg/cm}^2$, $\bar{\sigma}_{1c} = 10.00 \text{ kg/cm}^2$

$e_c = 0.770$, $\gamma_{dc} = 93.8$ pcf

METHOD OF LOADING: Undrained, Axial Compression Load Control

TESTING DETAILS : Specimen Diameter 3.60 cm

: Specimen Height 5.30 cm

: End Platens: Lubricated, Type 1

Fig. 4-1: Typical Type A Stress-Strain Curves

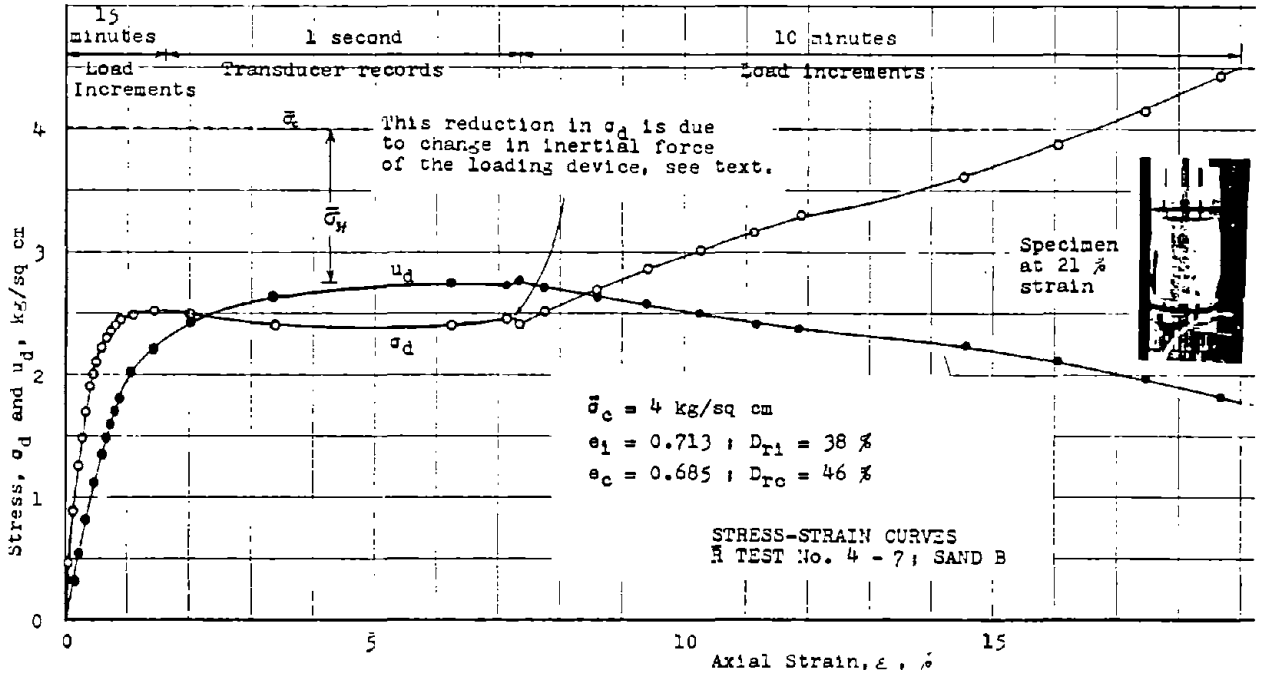

NOTE: $\sigma_d = \sigma_1 - \sigma_3$

u_d = induced pore pressure

Fig. 4-2 Type A-E Stress-Strain Curve (From Castro, 1969)

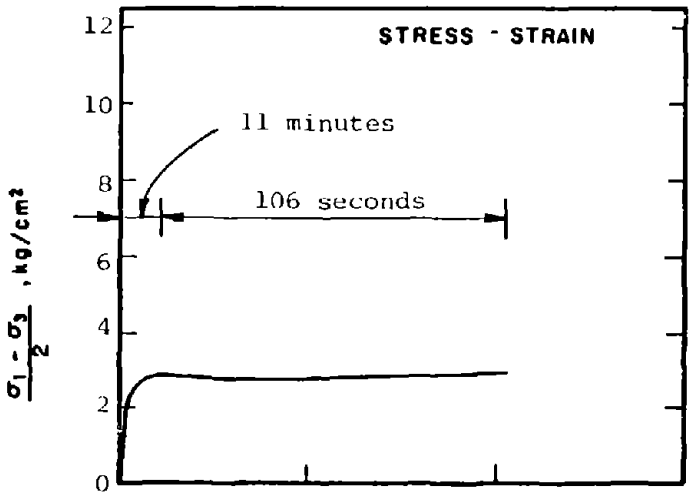

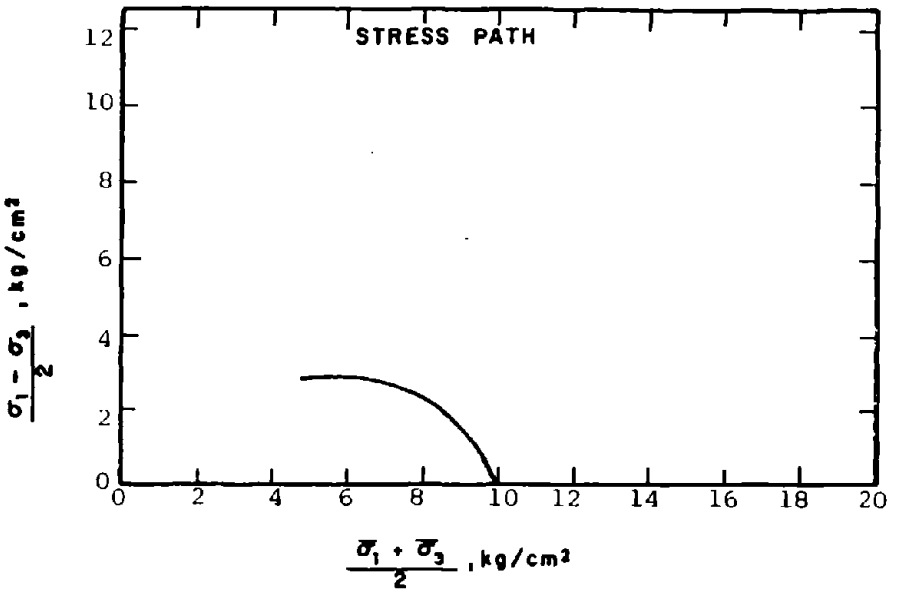

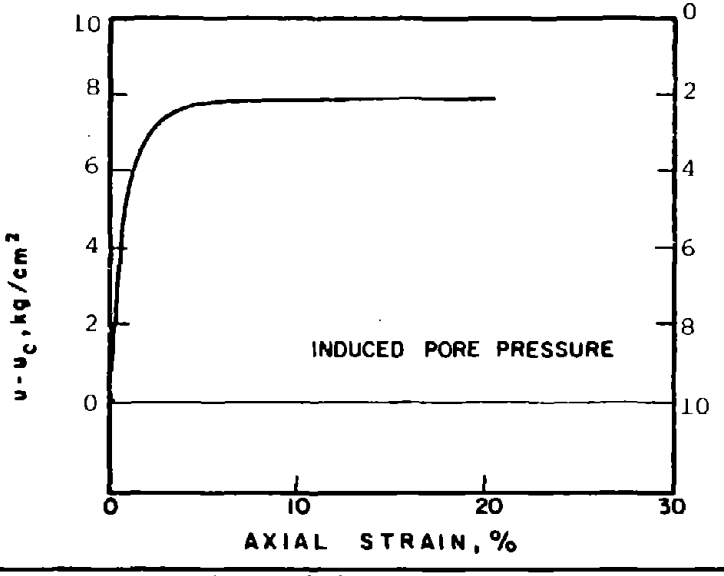

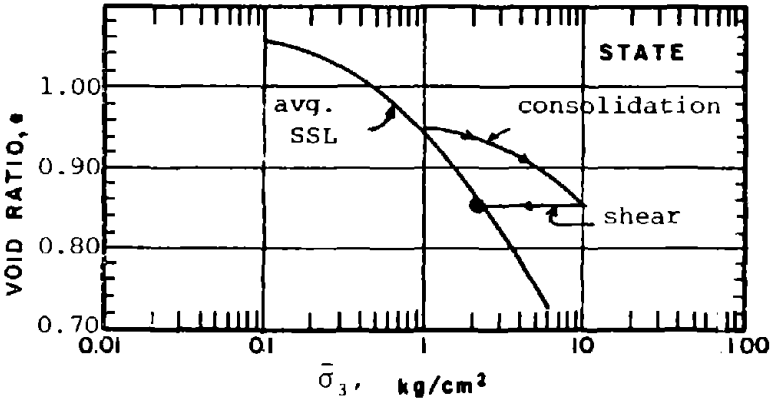

R-1015

SOIL	: Mine Tailings	METHOD OF LOADING:	Undrained, Axial Compression Load Control
STRUCTURE	: Compacted Moist		
STATE AFTER CONSOLIDATION:	$\bar{\sigma}_{3c}$ =10.00 kg/cm^2, $\bar{\sigma}_{1c}$ =10.00 kg/cm^2	TESTING DETAILS	: Specimen Diameter 3.60 cm
	e_c = 0.851, γ_{dc} = 90.3 pcf		: Specimen Height 5.30 cm
			: End Platens: Conventional

Fig. 4-3: Typical Type B Stress-Strain Curves

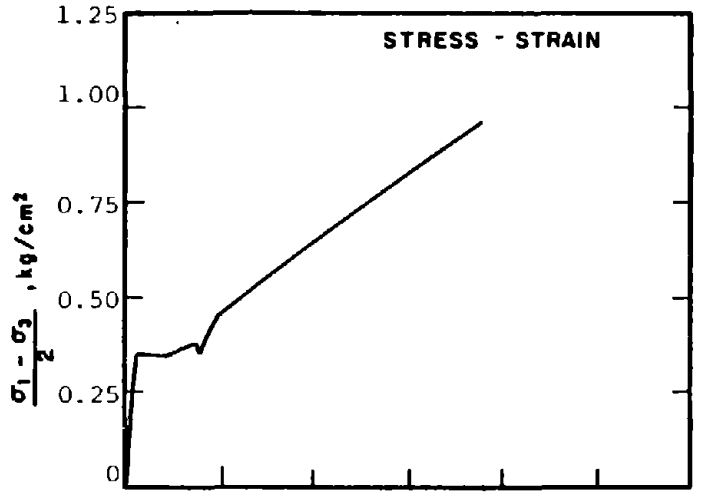

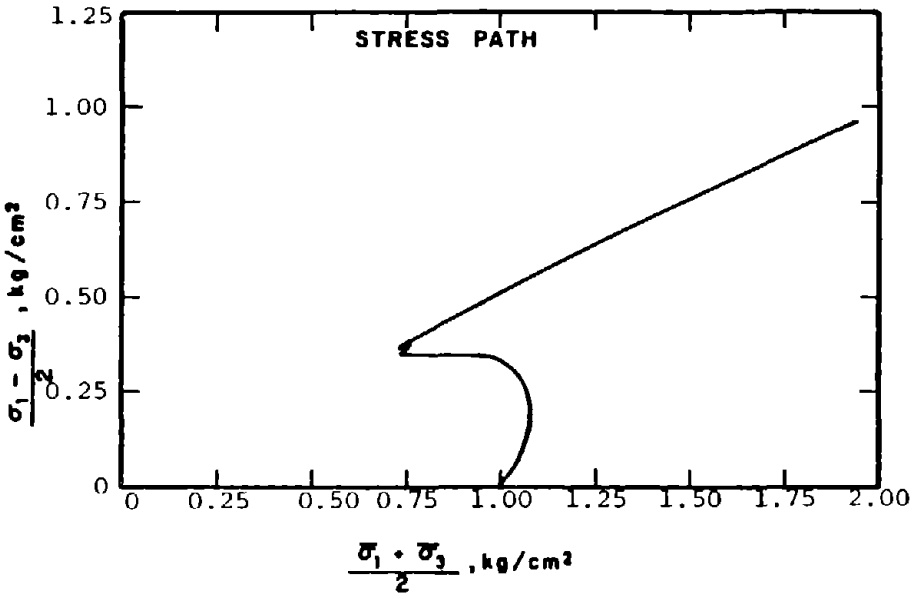

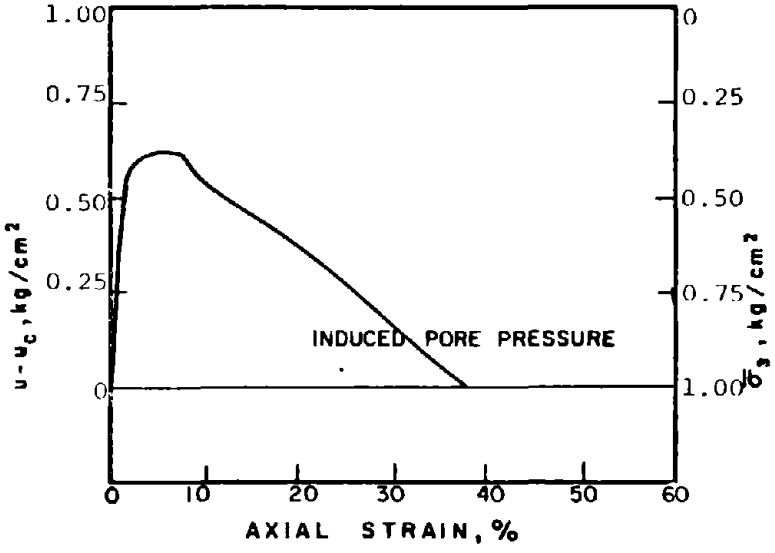

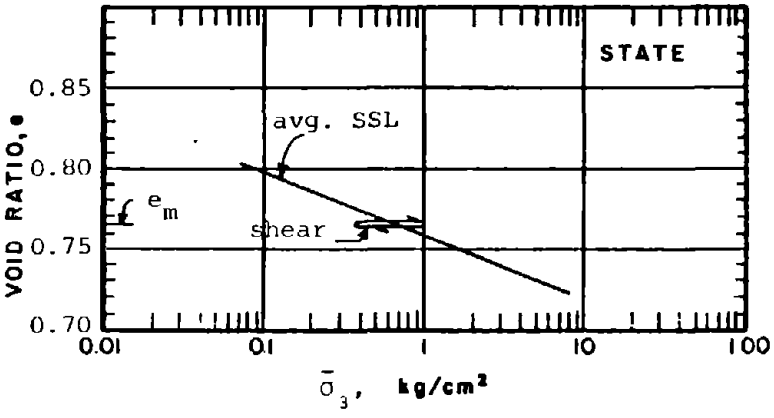

R-618

SOIL : Banding Sand #6

STRUCTURE : Compacted Moist

STATE AFTER CONSOLIDATION: $\bar{\sigma}_{3c}$ = 1.00 kg/cm², $\bar{\sigma}_{1c}$ = 1.00 kg/cm²
e_c = 0.765, γ_{dc} = 94.0 pcf

METHOD OF LOADING: Undrained Axial Compression
Load Control

TESTING DETAILS : Specimen Diameter 3.60 cm
: Specimen Height 5.30 cm
: End Platens: Lubricated, Type 1

Fig. 4-4: Type B-E Stress-Strain Curves

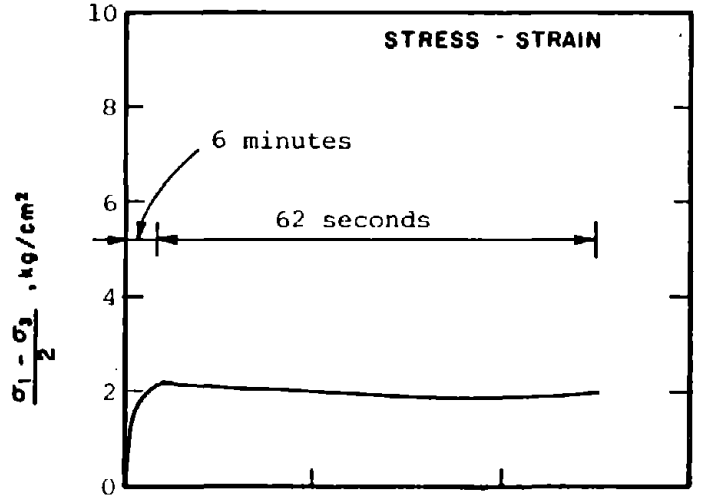

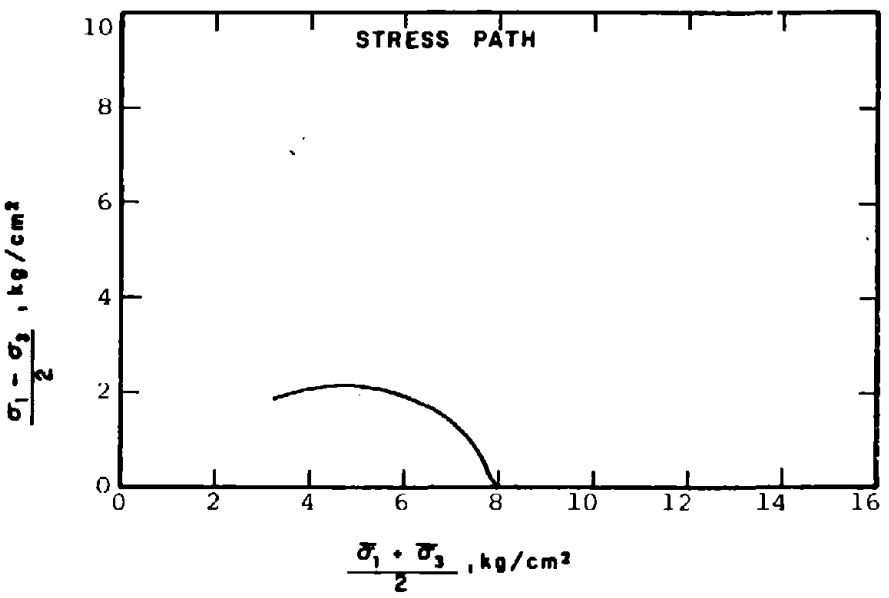

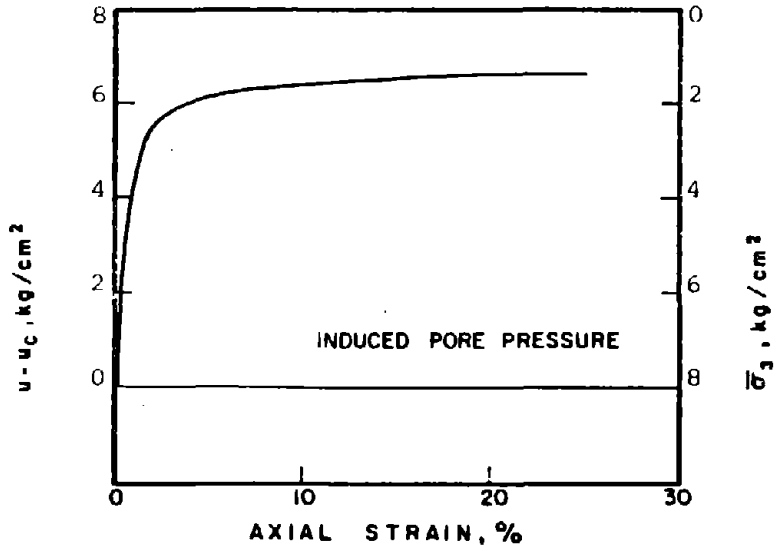

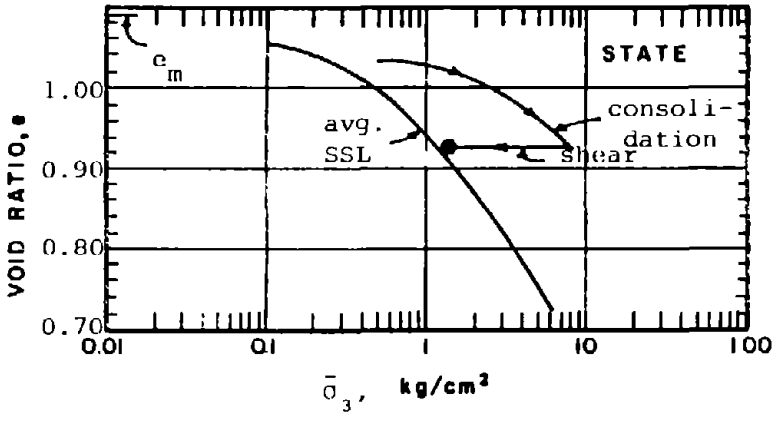

SOIL	: Mine Tailings	METHOD OF LOADING:	Undrained, Axial Compression Load Control
STRUCTURE	: Compacted Moist		
STATE AFTER CONSOLIDATION:	$\bar{\sigma}_{3c}$ =8.00 kg/cm², $\bar{\sigma}_{1c}$ =8.00 kg/cm²	TESTING DETAILS	: Specimen Diameter 3.60 cm
	e_c =0.921 , γ_{dc} = 87.0 pcf		: Specimen Height 5.30 cm
			: End Platens: Lubricated, Type 1

R-1002

Fig. 4-5: Type A-B Stress-Strain Curves

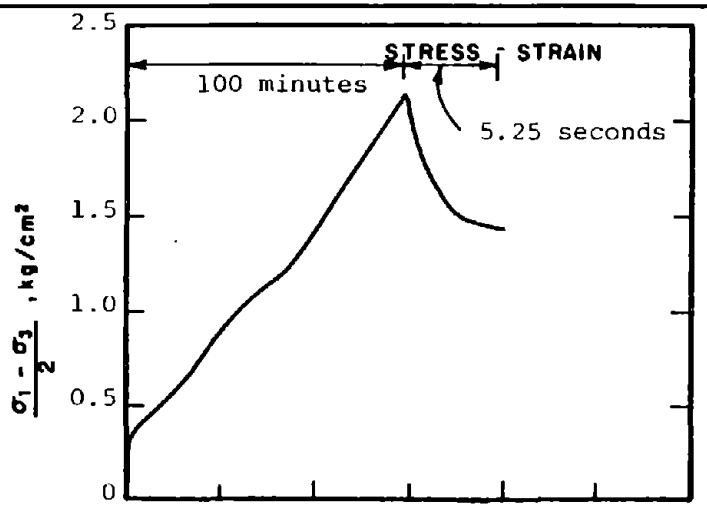

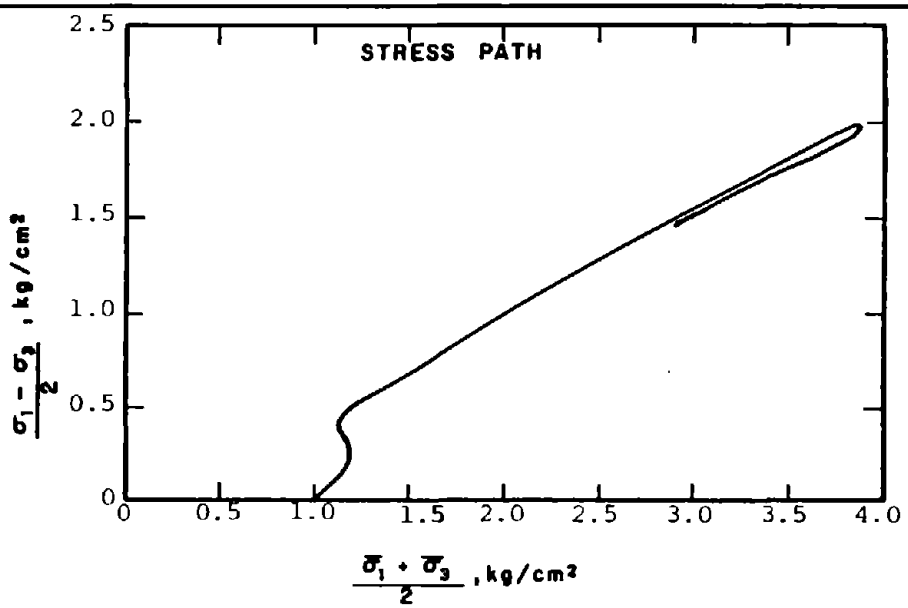

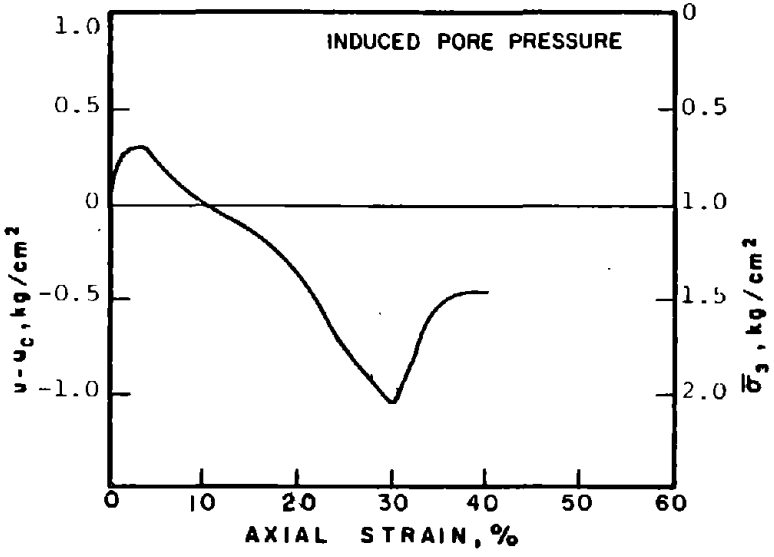

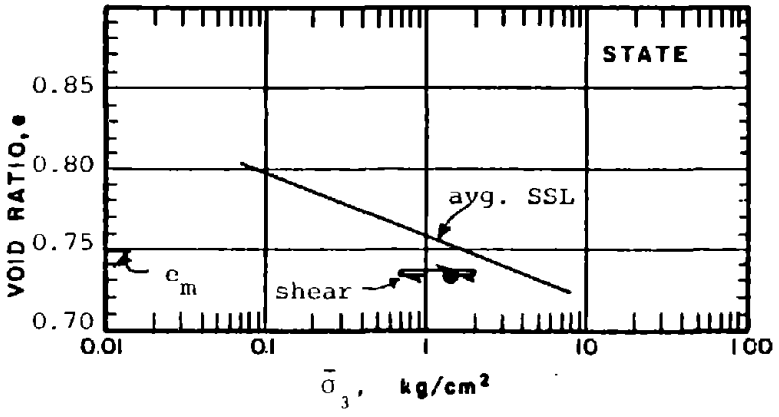

SOIL	: Banding Sand #6	METHOD OF LOADING:	Undrained Axial Compression Load Control
STRUCTURE	: Compacted Moist		
STATE AFTER CONSOLIDATION:	$\bar{\sigma}_{3c}$ = 1.00 kg/cm², $\bar{\sigma}_{1c}$ = 1.00 kg/cm²	TESTING DETAILS	: Specimen Diameter 3.60 cm
	e_c = 0.734, γ_{dc} = 95.7 pcf		: Specimen Height 5.30 cm
			: End Platens: Lubricated, Type 1

R-619

Fig. 4-6: Typical Type C Stress-Strain Curves

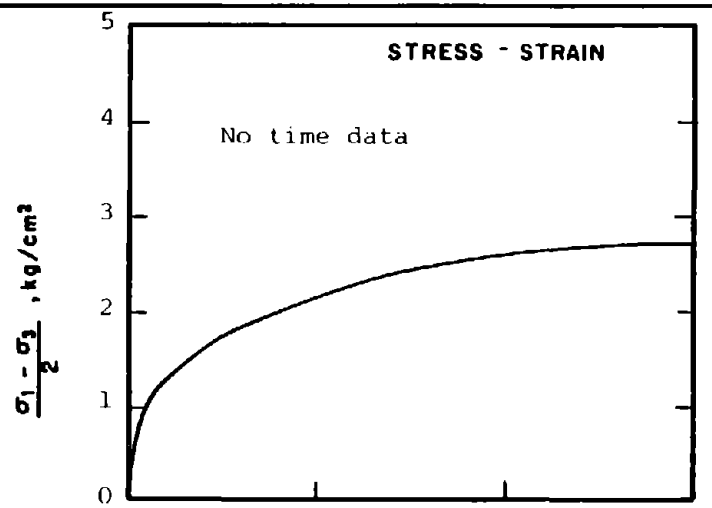

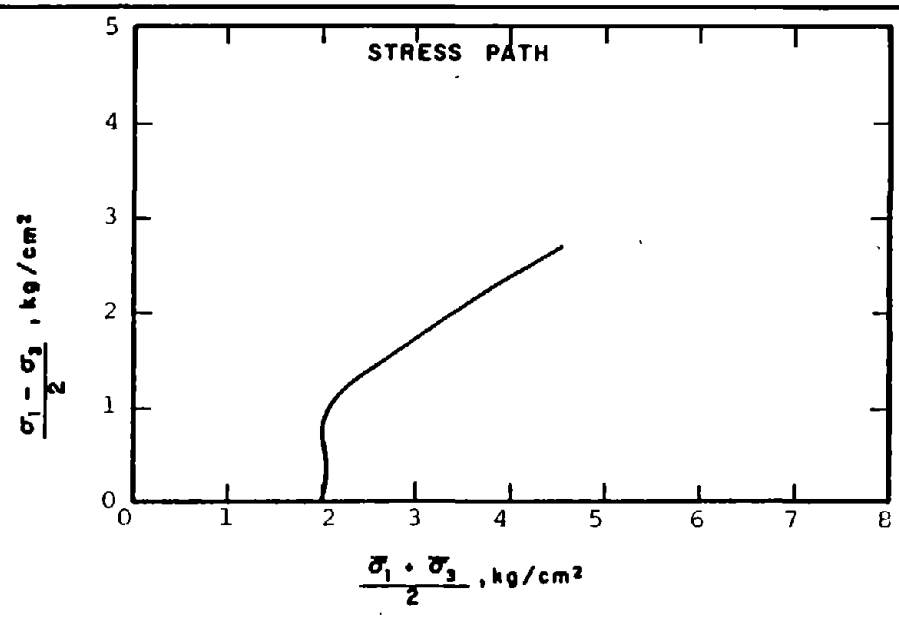

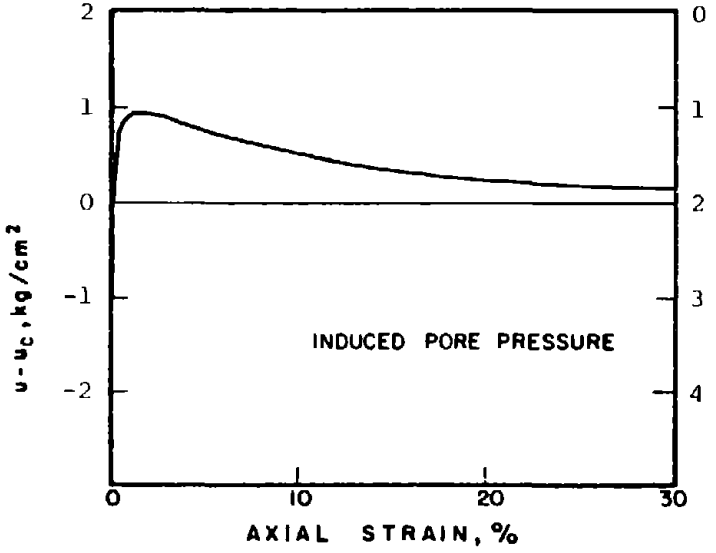

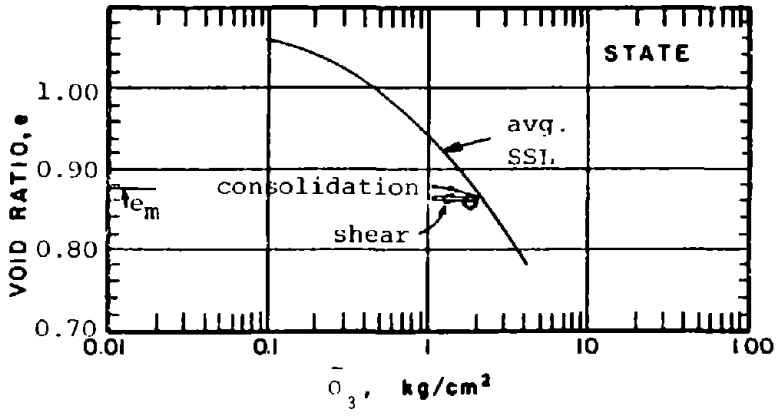

SOIL	: Mine Tailings	METHOD OF LOADING:	Undrained, Axial Compression Load Control
STRUCTURE	: Compacted Moist		
STATE AFTER CONSOLIDATION:	$\bar{\sigma}_{3c}$ = 2.00 kg/cm², $\bar{\sigma}_{1c}$ = 2.00 kg/cm²	TESTING DETAILS	: Specimen Diameter 3.60 cm
	e_c = 0.863, γ_{dc} = 89.8 pcf		: Specimen Height 5.30 cm
			: End Platens: Lubricated, Type 2

R-1026

Fig. 4-7: Typical Type D Stress-Strain Curves

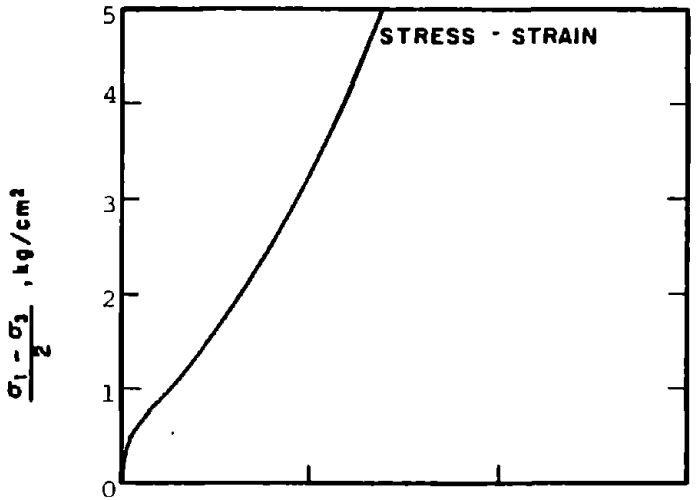

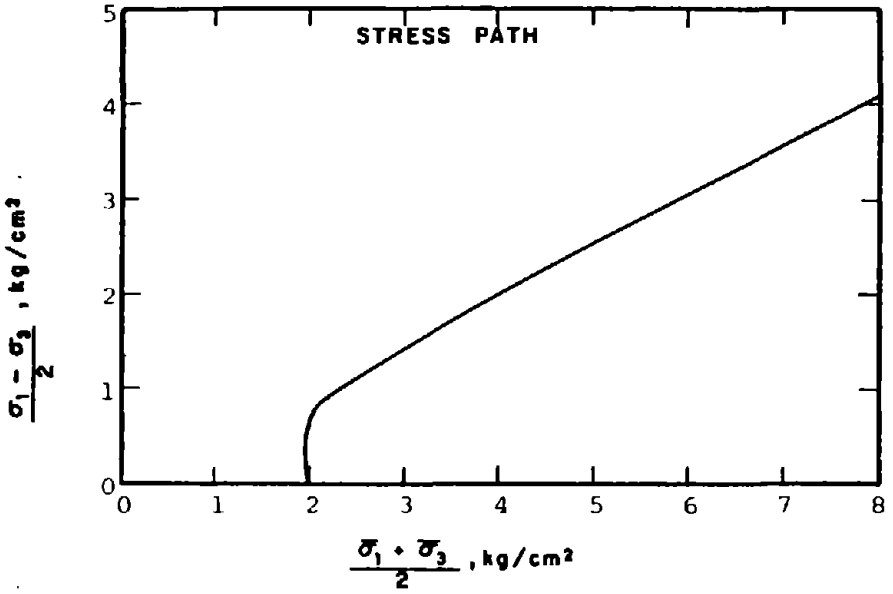

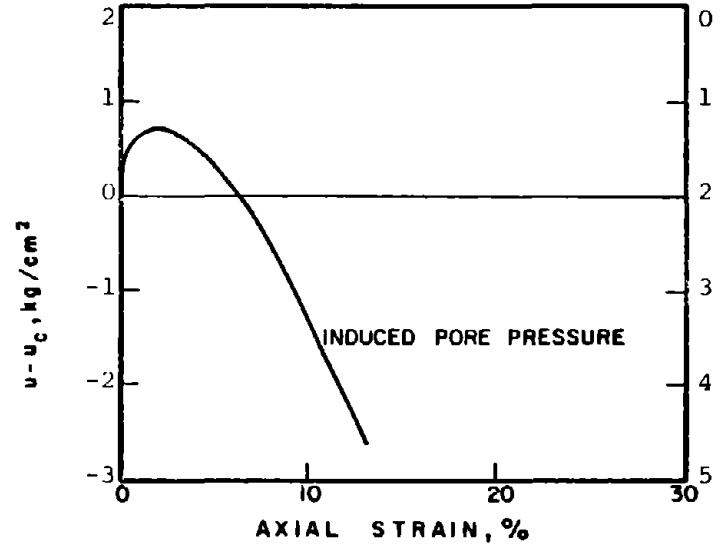

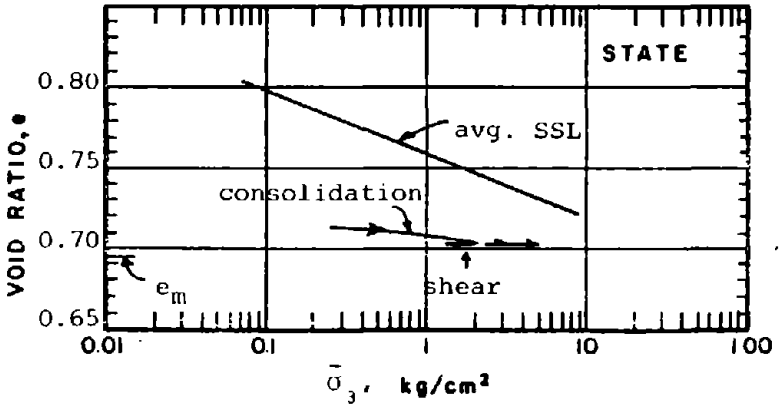

SOIL	: Banding Sand #6	METHOD OF LOADING:	Undrained, Axial Compression Load Control
STRUCTURE	: Compacted Moist		
STATE AFTER CONSOLIDATION:	$\bar{\sigma}_{3c}$ = 2.00 kg/cm², $\bar{\sigma}_{1c}$ = 2.00 kg/cm²	TESTING DETAILS	: Specimen Diameter 3.60 cm
	e_c = 0.704, γ_{dc} = 97.4 pcf		: Specimen Height 5.30 cm
			: End Platens: Lubricated, Type 1

R-617

Fig. 4-8: Typical Type E Stress-Strain Curves

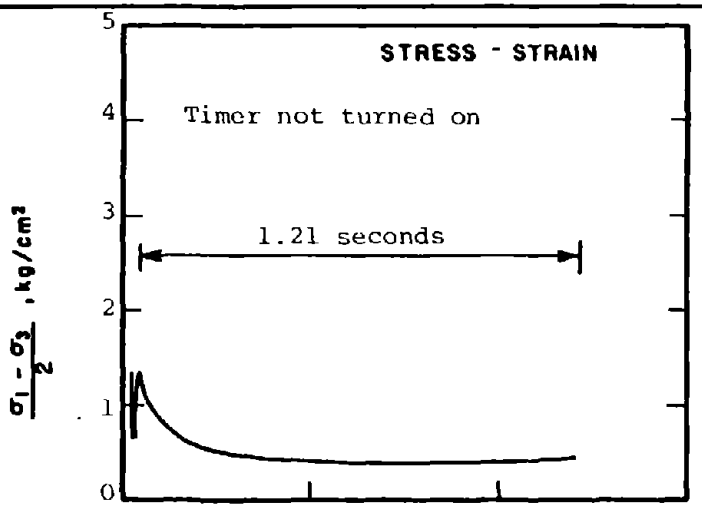

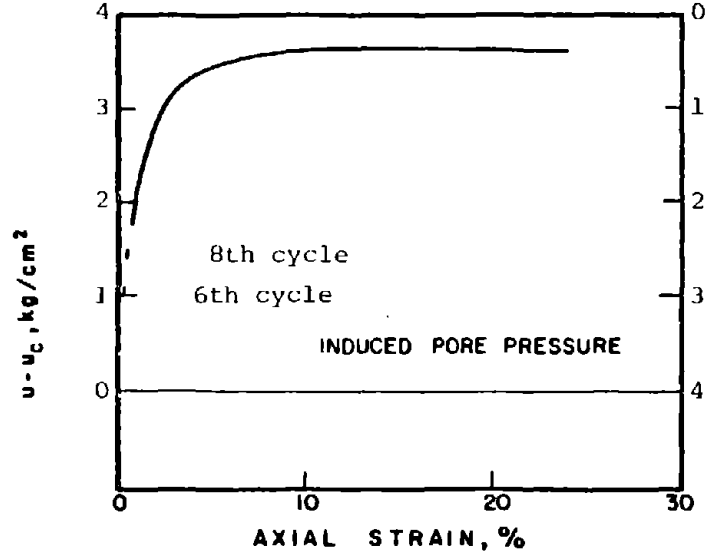

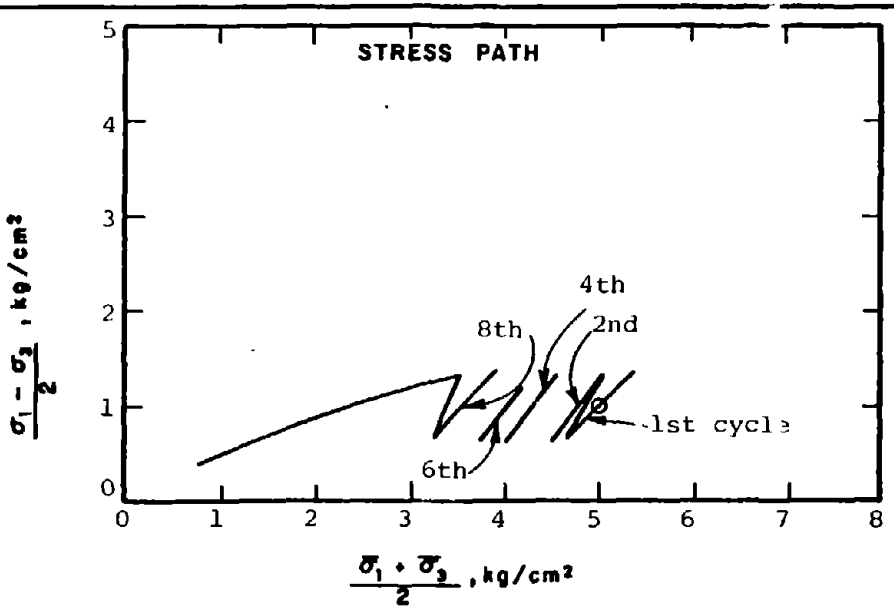

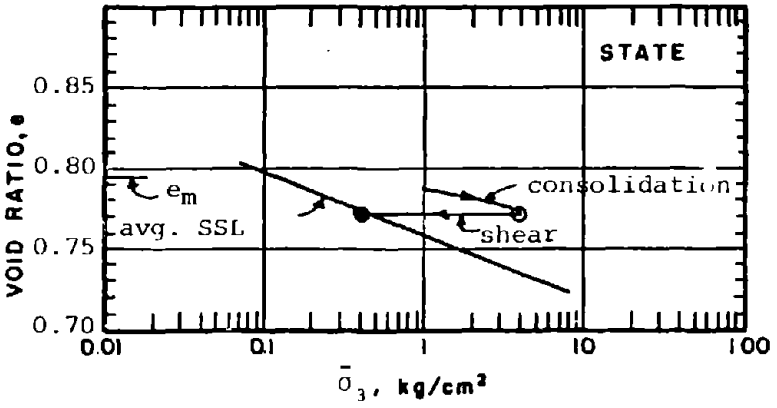

SOIL	: Banding Sand #6	METHOD OF LOADING:	Undrained, Cyclic Axial Compression Load Control
STRUCTURE	: Compacted Moist		$(\sigma_1 - \sigma_3)_{cy}$ = 0.72 ksc
STATE AFTER CONSOLIDATION:	$\bar{\sigma}_{3c}$ = 4.00 kg/cm², $\bar{\sigma}_{1c}$ = 6.00 kg/cm²	TESTING DETAILS	: Specimen Diameter 3.60 cm
	e_c = 0.771, γ_{dc} = 93.7 pcf		: Specimen Height 5.30 cm
			: End Platens: Lubricated, Type 1

CAR-608

Fig. 4-9: Typical Type F Stress-Strain Curves

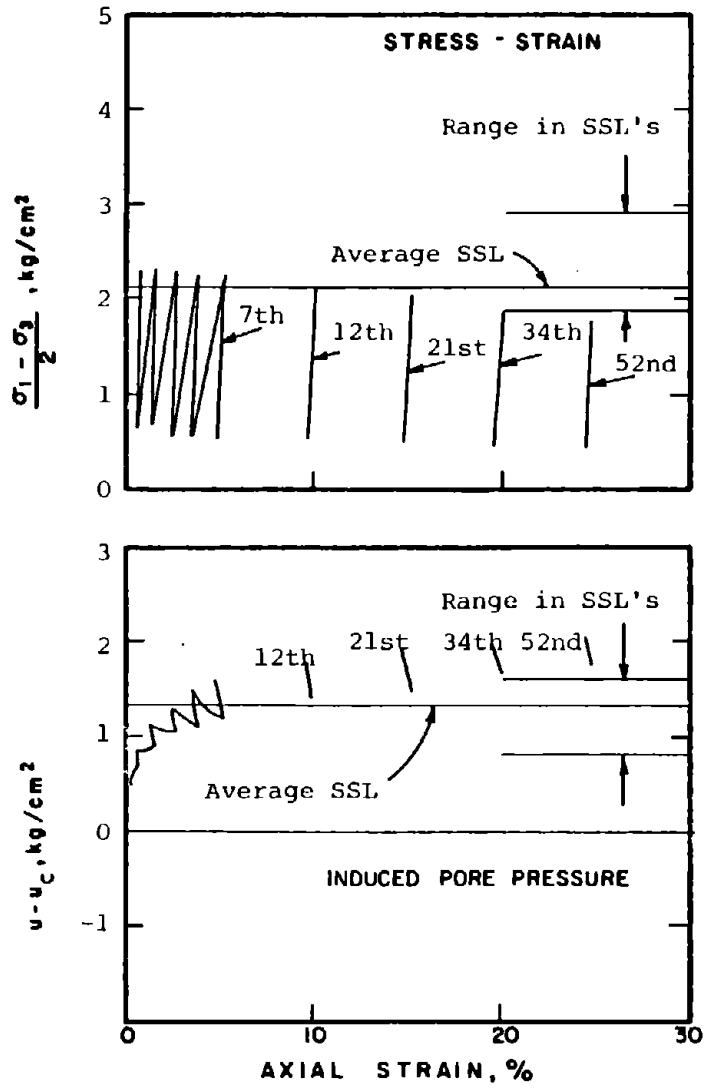

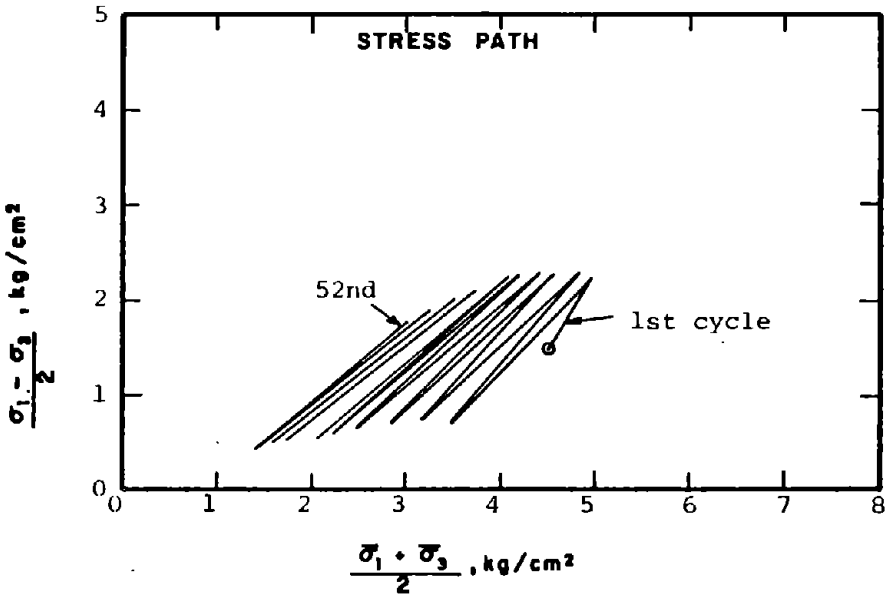

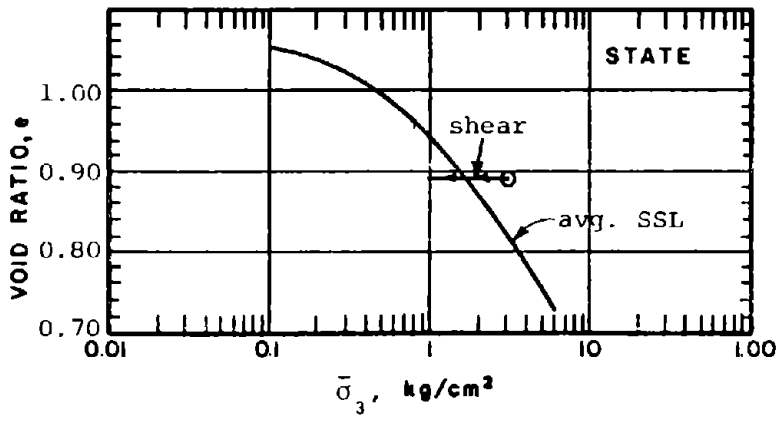

SOIL	: Mine Tailings	METHOD OF LOADING:	Undrained, Cyclic Axial Compression Load Control $(\sigma_1 - \sigma_3)_{cy}$ = 1.67 ksc
STRUCTURE	: Compacted Moist		
STATE AFTER CONSOLIDATION:	$\bar{\sigma}_{3c}$ = 3.00 kg/cm², $\bar{\sigma}_{1c}$ = 6.00 kg/cm²	TESTING DETAILS	: Specimen Diameter 3.60 cm
	e_c = 0.891, γ_{dc} = 88.4 pcf		: Specimen Height 5.30 cm
			: End Platens: Lubricated, Type 2

CAR-1007b

Fig. 4-10: Typical Type G Stress-Strain Curves

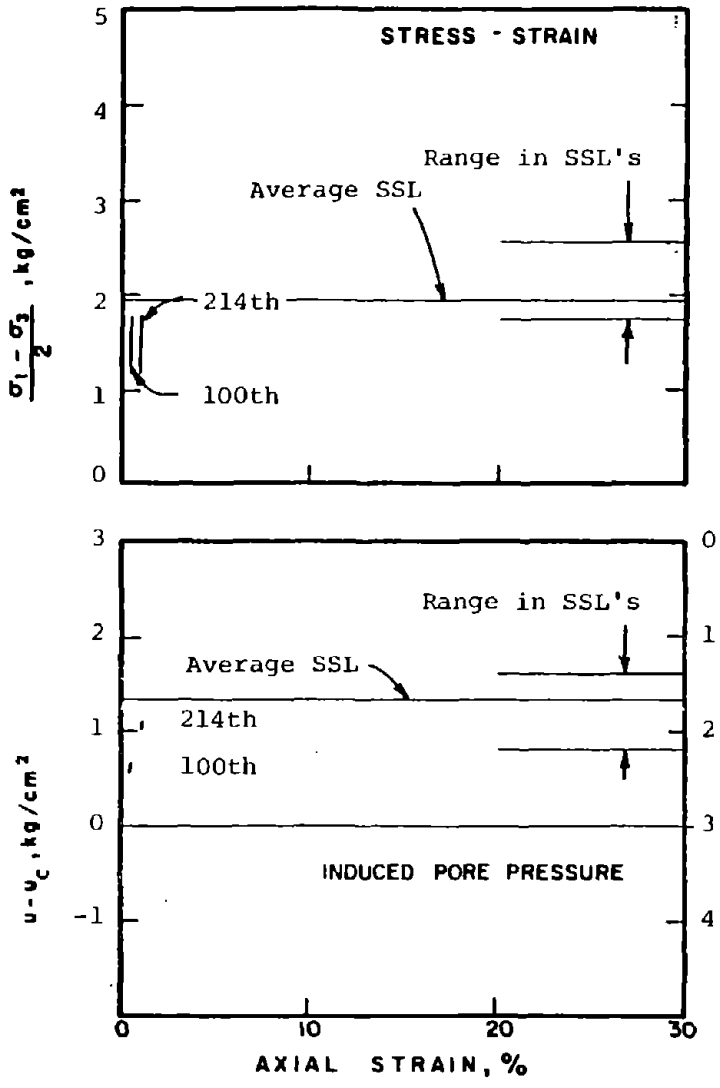

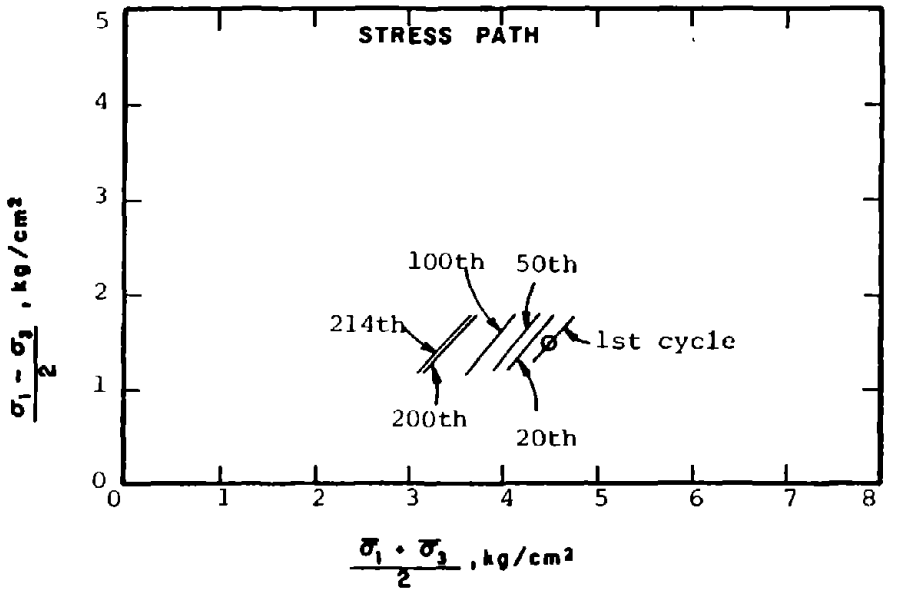

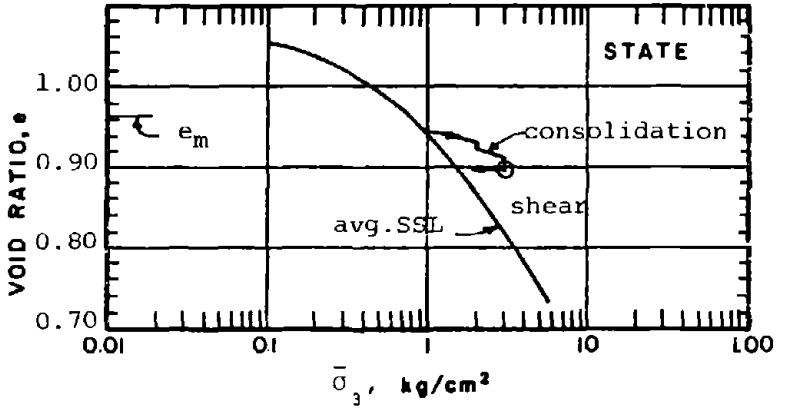

CAR-1007

SOIL : Mine Tailings

STRUCTURE : Compacted Moist

STATE AFTER CONSOLIDATION: $\bar{\sigma}_{3c}$ = 3.00 kg/cm², $\bar{\sigma}_{1c}$ = 6.00 kg/cm²
e_c = 0.899, γ_{dc} = 88.1 pcf

METHOD OF LOADING: Undrained, Cyclic Axial Compression
Load Control
$(\sigma_1 - \sigma_3)_{cy}$ = 0.61 ksc

TESTING DETAILS : Specimen Diameter 3.60 cm
: Specimen Height 5.30 cm
: End Platens: Lubricated, Type 2

Fig. 4-11: Typical Type H Stress-Strain Curves

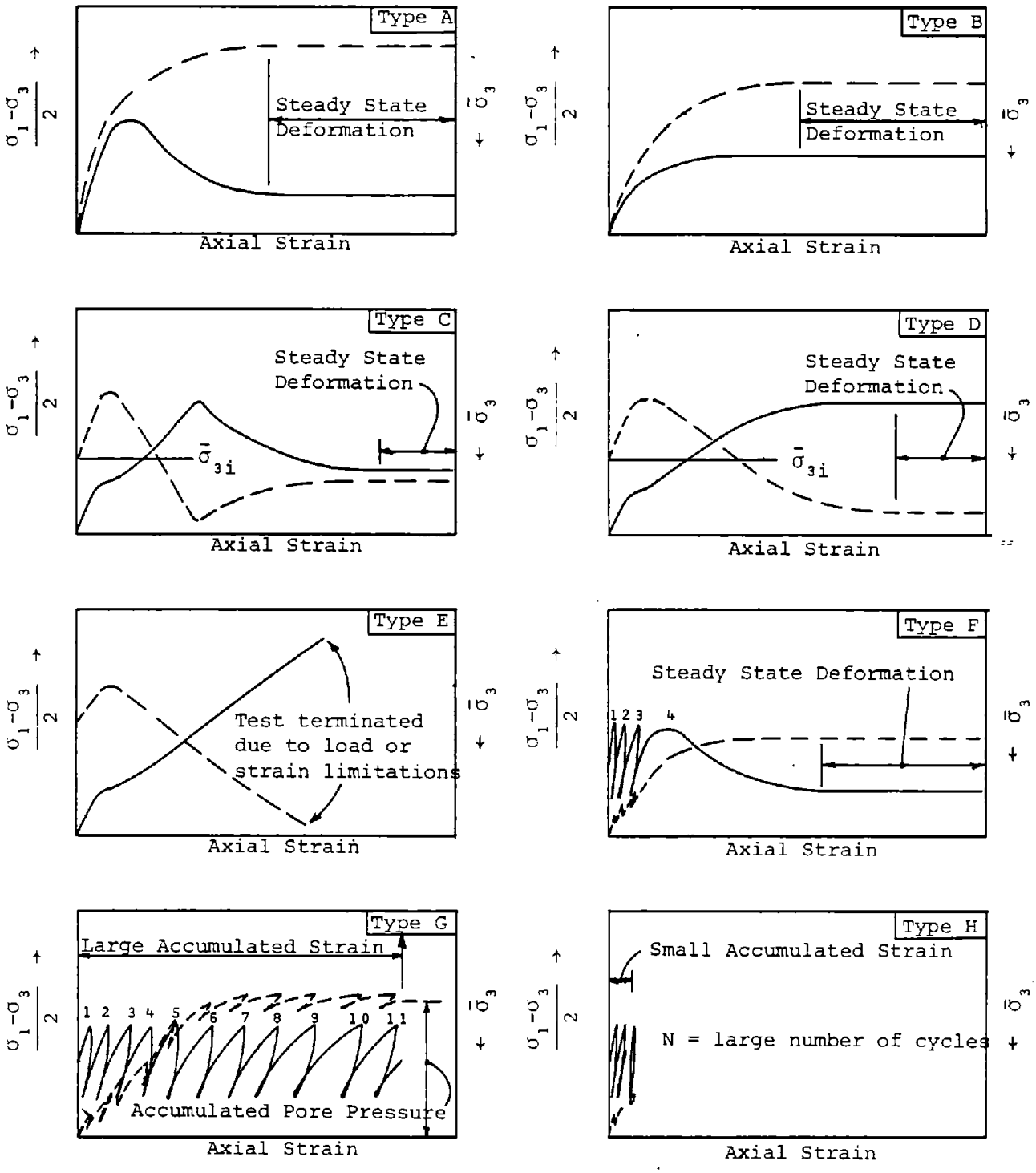

Fig. 4-12: Schematic Illustrations or Types of Stress-Strain Curves Observed

LEGEND

1) Types of stress-strain curves:

Symbol	Type
●	A
⏃	B-E
■	C
o	E

See text for discussion

2) Avg. SSL indicates average steady state line

3) Where more than one test had the same consolidation state, the numbers next to the data points indicate the number of tests represented by the point.

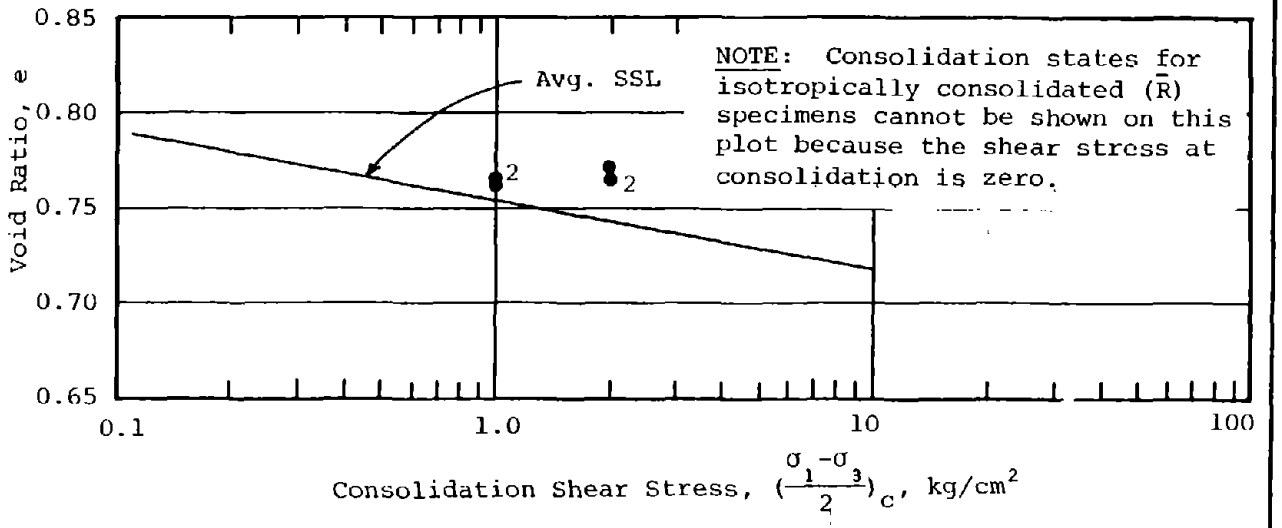

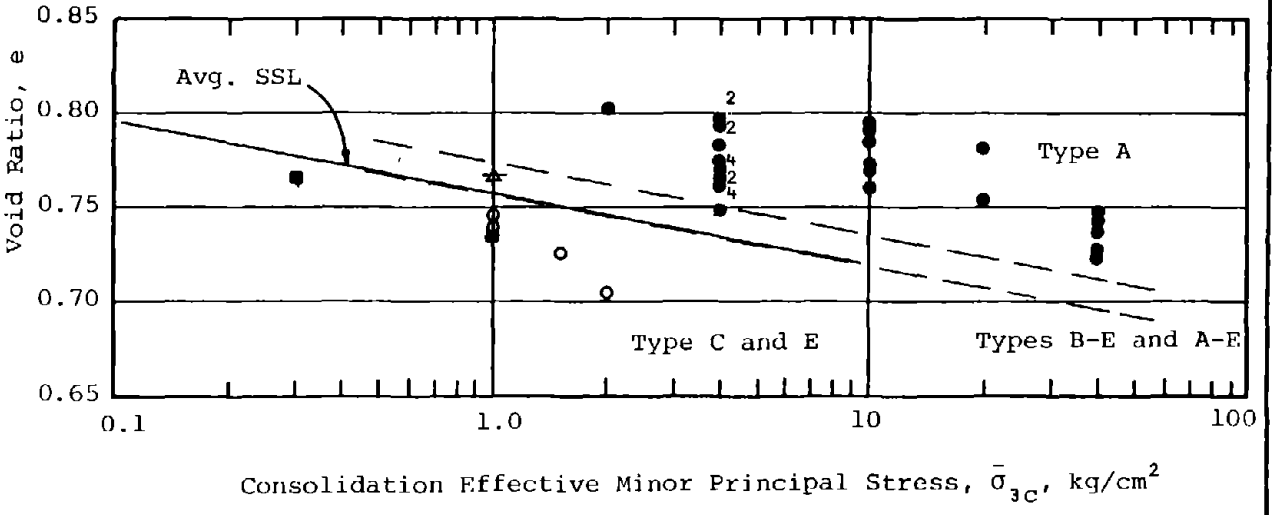

Fig. 4-13: Types of Stress-Strain Curves Observed for Different Consolidation States for R̄ and AR̄ Tests on Banding Sand #6

LEGEND

1) Types of stress-strain curves:

Symbol	Type
●	A
▲	B
★	A-B
▼	D

See text for discussion

2) Avg. SSL indicates average steady state line

3) Where more than one test had the same consolidation state, the numbers next to the data points indicate the number of tests represented by the point.

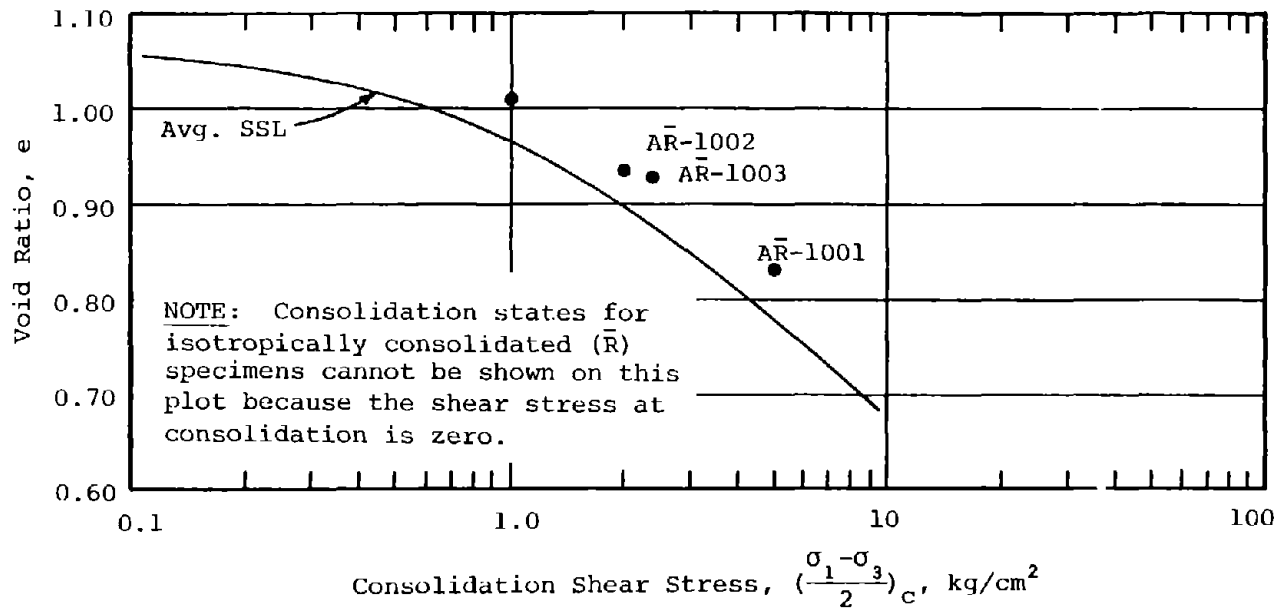

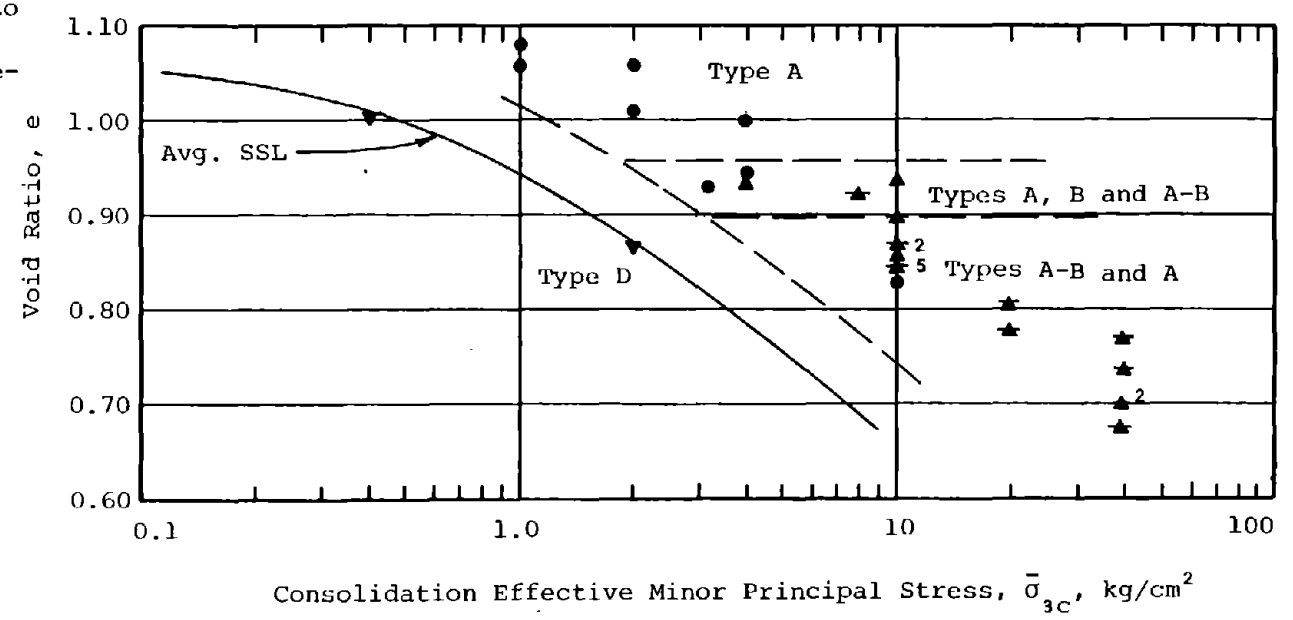

Fig. 4-14: Types of Stress-Strain Curves Observed for Different Consolidation States for R̄ and AR on Mine Tailings

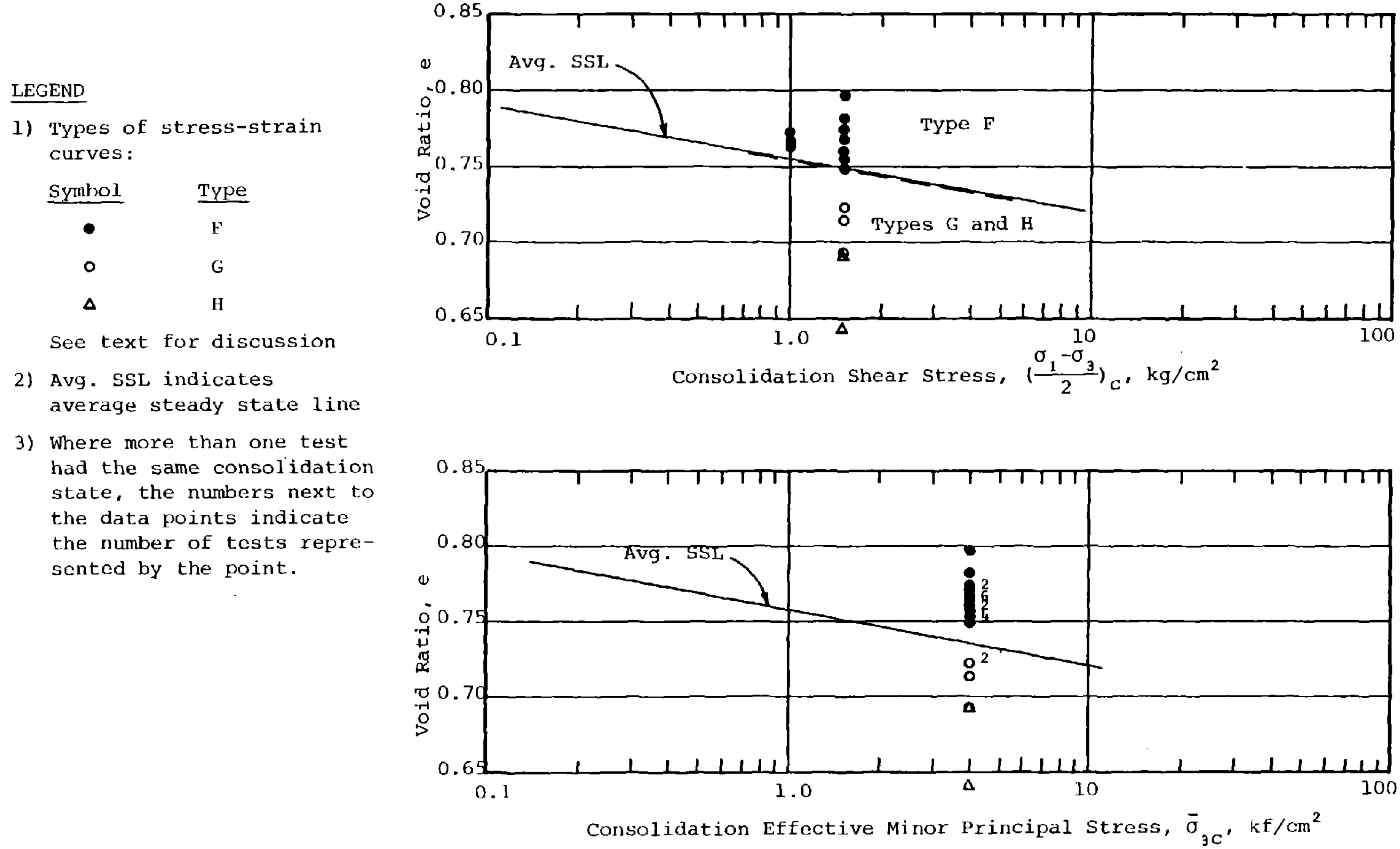

Fig. 4-15: Types of Stress-Strain Curves Observed for Different Consolidation States for CA$\bar{R}$ Tests on Banding Sand #6

LEGEND

1) Types of stress-strain curves:

Symbol	Type
●	F
o	G
△	H

See text for discussion

2) Avg. SSL indicates average steady state line

3) Where more than one test had the same consolidation state, the numbers next to the data points indicate the number of tests represented by the point.

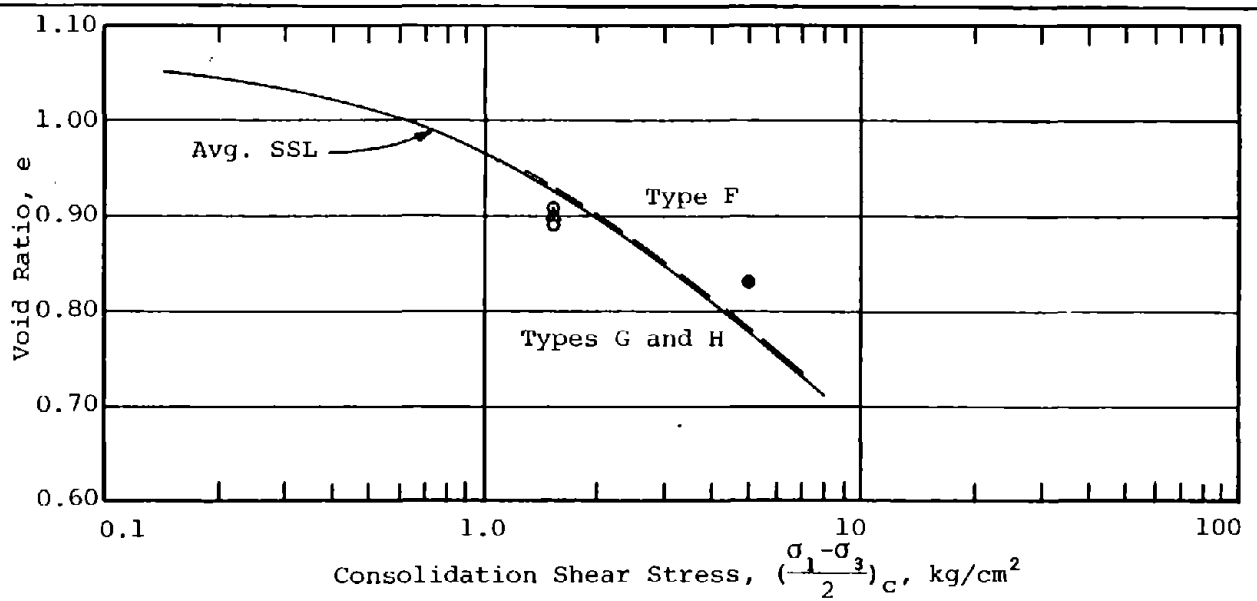

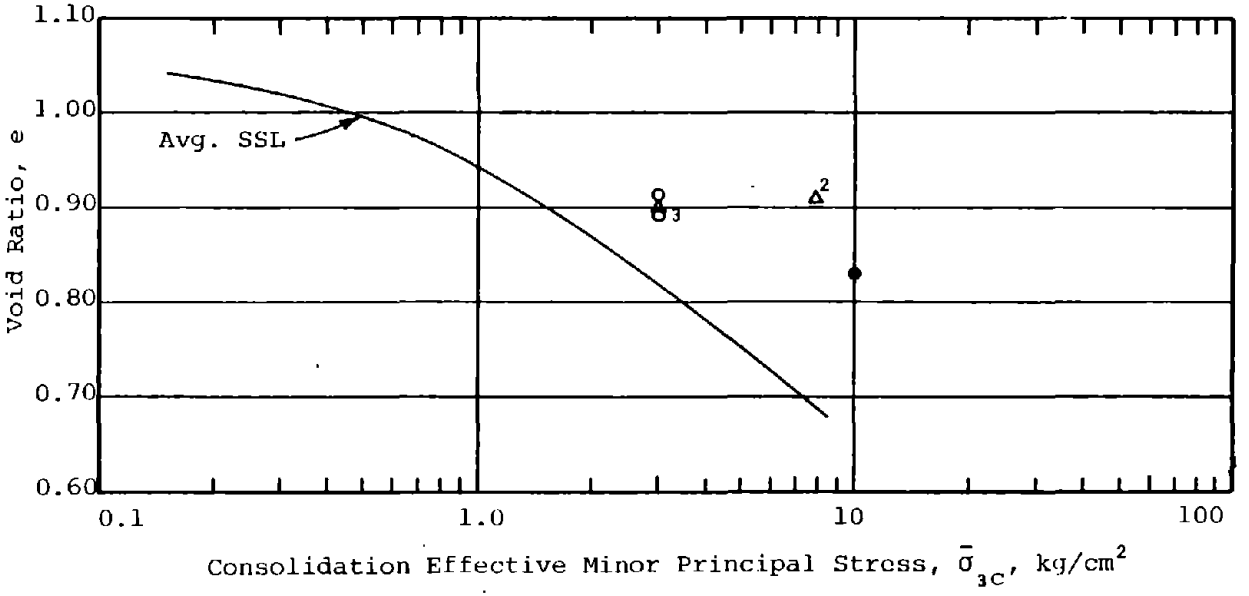

Fig. 4-16: Types of Stress-Strain Curves Observed for Different Consolidation States for CAR̄ Tests on Mine Tailings

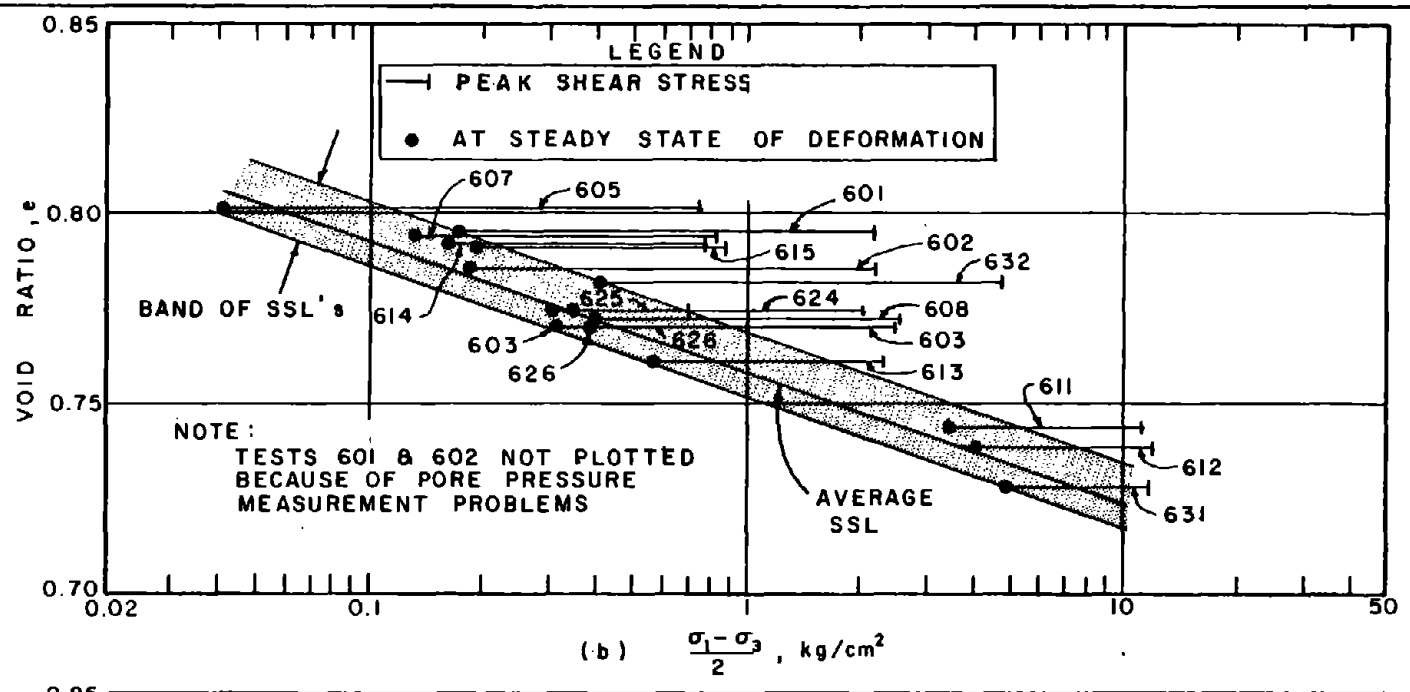

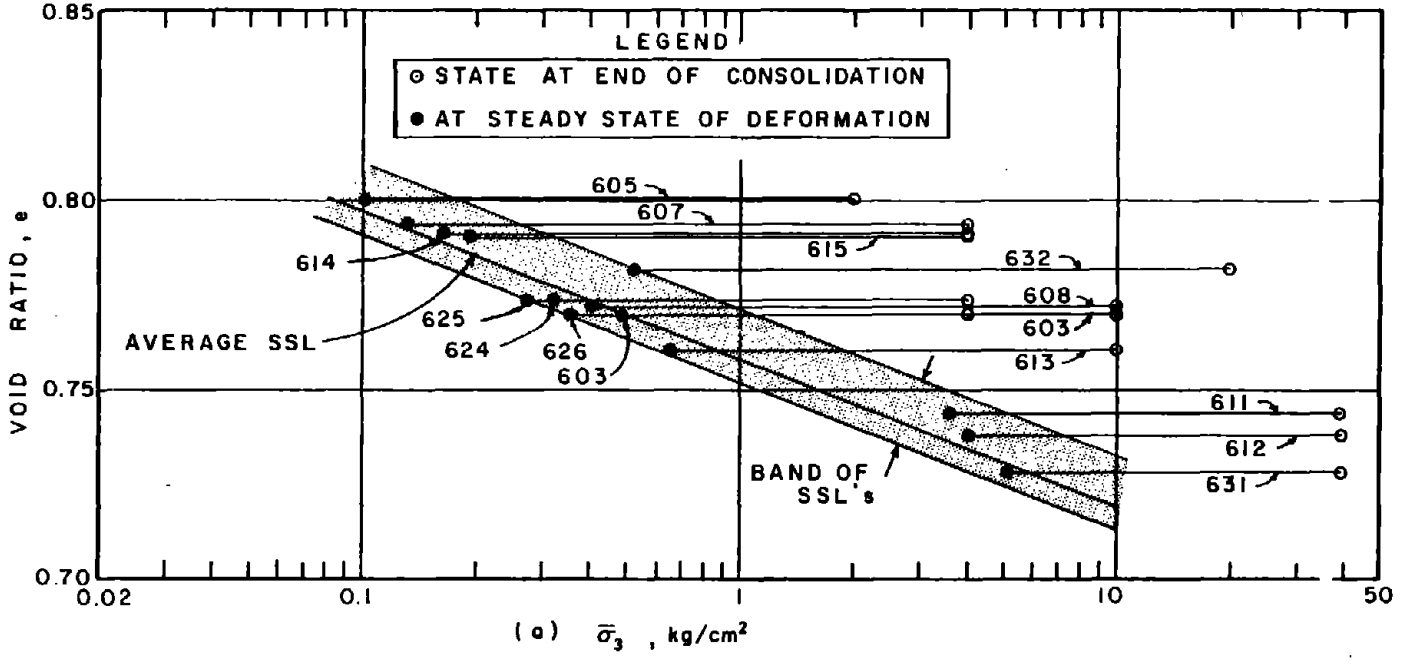

Fig. 5-1: Steady State Lines from $\bar{R}$ Tests on Banding Sand #6

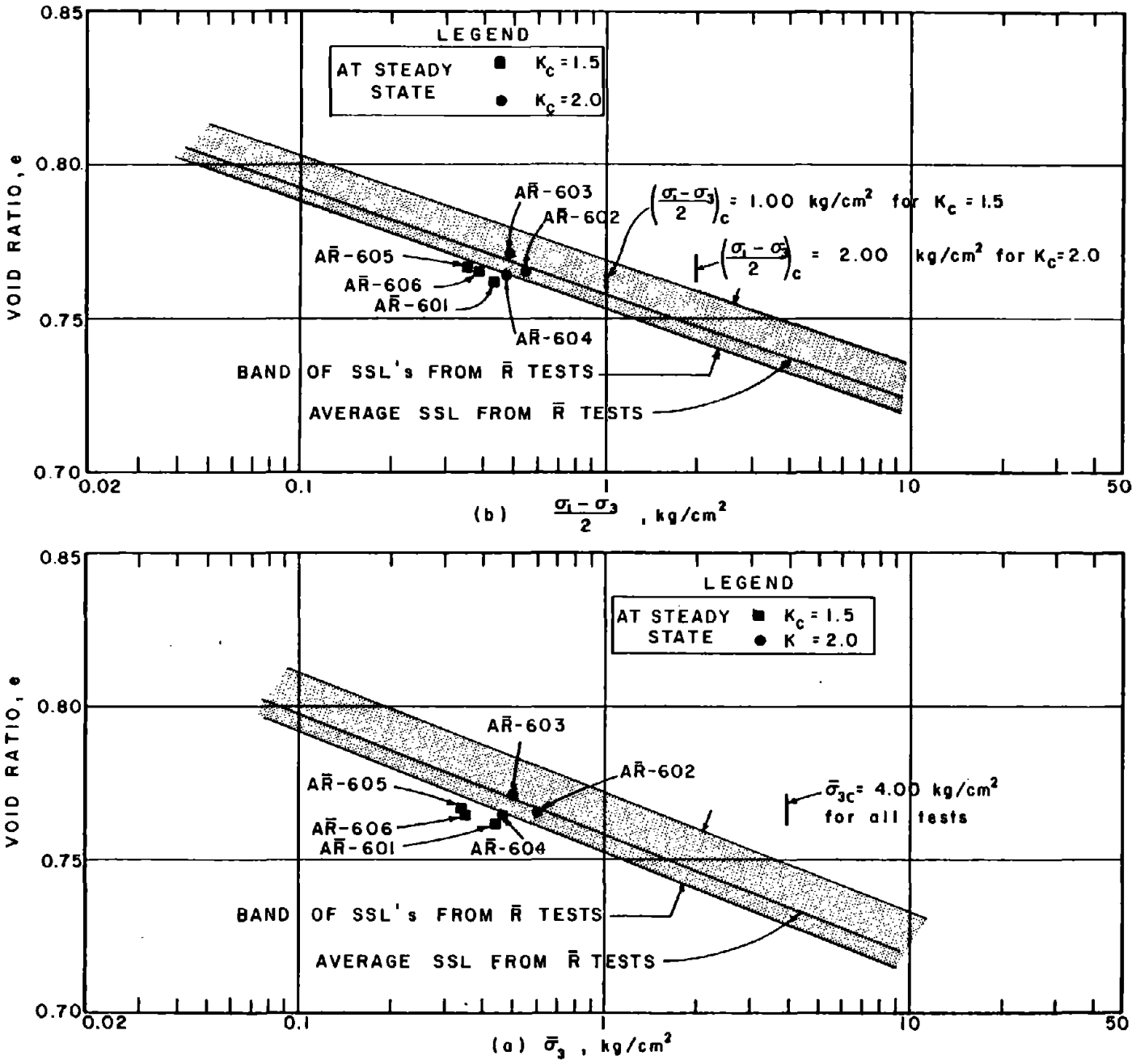

Fig. 5-2: Steady State Points from AR̄ Tests on Banding Sand #6

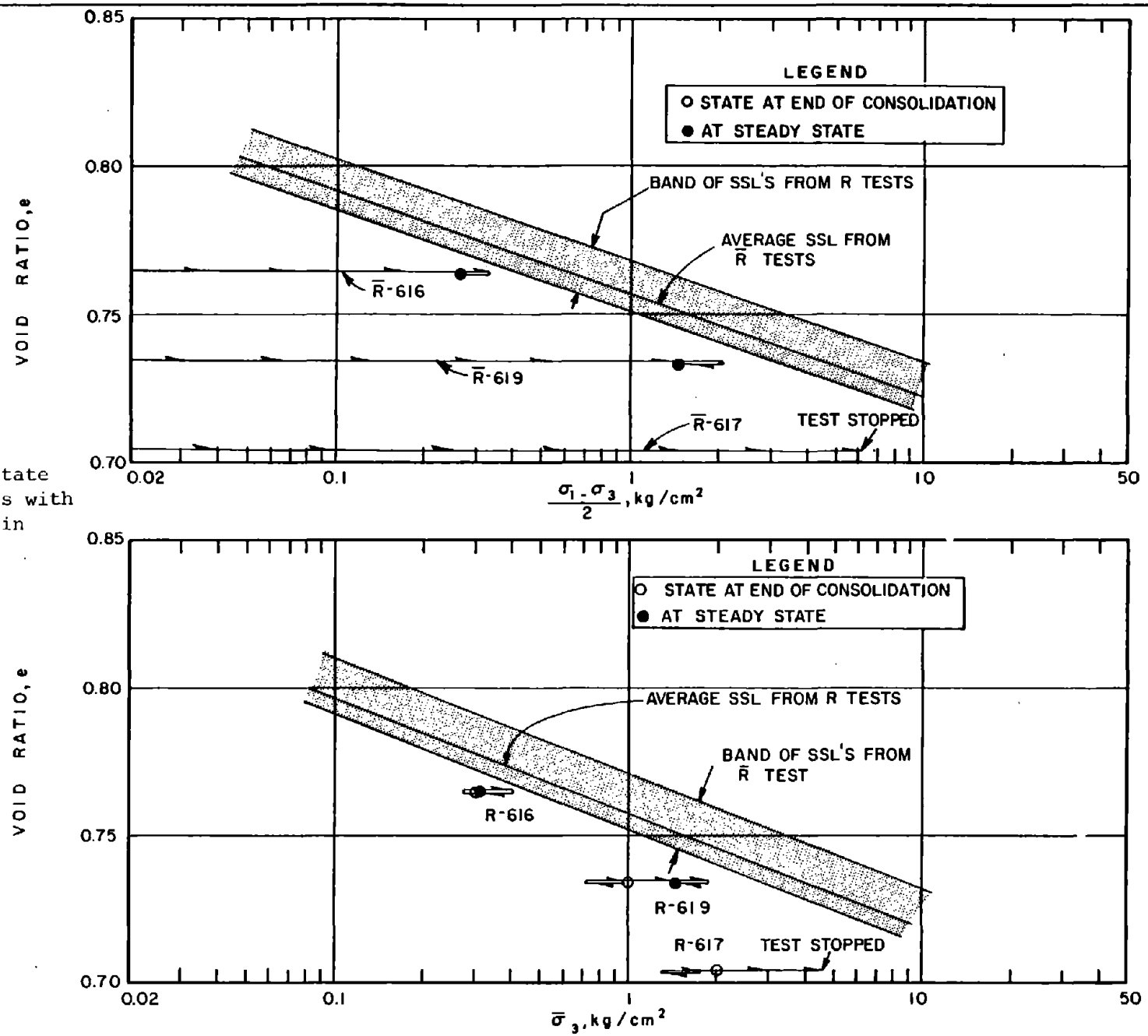

Fig. 5-3 Steady State Points from R-Tests with Type C Stress-Strain Curves.

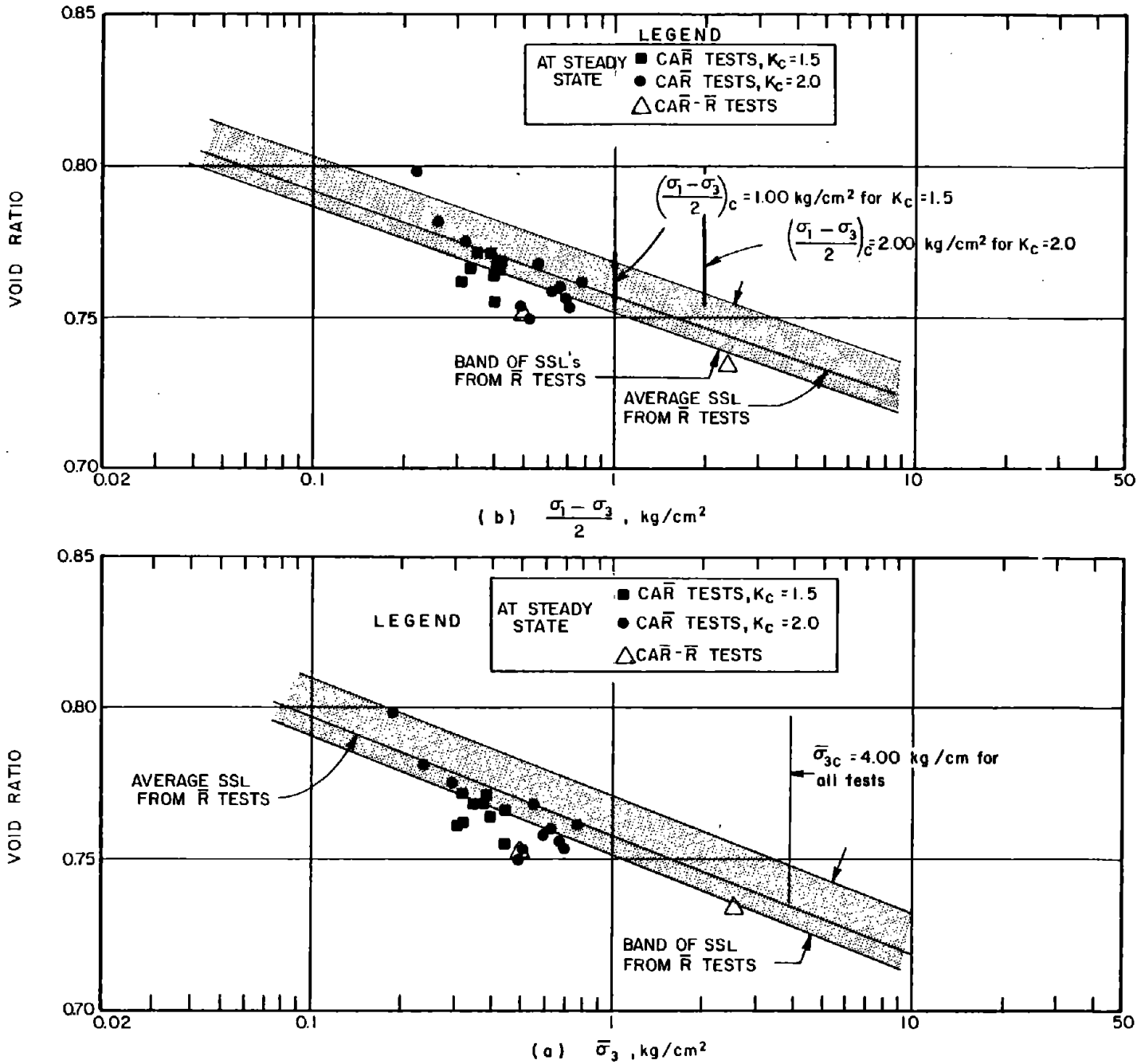

Fig. 5-4: Steady State Points from CAR̄ and CAR̄-R̄ Tests on Banding Sand #6

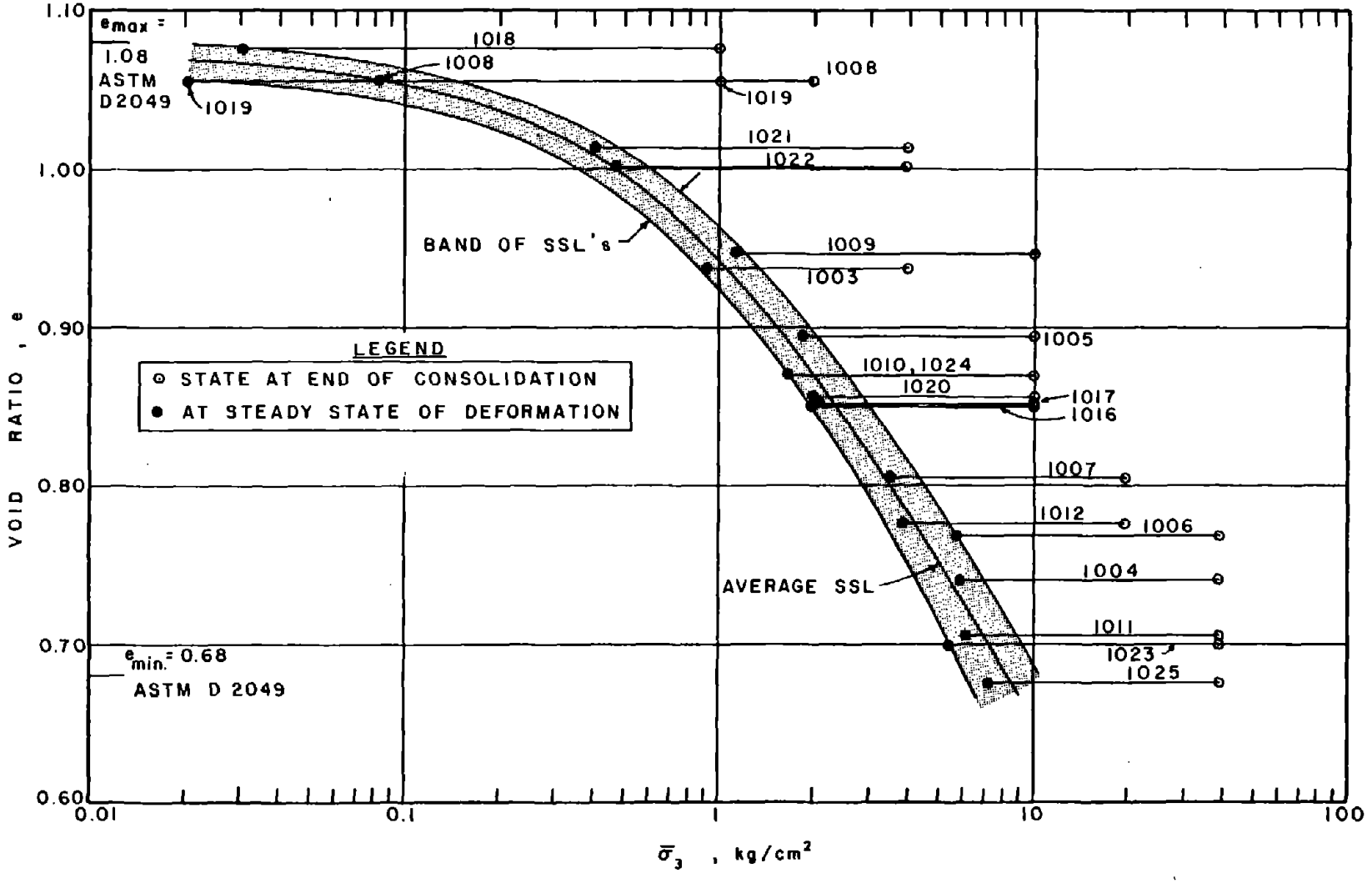

Fig. 5-5: Steady State Lines from $\bar{R}$-Tests on Mine Tailings

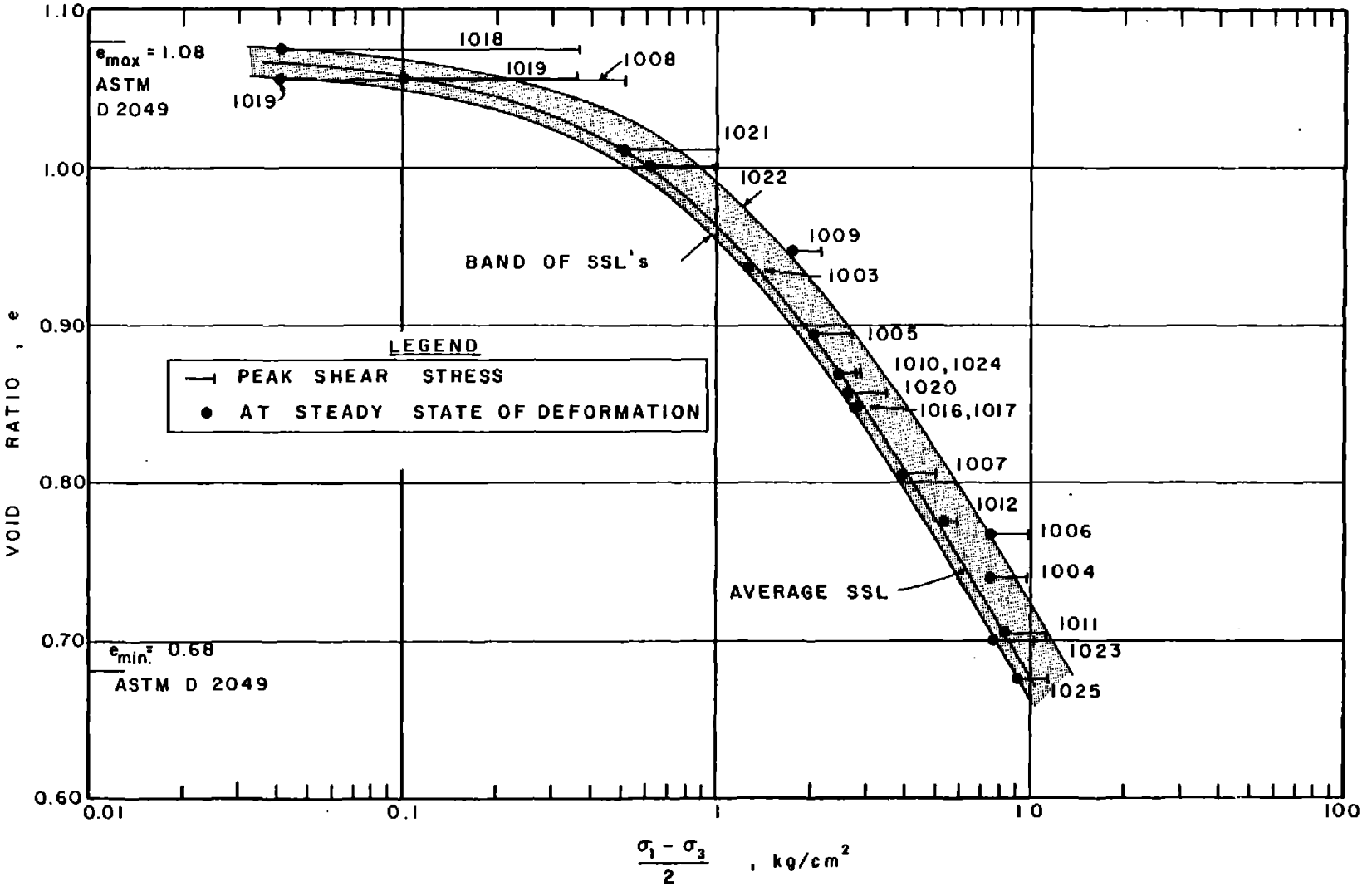

Fig. 5-6: Steady State Lines from $\bar{R}$-Tests on Mine Tailings

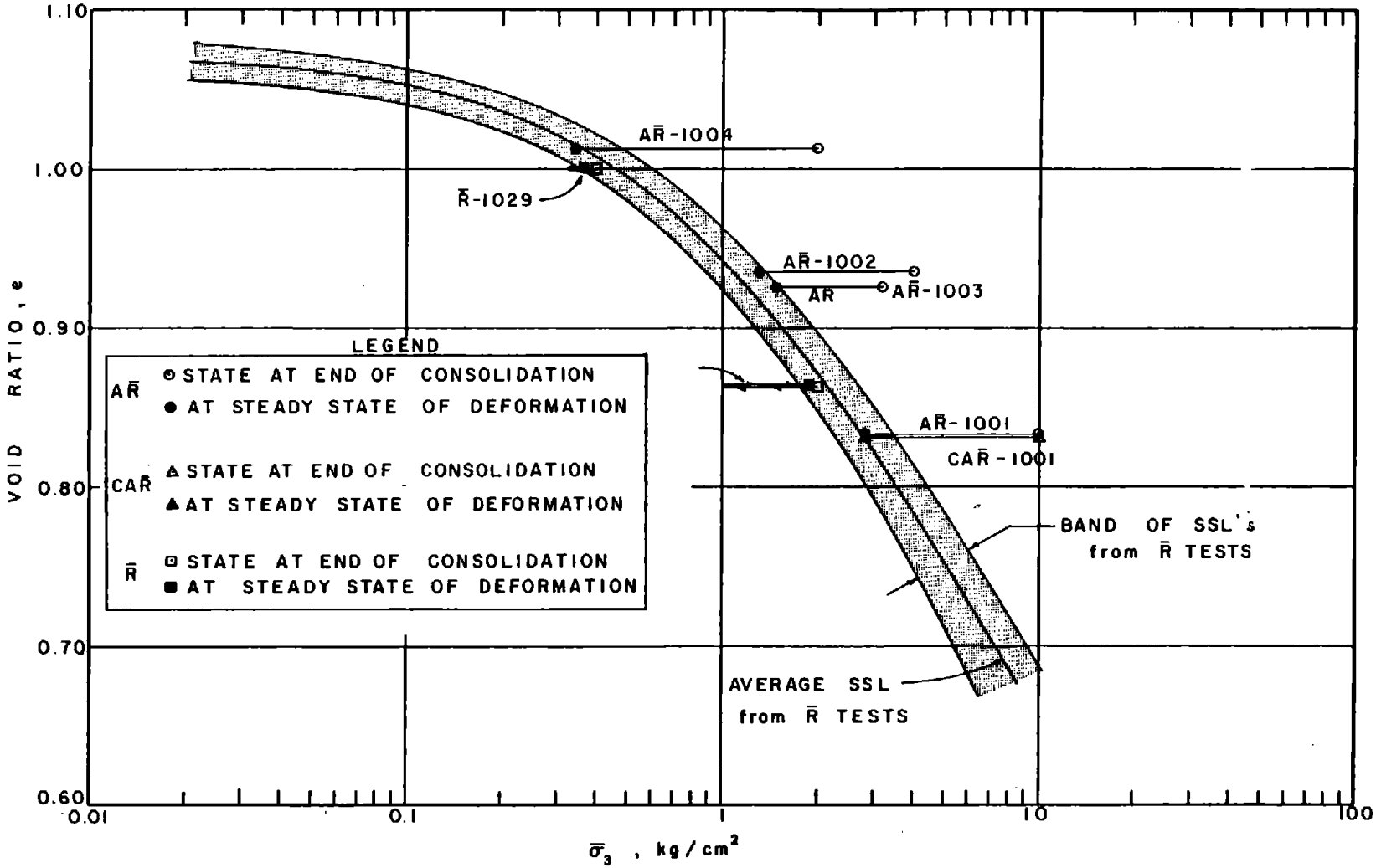

Fig. 5-7: Steady State Points from AR̄-Tests, R̄-Tests with Type D Stress-Strain Curves and CAR̄-Tests on Mine Tailings

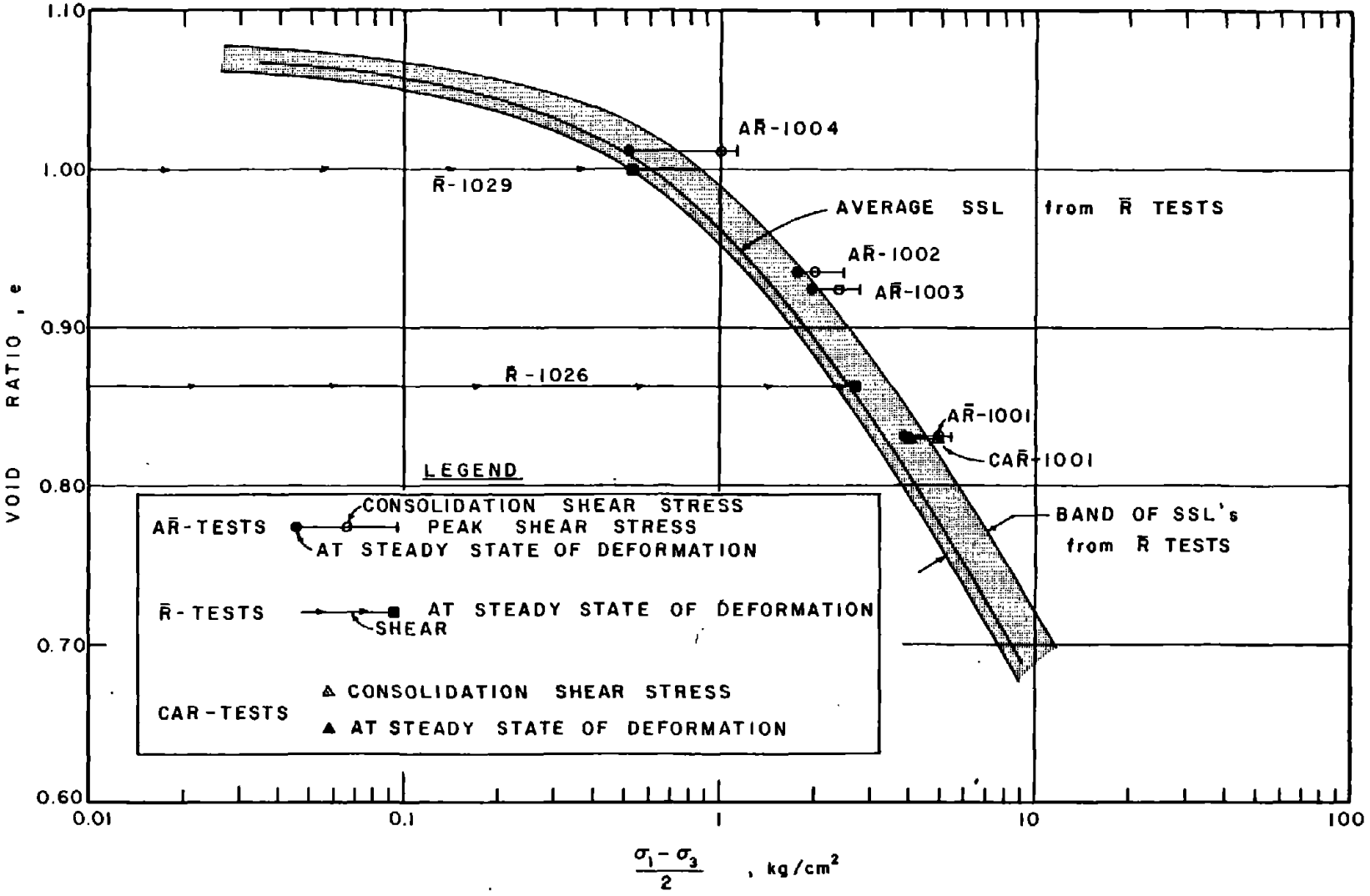

Fig. 5-8: Steady State Points from AR̄-Tests, R̄-Tests with Type D Stress-Strain Curves and CAR̄-Tests on Mine Tailings

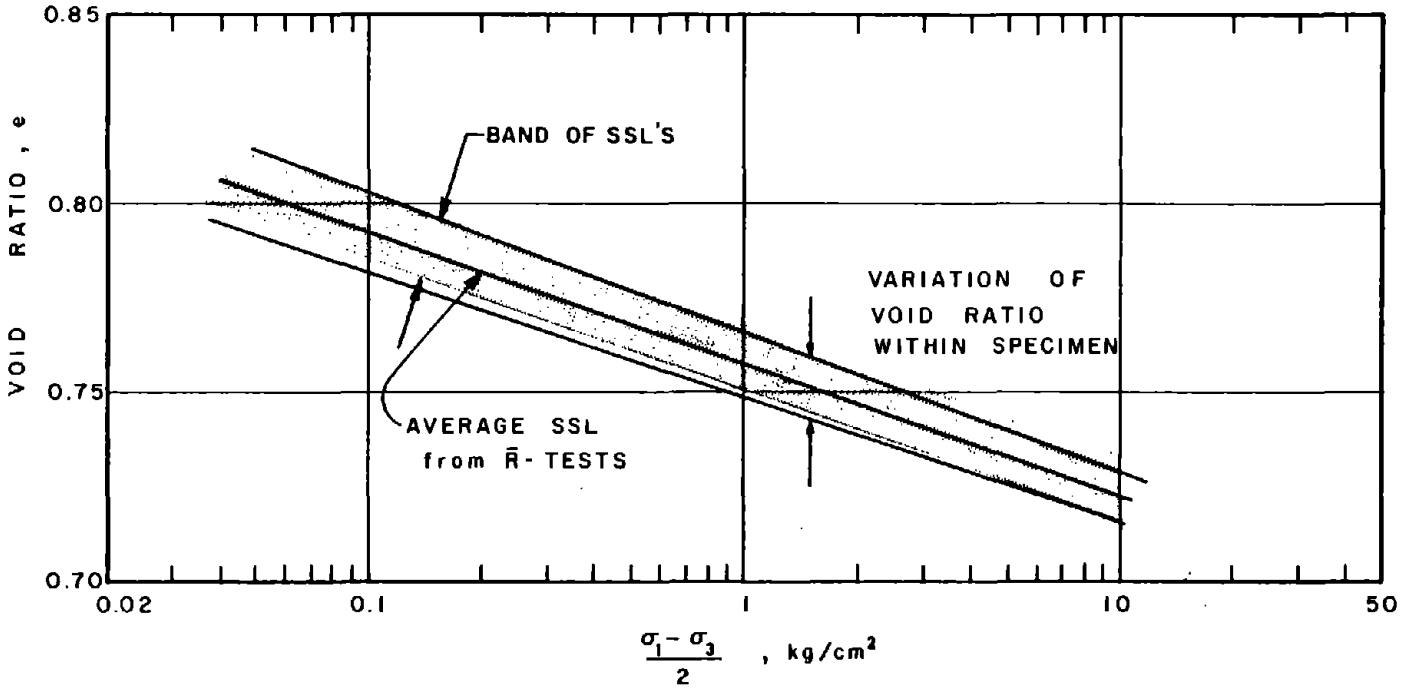

Fig. 5-9: Variations in SSL Due to Nonuniformity of Individual Specimens

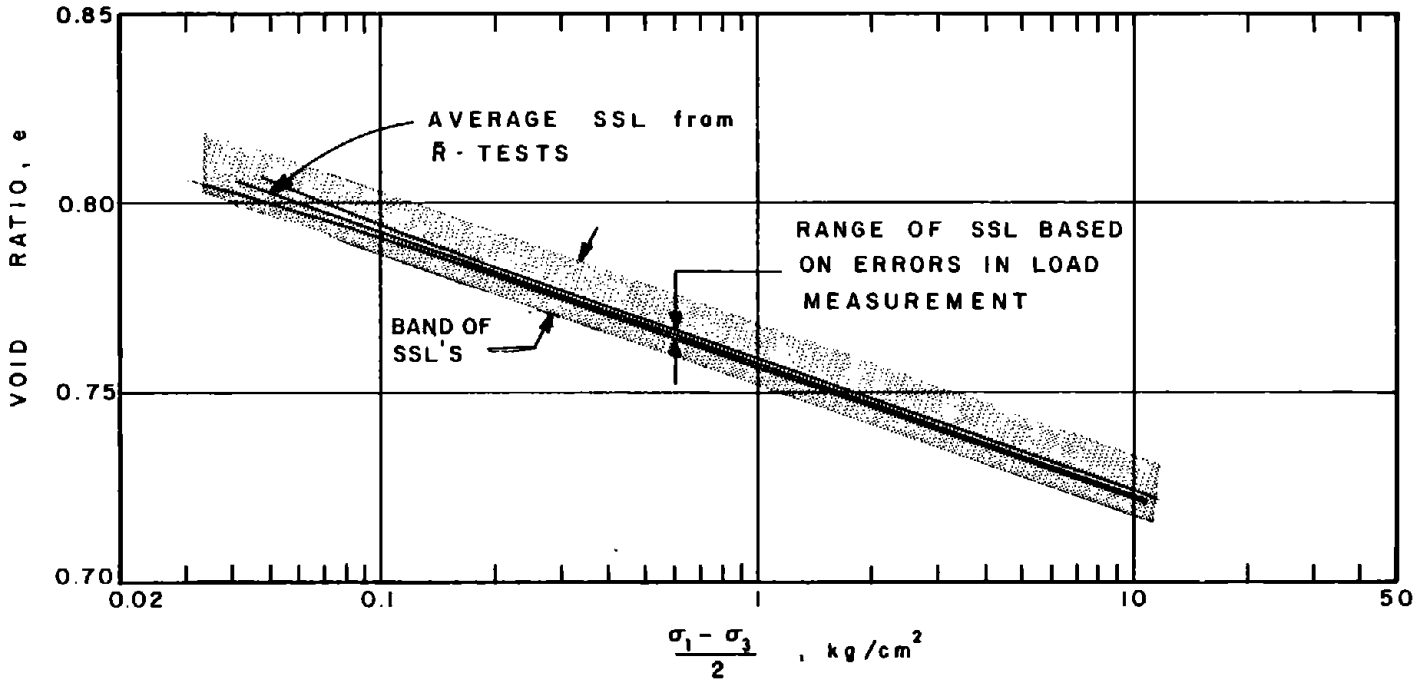

Fig. 5-10: Estimated Range in SSL Due to Errors in Load Measurement

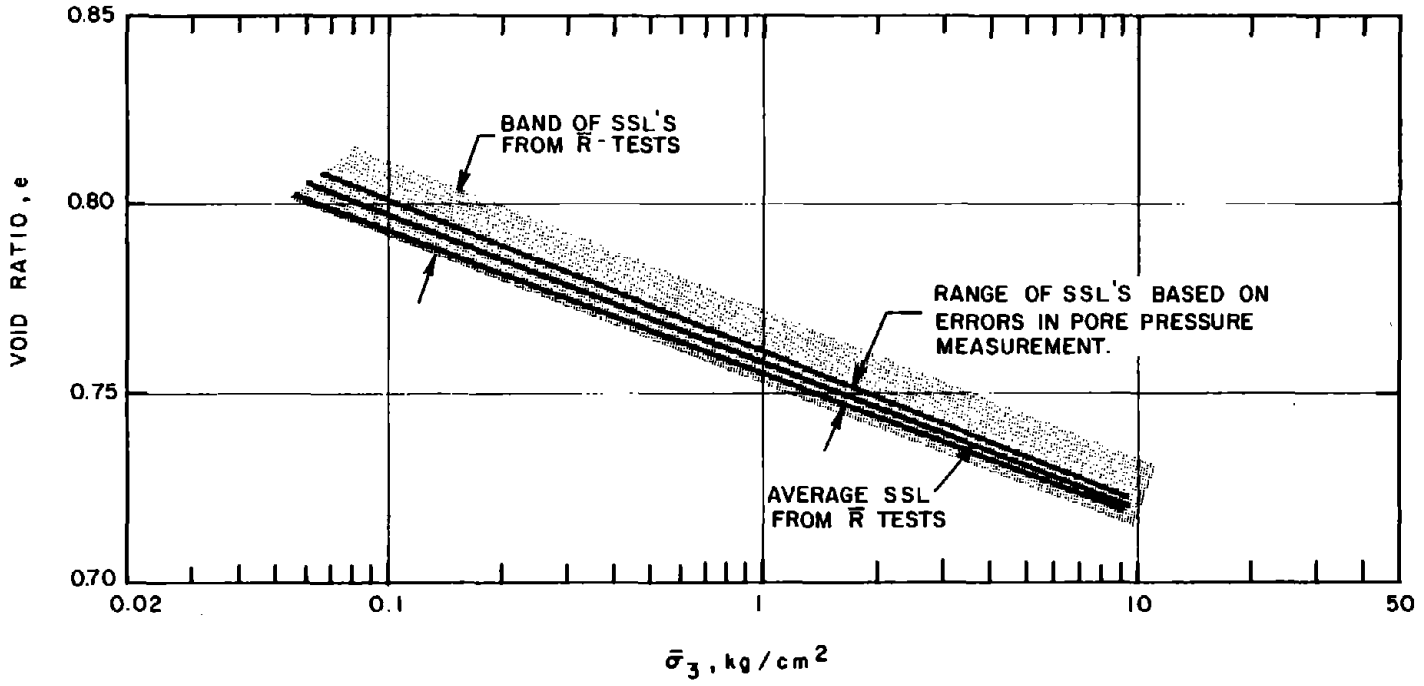

Fig. 5-11 Estimated Range in SSL Due to Errors in Pore Pressure Measurement

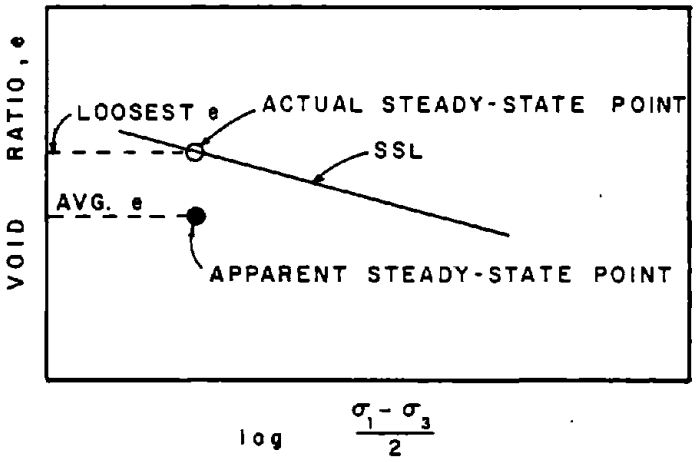

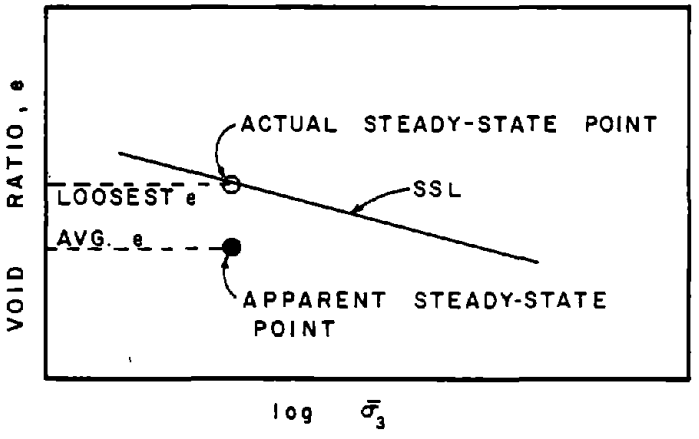

Fig. 5-12: Variation of Apparent Steady State Point From SSL Due to Variation in Void Ratio Within the Specimen.

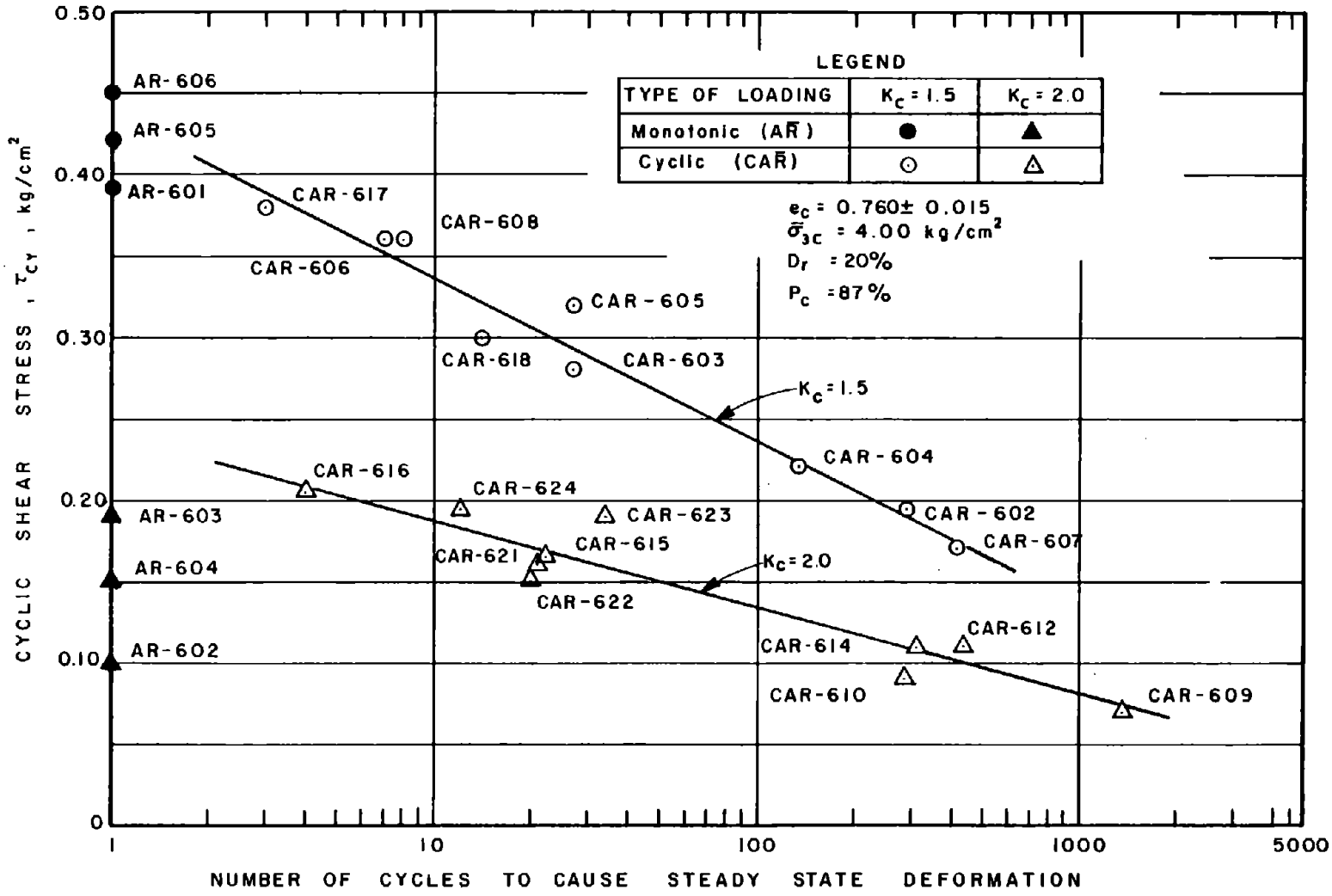

Fig. 5-13: Cyclic Shear Stress vs. Number of Cycles to Cause Steady State Deformation.

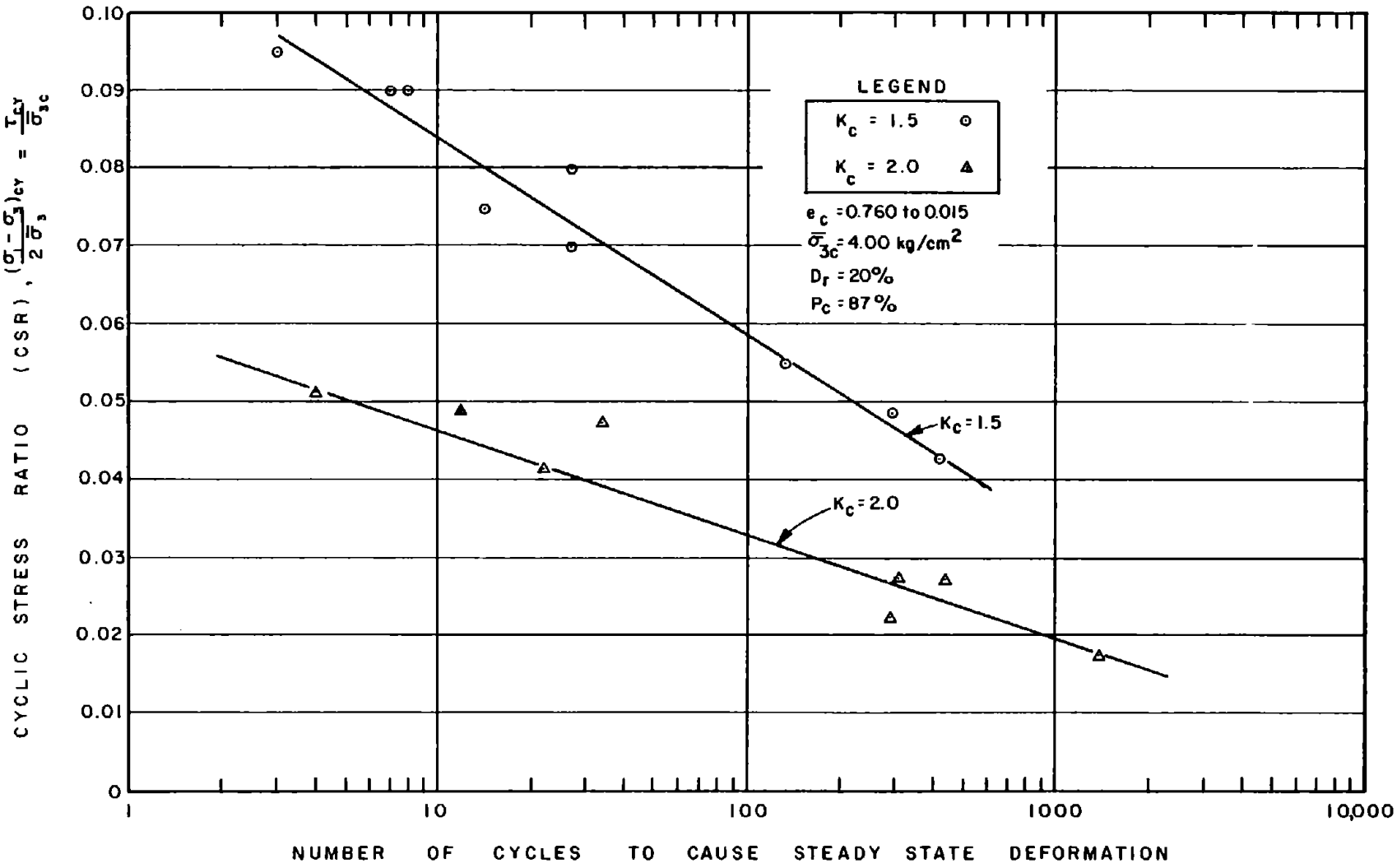

Fig. 5-14: Cyclic Stress Ratio vs. Number of Cycles to Cause Steady State Deformation in CAR Tests on Banding Sand #6

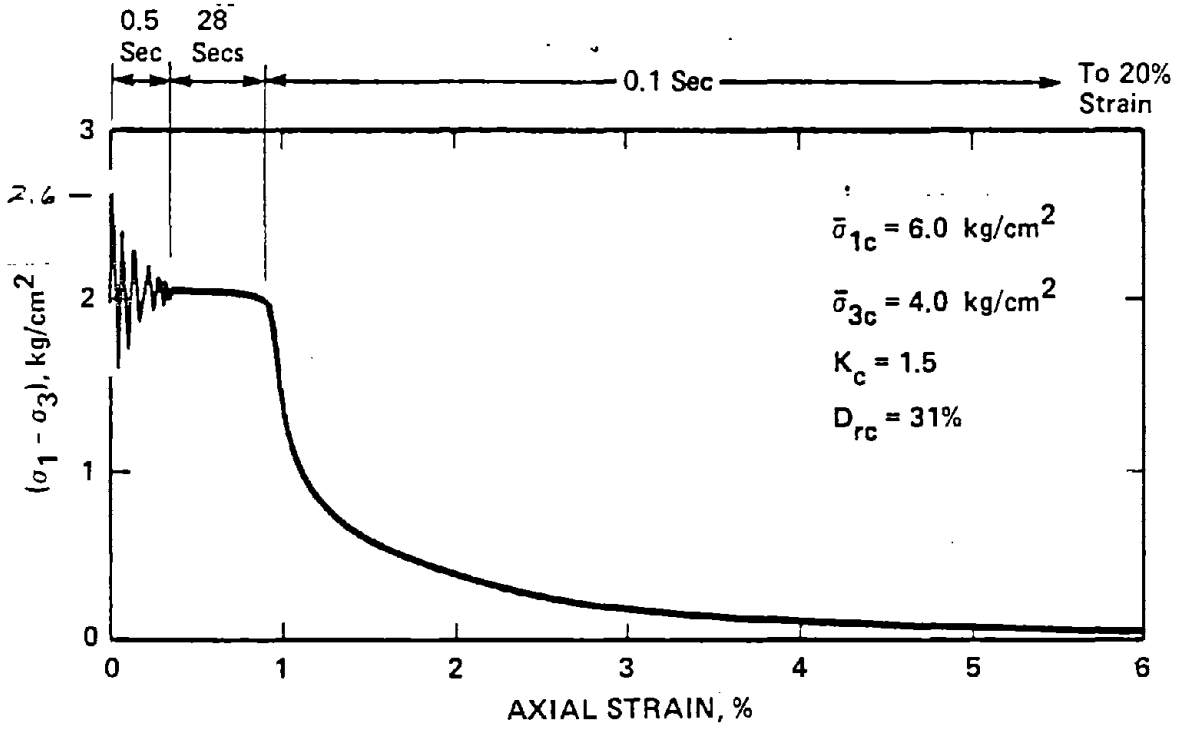

Fig. 5-15: Example of Creep Prior to Steady State Deformation (From Castro, 1978)

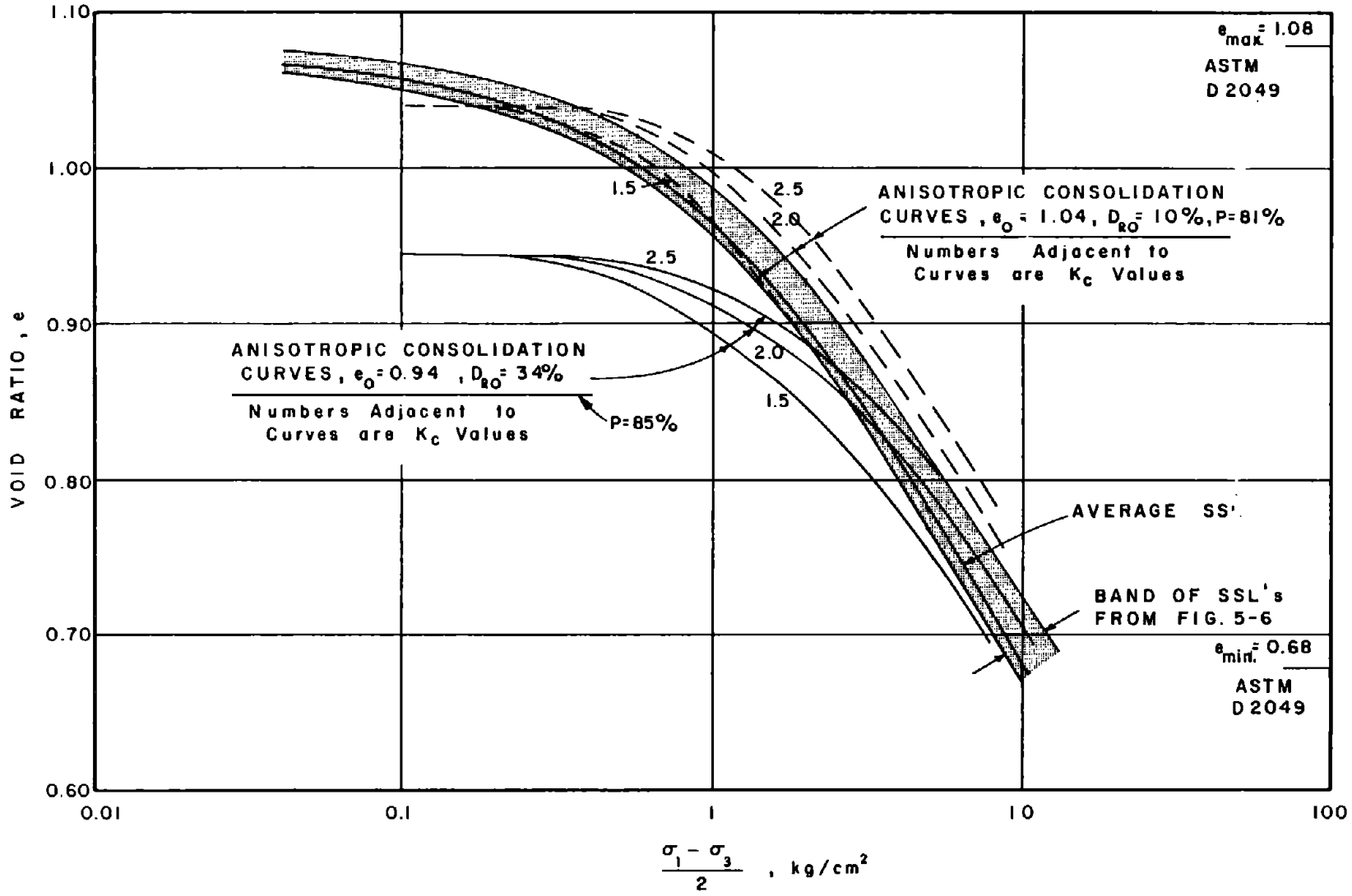

Fig. 5-16: Anisotropic Consolidation Curves for Mine Tailings Specimens Compared to Steady State Line.

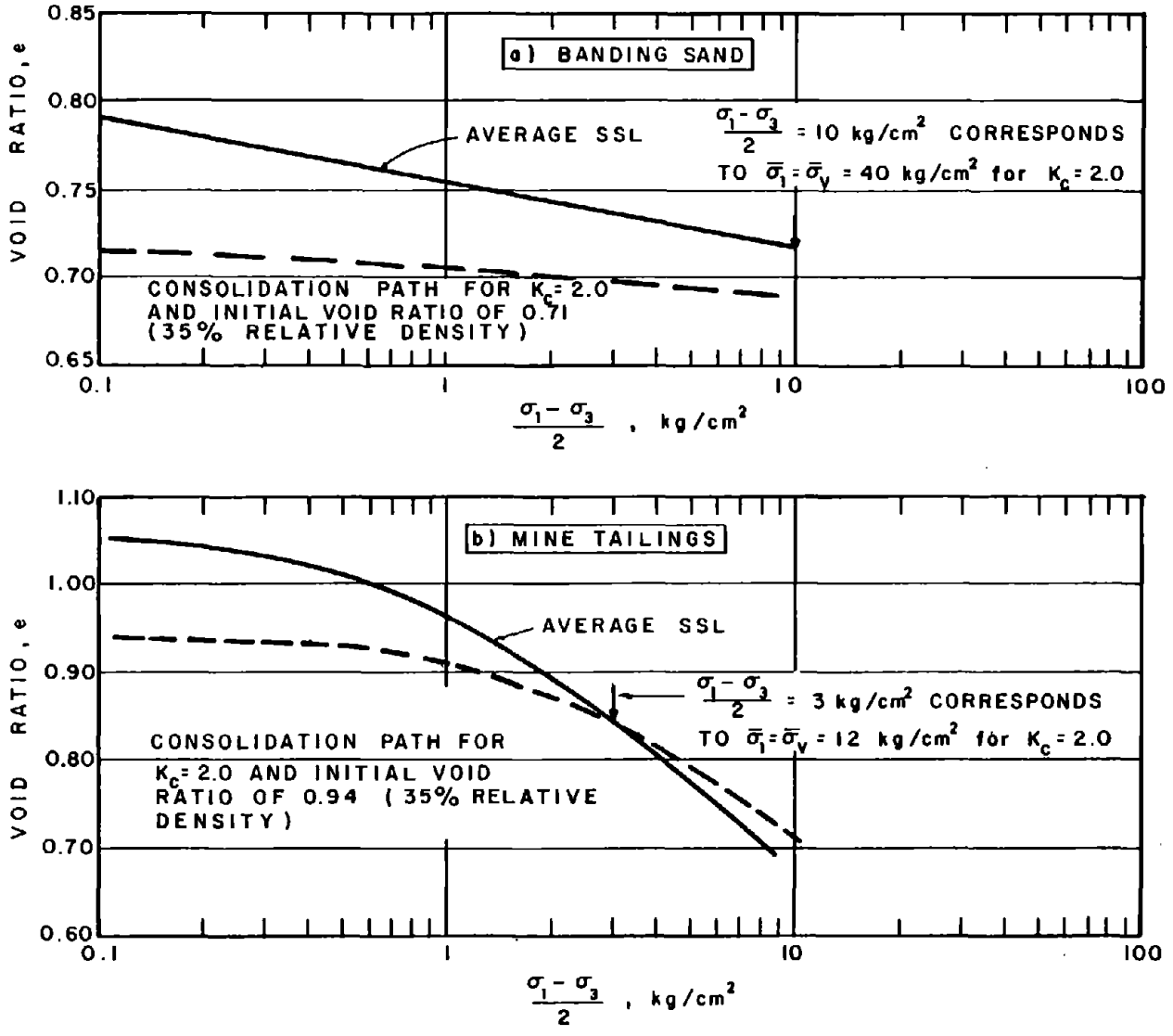

Fig. 5-17: Consolidation Curves for Banding Sand and Mine Tailings Placed at 35% Relative Density

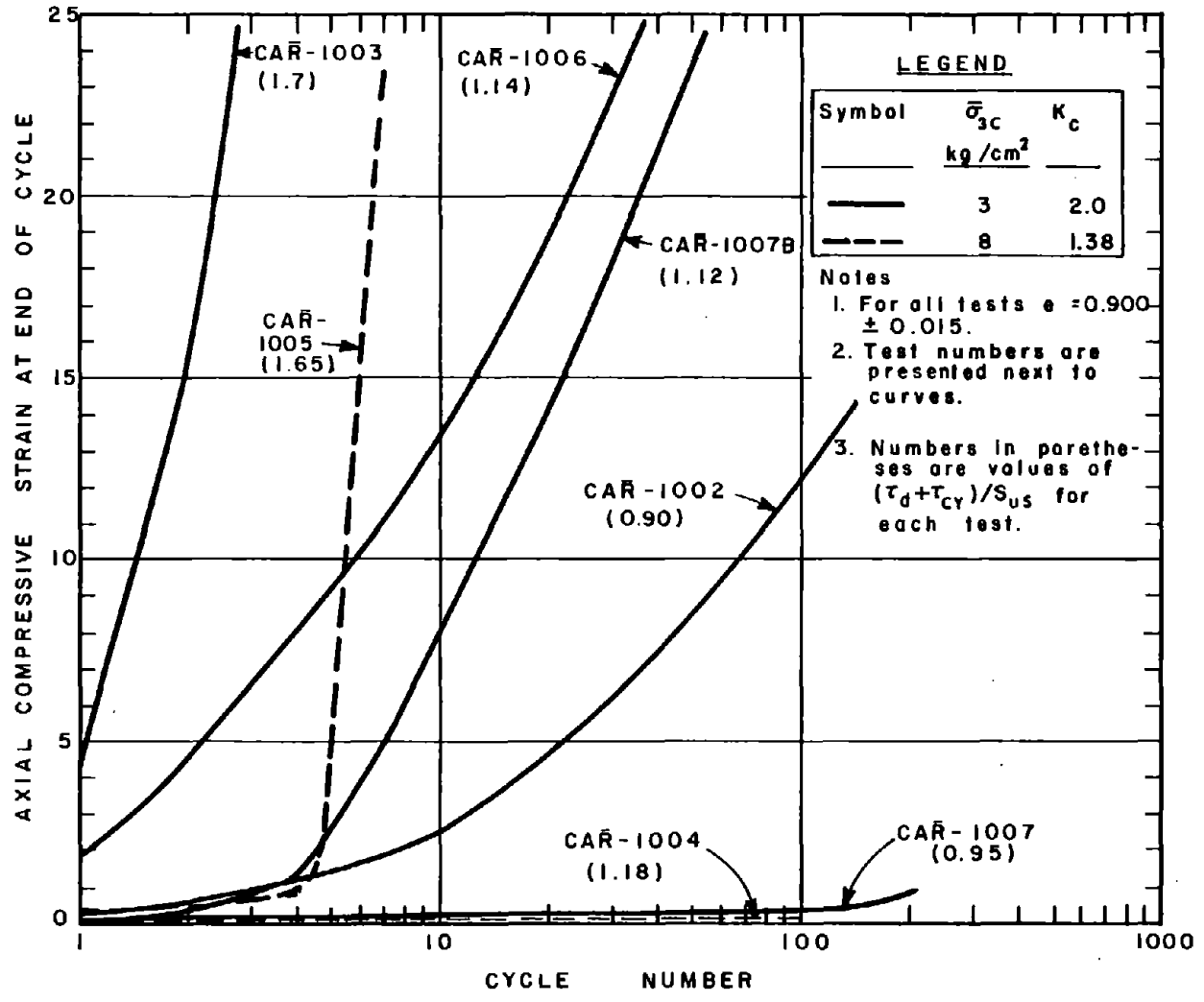

Fig. 5-18: Strain Accumulation for CAR̄ Tests on Mine Tailings with τ_{st} less than τ_{ss}.

LEGEND

1) Types of stress-strain curves:

Symbol	Type
●	F
o	G
Δ	H

See text for discussion

2) Avg. SSL indicates average steady state line

3) Where more than one test had the same consolidation state, the numbers next to the data points indicate the number of tests represented by the point.

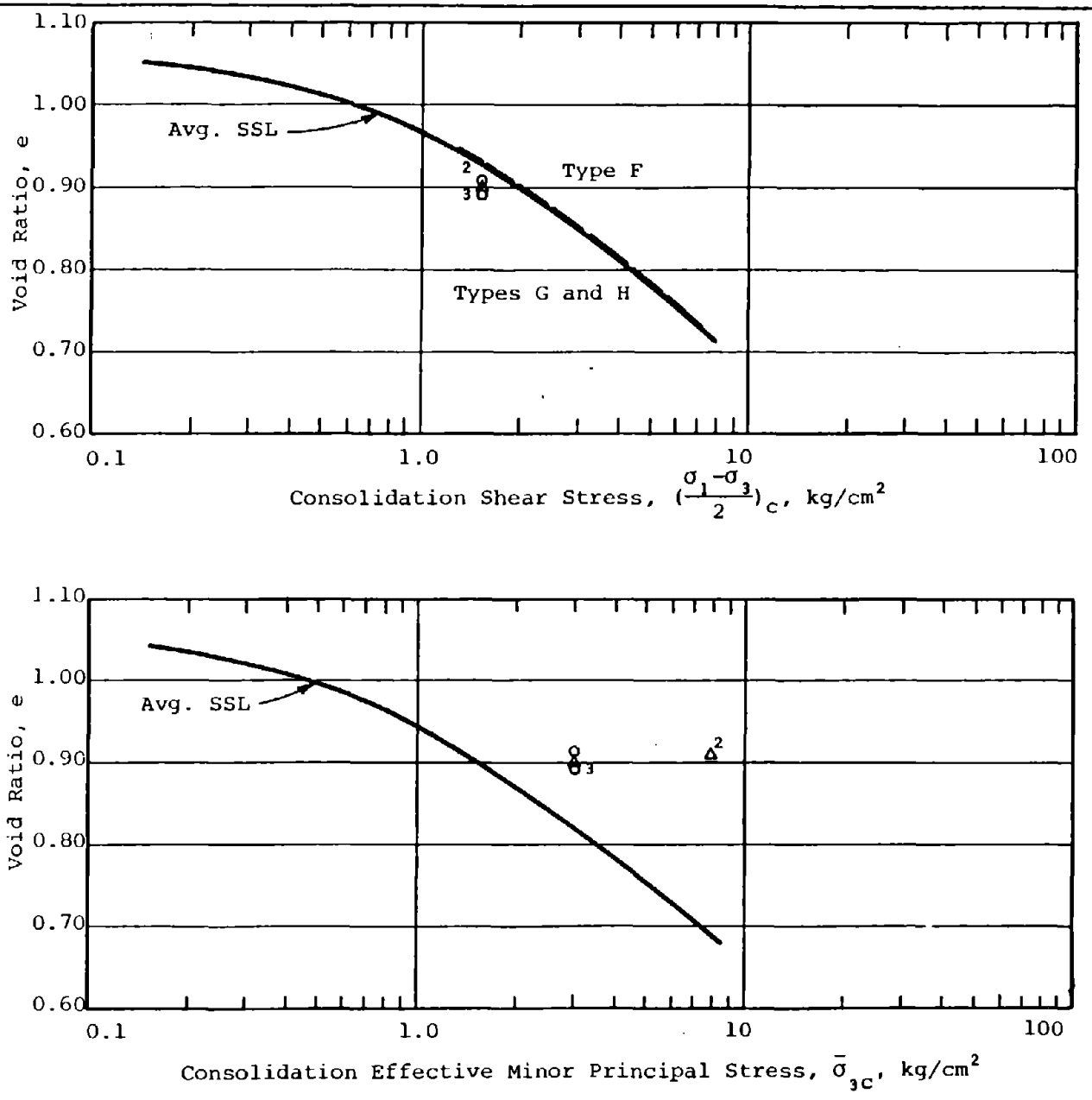

Fig. 5-19: Consolidation States for CAR̄ Tests on Mine Tailings with τ_d less than S_{us}

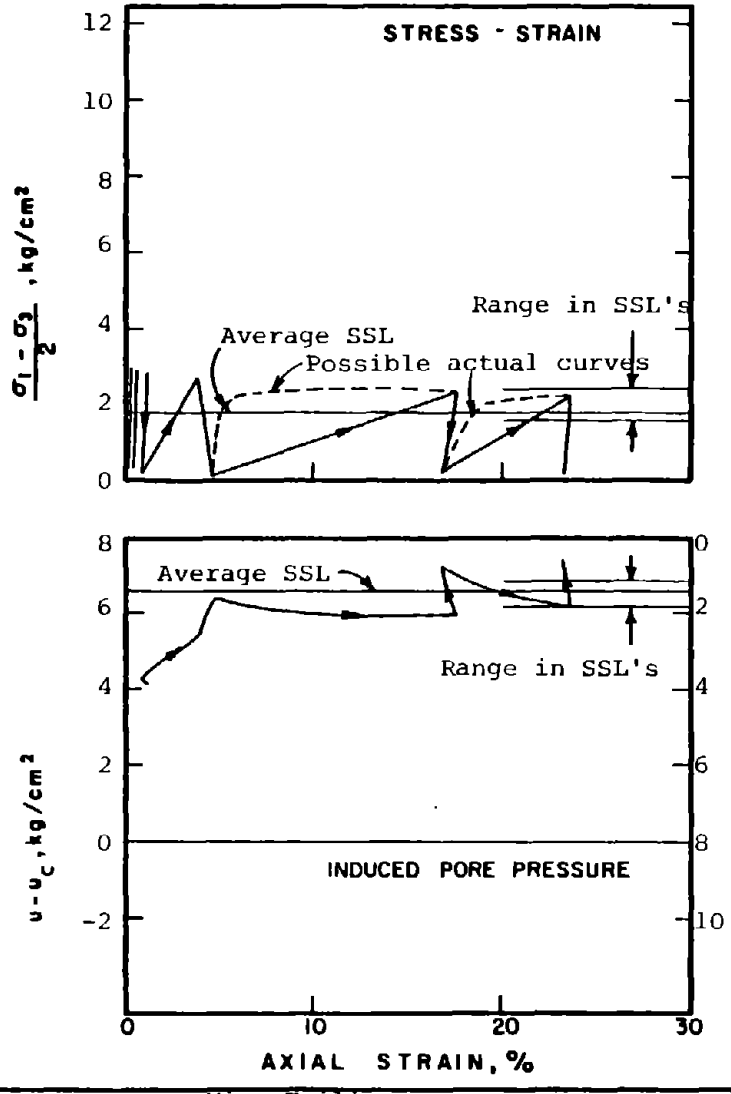

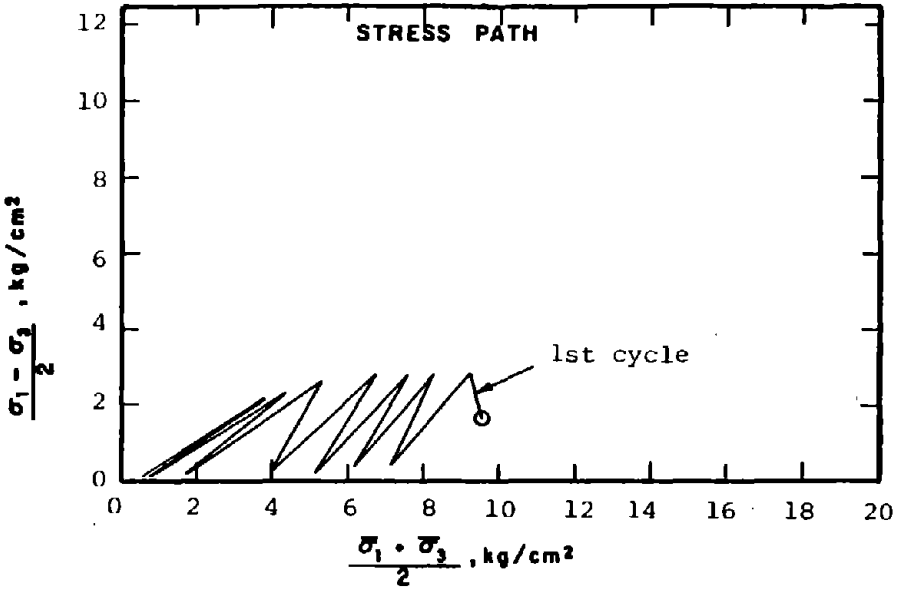

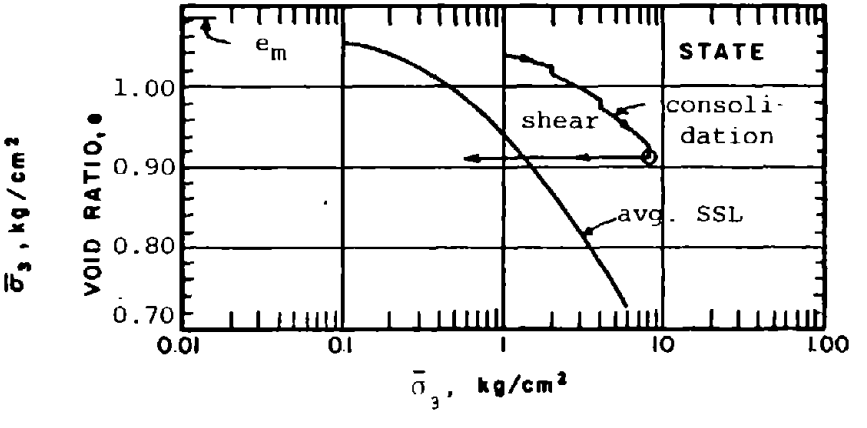

CAR-1005

SOIL : Mine Tailings

STRUCTURE : Compacted Moist

STATE AFTER CONSOLIDATION: $\bar{\sigma}_{3c}$ = 8.00 kg/cm², $\bar{\sigma}_{1c}$ = 11.00kg/cm²

e_c = 0.910, γ_{dc} = 87.6 pcf

METHOD OF LOADING: Undrained, Cyclic Axial Compression Load Control

$(\sigma_1 - \sigma_3)_{cy}$ = 2.66 ksc

TESTING DETAILS : Specimen Diameter 3.60 cm

: Specimen Height 5.30 cm

: End Platens: Lubricated, Type 2

Fig. 5-20: Stress-Strain Curves from Test CAR-1005

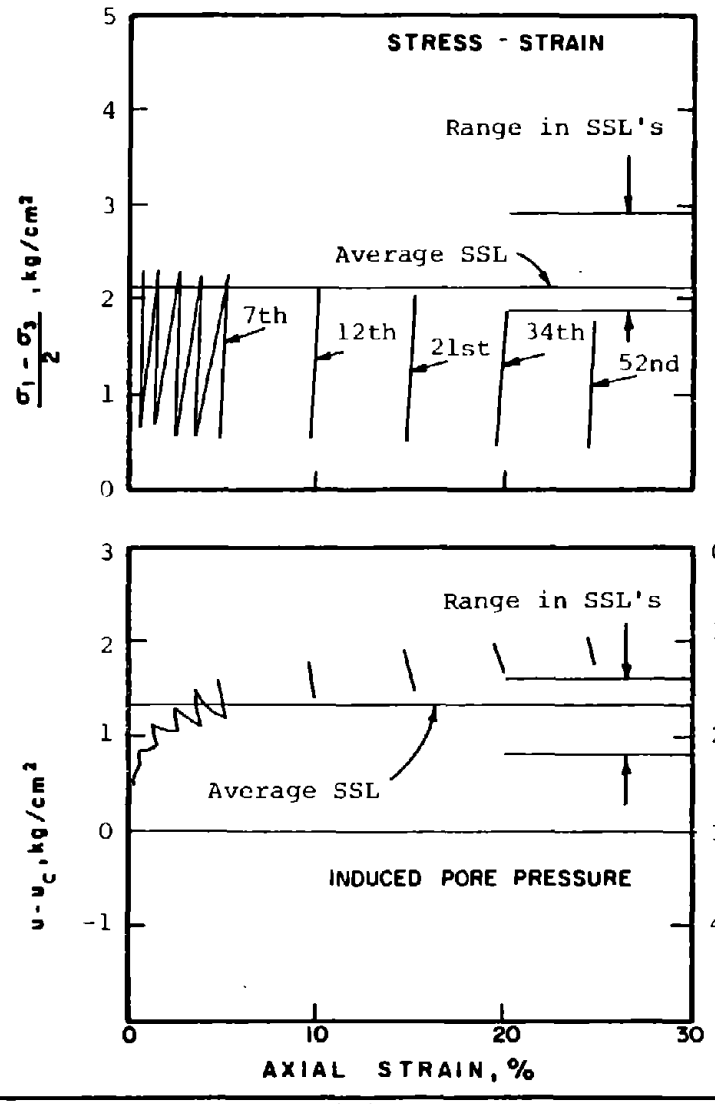

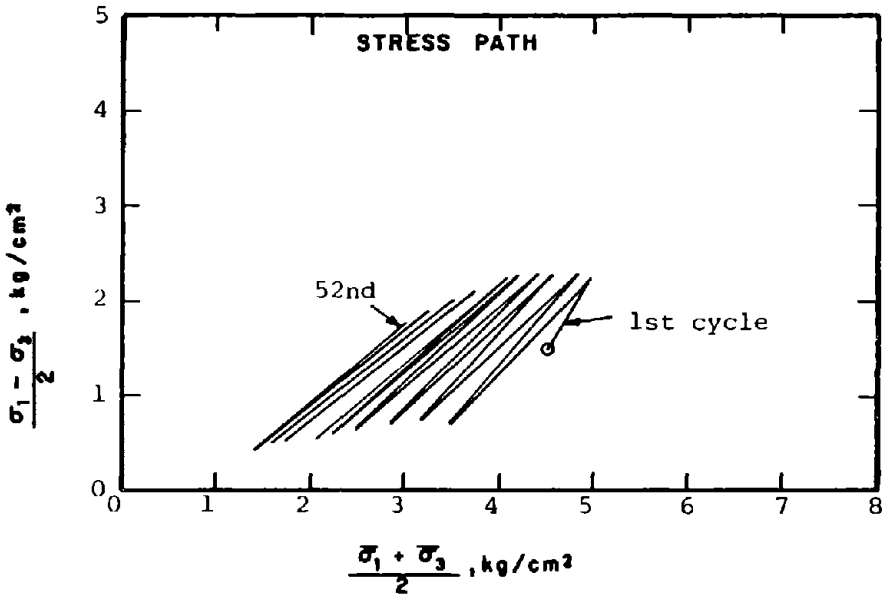

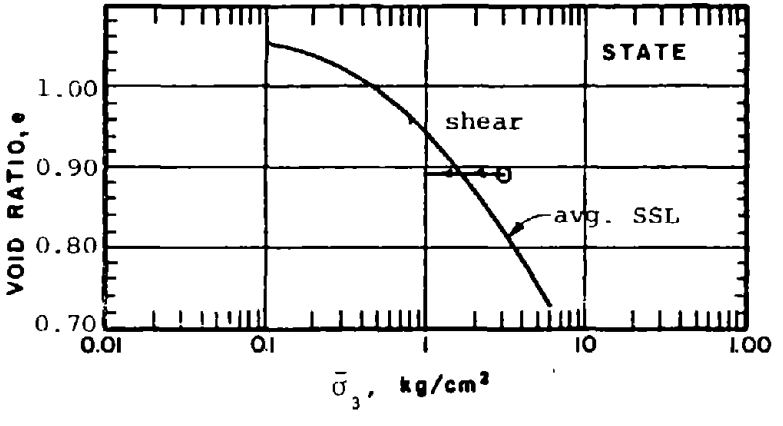

CAR-1007B

SOIL : Mine Tailings

STRUCTURE : Compacted Moist

STATE AFTER CONSOLIDATION: $\bar{\sigma}_{3c}$ = 3.00 kg/cm², $\bar{\sigma}_{1c}$ = 6.00 kg/cm²

e_c = 0.891, γ_{dc} = 88.4 pcf

METHOD OF LOADING: Undrained, Cyclic Axial Compression
Load Control
$(\sigma_1 - \sigma_3)_{cy}$ = 1.67 ksc

TESTING DETAILS : Specimen Diameter 3.60 cm
: Specimen Height 5.30 cm
: End Platens: Lubricated, Type 2

Fig. 5-21: Stress-Strain Curves from Test CAR-1007B

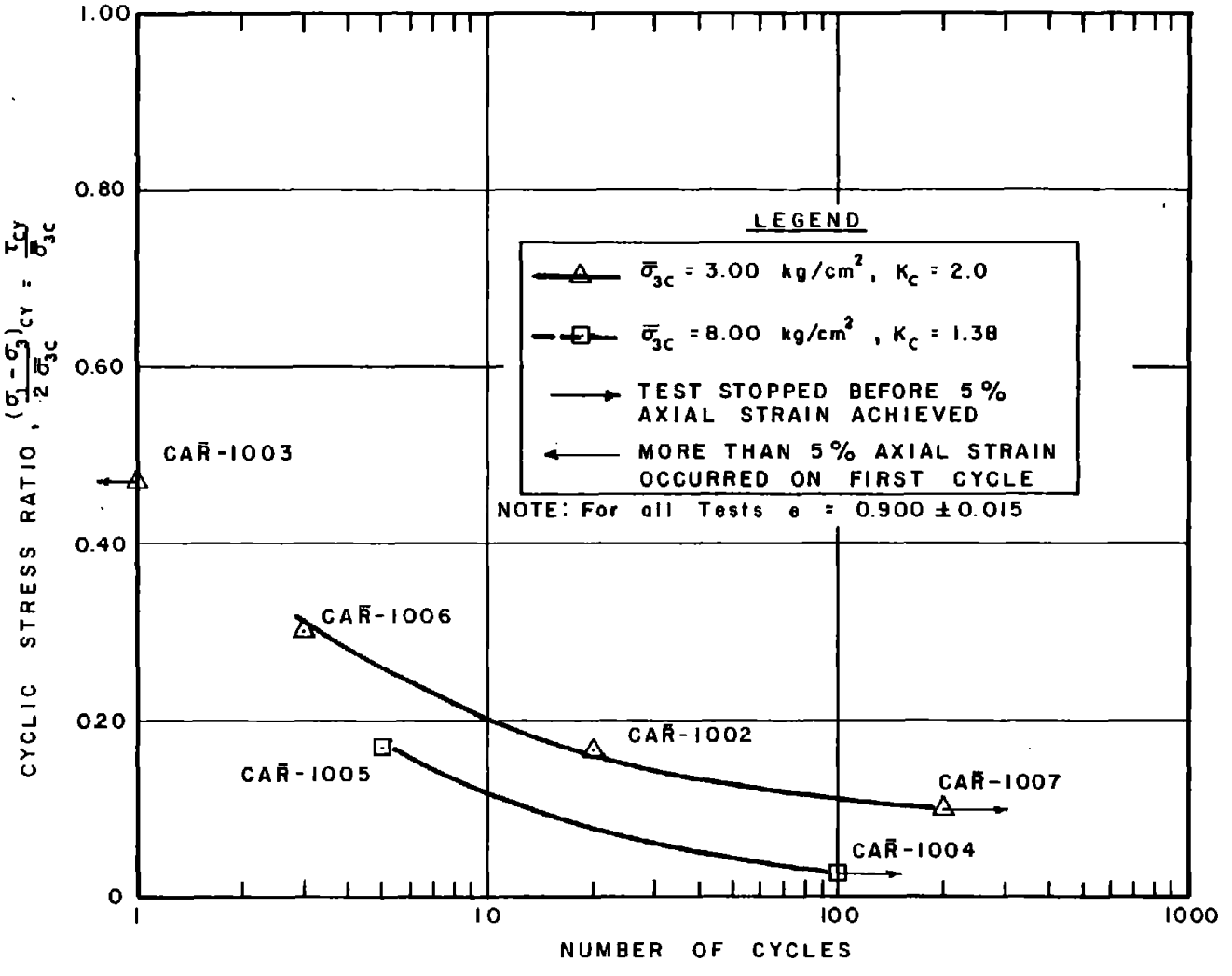

Fig. 5-22: Cyclic Stress Ratio vs. Number of Cycles to Accumulate 5% Axial Strain for CAR̄ Tests on Mine Tailings with τ_d less than S_{us}. (Cyclic mobility tests [$\tau_d < S_{us}$]).

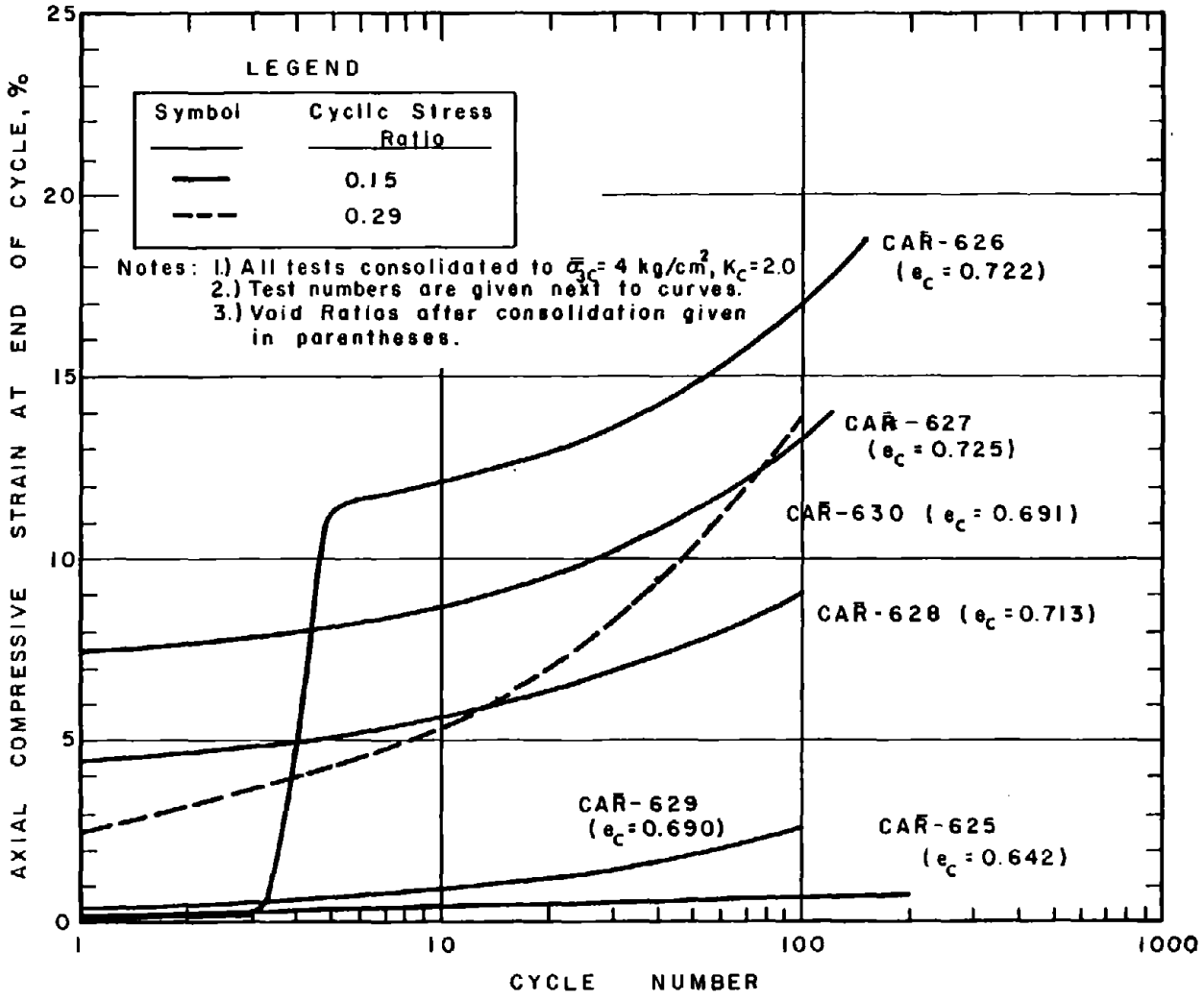

Fig. 5-23: Strain Accumulation for CAR̄ Tests on Banding Sand #6 with $\tau_d + \tau_{cy}$ Less Than S_{us}.

LEGEND

1) Types of stress-strain curves:

Symbol	Type
●	F
o	G
Δ	H

See text for discussion

2) Avg. SSL indicates average steady state line

3) Where more than one test had the same consolidation state, the numbers next to the data points indicate the number of tests represented by the point.

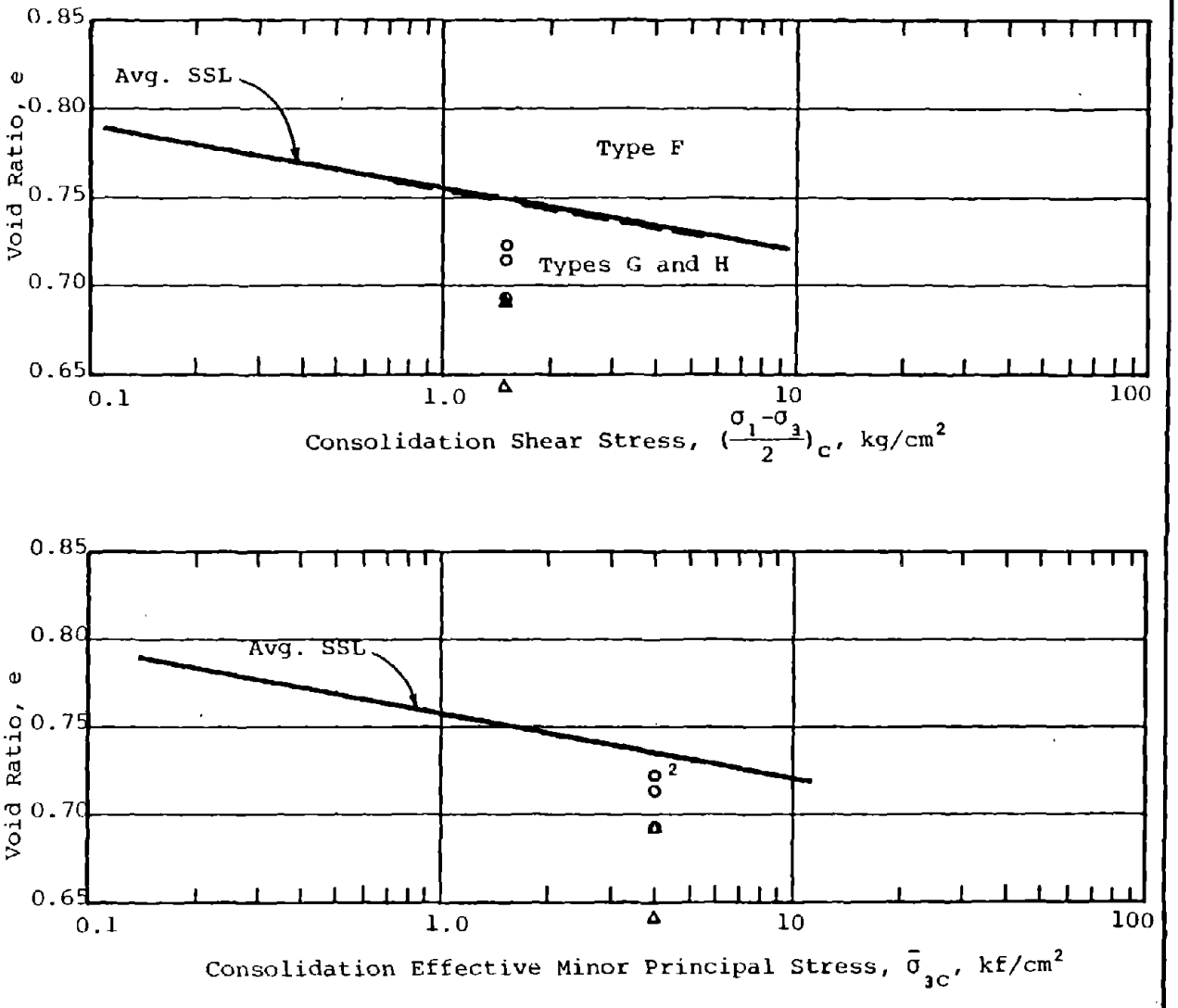

Fig. 5-24: Consolidation States for CAR̄ Tests on Banding Sand #6 with τ_d less than S_{us}

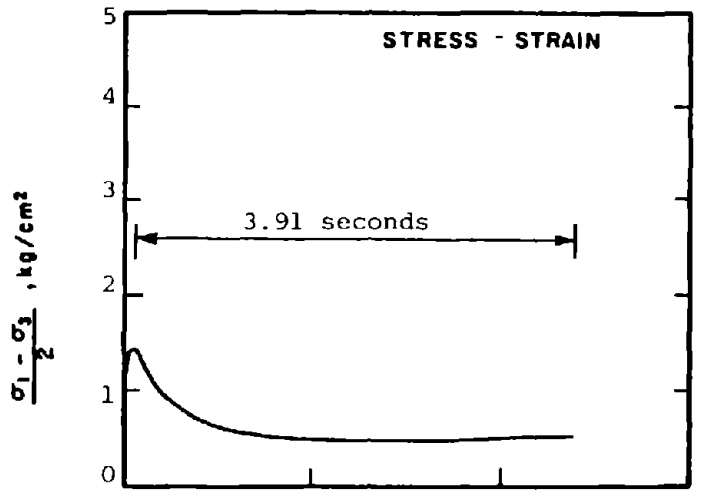

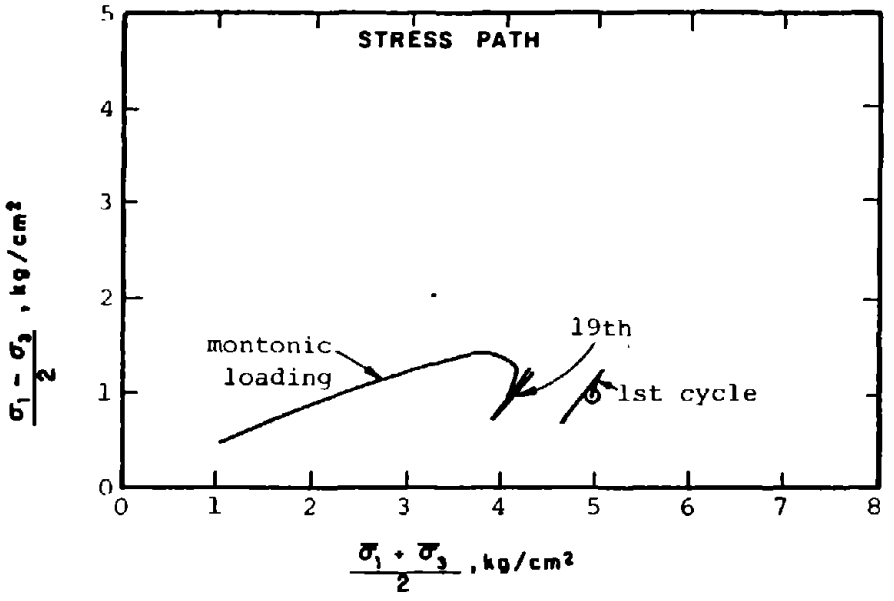

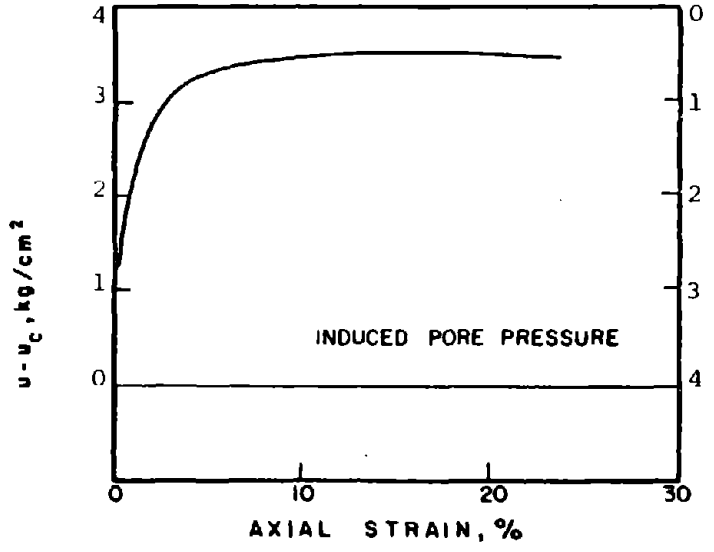

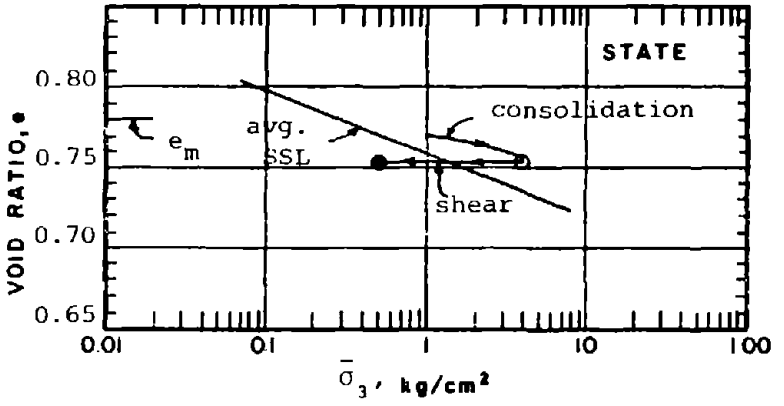

CAR̄-R̄-631

SOIL : Banding Sand #6

STRUCTURE : Compacted Moist

STATE AFTER CONSOLIDATION: $\bar{\sigma}_{3c} = 4.00$ kg/cm², $\bar{\sigma}_{1c} = 6.00$ kg/cm²
$e_c = 0.752$, $\gamma_{dc} = 94.7$ pcf

METHOD OF LOADING: Undrained, Cyclic Axial Compression
Load Control
$(\sigma_1 - \sigma_3)_{cy} = 0.59$ ksc

TESTING DETAILS : Specimen Diameter 3.60 cm
: Specimen Height 5.30 cm
: End Platens: Lubricated, Type 2

Fig. 5-25: Stress-Strain Curves From Test CAR̄-R̄-631

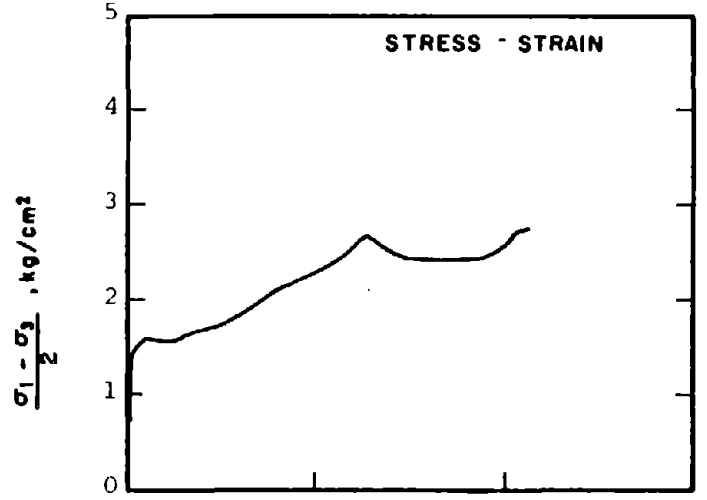

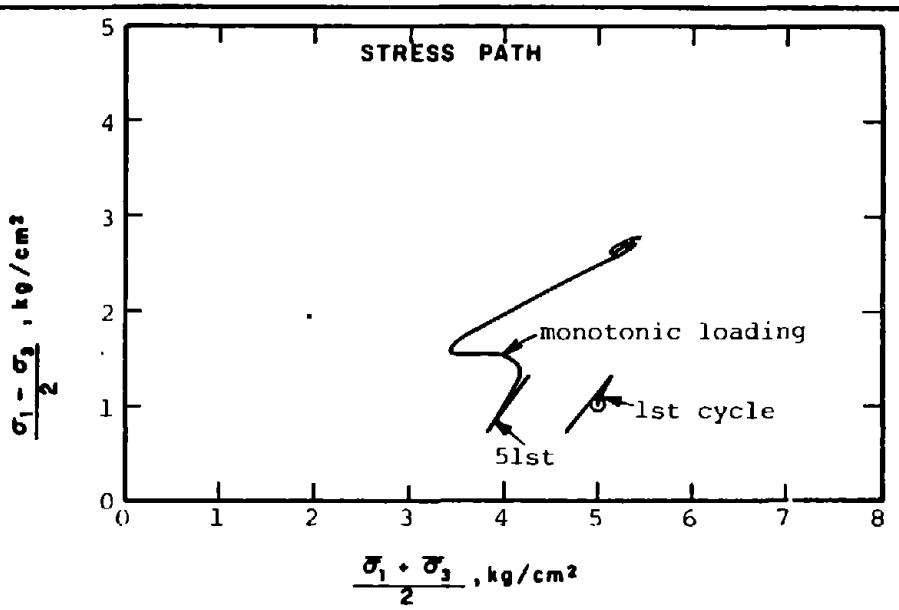

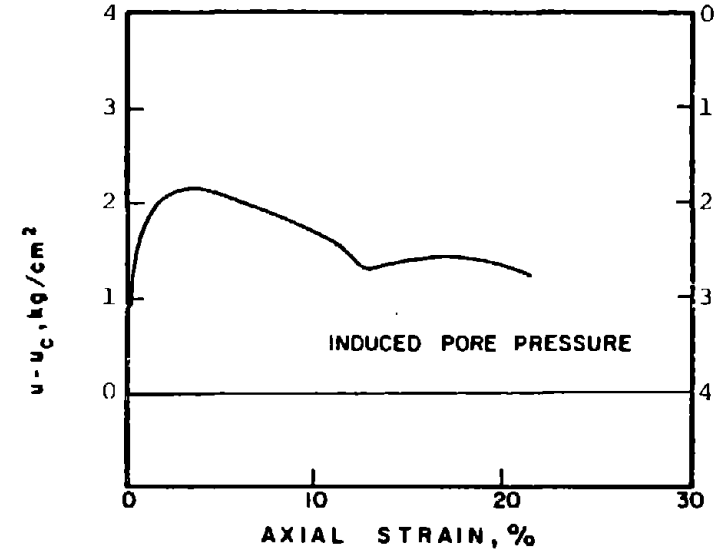

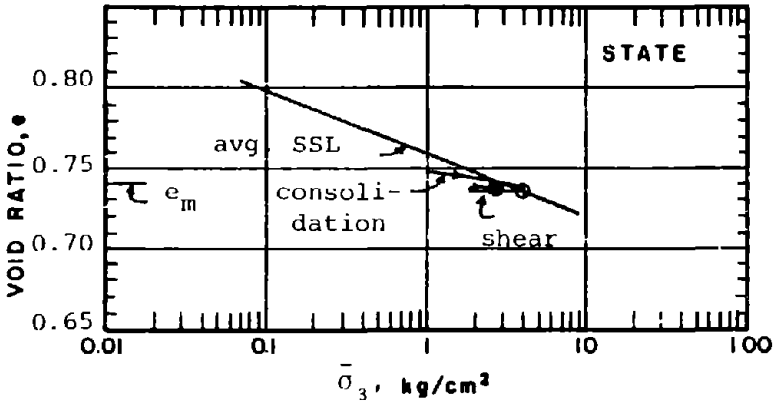

CAR-R-632

SOIL : Banding Sand #6

STRUCTURE : Compacted Moist

STATE AFTER CONSOLIDATION: $\bar{\sigma}_{3c}$ = 4.00 kg/cm², $\bar{\sigma}_{1c}$ = 6.00 kg/cm²
e_c = 0.734, γ_{dc} = 95.7 pcf

METHOD OF LOADING: Undrained, Cyclic Axial Compression
Load Control
$(\sigma_1 - \sigma_3)_{cy}$ = 0.59 ksc

TESTING DETAILS : Specimen Diameter 3.60 cm
: Specimen Height 5.30 cm
: End Platens: Lubricated, Type 2

Test 5-26: Stress-Strain Curves From Test CAR-R-632

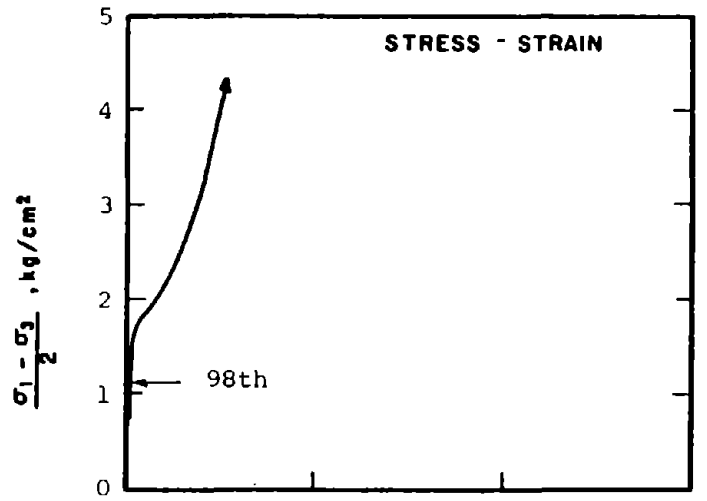

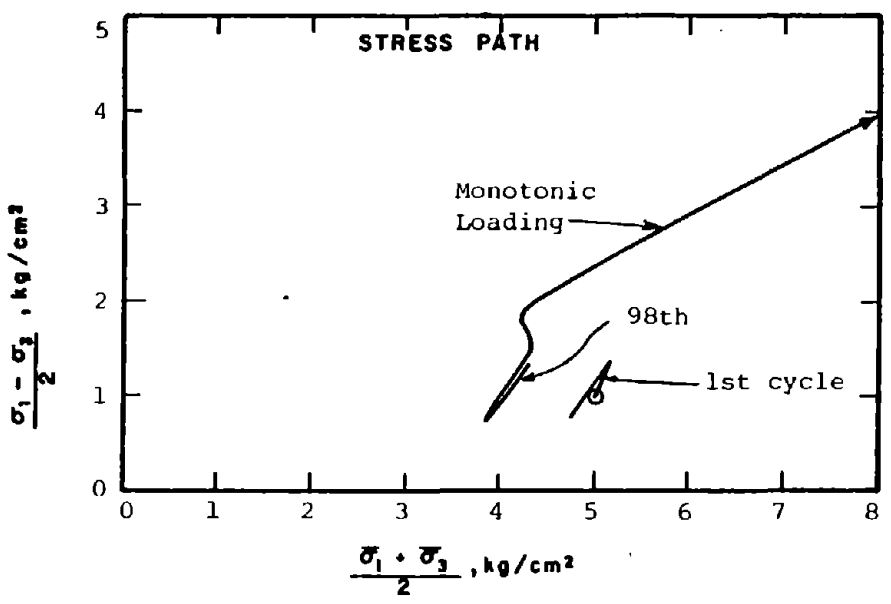

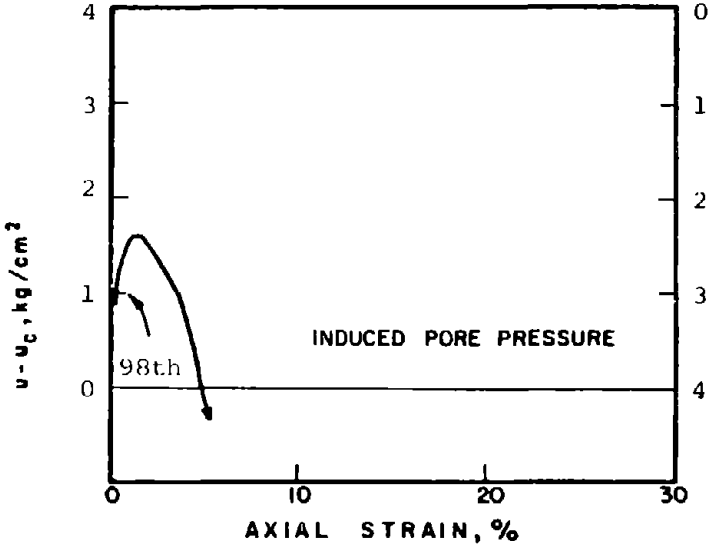

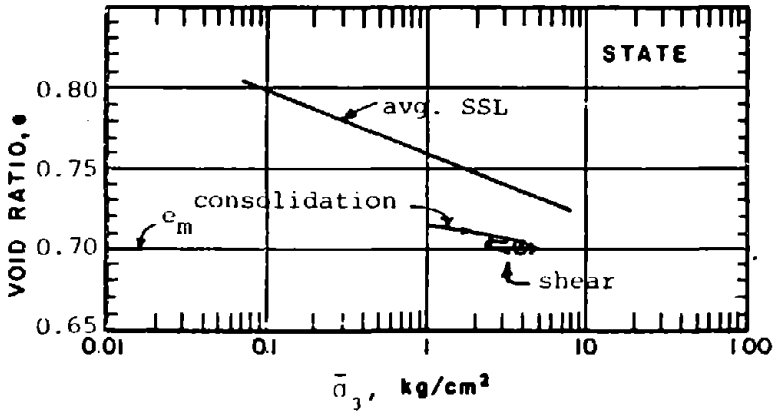

CAR-R-633

SOIL : Banding Sand #6

STRUCTURE : Compacted Moist

STATE AFTER CONSOLIDATION: $\bar{\sigma}_{3c} = 4.00$ kg/cm^2, $\bar{\sigma}_{1c} = 6.00$ kg/cm^2

$e_c = 0.701$, $\gamma_{dc} = 97.6$ pcf

METHOD OF LOADING: Undrained, Cyclic Axial Compression Load Control

$(\sigma_1 - \sigma_3)_{cy} = 0.60$ ksc

TESTING DETAILS : Specimen Diameter 3.60 cm

: Specimen Height 5.30 cm

: End Platens: Lubricated, Type 2

Fig. 5-27: Stress-Strain Curves From Test CAR-R-633

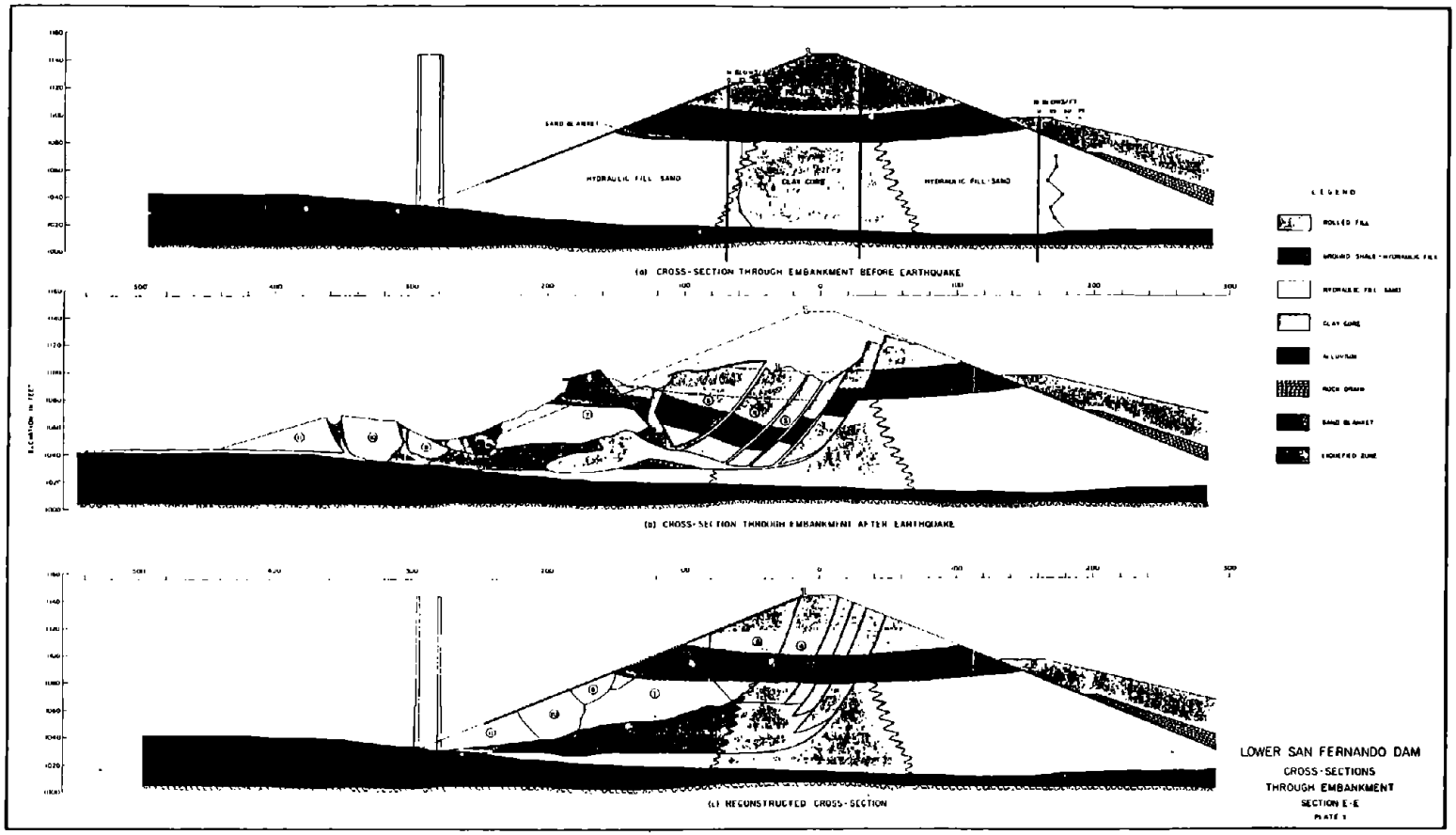

Fig. 6-1: Cross Sections of Failure of Lower San Fernando Dam (from Seed et al, 1975)

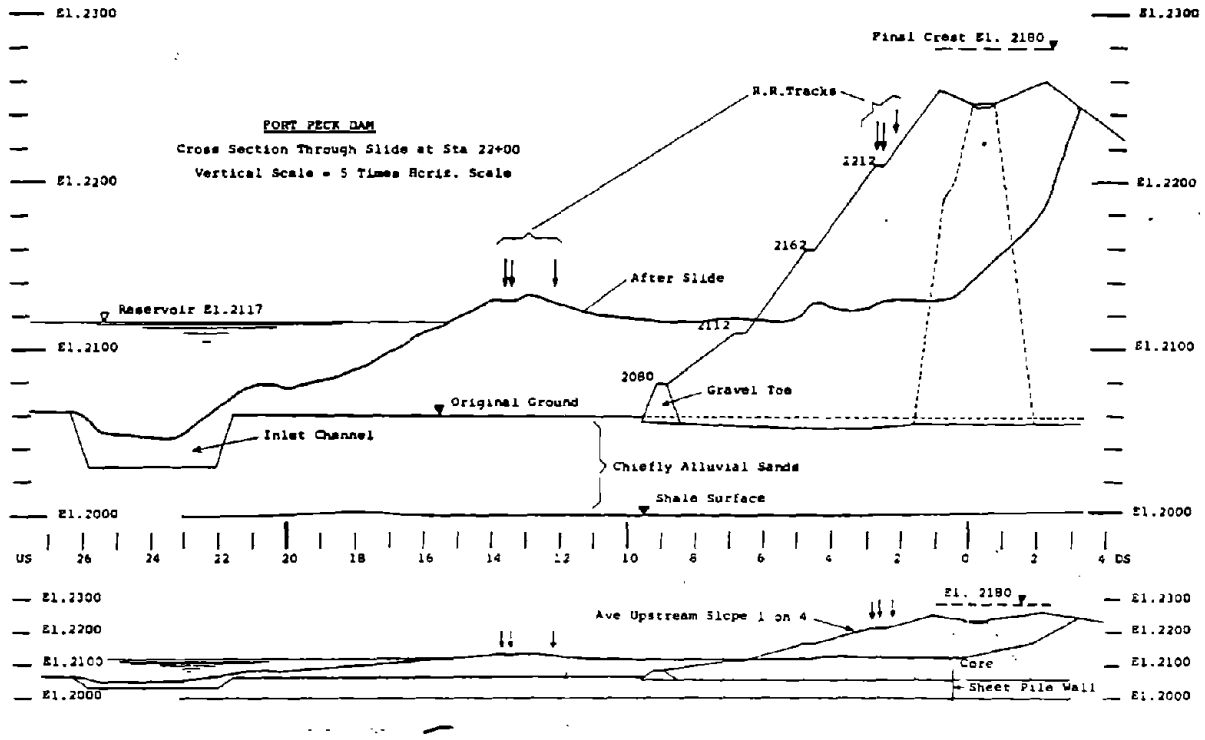

Fig. 6-2: Cross-Sections of Failure of Fort Peck Dam, From Casagrande, 1965

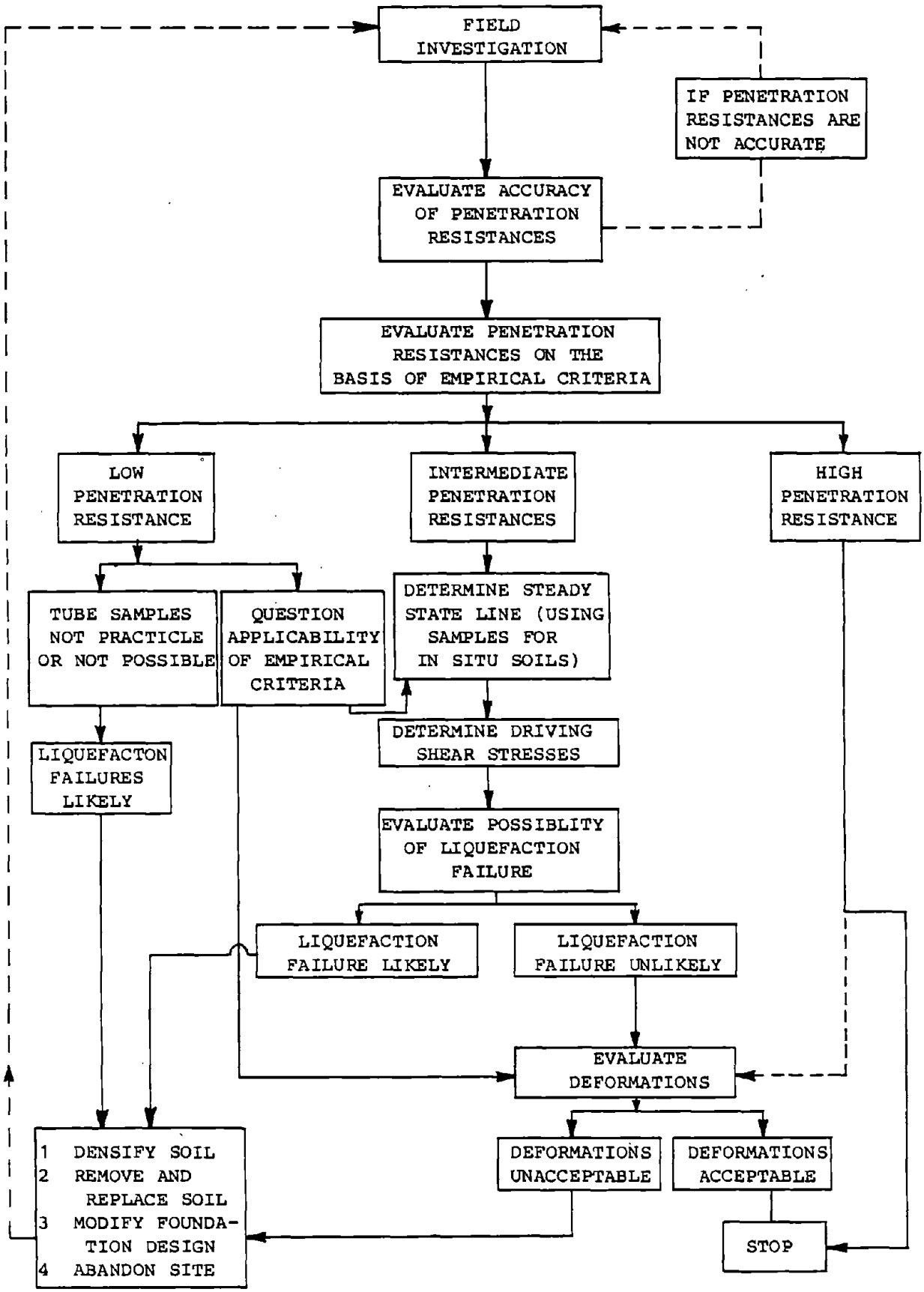

FIG. 6-3 FLOW CHART FOR PROPOSED METHOD OF GEOTECHNICAL EARTHQUAKE ENGINEERING

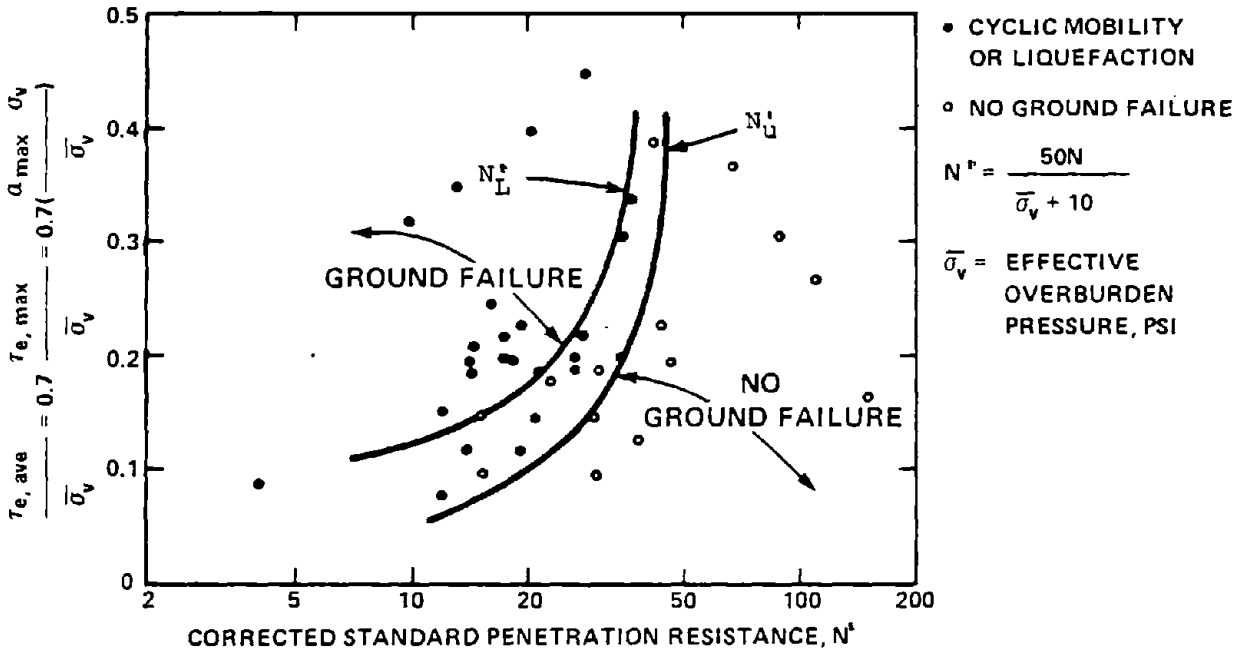

Fig. 6-4: Correlation Between Blowcounts in Sands and Earthquake Induced Ground Failure

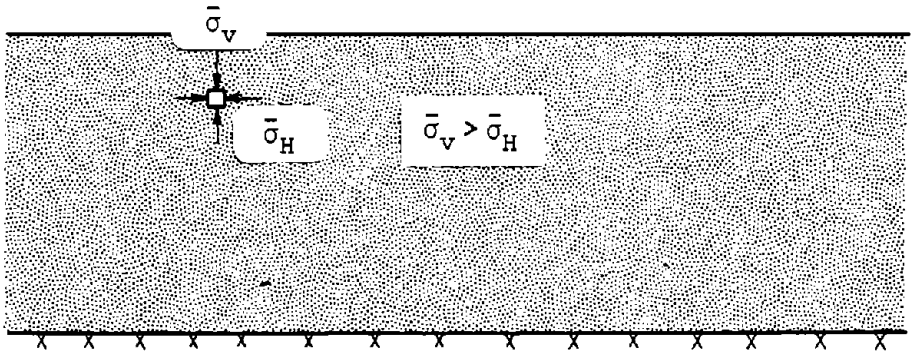

a) "Locked-in" shear stresses due to anisotropic consolidation beneath level ground

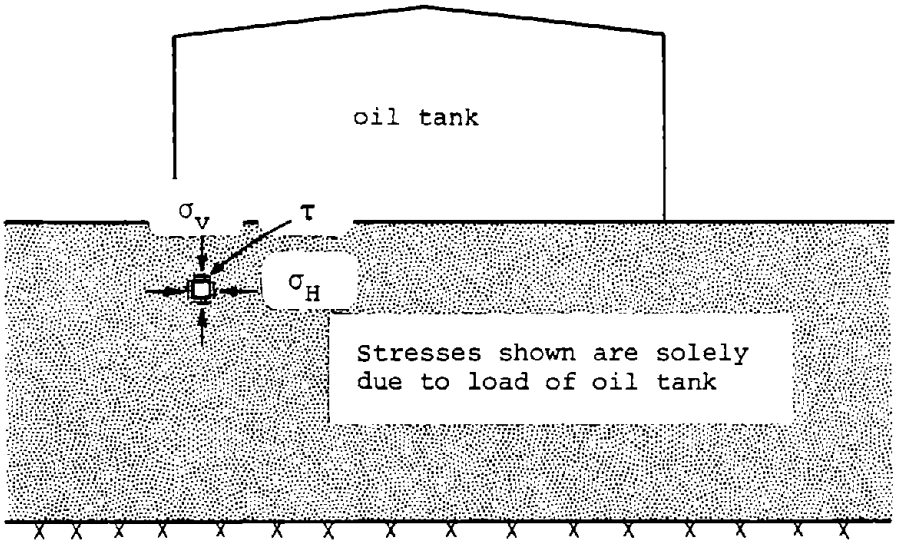

b) "Driving" shear stresses due to load of oil tank

Fig. 6-5 Examples of "Locked-in" and "Driving" Shear Stresses

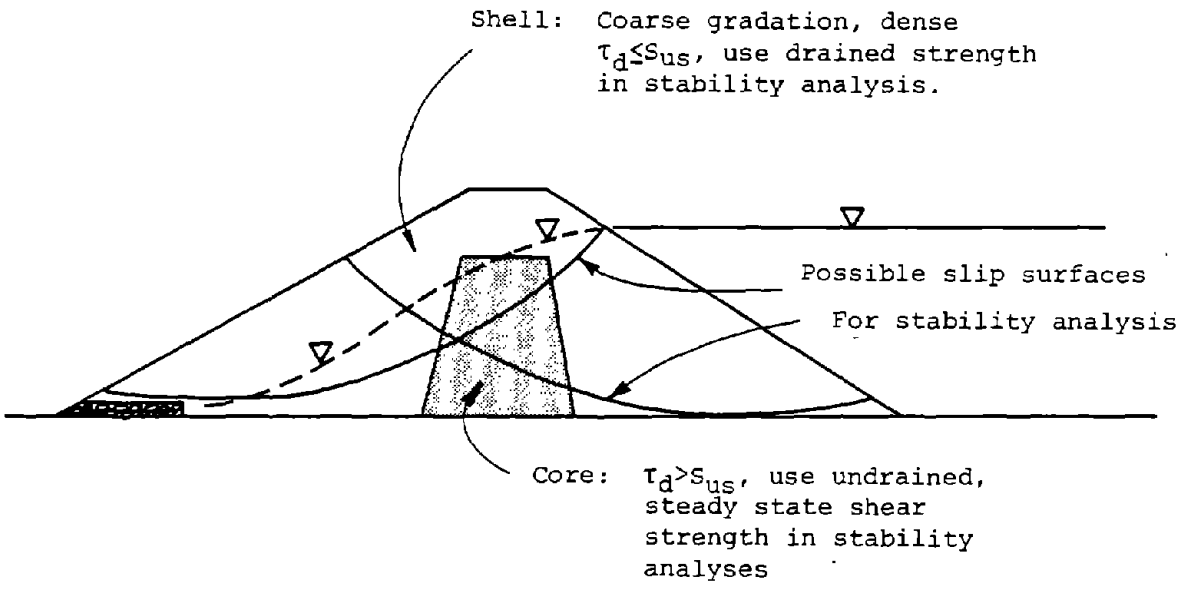

Fig. 6-6 Example of Stability Analyses to Evaluate Liquefaction Potential.

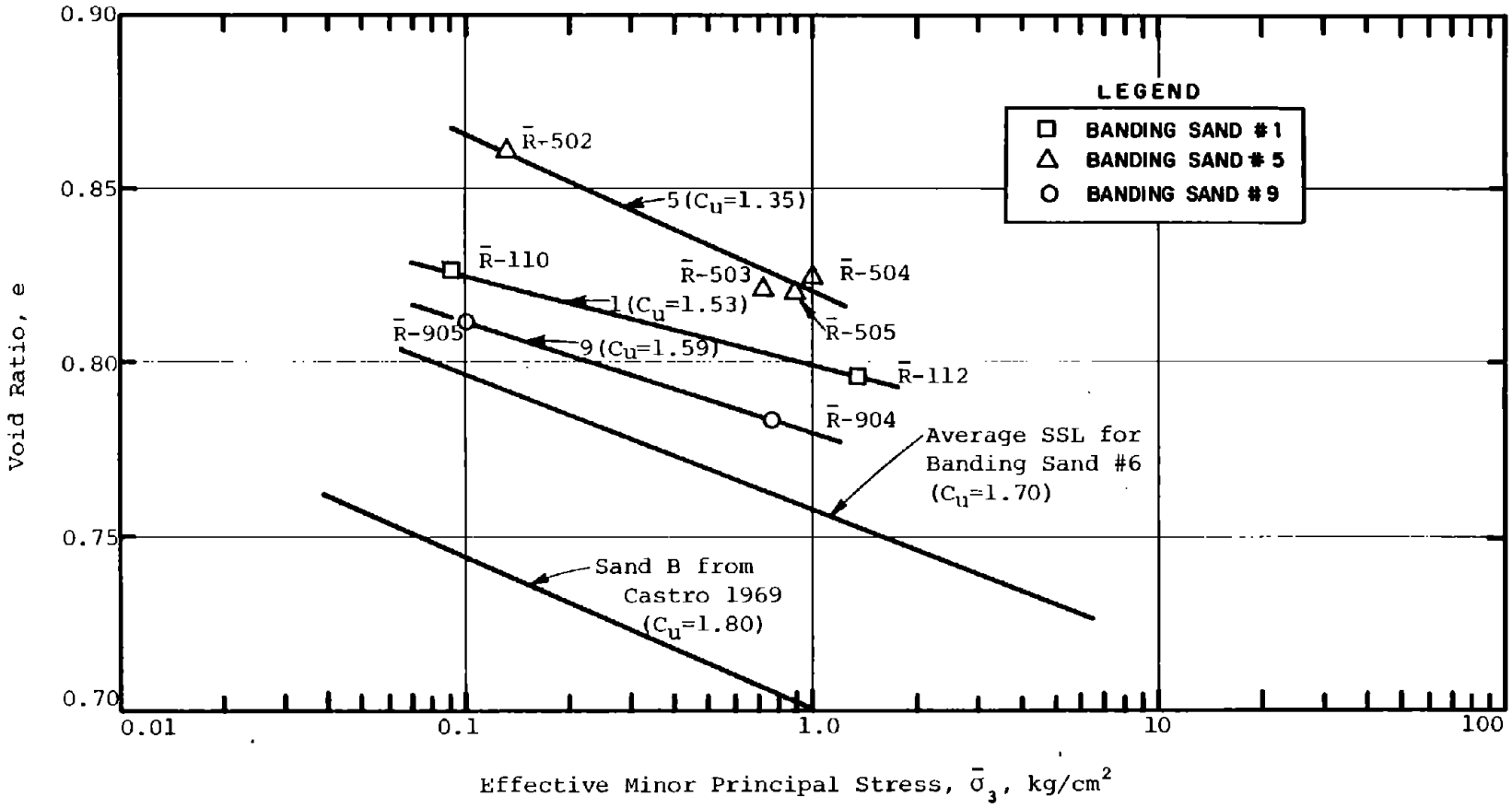

Fig. 6-7 Steady State Lines for Banding Sands Plotted in Terms of Void Ratio vs. $\bar{\sigma}_3$.

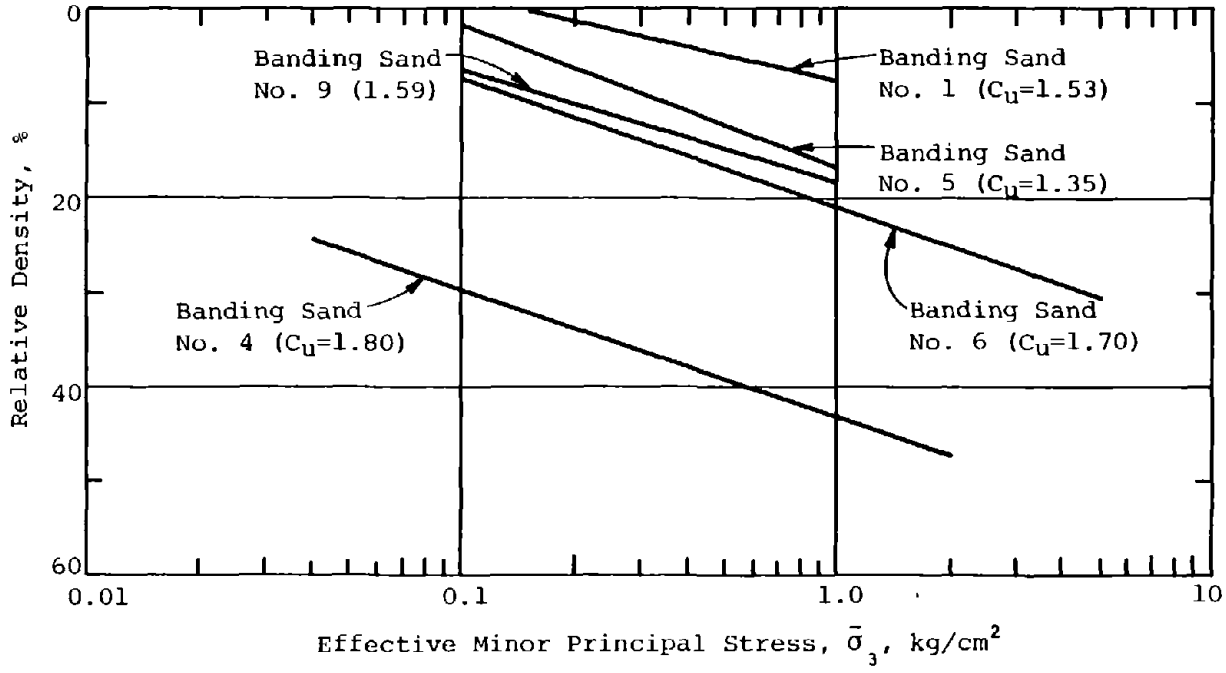

Fig. 6-8 Steady State Lines for Banding Sands Plotted in Terms of Relative Density vs. $\bar{\sigma}_3$

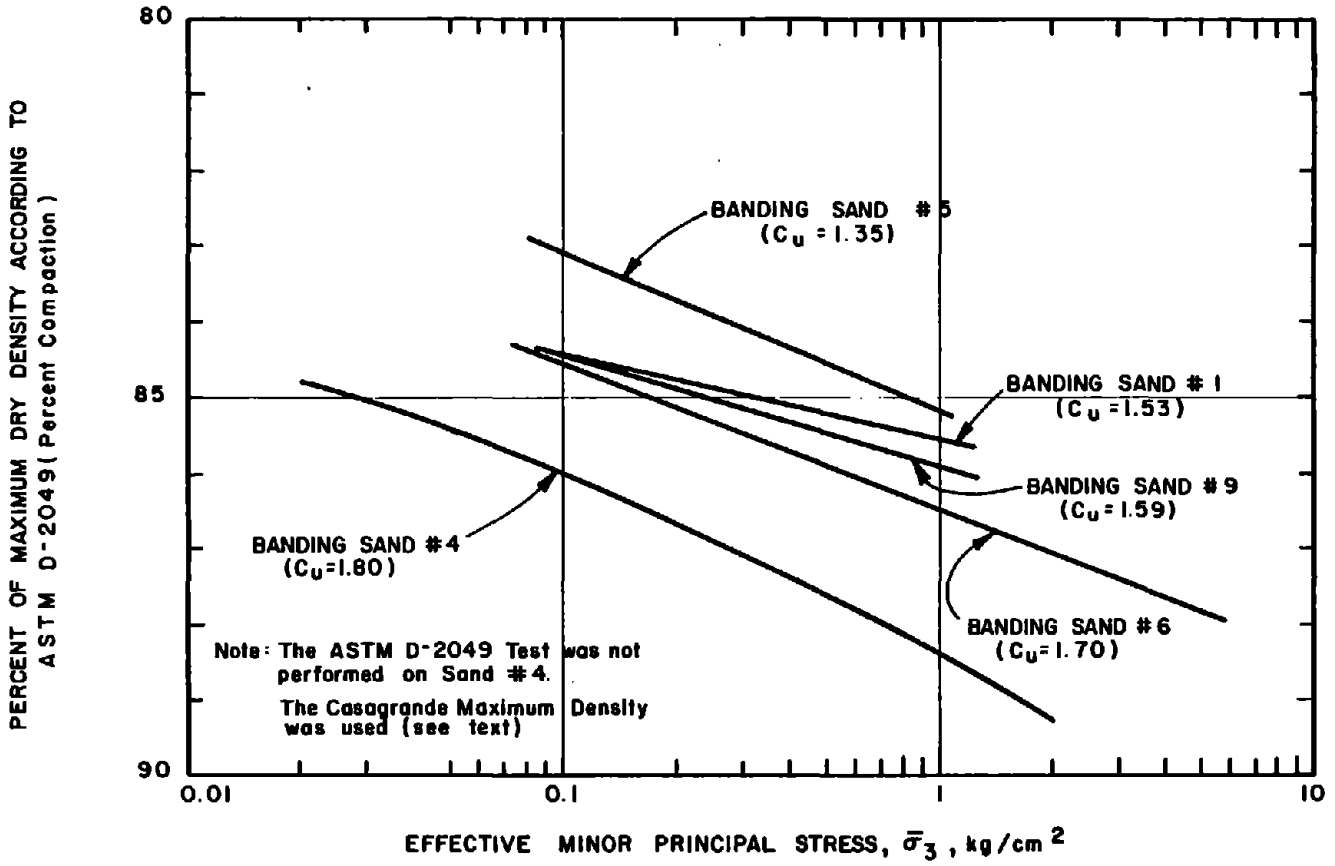

Fig. 6-9 Steady State Lines for Banding Sands Plotted in Terms of Percent Compaction vs $\bar{\sigma}_3$

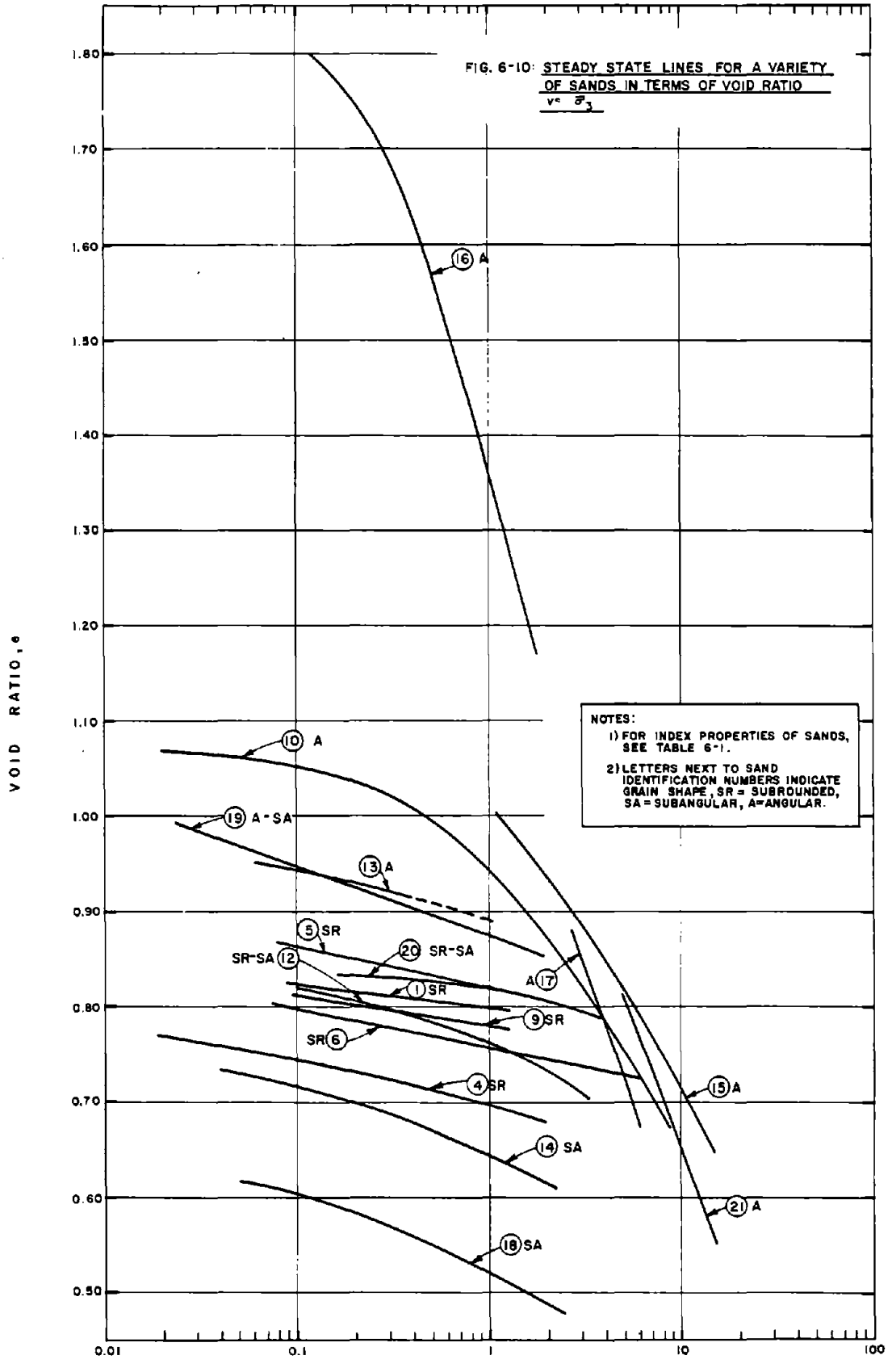

FIG. 6-10: STEADY STATE LINES FOR A VARIETY OF SANDS IN TERMS OF VOID RATIO vs $\bar{\sigma}_3$

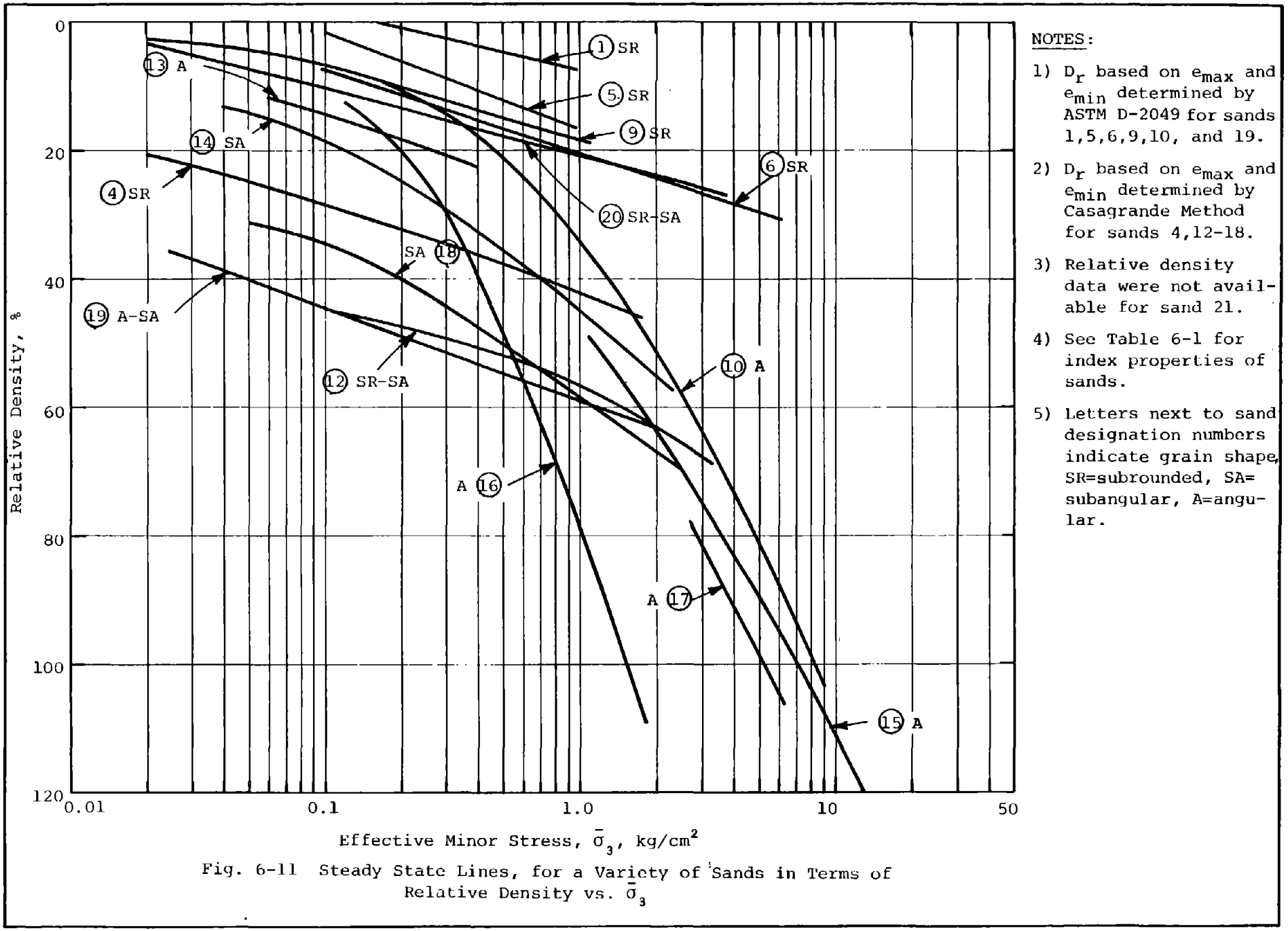

NOTES:

1) D_r based on e_{max} and e_{min} determined by ASTM D-2049 for sands 1,5,6,9,10, and 19.
2) D_r based on e_{max} and e_{min} determined by Casagrande Method for sands 4,12-18.
3) Relative density data were not available for sand 21.
4) See Table 6-1 for index properties of sands.
5) Letters next to sand designation numbers indicate grain shape, SR=subrounded, SA=subangular, A=angular.

Fig. 6-11 Steady State Lines, for a Variety of Sands in Terms of Relative Density vs. $\bar{\sigma}_3$

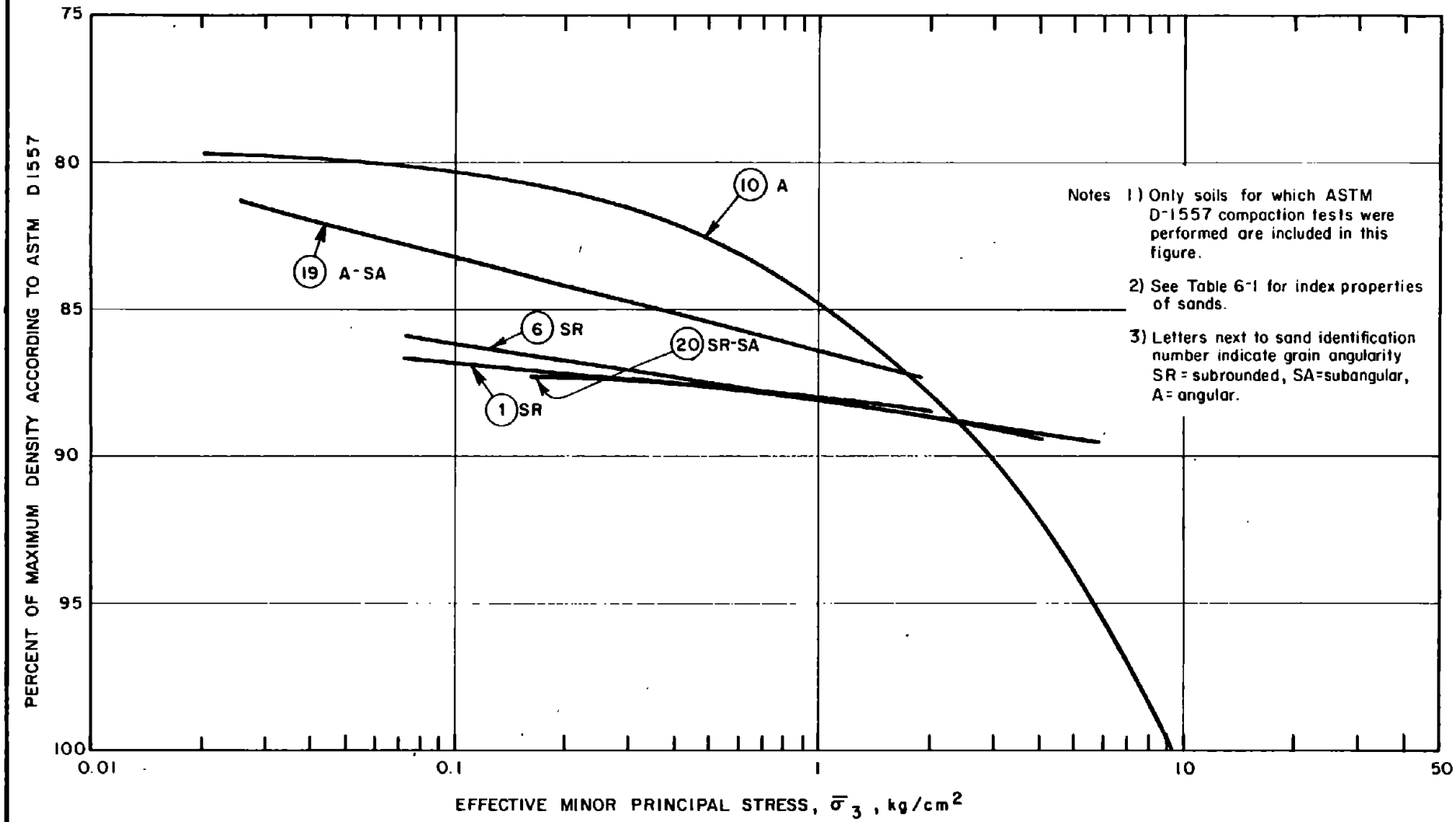

Fig. 6-12: Steady State Lines For a Variety of Sands in Terms of Percent Compaction vs. $\bar{\sigma}_3$.

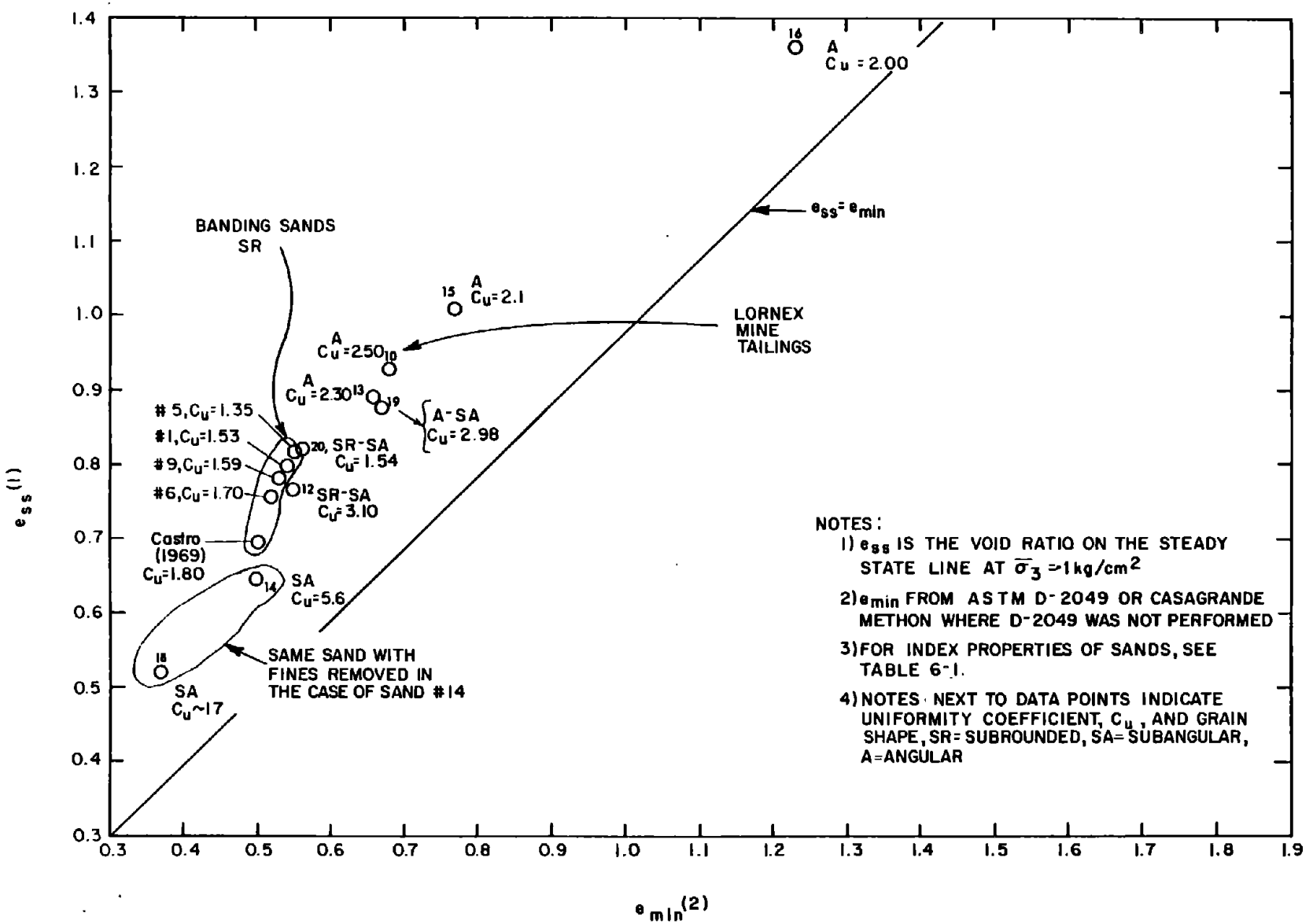

Fig. 6-13: Plot of e_{ss} vs. e_{min} for a Variety of Sands

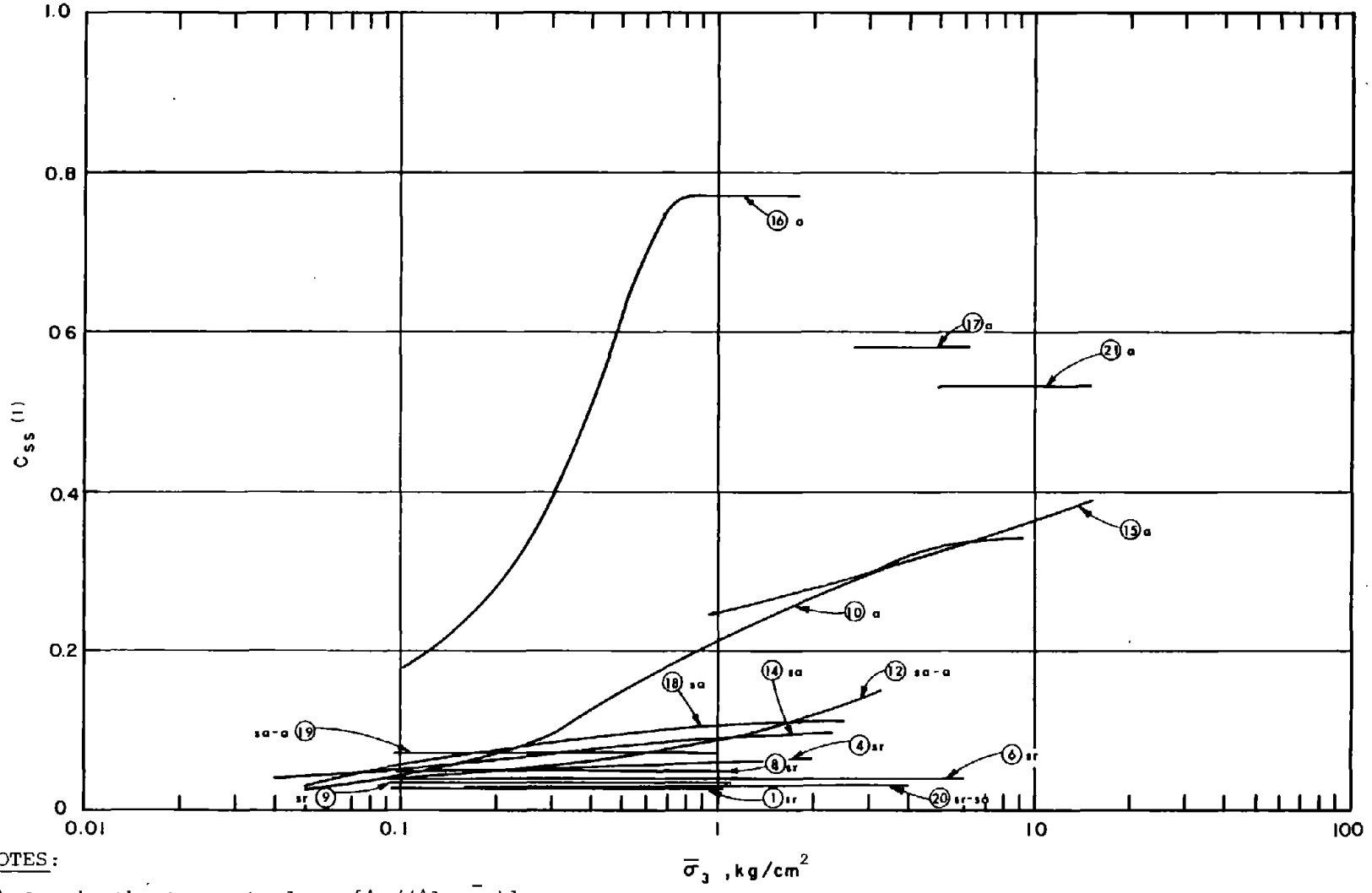

NOTES:

1) C_{ss} is the tangent slope $[\Delta e/(\Delta \log \bar{\sigma}_3)]$ of the steady state line.
2) For index properties of sands, see Table 6-1.

Fig. 6-14: Plot of C_{ss} vs. $\bar{\sigma}_3$ For a Variety of Sands

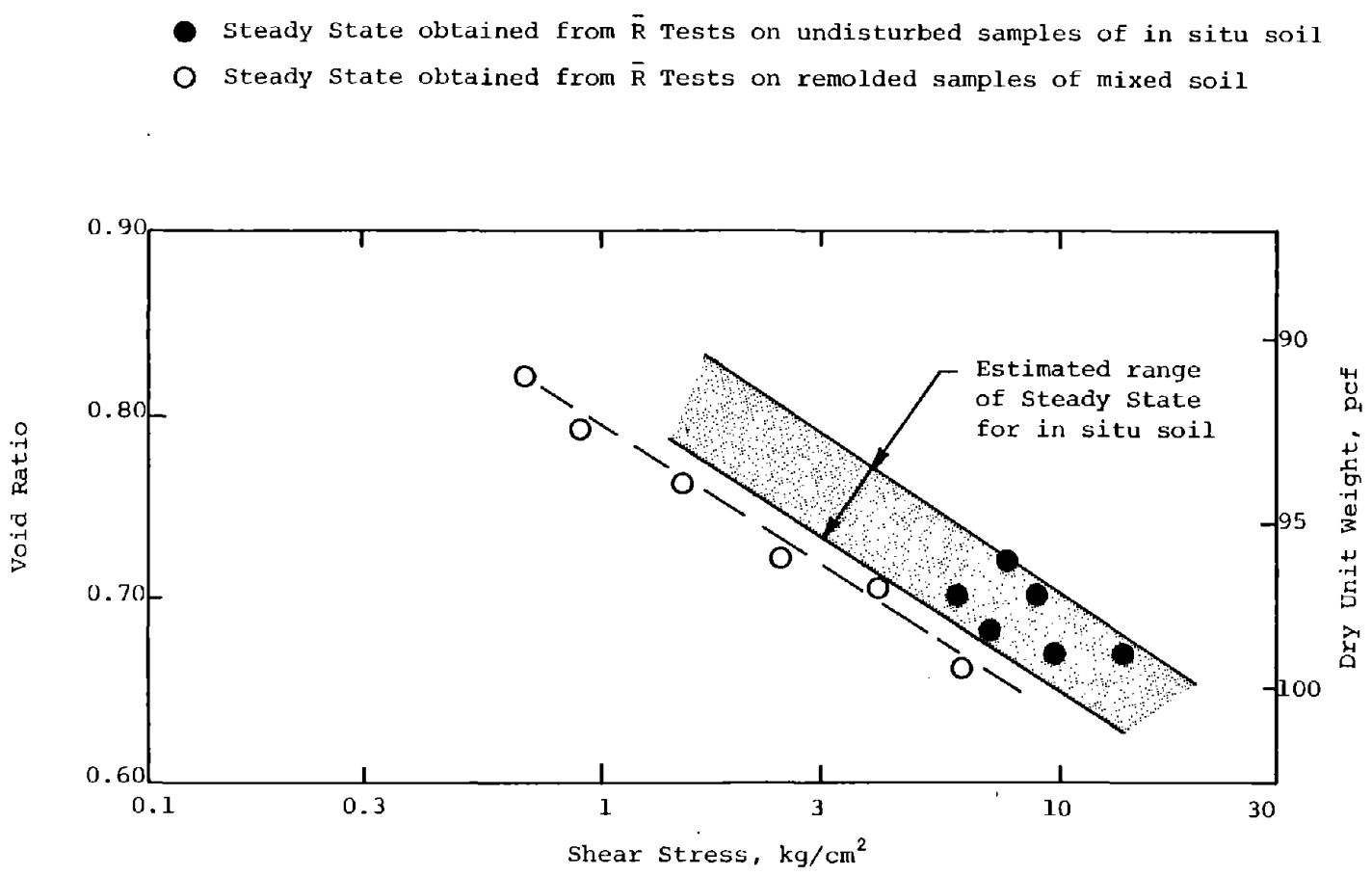

Fig. 6-15 Correcting Steady State Data for Void Ratio Changes During Triaxial Consolidation.

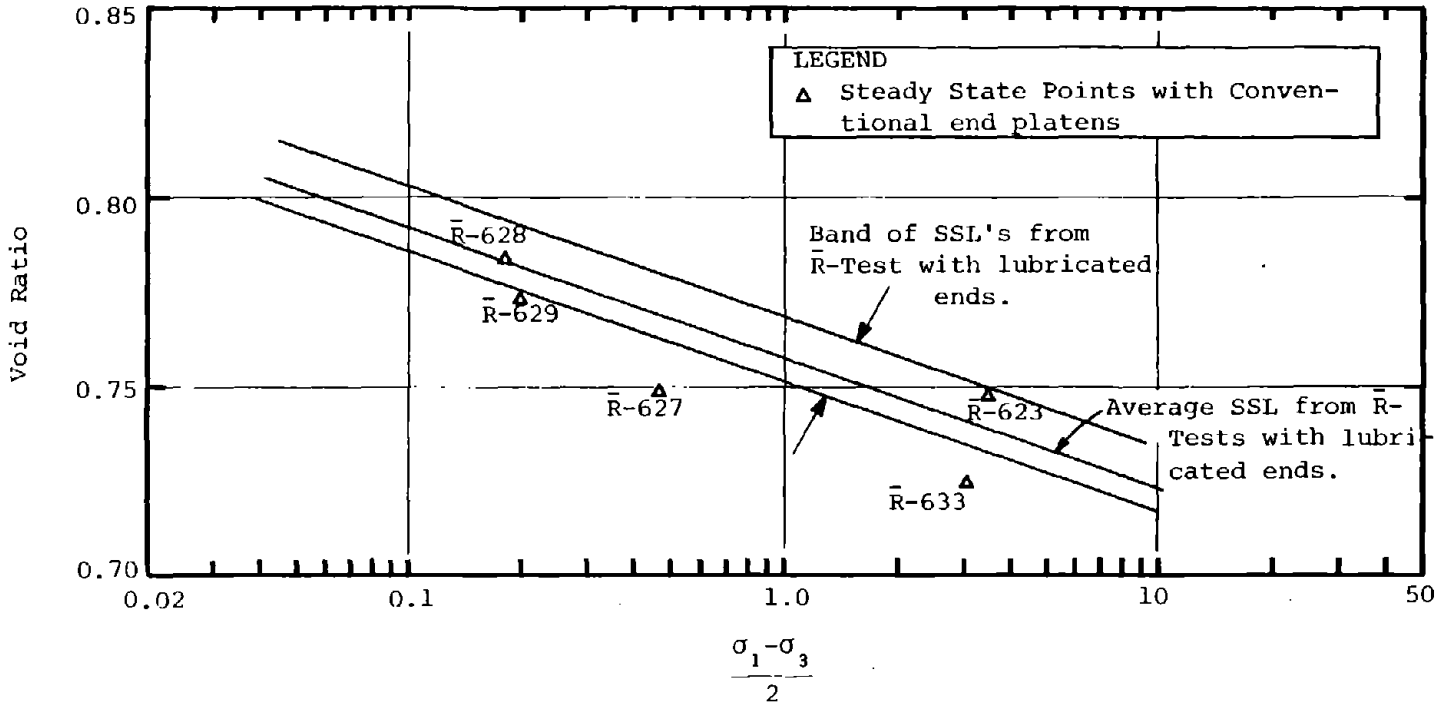

Fig. 7-1 Comparisons of Lubricated and Conventional End Platens for Banding Sand No. 6

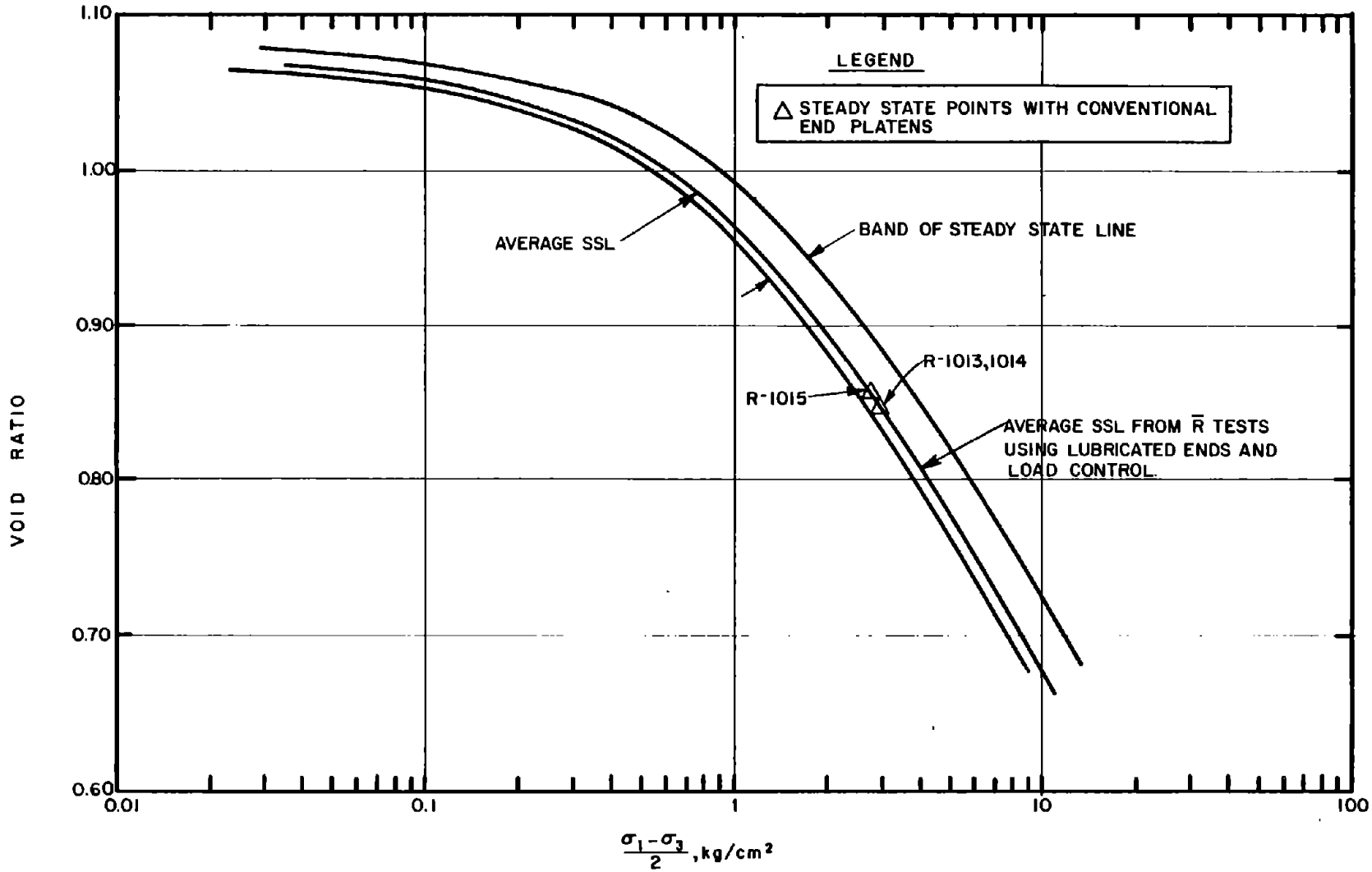

Fig. 7-2: Comparisons of Lubricated and Conventional End Platens for Mine Tailings

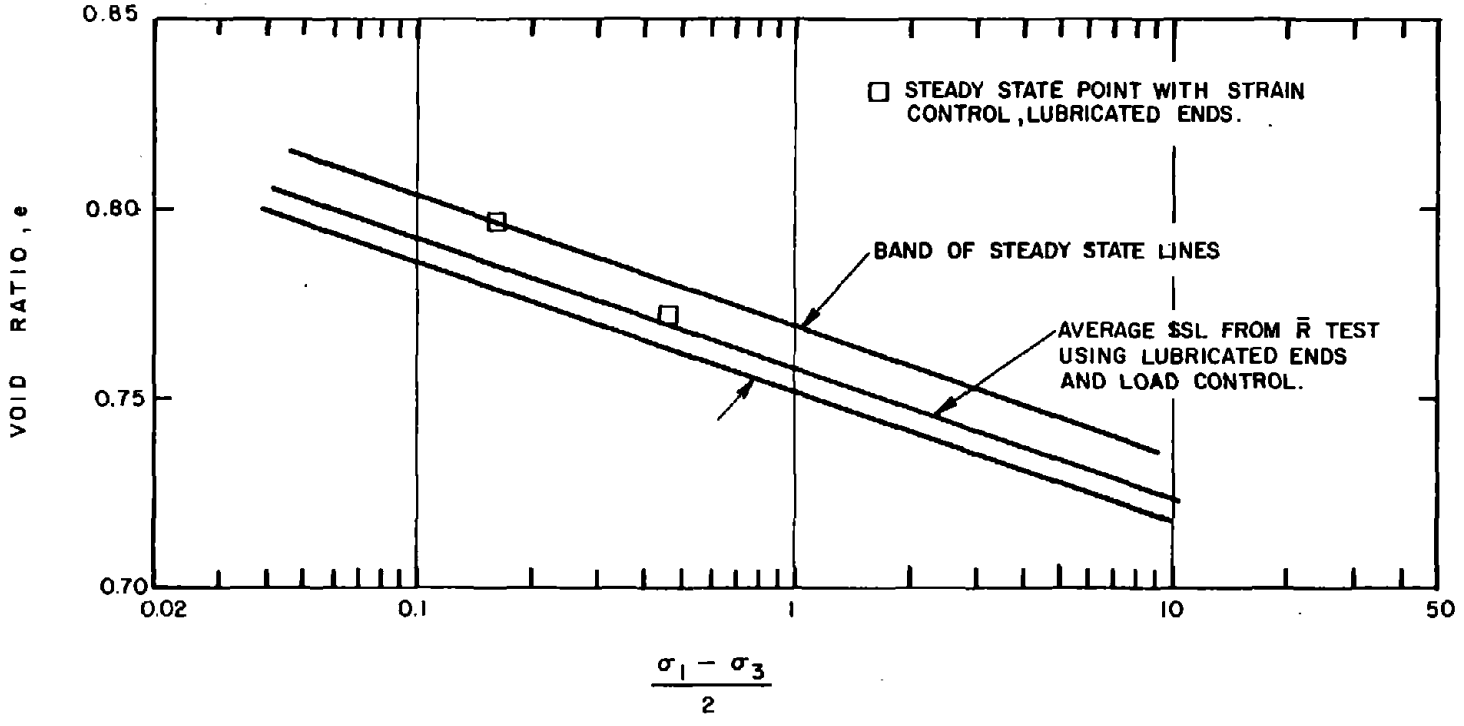

Fig. 7-3 Comparisons of Strain and Load Control for Banding Sand No. 6

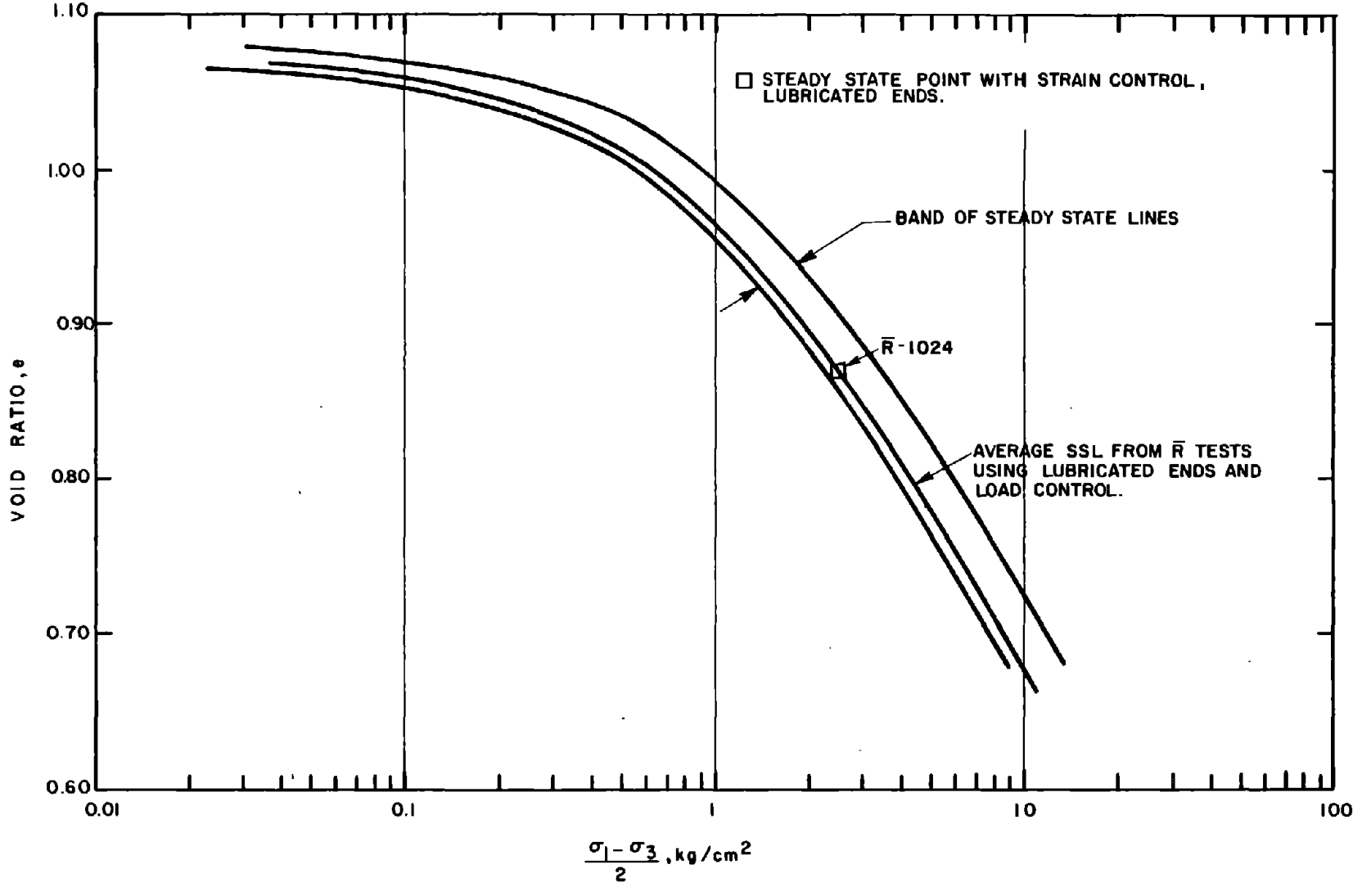

Fig 7-4 Comparisons of Strain and Load Control for Mine Tailings

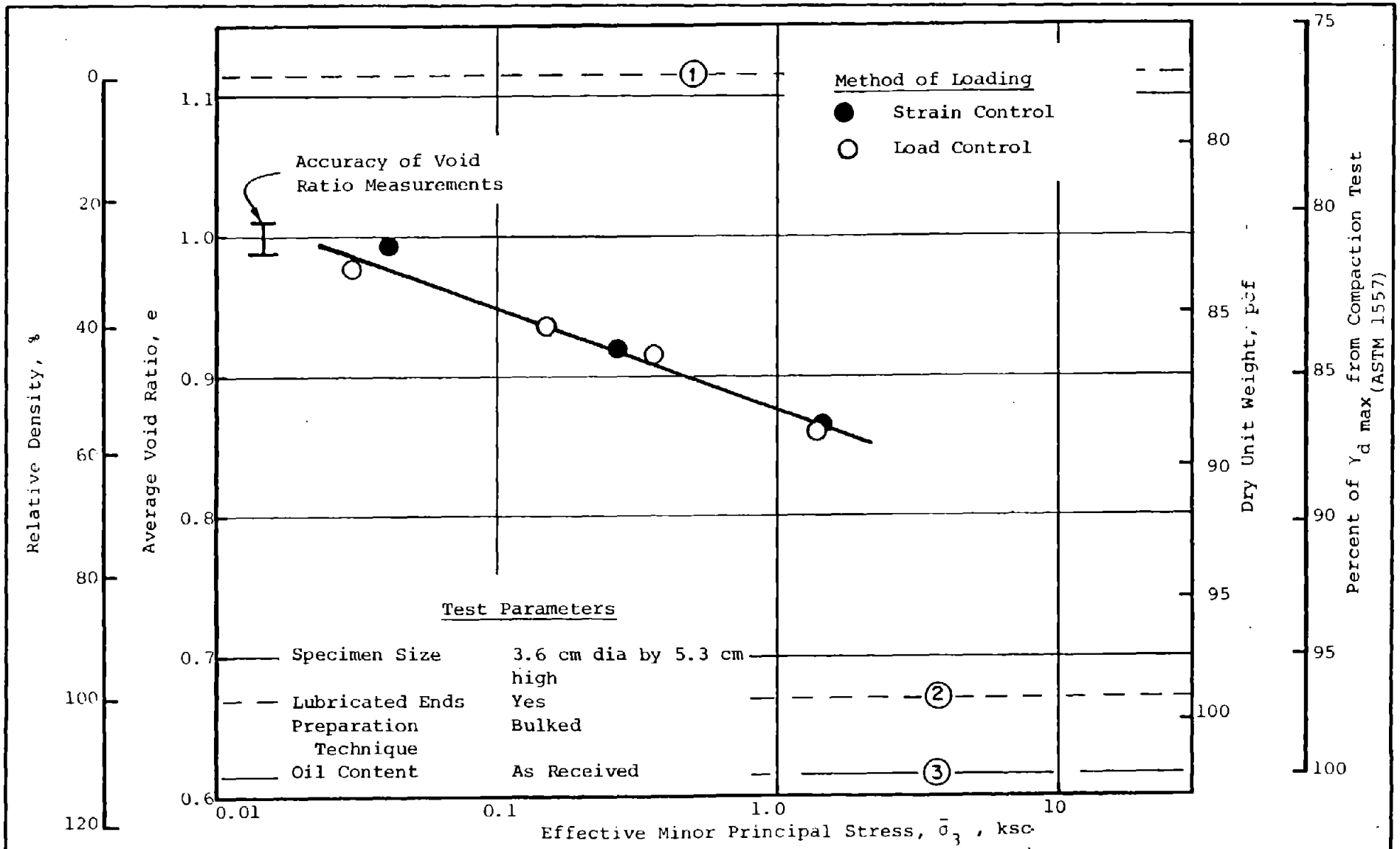

(1) Minimum Density (ASTM 2049)
(2) Maximum Density (ASTM 2049-Wet Method)
(3) Maximum Unit Weight (ASTM 1557-Method A)

Fig. 7-5 Comparisons of Strain and Load Control For Sand No. 19 (See Table 6-1)

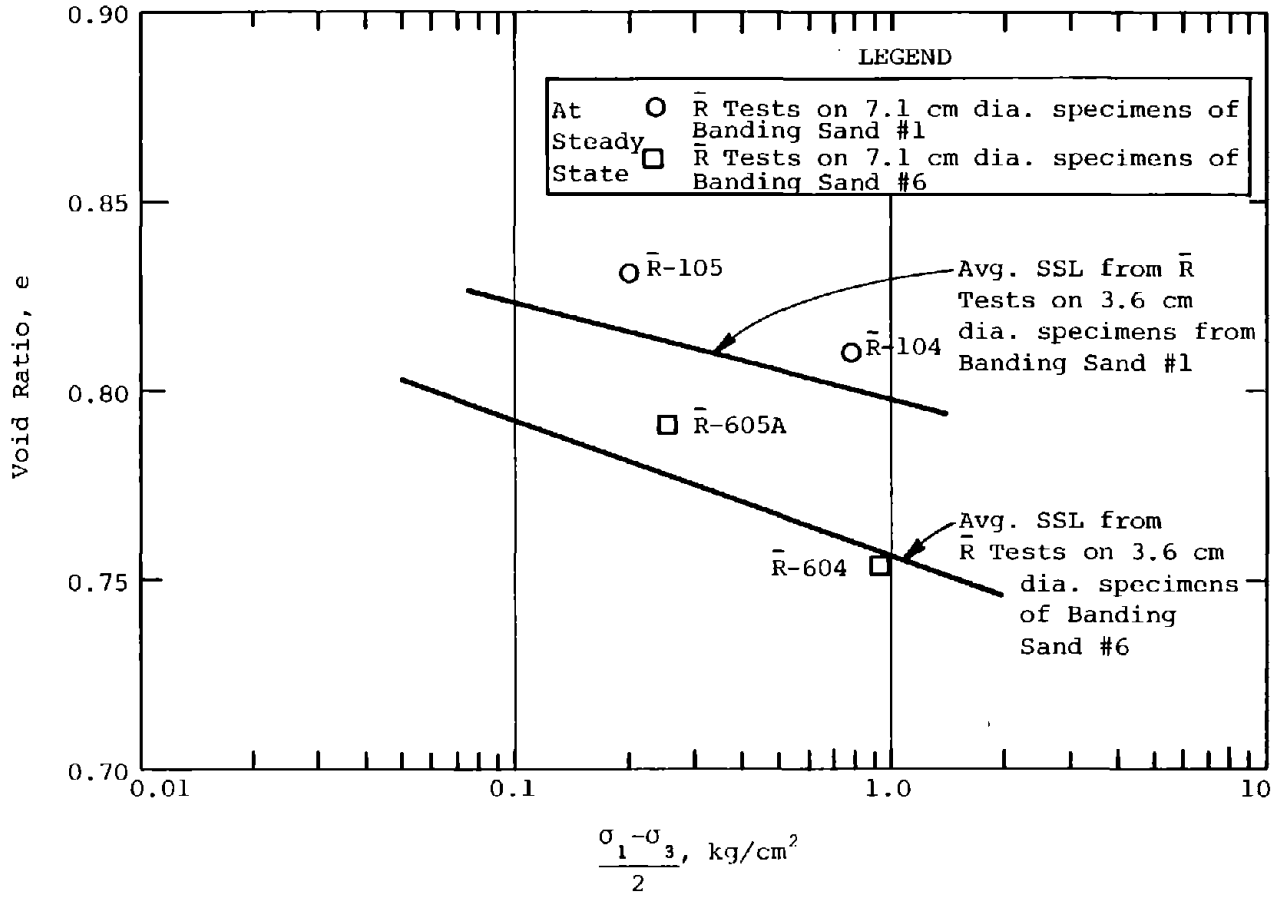

Fig. 7-6 Effect of Specimen Size on Steady State Line for Banding Sand

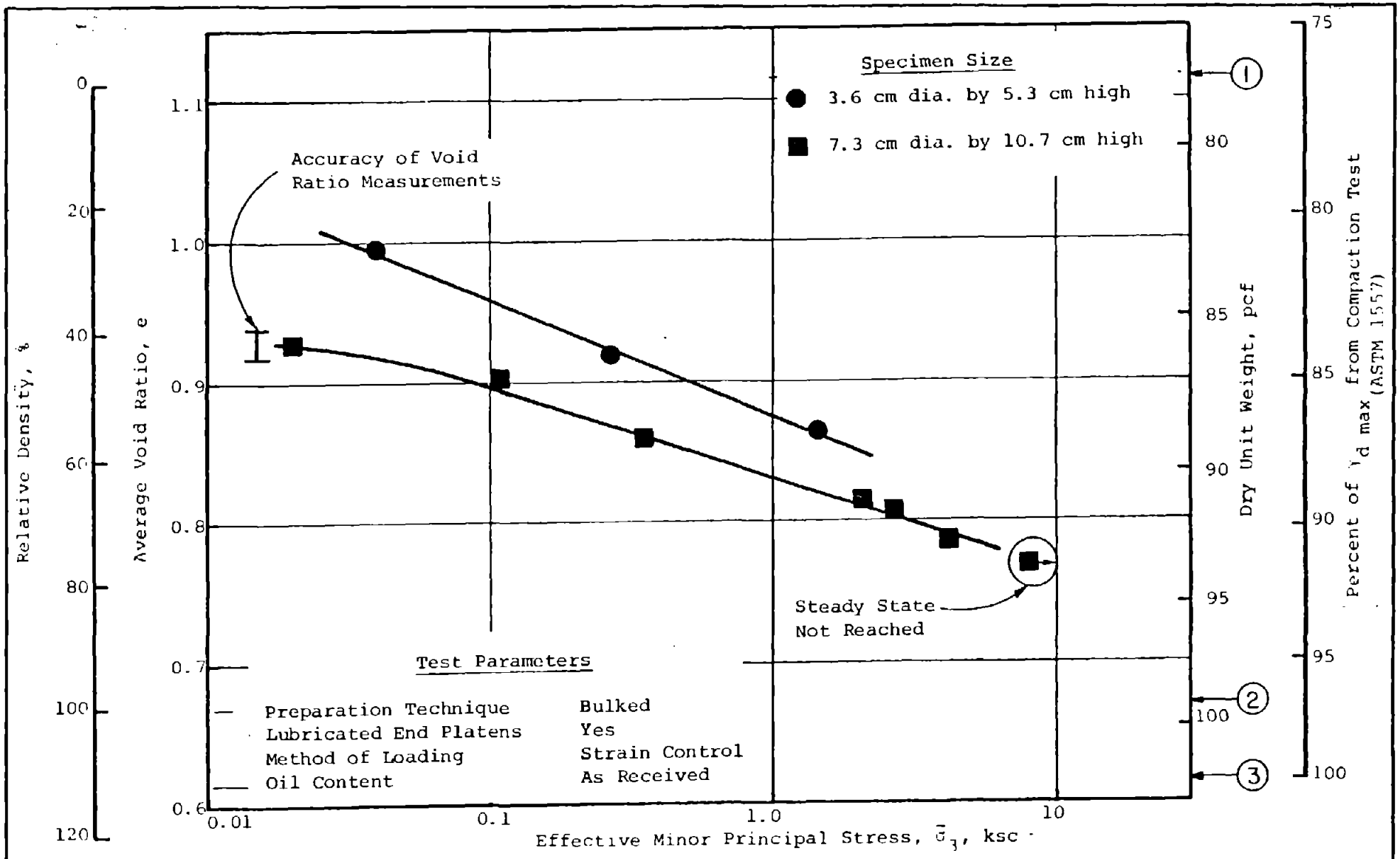

(1) Minimum Density (ASTM 2049)
(2) Maximum Density (ASTM 2049-Wet Method)
(3) Maximum Unit Weight (ASTM 1557-Method A)

Fig. 7.7 Effect of Specimen Size on Steady State Line For Sand No. 19 (See Table 6-1)

APPENDIX A

TRIAXIAL TEST RESULTS

APPENDIX A

TRIAXIAL TEST RESULTS

This appendix contains both tabular summaries and graphical presentations of results of all of the triaxial tests performed for this study. The table titles are given in the attached list of tables. Individiual test plots are grouped according to soil type and test type, as indicated in the attached list of figures. Within each group the test figures are in order by test number. For each test, the figure contains plots of 1) shear-stress, $(\sigma_1 - \sigma_3)/2$, vs axial strain; 2) induced pore pressure, $u-u_c$, vs axial strain; 3) effective stress path, $(\sigma_1 - \sigma_3)/2$ vs $(\bar{\sigma}_1 + \bar{\sigma}_3)/2$, and 4) state, void ratio vs $\bar{\sigma}_3$.

In the tables, the types of stress-strain curves observed in the tests are given, and Fig. A-1 contains schematic illustrations of the eight different types of stress-strain curves, as discussed in detail in Section 4 of the report.

It will be noted in the tables and the test plots that some test numbers in the numerical sequence are missing. The missing numbers correspond to tests in which leakage, low saturation or equipment problems forced termination of the tests or rendered the results meaningless.

APPENDIX A

LIST OF TABLES

LIST OF FIGURES

TABLE A-1 - SUMMARY OF TEST RESULTS - BANDING SAND #6
ISOTROPICALLY CONSOLIDATED-UNDRAINED
AXIAL COMPRESSION ($\bar{R}$) TESTS

Test No.	Specimen Dia. cm	Specimen Ht. cm	Void Ratio[1] In Mold e_m	Void Ratio[1] Under 30" Hg e_i	Void Ratio[1] After Consolidation e_c	Effective Consolidation Stress $\bar{\sigma}_{3c}$ kg/cm²	Consolidation Stress Ratio $\bar{\sigma}_{1c}/\bar{\sigma}_{3c}$	Back Pressure u_c kg/cm²	B Value	End Caps [2]	Method of Loading [3]	Type of Stress-Strain Behavior [4]	Time to Peak Shear Stress min	Time from Peak to 25% Axial Strain sec	Peak Shear Stress $\frac{\sigma_1-\sigma_3}{2}$ kg/cm²	Steady State Shear Stress $\left(\frac{\sigma_1-\sigma_3}{2}\right)_s$ kg/cm²	Effective Stress at Steady State $\bar{\sigma}_{3s}$ kg/cm²
R̄-601	3.6	5.3	0.84	0.837	0.795	10	1.0	4.00	0.96	L1	LC	A	12	0.16	2.14	0.17	(5)
R̄-602	3.6	5.3	0.83	0.825	0.785	10	1.0	5.00	0.96	L1	LC	A	15	0.07	2.24	0.18	(5)
R̄-603	3.6	5.3	0.81	0.805	0.770	10	1.0	4.00	0.95	L1	LC	A	18	0.08	2.53	0.31	0.48
R̄-604	7.1	10.7	0.83	0.793	0.754	20	1.0	8.00	0.97	L1	LC	A	13	0.68	5.69	0.92	0.96
R̄-605A	7.1	10.7	0.84	0.819	0.791	10	1.0	5.00	0.97	L1	LC	A	10	0.73	2.56	0.25	(5)
R̄-605	3.6	5.3	0.82	0.810	0.801	2	1.0	5.00	0.94[6]	L	LC	A	13	1.53	0.41	0.04	0.10
R̄-607	3.6	5.3	0.83	0.814	0.794	4	1.0	5.00	0.95	L1	LC	A	13	1.54	0.83	0.13	0.13
R̄-608	3.6	5.3	0.82	0.809	0.772	10	1.0	5.00	0.95	L1	LC	A	15	1.10	2.56	0.39	0.39
R̄-611	3.6	5.3	0.82	0.810	0.744	40	1.0	6.00	0.95	L1	LC	A	18	0.90	11.46	3.48	3.60
R̄-612	3.6	5.3	0.80	0.801	0.738	40	1.0	6.00	0.98	L1	LC	A	19	0.71	12.27	4.08	4.08
R̄-613	3.6	5.3	0.80	0.793	0.761	10	1.0	5.00	0.94	L1	LC	A	12	1.89	2.31	0.56	0.64
R̄-614	3.6	5.3	0.82	0.810	0.792	4	1.0	6.00	0.96	L1	LC	A	12	1.27	0.78	0.16	0.16
R̄-615	3.6	5.3	0.81	0.810	0.791	4	1.0	4.00	1.00	L1	LC	A	14	1.65	0.88	0.19	0.19
R̄-616	3.6	5.3	0.76	0.772	0.765	0.30	1.0	5.00	1.00	L1	LC	C	21	-	0.33	0.26	0.30
R̄-617	3.6	5.3	0.69	0.713[7]	0.704	2	1.0	4.00	0.97	L1	LC	E	-	-	-	-	-
R̄-618	3.6	5.3	0.76	0.765	0.765	1	1.0	10.00	0.88[8]	L1	LC	A-E	-	-	-	-	-
R̄-619	3.6	5.3	0.75	0.734	0.734	1	1.0	14.00	0.94[9]	L1	LC	C	100	5.25	2.11	1.44	1.45
R̄-620	3.6	5.3	0.74	0.747	0.747	1	1.0	7.00	0.97	L1	LC	E	-	-	-	-	-
R̄-621	3.6	5.3	0.73	0.728	0.726	1.50	1.0	9.00	0.86[10]	L1	LC	E	-	-	-	-	-
R̄-622	3.6	5.3	0.74	0.738	0.738	1	1.0	7.00	0.86	L1	LC	E	-	-	-	-	-
R̄-623	3.6	5.3	0.81	0.806	0.748	40	1.0	6.00	0.94	C	LC	A	18	0.88	11.40	3.47	3.87
R̄-624	3.6	5.3	0.79	0.789	0.774	4	1.0	5.00	0.98	L1	LC	A	18	2.06	1.10	0.34	0.31
R̄-625	3.6	5.3	0.79	0.789	0.774	4	1.0	5.00	0.97	L1	LC	A	17	1.70	1.06	0.30	0.27
R̄-626	3.6	5.3	0.79	0.785	0.770	4	1.0	5.00	0.95	L1	LC	A	17	3.46	1.00	0.38	0.35
R̄-627	3.6	8.1	-	0.763	0.749	4	1.0	5.00	0.97	C	LC	A	19	1.57	1.16	0.47	0.51
R̄-628	3.6	8.1	-	0.803	0.784	4	1.0	5.00	0.98	C	LC	A	15	2.33	0.92	0.18	0.18
R̄-629	3.6	8.1	-	0.791	0.773	4	1.0	5.00	0.98	C	LC	A	15	30	0.95	0.20	0.18
R̄-631	3.6	5.3	0.79	0.790	0.728	40	1.0	5.00	1.00	L2	LC	A	19	0.67	11.94	4.96	5.12
R̄-632	3.6	5.3	0.85	0.841	0.782	20	1.0	5.00	1.00	L2	LC	A	15	1.34	4.80	0.41	0.52
R̄-633	3.6	8.1	-	0.791	0.725	40	1.0	5.00	0.97	C	LC	A	18	1.39	11.39	3.02	3.20
R̄-634	3.6	5.3	0.83	0.819	0.796	4	1.0	5.00	0.97	L2	SC	A	1.4	3408	0.90	0.16	0.17
R̄-635	3.6	5.3	0.79	0.791	0.772	4	1.0	5.00	0.96	L2	SC	A	1.3	3432	1.07	0.47	0.47

Notes:
(1) G = 2.66
(2) C - Conventional Ends
L1 - Lubricated, Type 1
L2 - Lubricated, Type 2
(3) LC - Load Control
SC - Strain Control
(4) For description of symbols see Section 4, Stress-Strain Curves
(5) Pore Pressure record shows effective stress equal to zero at low strain.
(6) B = 0.94 at u_c = 4.00 kg/cm²
(7) Under 7.5 in. Hg vacuum
(8) B = 0.88 at u_c = 7.00 kg/cm²
(9) B = 0.94 at u_c = 4.00 kg/cm²
(10) B = 0.86 at u_c = 7.00 kg/cm²

TABLE A-2 - SUMMARY OF $\bar{R}$-TEST RESULTS - MINE TAILINGS
ISOTROPICALLY CONSOLIDATED-UNDRAINED
AXIAL COMPRESSION ($\bar{R}$) TESTS

Test No.	Specimen Dia. cm	Specimen Ht. cm	Void Ratio[1] In Mold e_m	Void Ratio[1] Under 30" Hg e_i	Void Ratio[1] After Consolidation e_c	Effective Consolidation Stress $\bar{\sigma}_{3c}$ kg/cm²	Consolidation Stress Ratio $\bar{\sigma}_{1c}/\bar{\sigma}_{3c}$	Back Pressure u_c kg/cm²	B Value	End Caps [2]	Method of Loading [3]	Type of Stress-Strain Behavior [4]	Time to Peak Shear Stress min	Time from Peak to 25% Axial Strain sec	Peak Shear Stress $\frac{\sigma_1-\sigma_3}{2}$ kg/cm²	Steady State Shear Stress $\left(\frac{\sigma_1-\sigma_3}{2}\right)_{ss}$ kg/cm²	Effective Stress at Steady State $\bar{\sigma}_{3s}$ kg/cm²
$\bar{R}$-1002	3.6	5.3	1.09	1.034	0.921	8	1.0	8.00	1.00	L1	LC	A-B	6	62	2.18	1.78	1.37
$\bar{R}$-1003	3.6	5.3	1.01	0.977	0.938	4	1.0	6.00	0.97	L2	LC	B	-	-	1.15	1.26	0.92
$\bar{R}$-1004	3.6	5.3	1.18	1.096	0.740	40	1.0	4.00	0.98	L2	LC	A-B	14	43	9.66	7.40	5.80
$\bar{R}$-1005	3.6	5.3	1.03	1.022	0.896	10	1.0	5.00	1.00	L2	LC	A-B	10	330	2.72	2.03	1.82
$\bar{R}$-1006	3.6	5.3	1.17	1.099	0.769	40	1.0	5.00	0.97	L2	LC	A-B	14	62	9.81	7.48	5.73
$\bar{R}$-1007	3.6	5.3	1.04	1.008	0.806	20	1.0	6.00	0.97	L2	LC	A-B	14	135	5.12	3.90	3.56
$\bar{R}$-1008	3.6	5.3	1.18	1.070	1.058	2	1.0	6.00	0.98	L2	LC	A	7	59.3	0.52	0.10	0.08
$\bar{R}$-1009	3.6	5.3	1.15	1.092	0.948	10	1.0	4.00	1.00	L2	LC	B	8	27.5	2.18	1.79	1.18
$\bar{R}$-1010	3.6	5.3	1.05	0.999	0.870	10	1.0	7.00	0.94[6]	L2	LC	A-B	10	1.55	2.80	2.43	1.63
$\bar{R}$-1011	3.6	5.3	1.00	0.979	0.705	40	1.0	5.00	1.00	L2	LC	A-B	14	9.5	11.51	8.26	6.16
$\bar{R}$-1012	3.6	5.3	0.95	0.928	0.777	20	1.0	6.00	1.00	L2	LC	B	12	111	5.97	5.27	3.88
$\bar{R}$-1013	3.48	7.59	-	0.952	0.845	10	1.0	6.00	0.97	C	LC	B	11	2.60	3.64	2.99	2.44
$\bar{R}$-1014	3.49	7.41	-	0.954	0.845	10	1.0	5.00	0.97	C	LC	B	10	93	3.60	2.94	2.30
$\bar{R}$-1015	3.49	8.02	-	0.945	0.851	10	1.0	4.00	0.97	C	LC	B	11	106	2.84	2.75	2.10
$\bar{R}$-1016	3.6	5.3	0.98	0.958	0.849	10	1.0	4.00	1.00	L2	LC	B	-	-	2.76	2.75	2.01
$\bar{R}$-1017	3.6	5.3	0.98	0.952	0.850	10	1.0	5.00	1.00	L2	LC	B	11	632	2.71	2.85	2.00
$\bar{R}$-1018	3.6	5.3	1.14	1.078	1.078	1	1.0	5.00	0.97	L2	LC	A	12	1.56	0.37	0.04	0.03
$\bar{R}$-1019	3.6	5.3	1.12	1.056	1.056	1	1.0	6.00	0.95	L2	LC	A	13	(5)	0.36	0.04	0.02
$\bar{R}$-1020	3.6	5.3	1.01	0.977	0.858	10	1.0	5.00	0.98	L2	LC	B	10	19.3	3.52	2.60	2.00
$\bar{R}$-1021	3.6	5.3	1.18	1.090	1.013	4	1.0	5.00	0.98	L2	LC	A	16	11	1.01	0.51	0.40
$\bar{R}$-1022	3.6	5.3	1.15	1.073	1.001	4	1.0	5.00	0.97	L2	LC	A	16	5.1	1.00	0.61	0.47
$\bar{R}$-1023	3.6	5.3	1.04	0.997	0.700	40	1.0	5.00	0.97	L2	LC	A-B	15	159	10.09	7.78	5.36
$\bar{R}$-1024	3.6	5.3	1.05	1.009	0.870	10	1.0	6.00	0.94[7]	L2	SC	A-B	5.73	1802	2.83	2.42	1.64
$\bar{R}$-1025	3.6	5.3	0.94	0.754	0.675	40	1.0	5.00	1.00	L2	LC	A-B	17	952	11.66	9.09	7.20
$\bar{R}$-1026	3.6	5.3	0.87	0.872	0.863	2	1.0	5.00	0.97	L2	LC	D	-	-	-	-	-
$\bar{R}$-1029	3.6	5.3	1.00	0.997	1.000	0.40	1.0	9.60	0.93[8]	L2	LC	D	-	-	-	-	-

Notes: (1) G = 2.68
(2) C - Conventional Ends
L1 - Lubricated, Type 1
L2 - Lubricated, Type 2
(3) LC - Load Control
SC - Strain Control
(4) For description of symbols see Section 4, Stress-Strain Curves
(5) Recorder speed too slow to interpret time data
(6) B-value = 0.94 at u_c = 6.00 kg/cm²
(7) B-value = 0.94 at u_c = 5.00 kg/cm²
(8) B-value = 0.93 at u_c = 9.00 kg/cm²

TABLE A-3 - SUMMARY OF $\bar{R}$-TEST RESULTS - BANDING SANDS #1, 5 AND 9
ISOTROPICALLY CONSOLIDATED-UNDRAINED
AXIAL COMPRESSION ($\bar{R}$) TESTS

Test No.	Specimen Dia. (cm)	Specimen Ht. (cm)	Void Ratio[1] In Mold e_m	Void Ratio[1] Under 30" Hg e_i	Void Ratio[1] After Consolidation e_c	Effective Consolidation Stress $\bar{\sigma}_{3c}$ kg/cm²	Consolidation Stress Ratio $\bar{\sigma}_{1c}/\bar{\sigma}_{3c}$	Back Pressure u_c kg/cm²	B Value	End Caps [2]	Method of Loading [3]	Type of Stress-Strain Behavior [4]	Time to Peak Shear Stress min	Time from Peak to 25% Axial Strain sec	Peak Shear Stress $\frac{\sigma_1-\sigma_3}{2}$ kg/cm²	Steady State Shear Stress $\left(\frac{\sigma_1-\sigma_3}{2}\right)_s$ kg/cm²	Effective Stress at Steady State $\bar{\sigma}_{3s}$ kg/cm²
$\bar{R}$-104[8]	7.1	10.7	0.84	0.839	0.810	14	1.0	6.00	0.95	L1	LC	A	19	0.67	3.95	0.78	0.50
$\bar{R}$-105[8]	7.1	10.7	0.84	0.839	0.831	4	1.0	6.00	0.97	L1	LC	A	17	1.05	1.08	0.20	-
$\bar{R}$-108[8]	3.6	5.3	0.88	0.857	0.817	10	1.0	4.00	0.97	L1	LC	A	13	0.67	2.21	0.16	-
$\bar{R}$-110[8]	3.6	5.3	0.85	0.835	0.826	2	1.0	5.00	0.96	L1	LC	A	14	1.28	0.41	0.08	0.09
$\bar{R}$-112[8]	3.6	5.3	0.85	0.839	0.796	20	1.0	4.00	0.95	L1	LC	A	19	0.80	5.98	1.30	1.32
$\bar{R}$-502[9]	3.6	5.3	0.89	0.89[6]	0.861	4	1.0	10.00	0.89[5]	L1	LC	A	9	1.82	0.89	0.13	0.13
$\bar{R}$-503[9]	3.6	5.3	0.89	0.877	0.821	20	1.0	5.00	0.94	L1	LC	A	16	0.80	4.52	0.67	0.72
$\bar{R}$-504[9]	3.6	5.3	0.88	0.872	0.824	20	1.0	6.00	0.97	L1	LC	A	18	1.08	5.26	0.98	1.00
$\bar{R}$-505[9]	3.6	5.3	0.88	0.873	0.820	20	1.0	5.00	1.00	L1	LC	A	16	0.75	5.13	0.86	0.88
$\bar{R}$-904[10]	3.6	5.3	0.84	0.834	0.783	20	1.0	5.00	0.98	L1	LC	A	16	1.46	5.13	0.63	0.76
$\bar{R}$-905[10]	3.6	5.3	0.86	0.840	0.812	4	1.0	5.00	0.97	L1	LC	A	13	(7)	0.80	0.08	0.10

Notes:

(1) G = 2.66
(2) L1 - Lubricated, Type 1
L2 - Lubricated, Type 2
(3) LC - Load Control
(4) L - Liquefaction
(5) B-value = 0.89 at u = 9.00 kg/cm²
(6) Under 15 in Hg vacuum
(7) Timer not turned on
(8) Banding Sand #5 specimen
(9) Banding Sand #5 specimen
(10) Banding Sand #9 specimen

TABLE A-4 - SUMMARY OF $\bar{A}R$-TEST RESULTS - BANDING SAND #6
ANISOTROPICALLY CONSOLIDATED-UNDRAINED
AXIAL COMPRESSION ($\bar{A}R$) TESTS

Test No.	Specimen Dia. cm	Specimen Ht. cm	Void Ratio[1] In Mold e_m	Void Ratio[1] Under 30" Hg e_i	Void Ratio[1] After Consolidation e_c	Effective Consolidation Stress $\bar{\sigma}_{3c}$ kg/cm^2	Consolidation Stress Ratio $\bar{\sigma}_{1c}/\bar{\sigma}_{3c}$	Back Pressure u_c kg/cm^2	B Value	End Caps (2)	Method of Loading (3)	Type of Stress-Strain Behavior (4)	Time to Peak Shear Stress min	Time from Peak to 25% Axial Strain sec	Peak Shear Stress $\frac{\sigma_1-\sigma_3}{2}$ kg/cm^2	Steady State Shear Stress $\left(\frac{\sigma_1-\sigma_3}{2}\right)_s$ kg/cm^2	Effective Stress at Steady State $\bar{\sigma}_{3s}$ kg/cm^2
$\bar{A}R$-601	3.6	5.3	0.78	0.781	0.762	4	1.5	5.00	0.99	L1	LC	A	12	1.35	1.41	0.43	0.44
$\bar{A}R$-602	3.6	5.3	0.79	0.790	0.765	4	2.0	5.00	1.00	L1	LC	A	15	2.32	2.10	0.54	0.60
$\bar{A}R$-603	3.6	5.3	0.79	0.800	0.771	4	2.0	5.00	1.00	L2	LC	A	6	1[5]	2.19	0.48	0.50
$\bar{A}R$-604	3.6	5.3	0.79	0.790	0.764	4	2.0	5.00	1.00	L2	LC	A	11	1.01	2.15	0.46	0.46
$\bar{A}R$-605	3.6	5.3	0.78	0.787	0.766	4	1.5	5.00	0.98	L2	LC	A	13	1.35	1.42	0.35	0.34
$\bar{A}R$-606	3.6	5.3	0.78	0.786	0.765	4	1.5	5.00	0.97	L2	LC	A	14	1.36	1.45	0.38	0.35

Notes: (1) G = 2.66
(2) L1 - Lubricated, Type 1
L2 - Lubricated, Type 2
(3) LC - Load Control
(4) L - Liquefaction
(5) Recorder speed too slow to interpret time data

081

TABLE A-5 - SUMMARY OF $A\bar{R}$-TEST RESULTS - MINE TAILINGS
ANISOTROPICALLY CONSOLIDATED-UNDRAINED
AXIAL COMPRESSION ($A\bar{R}$) TESTS

Test No.	Specimen Dia. cm	Specimen Ht. cm	Void Ratio(1) In Mold e_m	Void Ratio(1) Under 30" Hg e_i	Void Ratio(1) After Consolidation e_c	Effective Consolidation Stress $\bar{\sigma}_{3c}$ kg/cm^2	Consolidation Stress Ratio $\bar{\sigma}_{1c}/\bar{\sigma}_{3c}$	Back Pressure u_c kg/cm^2	B Value	End Caps (2)	Method of Loading (3)	Type of Stress-Strain Behavior (4)	Time to Peak Shear Stress min	Time from Peak to 25% Axial Strain sec	Peak Shear Stress $\frac{\sigma_1-\sigma_3}{2}$ kg/cm^2	Steady State Shear Stress $\left(\frac{\sigma_1-\sigma_3}{2}\right)_s$ kg/cm^2	Effective Stress at Steady State $\bar{\sigma}_{3s}$ kg/cm^2
$A\bar{R}$-1001	3.6	5.3	1.10	1.051	0.832	10	2.0	5.00	0.98	L2	LC	A	35	29.0	5.55	3.87	2.98
$A\bar{R}$-1002	3.6	5.3	1.10	1.032	0.936	4	2.0	5.00	0.97	L2	LC	A	14	37.2	2.49	1.74	1.30
$A\bar{R}$-1003	3.6	5.3	1.08	1.020	0.926	3.20	2.5	5.00	0.96	L2	LC	A	9	58	2.81	1.98	1.48
$A\bar{R}$-1004	3.6	5.3	1.16	1.083	1.012	2	2.0	5.00	0.97	L2	LC	A	5	47.2	1.14	0.52	0.34

Notes: (1) G = 2.68
(2) L1 - Lubricated, Type 1
L2 - Lubricated, Type 2
(3) LC - Load Control
(4) L - Liquefaction

TABLE A-6 - SUMMARY OF CAR̄ TEST RESULTS - BANDING SAND #6
ANISOTROPICALLY CONSOLIDATED-UNDRAINED CYCLIC AXIAL COMPRESSION (CAR̄) TESTS

Test No.	Specimen Dia.	Specimen Ht.	Void Ratio(1) In Mold	Void Ratio(1) Under 30" Hg Vacuum	Void Ratio(1) After Consolidation	Effective Consolidation Stress $\bar{\sigma}_{3c}$	Consolidation Stress Ratio $\bar{\sigma}_{1c}/\bar{\sigma}_{3c}$	Back Pressure u_c	B Value	End Caps (2)	Cyclic Shear Stress $\left(\frac{\sigma_1-\sigma_3}{2}\right)_{cy}$	At Steady State: Number of Cycles of Loading	At Steady State: $\left(\frac{\sigma_1-\sigma_3}{2}\right)_{ss}$	At Steady State: $\bar{\sigma}_{3ss}$
	cm	cm	e_m	e_i	e_c	kg/cm²		kg/cm²			kg/cm²		kg/cm²	kg/cm²
CAR̄-602	3.6	5.3	0.79	0.785	0.766	4	1.5	5.00	0.97	L1	0.20	290	0.41	0.45
CAR̄-603	3.6	5.3	0.78	0.775	0.755	4	1.5	5.00	0.91(4)	L1	0.28	27	0.40	0.45
CAR̄-604	3.6	5.3	0.79	0.785	0.768	4	1.5	5.00	0.94	L1	0.22	132	0.42	0.38
CAR̄-605	3.6	5.3	0.79	0.783	0.764	4	1.5	6.00	0.97	L2	0.32	27	0.40	0.40
CAR̄-606	3.6	5.3	0.79	0.782	0.762	4	1.5	5.00	0.95	L2	0.36	7	0.36	0.32
CAR̄-607	3.6	5.3	0.79	0.786	0.768	4	1.5	5.00	0.95	L1	0.17	415	0.40	0.35
CAR̄-608	3.6	5.3	0.79	0.788	0.771	4	1.5	6.00	0.93	L1	0.36	8	0.39	0.39
CAR̄-609	3.6	5.3	0.79	0.780	0.760	4	2.0	6.00	0.93	L1	0.07	1394	0.67	0.63
CAR̄-610	3.6	5.3	0.79	0.780	0.756	4	2.0	5.00	0.95	L1	0.09	284	0.69	0.68
CAR̄-611	3.6	5.3	0.78	0.778	0.754	4	2.0	5.00	0.95	L1	0.11	451	0.71	0.70
CAR̄-612	3.6	5.3	0.78	0.784	0.758	4	2.0	5.00	0.96	L1	0.11	433	0.62	0.60
CAR̄-614	3.6	5.3	0.79	0.793	0.768	4	2.0	6.00	0.96	L1	0.11	309	0.56	0.56
CAR̄-615	3.6	5.3	0.78	0.784	0.762	4	2.0	5.00	0.97	L2	0.17	22	0.77	0.77
CAR̄-616	3.6	5.3	0.78	0.781	0.753	4	2.0	5.00	0.98	L2	0.21	4	0.49	0.51
CAR̄-617	3.6	5.3	0.79	0.791	0.771	4	1.5	5.00	0.98	L2	0.38	3	0.35	0.32
CAR̄-618	3.6	5.3	0.79	0.787	0.766	4	1.5	6.00	0.94(5)	L2	0.30	14(6)	0.33	0.31
CAR̄-621	3.6	5.3	0.87	0.856	0.799	4	2.0	5.00	0.97	L2	0.16	21	0.22	0.19
CAR̄-622	3.6	5.3	0.84	0.821	0.782	4	2.0	5.00	1.00	L2	0.15	20	0.26	0.24
CAR̄-623	3.6	5.3	0.82	0.812	0.775	4	2.0	5.00	0.97	L2	0.19	34	0.32	0.30
CAR̄-624	3.6	5.3	0.78	0.778	0.749	4	2.0	5.00	0.97	L2	0.20	12	0.52	0.50
CAR̄-625	3.6	5.3	0.65	0.655	0.642	4	2.0	6.00	0.94(7)	L2	0.60	201	-	-
CAR̄-626	3.6	5.3	0.74	0.745	0.722	4	2.0	5.00	0.96	L2	0.60	154	-	-
CAR̄-627	3.6	5.3	0.74	0.744	0725	4	2.0	5.00	0.98	L2	0.61	122	-	-
CAR̄-628	3.6	5.3	0.72	0.731	0.713	4	2.0	5.00	0.97	L2	0.59	100	-	-
CAR̄-629	3.6	5.3	0.70	0.705	0.690	4	2.0	5.00	0.96	L2	0.59	103	-	-
CAR̄-630	3.6	5.3	0.70	0.707	0.691	4	2.0	5.00	0.98	L2	1.09	101	-	-
CAR̄-631	3.6	5.3	0.78	0.770	0.752	4	1.5	5.00	0.98	L2	0.30	19	0.50	0.50
CAR̄-632	3.6	5.3	0.74	0.749	0.734	4	1.5	5.00	0.97	L2	0.30	51	2.40	2.60
CAR̄-633	3.6	5.3	0.70	0.715	0.701	4	1.5	5.00	0.98	L2	0.30	98	-	-

Notes:
(1) G = 2.66
(2) L1 - Lubricated, Type 1
L2 - Lubricated, Type 2
(3) D - Dilation, L - Liquefaction under Monotonic Loading
(4) B = 0.91 at u = 4.00 kg/cm²
(5) B = 0.94 at u = 5.00 kg/cm²
(6) Cycling stopped after 13 cycles, stresses and strains stable for 40 min., liquefaction on 14th cycle
(7) B = 0.94 at u = 5.00 kg/cm²
(8) Load cycled until 1.0 kg/cm² pore pressure build up. Specimen then loaded monotonically.
(9) All tests were load controlled.

TABLE A-7 - SUMMARY OF CAR̄ TEST RESULTS - MINE TAILINGS
ANISOTROPICALLY CONSOLIDATED-UNDRAINED CYCLIC
AXIAL COMPRESSION (CAR̄) TESTS

Test No.	Specimen Dia. cm	Specimen Ht. cm	Void Ratio(1) In Mold e_m	Void Ratio(1) Under 30" Hg Vacuum e_i	Void Ratio(1) After Consolidation e_c	Effective Consolidation Stress $\bar{\sigma}_{3c}$ kg/cm²	Consolidation Stress Ratio $\bar{\sigma}_{1c}/\bar{\sigma}_{3c}$	Back Pressure u_c kg/cm²	B Value	End Caps (2)	Cyclic Shear Stress $\left(\frac{\sigma_1 - \sigma_3}{2}\right)_{cy}$ kg/cm²	At Steady State: Number of Cycles of Loading	At Steady State: $\left(\frac{\sigma_1 - \sigma_3}{2}\right)_s$ kg/cm²	At Steady State: $\bar{\sigma}_{3s}$ kg/cm²
CAR̄-1001	3.6	5.3	1.12	1.040	0.831	10	2.0	5.00	0.97	L2	0.42	786	4.12	2.88
CAR̄-1002	3.6	5.3	0.94	0.930	0.887	3	2.0	5.00	0.97	L2	0.48	141	-	-
CAR̄-1003	3.6	5.3	0.98	0.955	0.911	3	2.0	5.00	0.98	L2	1.05	2	-	-
CAR̄-1004	3.6	5.3	1.08	1.042	0.914	8	1.38	5.00	0.98	L2	0.50	107	-	-
CAR̄-1005	3.6	5.3	1.08	1.040	0.910	8	1.38	5.00	0.96	L2	1.33	9	-	-
CAR̄-1006	3.6	5.3	0.95	0.937	0.895	3	2.0	5.00	0.97	L2	0.77	52	-	-
CAR̄-1007	3.6	5.3	0.96	0.946	0.899	3	2.0	6.00	0.95	L2	0.31	214	-	-
CAR̄-1007B	3.6	5.3	-	-	0.891(3)	3	2.0	6.00	0.95	L2	0.84	52	-	-

Notes: (1) G = 2.68
(2) L2 - Lubricated, Type 2
(3) Specimen from test CAR-1007 was reconsolidated after cycles and subject to higher cyclic stress (Test CAR-1007B)
(4) All tests were load controlled.

Geotechnical Engineers Inc.

Project 80696
March 1, 1982

Note: See Section 4 of report for discussion.

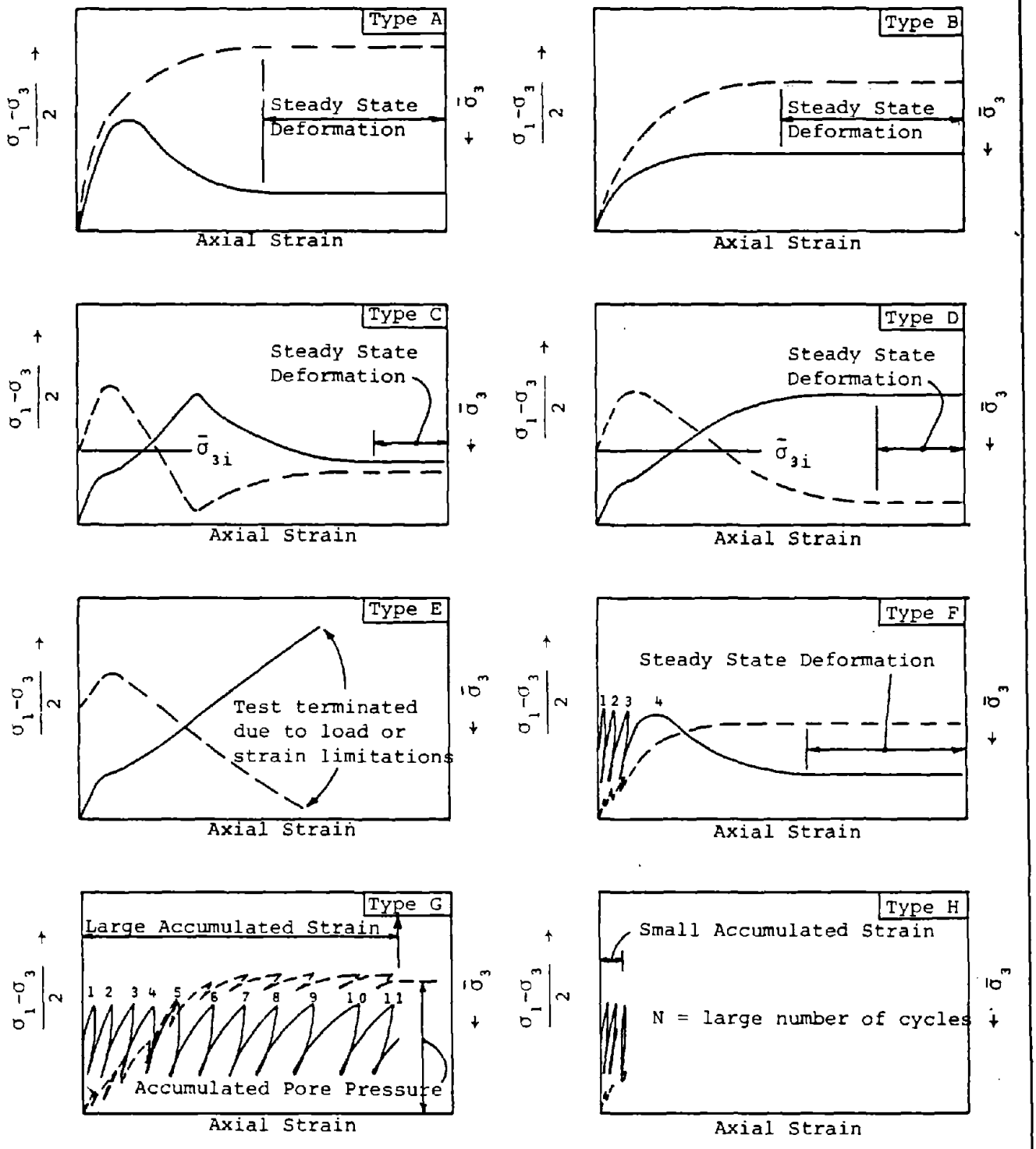

LEGEND

——— Shear Stress $\frac{\sigma_1-\sigma_3}{2}$, vs. axial strain

---- Effective minor principal stress, $\bar{\sigma}_3$, vs. axial strain

Fig. A-1: Schematic Illustrations or Types of Stress-Strain Curves Observed

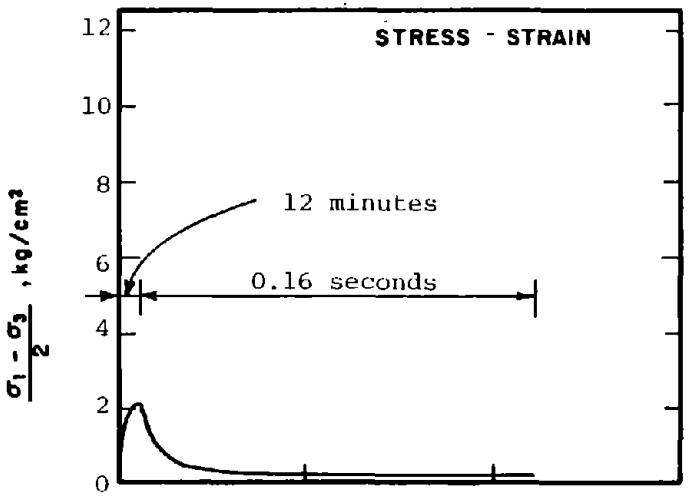

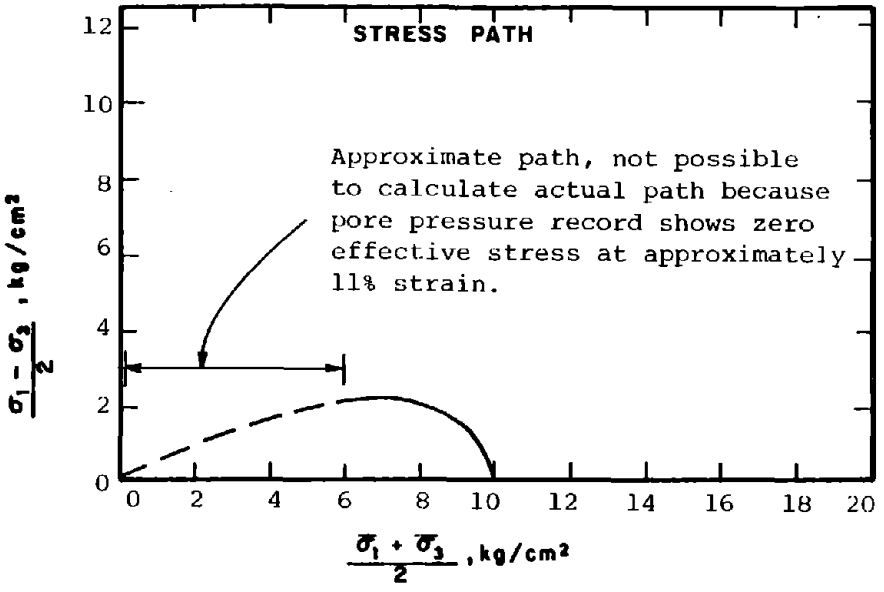

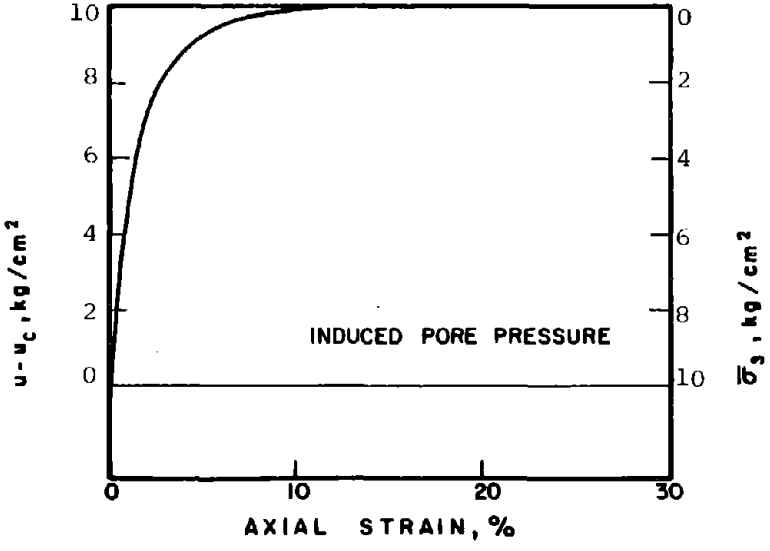

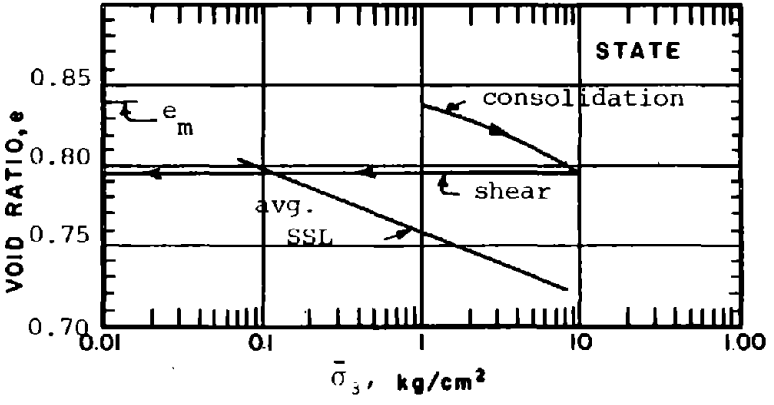

SOIL	: Banding Sand #6	METHOD OF LOADING:	Undrained, Axial Compression Load Control
STRUCTURE	: Compacted Moist		
STATE AFTER CONSOLIDATION:	$\bar{\sigma}_{3c}$ = 10.00 kg/cm², $\bar{\sigma}_{1c}$ = 10.00 kg/cm²	TESTING DETAILS	: Specimen Diameter 3.60 cm
	e_c = 0.795, γ_{dc} = 92.5 pcf		: Specimen Height 5.30 cm
			: End Platens: Lubricated, Type 1

R-601

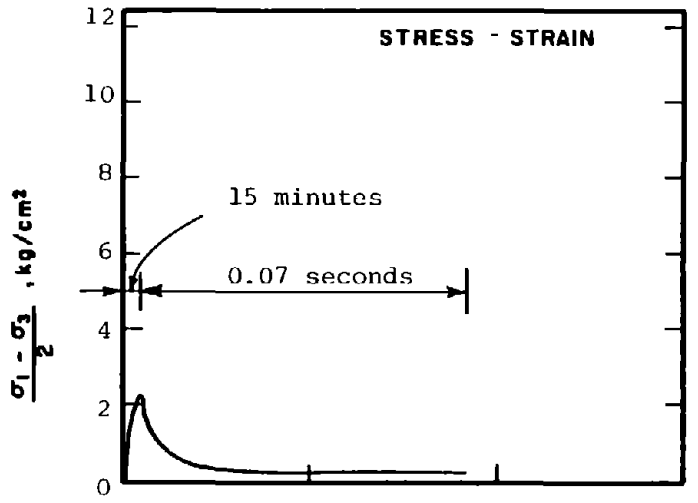

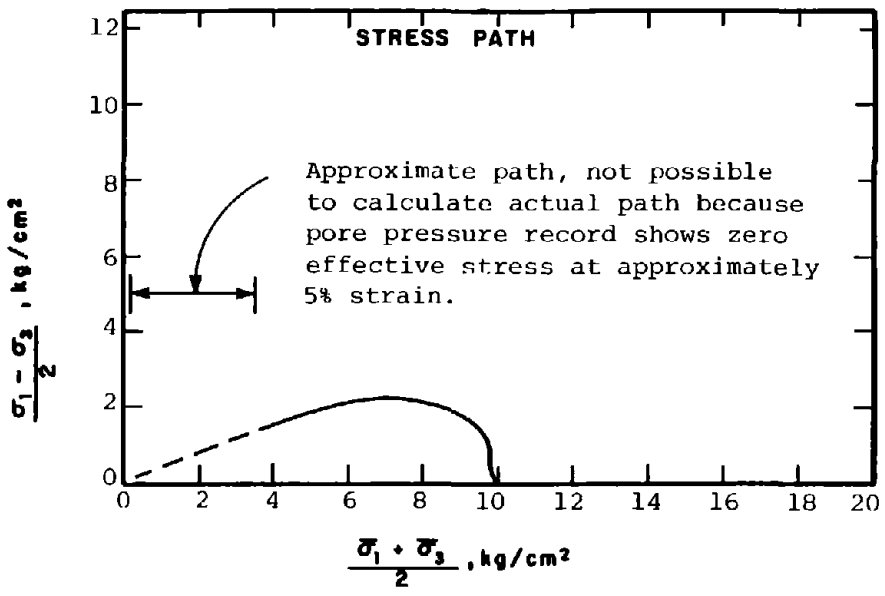

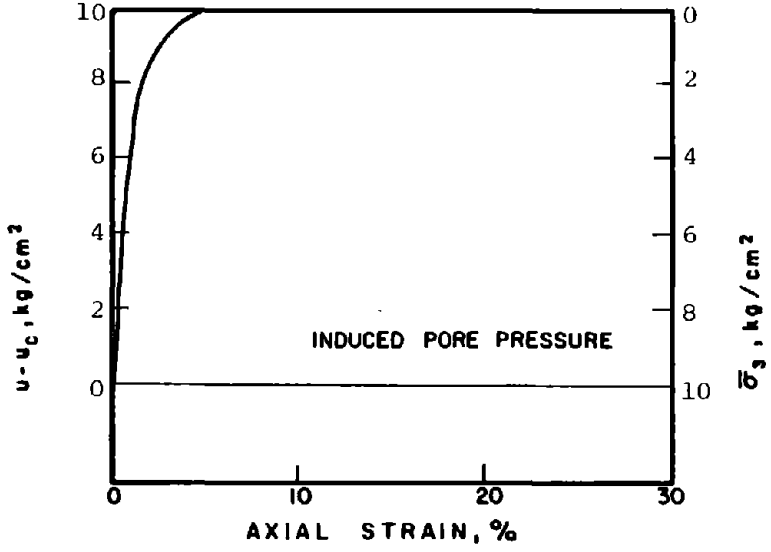

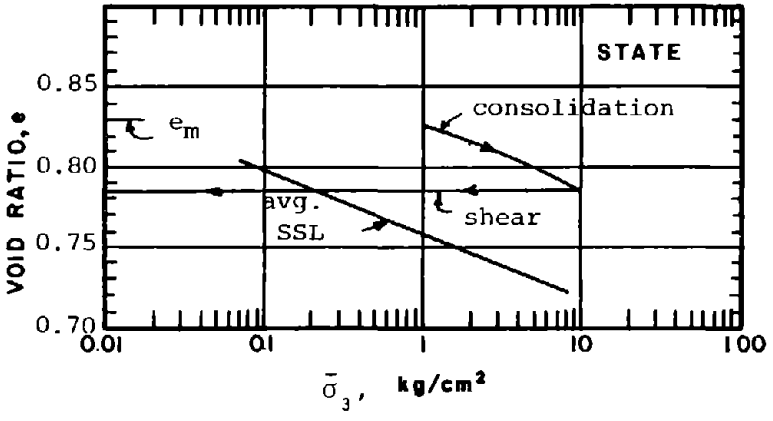

SOIL	: Banding Sand #6	METHOD OF LOADING:	Undrained, Axial Compression Load Control
STRUCTURE	: Compacted Moist		
STATE AFTER CONSOLIDATION:	$\bar{\sigma}_{3c}$ = 10.00kg/cm², $\bar{\sigma}_{1c}$ =10.00 kg/cm²	TESTING DETAILS	: Specimen Diameter 3.60 cm
	e_c = 0.785, γ_{dc} = 93.0 pcf		: Specimen Height 5.30 cm
			: End Platens: Lubricated, Type 1

R-602-

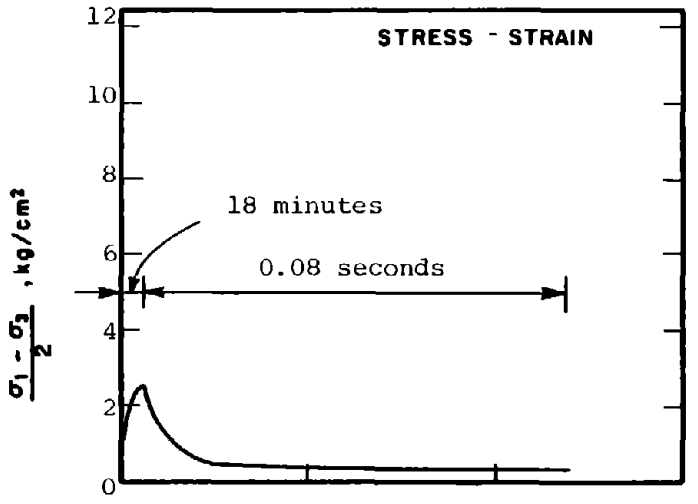

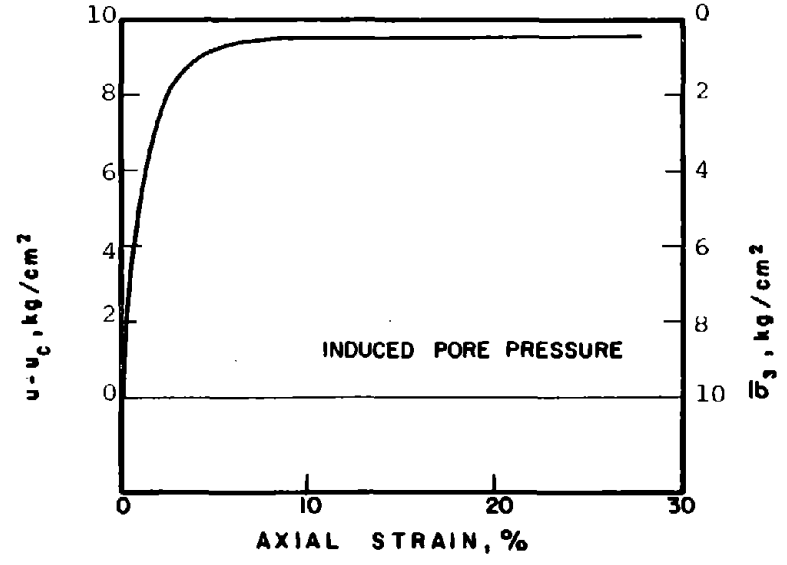

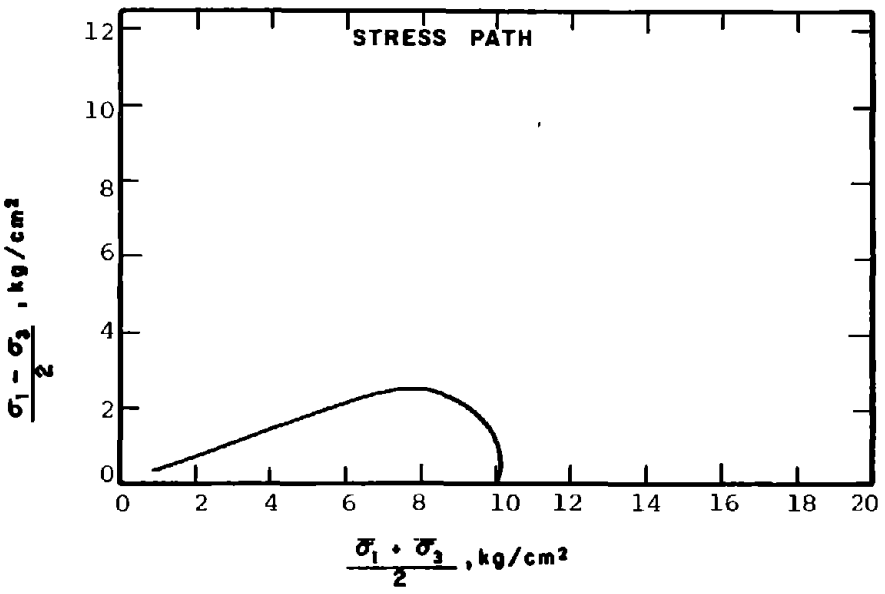

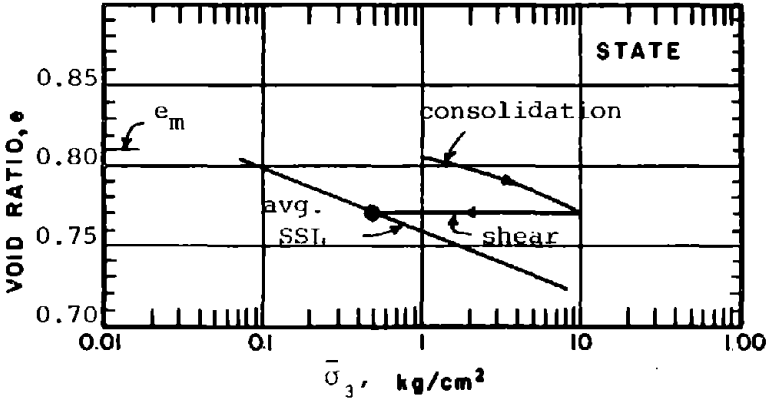

SOIL	: Banding Sand #6	METHOD OF LOADING:	Undrained, Axial Compression Load Control
STRUCTURE	: Compacted Moist		
STATE AFTER CONSOLIDATION:	$\bar{\sigma}_{3c} = 10.00\,kg/cm^2$, $\bar{\sigma}_{1c} = 10.00\,kg/cm^2$	TESTING DETAILS	: Specimen Diameter 3.60 cm
	$e_c = 0.770$, $\gamma_{dc} = 93.8$ pcf		: Specimen Height 5.30 cm
			: End Platens: Lubricated, Type 1

R-603

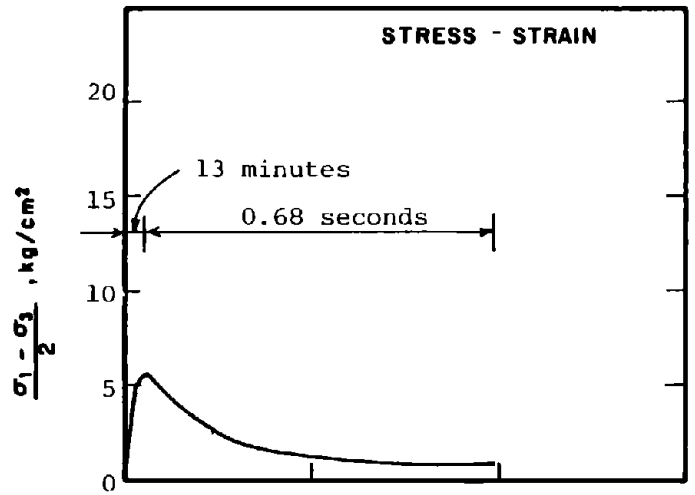

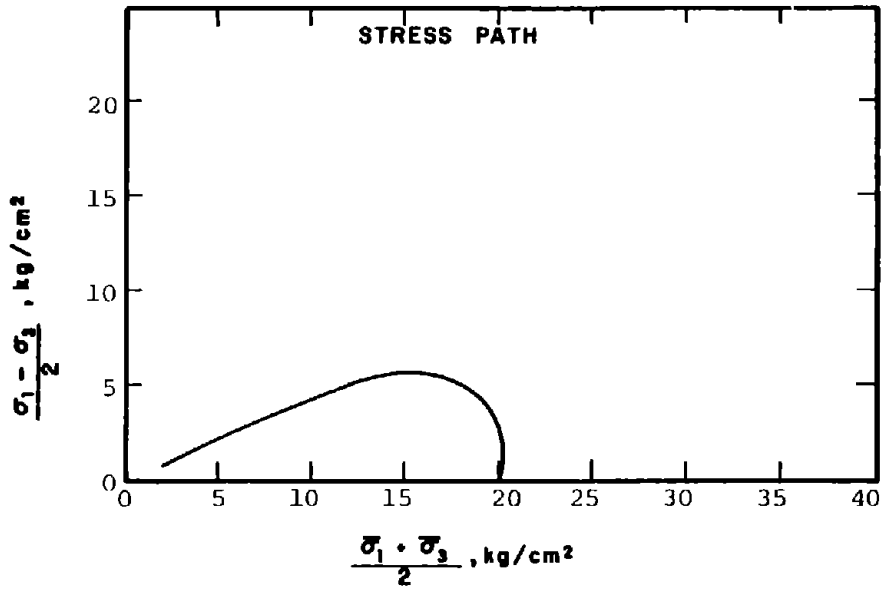

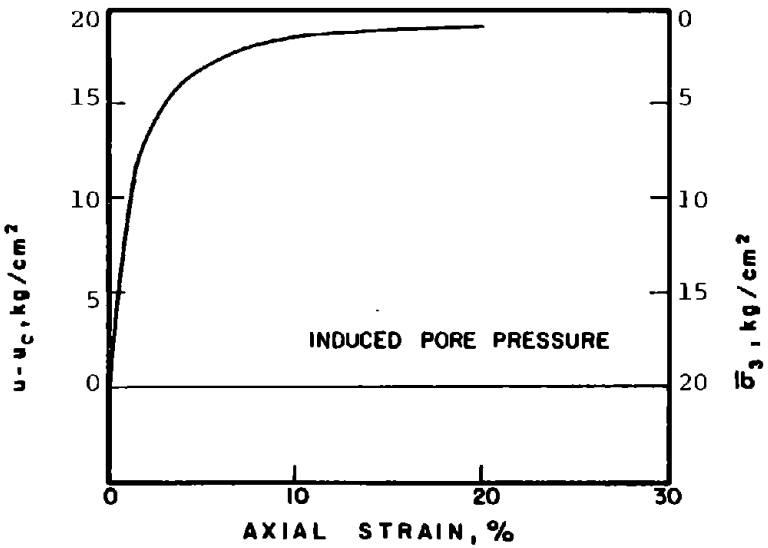

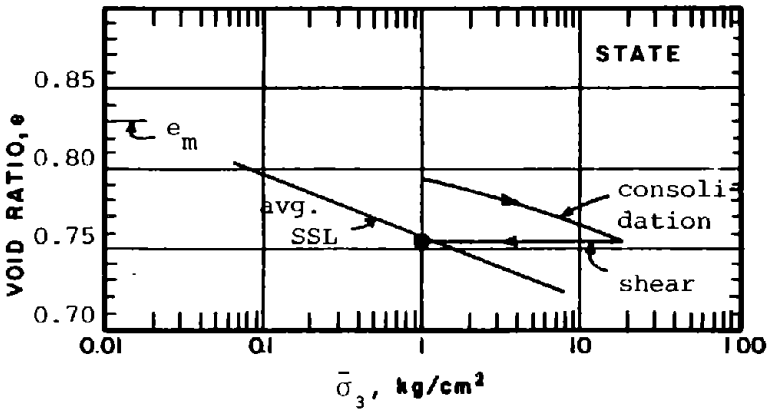

SOIL	: Banding Sand #6	METHOD OF LOADING:	Undrained, Axial Compression Load Control
STRUCTURE	: Compacted Moist		
STATE AFTER CONSOLIDATION:	$\bar{\sigma}_{3c}$ = 20.00 kg/cm², $\bar{\sigma}_{1c}$ = 20.00 kg/cm²	TESTING DETAILS	: Specimen Diameter 3.60 cm
	e_c = 0.754, γ_{dc} = 94.6 pcf		: Specimen Height 5.30 cm
			: End Platens: Lubricated, Type 1

R-604

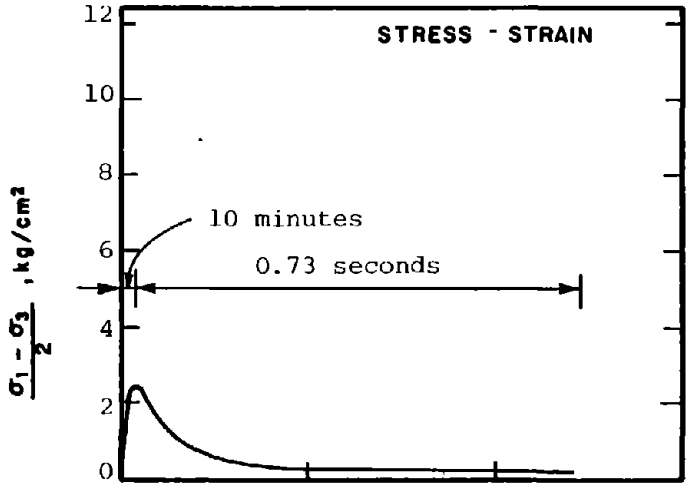

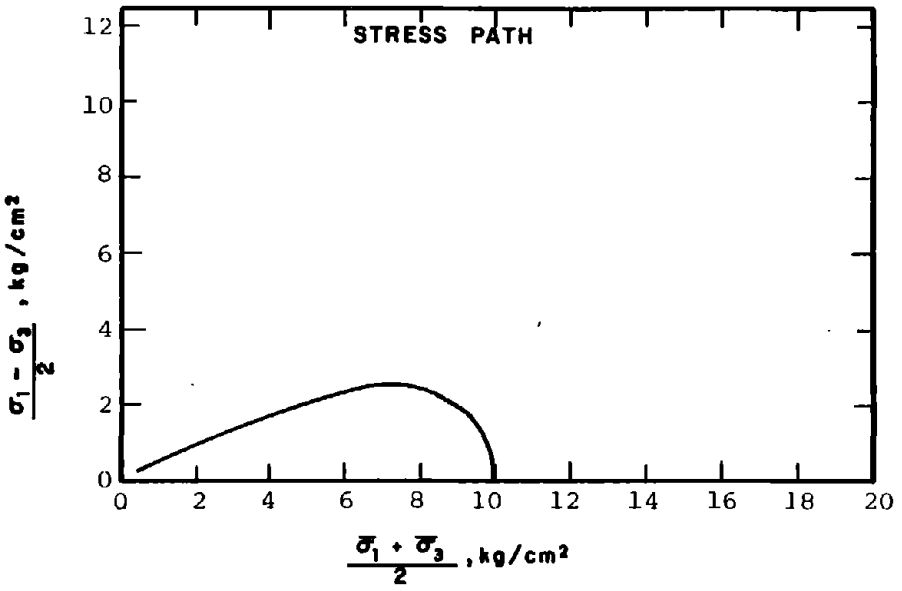

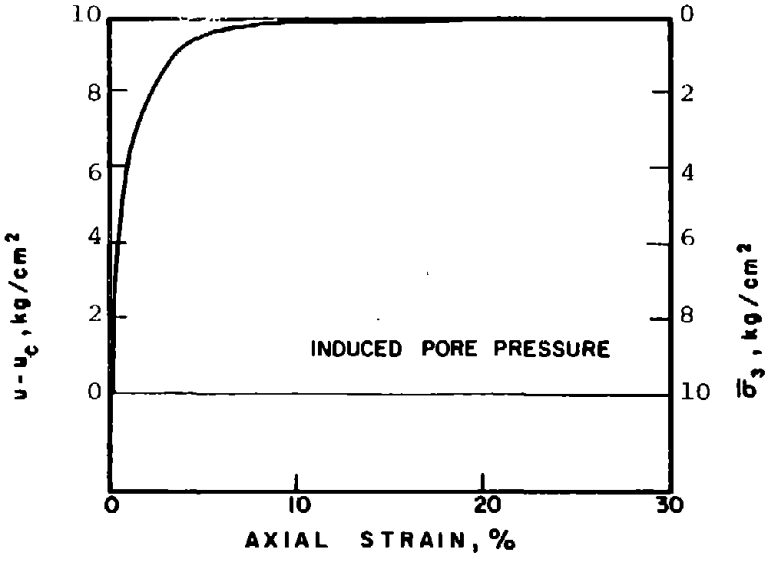

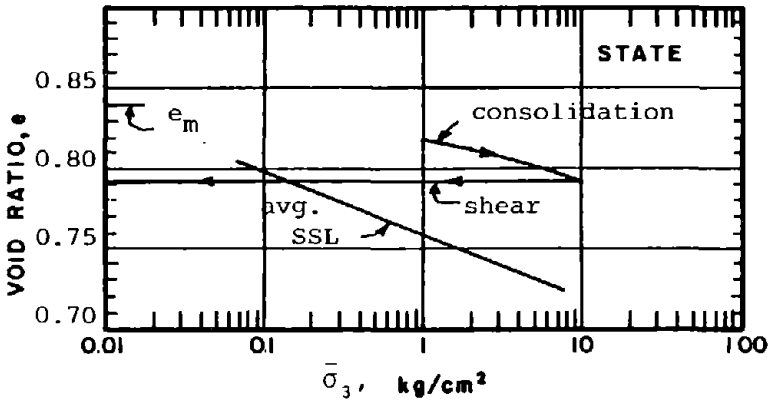

SOIL	: Banding Sand #6	METHOD OF LOADING:	Undrained, Axial Compression Load Control
STRUCTURE	: Compacted Moist		
STATE AFTER CONSOLIDATION:	$\bar{\sigma}_{3c}$ =10.00 kg/cm², $\bar{\sigma}_{1c}$ =10.00 kg/cm² e_c = 0.791, γ_{dc} = 92.7 pcf	TESTING DETAILS	: Specimen Diameter 7.10 cm : Specimen Height 10.70 cm : End Platens: Lubricated, Type 1

R-605A

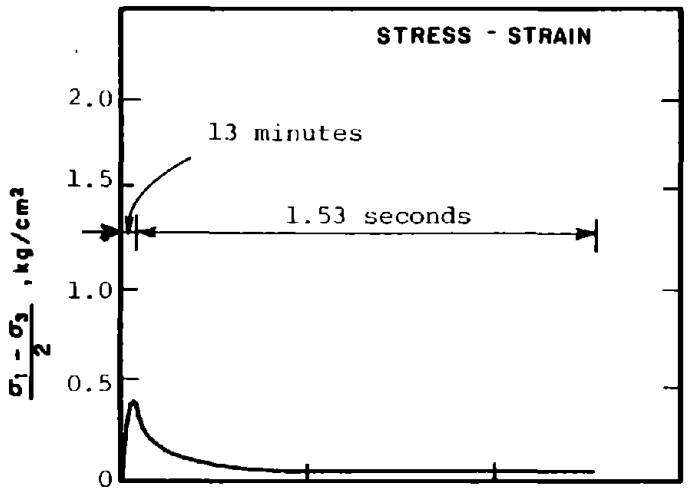

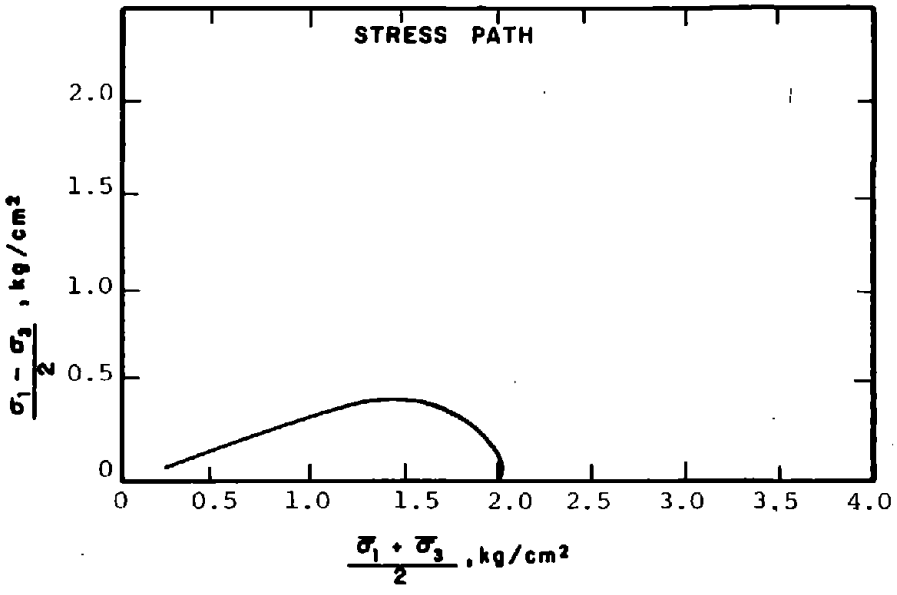

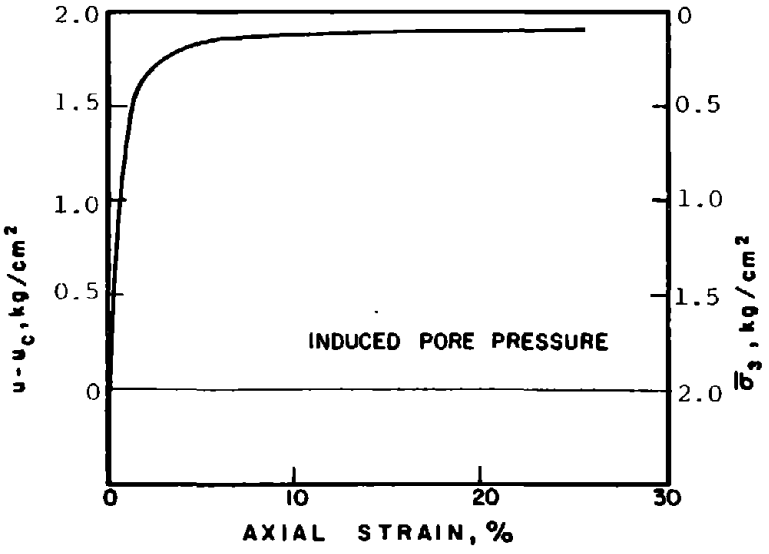

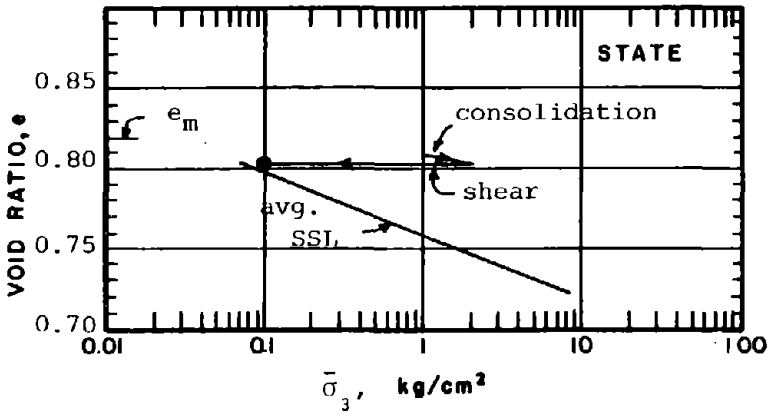

SOIL	: Banding Sand #6	METHOD OF LOADING:	Undrained, Axial Compression Load Control
STRUCTURE	: Compacted Moist		
STATE AFTER CONSOLIDATION:	$\bar{\sigma}_{3c}$ = 2.00 kg/cm², $\bar{\sigma}_{1c}$ = 2.00 kg/cm²	TESTING DETAILS	: Specimen Diameter 3.60 cm
	e_c = 0.801, γ_{dc} = 92.2 pcf		: Specimen Height 5.30 cm
			: End Platens: Lubricated, Type 1

R-605

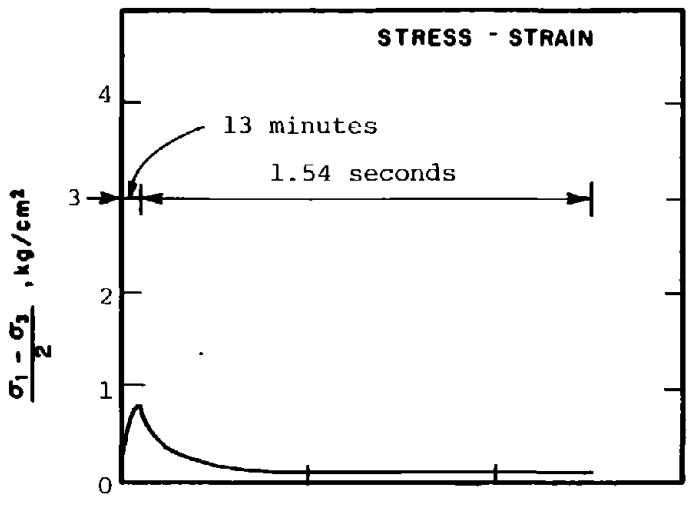

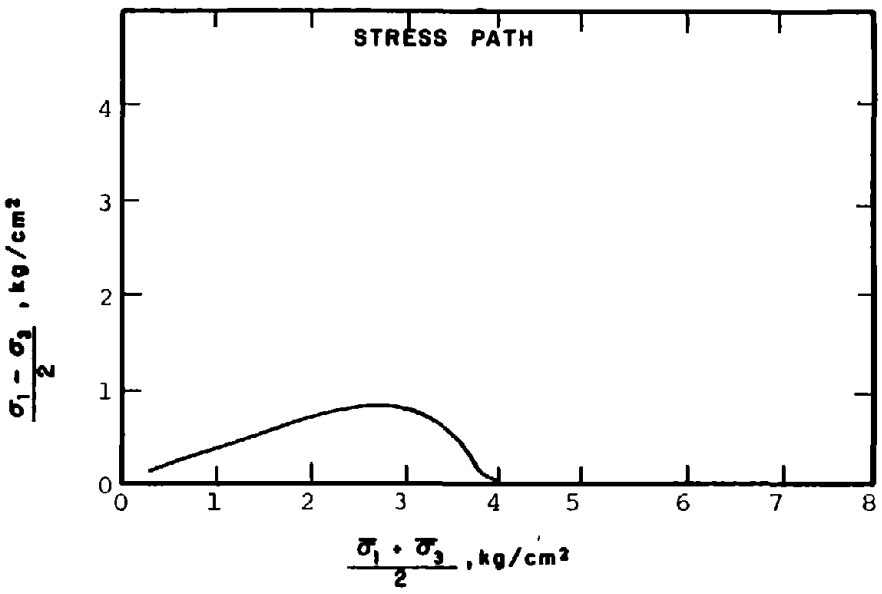

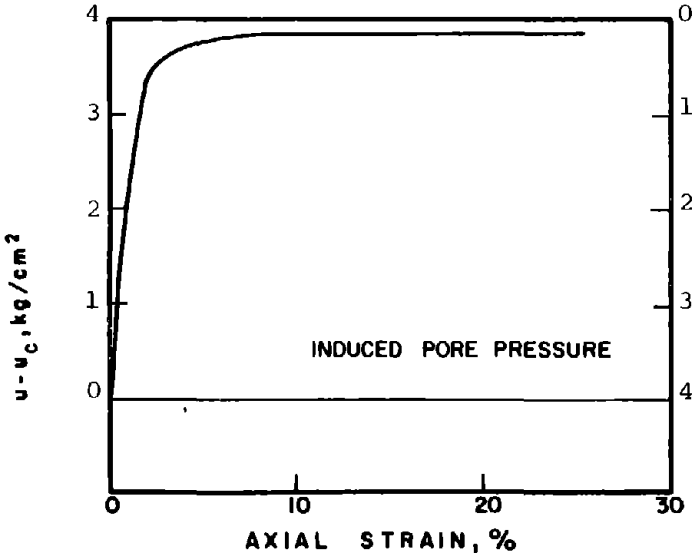

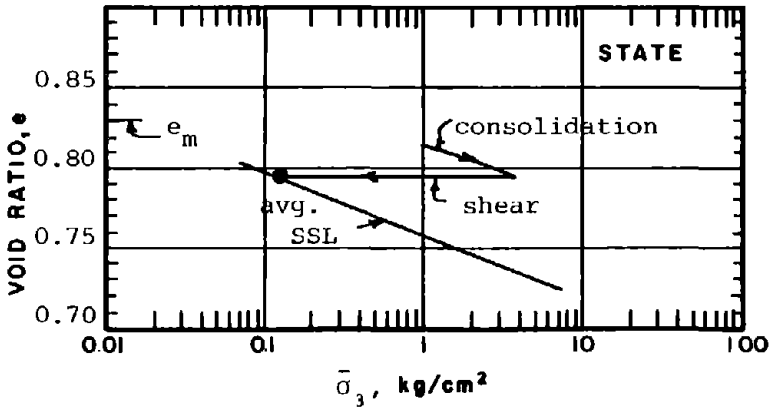

SOIL	: Banding Sand #6	METHOD OF LOADING:	Undrained, Axial Compression Load Control
STRUCTURE	: Compacted Moist		
STATE AFTER CONSOLIDATION:	$\bar{\sigma}_{3c}$ = 4.00 kg/cm², $\bar{\sigma}_{1c}$ = 4.00 kg/cm²	TESTING DETAILS	: Specimen Diameter 3.60 cm
	e_c = 0.794, γ_{dc} = 92.5 pcf		: Specimen Height 5.30 cm
			: End Platens: Lubricated, Type 1

R-607

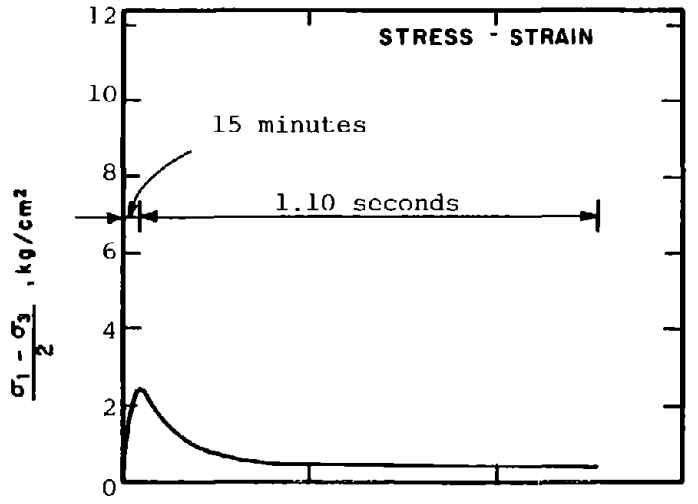

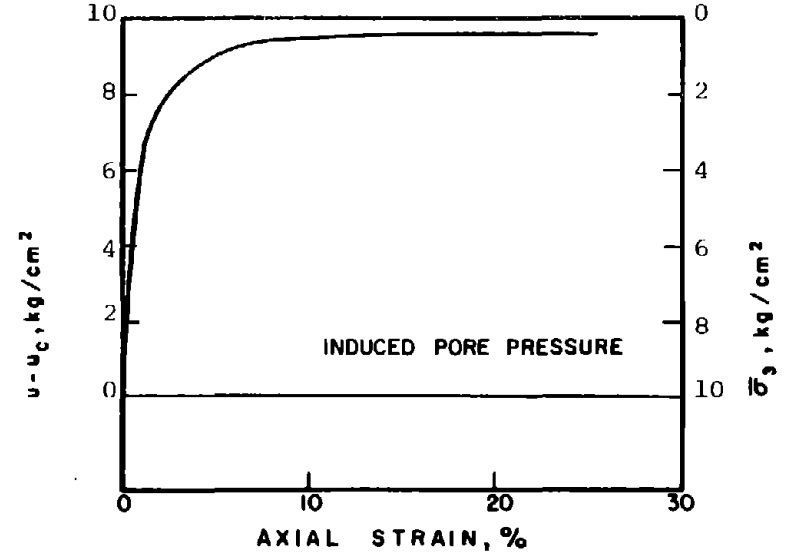

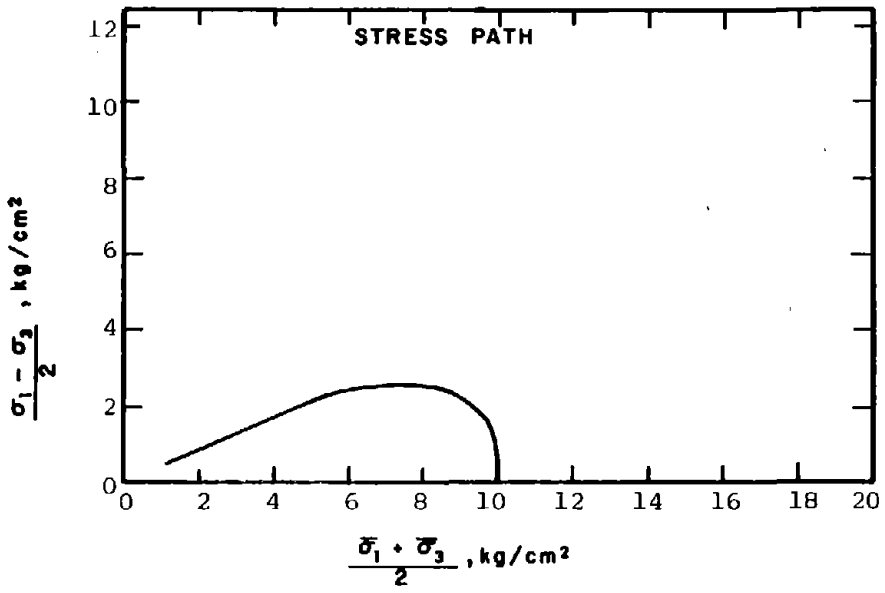

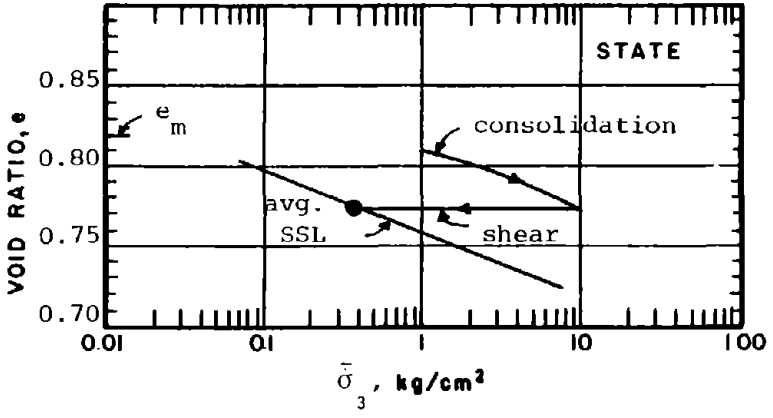

SOIL	: Banding Sand #6	METHOD OF LOADING:	Undrained, Axial Compression Load Control
STRUCTURE	: Compacted Moist		
STATE AFTER CONSOLIDATION:	$\bar{\sigma}_{3c} = 10.00$ kg/cm², $\bar{\sigma}_{1c} = 10.00$ kg/cm² $e_c = 0.772$, $\gamma_{dc} = 93.7$ pcf	TESTING DETAILS	: Specimen Diameter 3.60 cm : Specimen Height 5.30 cm : End Platens: Lubricated, Type 1

R-608

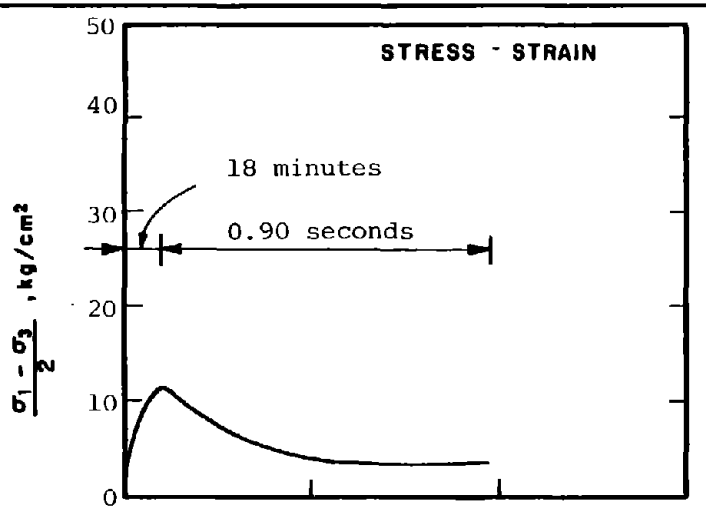

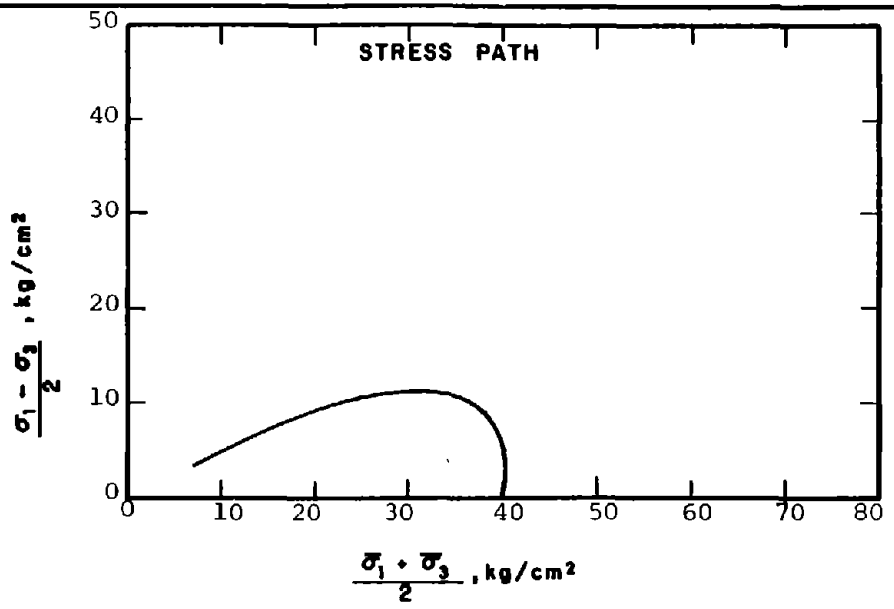

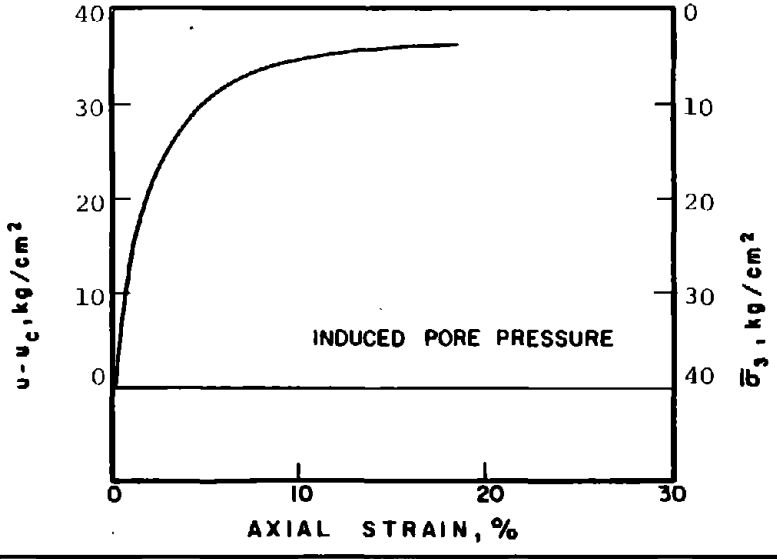

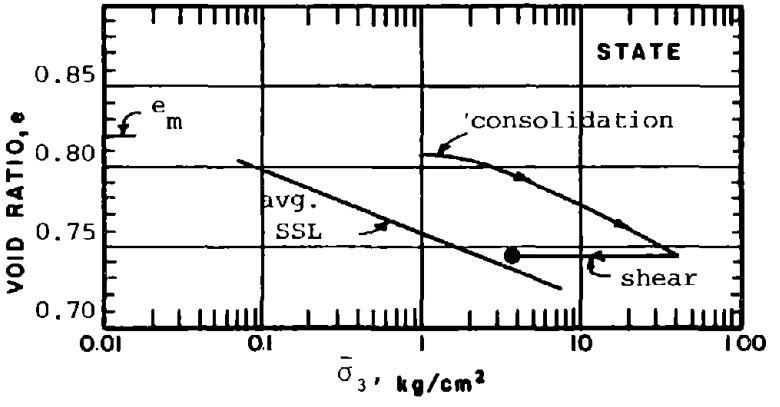

R-611

SOIL : Banding Sand #6

STRUCTURE : Compacted Moist

STATE AFTER CONSOLIDATION: $\bar{\sigma}_{3c} = 40.00$ kg/cm², $\bar{\sigma}_{1c} = 40.00$ kg/cm²
$e_c = 0.744$, $\gamma_{dc} = 95.2$ pcf

METHOD OF LOADING: Undrained, Axial Compression
Load Control

TESTING DETAILS : Specimen Diameter 3.60 cm
: Specimen Height 5.30 cm
: End Platens: Lubricated; Type 1

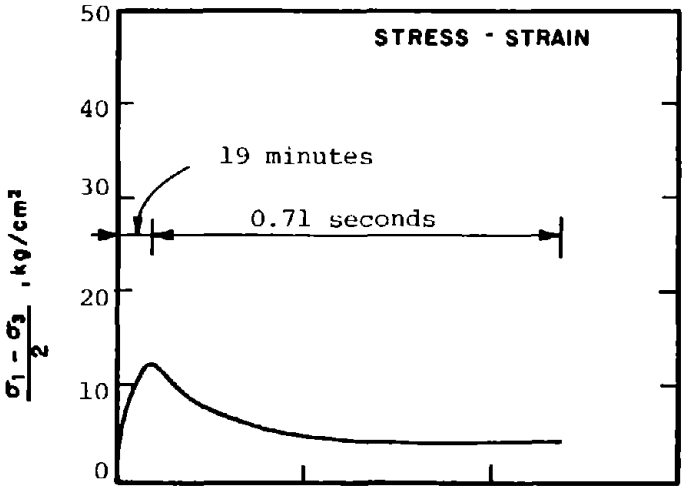

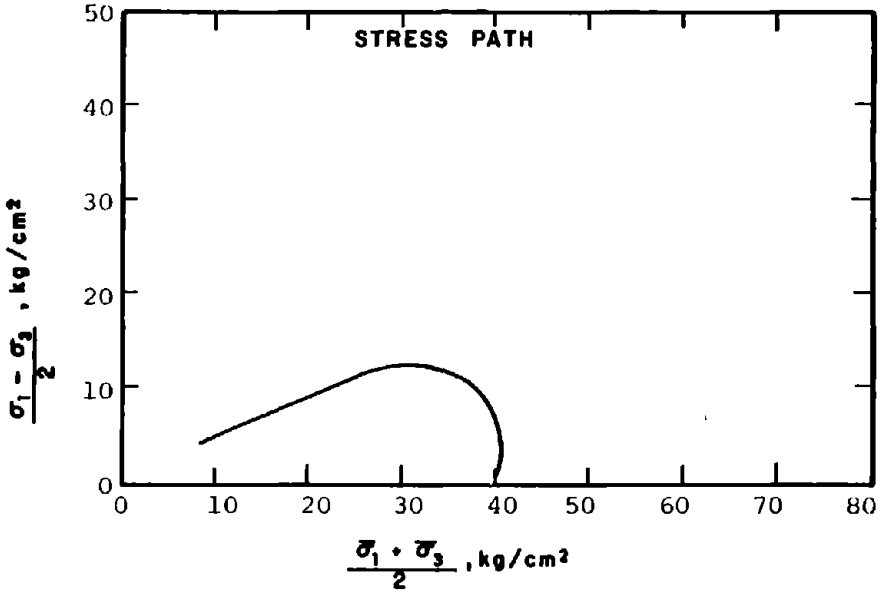

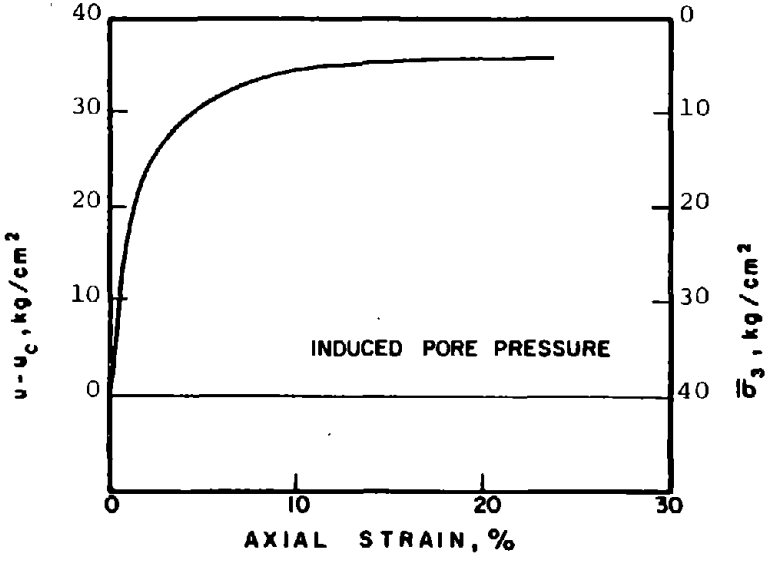

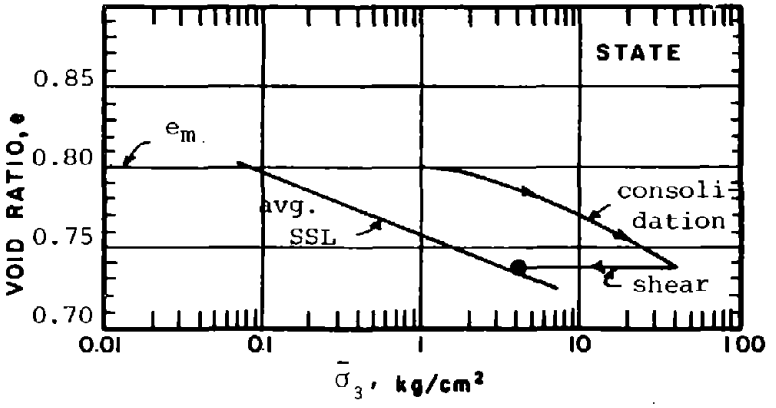

SOIL	: Banding Sand #6	METHOD OF LOADING:	Undrained, Axial Compression Load Control
STRUCTURE	: Compacted Moist		
STATE AFTER CONSOLIDATION:	$\bar{\sigma}_{3c}$ =40.00 kg/cm^2, $\bar{\sigma}_{1c}$ =40.00 kg/cm^2 e_c = 0.738, γ_{dc} = 95.5 pcf	TESTING DETAILS	: Specimen Diameter 3.60 cm : Specimen Height 5.30 cm : End Platens: Lubricated, Type 1

R-612

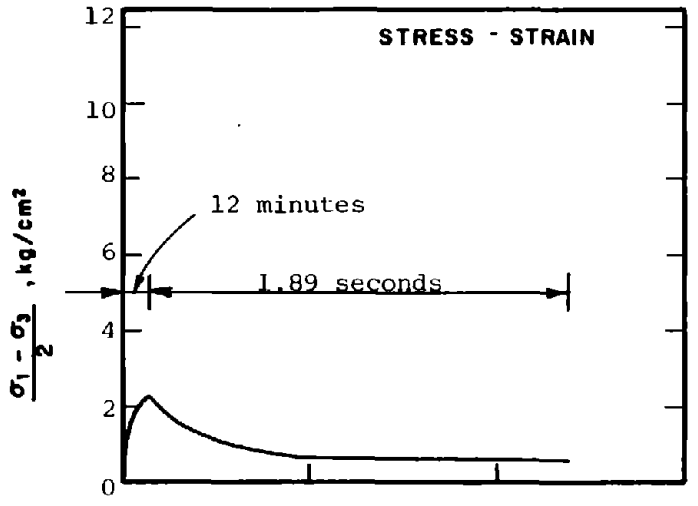

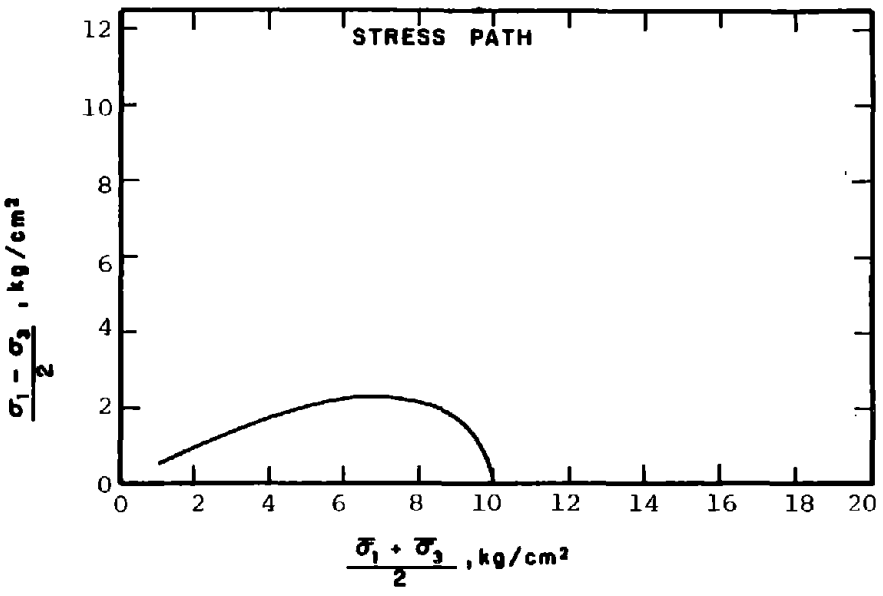

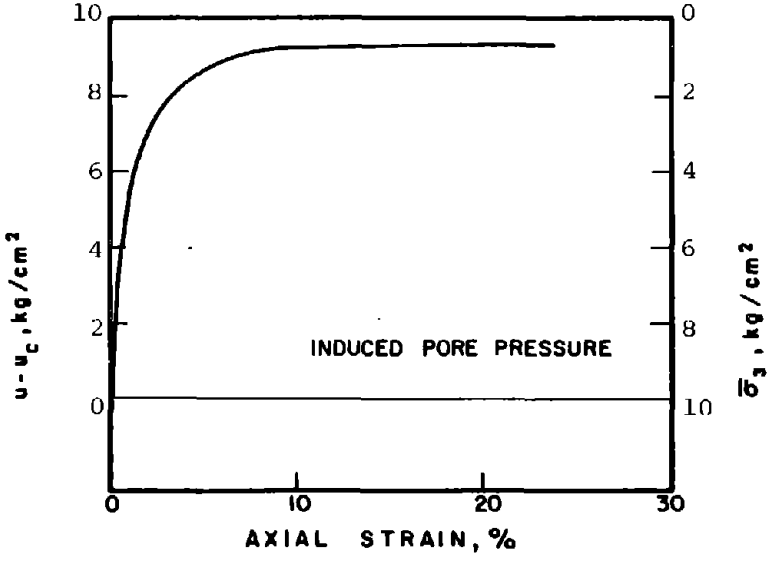

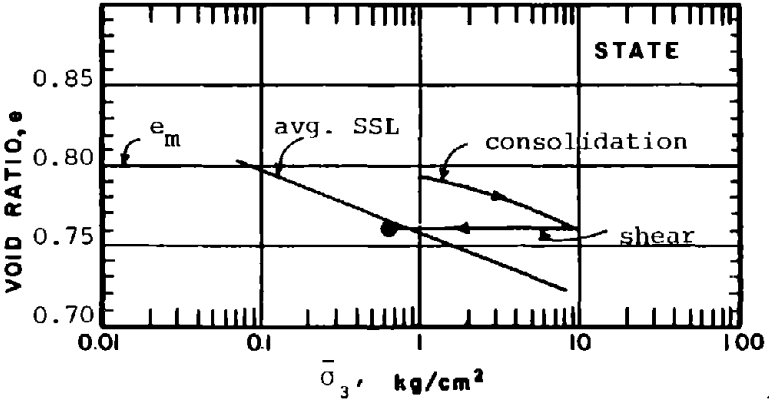

SOIL	: Banding Sand #6	METHOD OF LOADING:	Undrained, Axial Compression Load Control
STRUCTURE	: Compacted Moist		
STATE AFTER CONSOLIDATION:	$\bar{\sigma}_{3c}$ = 10.00 kg/cm², $\bar{\sigma}_{1c}$ = 10.00 kg/cm² e_c = 0.761, γ_{dc} = 94.2 pcf	TESTING DETAILS	: Specimen Diameter 3.60 cm : Specimen Height 5.30 cm : End Platens: Lubricated, Type 1

R-613

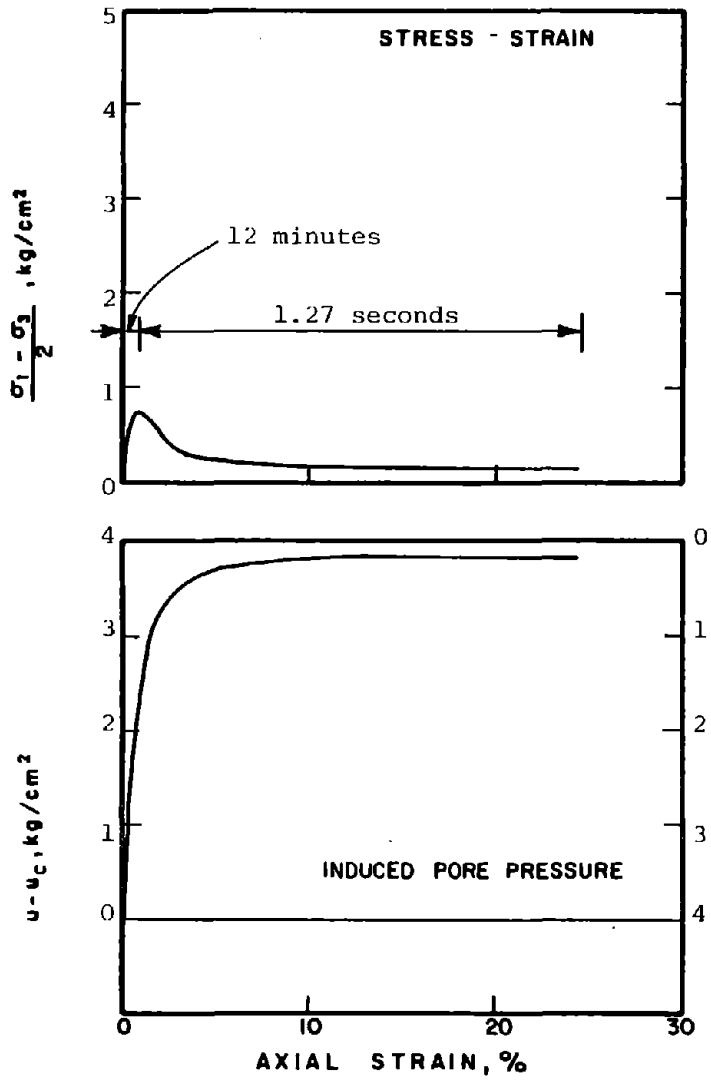

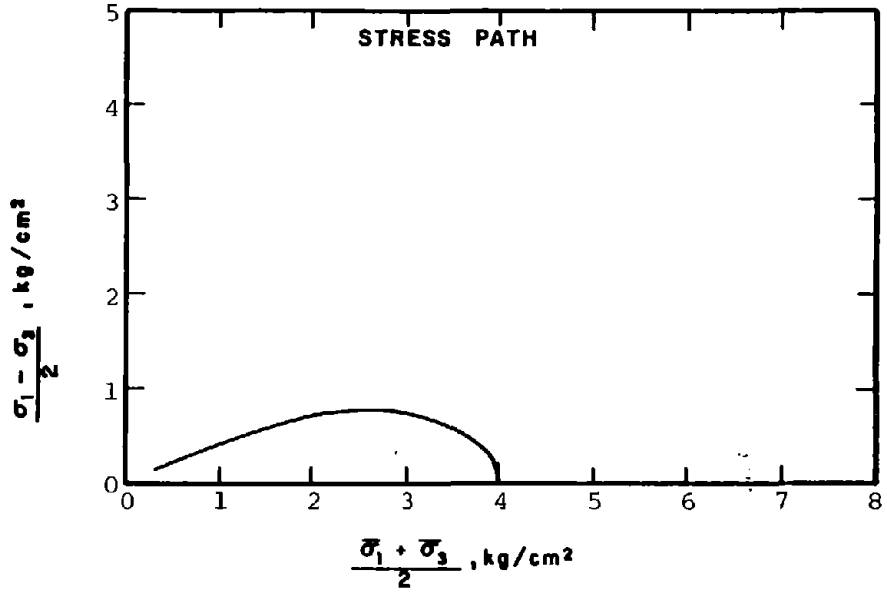

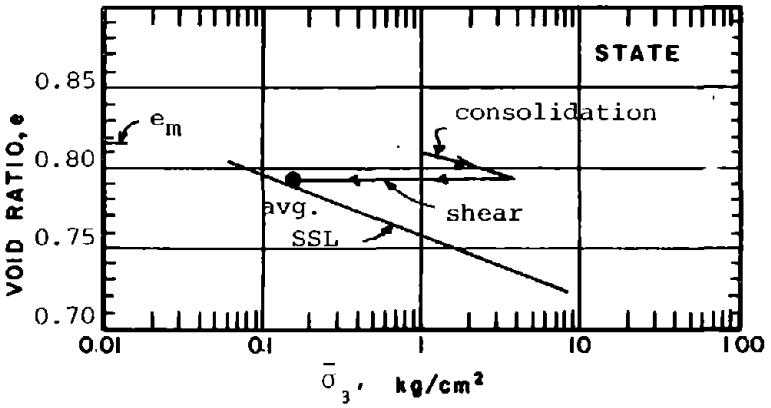

SOIL : Banding Sand #6

STRUCTURE : Compacted Moist

STATE AFTER CONSOLIDATION: $\bar{\sigma}_{3c} = 4.00$ kg/cm^2, $\bar{\sigma}_{1c} = 4.00$ kg/cm^2

$e_c = 0.792$, $\gamma_{dc} = 92.6$ pcf

METHOD OF LOADING: Undrained, Axial Compression
Load Control

TESTING DETAILS : Specimen Diameter 3.60 cm
: Specimen Height 5.30 cm
: End Platens: Lubricated, Type 1

R-614

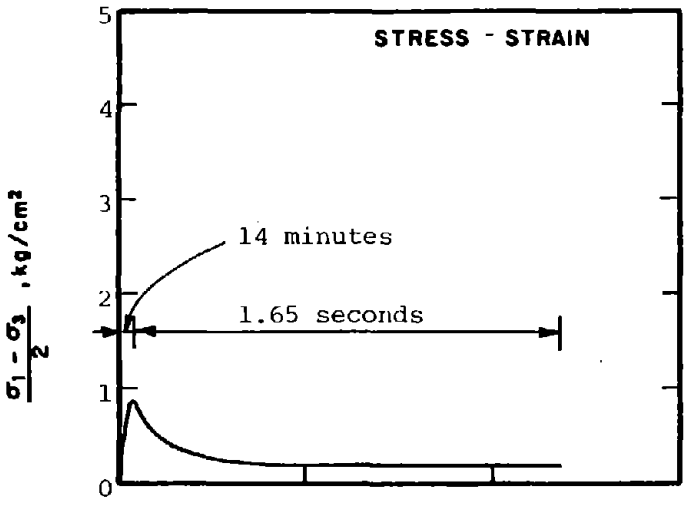

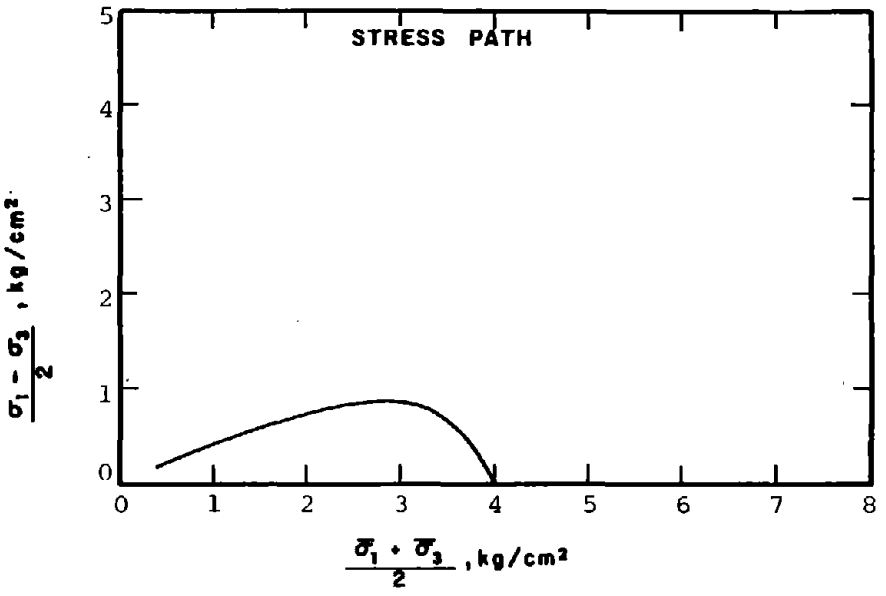

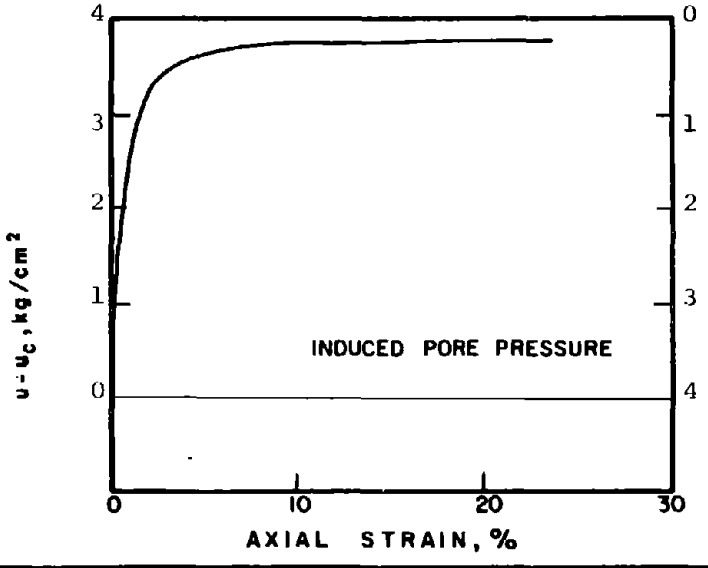

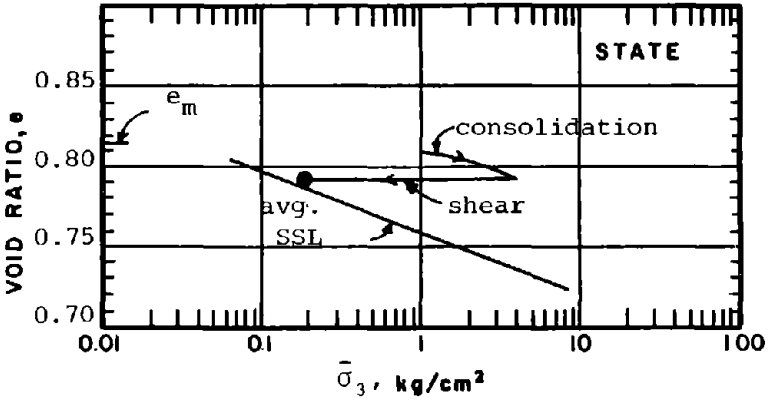

SOIL	: Banding Sand #6	METHOD OF LOADING:	Undrained, Axial Compression Load Control
STRUCTURE	: Compacted Moist		
STATE AFTER CONSOLIDATION:	$\bar{\sigma}_{3c}$ = 4.00 kg/cm², $\bar{\sigma}_{1c}$ = 4.00 kg/cm² e_c = 0.791, γ_{dc} = 92.7 pcf	TESTING DETAILS	: Specimen Diameter 3.60 cm : Specimen Height 5.30 cm : End Platens: Lubricated, Type 1

R-615

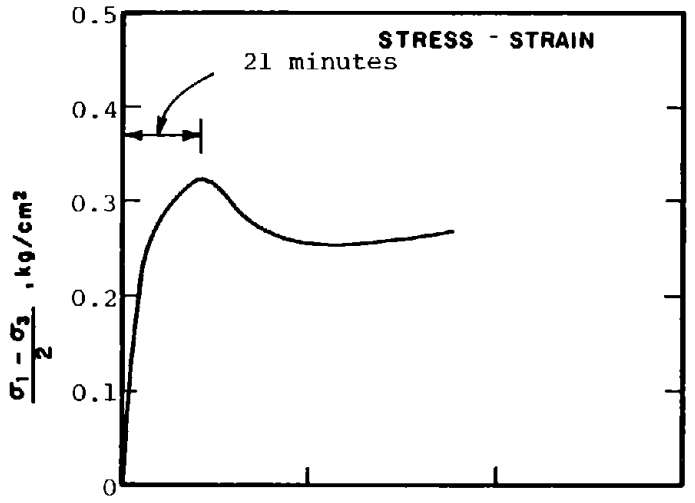

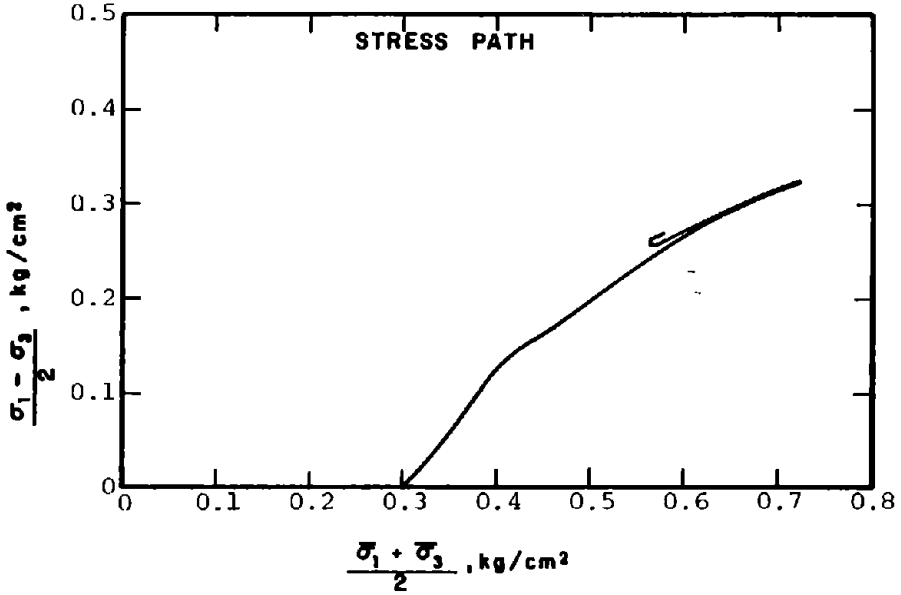

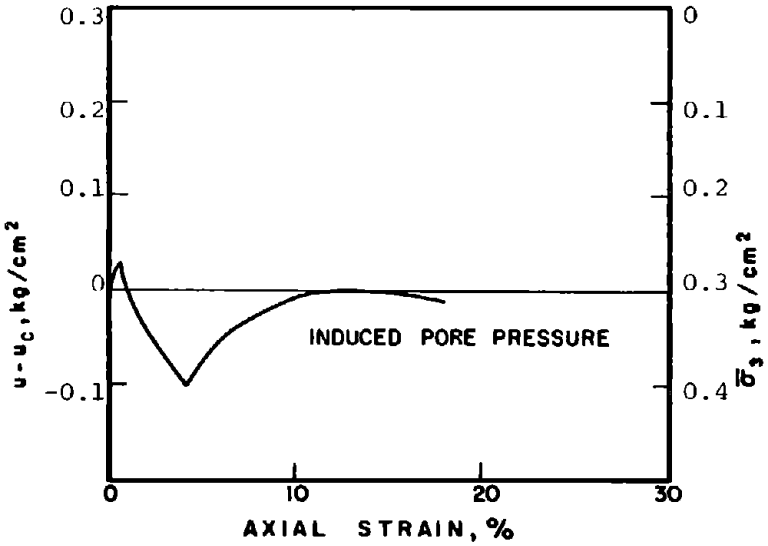

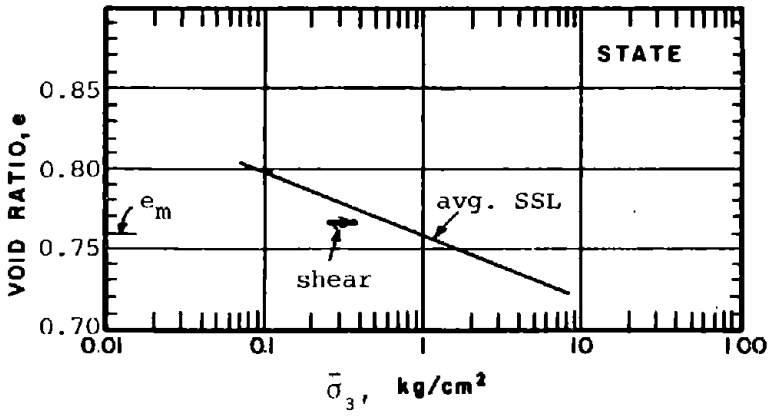

861

R-616

SOIL : Banding Sand #6

STRUCTURE : Compacted Moist

STATE AFTER CONSOLIDATION: $\bar{\sigma}_{3c} = 0.30$ kg/cm^2, $\bar{\sigma}_{1c} = 0.30$ kg/cm^2

$e_c = 0.765$, $\gamma_{dc} = 94.0$ pcf

METHOD OF LOADING: Undrained, Axial Compression
Load Control

TESTING DETAILS : Specimen Diameter 3.60 cm
: Specimen Height 5.30 cm
: End Platens: Lubricated, Type 1

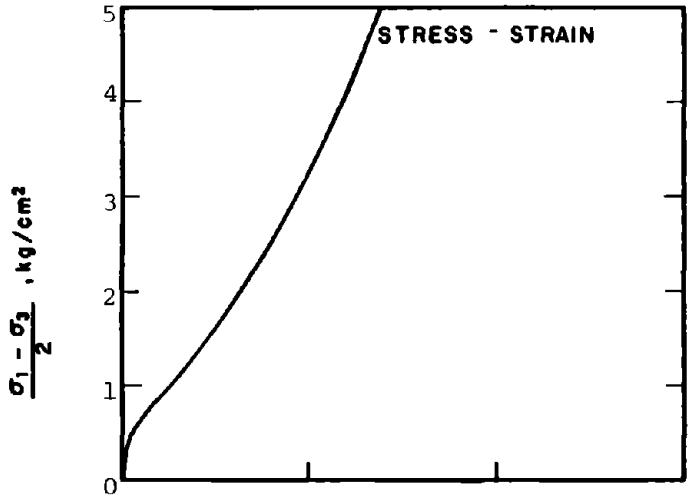

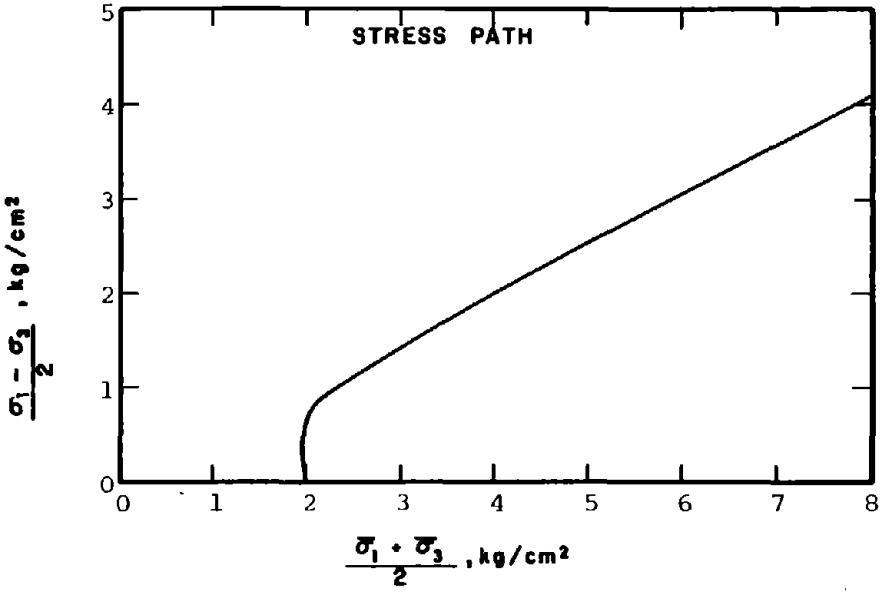

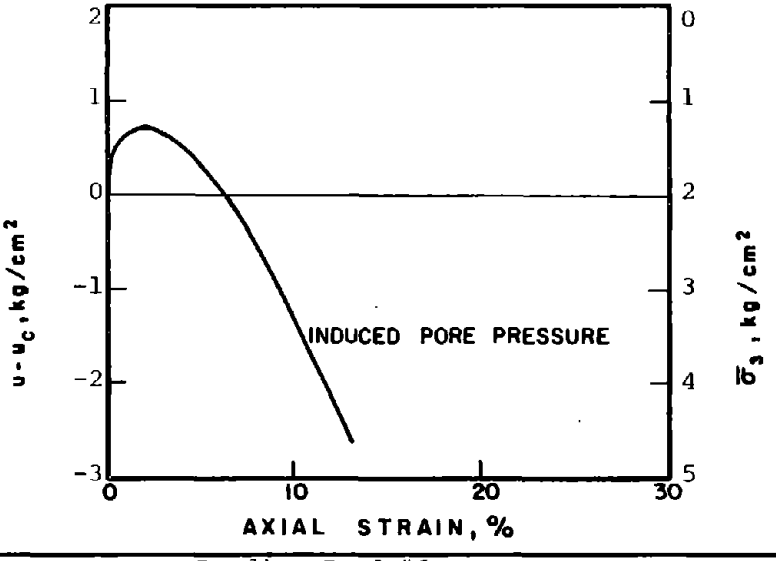

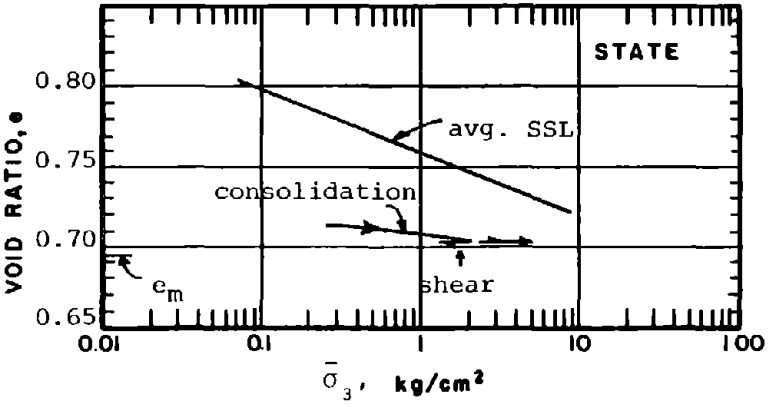

R-612

SOIL : Banding Sand #6

STRUCTURE : Compacted Moist

STATE AFTER CONSOLIDATION: $\bar{\sigma}_{3c}$ = 2.00 kg/cm², $\bar{\sigma}_{1c}$ = 2.00 kg/cm²
e_c = 0.704, γ_{dc} = 97.4 pcf

METHOD OF LOADING: Undrained, Axial Compression
Load Control

TESTING DETAILS : Specimen Diameter 3.60 cm
: Specimen Height 5.30 cm
: End Platens: Lubricated, Type 1

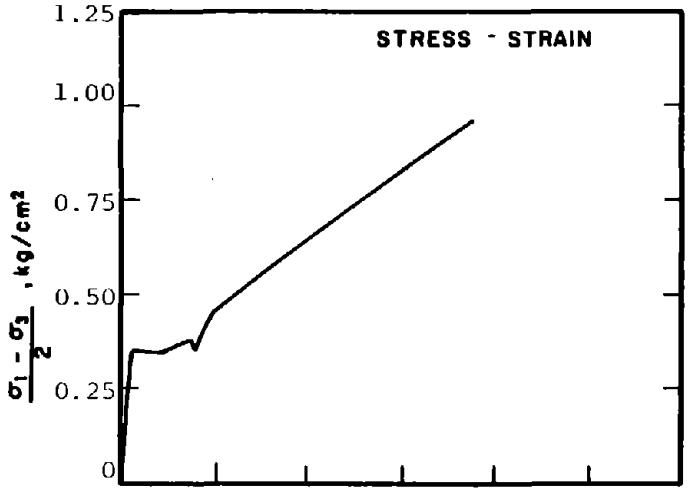

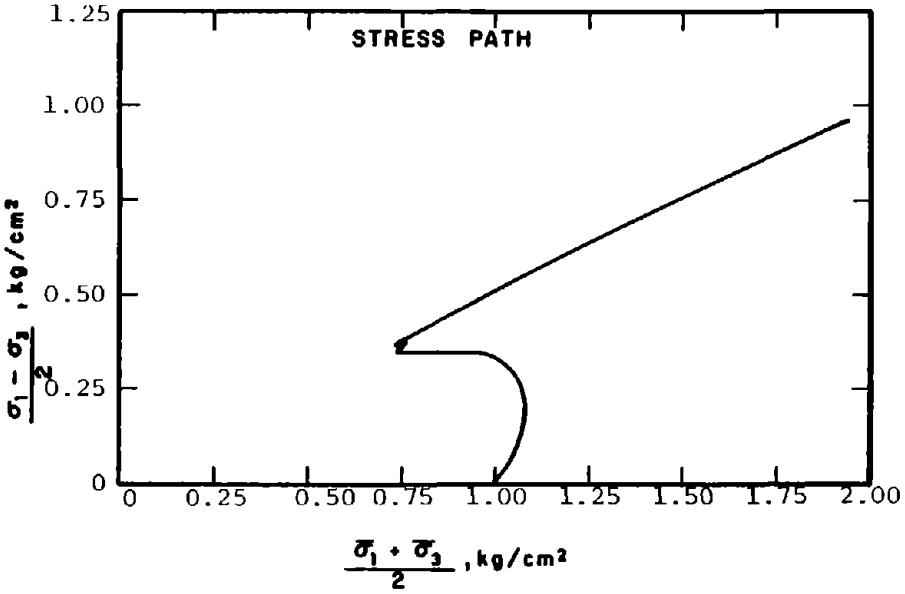

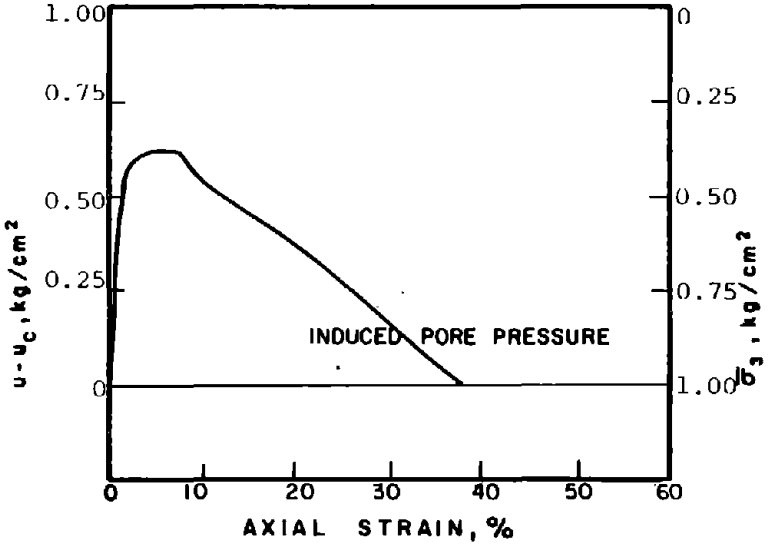

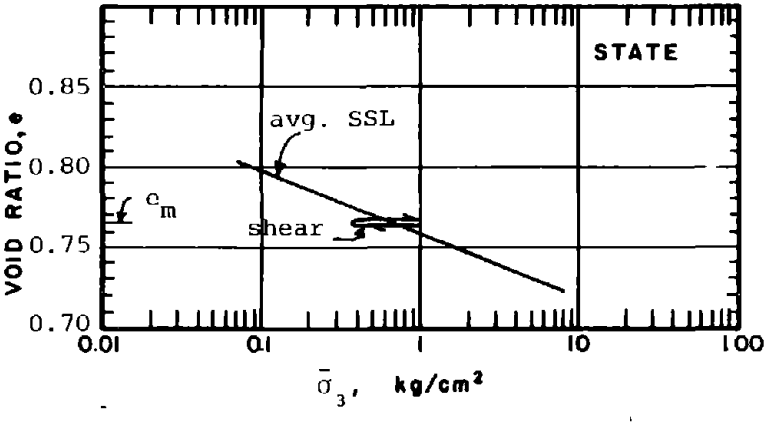

200

R-618

SOIL	: Banding Sand #6	METHOD OF LOADING:	Undrained Axial Compression Load Control
STRUCTURE	: Compacted Moist		
STATE AFTER CONSOLIDATION:	$\bar{\sigma}_{3c}$ = 1.00 kg/cm², $\bar{\sigma}_{1c}$ = 1.00 kg/cm² e_c = 0.765, γ_{dc} = 94.0 pcf	TESTING DETAILS	: Specimen Diameter 3.60 cm : Specimen Height 5.30 cm : End Platens: Lubricated, Type 1

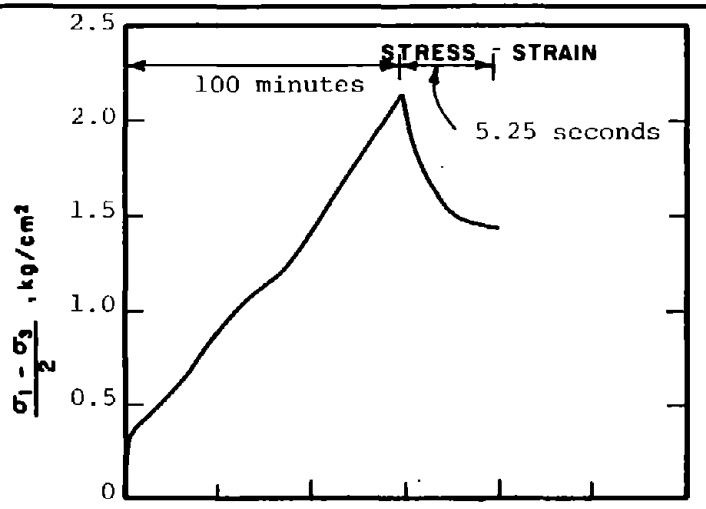

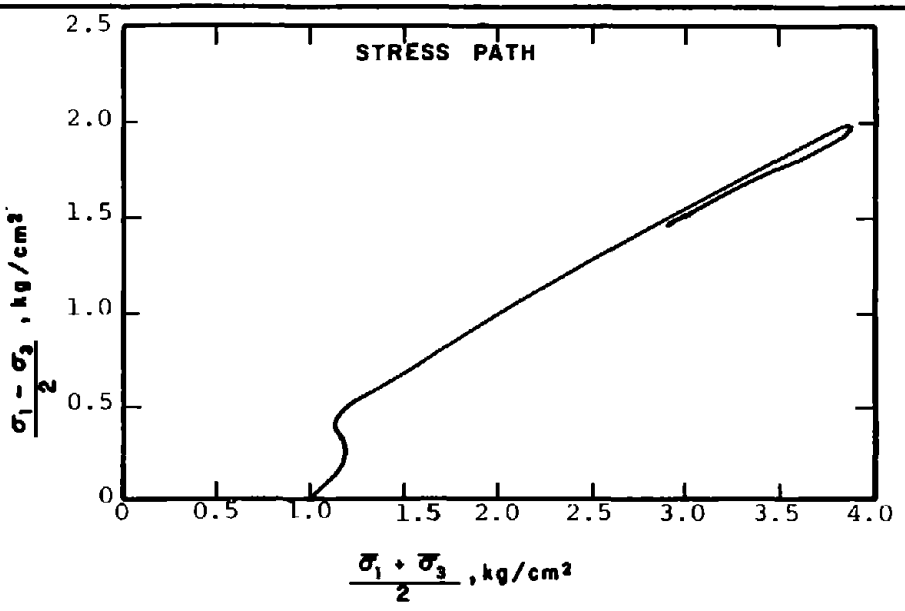

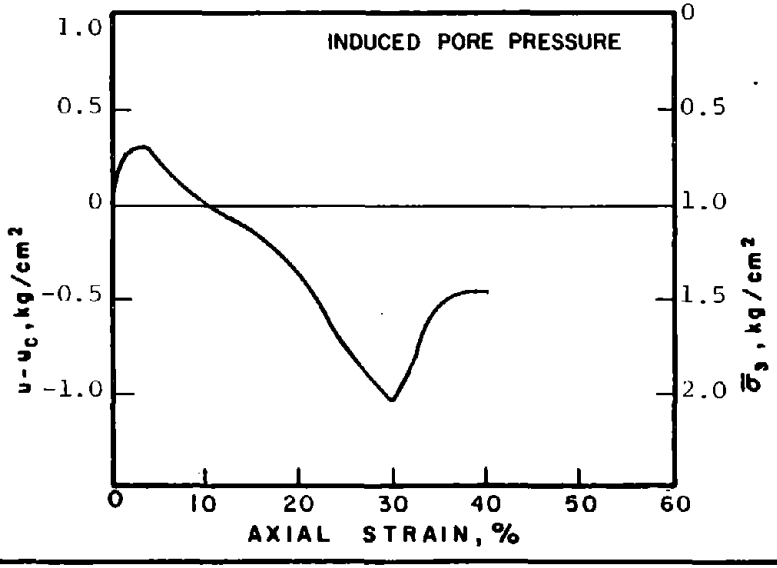

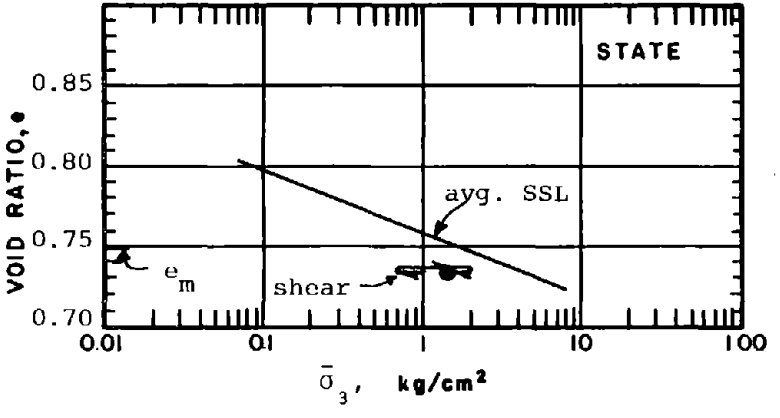

SOIL	: Banding Sand #6	METHOD OF LOADING:	Undrained Axial Compression Load Control
STRUCTURE	: Compacted Moist		
STATE AFTER CONSOLIDATION:	$\bar{\sigma}_{3c}$ = 1.00 kg/cm², $\bar{\sigma}_{1c}$ = 1.00 kg/cm²	TESTING DETAILS	: Specimen Diameter 3.60 cm
	e_c = 0.734, γ_{dc} = 95.7 pcf		: Specimen Height 5.30 cm
			: End Platens: Lubricated, Type 1

R-619

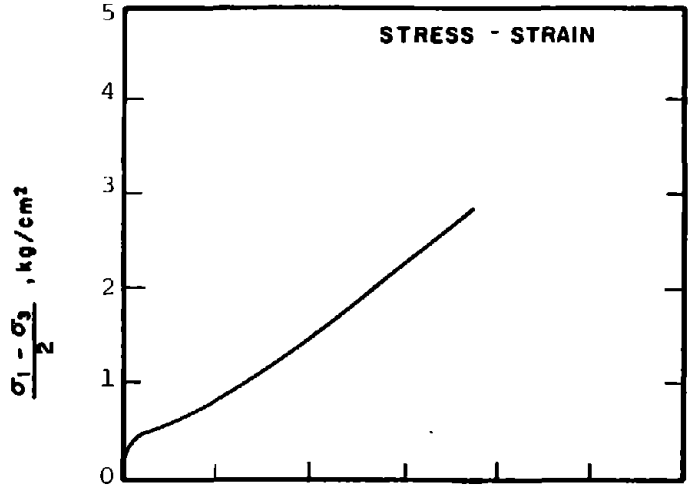

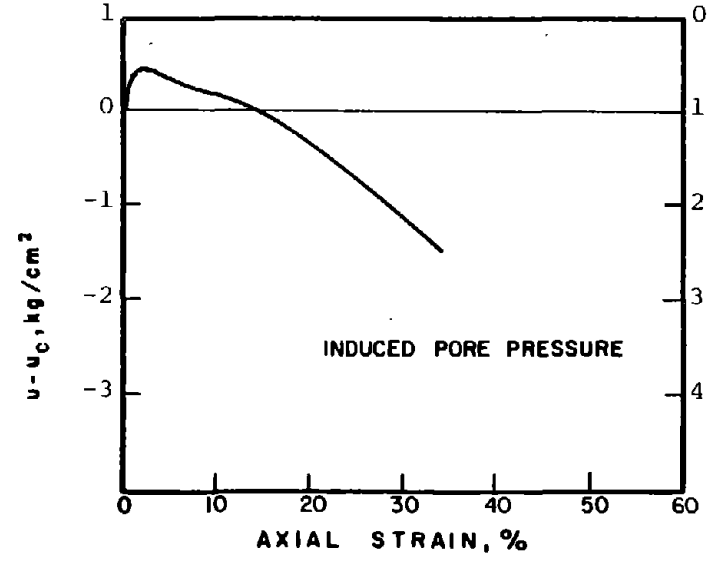

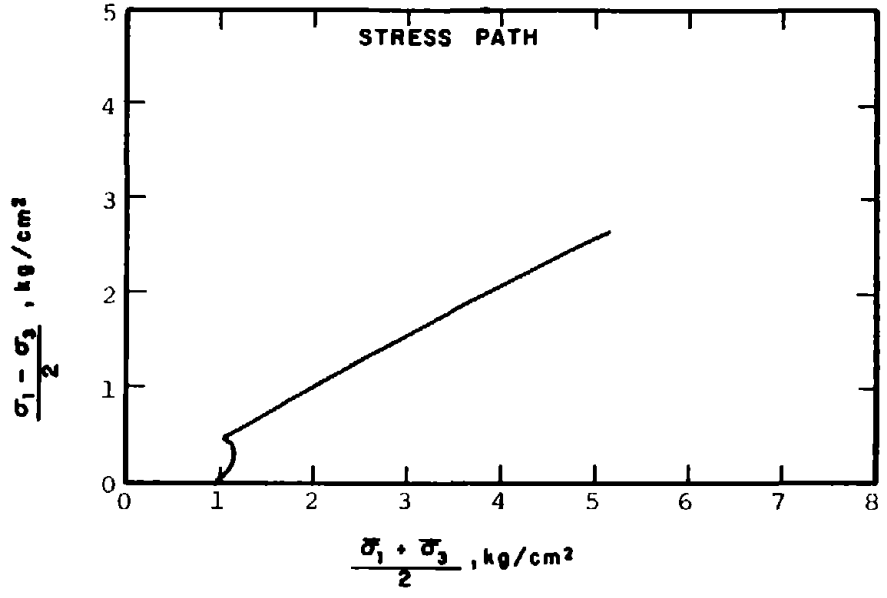

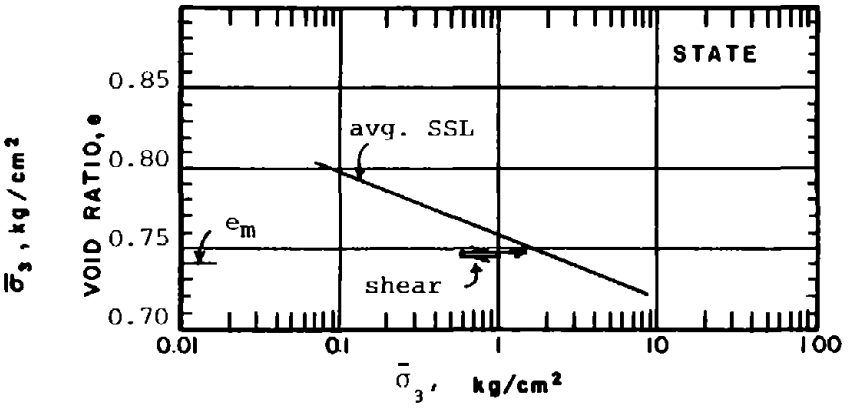

SOIL	: Banding Sand #6	METHOD OF LOADING:	Undrained, Axial Compression Load Control
STRUCTURE	: Compacted Moist		
STATE AFTER CONSOLIDATION:	$\bar{\sigma}_{3c}$ = 1.00 kg/cm², $\bar{\sigma}_{1c}$ = 1.00 kg/cm² e_c = 0.747, γ_{dc} = 95.0 pcf	TESTING DETAILS	: Specimen Diameter 3.60 cm : Specimen Height 5.30 cm : End Platens: Lubricated, Type 1

R-620

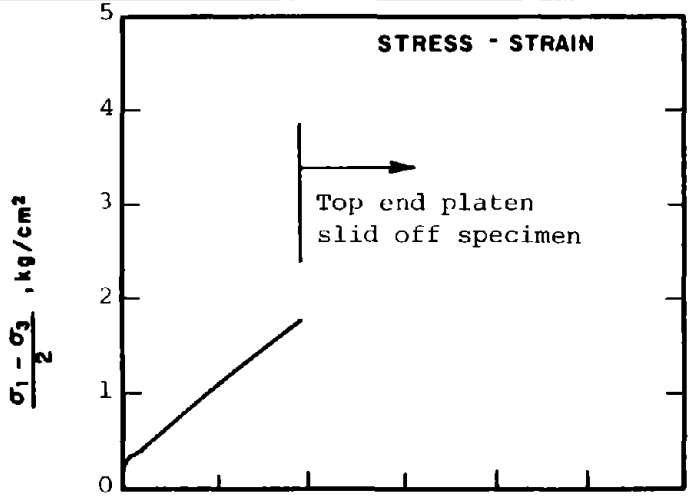

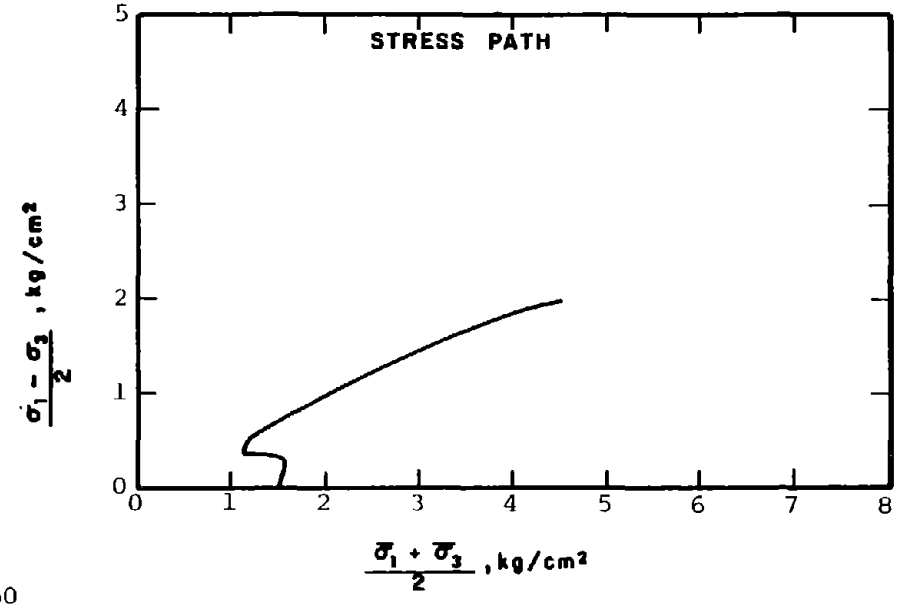

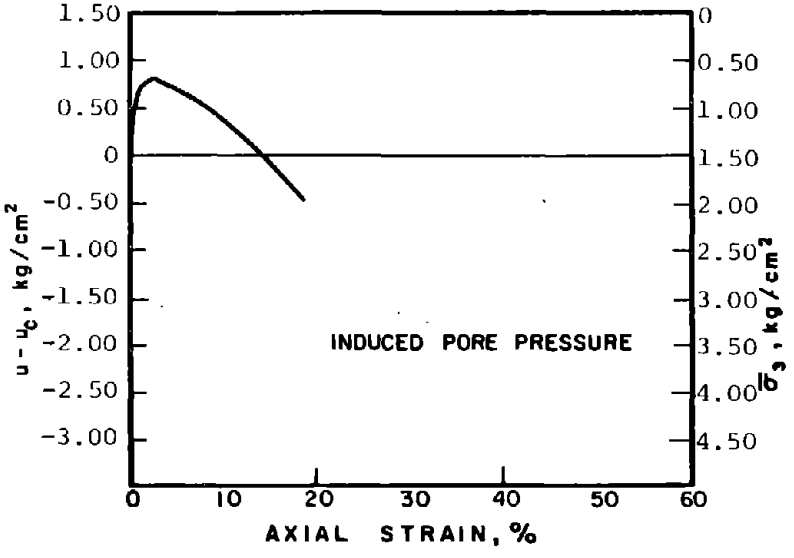

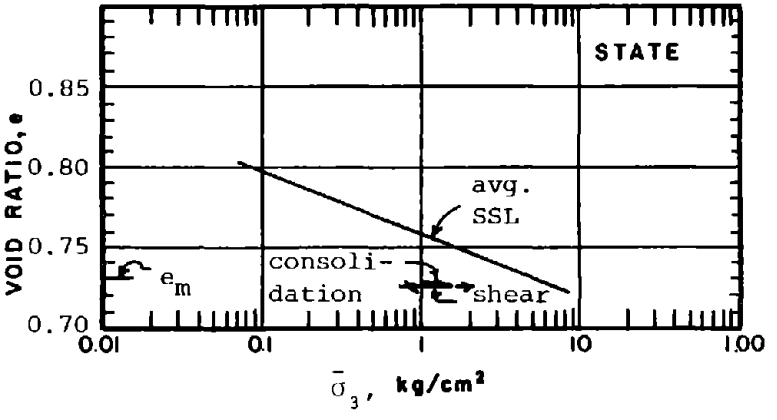

SOIL	: Banding Sand #6	METHOD OF LOADING:	Undrained, Axial Compression Load Control
STRUCTURE	: Compacted Moist		
STATE AFTER CONSOLIDATION:	$\bar{\sigma}_{3c}$ = 1.50 kg/cm², $\bar{\sigma}_{1c}$ = 1.50 kg/cm²	TESTING DETAILS	: Specimen Diameter 3.60 cm
	e_c = 0.726, γ_{dc} = 96.2 pcf		: Specimen Height 5.30 cm
			: End Platens: Lubricated, Type 1

R-621

203

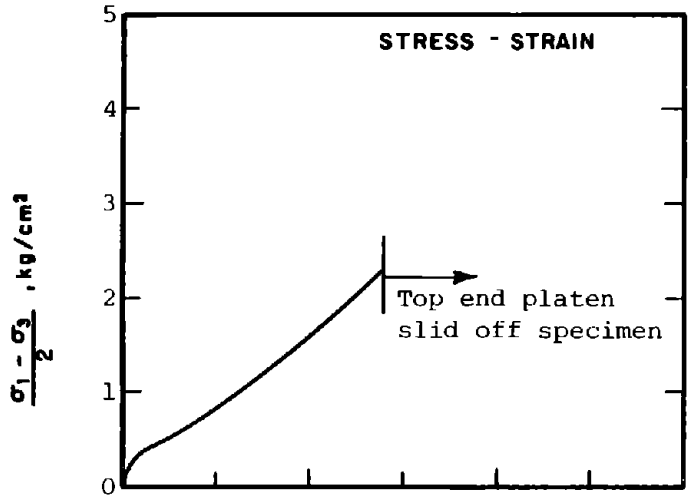

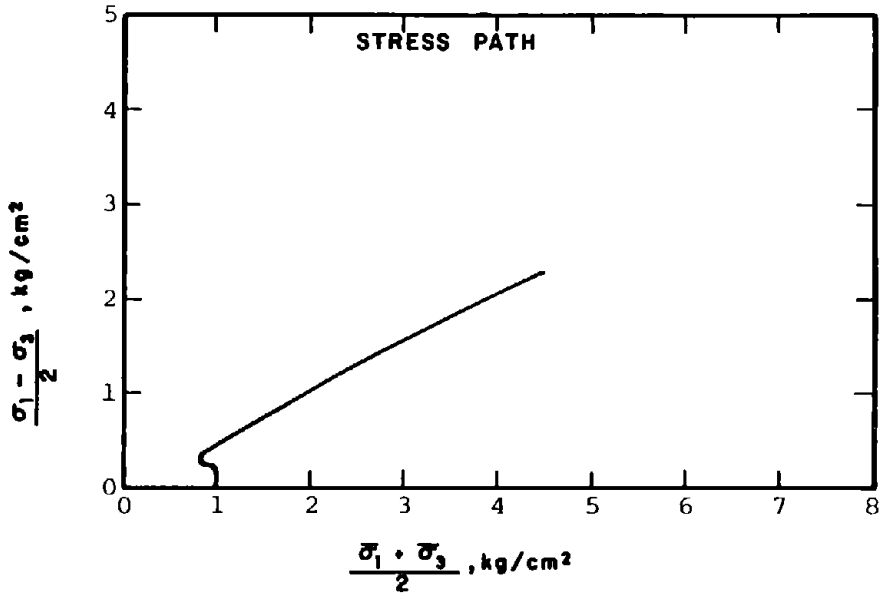

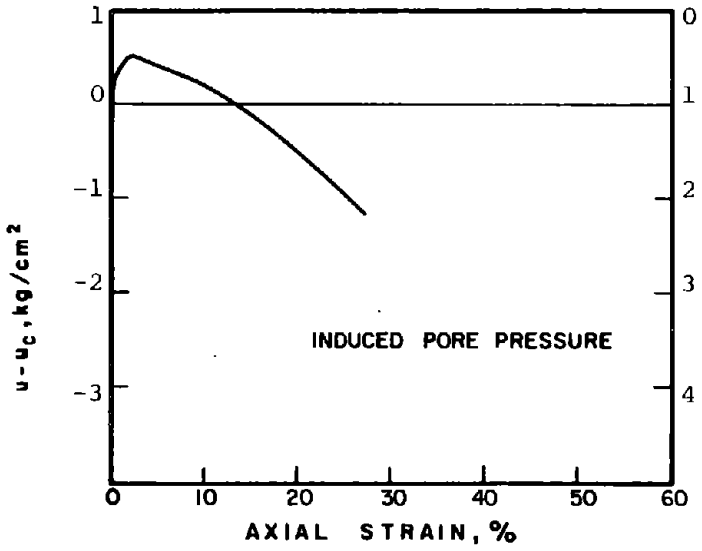

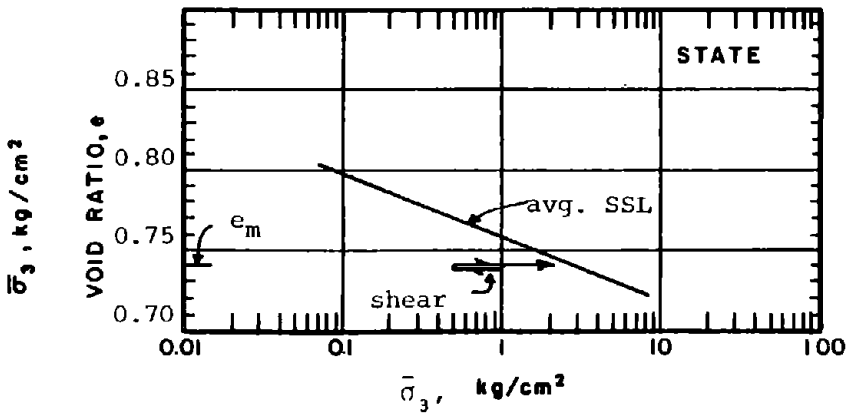

SOIL	: Banding Sand #6	METHOD OF LOADING:	Undrained, Axial Compression Load Control
STRUCTURE	: Compacted Moist		
STATE AFTER CONSOLIDATION:	$\bar{\sigma}_{3c}$ = 1.00 kg/cm², $\bar{\sigma}_{1c}$ = 1.00 kg/cm²	TESTING DETAILS	: Specimen Diameter 3.60 cm
	e_c = 0.738 , γ_{dc} = 95.5 pcf		: Specimen Height 5.30 cm
			: End Platens: Lubricated, Type 1

R-622

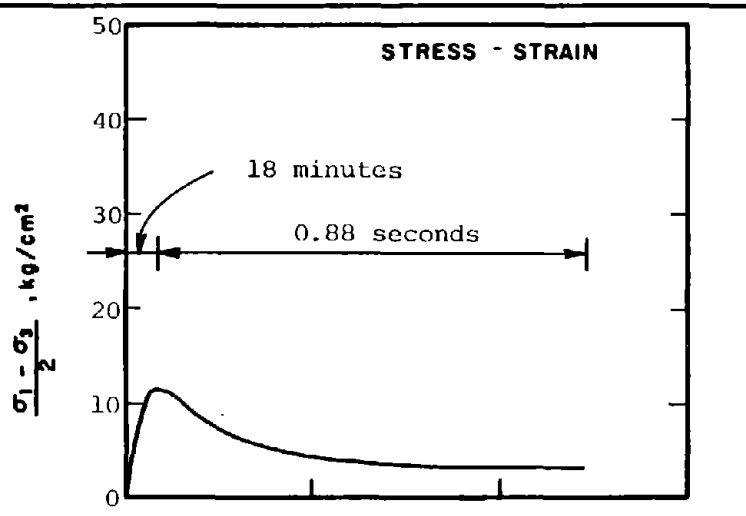

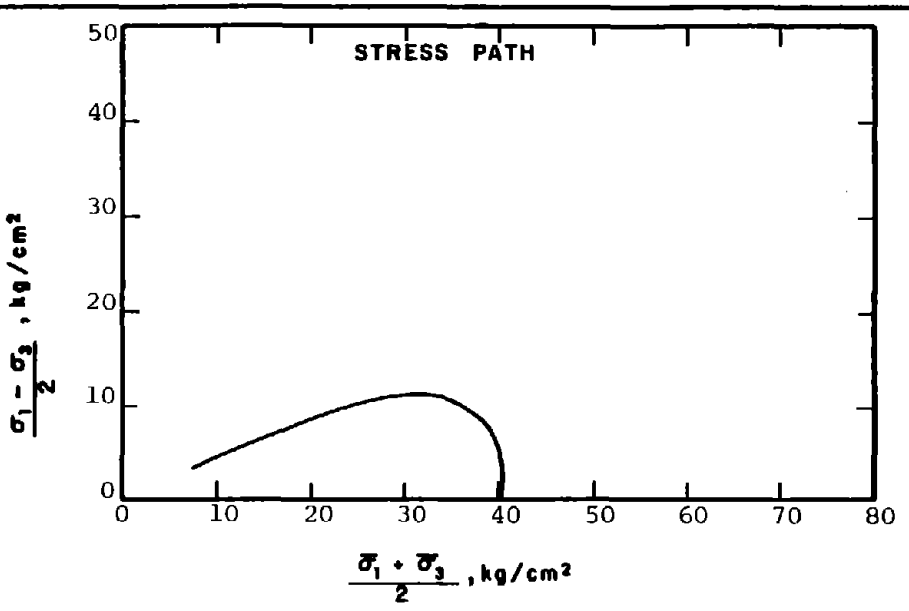

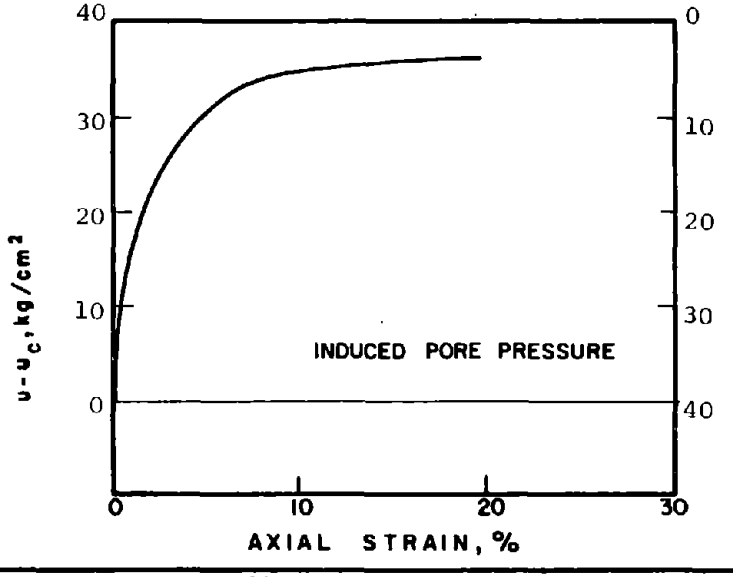

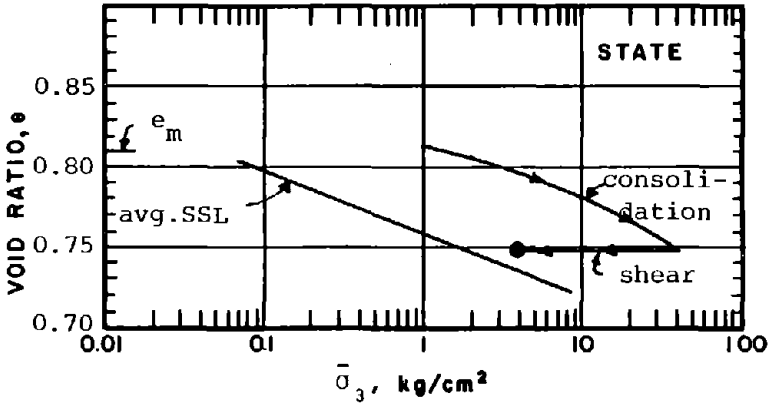

R-623

SOIL : Banding Sand #6

STRUCTURE : Compacted Moist

STATE AFTER CONSOLIDATION: $\bar{\sigma}_{3c} = 40.00$ kg/cm^2, $\bar{\sigma}_{1c} = 40.00$ kg/cm^2

$e_c = 0.748$, $\gamma_{dc} = 95.0$ pcf

METHOD OF LOADING: Undrained, Axial Compression
Load Control

TESTING DETAILS : Specimen Diameter 3.60 cm
: Specimen Height 5.30 cm
: End Platens: Conventional

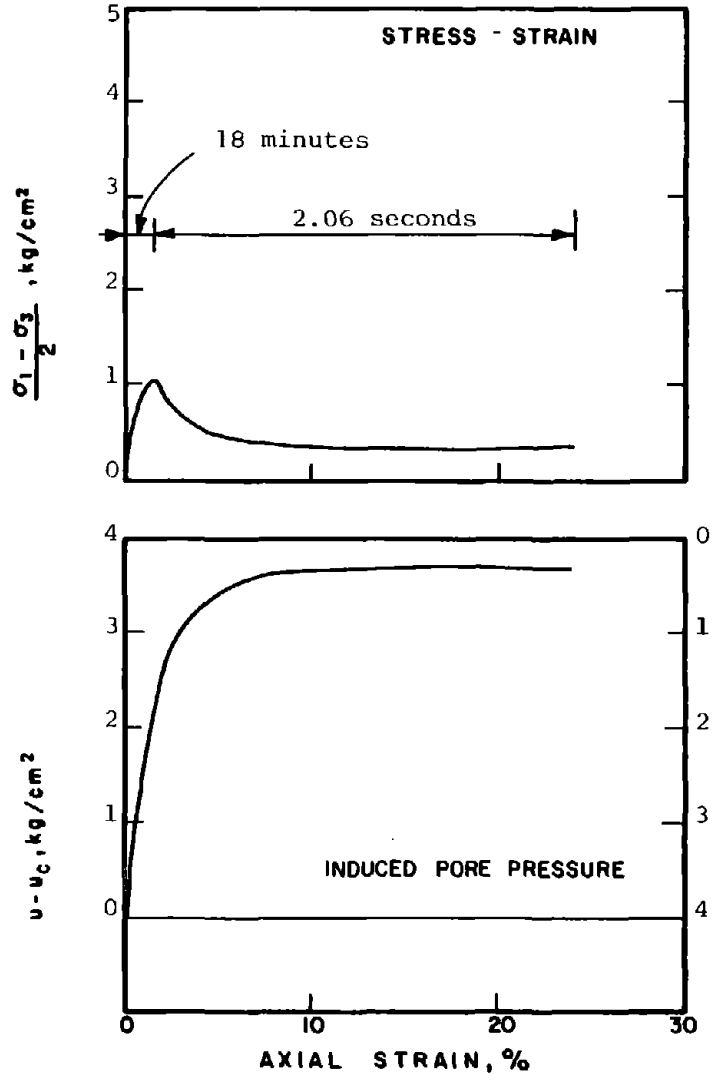

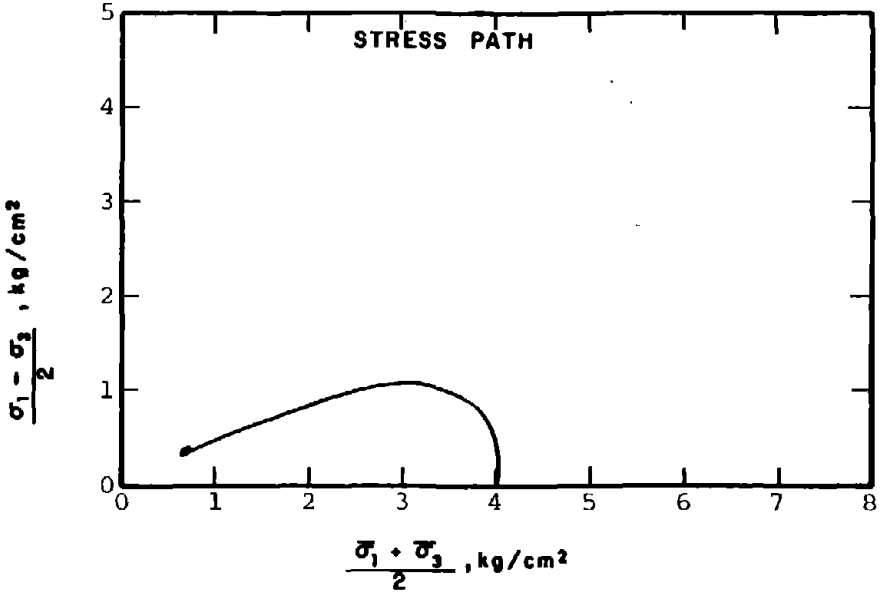

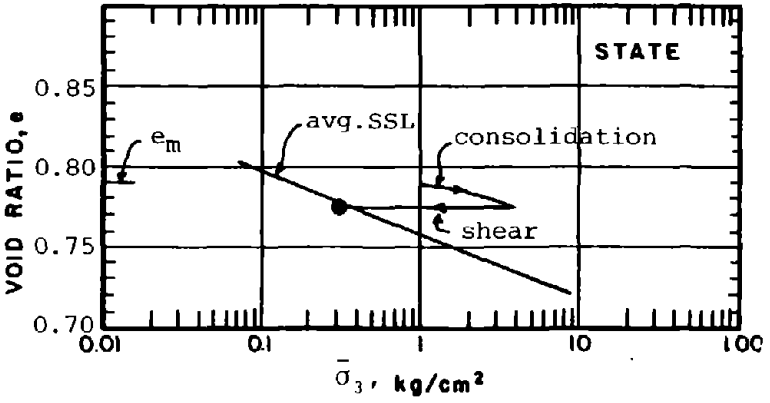

R-624

SOIL : Banding Sand #6

STRUCTURE : Compacted Moist

STATE AFTER CONSOLIDATION: $\bar{\sigma}_{3c} = 4.00$ kg/cm^2, $\bar{\sigma}_{1c} = 4.00$ kg/cm^2

$e_c = 0.774$, $\gamma_{dc} = 93.6$ pcf

METHOD OF LOADING: Undrained, Axial Compression
Load Control

TESTING DETAILS : Specimen Diameter 3.60 cm
: Specimen Height 5.30 cm
: End Platens: Lubricated, Type 1

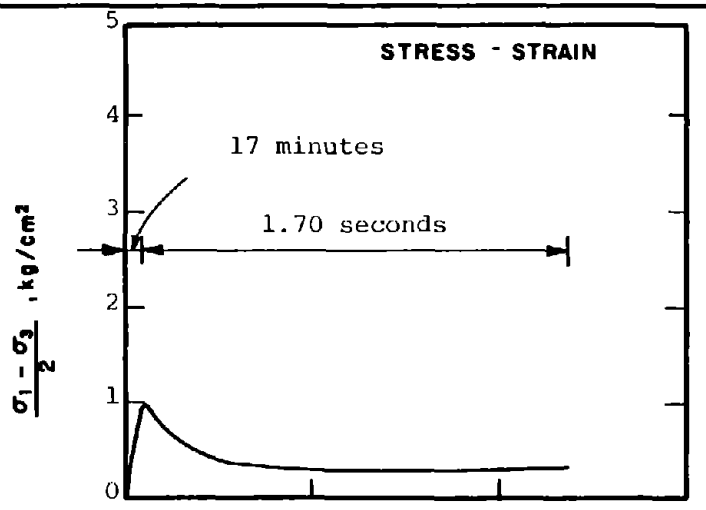

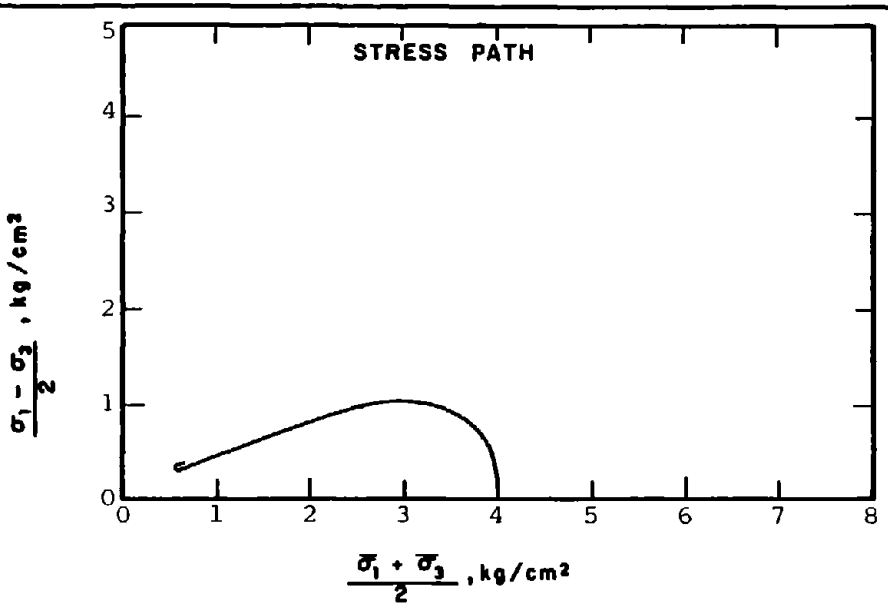

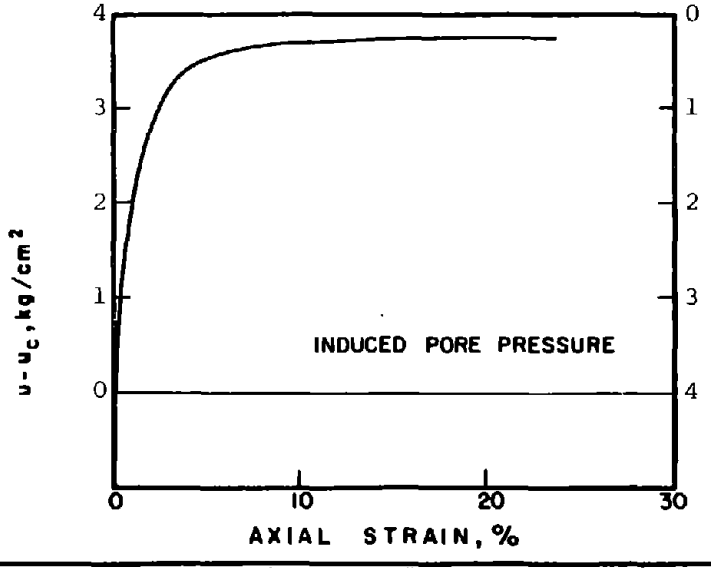

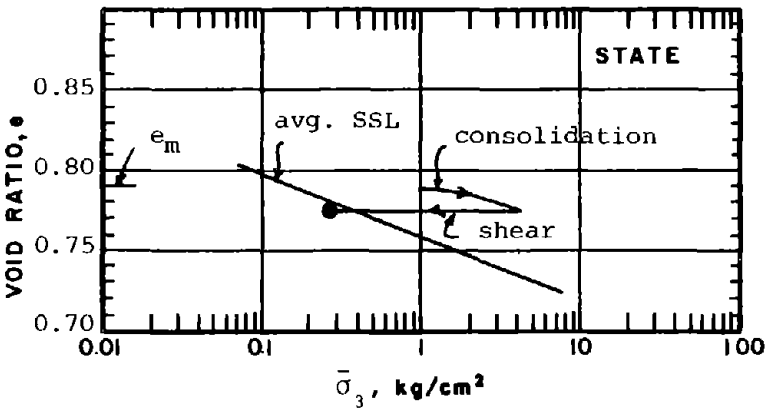

SOIL	: Banding Sand #6	METHOD OF LOADING:	Undrained, Axial Compression Load Control
STRUCTURE	: Compacted Moist		
STATE AFTER CONSOLIDATION:	$\bar{\sigma}_{3c}$ = 4.00 kg/cm², $\bar{\sigma}_{1c}$ = 4.00 kg/cm² e_c = 0.774, γ_{dc} = 93.6 pcf	TESTING DETAILS	: Specimen Diameter 3.60 cm : Specimen Height 5.30 cm : End Platens: Lubricated, Type 1

R-625

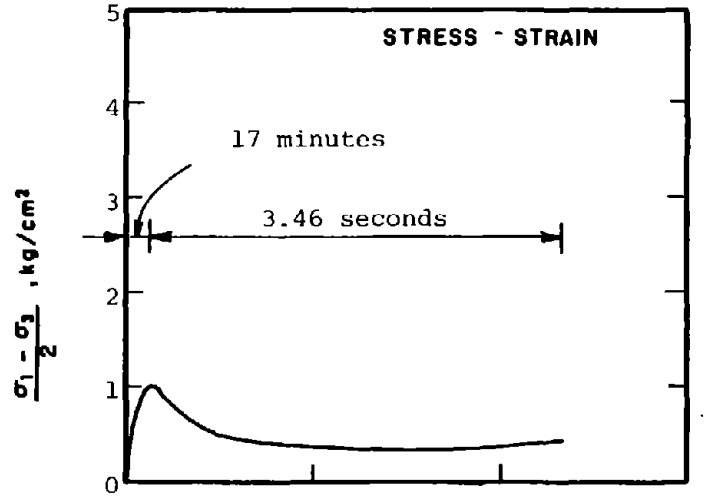

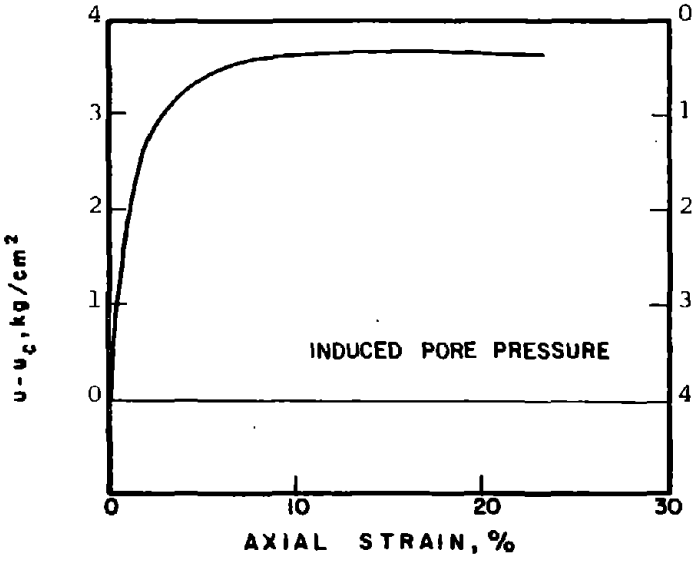

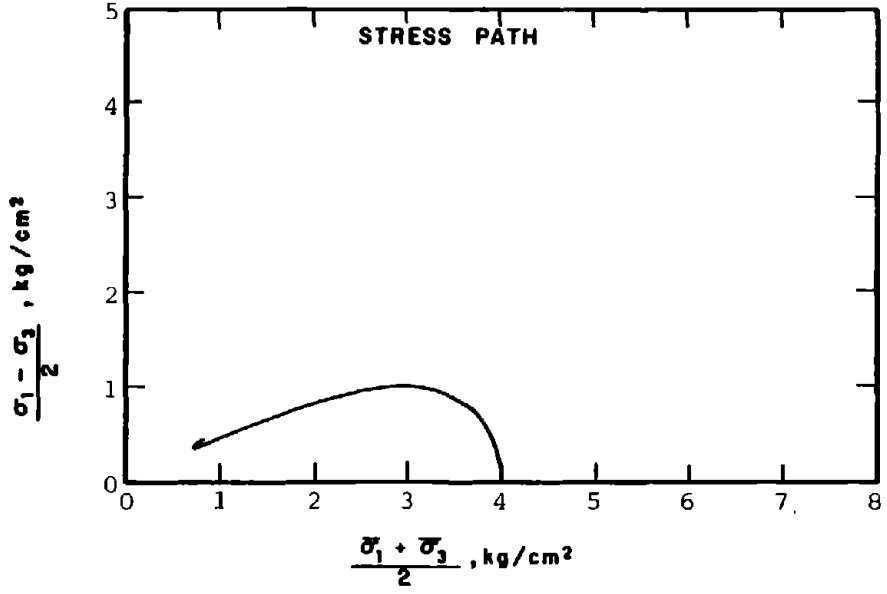

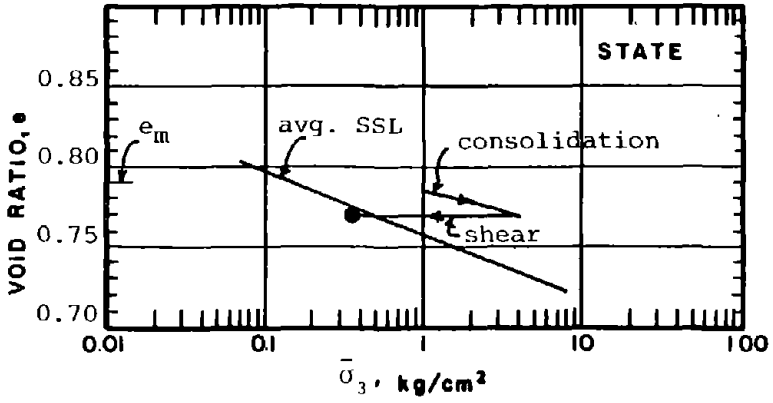

SOIL	: Banding Sand #6	METHOD OF LOADING:	Undrained, Axial Compression Load Control
STRUCTURE	: Compacted Moist		
STATE AFTER CONSOLIDATION:	$\bar{\sigma}_{3c}$ = 4.00 kg/cm², $\bar{\sigma}_{1c}$ = 4.00 kg/cm² e_c = 0.770, γ_{dc} = 93.8 pcf	TESTING DETAILS	: Specimen Diameter 3.60 cm : Specimen Height 5.30 cm : End Platens: Lubricated, Type 1

R-626

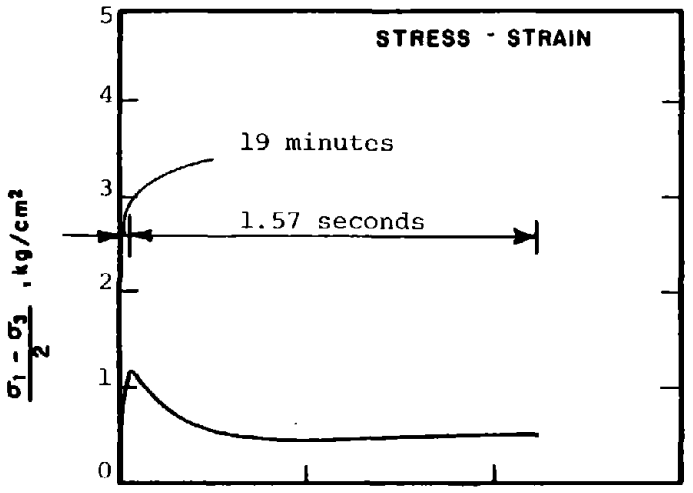

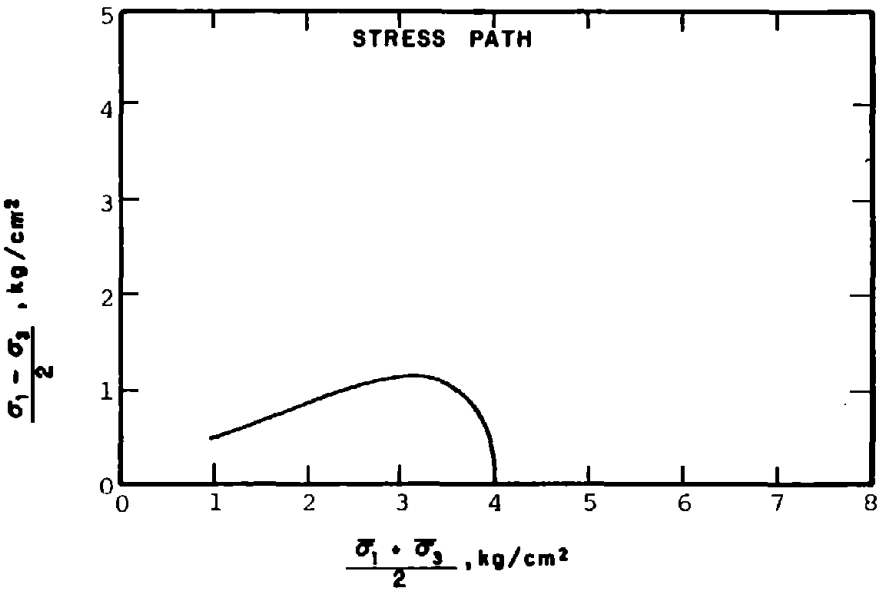

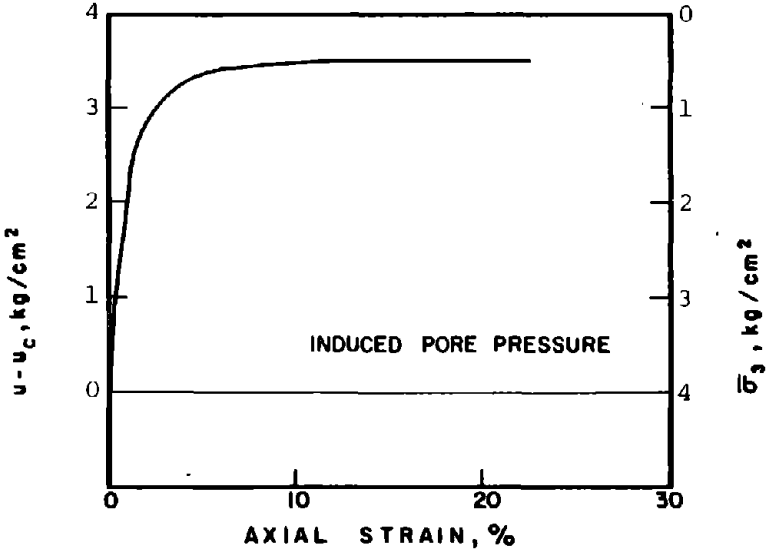

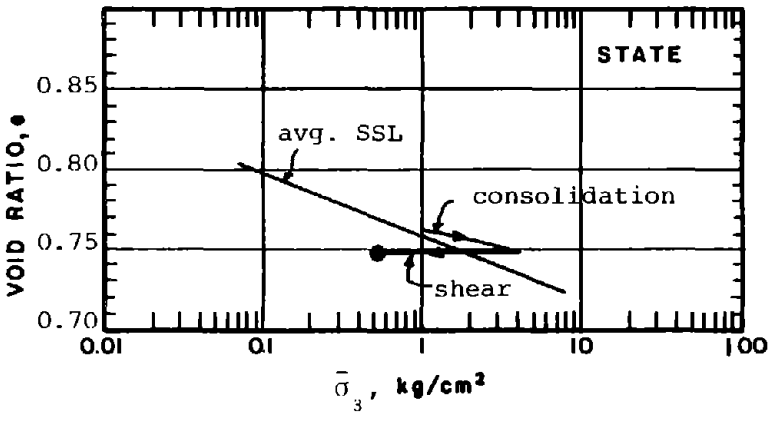

R-627

SOIL : Banding Sand #6

STRUCTURE : Compacted Moist

STATE AFTER CONSOLIDATION: $\bar{\sigma}_{3c} = 4.00$ kg/cm^2, $\bar{\sigma}_{1c} = 4.00$ kg/cm^2

$e_c = 0.749$, $\gamma_{dc} = 94.9$ pcf

METHOD OF LOADING: Undrained, Axial Compression
Load Control

TESTING DETAILS : Specimen Diameter 3.60cm
: Specimen Height 8.10cm
: End Platens: Conventional

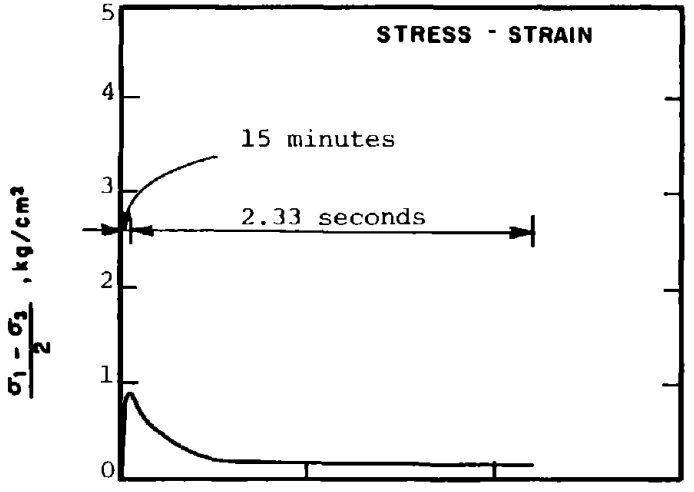

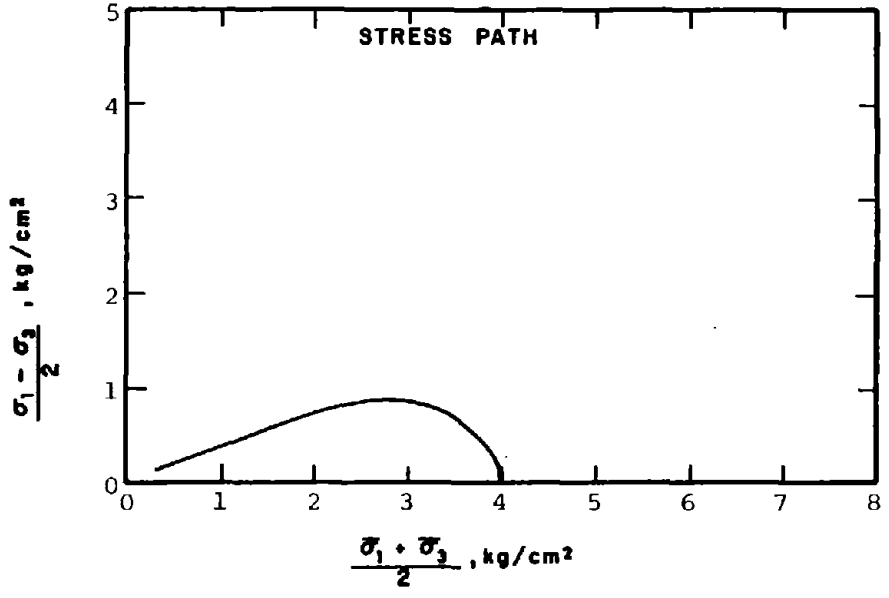

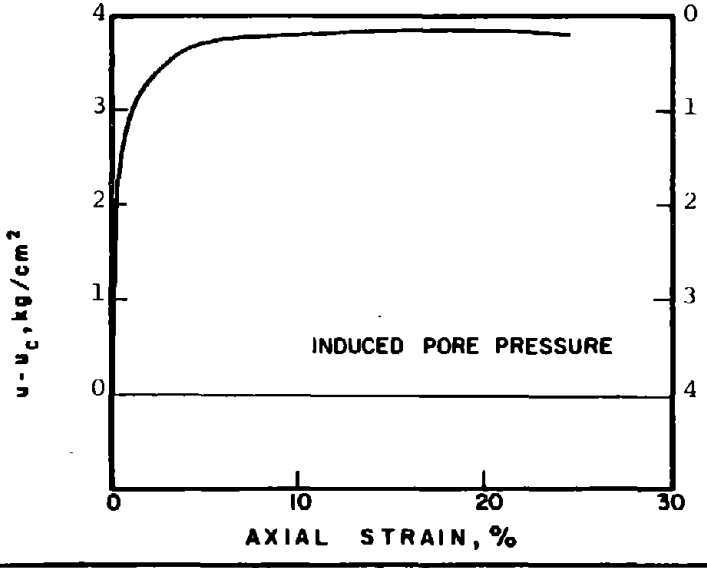

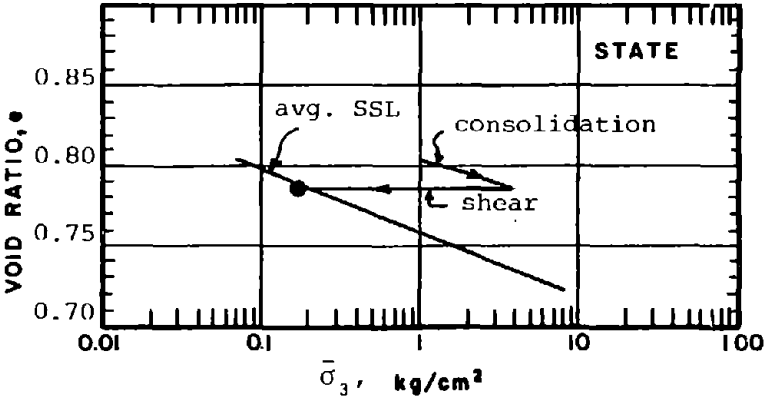

SOIL	: Banding Sand #6	METHOD OF LOADING:	Undrained, Axial Compression Load Control
STRUCTURE	: Compacted Moist		
STATE AFTER CONSOLIDATION:	$\bar{\sigma}_{3c}$ = 4.00 kg/cm^2, $\bar{\sigma}_{1c}$ = 4.00 kg/cm^2 e_c = 0.784, γ_{dc} = 93.0 pcf	TESTING DETAILS	: Specimen Diameter 3.60 cm : Specimen Height 8.10 cm : End Platens: Conventional

R-628

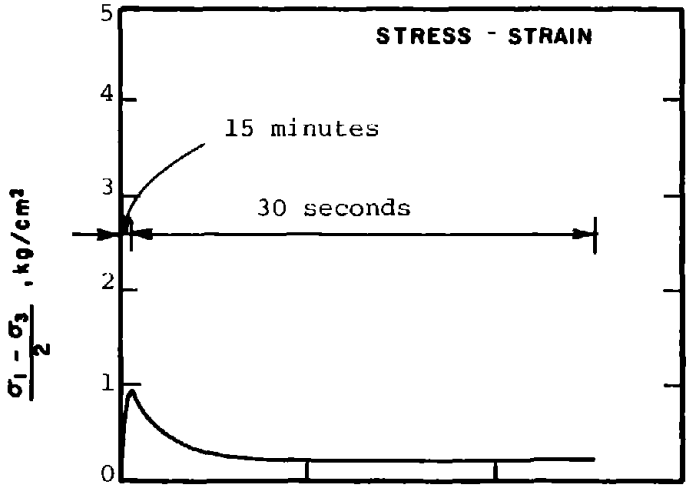

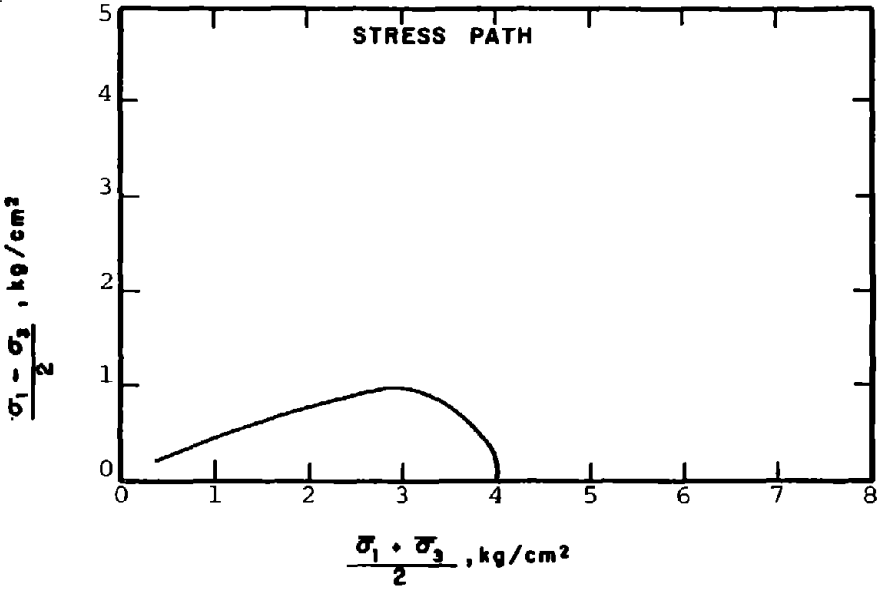

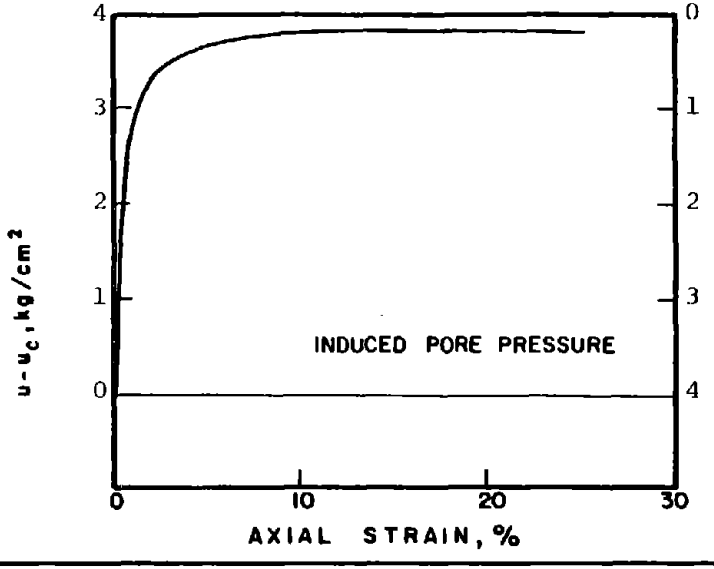

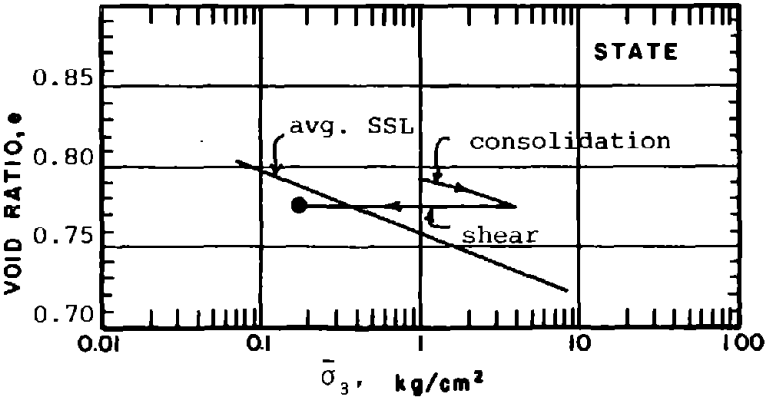

SOIL	: Banding Sand #6	METHOD OF LOADING:	Undrained, Axial Compression Load Control
STRUCTURE	: Compacted Moist		
STATE AFTER CONSOLIDATION:	$\bar{\sigma}_{3c}$ = 4.00 kg/cm², $\bar{\sigma}_{1c}$ = 4.00 kg/cm²	TESTING DETAILS	: Specimen Diameter 3.60 cm
	e_c = 0.773, γ_{dc} = 93.6 pcf		: Specimen Height 8.10 cm
			: End Platens: Conventional

R-629

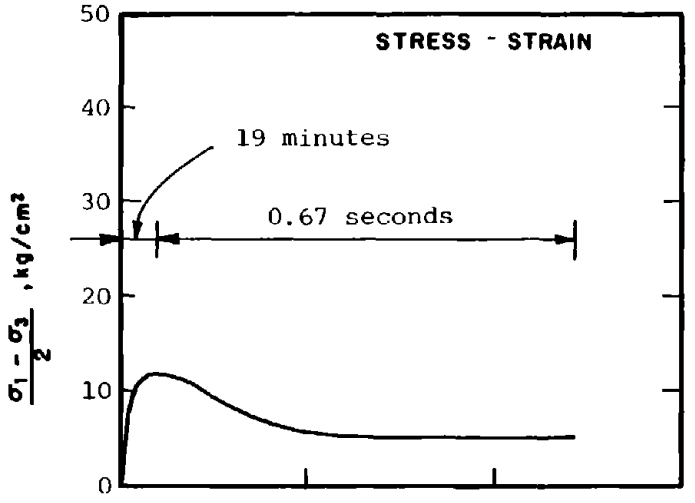

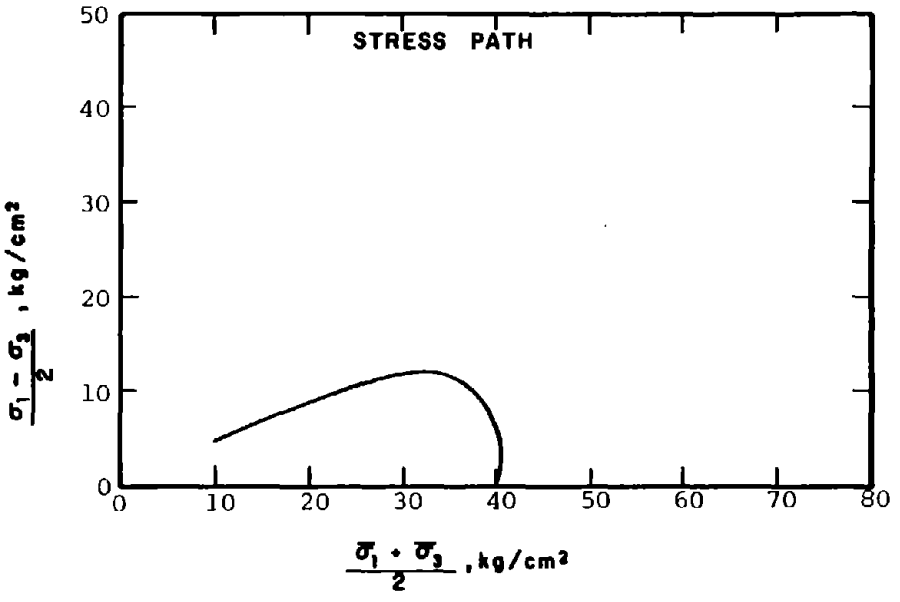

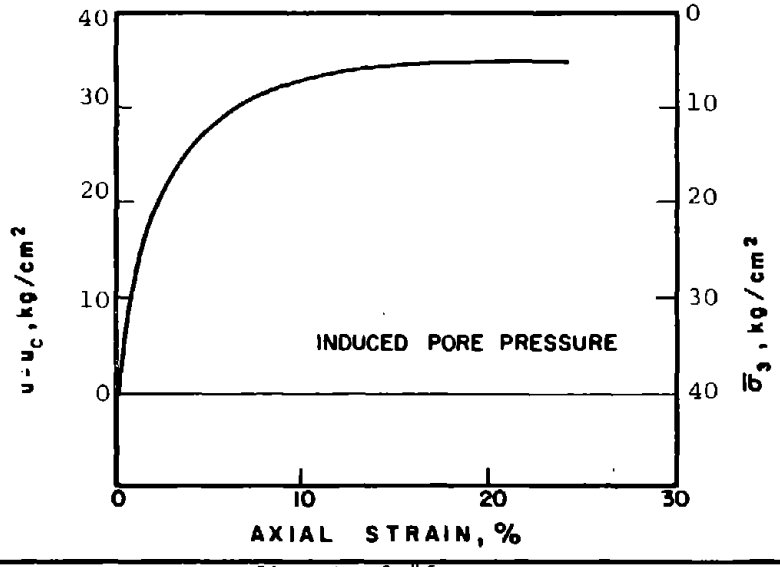

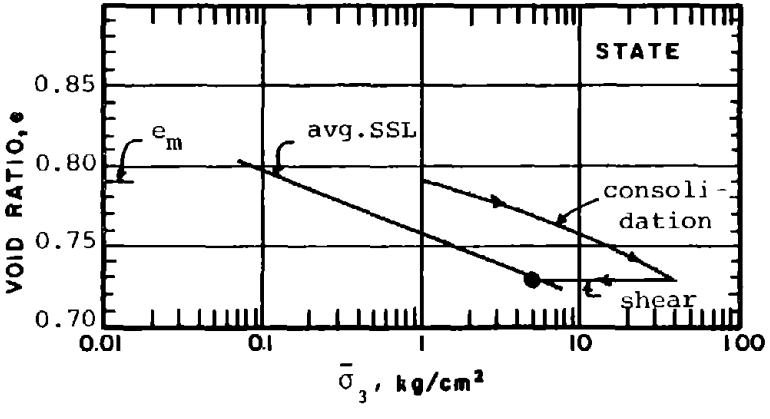

R-631

SOIL : Banding Sand #6

STRUCTURE : Compacted Moist

STATE AFTER CONSOLIDATION: $\bar{\sigma}_{3c} = 40.00$ kg/cm^2, $\bar{\sigma}_{1c} = 40.00$ kg/cm^2

$e_c = 0.728$, $\gamma_{dc} = 96.0$ pcf

METHOD OF LOADING: Undrained, Axial Compression
Load Control

TESTING DETAILS : Specimen Diameter 3.60 cm
: Specimen Height 5.30 cm
: End Platens: Lubricated, Type 2

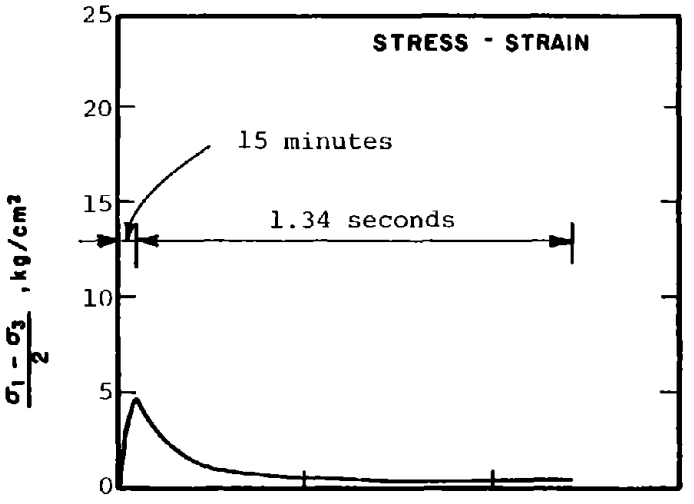

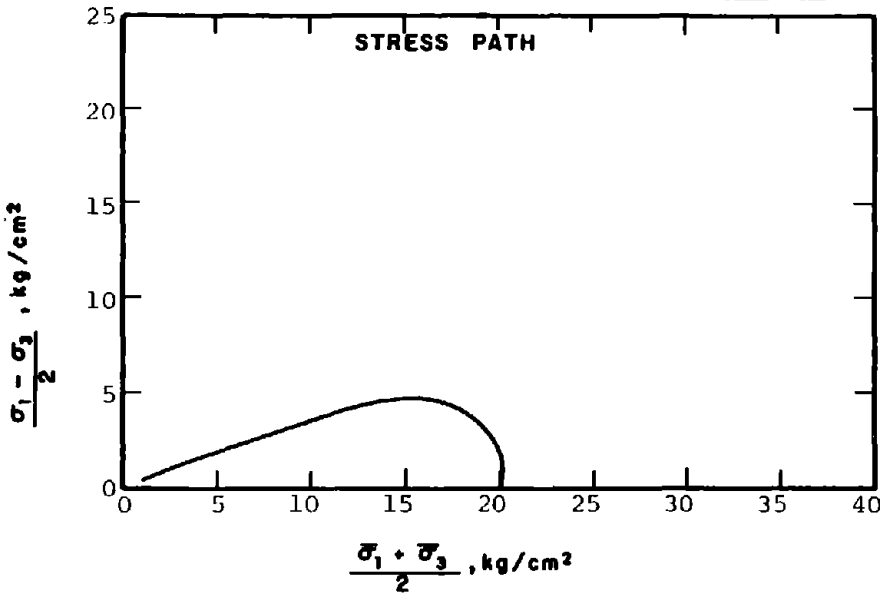

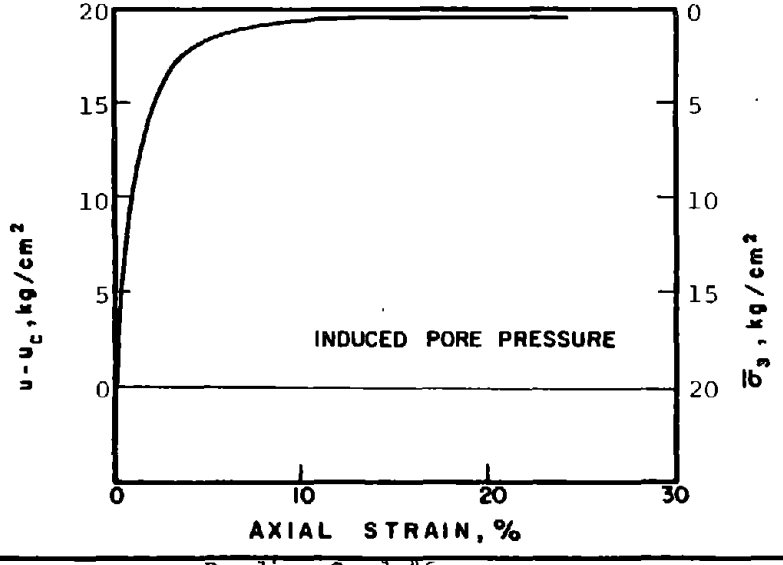

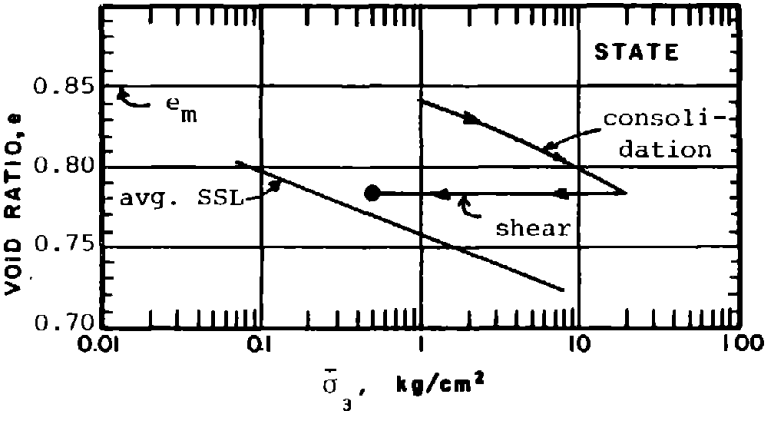

SOIL	: Banding Sand #6	METHOD OF LOADING:	Undrained, Axial Compression Load Control
STRUCTURE	: Compacted Moist		
STATE AFTER CONSOLIDATION:	$\bar{\sigma}_{3c}$ =20.00 kg/cm², $\bar{\sigma}_{1c}$ =20.00 kg/cm² e_c =0.782 , γ_{dc} = 93.1 pcf	TESTING DETAILS	: Specimen Diameter 3.60 cm : Specimen Height 5.30 cm : End Platens: Lubricated, Type 2

R-632

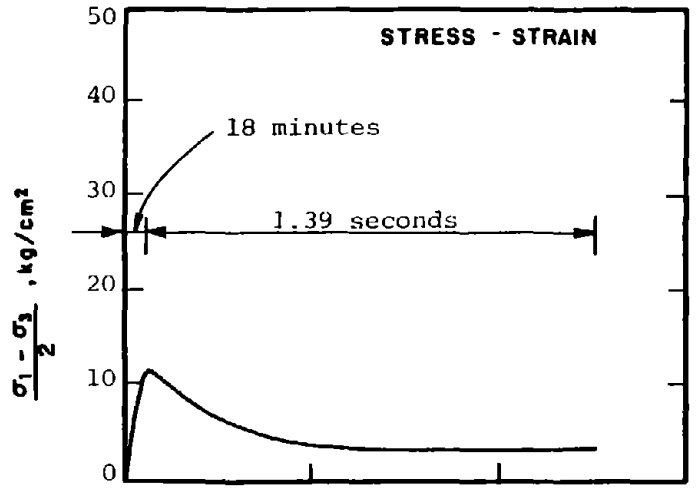

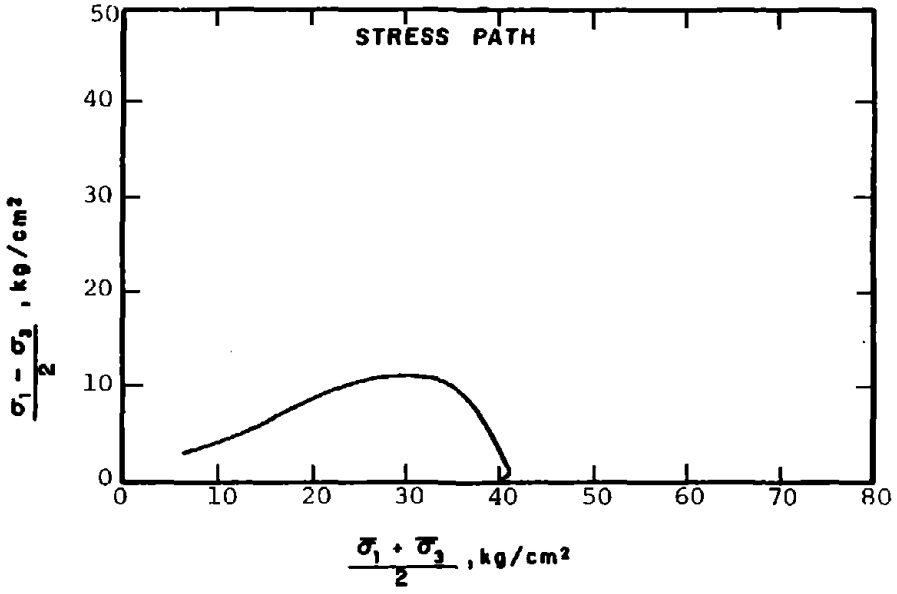

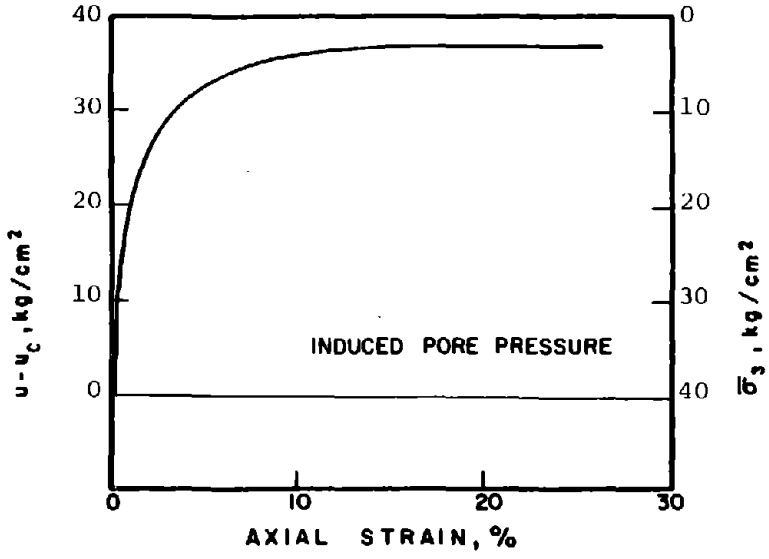

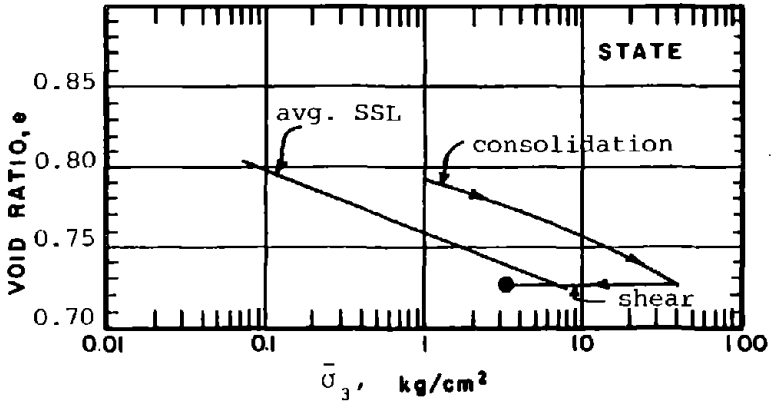

SOIL	: Banding Sand #6	METHOD OF LOADING:	Undrained, Axial Compression Load Control
STRUCTURE	: Compacted Moist		
STATE AFTER CONSOLIDATION:	$\bar{\sigma}_{3c}$ = 40.00kg/cm², $\bar{\sigma}_{1c}$ =40.00 kg/cm²	TESTING DETAILS	: Specimen Diameter 3.60 cm
	e_c = 0.725, γ_{dc} = 96.2 pcf		: Specimen Height 8.10 cm
			: End Platens: Conventional

R-633

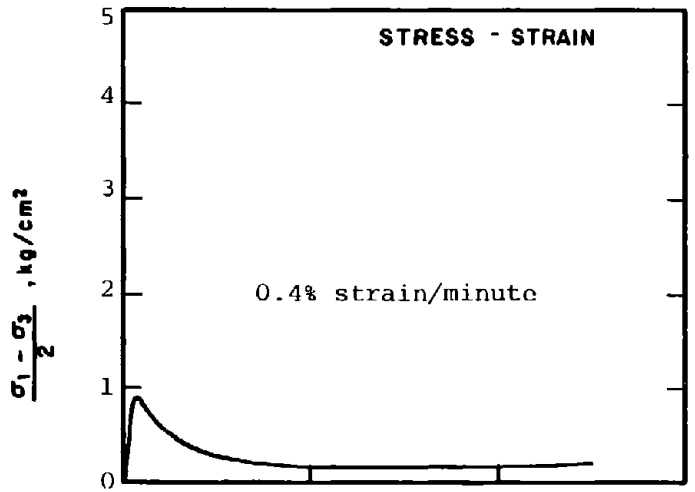

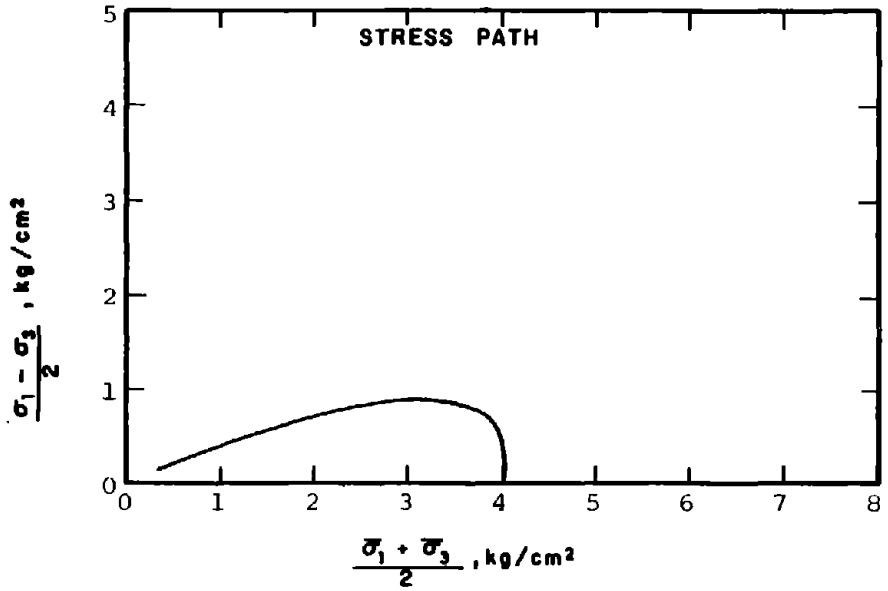

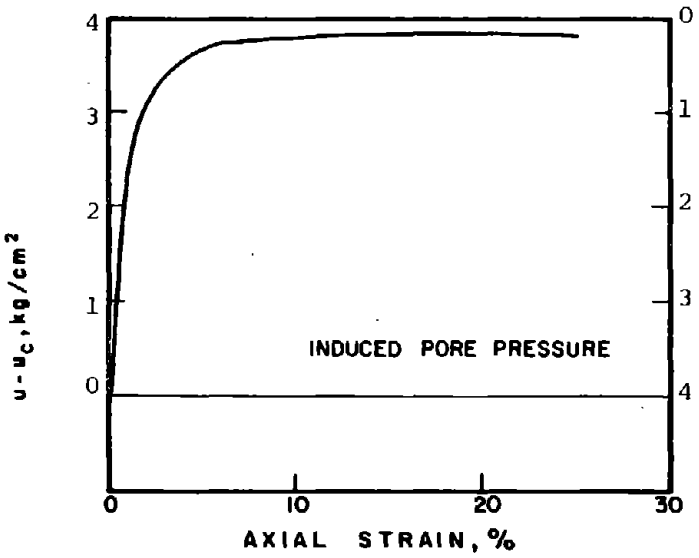

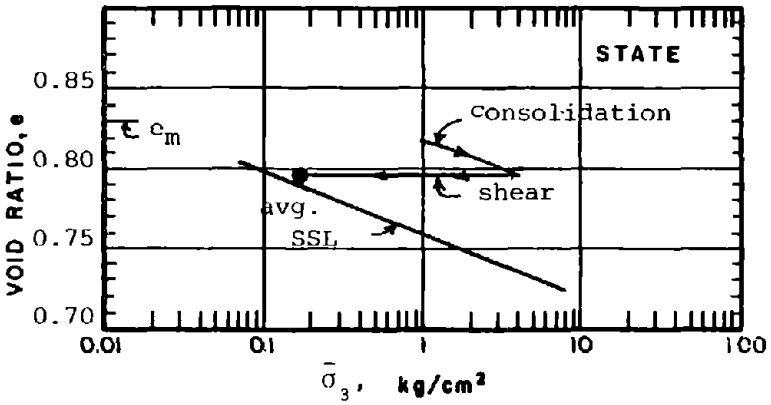

SOIL : Banding Sand #6

STRUCTURE : Compacted Moist

STATE AFTER CONSOLIDATION: $\bar{\sigma}_{3c}$ = 4.00 kg/cm², $\bar{\sigma}_{1c}$ = 4.00 kg/cm²
e_c = 0.796, γ_{dc} = 92.4 pcf

METHOD OF LOADING: Undrained, Axial Compression Strain Control

TESTING DETAILS : Specimen Diameter 3.60 cm
: Specimen Height 5.30 cm
: End Platens: Lubricated, Type 2

R-634

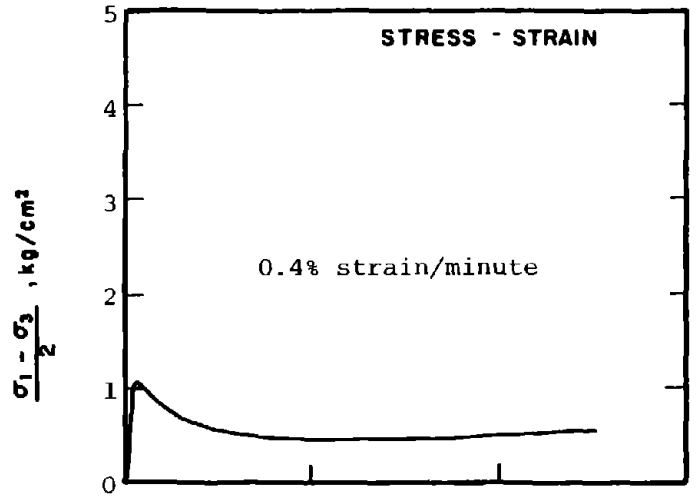

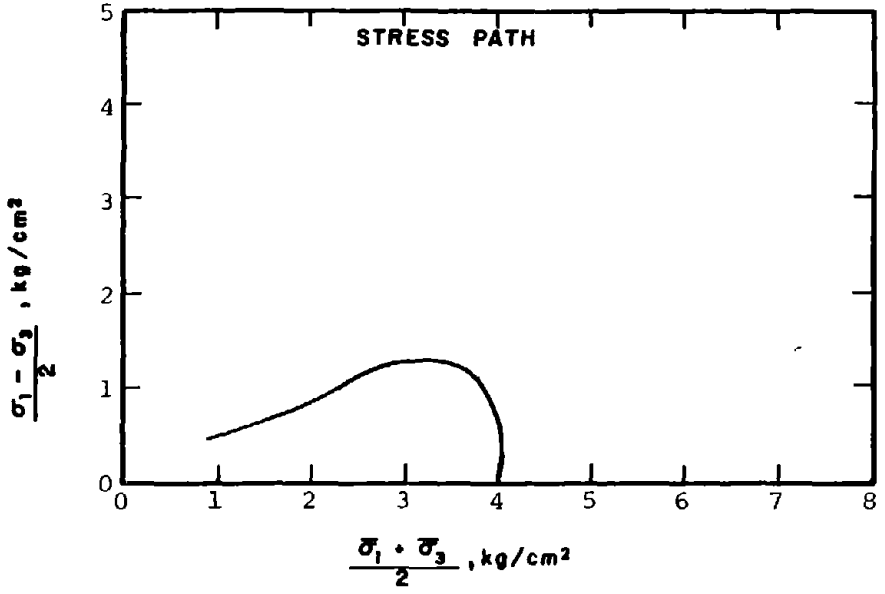

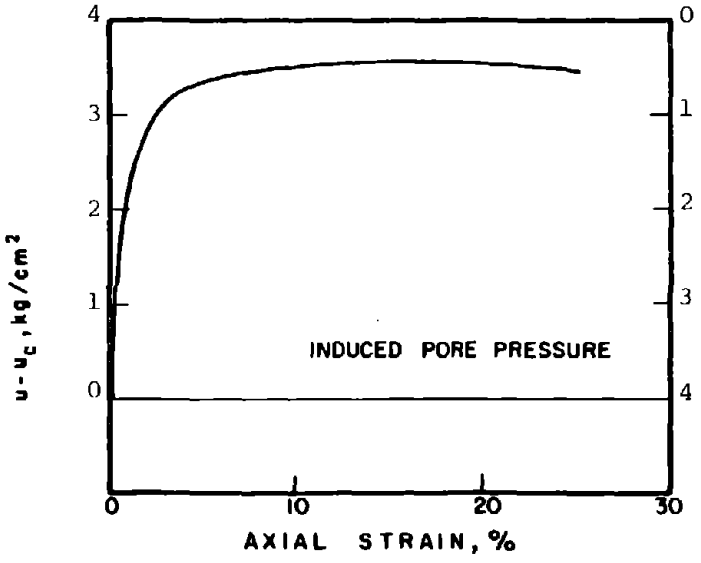

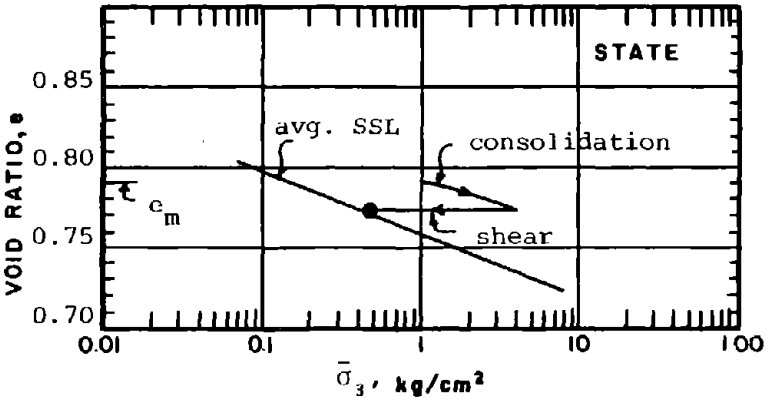

R-635

SOIL : Banding Sand #6

STRUCTURE : Compacted Moist

STATE AFTER CONSOLIDATION: $\bar{\sigma}_{3c}$ = 4.00 kg/cm², $\bar{\sigma}_{1c}$ = 4.00 kg/cm²

e_c =0.772 , γ_{dc} = 93.7 pcf

METHOD OF LOADING: Undrained, Axial Compression Strain Control

TESTING DETAILS : Specimen Diameter 3.60 cm

: Specimen Height 5.30 cm

: End Platens: Lubricated, Type 2

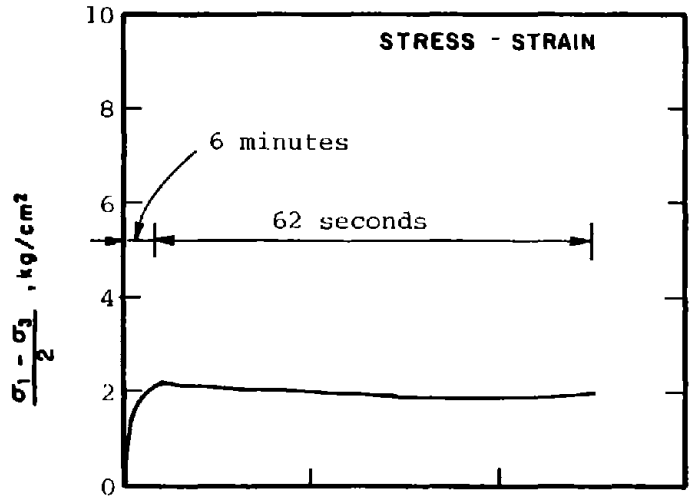

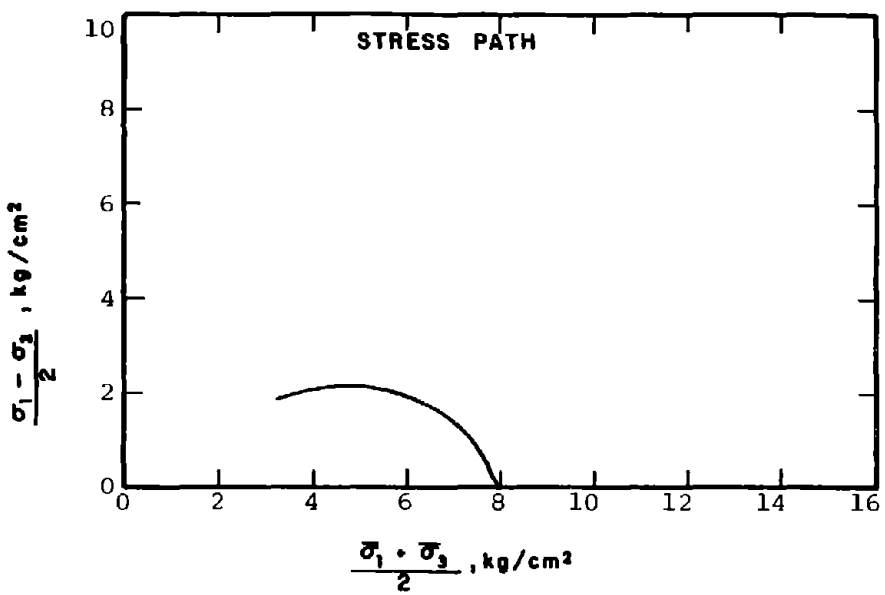

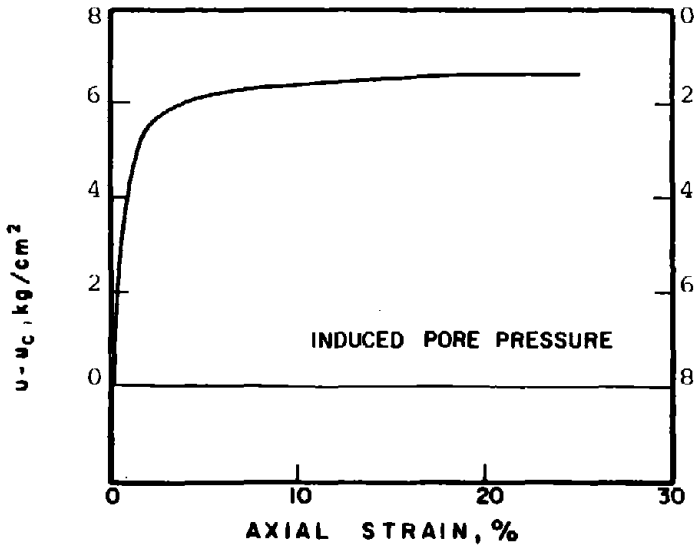

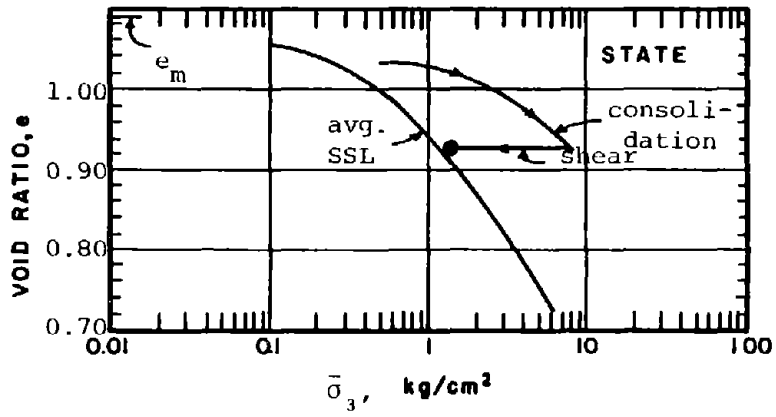

R-1002

SOIL : Mine Tailings

STRUCTURE : Compacted Moist

STATE AFTER CONSOLIDATION: $\bar{\sigma}_{3c}$ =8.00 kg/cm², $\bar{\sigma}_{1c}$ =8.00 kg/cm²
e_c =0.921 , γ_{dc} = 87.0 pcf

METHOD OF LOADING: Undrained, Axial Compression
Load Control

TESTING DETAILS : Specimen Diameter 3.60 cm
: Specimen Height 5.30 cm
: End Platens: Lubricated, Type 1

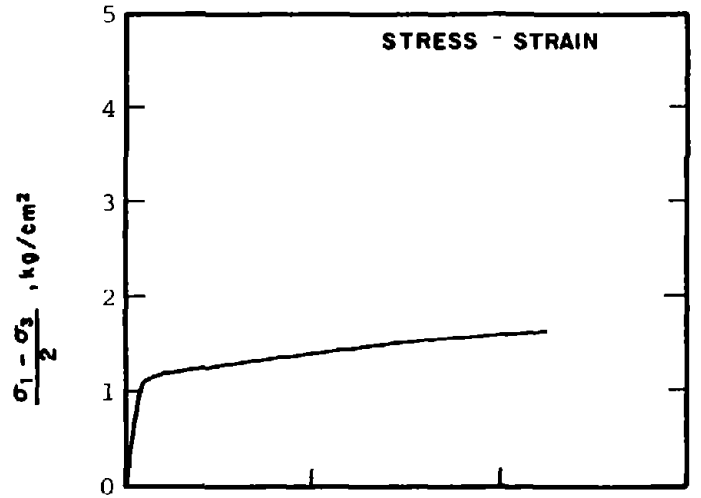

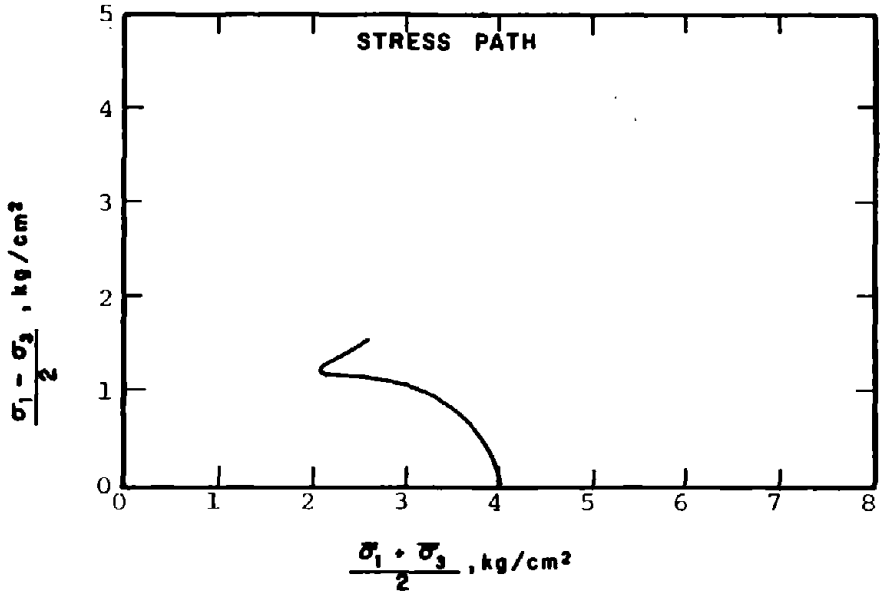

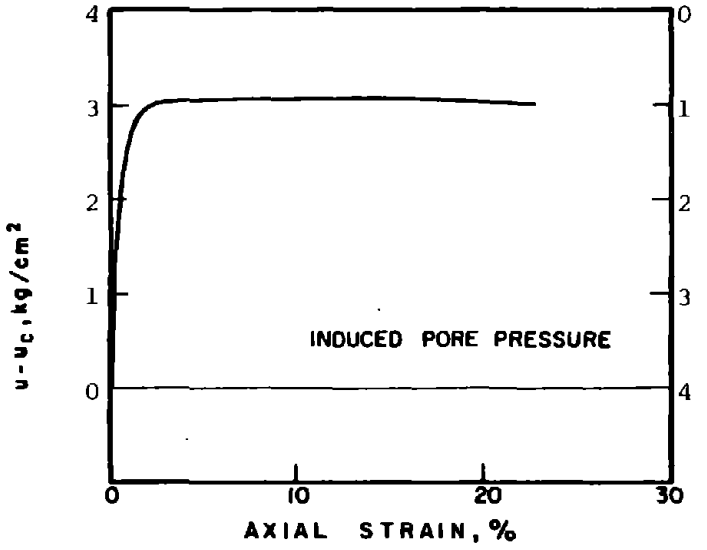

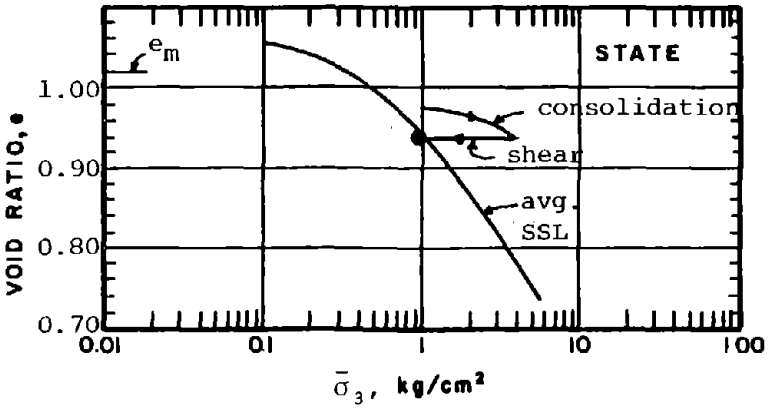

R-1003

SOIL : Mine Tailings

STRUCTURE : Compacted Moist

STATE AFTER CONSOLIDATION: $\bar{\sigma}_{3c}$ = 4.00 kg/cm², $\bar{\sigma}_{1c}$ = 4.00 kg/cm²
e_c = 0.938, γ_{dc} = 86.3 pcf

METHOD OF LOADING: Undrained, Axial Compression
Load Control

TESTING DETAILS : Specimen Diameter 3.60 cm
: Specimen Height 5.30 cm
: End Platens: Lubricated, Type 2

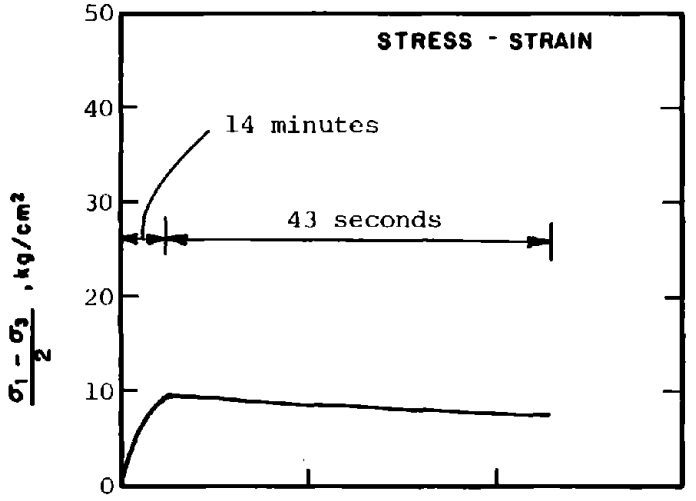

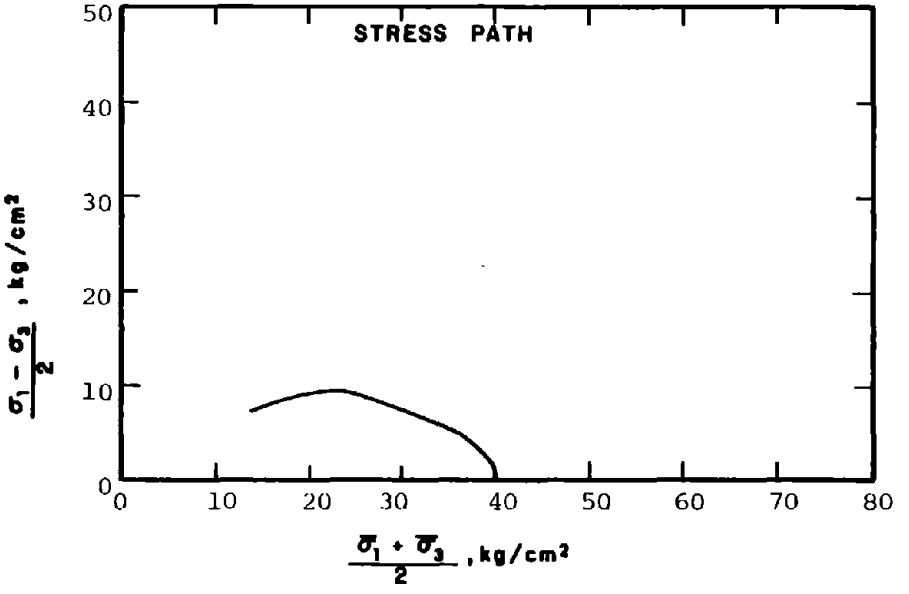

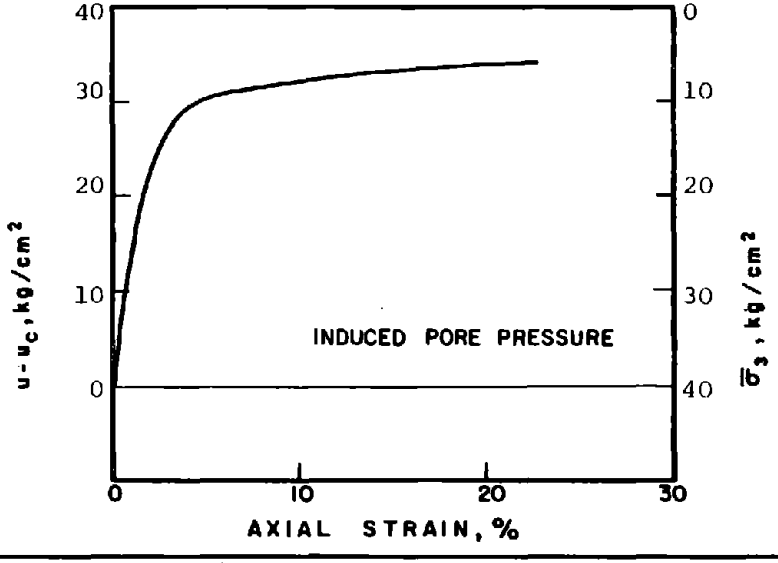

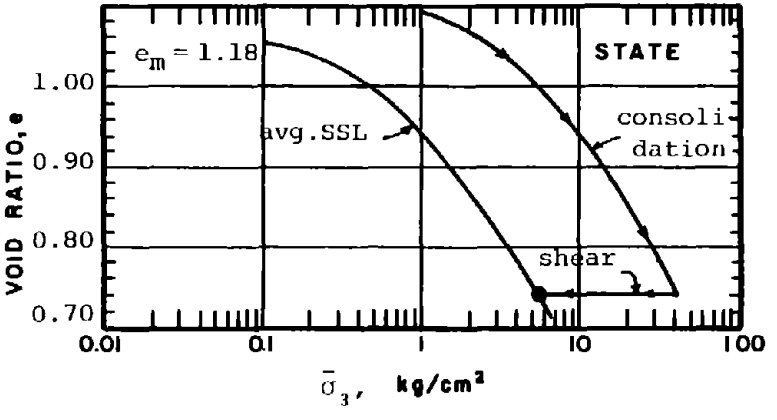

SOIL	: Mine Tailings	METHOD OF LOADING:	Undrained, Axial Compression Load Control
STRUCTURE	: Compacted Moist		
STATE AFTER CONSOLIDATION:	$\bar{\sigma}_{3c}$ =40.00 kg/cm², $\bar{\sigma}_{1c}$ =40.00 kg/cm²	TESTING DETAILS	: Specimen Diameter 3.60 cm
	e_c = 0.740, γ_{dc} = 96.1 pcf		: Specimen Height 5.30 cm
			: End Platens: Lubricated, Type 2

R-1004

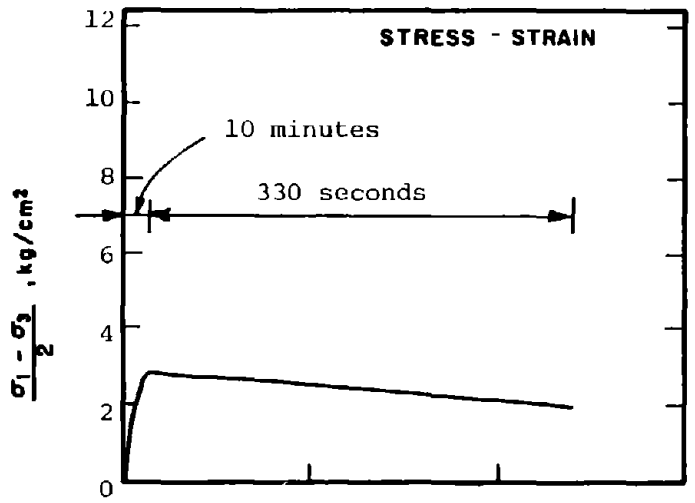

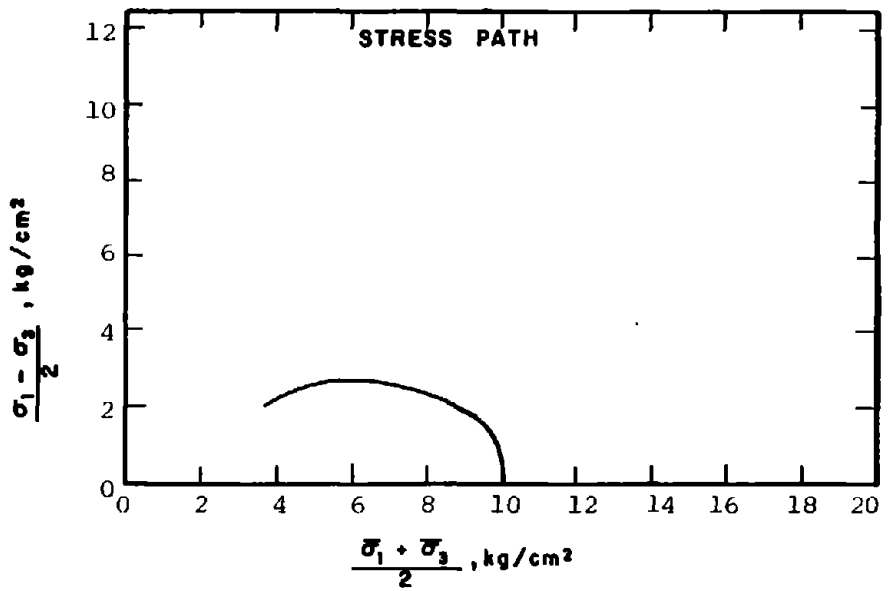

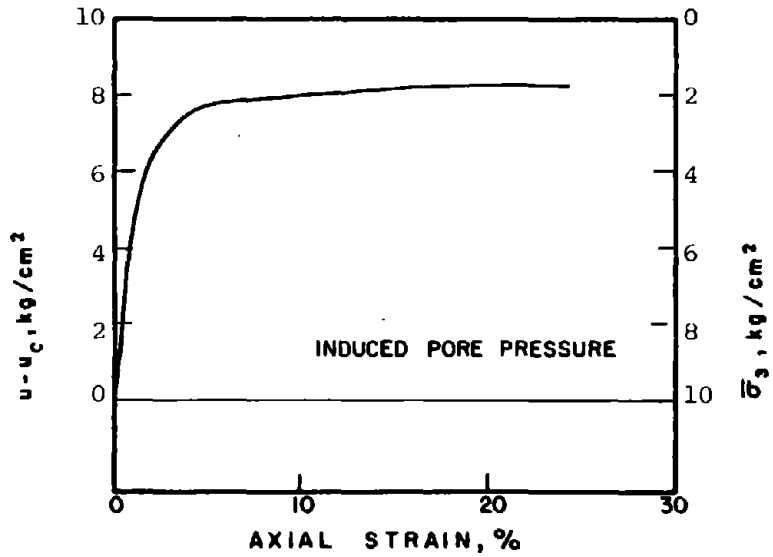

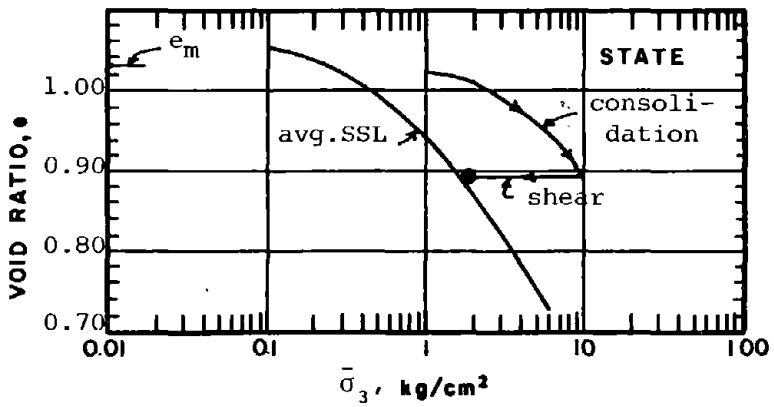

R-1005

SOIL : Mine Tailings

STRUCTURE : Compacted Moist

STATE AFTER CONSOLIDATION: $\bar{\sigma}_{3c}$ =10.00 kg/cm², $\bar{\sigma}_{1c}$ =10.00 kg/cm²

e_c = 0.896, γ_{dc} = 88.2 pcf

METHOD OF LOADING: Undrained, Axial Compression
Load Control

TESTING DETAILS : Specimen Diameter 3.60 cm
: Specimen Height 5.30 cm
: End Platens: Lubricated, Type 2

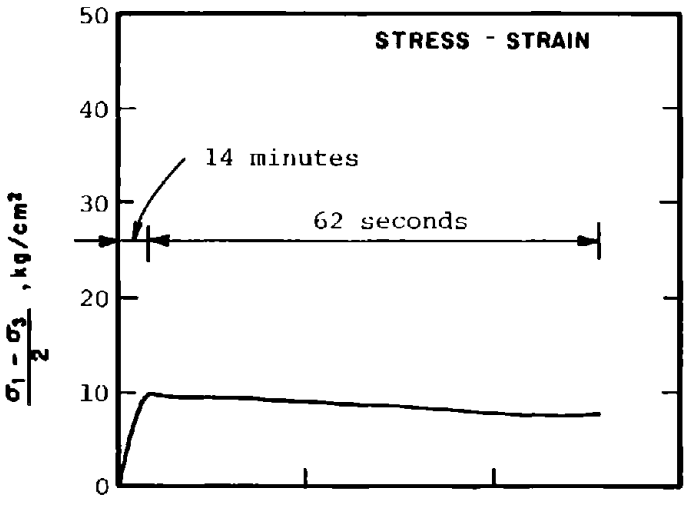

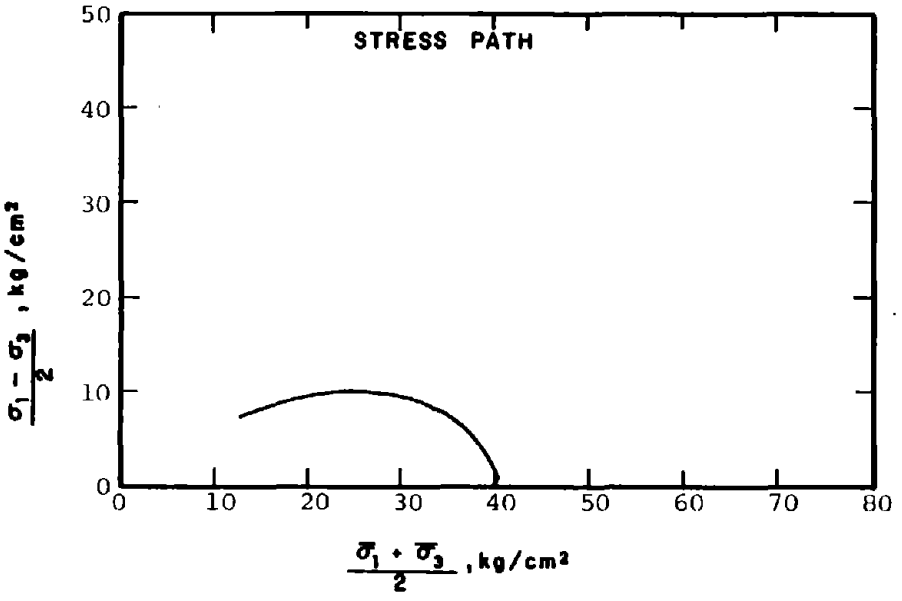

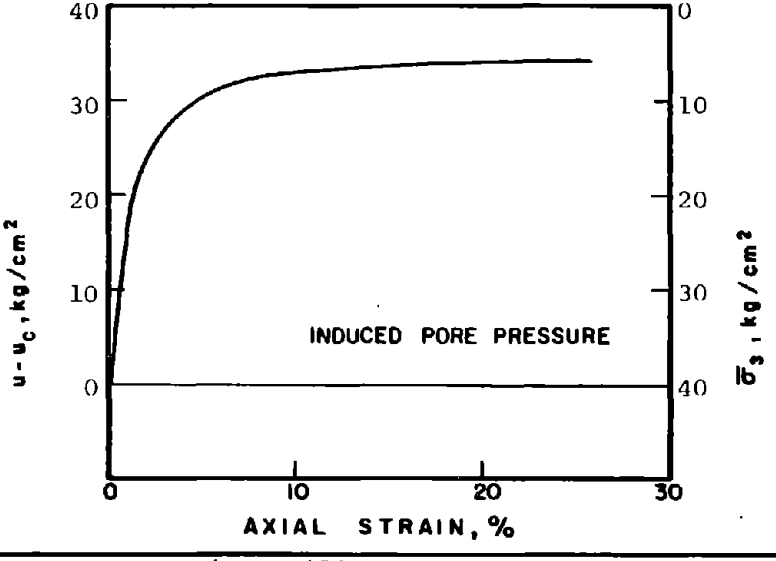

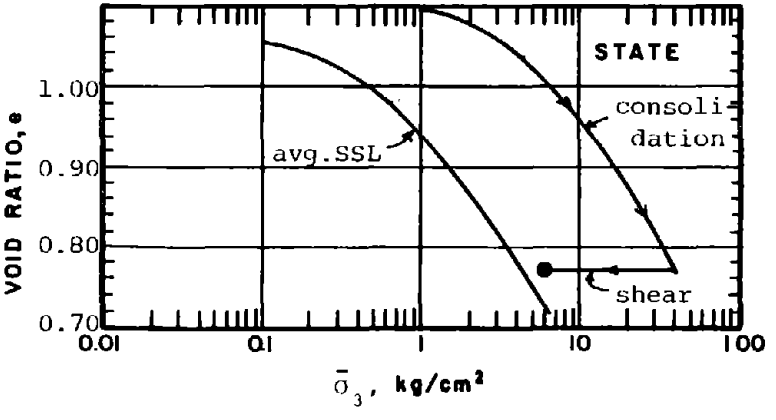

R-1009

SOIL : Mine Tailings

STRUCTURE : Compacted Moist

STATE AFTER CONSOLIDATION: $\bar{\sigma}_{3c}$ =40.00 kg/cm², $\bar{\sigma}_{1c}$ =40.00 kg/cm²

e_c = 0.769, γ_{dc} = 94.5 pcf

METHOD OF LOADING: Undrained, Axial Compression
Load Control

TESTING DETAILS : Specimen Diameter 3.60 cm
: Specimen Height 5.30 cm
: End Platens: Lubricated, Type 2

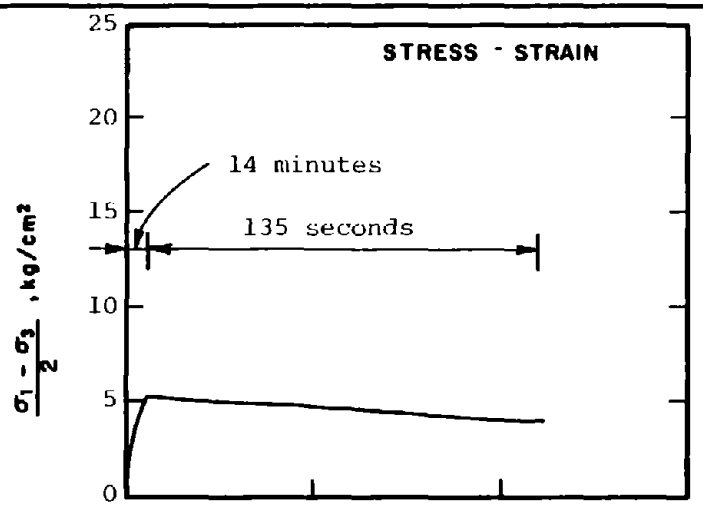

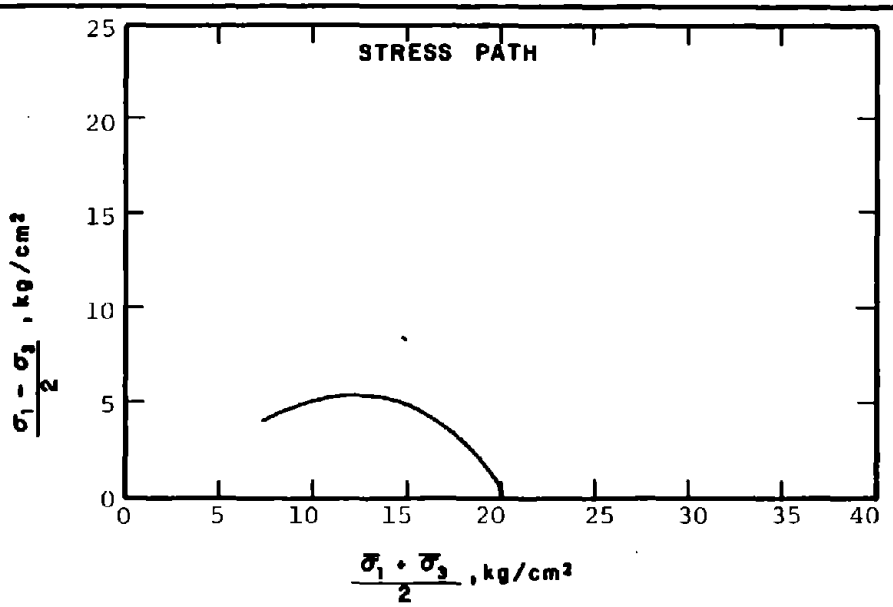

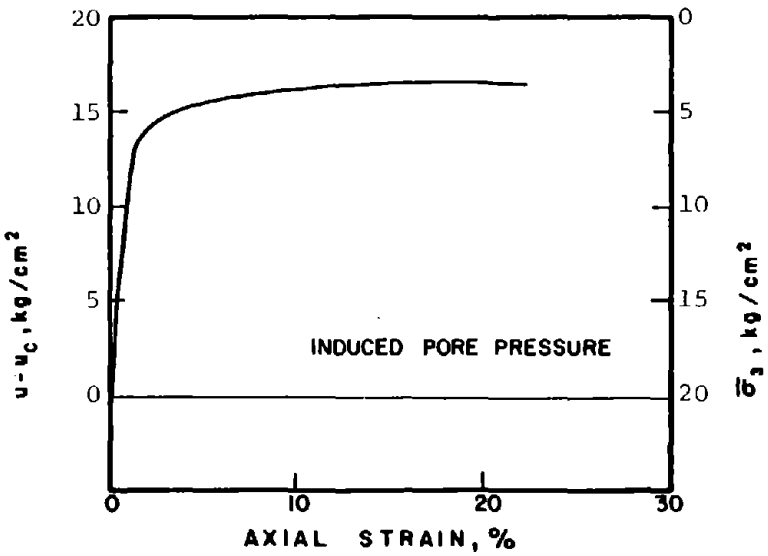

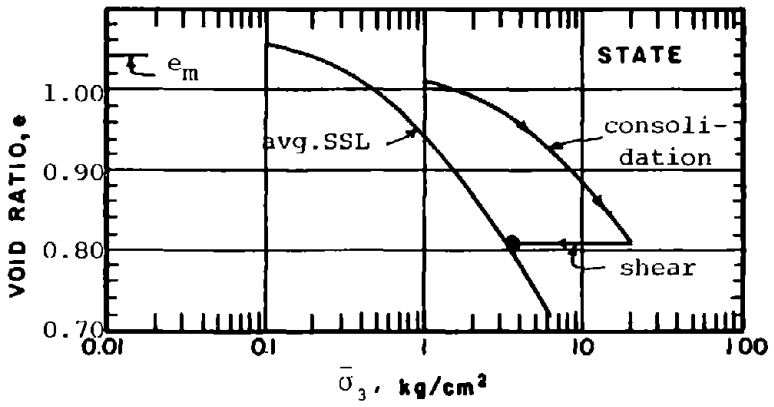

R-1007

SOIL : Mine Tailings

STRUCTURE : Compacted Moist

STATE AFTER CONSOLIDATION: $\bar{\sigma}_{3c}$ = 20.00 kg/cm², $\bar{\sigma}_{1c}$ = 20.00 kg/cm²

e_c = 0.806, γ_{dc} = 92.6 pcf

METHOD OF LOADING: Undrained, Axial Compression
Load Control

TESTING DETAILS : Specimen Diameter 3.60 cm
: Specimen Height 5.30 cm
: End Platens: Lubricated, Type 2

222

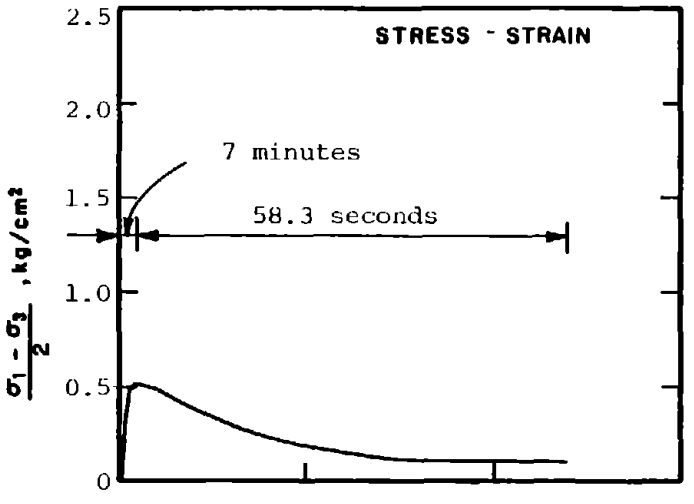

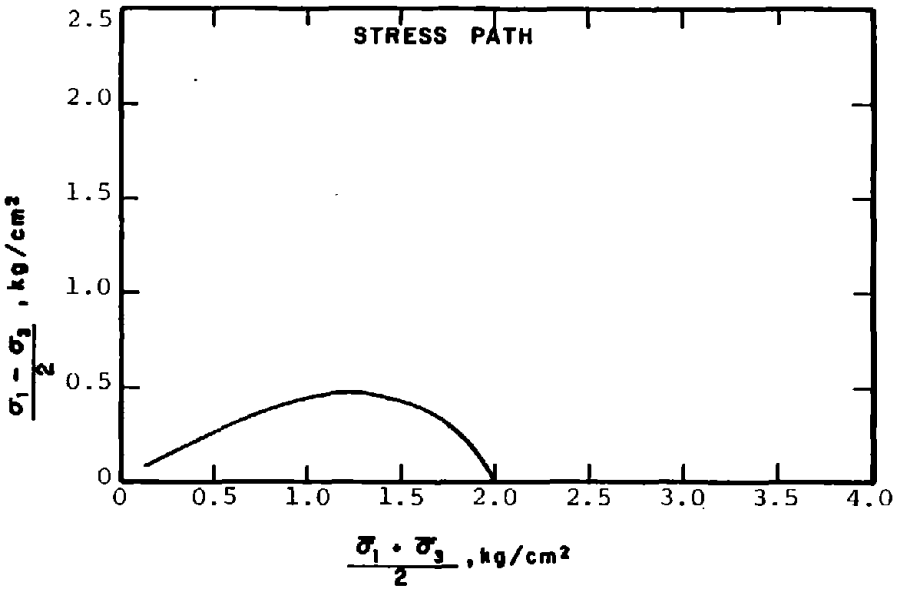

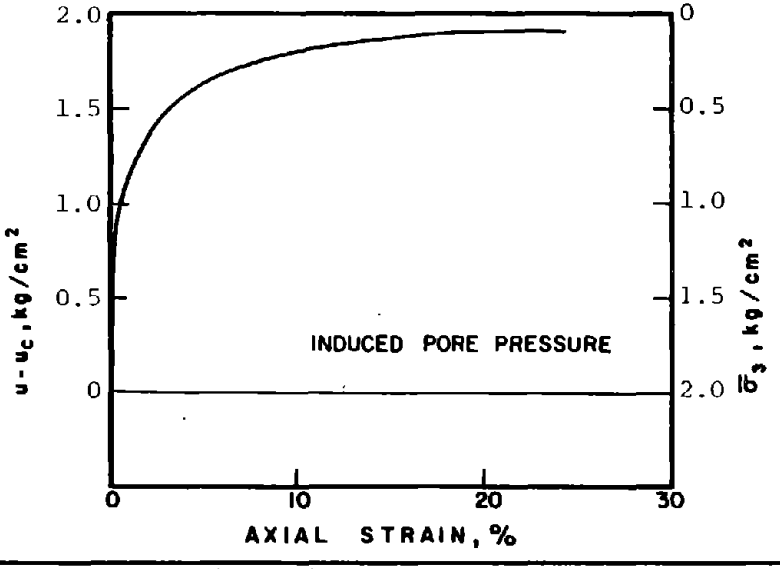

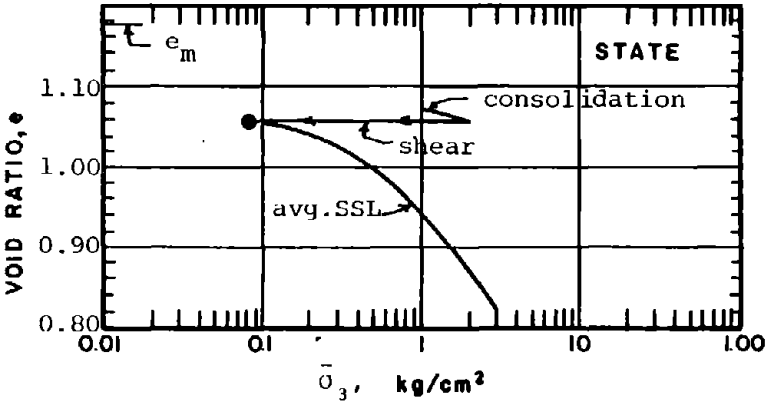

R-1008

SOIL : Mine Tailings

STRUCTURE : Compacted Moist

STATE AFTER CONSOLIDATION: $\bar{\sigma}_{3c}$ = 2.00 kg/cm², $\bar{\sigma}_{1c}$ = 2.00 kg/cm²

e_c = 1.058, γ_{dc} = 81.2 pcf

METHOD OF LOADING: Undrained, Axial Compression
Load Control

TESTING DETAILS : Specimen Diameter 3.60 cm
: Specimen Height 5.30 cm
: End Platens: Lubricated, Type 2

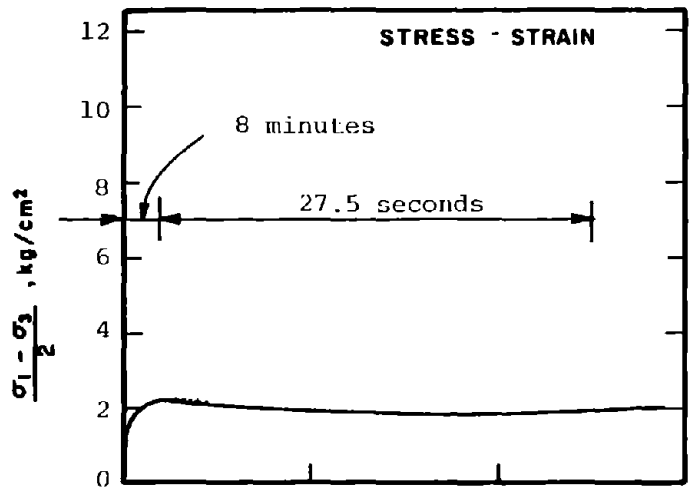

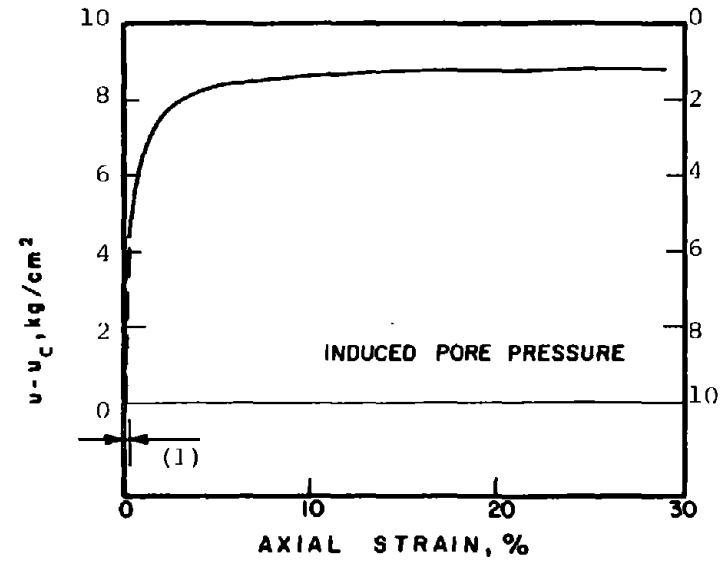

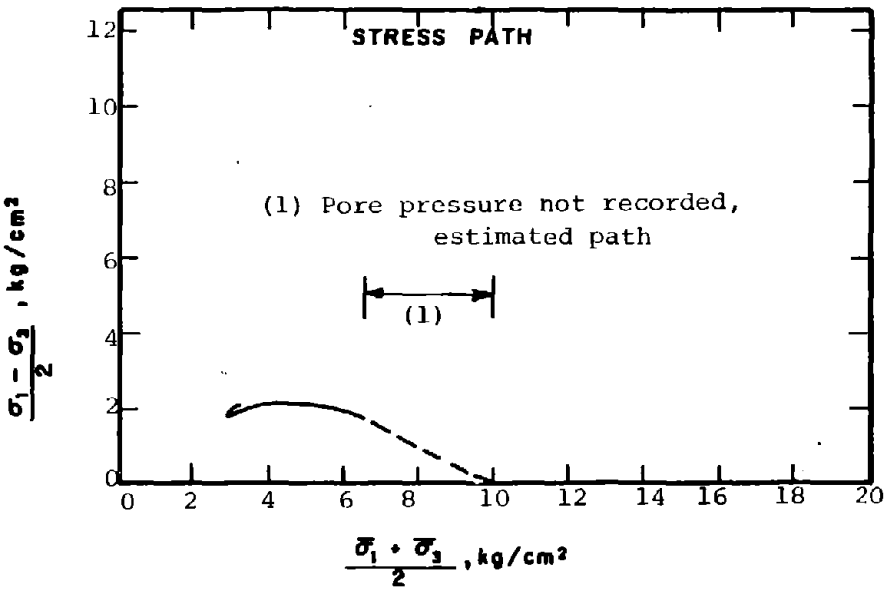

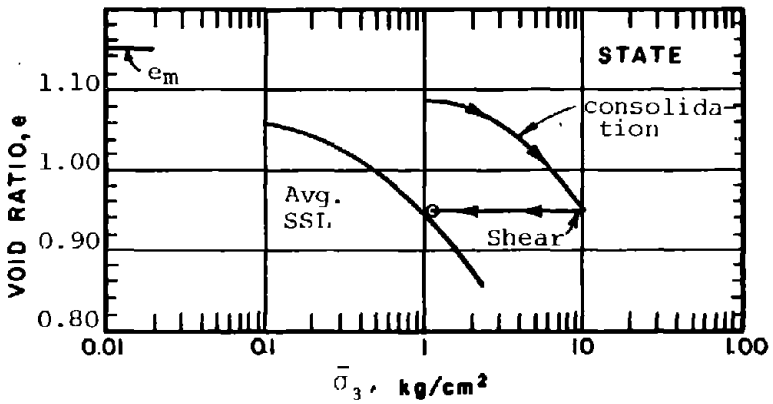

R-1009

SOIL : Mine Tailings

STRUCTURE : Compacted Moist

STATE AFTER CONSOLIDATION: $\bar{\sigma}_{3c} = 10.00 kg/cm^2$, $\bar{\sigma}_{1c} = 10.00 kg/cm^2$

$e_c = 0.948$, $\gamma_{dc} = 85.8$ pcf

METHOD OF LOADING: Undrained, Axial Compression Load Control

TESTING DETAILS : Specimen Diameter 3.60 cm

: Specimen Height 5.30 cm

: End Platens: Lubricated, Type 2

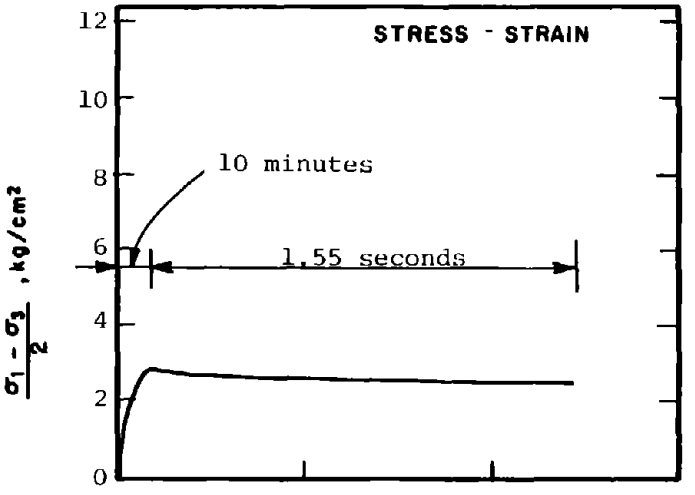

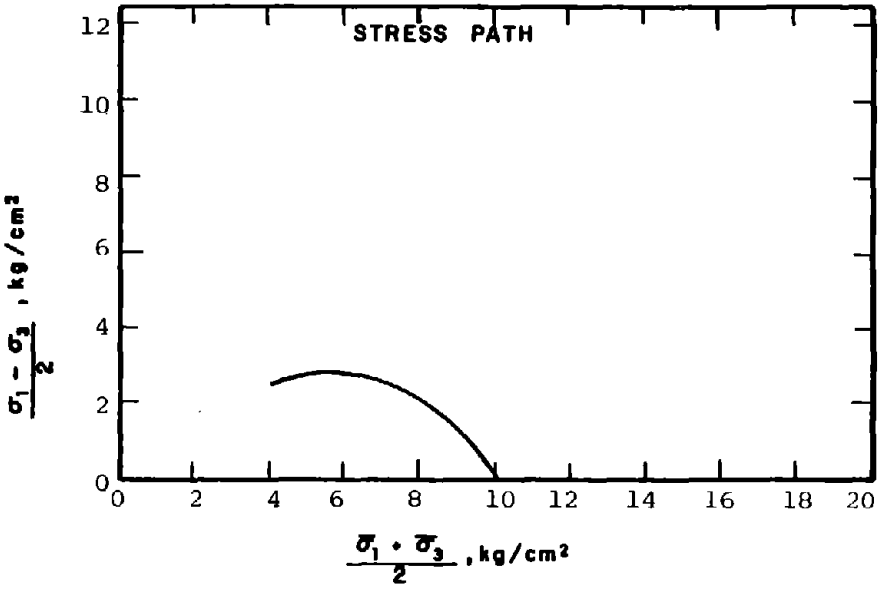

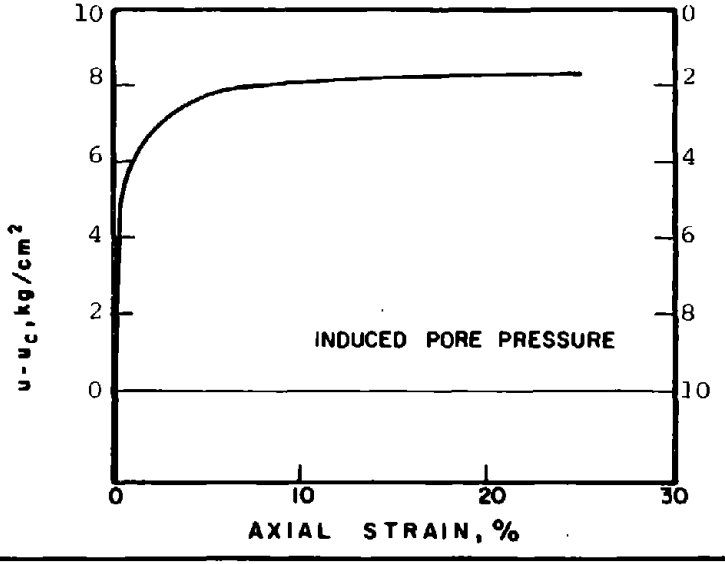

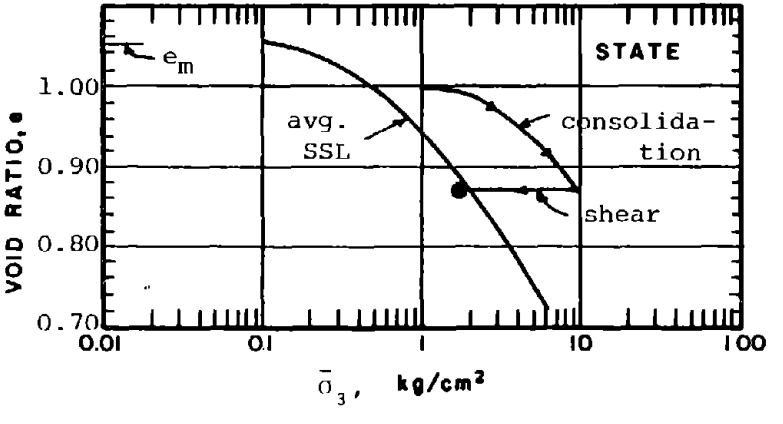

R-1010

SOIL : Mine Tailings

STRUCTURE : Compacted Moist

STATE AFTER CONSOLIDATION: $\bar{\sigma}_{3c}$ = 10.00kg/cm², $\bar{\sigma}_{1c}$ =10.00 kg/cm²
e_c = 0.870, γ_{dc} = 89.4 pcf

METHOD OF LOADING: Undrained, Axial Compression
Load Control

TESTING DETAILS : Specimen Diameter 3.60 cm
: Specimen Height 5.30 cm
: End Platens: Lubricated, Type 2

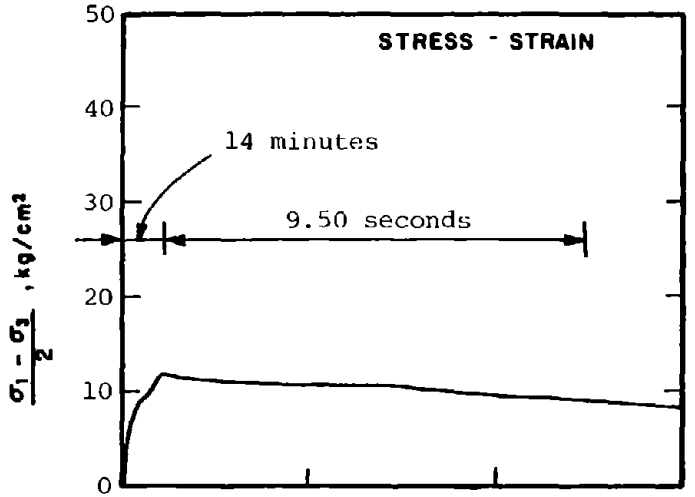

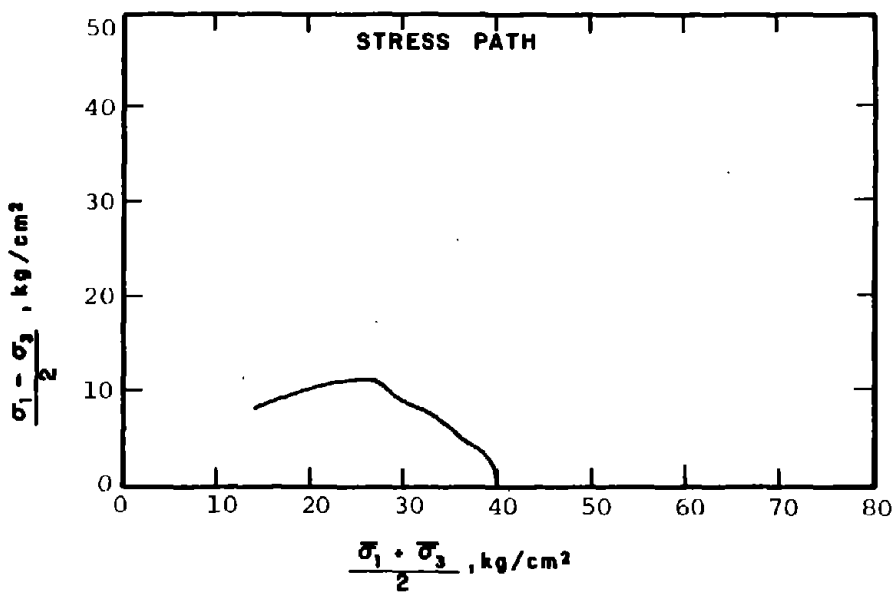

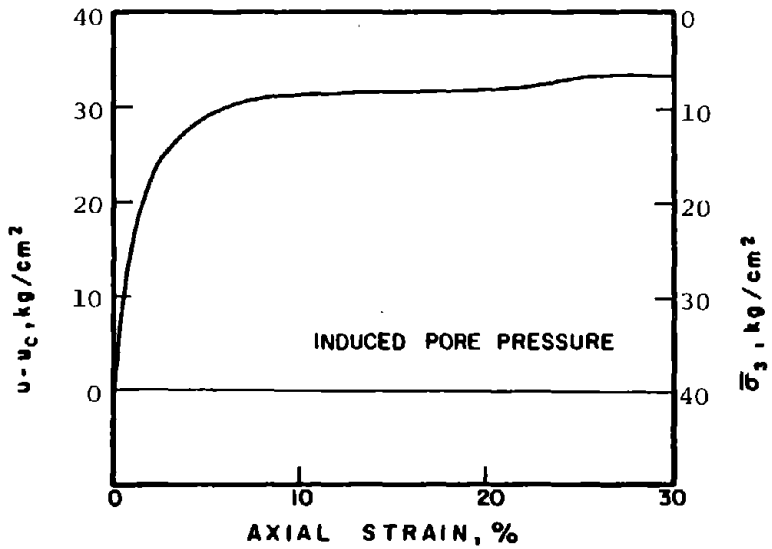

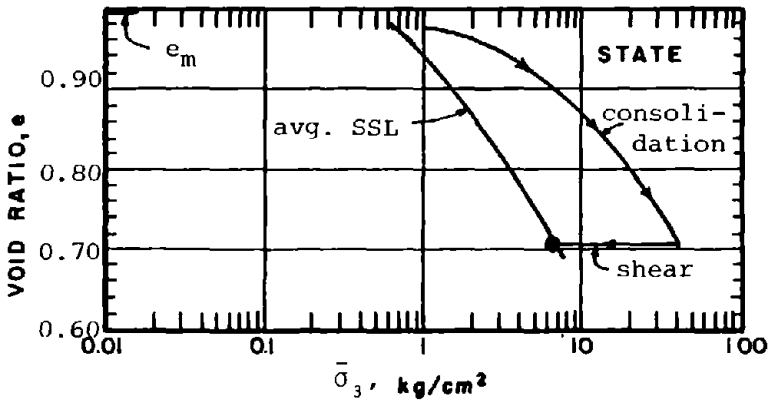

R-1011

SOIL : Mine Tailings

STRUCTURE : Compacted Moist

STATE AFTER CONSOLIDATION: $\bar{\sigma}_{3c}$ = 40.00kg/cm², $\bar{\sigma}_{1c}$ =40.00 kg/cm²
e_c = 0.705, γ_{dc} = 98.1 pcf

METHOD OF LOADING: Undrained, Axial Compression
Load Control

TESTING DETAILS : Specimen Diameter 3.60cm
: Specimen Height 5.30cm
: End Platens: Lubricated, Type 2

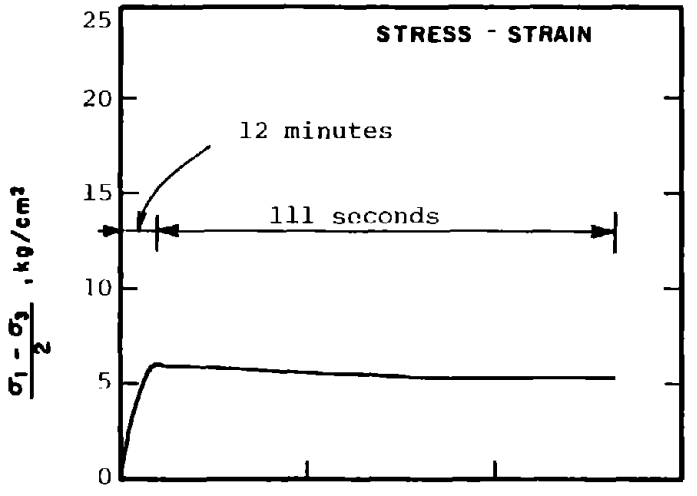

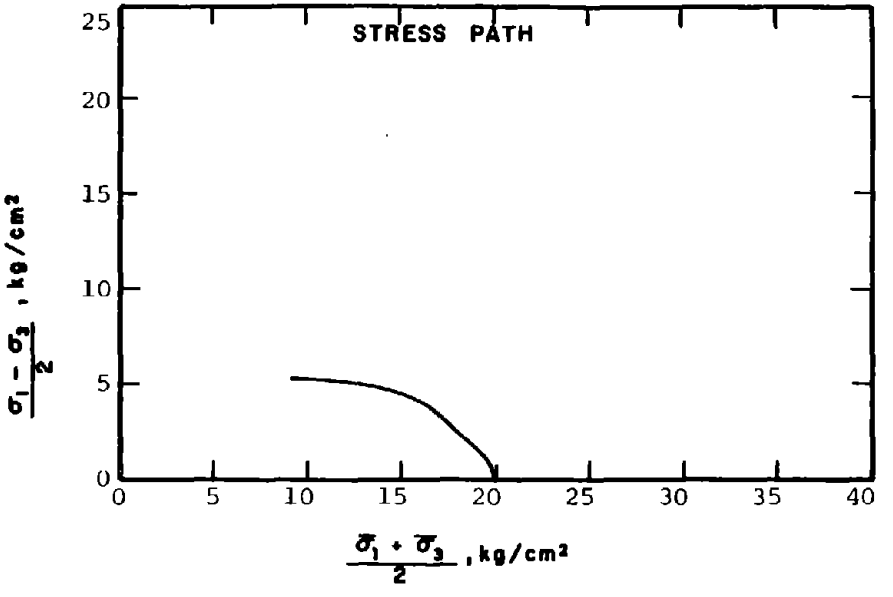

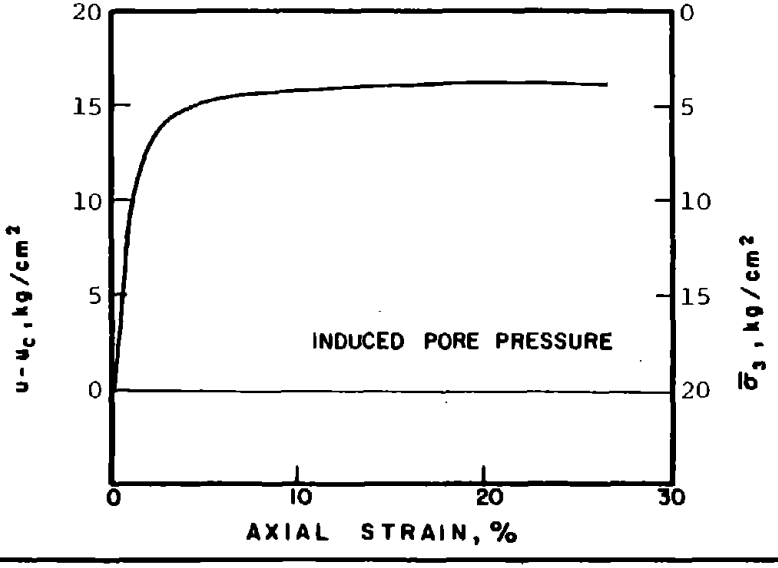

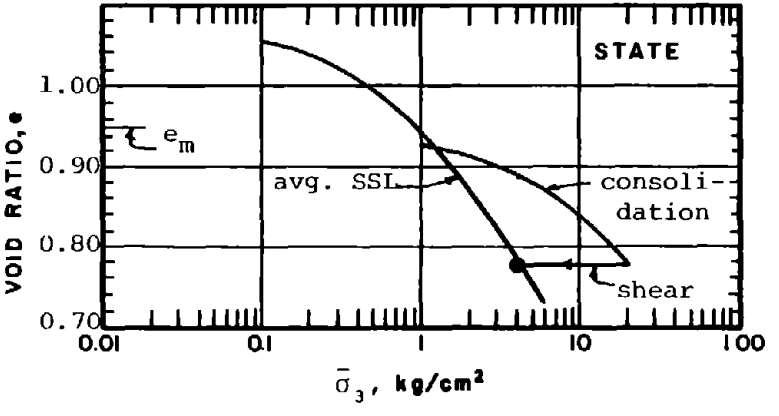

SOIL	: Mine Tailings	METHOD OF LOADING:	Undrained, Axial Compression Load Control
STRUCTURE	: Compacted Moist		
STATE AFTER CONSOLIDATION:	$\bar{\sigma}_{3c}$ =20.00 kg/cm², $\bar{\sigma}_{1c}$ =20.00 kg/cm² e_c =0.777 , γ_{dc} = 94.1 pcf	TESTING DETAILS	: Specimen Diameter 3.60 cm : Specimen Height 5.30 cm : End Platens: Lubricated, Type 2

R-1012

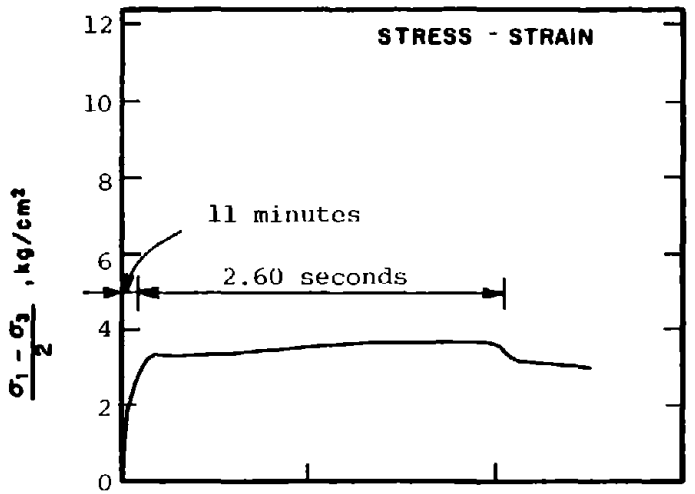

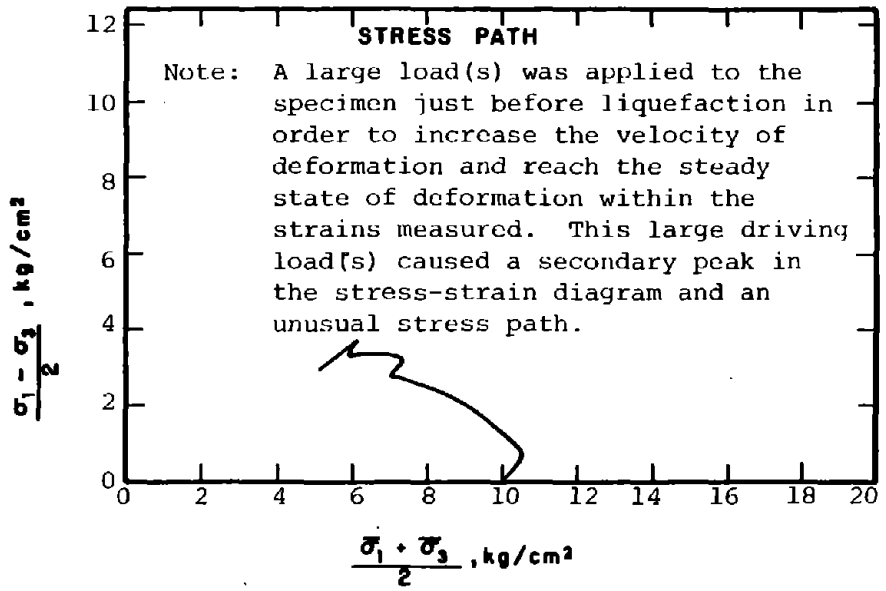

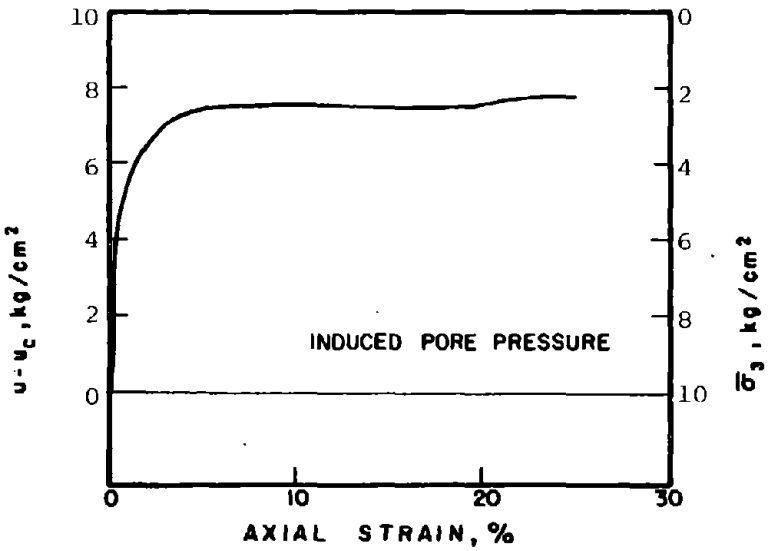

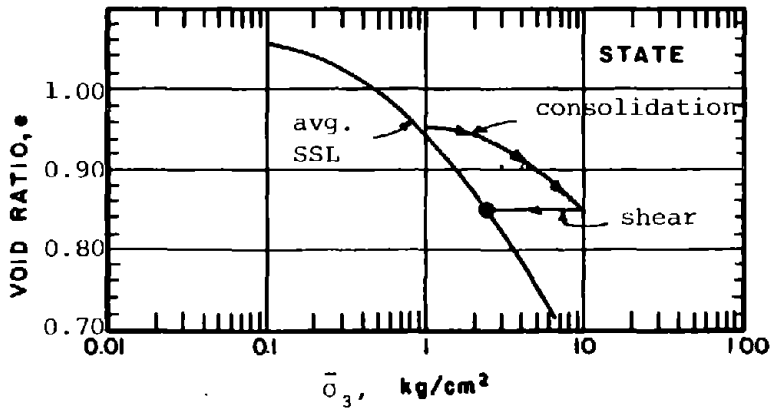

R-1013

SOIL : Mine Tailings

STRUCTURE : Compacted Moist

STATE AFTER CONSOLIDATION: $\bar{\sigma}_{3c}$ =10.00 kg/cm², $\bar{\sigma}_{1c}$ =10.00 kg/cm²

e_c = 0.845, γ_{dc} = 90.6 pcf

METHOD OF LOADING: Undrained, Axial Compression Load Control

TESTING DETAILS : Specimen Diameter 3.60 cm

: Specimen Height 5.30 cm

: End Platens: Conventional

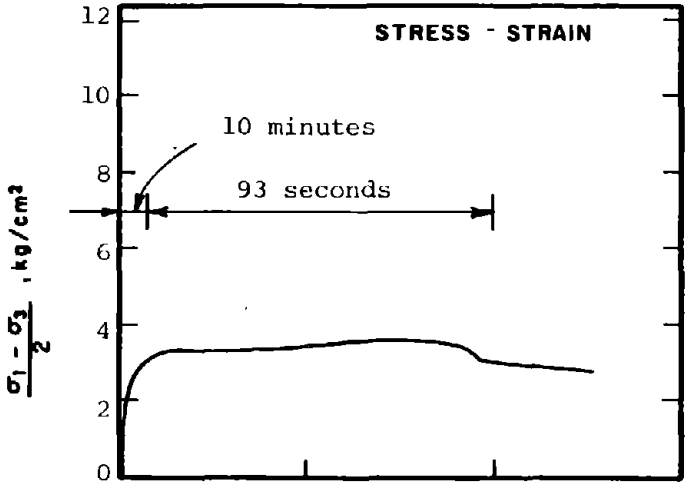

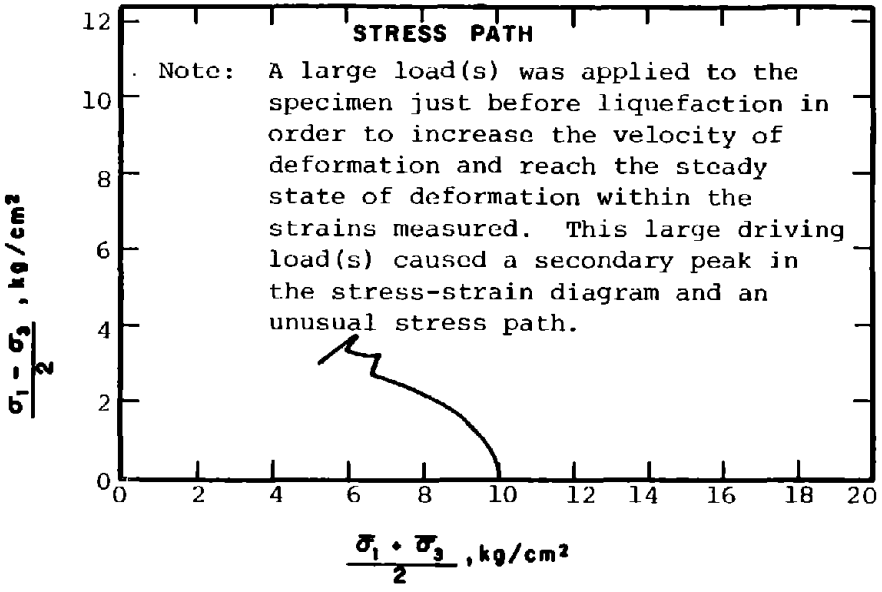

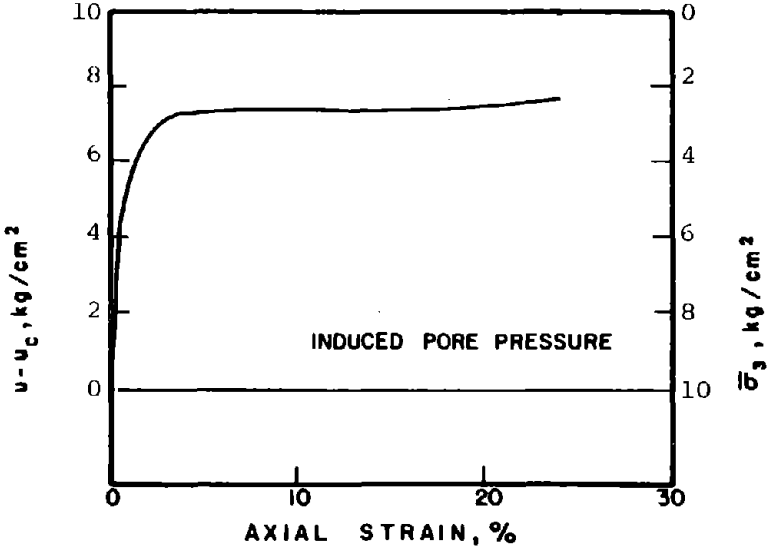

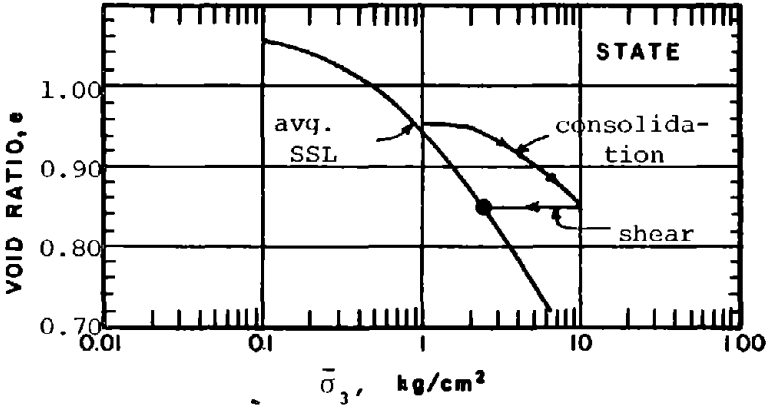

SOIL	: Mine Tailings	METHOD OF LOADING:	Undrained, Axial Compression Load Control
STRUCTURE	: Compacted Moist		
STATE AFTER CONSOLIDATION:	$\bar{\sigma}_{3c}$ =10.00 kg/cm², $\bar{\sigma}_{1c}$ =10.00 kg/cm²	TESTING DETAILS	: Specimen Diameter 3.60 cm
	e_c = 0.845, γ_{dc} = 90.6 pcf		: Specimen Height 5.30 cm
			: End Platens: Conventional

R-1014

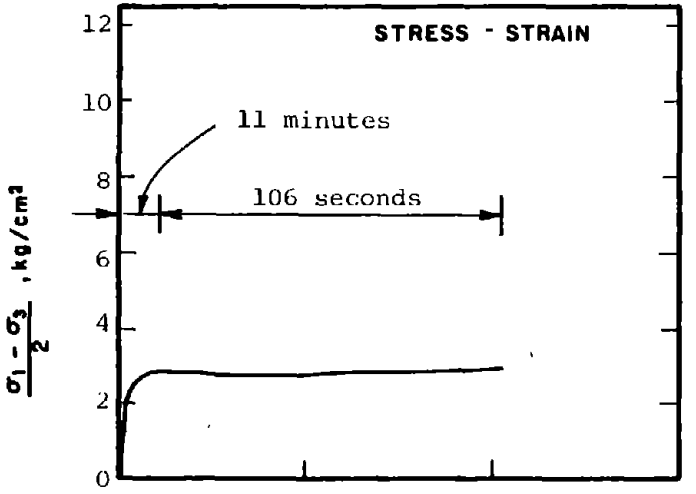

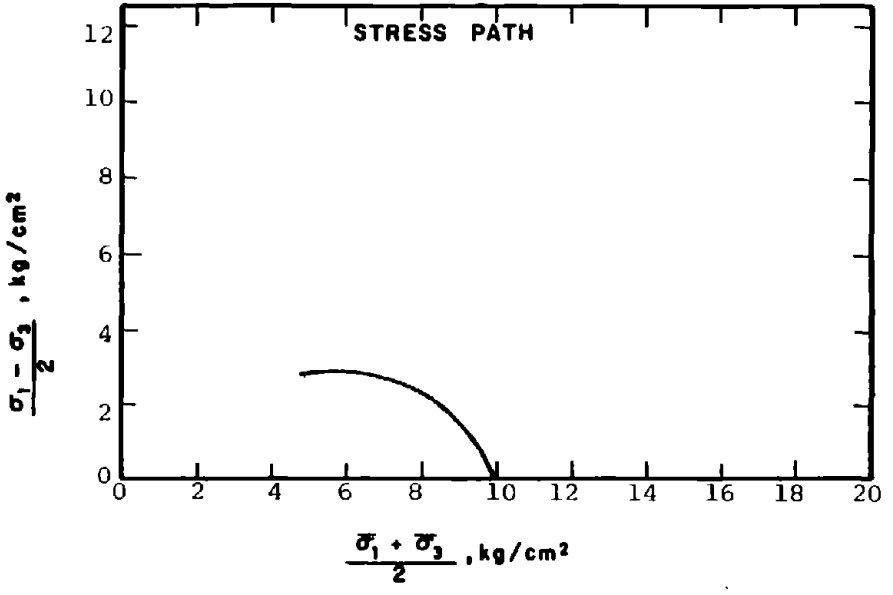

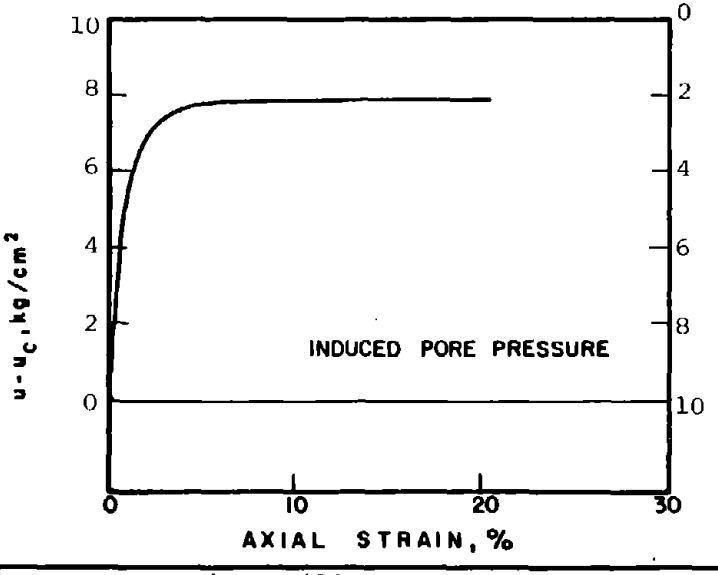

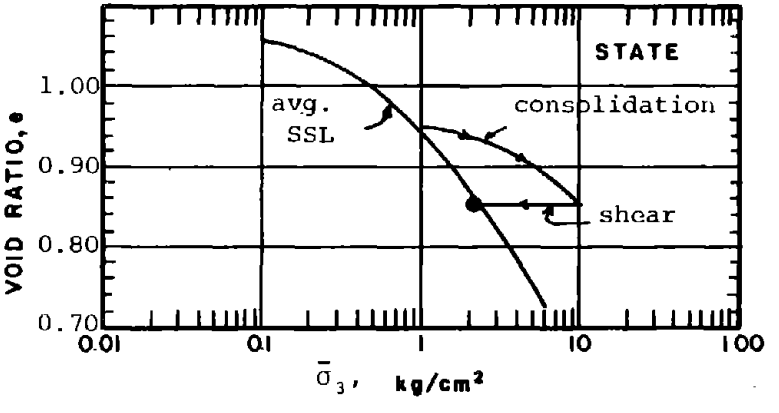

R-1015

SOIL : Mine Tailings

STRUCTURE : Compacted Moist

STATE AFTER CONSOLIDATION: $\bar{\sigma}_{3c}$ =10.00 kg/cm^2, $\bar{\sigma}_{1c}$ =10.00 kg/cm^2

e_c = 0.851, γ_{dc} = 90.3 pcf

METHOD OF LOADING: Undrained, Axial Compression
Load Control

TESTING DETAILS : Specimen Diameter 3.60 cm
: Specimen Height 5.30 cm
: End Platens: Conventional

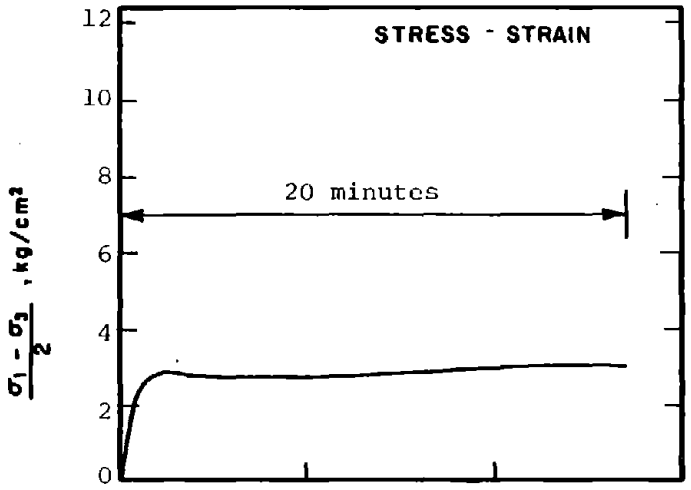

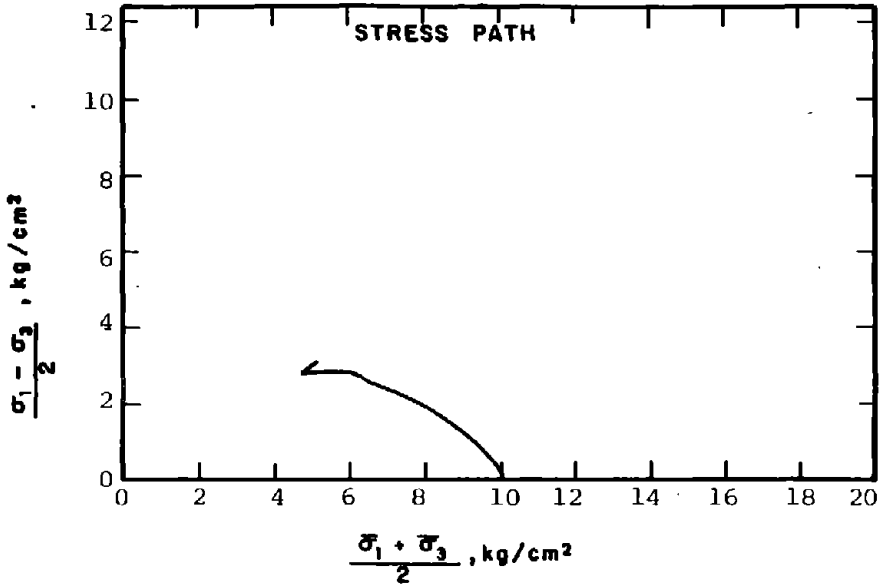

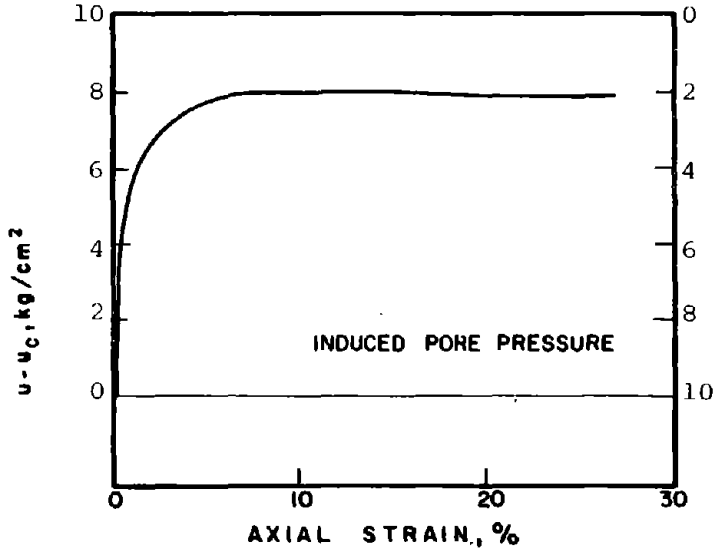

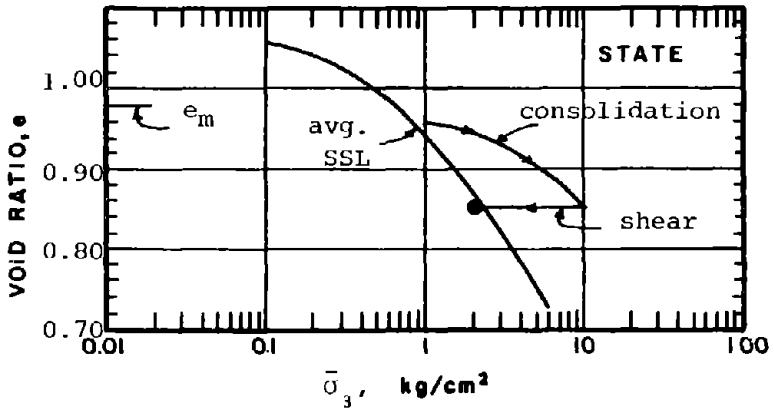

R-1016

SOIL : Mine Tailings

STRUCTURE : Compacted Moist

STATE AFTER CONSOLIDATION: $\bar{\sigma}_{3c}$ =10.00 kg/cm^2, $\bar{\sigma}_{1c}$ =10.00 kg/cm^2

e_c = 0.849, γ_{dc} = 90.4 pcf

METHOD OF LOADING: Undrained, Axial Compression
Load Control

TESTING DETAILS : Specimen Diameter 3.60 cm
: Specimen Height 5.30 cm
: End Platens: Lubricated, Type 2

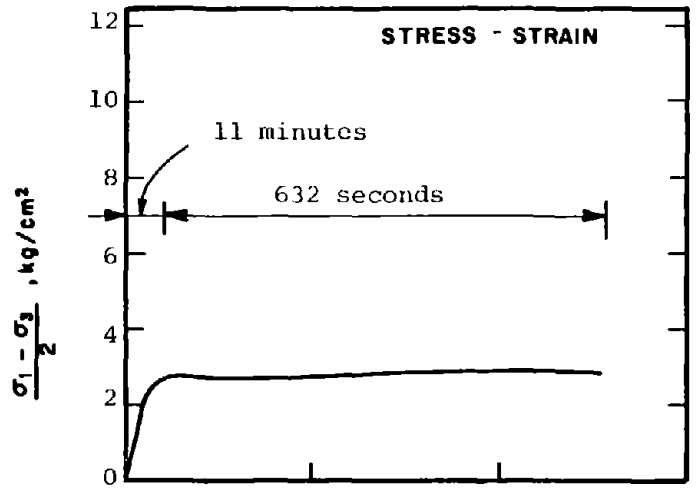

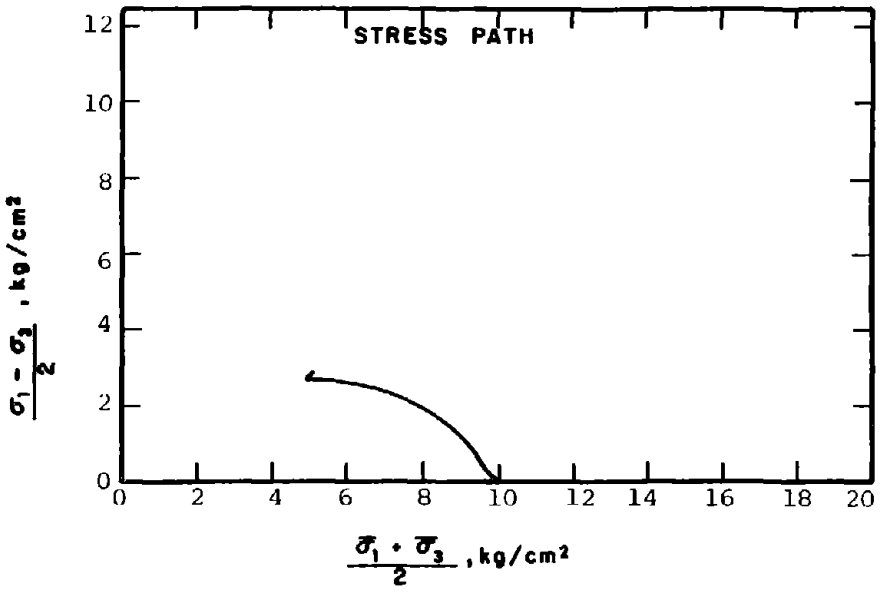

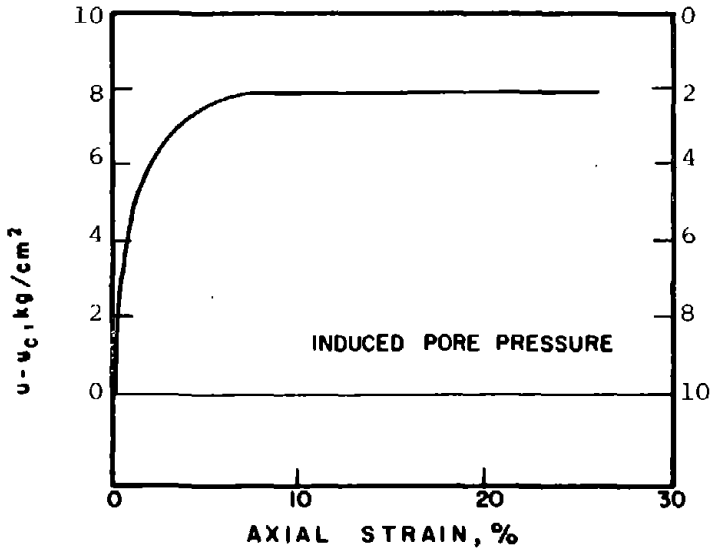

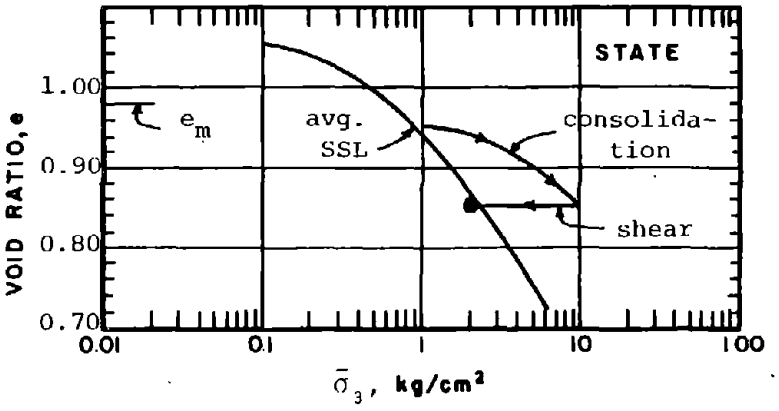

R-1017

SOIL : Mine Tailings

STRUCTURE : Compacted Moist

STATE AFTER CONSOLIDATION: $\bar{\sigma}_{3c}$ =10.00 kg/cm², $\bar{\sigma}_{1c}$ =10.00 kg/cm²

e_c = 0.850, γ_{dc} = 90.4 pcf

METHOD OF LOADING: Undrained, Axial Compression Load Control

TESTING DETAILS : Specimen Diameter 3.60 cm

: Specimen Height 5.30 cm

: End Platens: Lubricated, Type 2

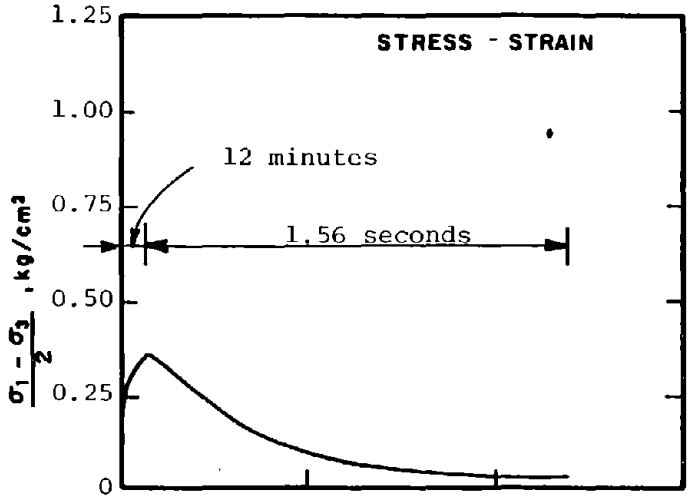

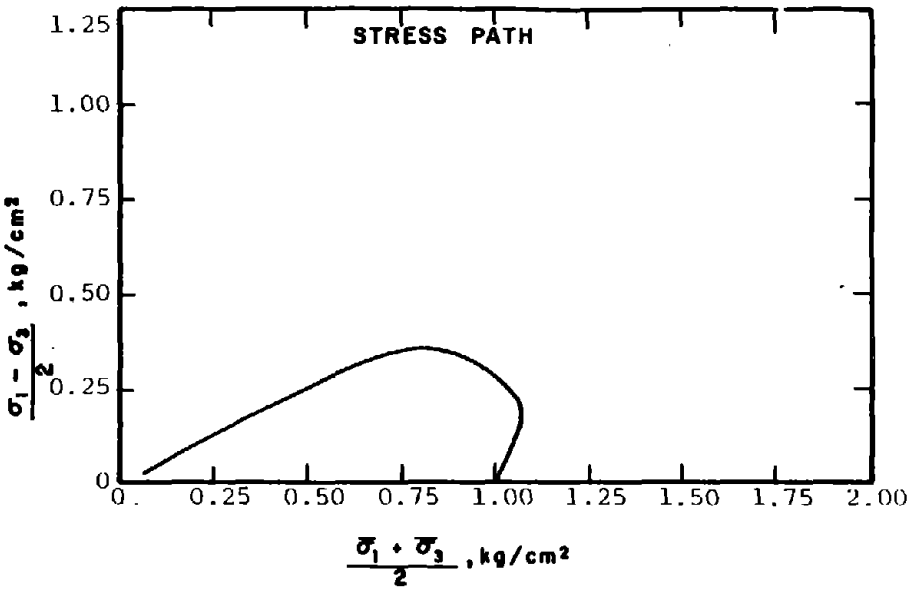

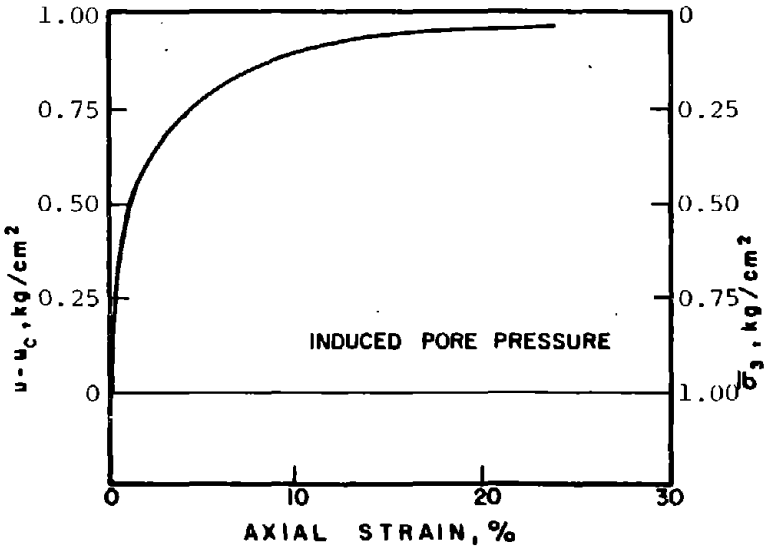

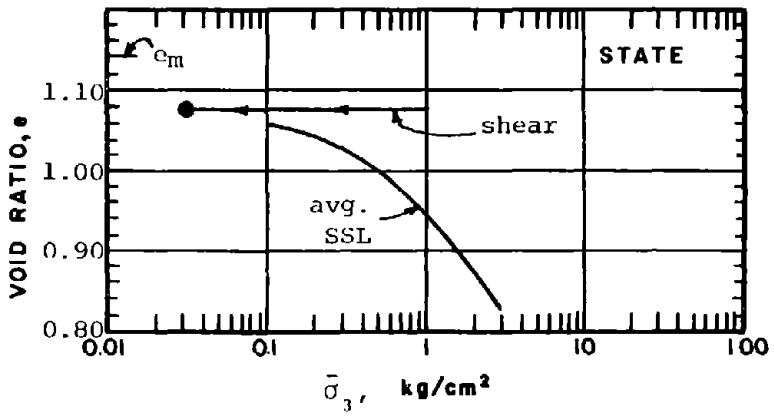

R-1018

SOIL : Mine Tailings

STRUCTURE : Compacted Moist

STATE AFTER CONSOLIDATION: $\bar{\sigma}_{3c}$ = 1.00 kg/cm², $\bar{\sigma}_{1c}$ = 1.00 kg/cm²
e_c = 1.078, γ_{dc} = 80.5 pcf

METHOD OF LOADING: Undrained, Axial Compression
Load Control

TESTING DETAILS : Specimen Diameter 3.60 cm
: Specimen Height 5.30 cm
: End Platens: Lubricated, Type 2

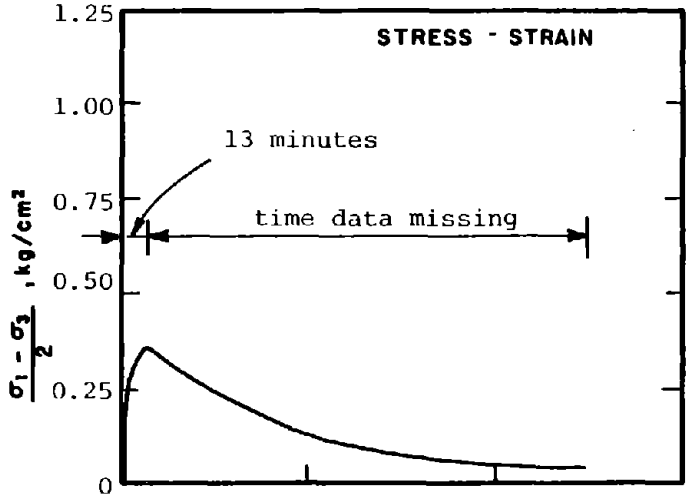

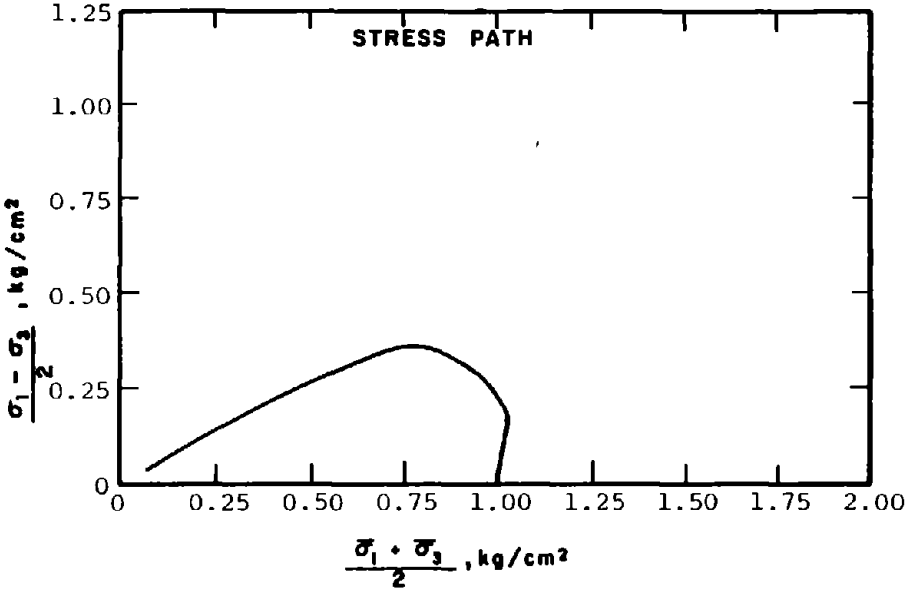

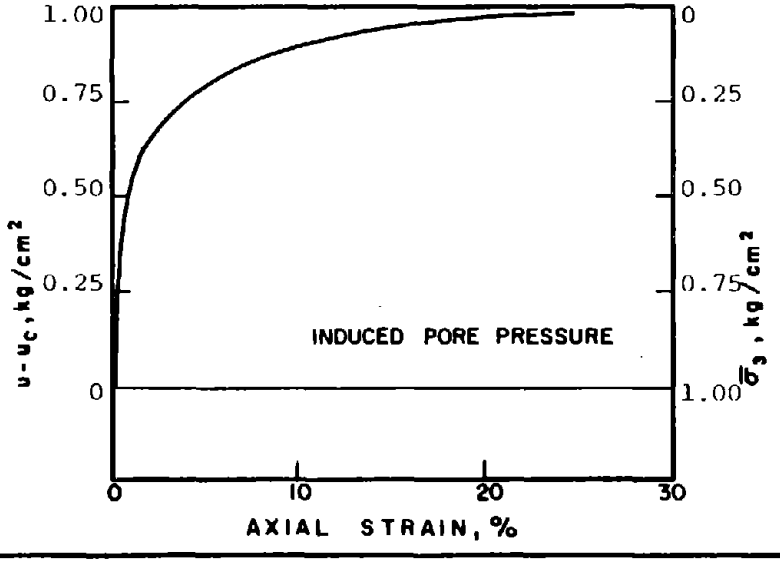

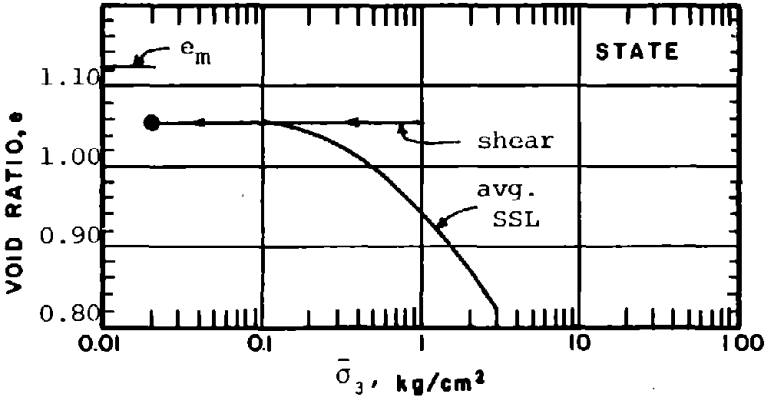

R-1019

SOIL : Mine Tailings

STRUCTURE : Compacted Moist

STATE AFTER CONSOLIDATION: $\bar{\sigma}_{3c} = 1.00$ kg/cm^2, $\bar{\sigma}_{1c} = 1.00$ kg/cm^2

$e_c = 1.056$, $\gamma_{dc} = 81.3$ pcf

METHOD OF LOADING: Undrained, Axial Compression
Load Control

TESTING DETAILS : Specimen Diameter 3.60 cm
: Specimen Height 5.30 cm
: End Platens: Lubricated, Type 2

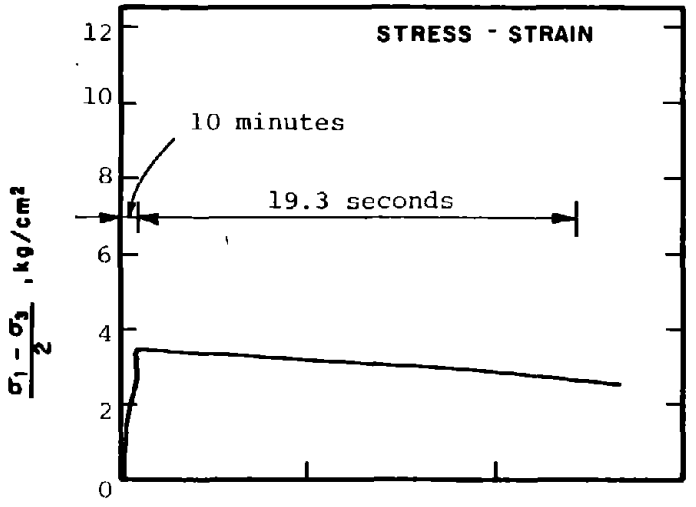

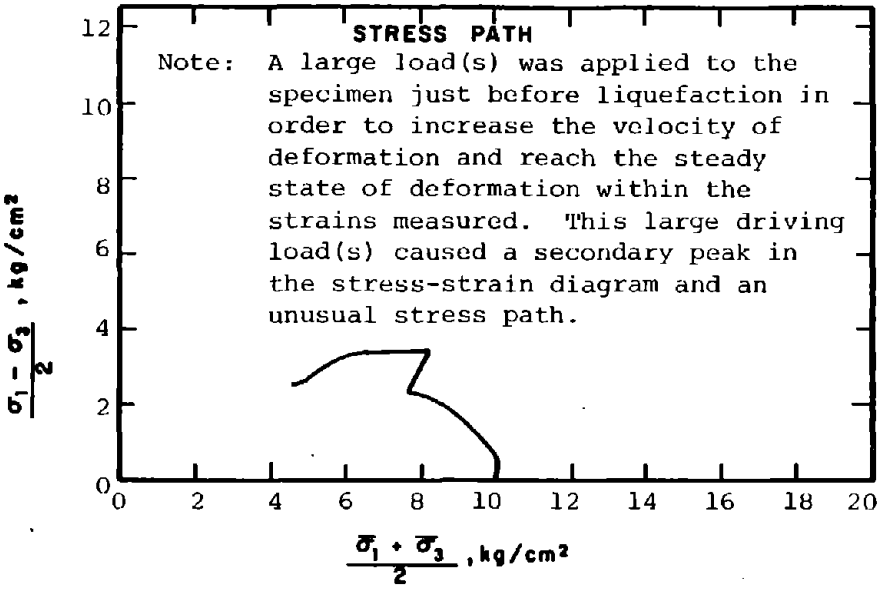

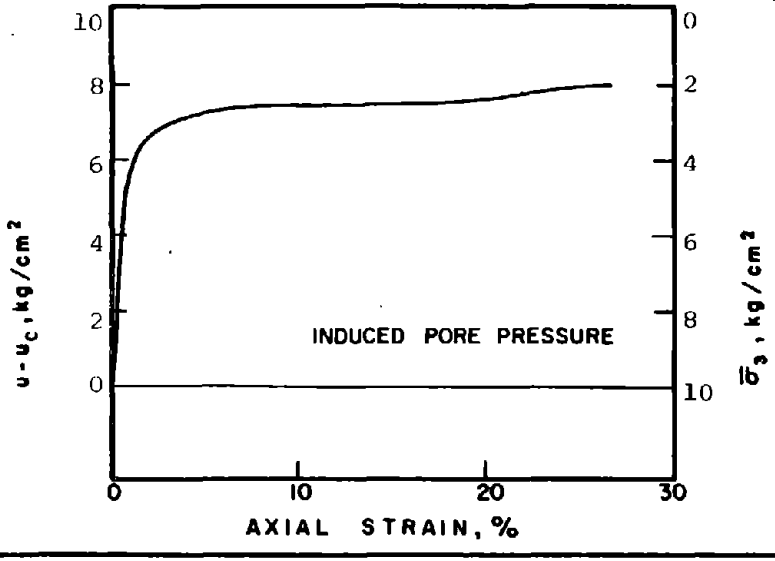

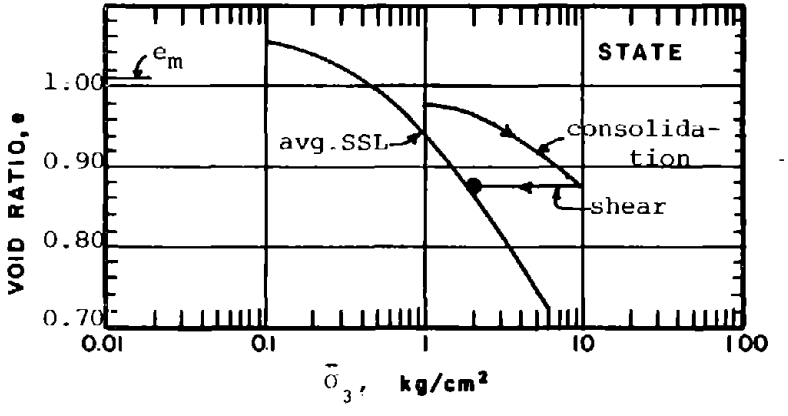

R-1020

SOIL : Mine Tailings

STRUCTURE : Compacted Moist

STATE AFTER CONSOLIDATION: $\bar{\sigma}_{3c} = 10.00 kg/cm^2$, $\bar{\sigma}_{1c} = 10.00$ kg/cm²

$e_c = 0.858$, $\gamma_{dc} = 90.0$ pcf

METHOD OF LOADING: Undrained, Axial Compression Load Control

TESTING DETAILS : Specimen Diameter 3.60 cm

: Specimen Height 5.30 cm

: End Platens: Lubricated, Type 2

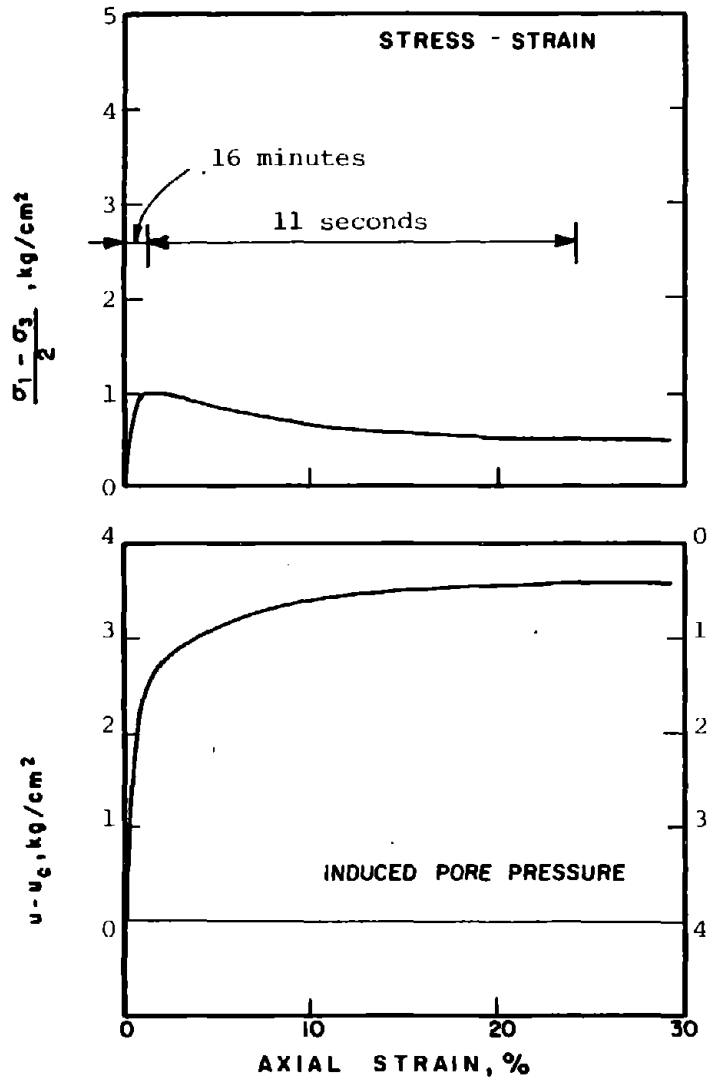

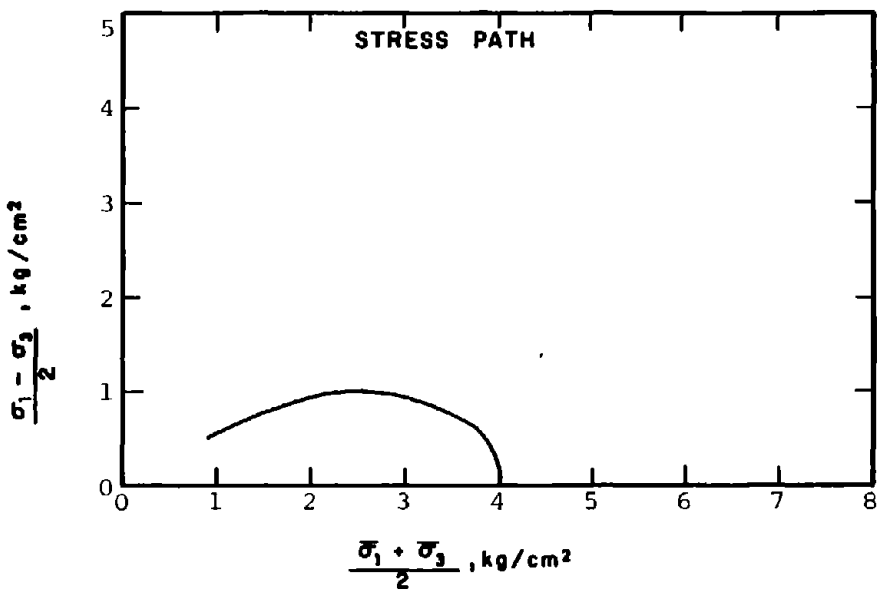

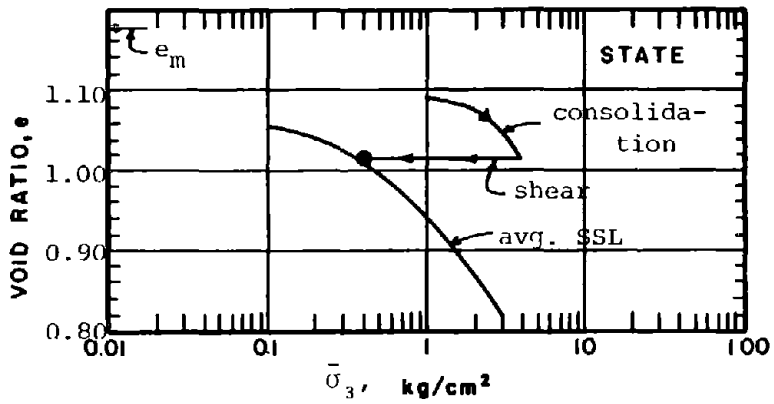

SOIL	: Mine Tailings	METHOD OF LOADING:	Undrained, Axial Compression Load Control
STRUCTURE	: Compacted Moist		
STATE AFTER CONSOLIDATION:	$\bar{\sigma}_{3c}$ = 4.00 kg/cm², $\bar{\sigma}_{1c}$ = 4.00 kg/cm²	TESTING DETAILS	: Specimen Diameter 3.60 cm
	e_c = 1.013, γ_{dc} = 83.1 pcf		: Specimen Height 5.30 cm
			: End Platens: Lubricated, Type 2

R-1021

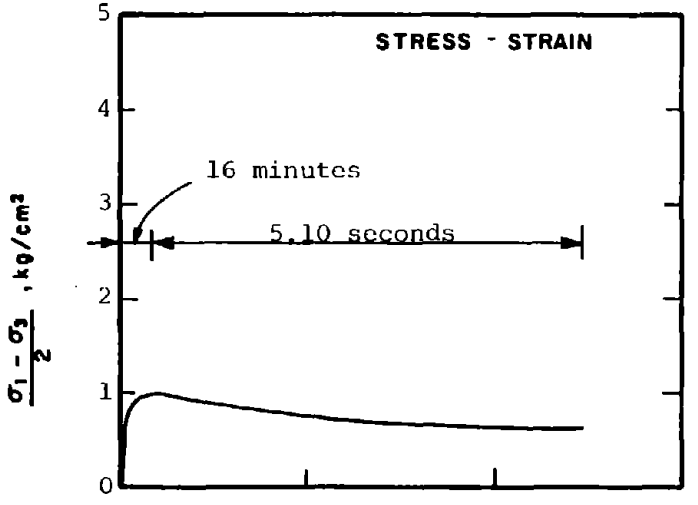

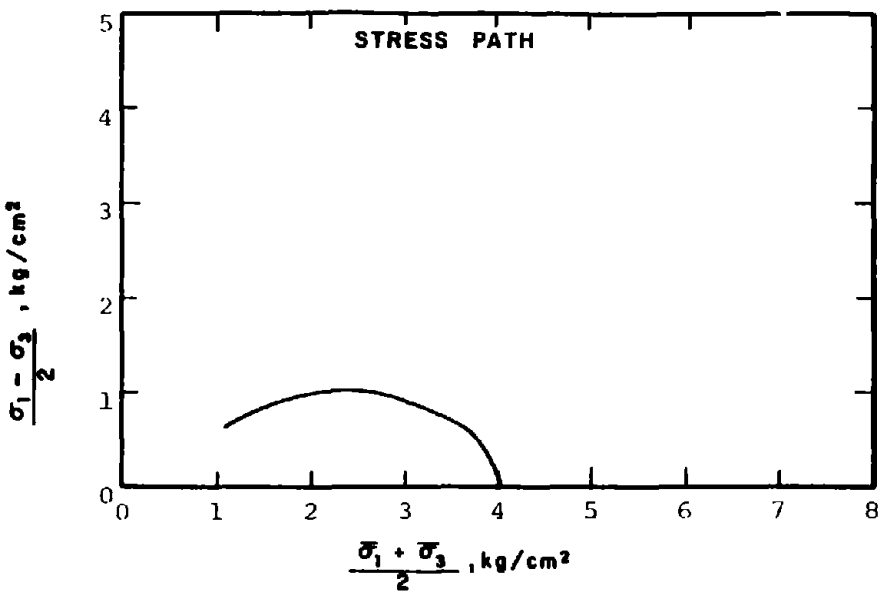

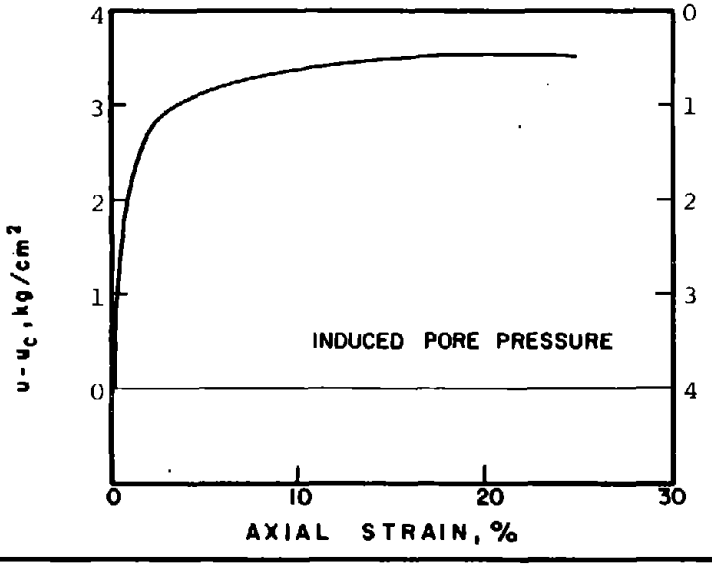

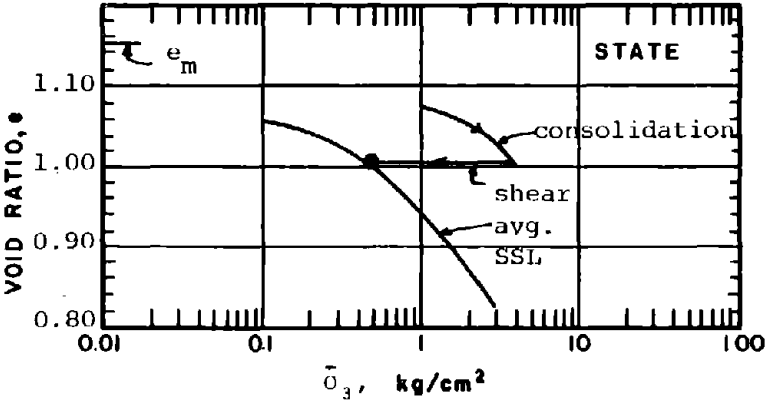

SOIL	: Mine Tailings	METHOD OF LOADING:	Undrained, Axial Compression Load Control
STRUCTURE	: Compacted Moist		
STATE AFTER CONSOLIDATION:	$\bar{\sigma}_{3c}$ = 4.00 kg/cm², $\bar{\sigma}_{1c}$ = 4.00 kg/cm²	TESTING DETAILS	: Specimen Diameter 3.60 cm
	e_c = 1.001 , γ_{dc} = 83.6 pcf		: Specimen Height 5.30 cm
			: End Platens: Lubricated, Type 2

R-1022

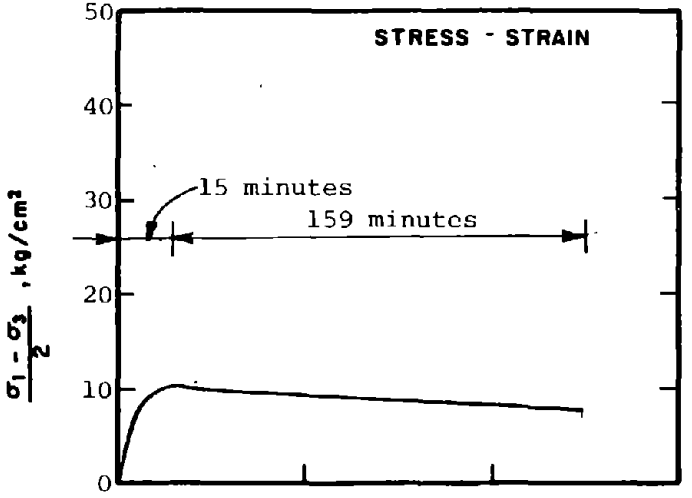

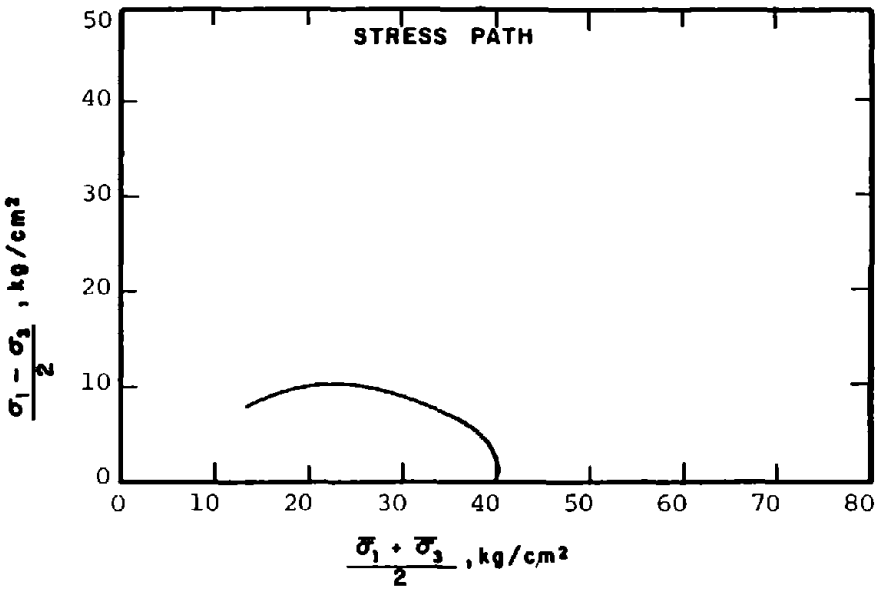

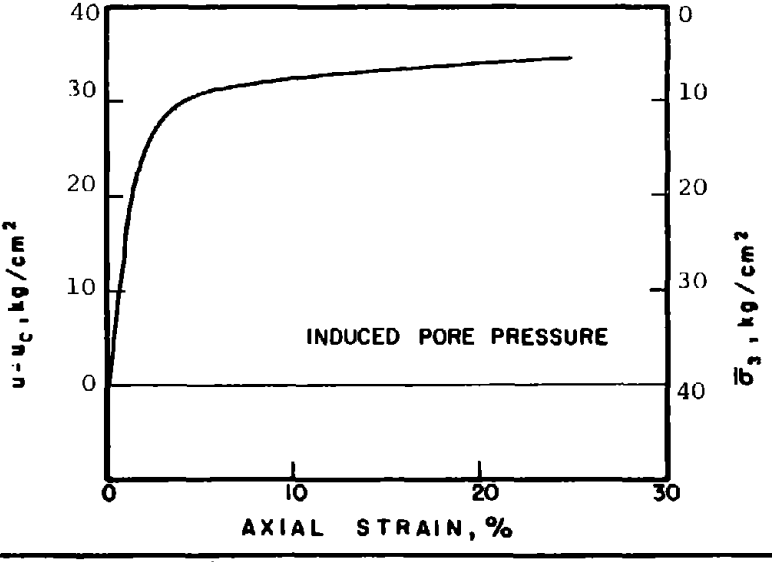

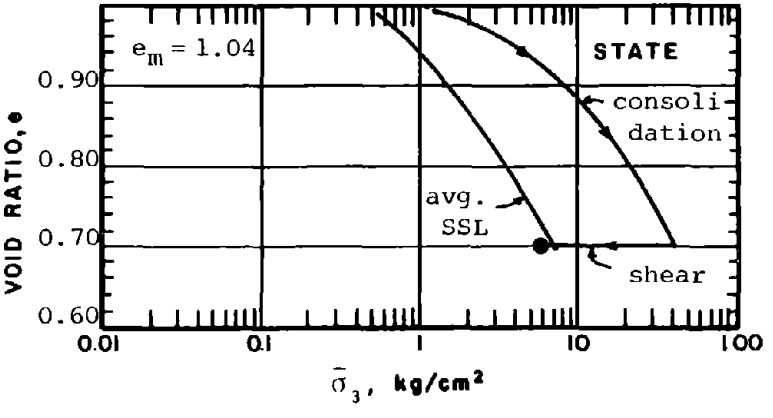

R-1023

SOIL : Mine Tailings

STRUCTURE : Compacted Moist

STATE AFTER CONSOLIDATION: $\bar{\sigma}_{3c}$ = 40.00kg/cm², $\bar{\sigma}_{1c}$ =40.00 kg/cm²

e_c = 0.870, γ_{dc} = 89.4 pcf

METHOD OF LOADING: Undrained, Axial Compression Load Control

TESTING DETAILS : Specimen Diameter 3.60 cm

: Specimen Height 5.30 cm

: End Platens: Lubricated, Type 2

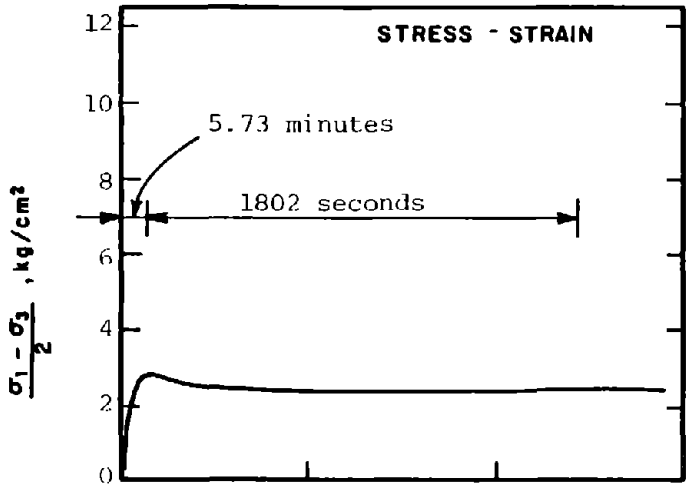

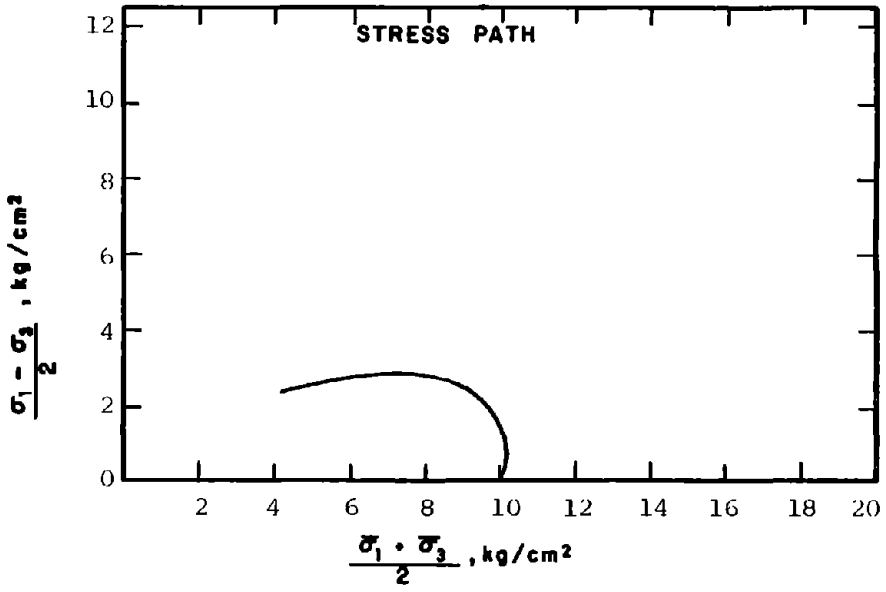

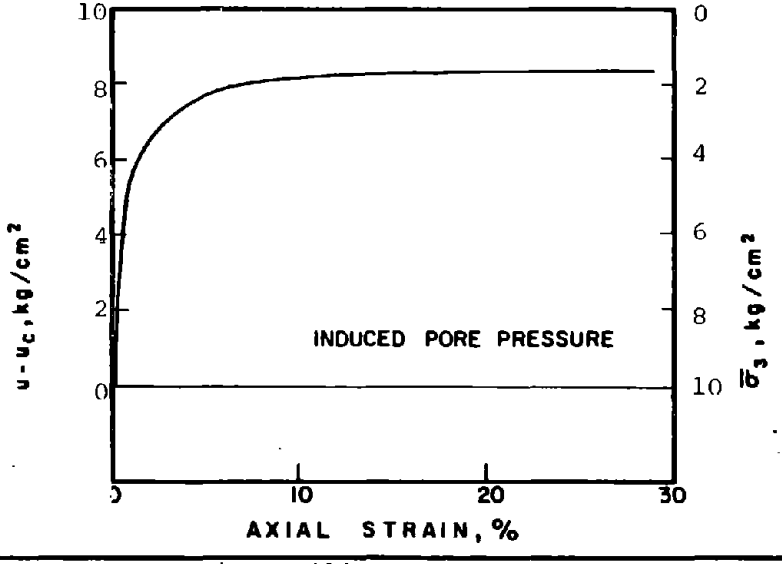

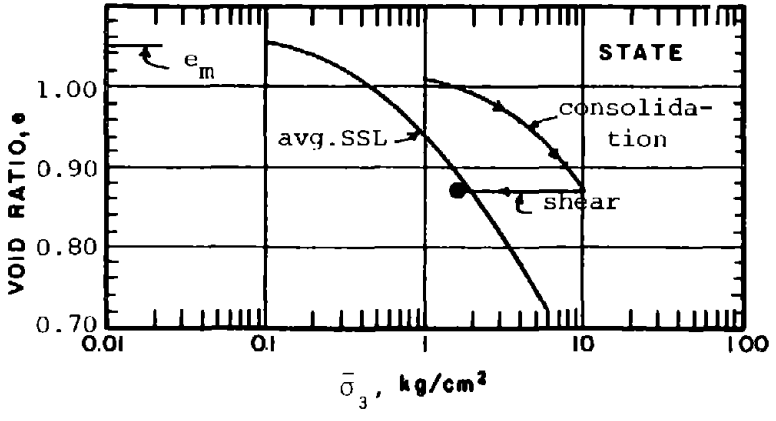

SOIL	: Mine Tailings	METHOD OF LOADING:	Undrained, Axial Compression Strain Control
STRUCTURE	: Compacted Moist		
STATE AFTER CONSOLIDATION:	$\bar{\sigma}_{3c}$ =10.00 kg/cm², $\bar{\sigma}_{1c}$ =10.00 kg/cm²	TESTING DETAILS	: Specimen Diameter 3.60 cm
	e_c = 0.870, γ_{dc} = 89.4 pcf		: Specimen Height 5.30 cm
			: End Platens: Lubricated, Type 2

R-1024

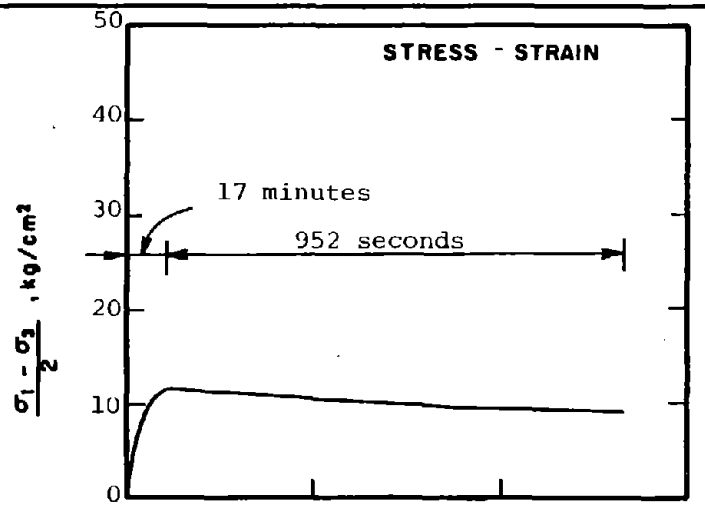

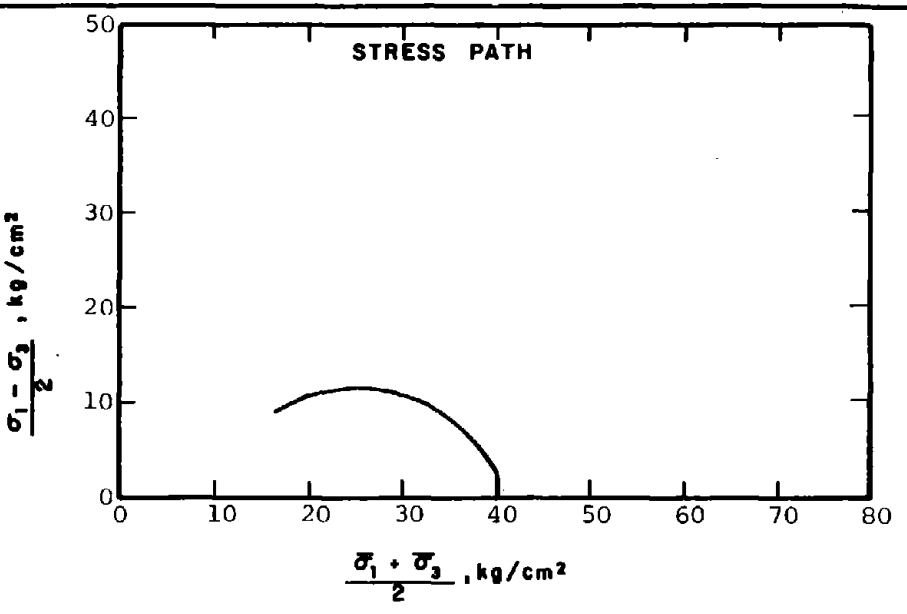

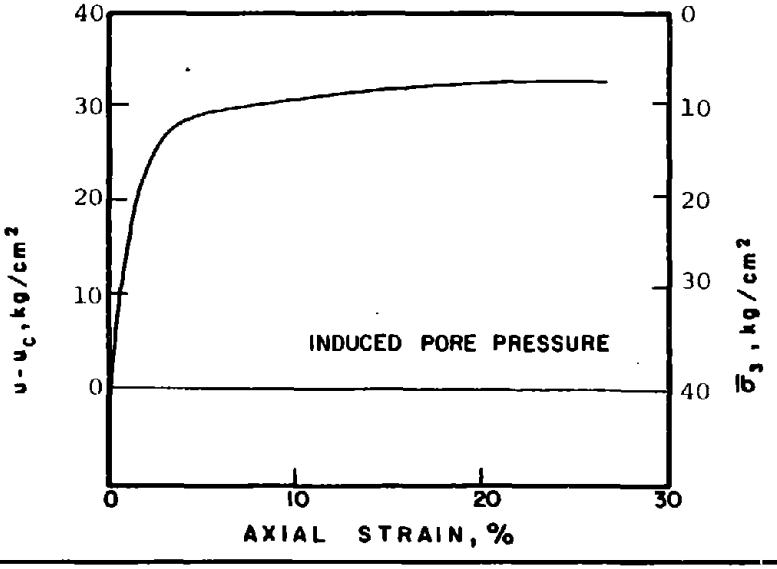

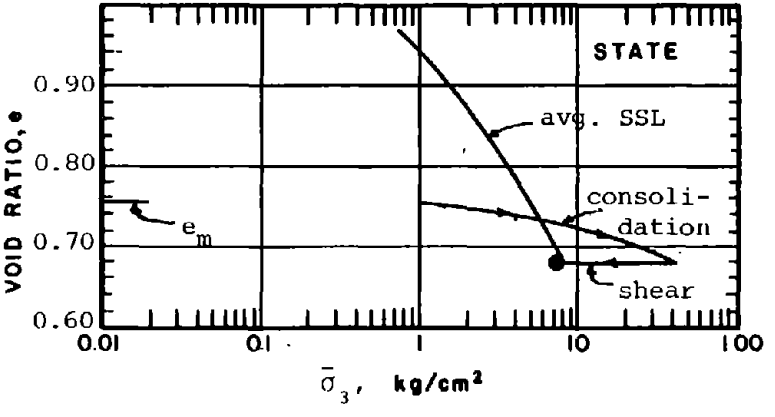

R-1025

SOIL : Mine Tailings

STRUCTURE : Compacted Moist

STATE AFTER CONSOLIDATION: $\bar{\sigma}_{3c}$ = 40.00 kg/cm², $\bar{\sigma}_{1c}$ = 40.00 kg/cm²

e_c = 0.675, γ_{dc} = 99.8 pcf

METHOD OF LOADING: Undrained, Axial Compression
Load Control

TESTING DETAILS : Specimen Diameter 3.60 cm
: Specimen Height 5.30 cm
: End Platens: Lubricated, Type 2

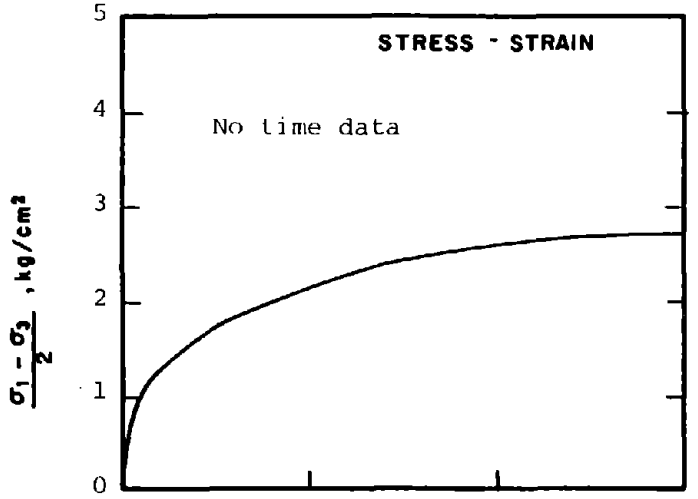

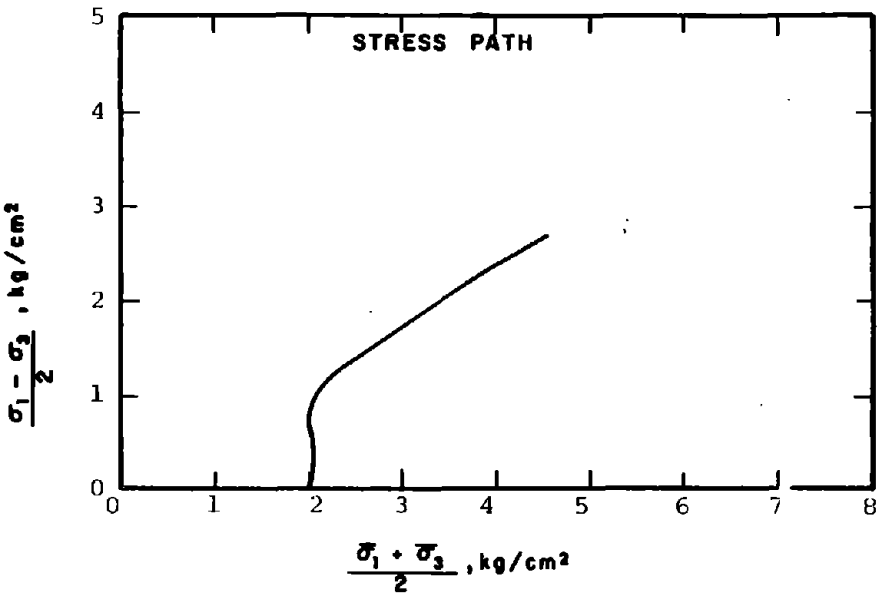

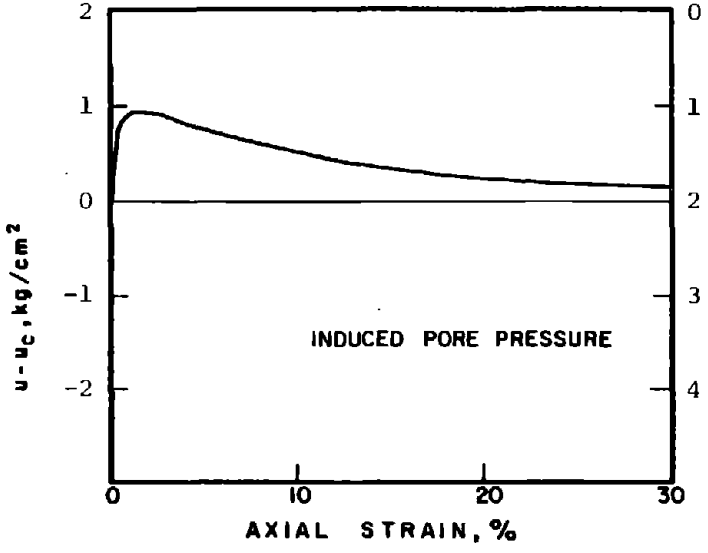

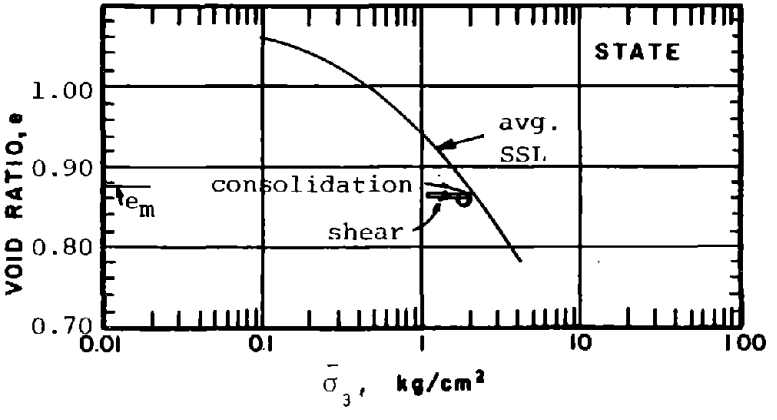

SOIL : Mine Tailings

STRUCTURE : Compacted Moist

STATE AFTER CONSOLIDATION: $\bar{\sigma}_{3c}$ = 2.00 kg/cm², $\bar{\sigma}_{1c}$ = 2.00 kg/cm²

e_c = 0.863 , γ_{dc} = 89.8 pcf

METHOD OF LOADING: Undrained, Axial Compression Load Control

TESTING DETAILS : Specimen Diameter 3.60 cm

: Specimen Height 5.30 cm

: End Platens: Lubricated, Type 2

R-1026

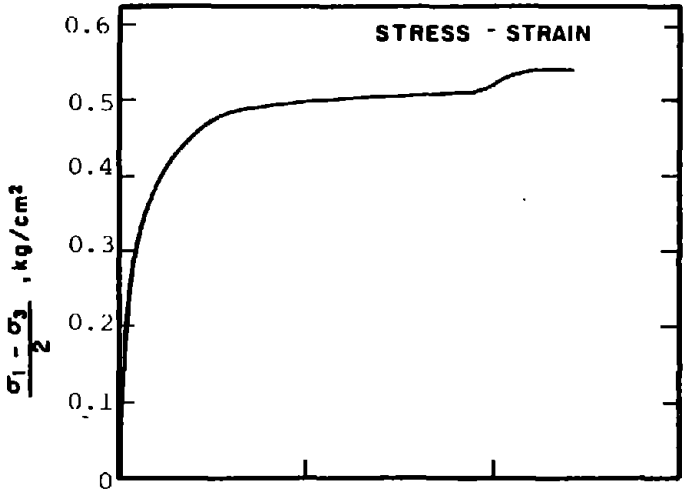

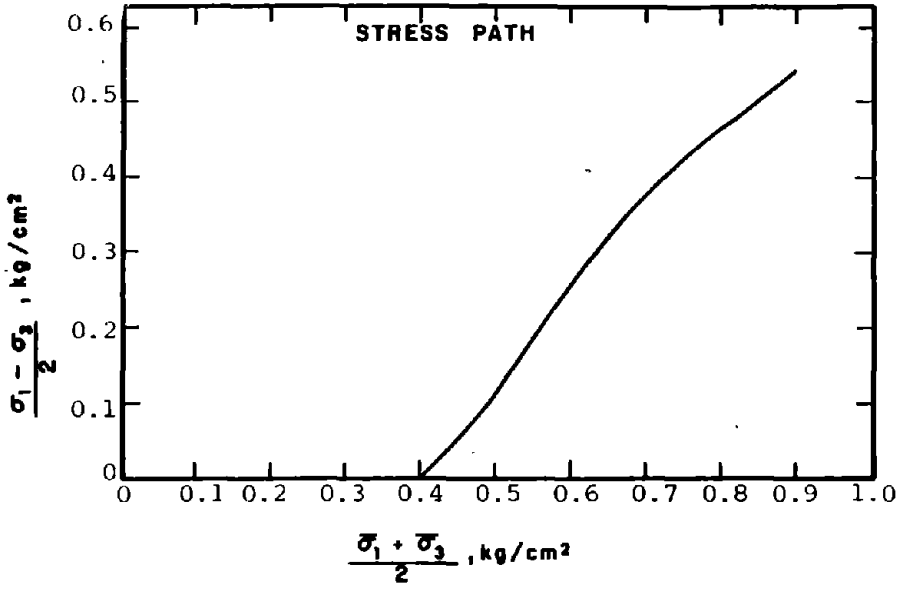

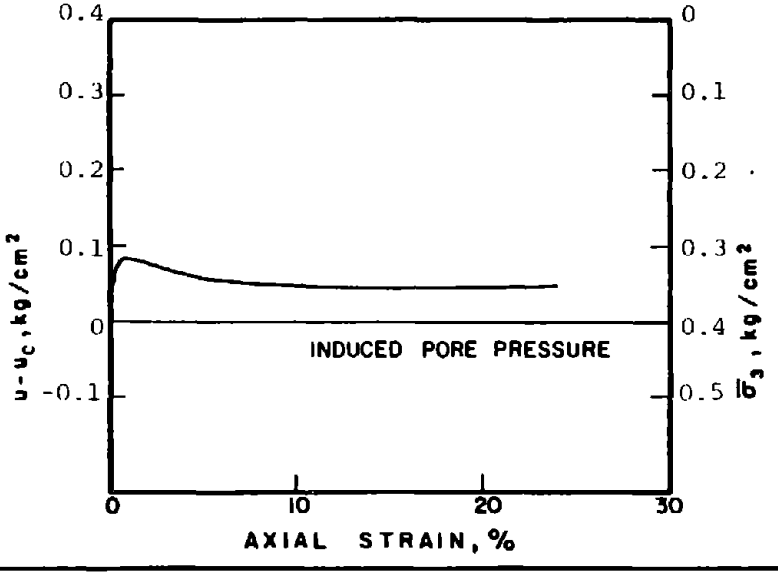

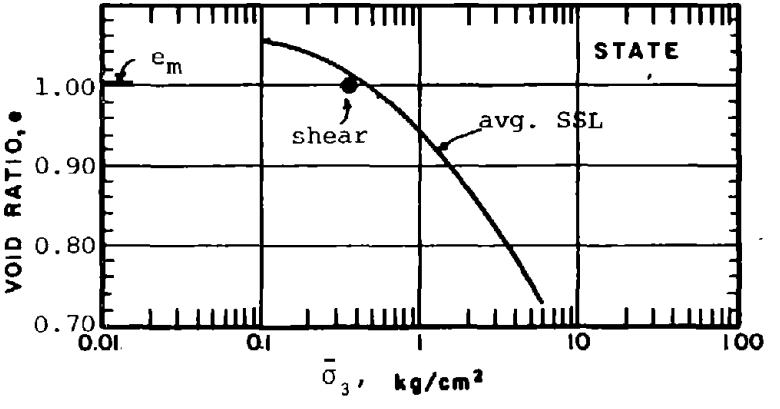

R-1029

SOIL : Mine Tailings

STRUCTURE : Compacted Moist

STATE AFTER CONSOLIDATION: $\bar{\sigma}_{3c} = 0.40$ kg/cm², $\bar{\sigma}_{1c} = 0.40$ kg/cm²

$e_c = 1.000$, $\gamma_{dc} = 83.6$ pcf

METHOD OF LOADING: Undrained, Axial Compression
Load Control

TESTING DETAILS : Specimen Diameter 3.60 cm
: Specimen Height 5.30 cm
: End Platens: Lubricated, Type 2

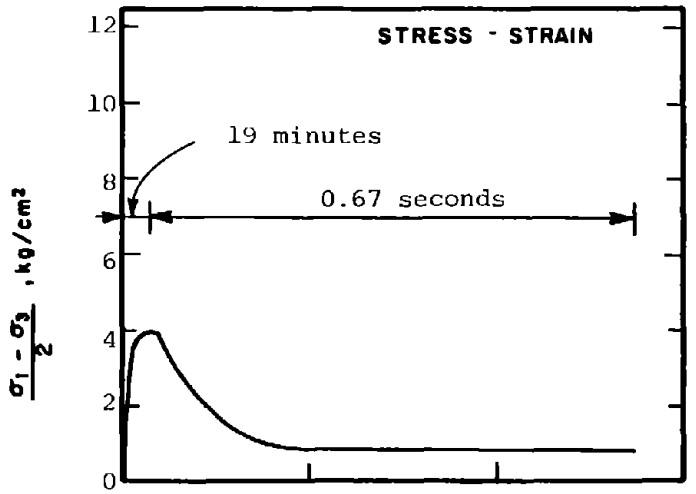

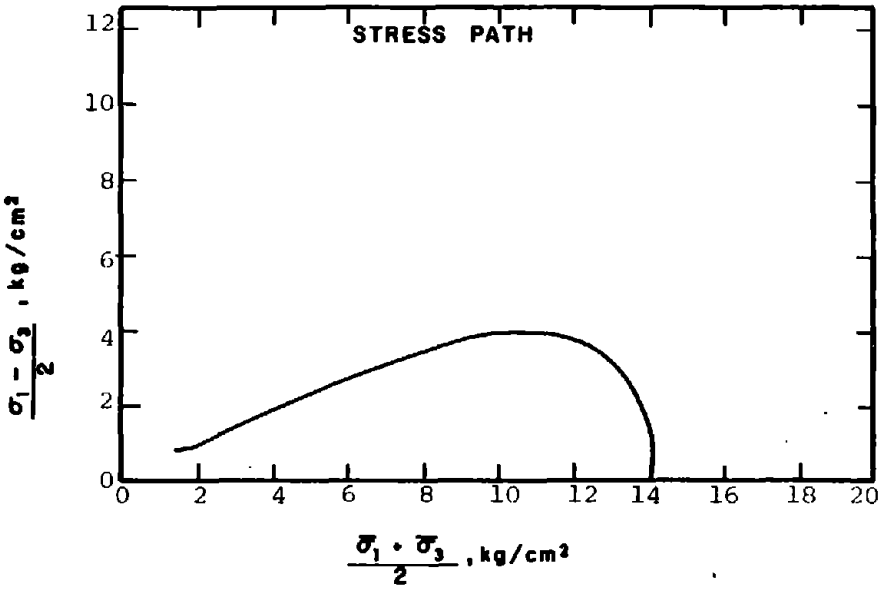

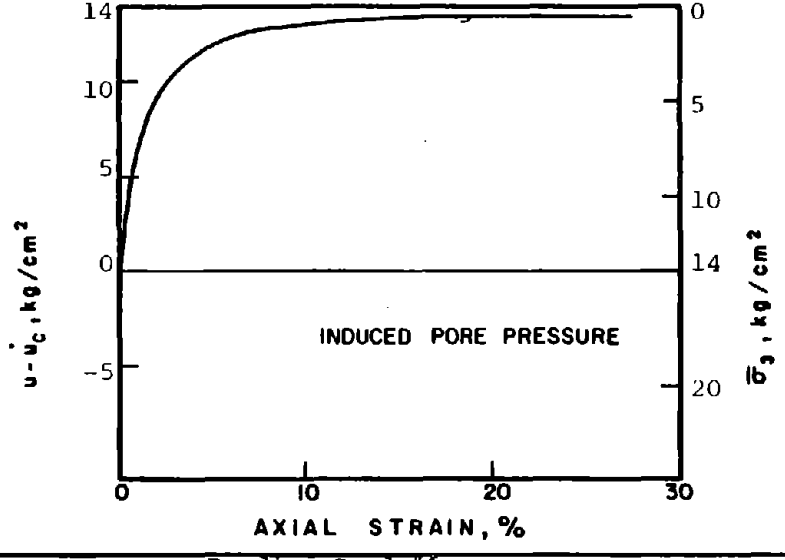

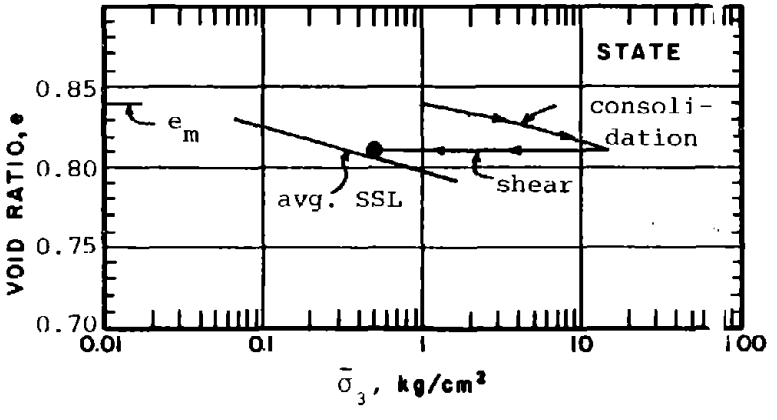

R-104

SOIL : Banding Sand #1

STRUCTURE : Compacted Moist

STATE AFTER CONSOLIDATION: $\bar{\sigma}_{3c}$ = 14.00 kg/cm², $\bar{\sigma}_{1c}$ = 14.00 kg/cm²

e_c = 0.810 , γ_{dc} = 91.7 pcf

METHOD OF LOADING: Undrained, Axial Compression
Load Control

TESTING DETAILS : Specimen Diameter 7.10 cm
: Specimen Height 10.70 cm
: End Platens: Lubricated, Type 1

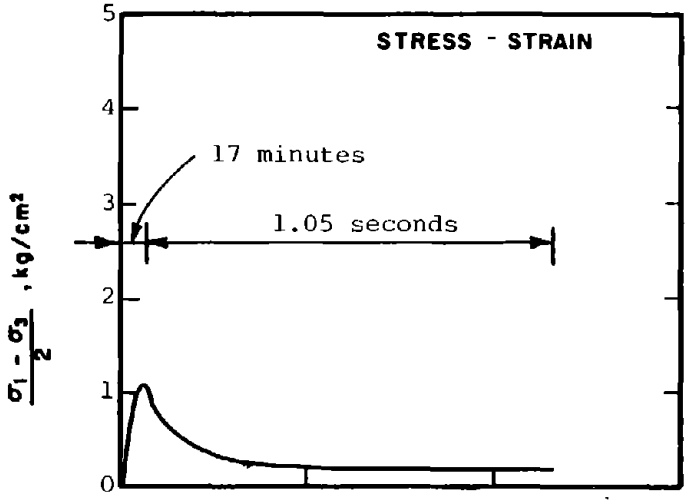

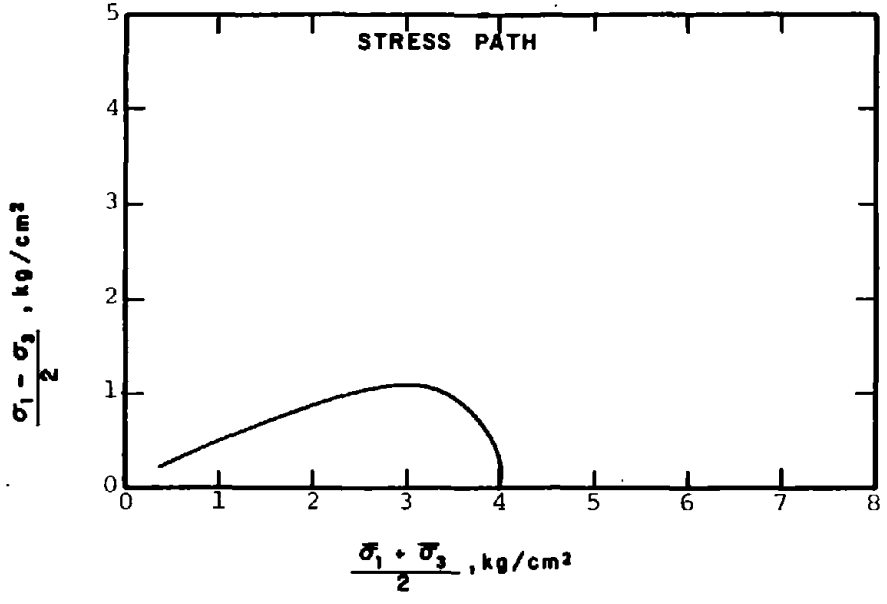

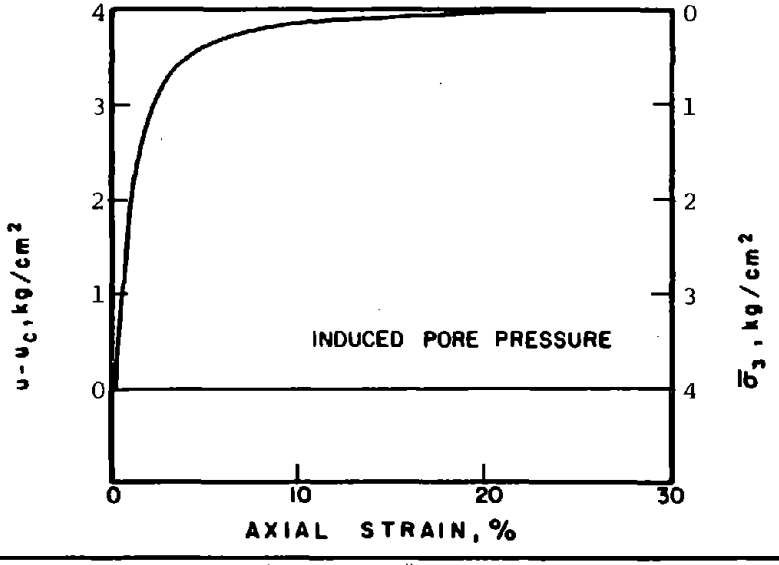

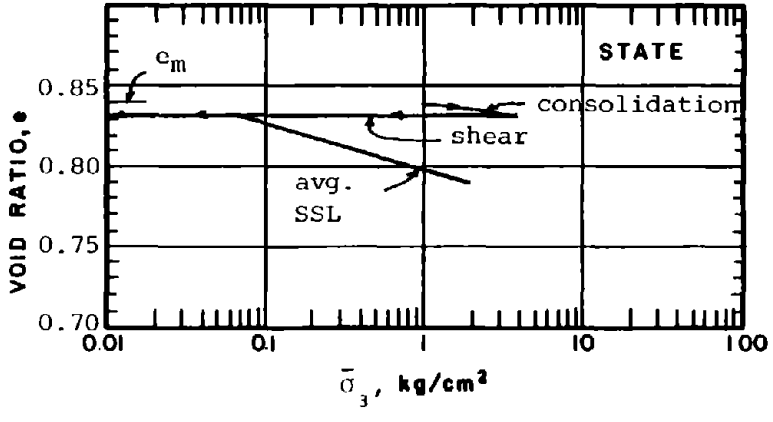

R-105

SOIL : Banding Sand #1

STRUCTURE : Compacted Moist

STATE AFTER CONSOLIDATION: $\bar{\sigma}_{3c} = 4.00$ kg/cm^2, $\bar{\sigma}_{1c} = 4.00$ kg/cm^2

$e_c = 0.831$, $\gamma_{dc} = 90.6$ pcf

METHOD OF LOADING: Undrained, Axial Compression
Load Control

TESTING DETAILS : Specimen Diameter 7.10 cm
: Specimen Height 10.70 cm
: End Platens: Lubricated, Type 1

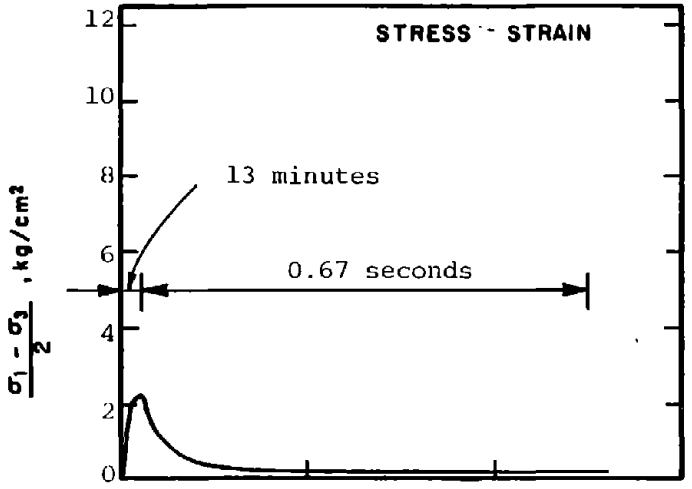

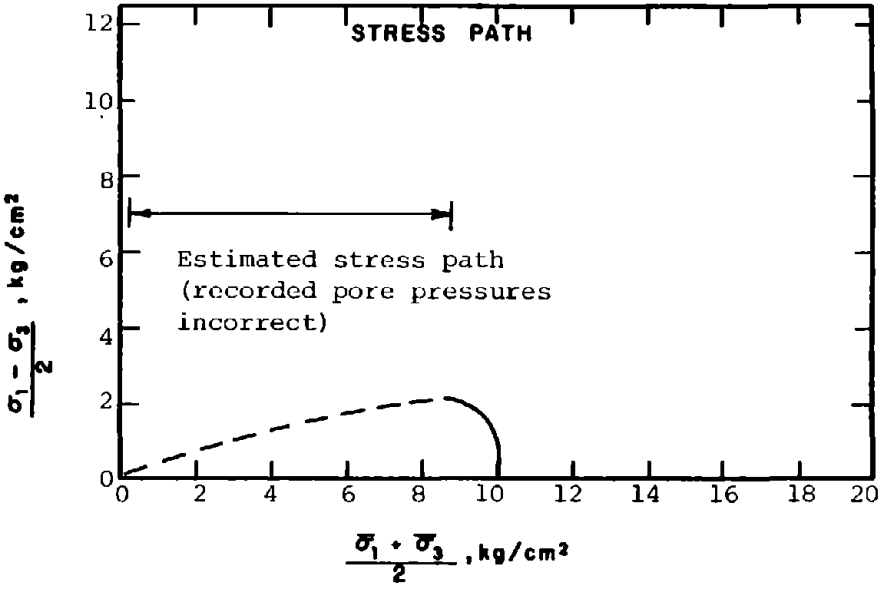

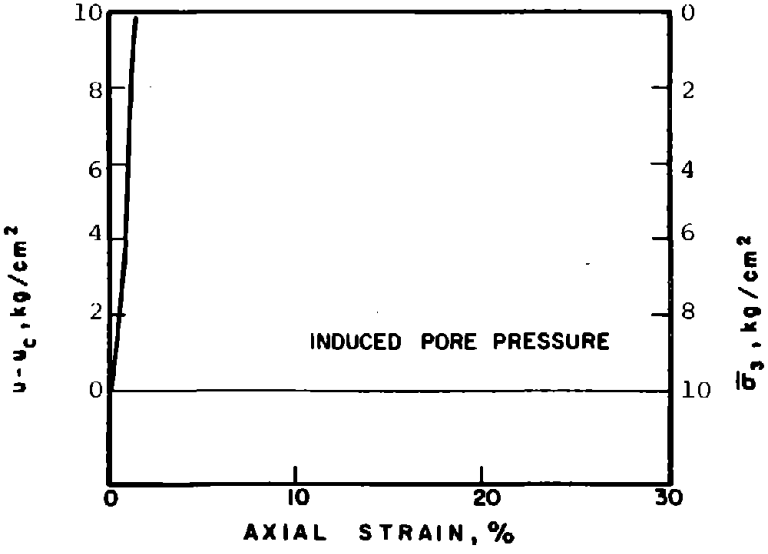

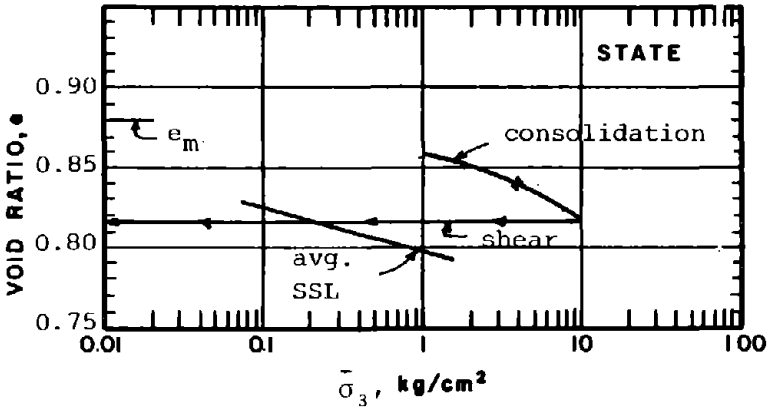

R-108

SOIL : Banding Sand #1

STRUCTURE : Compacted Moist

STATE AFTER CONSOLIDATION: $\bar{\sigma}_{3c}$ = 10.00 kg/cm², $\bar{\sigma}_{1c}$ = 10.00 kg/cm²

e_c = 0.817, γ_{dc} = 91.35 pcf

METHOD OF LOADING: Undrained, Axial Compression
Load Control

TESTING DETAILS : Specimen Diameter 3.60 cm
: Specimen Height 5.30 cm
: End Platens: Lubricated, Type 1

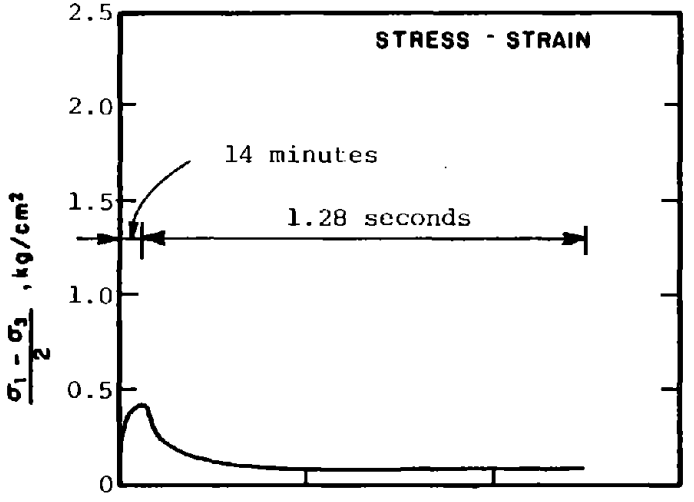

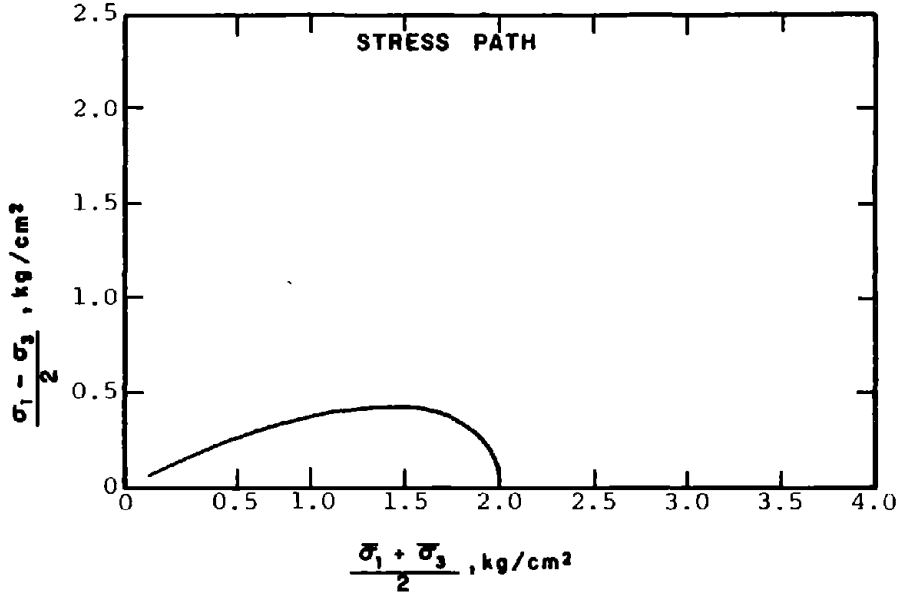

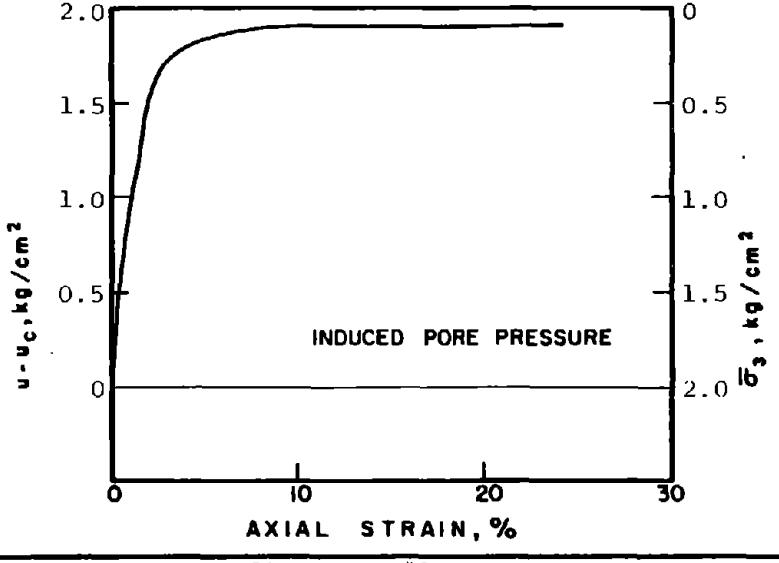

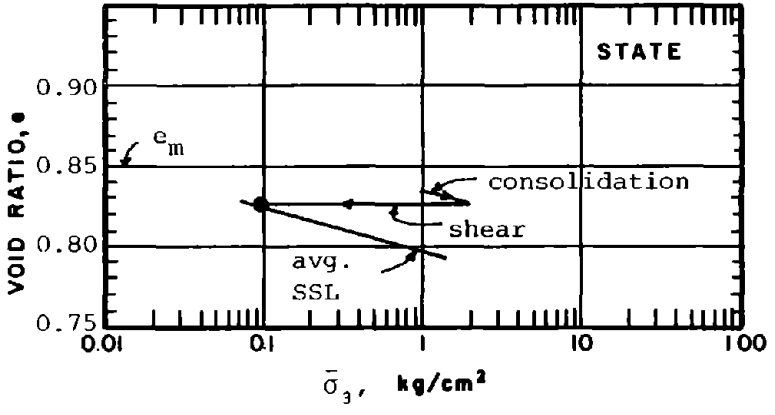

R-110

SOIL : Banding Sand #1

STRUCTURE : Compacted Moist

STATE AFTER CONSOLIDATION: $\bar{\sigma}_{3c} = 2.00\ kg/cm^2$, $\bar{\sigma}_{1c} = 2.00\ kg/cm^2$

$e_c = 0.826$, $\gamma_{dc} = 90.9$ pcf

METHOD OF LOADING: Undrained, Axial Compression
Load Control

TESTING DETAILS : Specimen Diameter 3.60 cm
: Specimen Height 5.30 cm
: End Platens: Lubricated, Type 1

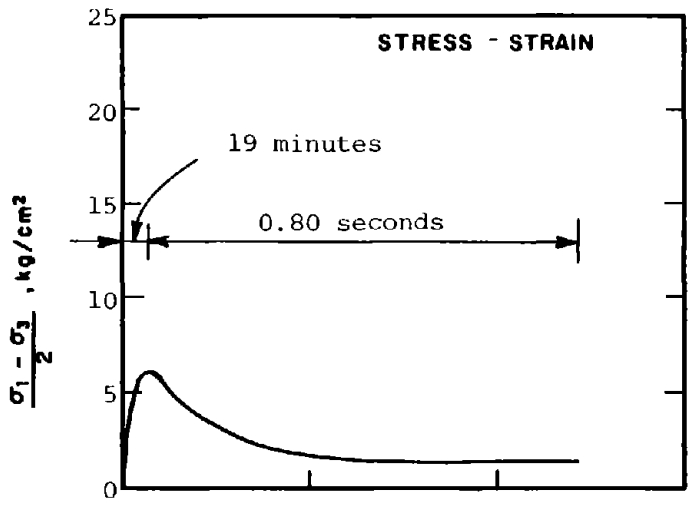

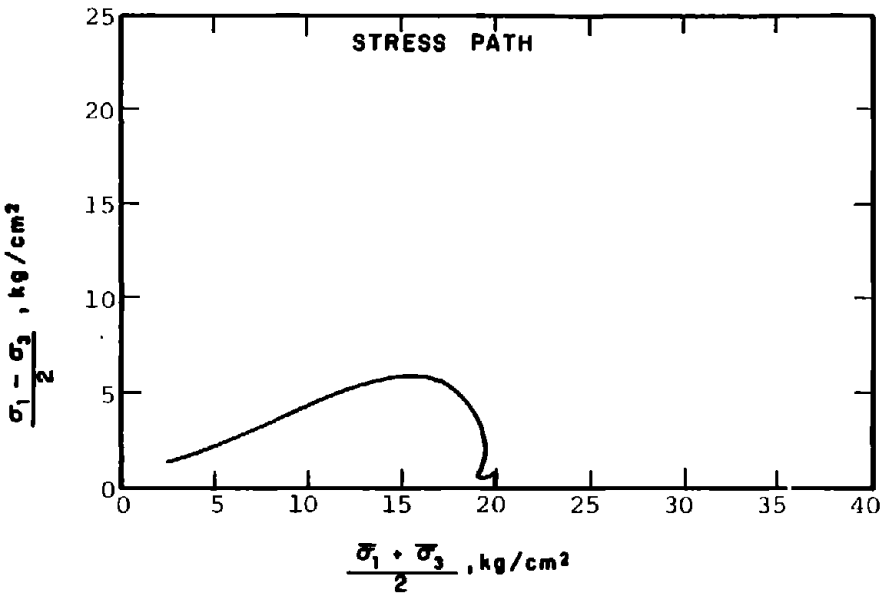

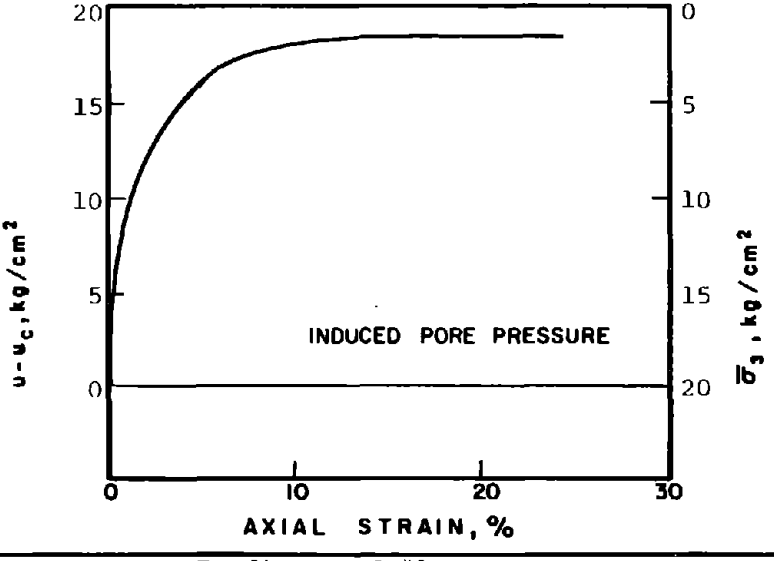

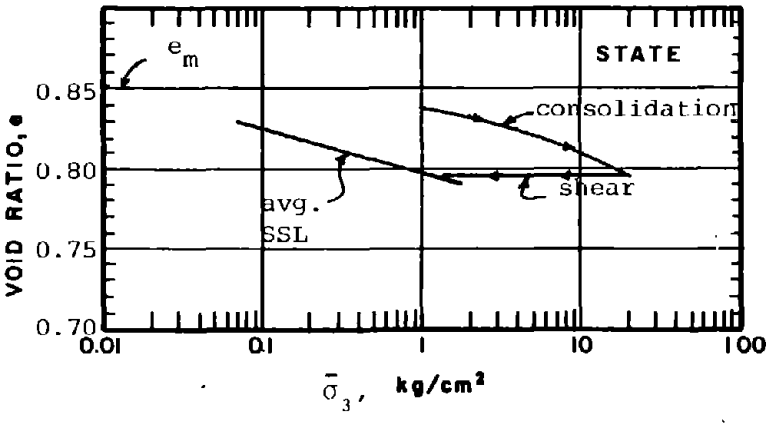

R-112

SOIL : Banding Sand #1

STRUCTURE : Compacted Moist

STATE AFTER CONSOLIDATION: $\bar{\sigma}_{3c} = 20.00$ kg/cm^2, $\bar{\sigma}_{1c} = 20.00$ kg/cm^2

$e_c = 0.796$, $\gamma_{dc} = 92.4$ pcf

METHOD OF LOADING: Undrained, Axial Compression
Load Control

TESTING DETAILS : Specimen Diameter 3.60 cm
: Specimen Height 5.30 cm
: End Platens: Lubricated, Type 1

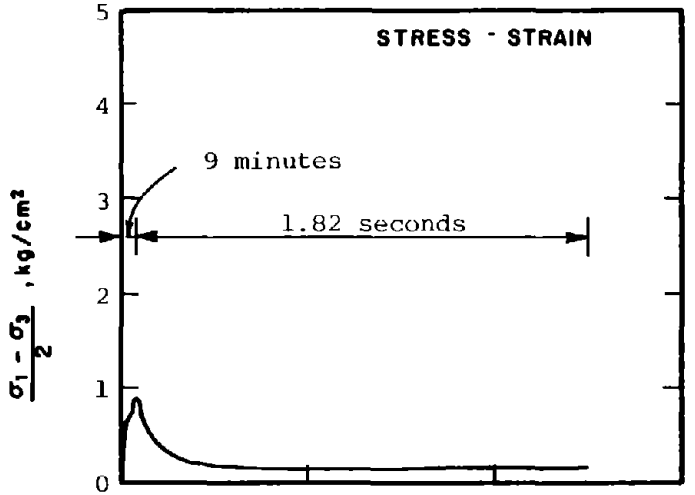

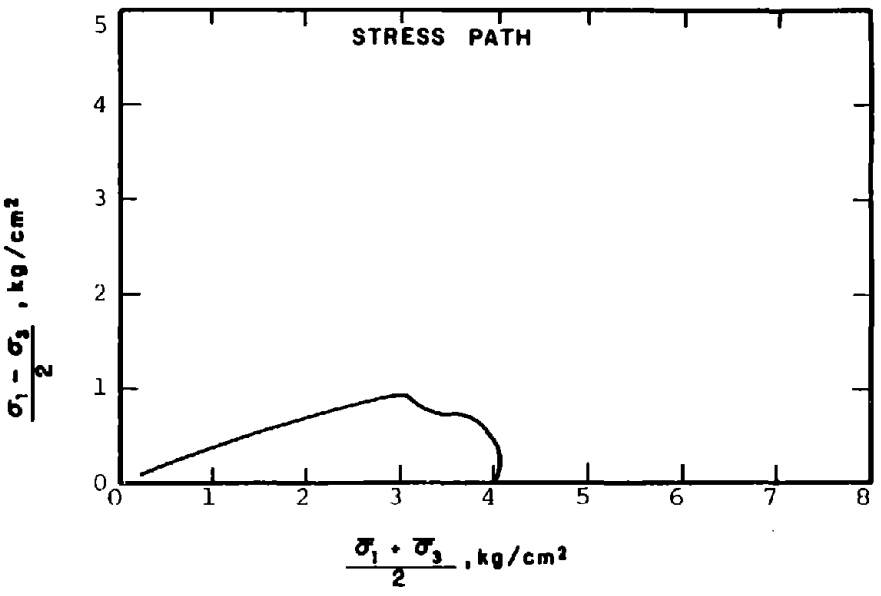

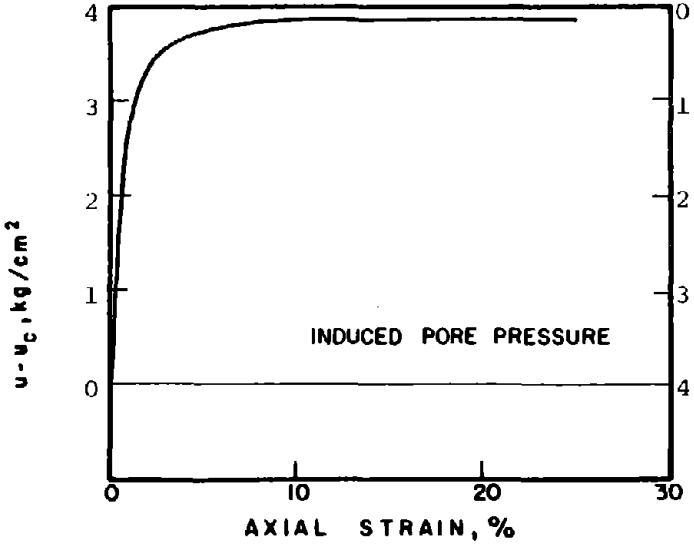

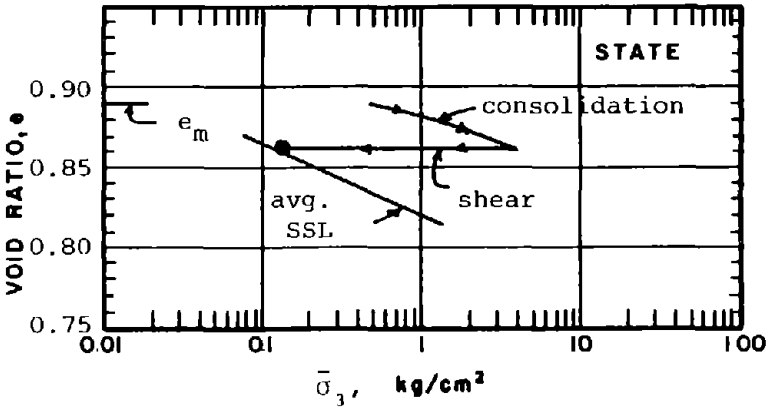

R-502

SOIL : Banding Sand #5

STRUCTURE : Compacted Moist

STATE AFTER CONSOLIDATION: $\bar{\sigma}_{3c} = 4.00$ kg/cm^2, $\bar{\sigma}_{1c} = 4.00$ kg/cm^2
$e_c = 0.861$, $\gamma_{dc} = 89.2$ pcf

METHOD OF LOADING: Undrained, Axial Compression
Load Control

TESTING DETAILS : Specimen Diameter 3.60 cm
: Specimen Height 5.30 cm
: End Platens: Lubricated, Type 1

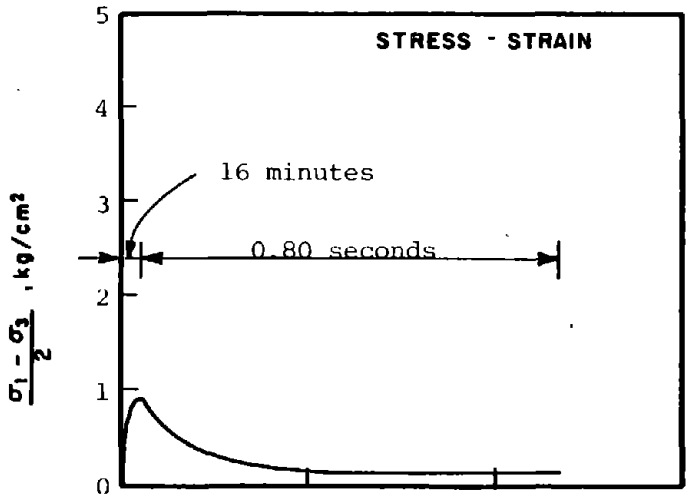

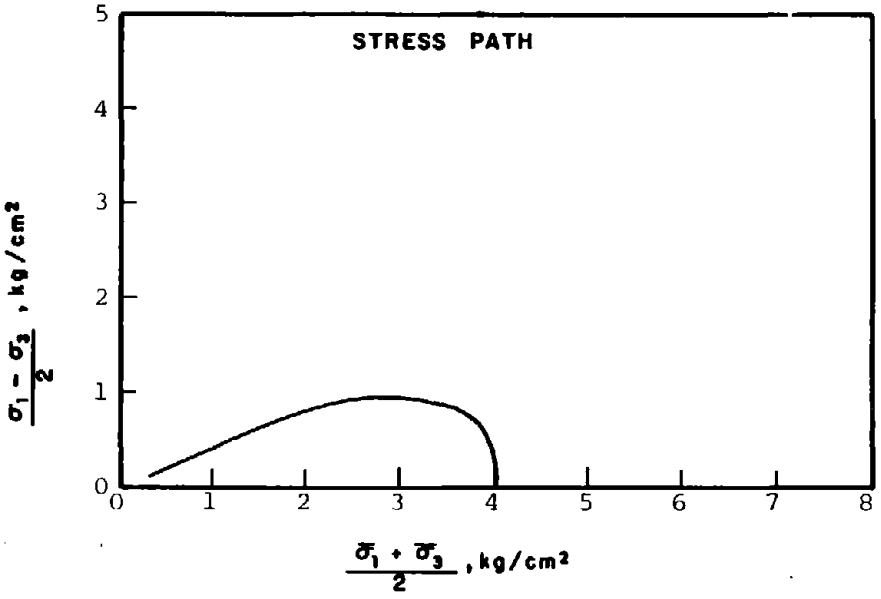

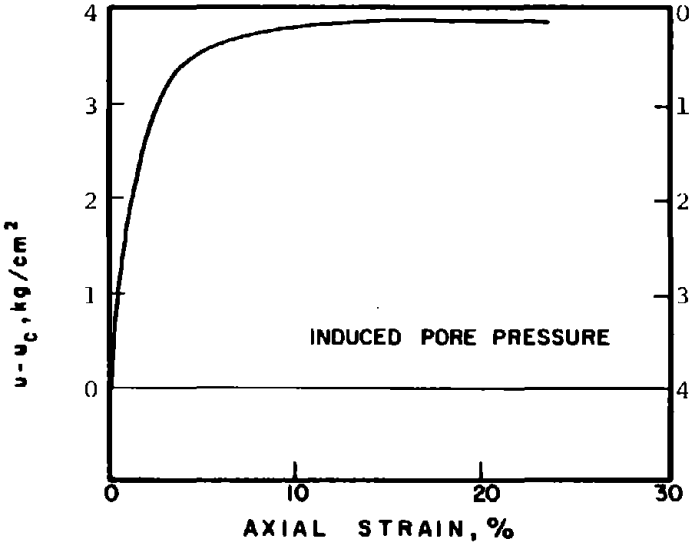

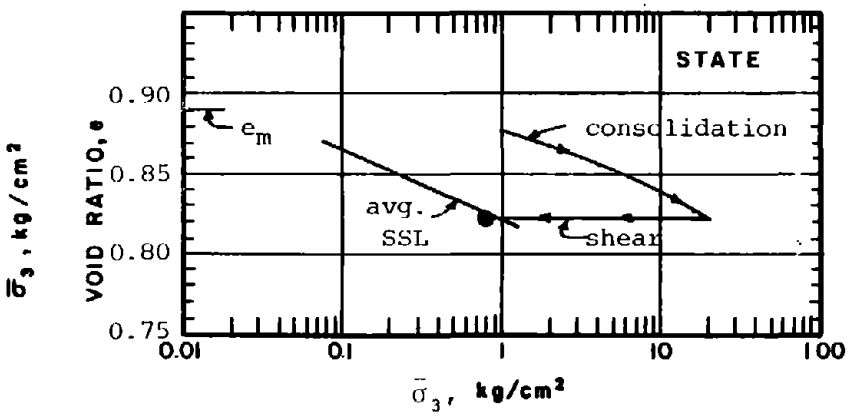

SOIL	: Banding Sand #5	METHOD OF LOADING:	Undrained, Axial Compression Load Control
STRUCTURE	: Compacted Moist		
STATE AFTER CONSOLIDATION:	$\bar{\sigma}_{3c}$ =20.00 kg/cm², $\bar{\sigma}_{1c}$ =20.00 kg/cm²	TESTING DETAILS	: Specimen Diameter 3.60 cm
	e_c = 0.821, γ_{dc} = 91.1 pcf		: Specimen Height 5.30 cm
			: End Platens: Lubricated, Type 1

R-503

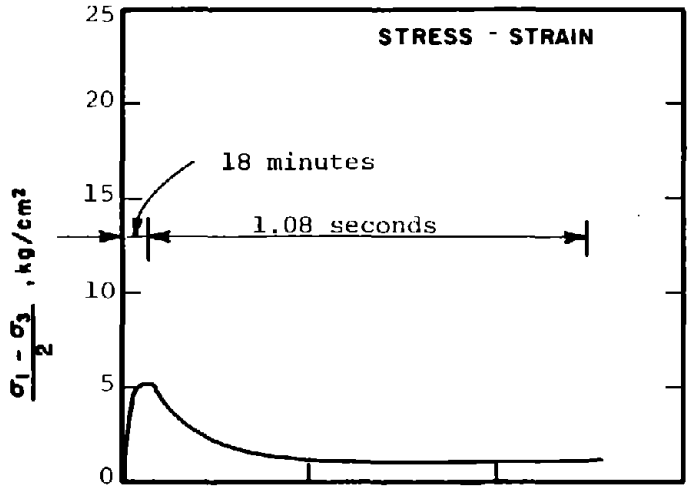

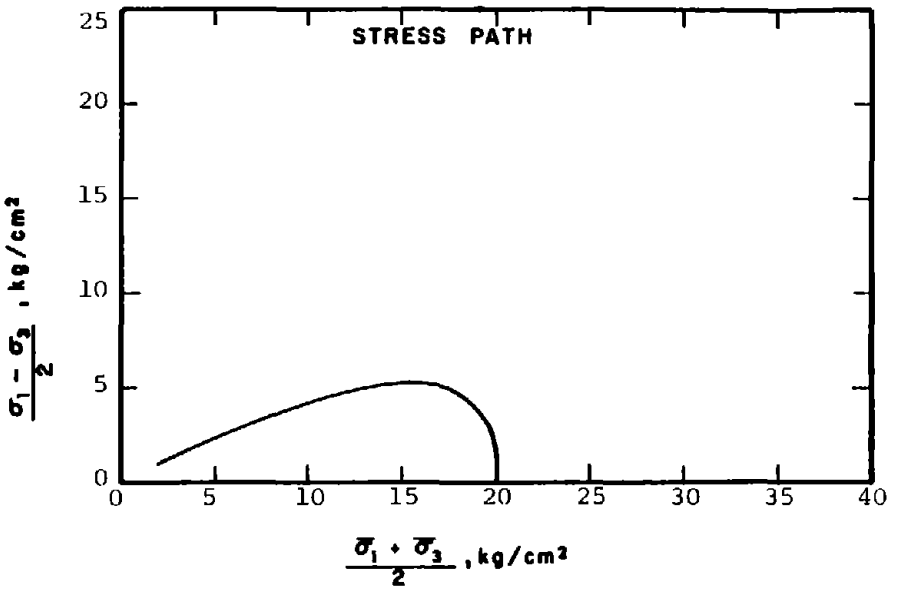

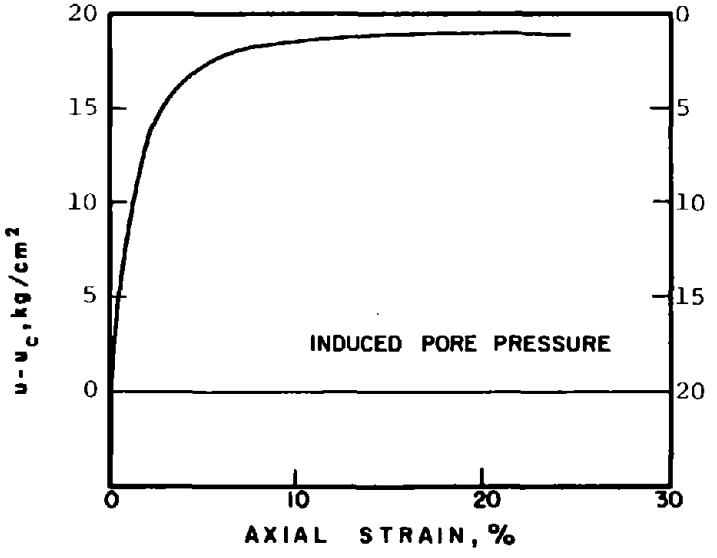

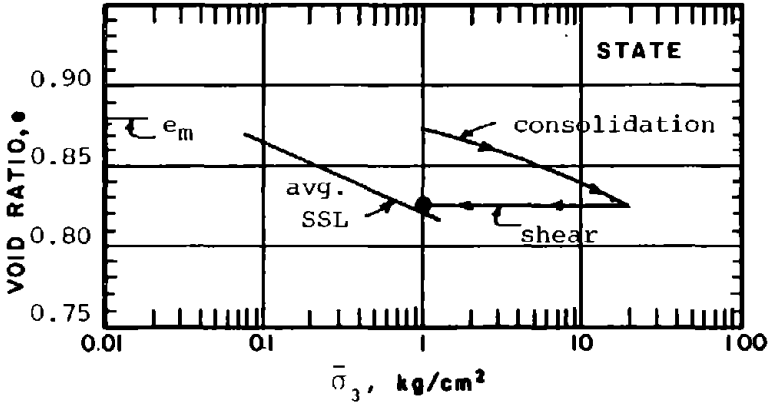

R-504

SOIL : Banding Sand #5

STRUCTURE : Compacted Moist

STATE AFTER CONSOLIDATION: $\bar{\sigma}_{3c}$ = 20.00kg/cm², $\bar{\sigma}_{1c}$ =20.00 kg/cm²

e_c = 0.824, γ_{dc} = 91.0 pcf

METHOD OF LOADING: Undrained, Axial Compression Load Control

TESTING DETAILS : Specimen Diameter 3.60 cm

: Specimen Height 5.30 cm

: End Platens: Lubricated

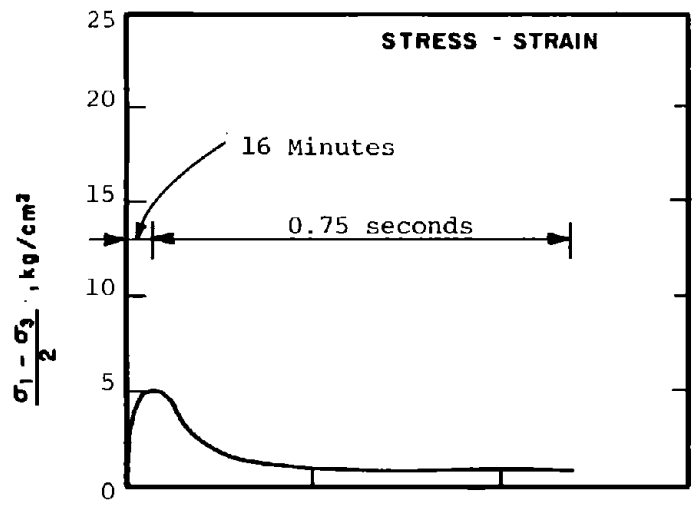

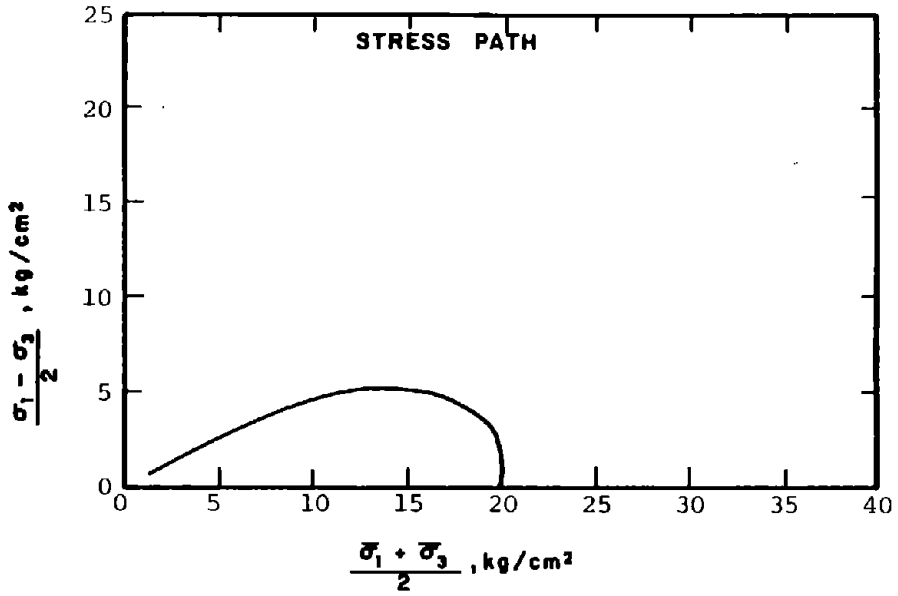

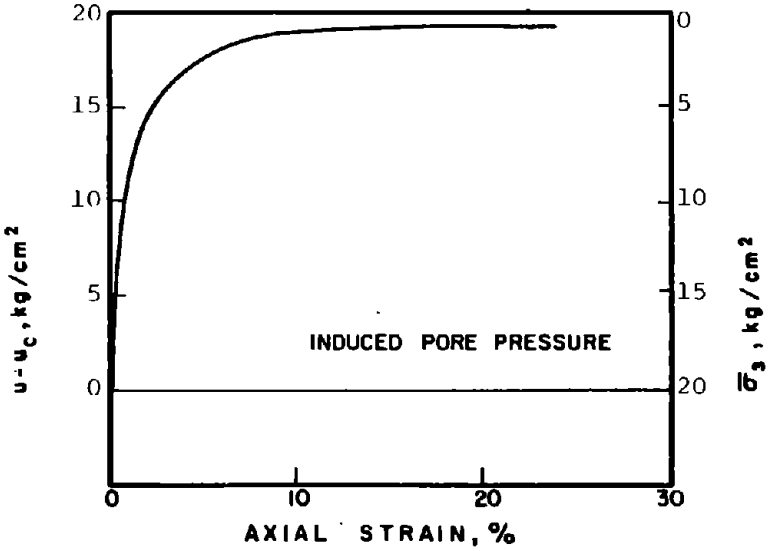

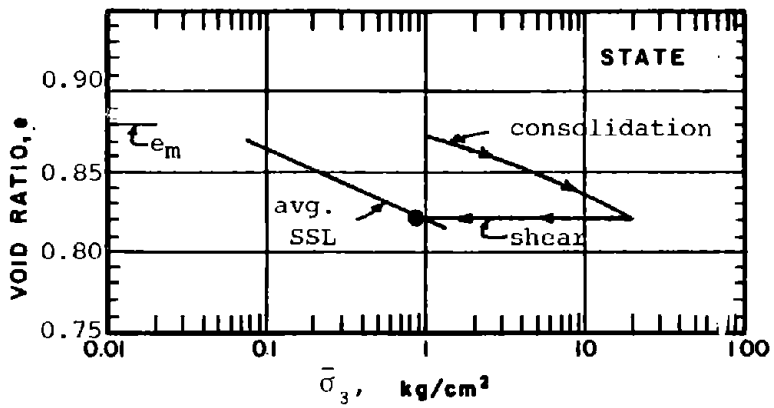

SOIL	: Banding Sand #5	METHOD OF LOADING:	Undrained, Axial Compression Load Control
STRUCTURE	: Compacted Moist		
STATE AFTER CONSOLIDATION:	$\bar{\sigma}_{3c}$ =20.00 kg/cm², $\bar{\sigma}_{1c}$ =20.00 kg/cm²	TESTING DETAILS	: Specimen Diameter 3.60 cm
	e_c = 0.820, γ_{dc} = 91.2 pcf		: Specimen Height 5.30 cm
			: End Platens: Lubricated, Type 1

R-505

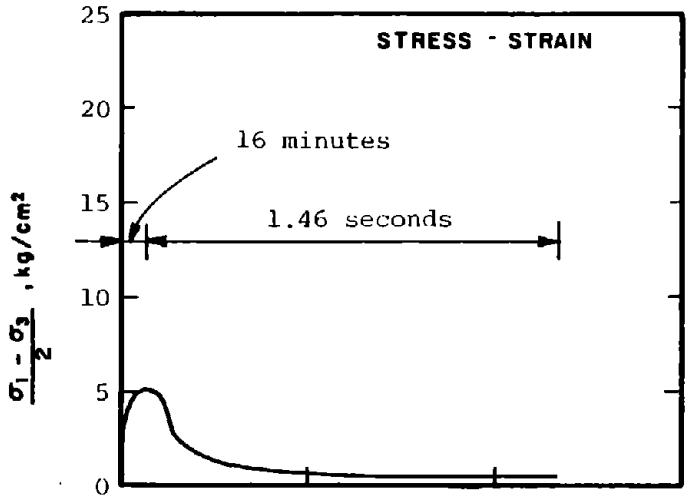

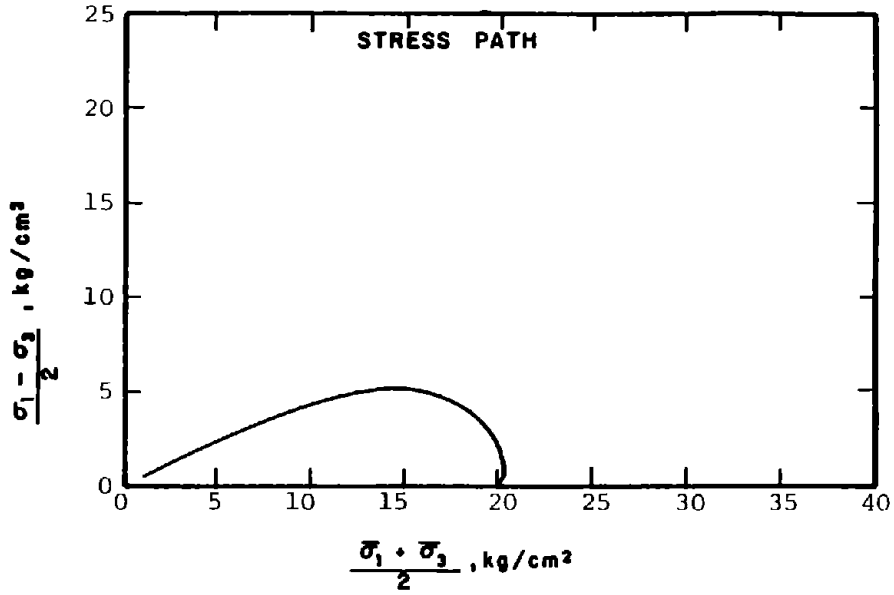

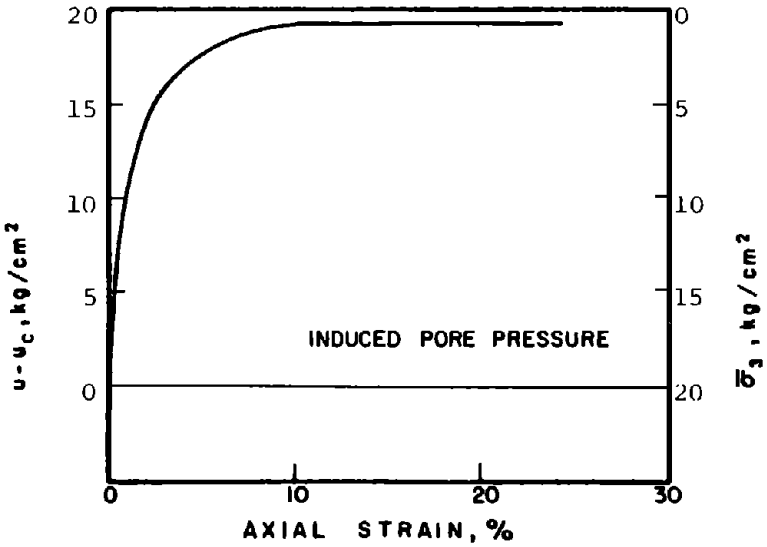

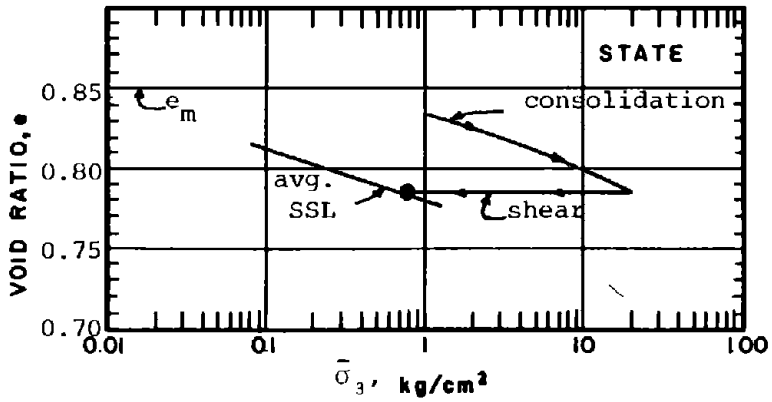

SOIL	: Banding Sand #9	METHOD OF LOADING:	Undrained, Axial Compression Load Control
STRUCTURE	: Compacted Moist		
STATE AFTER CONSOLIDATION:	$\bar{\sigma}_{3c}$ = 20.00kg/cm², $\bar{\sigma}_{1c}$ = 20.00kg/cm²	TESTING DETAILS	: Specimen Diameter 3.60 cm
	e_c = 0.783, γ_{dc} = 93.1 pcf		: Specimen Height 5.30 cm
			: End Platens: Lubricated, Type 1

R-904

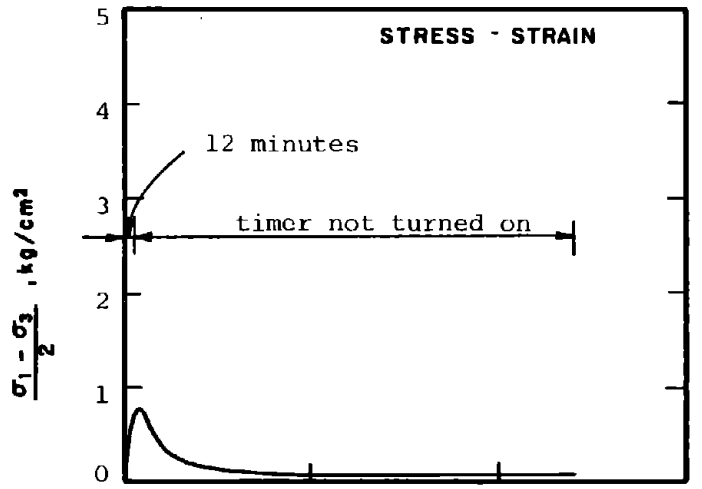

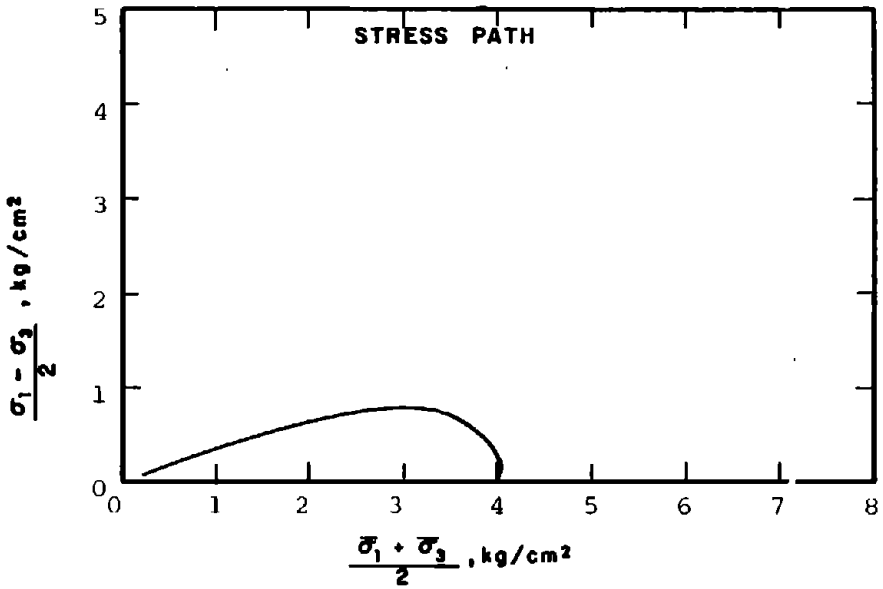

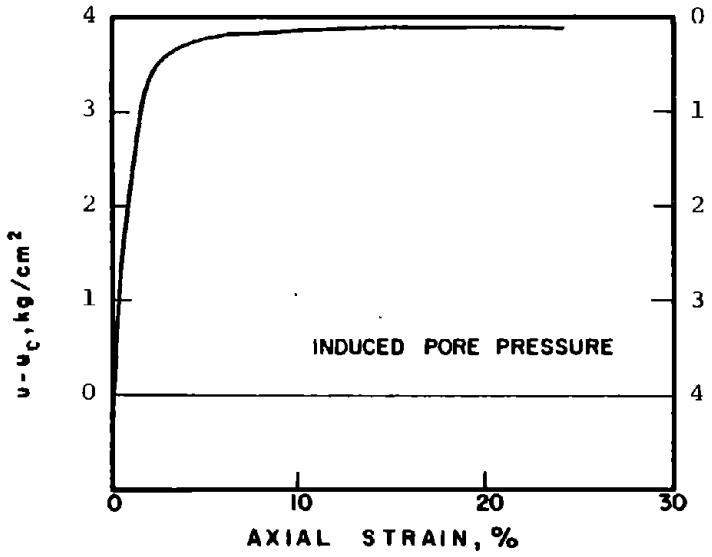

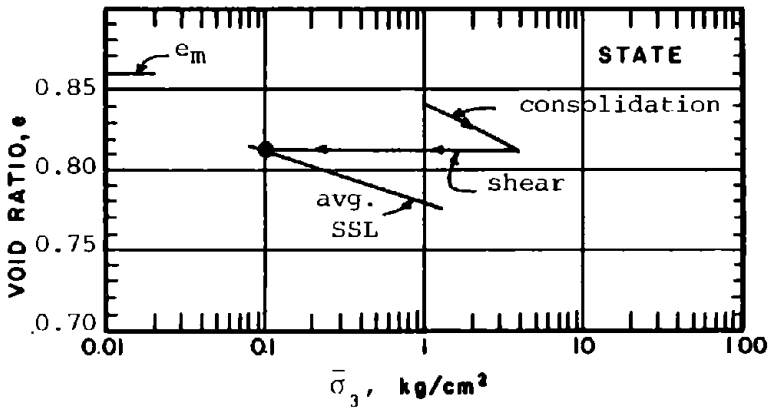

R-905

SOIL : Banding Sand #9

STRUCTURE : Compacted Moist

STATE AFTER CONSOLIDATION: $\bar{\sigma}_{3c} = 4.00\ kg/cm^2$, $\bar{\sigma}_{1c} = 4.00\ kg/cm^2$

$e_c = 0.812$, $\gamma_{dc} = 91.6$ pcf

METHOD OF LOADING: Undrained, Axial Compression
Load Control

TESTING DETAILS : Specimen Diameter 3.60 cm
: Specimen Height 5.30 cm
: End Platens: Lubricated, Type 2

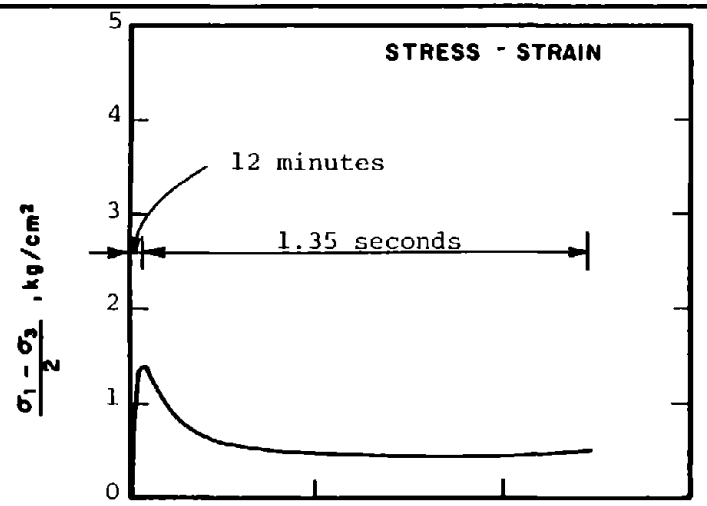

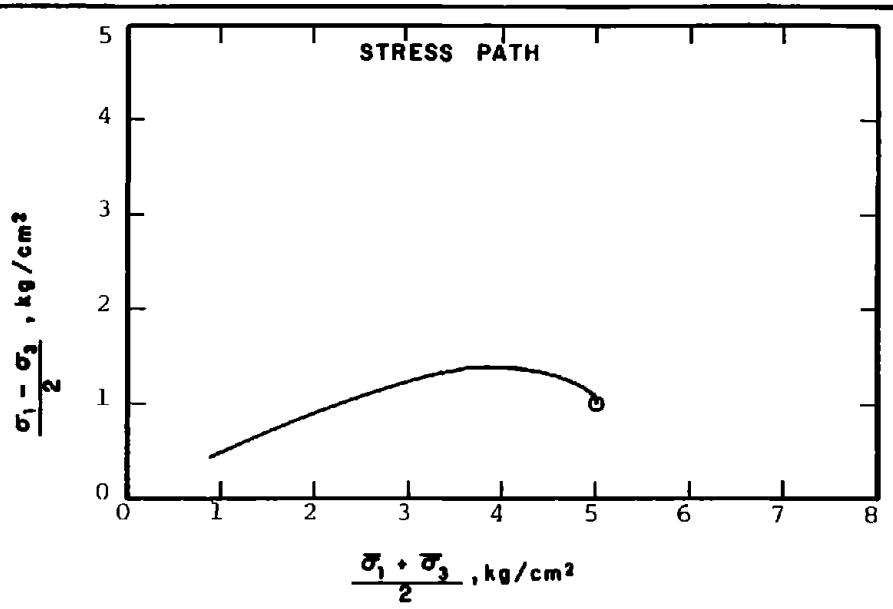

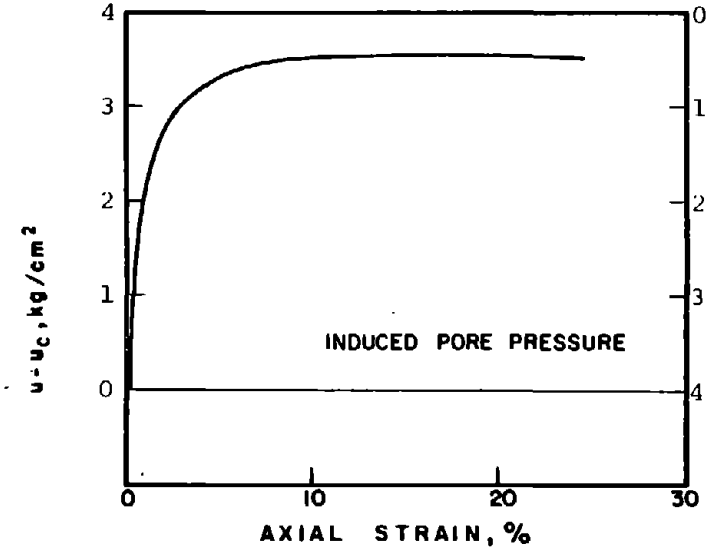

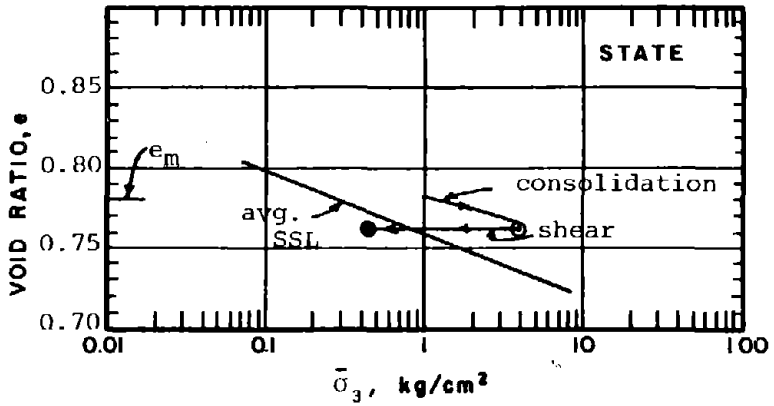

SOIL	: Banding Sand #6	METHOD OF LOADING:	Undrained, Axial Compression Load Control
STRUCTURE	: Compacted Moist		
STATE AFTER CONSOLIDATION:	$\bar{\sigma}_{3c}$ = 4.00 kg/cm², $\bar{\sigma}_{1c}$ = 6.00 kg/cm²	TESTING DETAILS	: Specimen Diameter 3.60 cm
	e_c = 0.762, γ_{dc} = 94.2 pcf		: Specimen Height 5.30 cm
			: End Platens: Lubricated, Type 1

AR-601

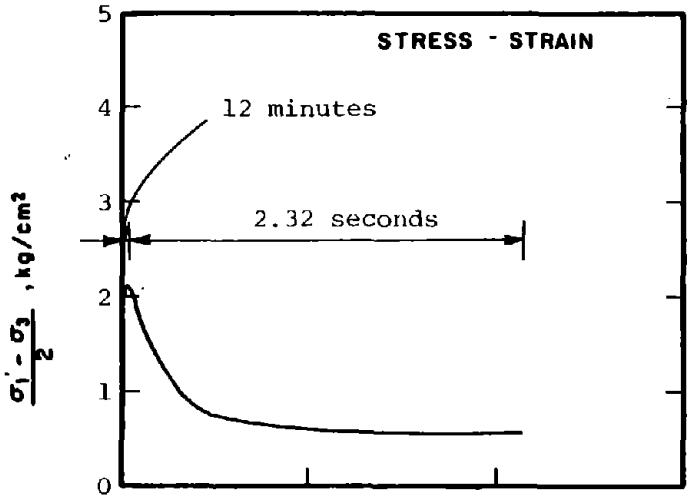

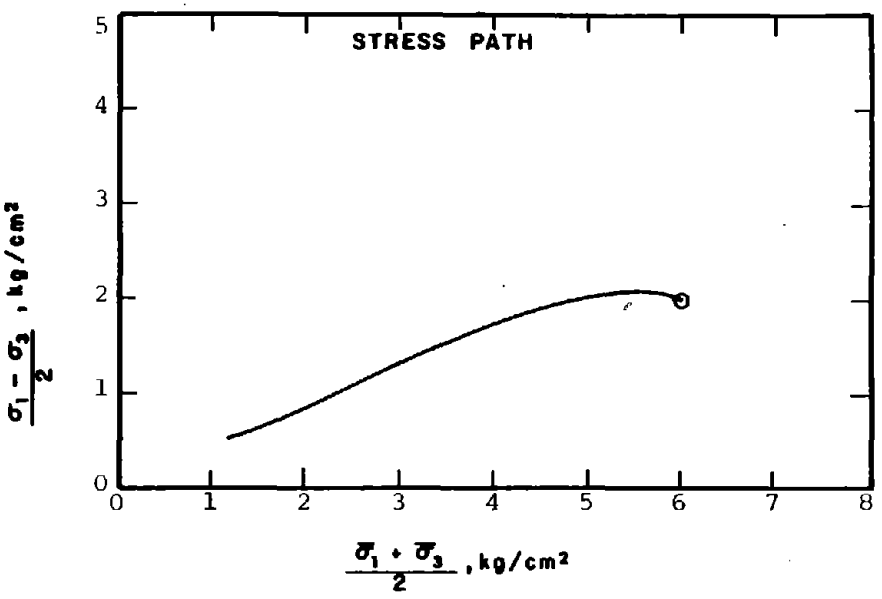

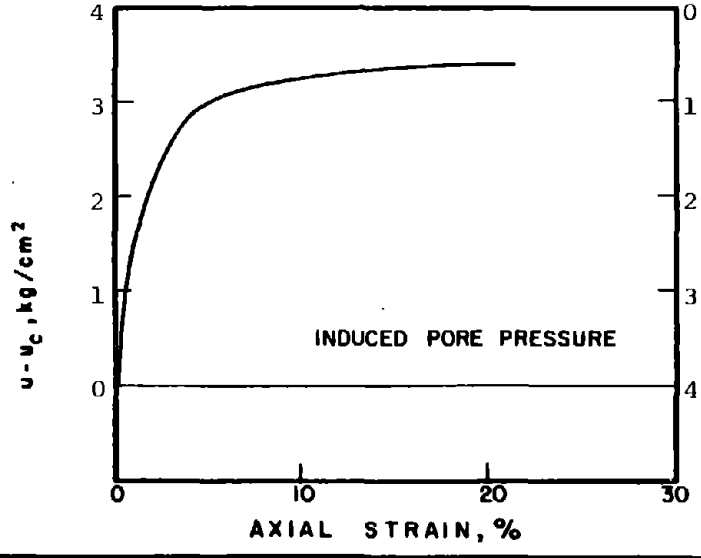

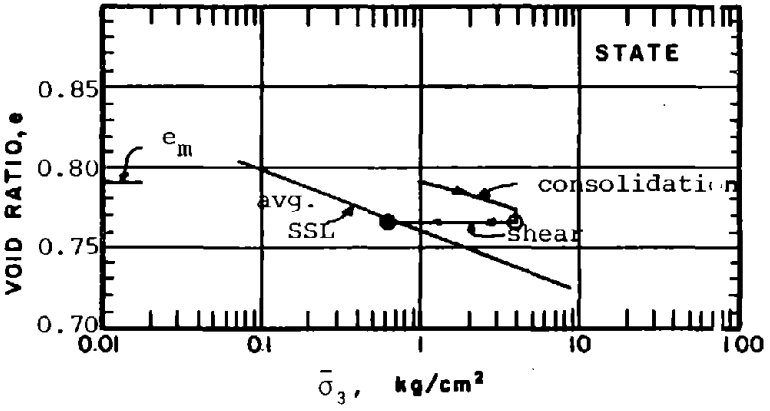

AR-602

SOIL : Banding Sand #6

STRUCTURE : Compacted Moist

STATE AFTER CONSOLIDATION: $\bar{\sigma}_{3c} = 4.00$ kg/cm^2, $\bar{\sigma}_{1c} = 8.00$ kg/cm^2

$e_c = 0.765$, $\gamma_{dc} = 94.0$ pcf

METHOD OF LOADING: Undrained, Axial Compression
Load Control

TESTING DETAILS : Specimen Diameter 3.60 cm
: Specimen Height 5.30 cm
: End Platens: Lubricated, Type 1

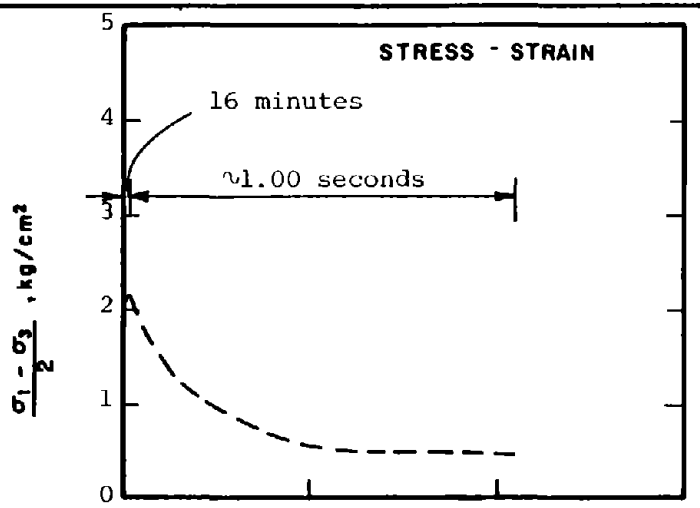

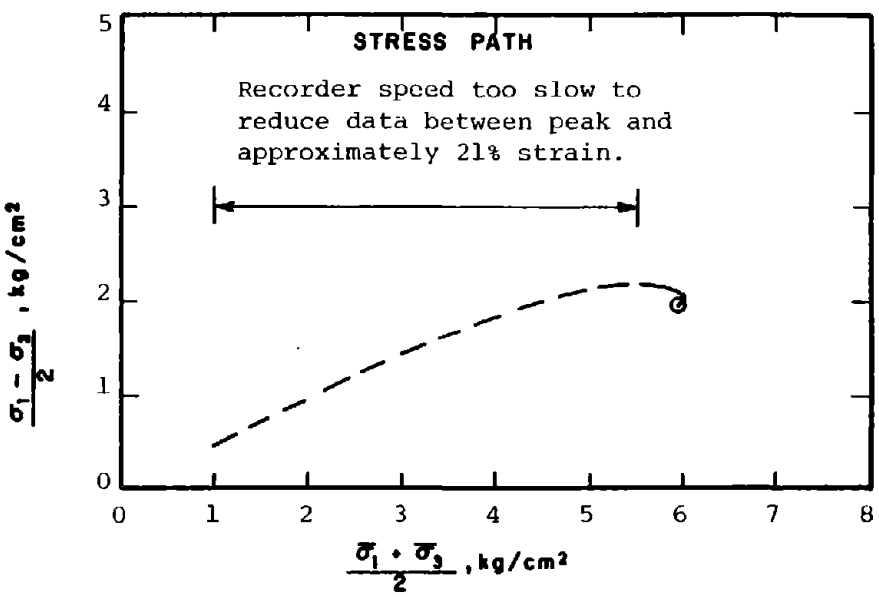

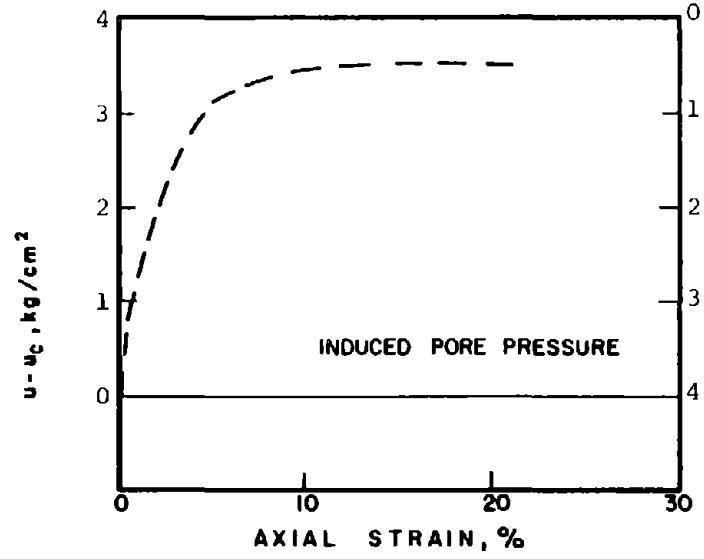

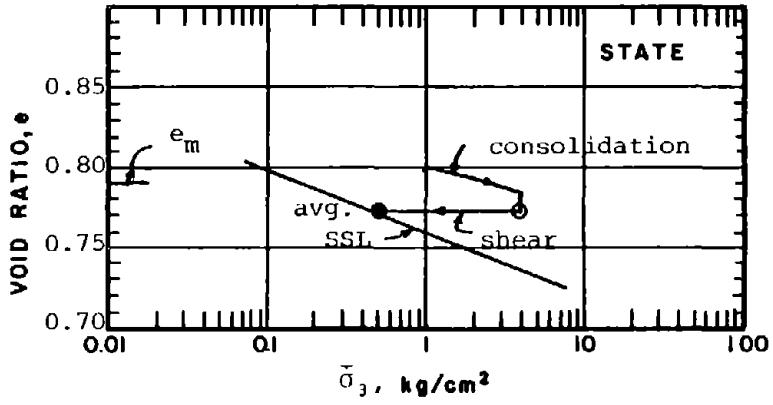

AR-603

SOIL : Banding Sand #6

STRUCTURE : Compacted Moist

STATE AFTER CONSOLIDATION: $\bar{\sigma}_{3c}$ = 4.00 kg/cm², $\bar{\sigma}_{1c}$ = 8.00 kg/cm²
e_c = 0.771, γ_{dc} = 93.7 pcf

METHOD OF LOADING: Undrained, Axial Compression
Load Control

TESTING DETAILS : Specimen Diameter 3.60 cm
: Specimen Height 5.30 cm
: End Platens: Lubricated, Type 2

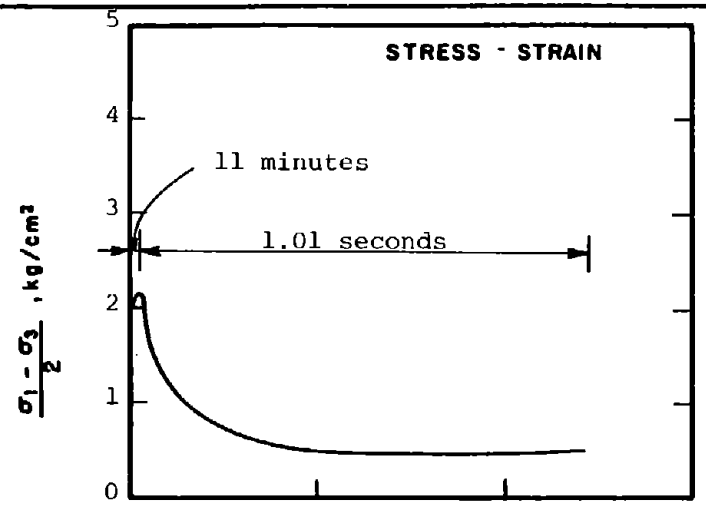

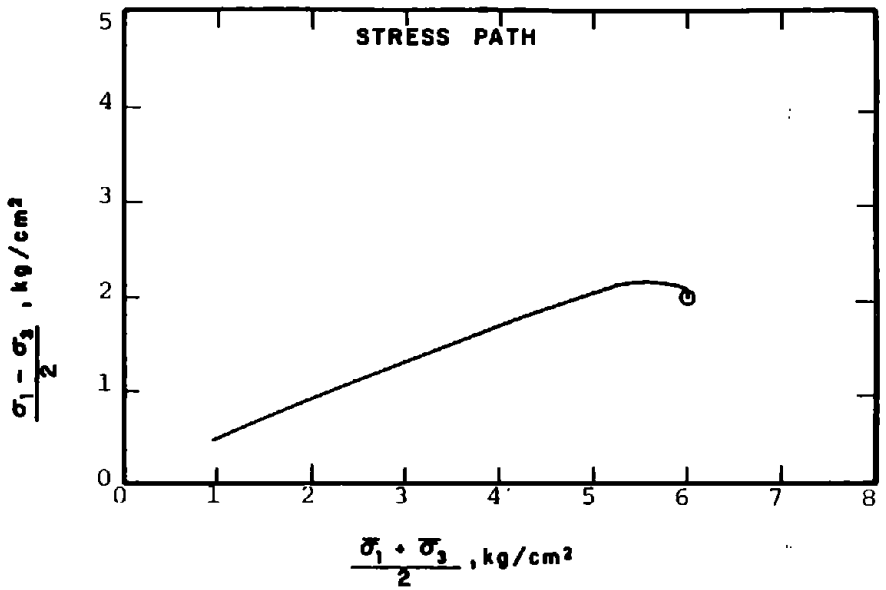

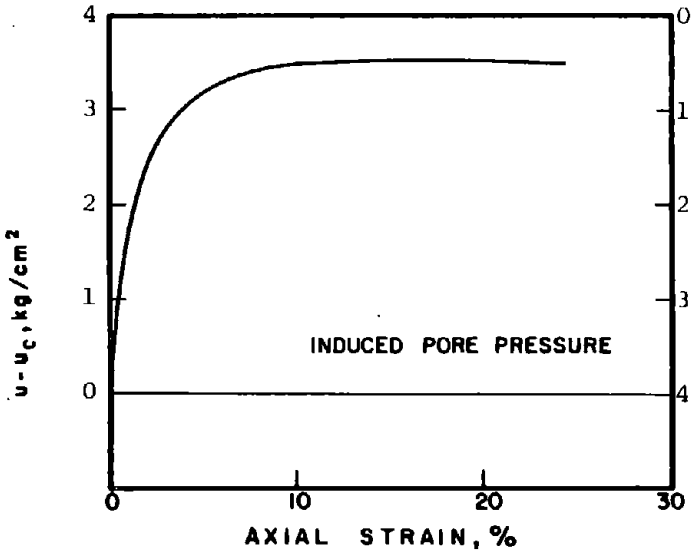

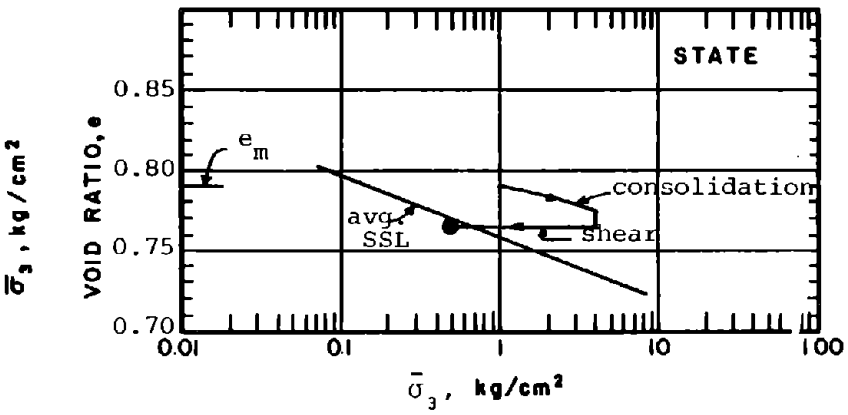

AR-604

SOIL : Banding Sand #6

STRUCTURE : Compacted Moist

STATE AFTER CONSOLIDATION: $\bar{\sigma}_{3c} = 4.00$ kg/cm^2, $\bar{\sigma}_{1c} = 8.00$ kg/cm^2
$e_c = 0.764$, $\gamma_{dc} = 94.1$ pcf

METHOD OF LOADING: Undrained, Axial Compression
Load Control

TESTING DETAILS : Specimen Diameter 3.60 cm
: Specimen Height 5.30 cm
: End Platens: Lubricated, Type 2

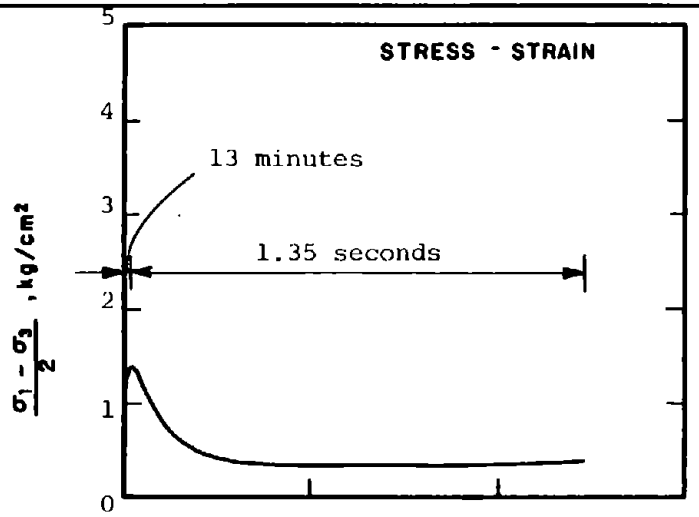

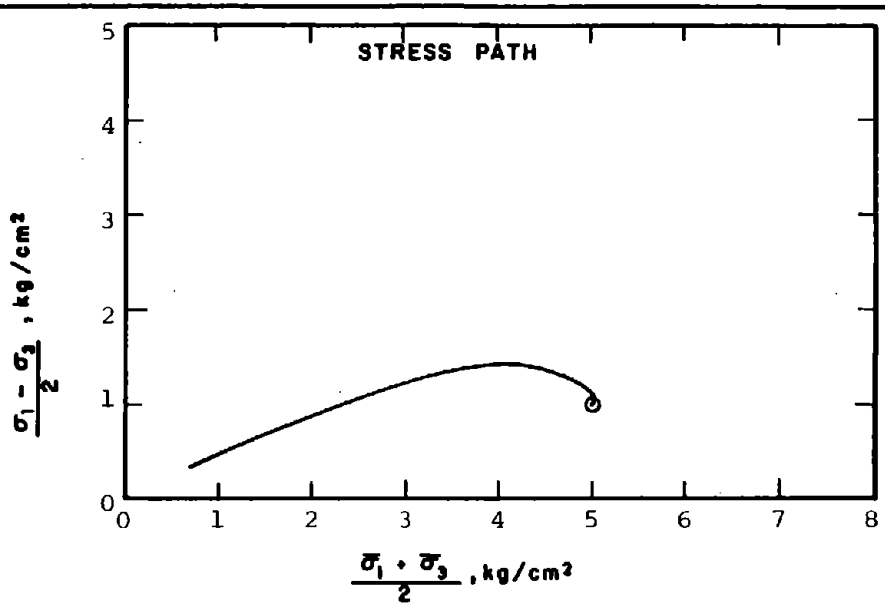

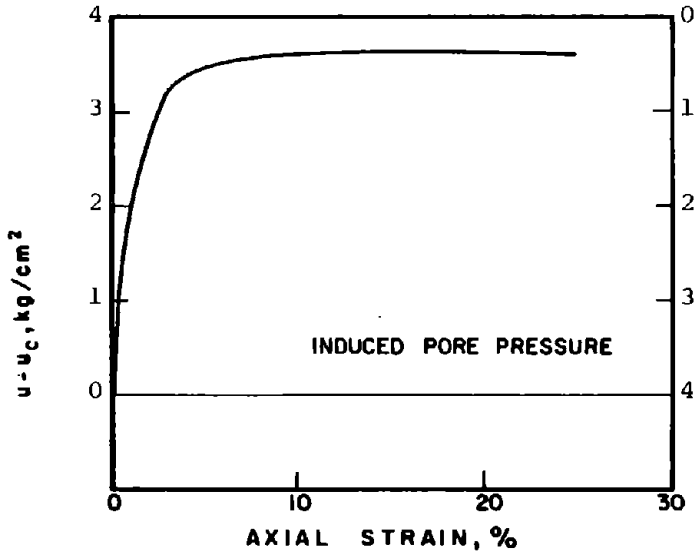

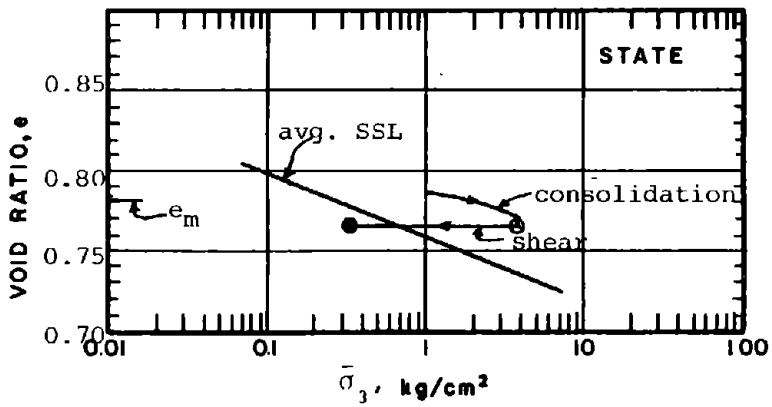

AR-605

SOIL : Banding Sand #6

STRUCTURE : Compacted Moist

STATE AFTER CONSOLIDATION: $\bar{\sigma}_{3c}$ = 4.00 kg/cm², $\bar{\sigma}_{1c}$ = 6.00 kg/cm²
e_c = 0.766, γ_{dc} = 94.0 pcf

METHOD OF LOADING: Undrained, Axial Compression
Load Control

TESTING DETAILS : Specimen Diameter 3.60 cm
: Specimen Height 5.30 cm
: End Platens: Lubricated, Type 2

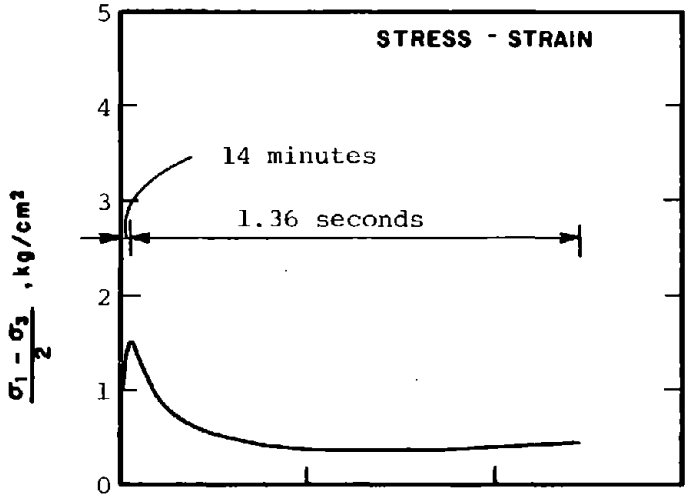

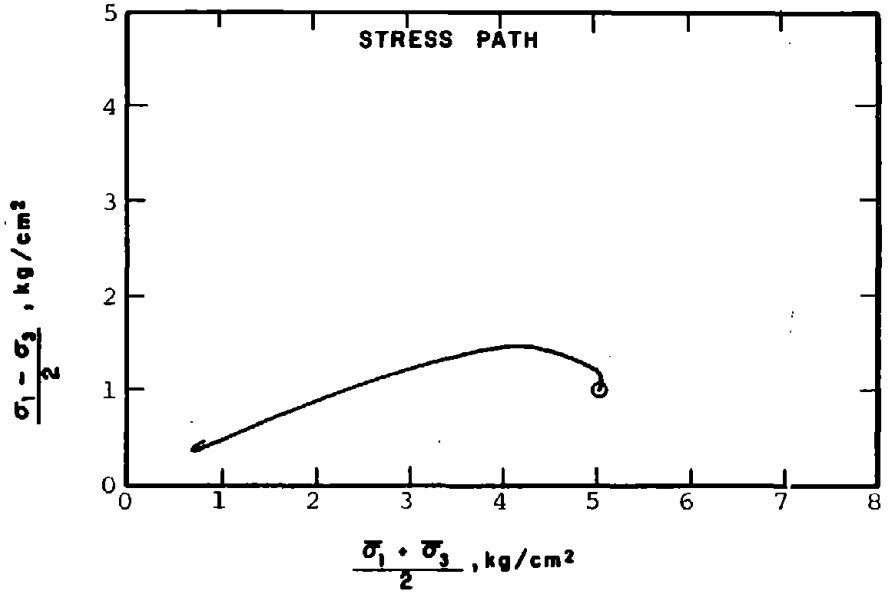

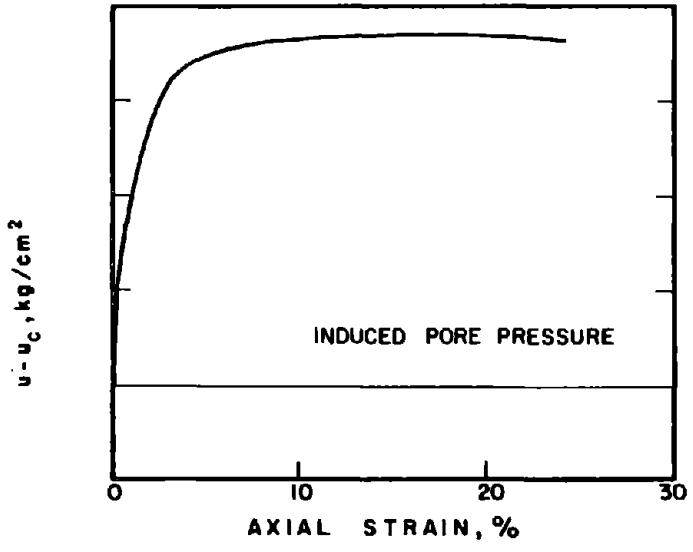

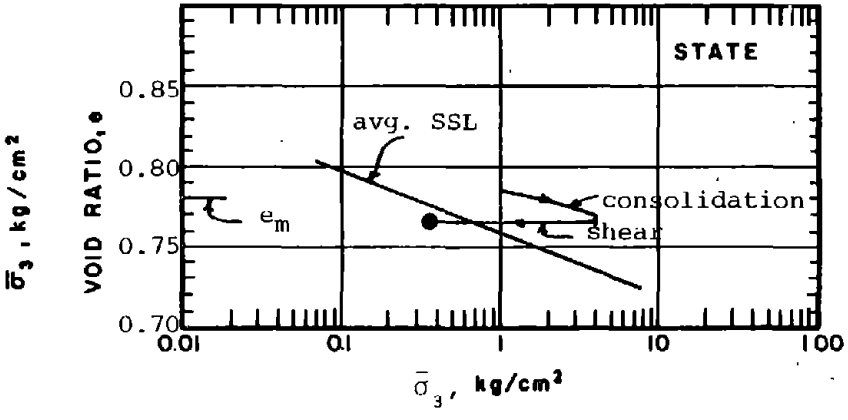

AR-606

SOIL : Banding Sand #6

STRUCTURE : Compacted Moist

STATE AFTER CONSOLIDATION: $\bar{\sigma}_{3c} = 4.00$ kg/cm^2, $\bar{\sigma}_{1c} = 6.00$ kg/cm^2

$e_c = 0.765$, $\gamma_{dc} = 94.0$ pcf

METHOD OF LOADING: Undrained, Axial Compression
Load Control

TESTING DETAILS : Specimen Diameter 3.60 cm
: Specimen Height 5.30 cm
: End Platens: Lubricated, Type 2

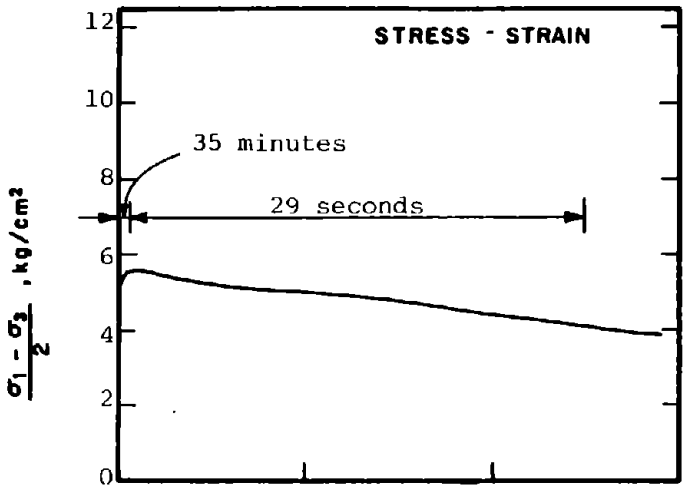

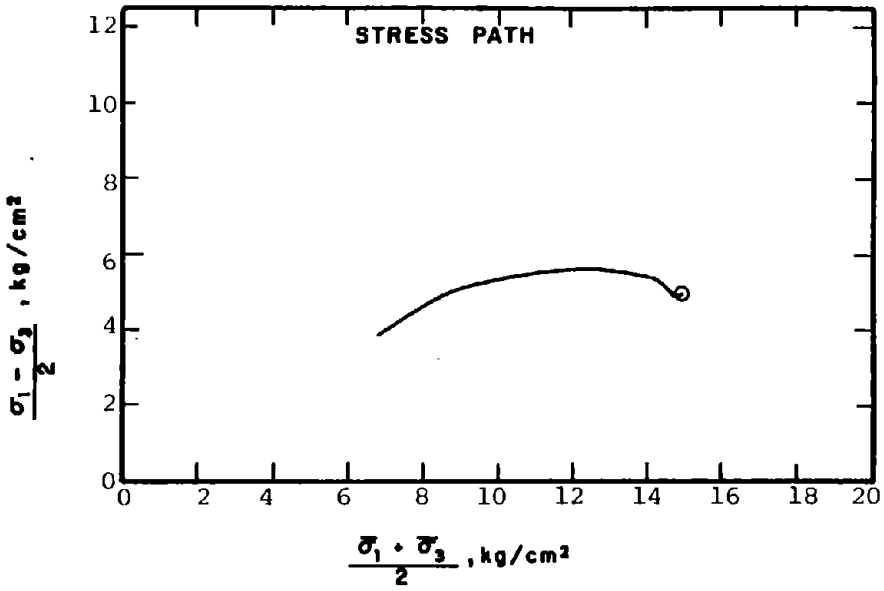

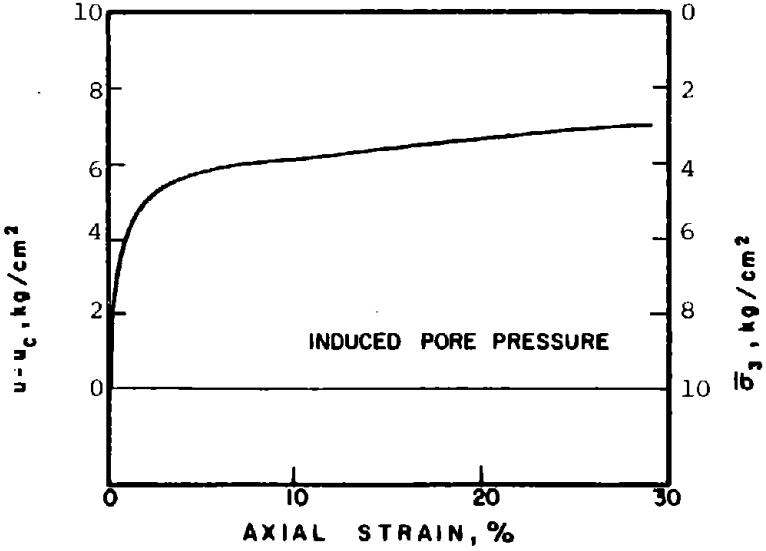

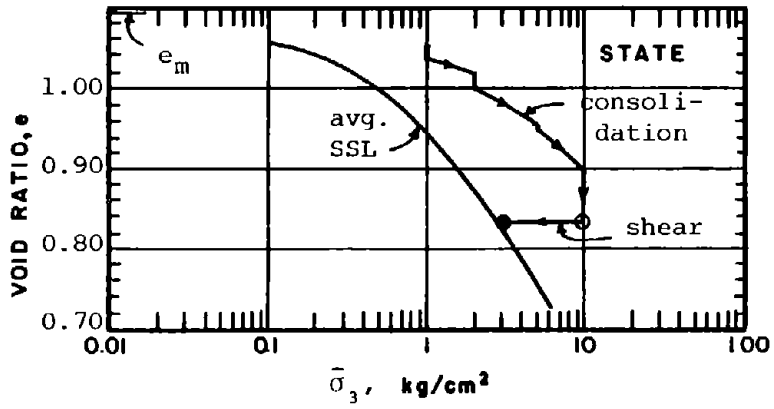

AR-1001

SOIL : Mine Tailings

STRUCTURE : Compacted Moist

STATE AFTER CONSOLIDATION: $\bar{\sigma}_{3c} = 10.00$ kg/cm^2, $\bar{\sigma}_{1c} = 20.00$ kg/cm^2

$e_c = 0.832$, $\gamma_{dc} = 91.3$ pcf

METHOD OF LOADING: Undrained, Axial Compression Load Control

TESTING DETAILS : Specimen Diameter 3.60 cm

: Specimen Height 5.30 cm

: End Platens: Lubricated, Type 2

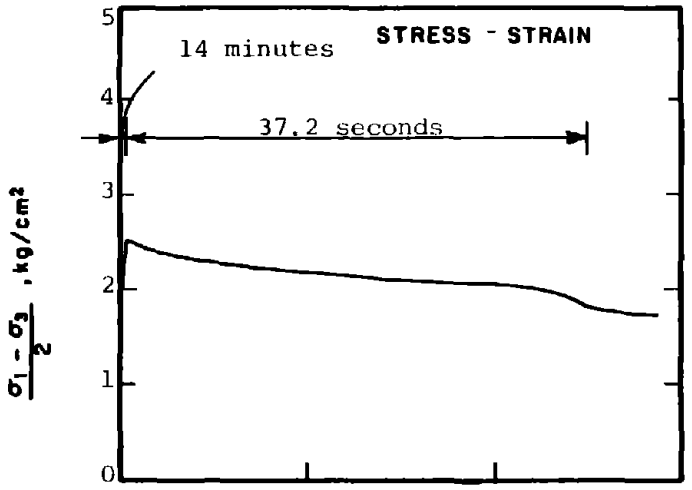

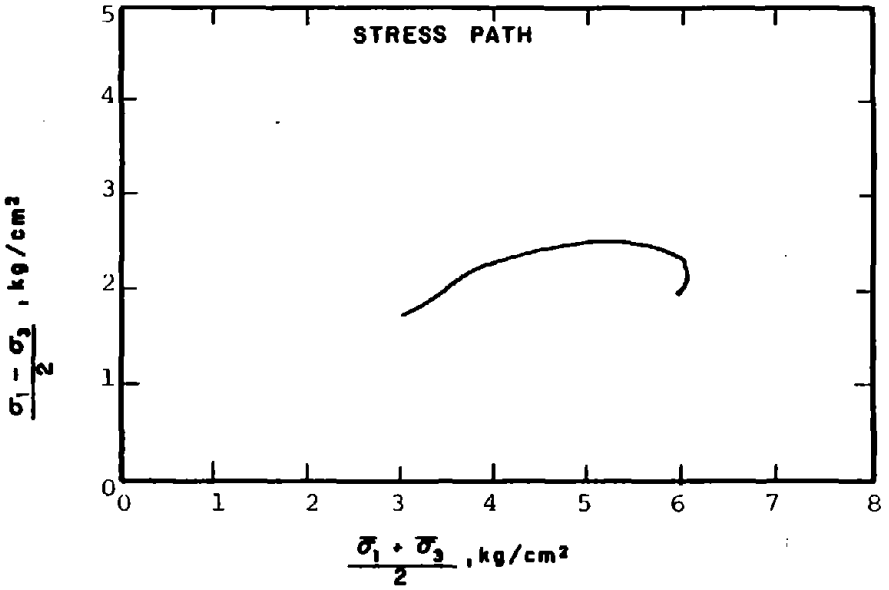

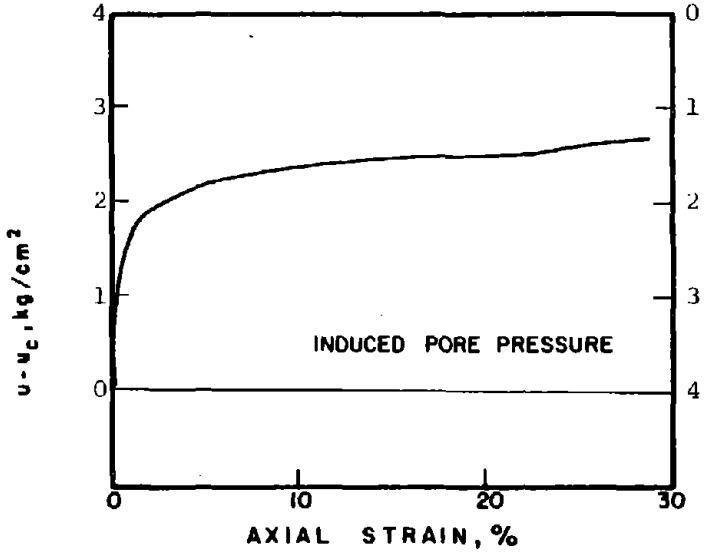

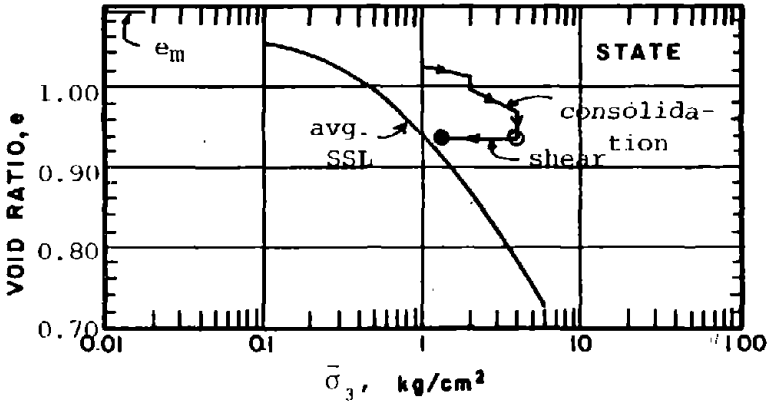

AR-1002

SOIL : Mine Tailings

STRUCTURE : Compacted Moist

STATE AFTER CONSOLIDATION: $\bar{\sigma}_{3c} = 4.00$ kg/cm², $\bar{\sigma}_{1c} = 8.00$ kg/cm²

$e_c = 0.936$, $\gamma_{dc} = 86.4$ pcf

METHOD OF LOADING: Undrained, Axial Compression Load Control

TESTING DETAILS : Specimen Diameter 3.60 cm

: Specimen Height 5.30 cm

: End Platens: Lubricated, Type 2

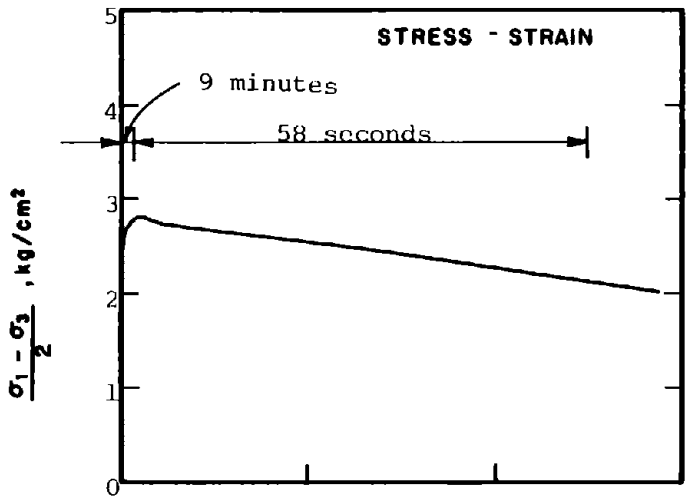

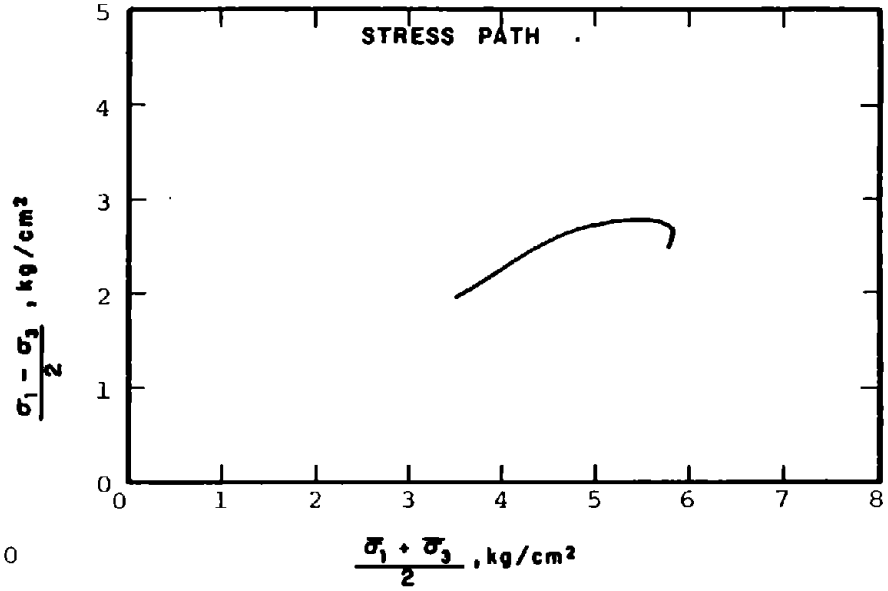

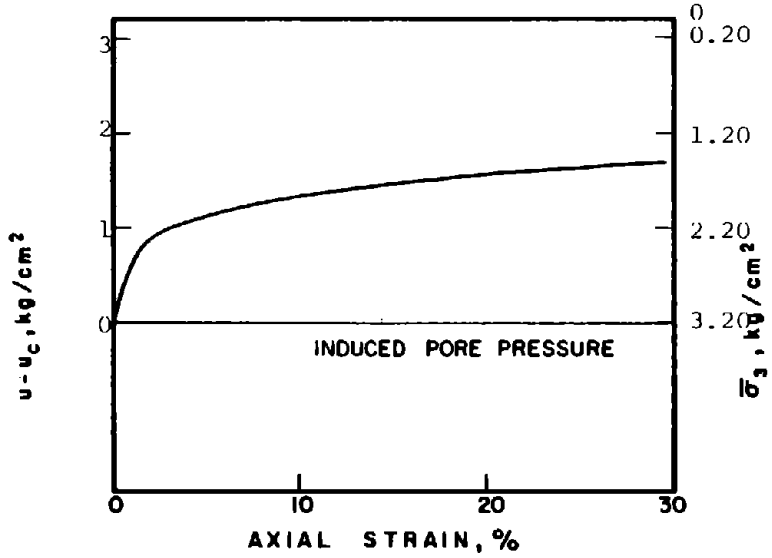

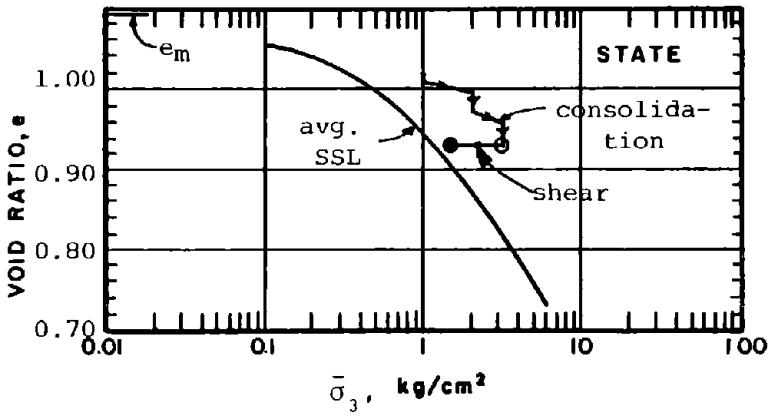

SOIL	: Mine Tailings	METHOD OF LOADING:	Undrained, Axial Compression Load Control
STRUCTURE	: Compacted Moist		
STATE AFTER CONSOLIDATION:	$\bar{\sigma}_{3c}$ = 3.20 kg/cm², $\bar{\sigma}_{1c}$ = 8.00 kg/cm²	TESTING DETAILS	: Specimen Diameter 3.60 cm
	e_c = 0.926, γ_{dc} = 86.8 pcf		: Specimen Height 5.30 cm
			: End Platens: Lubricated, Type 2

AR-1003

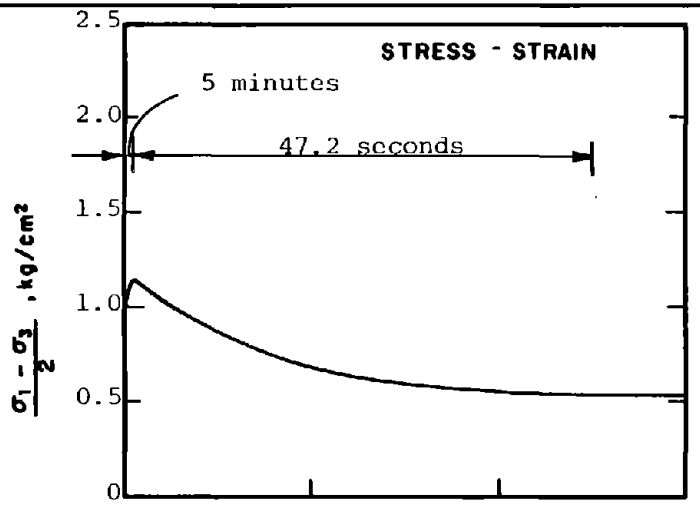

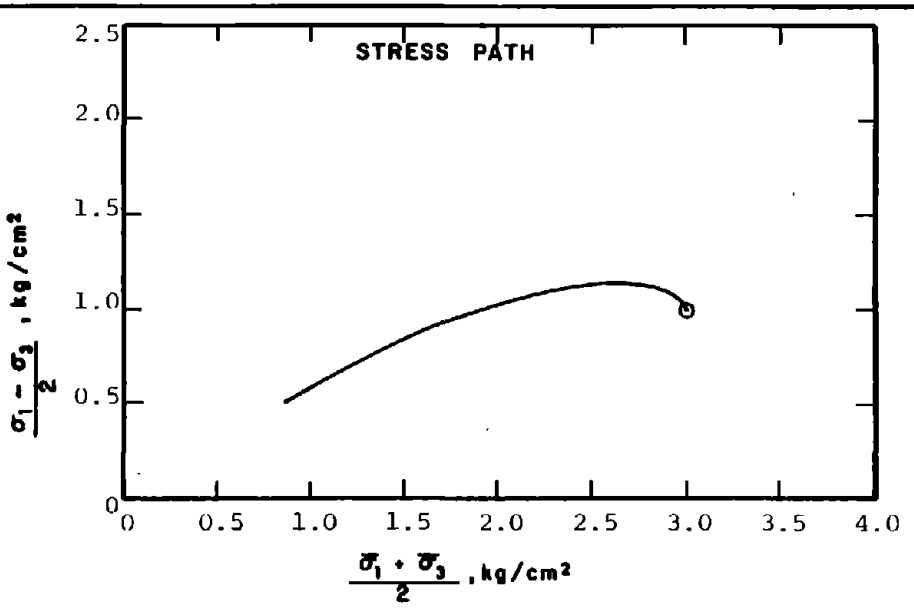

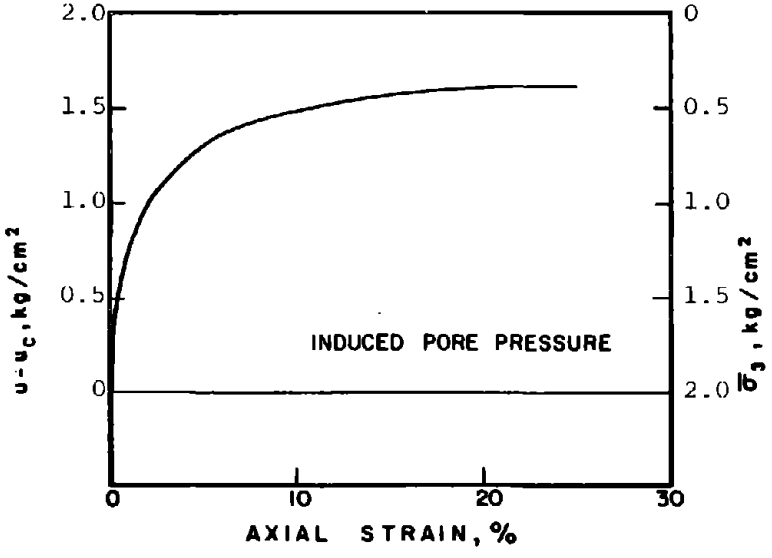

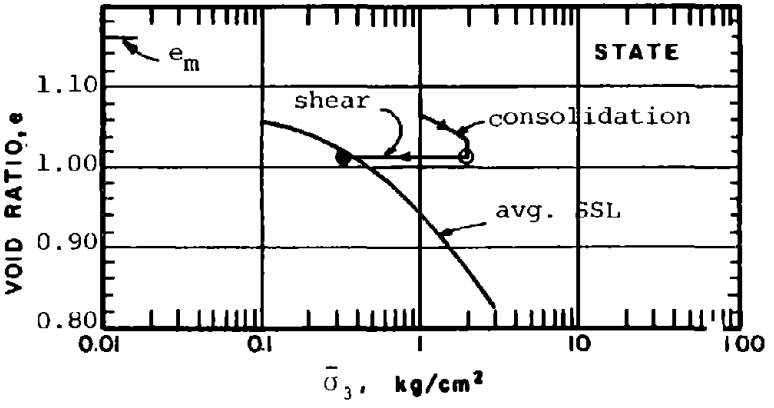

AR-1004

SOIL : Mine Tailings

STRUCTURE : Compacted Moist

STATE AFTER CONSOLIDATION: $\bar{\sigma}_{3c}$ = 2.00 kg/cm², $\bar{\sigma}_{1c}$ = 4.00 kg/cm²
e_c = 1.012 , γ_{dc} = 83.1 pcf

METHOD OF LOADING: Undrained, Axial Compression
Load Control

TESTING DETAILS : Specimen Diameter 3.60 cm
: Specimen Height 5.30 cm
: End Platens: Lubricated, Type 2

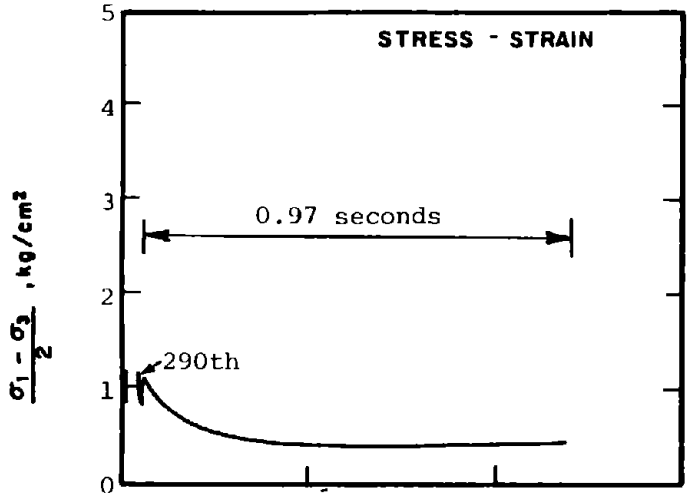

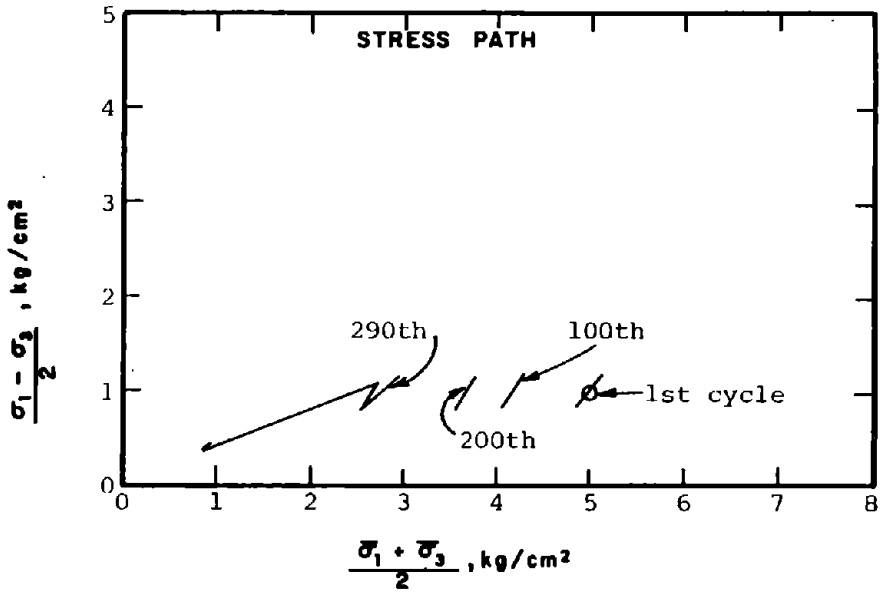

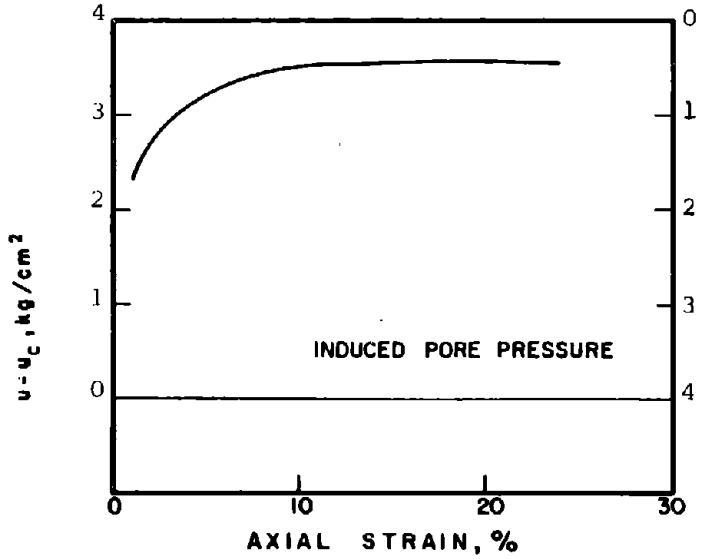

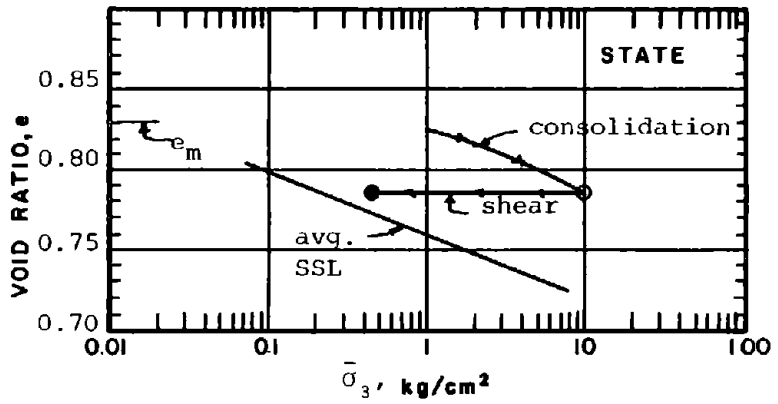

SOIL	: Banding Sand #6	METHOD OF LOADING:	Undrained, Cyclic Axial Compression
STRUCTURE	: Compacted Moist		Load Control
STATE AFTER CONSOLIDATION:	$\bar{\sigma}_{3c}$ = 4.00 kg/cm², $\bar{\sigma}_{1c}$ = 6.00 kg/cm²		$(\sigma_1 - \sigma_3)_{cy}$ = 0.39 ksc
	e_c = 0.766, γ_{dc} = 94.0 pcf	TESTING DETAILS :	Specimen Diameter 3.60 cm
		:	Specimen Height 5.30 cm
		:	End Platens: Lubricated, Type 2

CAR-602

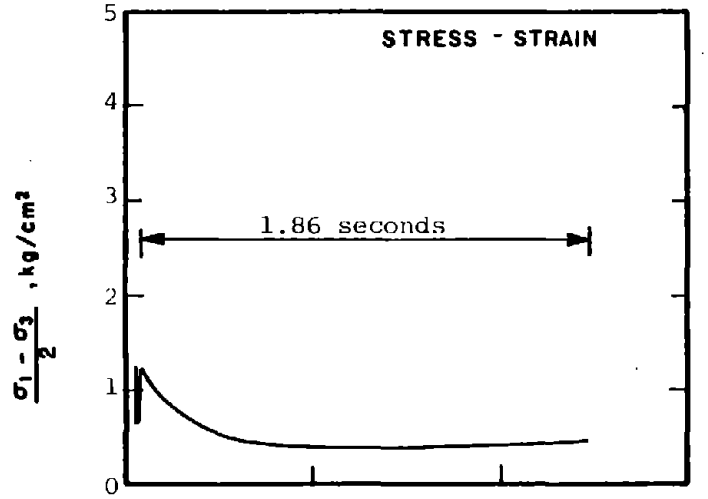

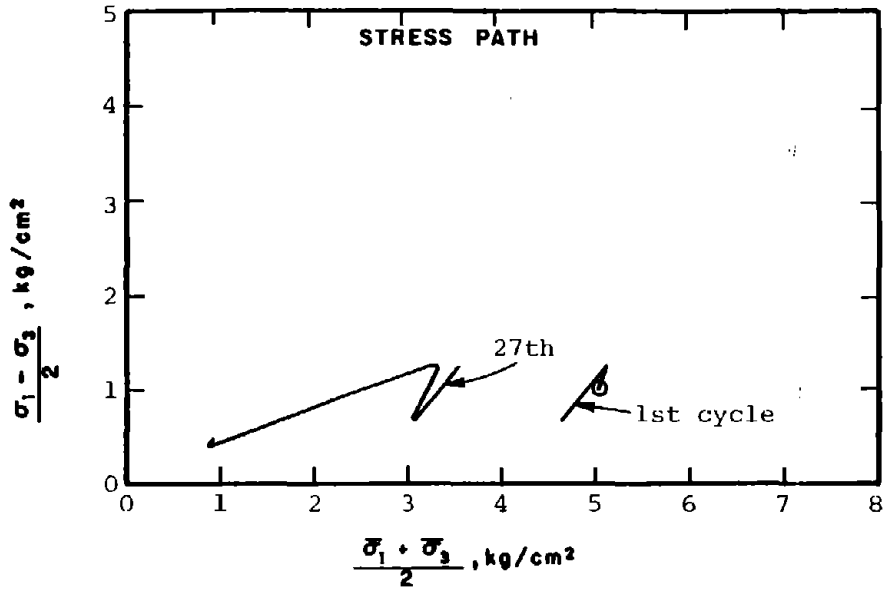

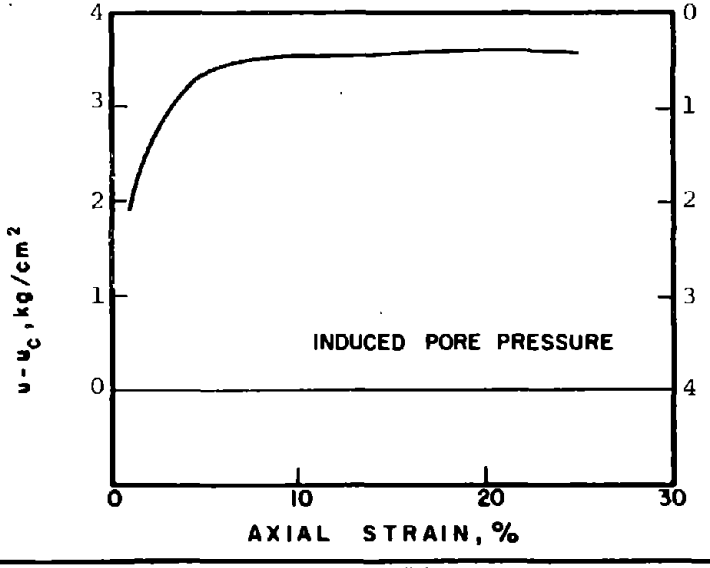

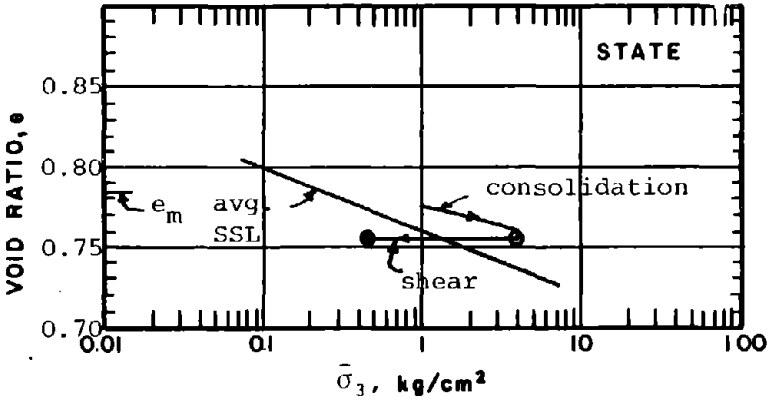

CAR-603

SOIL : Banding Sand #6

STRUCTURE : Compacted Moist

STATE AFTER CONSOLIDATION: $\bar{\sigma}_{3c}$ = 400 kg/cm², $\bar{\sigma}_{1c}$ = 6.00 kg/cm²

e_c = 0.755, γ_{dc} = 94.6 pcf

METHOD OF LOADING: Undrained, Cyclic Axial Compression Load Control

$(\sigma_1 - \sigma_3)_{cy}$ = 0.56 ksc

TESTING DETAILS : Specimen Diameter 3.60 cm

: Specimen Height 5.30 cm

: End Platens: Lubricated, Type 1

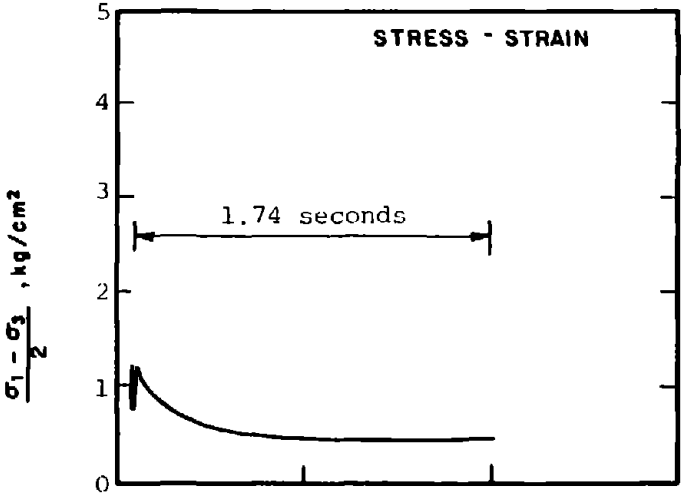

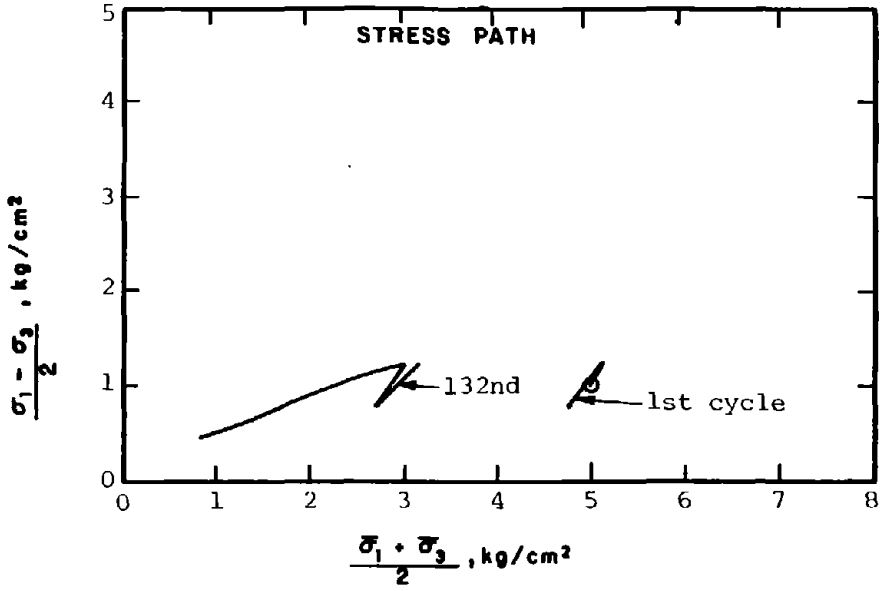

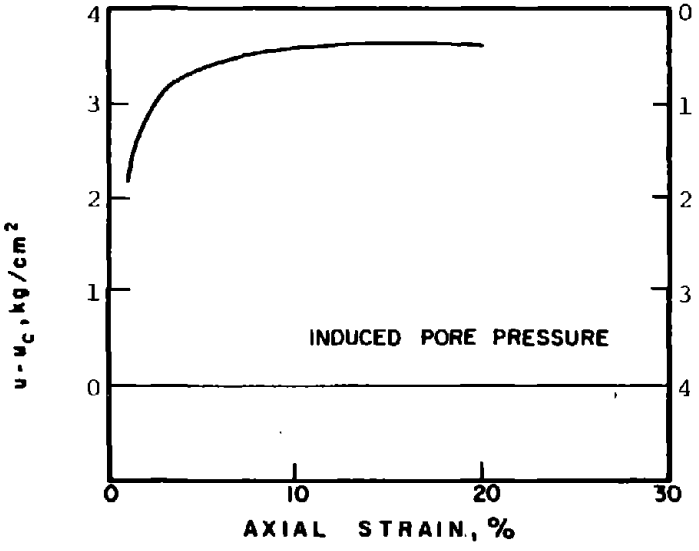

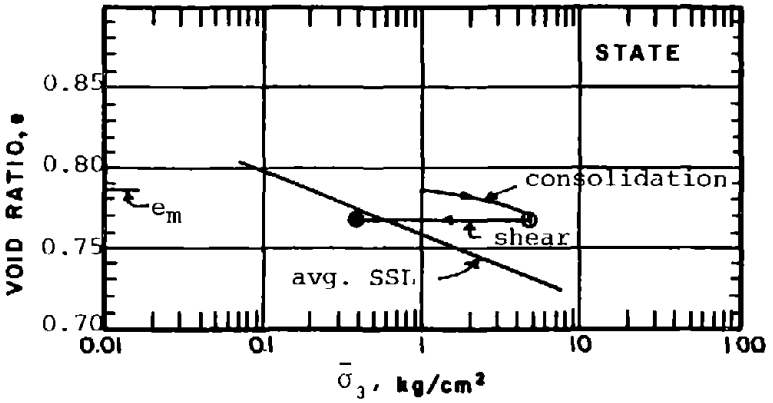

SOIL	: Banding Sand #6	METHOD OF LOADING:	Undrained, Cyclic Axial Compression
STRUCTURE	: Compacted Moist		Load Control
STATE AFTER CONSOLIDATION:	$\bar{\sigma}_{3c}$ = 4.00 kg/cm², $\bar{\sigma}_{1c}$ = 6.00 kg/cm²		$(\sigma_1 - \sigma_3)_{cy}$ = 0.44 ksc
	e_c = 0.768, γ_{dc} = 93.9 pcf	TESTING DETAILS :	Specimen Diameter 3.60 cm
		:	Specimen Height 5.30 cm
		:	End Platens: Lubricated, Type 1

CAR-604

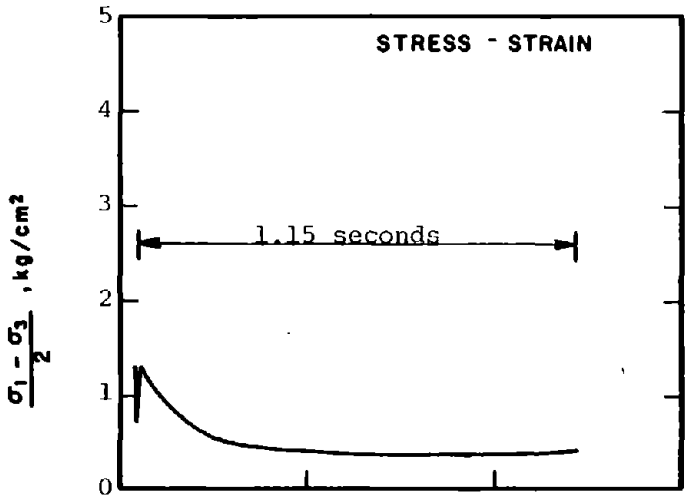

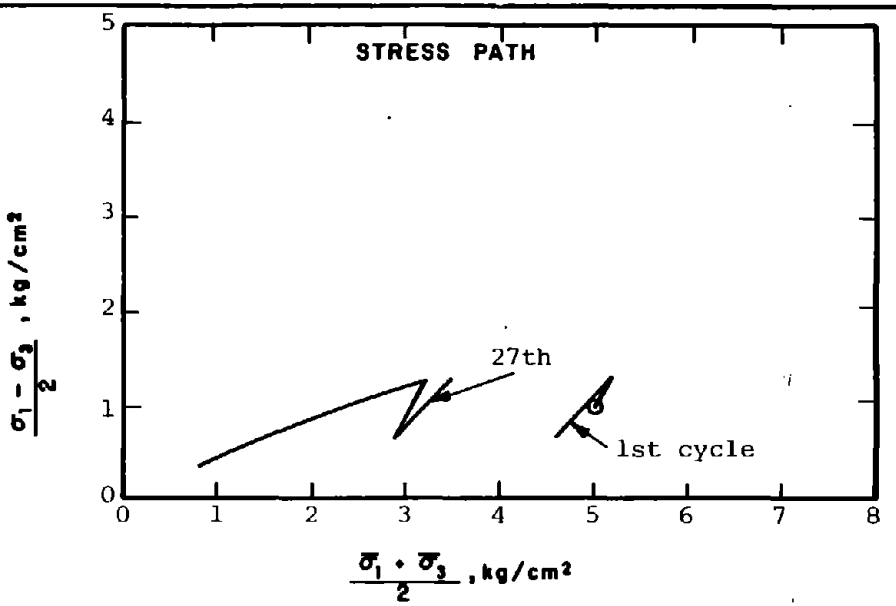

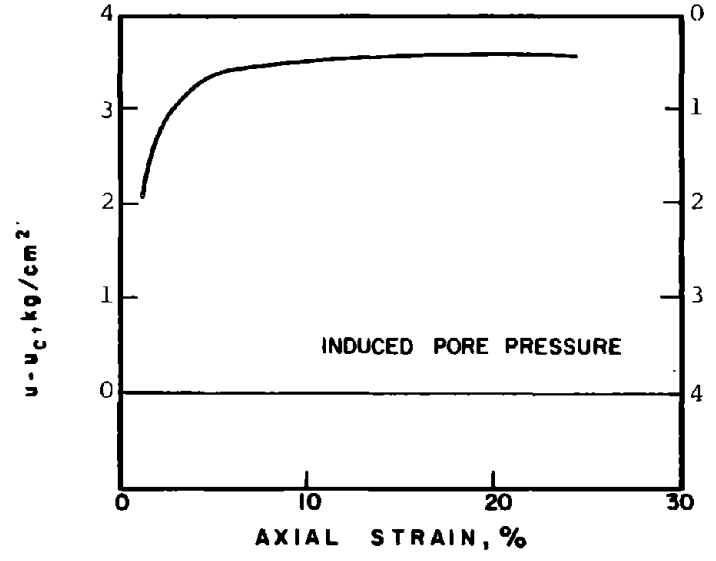

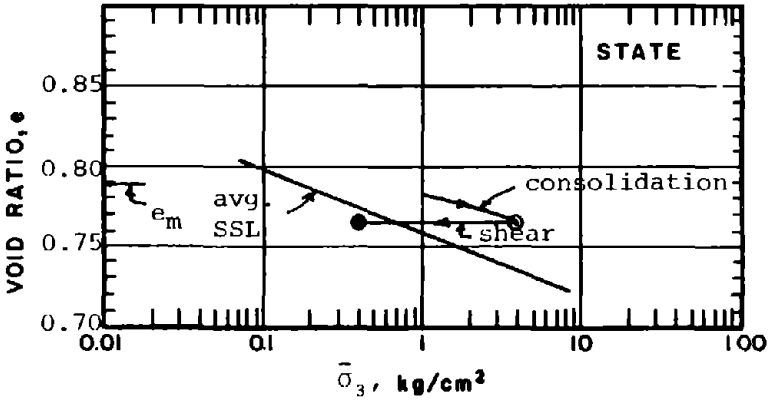

CAR-605

SOIL : Banding Sand #6

STRUCTURE : Compacted Moist

STATE AFTER CONSOLIDATION: $\bar{\sigma}_{3c}$ = 4.00 kg/cm², $\bar{\sigma}_{1c}$ = 6.00 kg/cm²

e_c = 0.764, γ_{dc} = 94.1 pcf

METHOD OF LOADING: Undrained, Cyclic Axial Compression Load Control

$(\sigma_1 - \sigma_3)_{cy}$ = 0.64 ksc

TESTING DETAILS : Specimen Diameter 3.60 cm

: Specimen Height 5.30 cm

: End Platens: Lubricated, Type 2

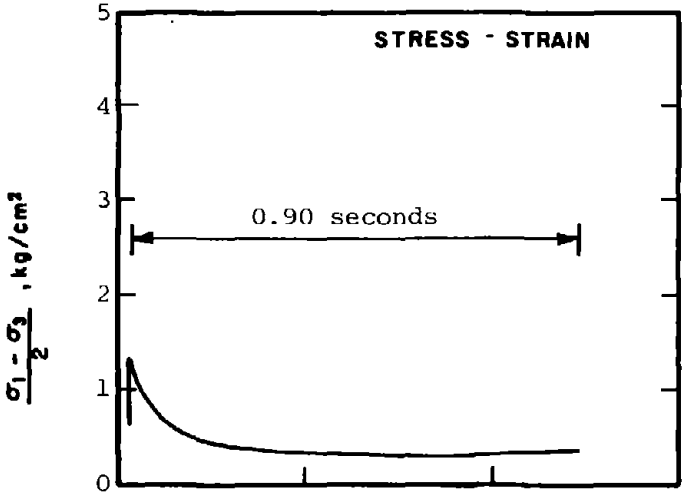

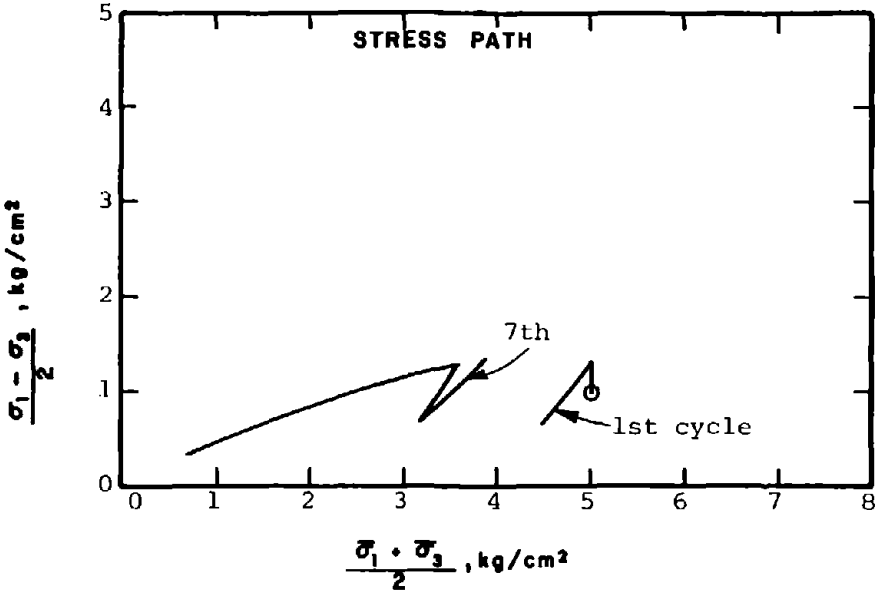

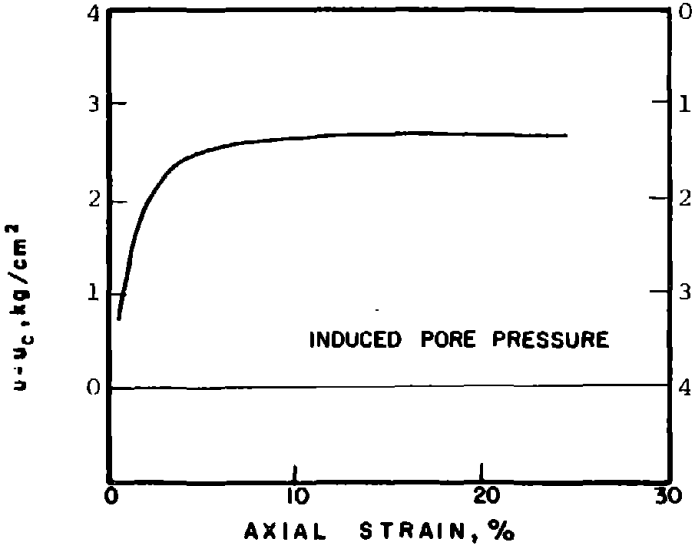

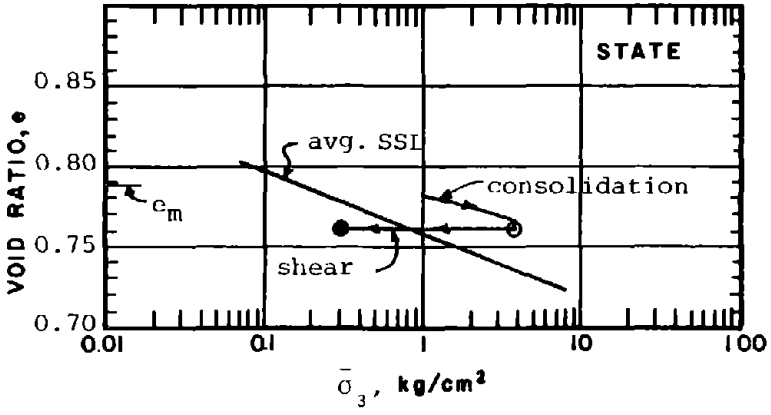

CAR-606

SOIL : Banding Sand #6

STRUCTURE : Compacted Moist

STATE AFTER CONSOLIDATION: $\bar{\sigma}_{3c}$ = 4.00 kg/cm², $\bar{\sigma}_{1c}$ = 6.00 kg/cm²
e_c = 0.762, γ_{dc} = 94.2 pcf

METHOD OF LOADING: Undrained, Cyclic Axial Compression
Load Control
$(\sigma_1 - \sigma_3)_{cy}$ = 0.72 ksc

TESTING DETAILS : Specimen Diameter 3.60 cm
: Specimen Height 5.30 cm
: End Platens: Lubricated, Type 2

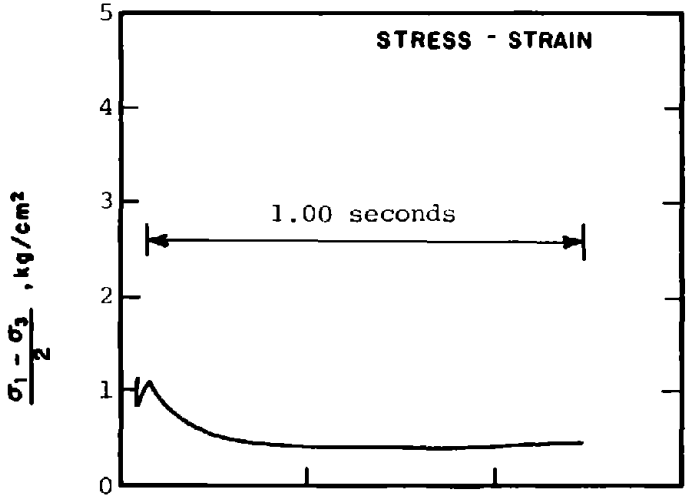

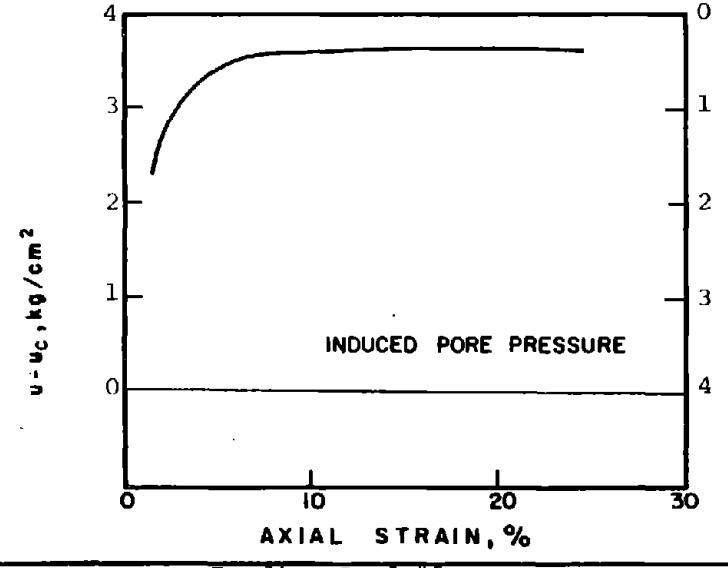

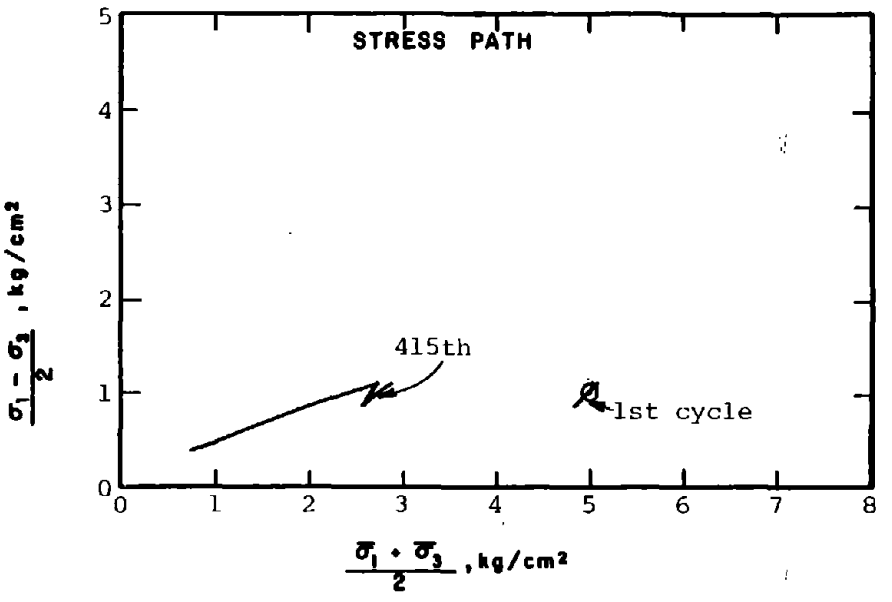

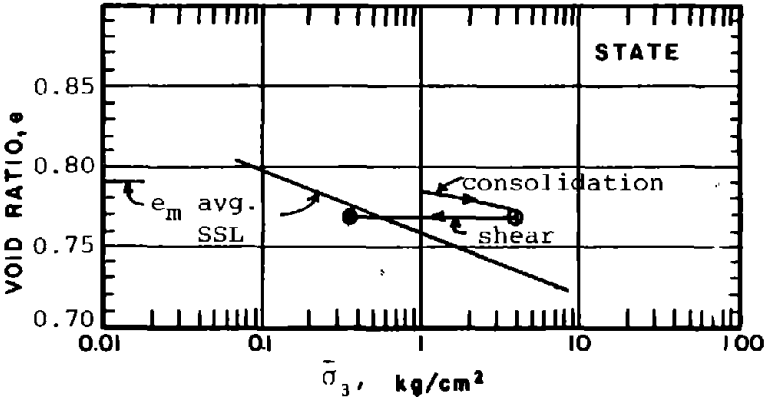

CAR-607

SOIL : Banding Sand #6

STRUCTURE : Compacted Moist

STATE AFTER CONSOLIDATION: $\bar{\sigma}_{3c}$ = 4.00 kg/cm², $\bar{\sigma}_{1c}$ = 6.00 kg/cm²

e_c = 0.768, γ_{dc} = 93.9 pcf

METHOD OF LOADING: Undrained, Cyclic Axial Compression
Load Control
$(\sigma_1 - \sigma_3)_{cy}$ = 0.34 ksc

TESTING DETAILS : Specimen Diameter 3.60 cm
: Specimen Height 5.30 cm
: End Platens: Lubricated, Type 1

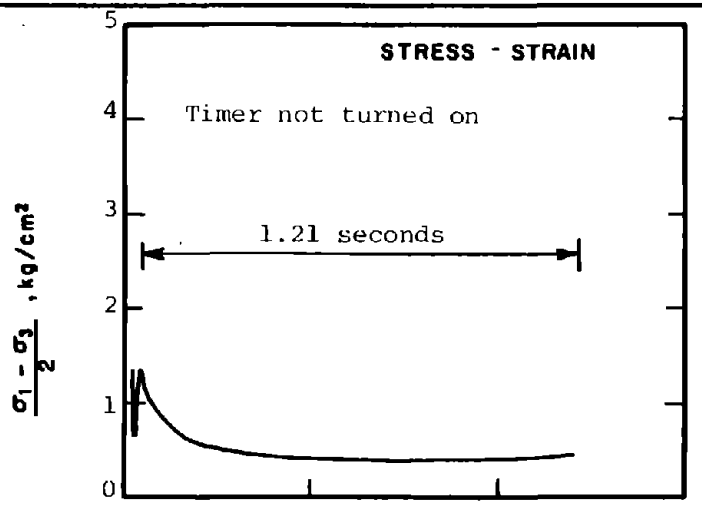

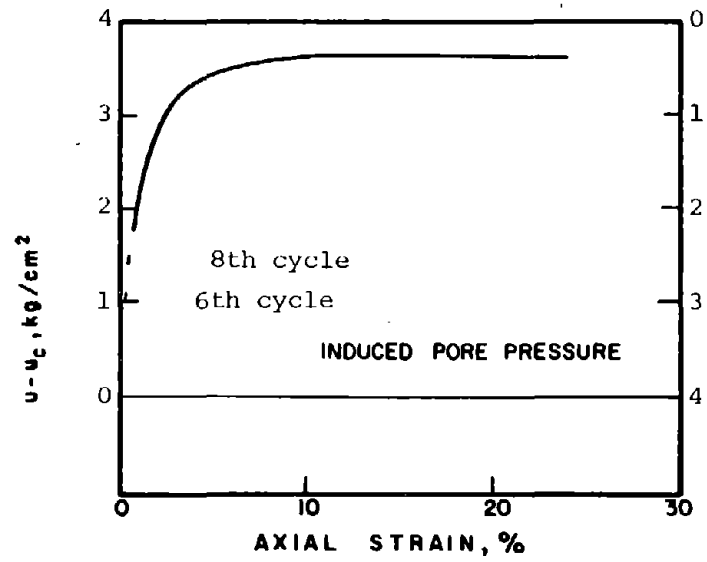

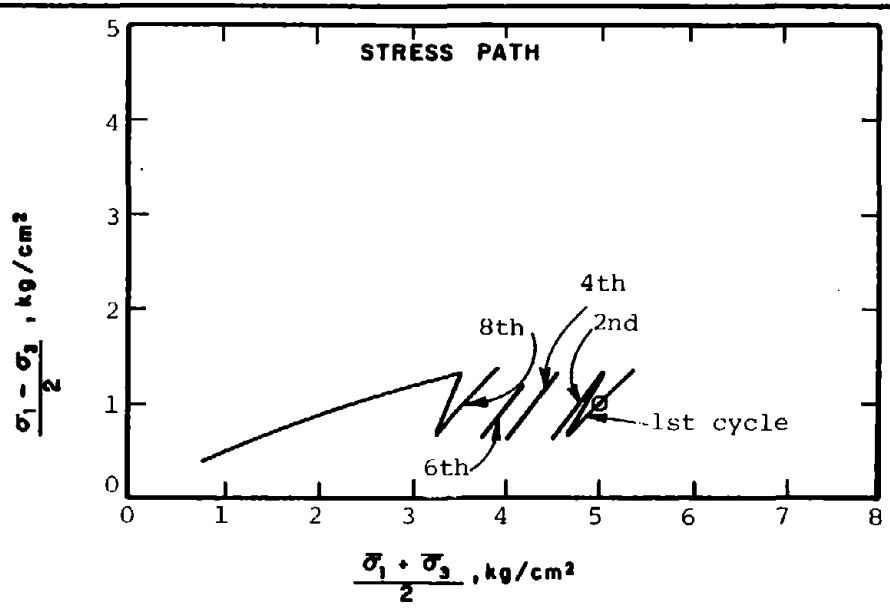

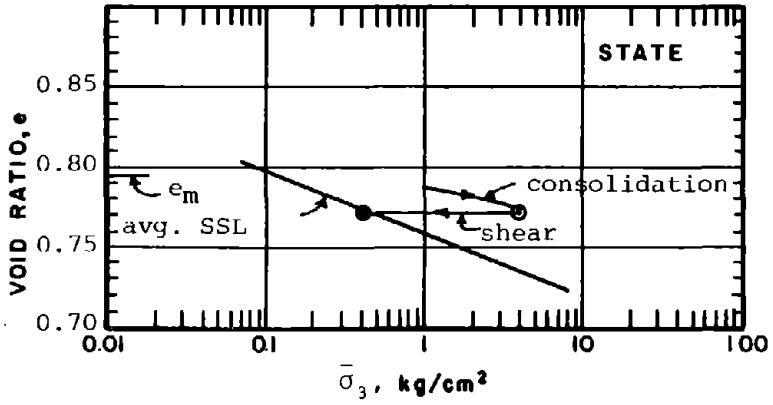

CAR-608

SOIL : Banding Sand #6

STRUCTURE : Compacted Moist

STATE AFTER CONSOLIDATION: $\bar{\sigma}_{3c} = 4.00$ kg/cm^2, $\bar{\sigma}_{1c} = 6.00$ kg/cm^2

$e_c = 0.771$, $\gamma_{dc} = 93.7$ pcf

METHOD OF LOADING: Undrained, Cyclic Axial Compression Load Control

$(\sigma_1 - \sigma_3)_{cy} = 0.72$ ksc

TESTING DETAILS : Specimen Diameter 3.60 cm

: Specimen Height 5.30 cm

: End Platens: Lubricated, Type 1

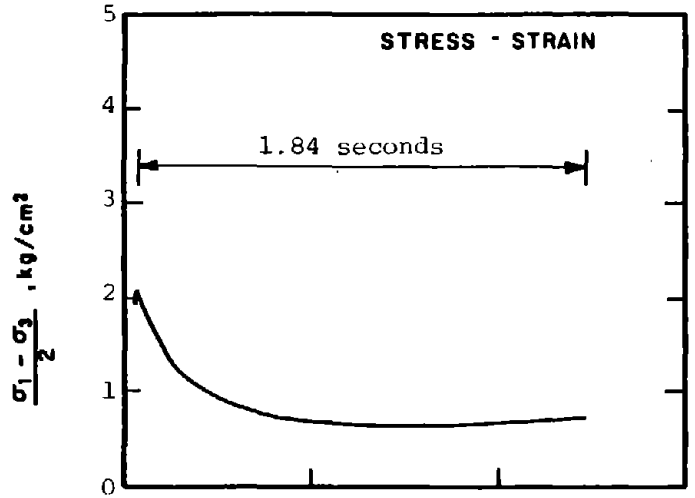

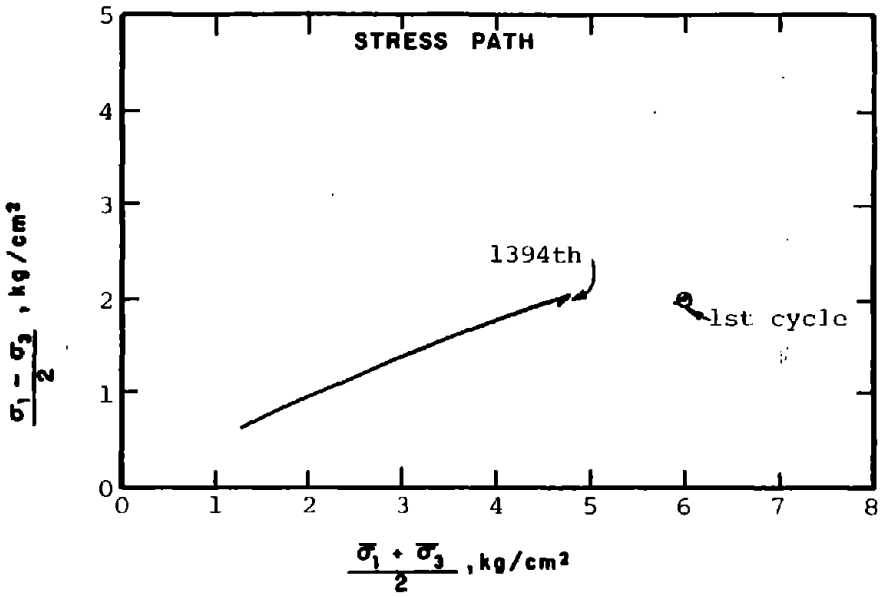

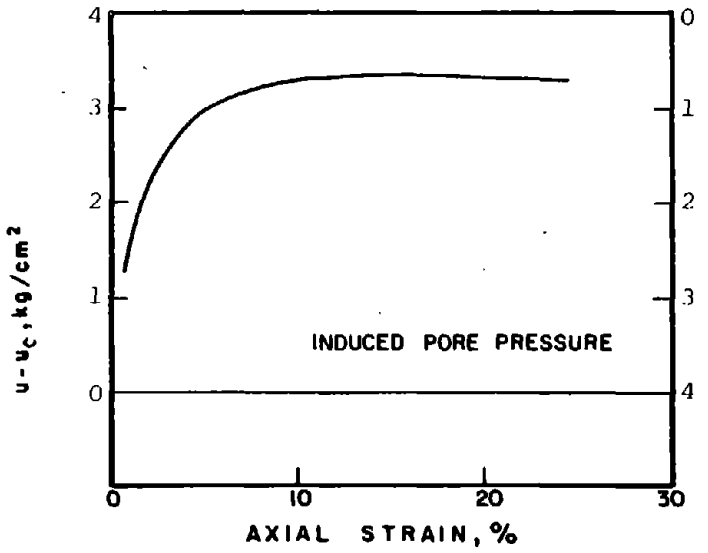

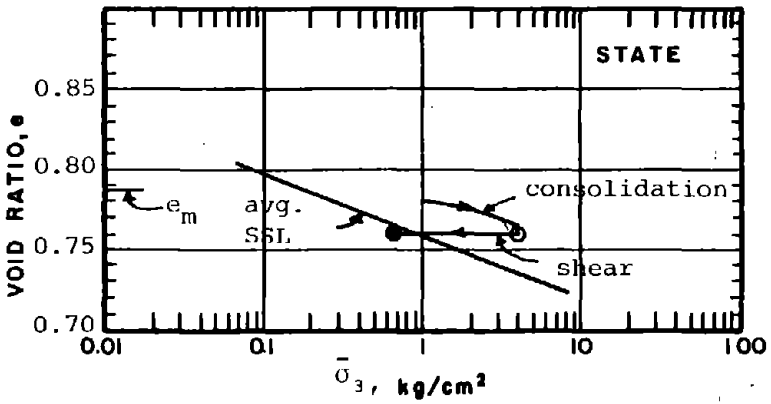

CAR-609

SOIL : Banding Sand #6

STRUCTURE : Compacted Moist

STATE AFTER CONSOLIDATION: $\bar{\sigma}_{3c}$ = 4.00 kg/cm², $\bar{\sigma}_{1c}$ = 8.00 kg/cm²
e_c = 0.760, γ_{dc} = 94.3 pcf

METHOD OF LOADING: Undrained, Cyclic Axial Compression
Load Control
$(\sigma_1 - \sigma_3)_{cy}$ = 0.14 ksc

TESTING DETAILS : Specimen Diameter 3.60 cm
: Specimen Height 5.30 cm
: End Platens: Lubricated, Type 1

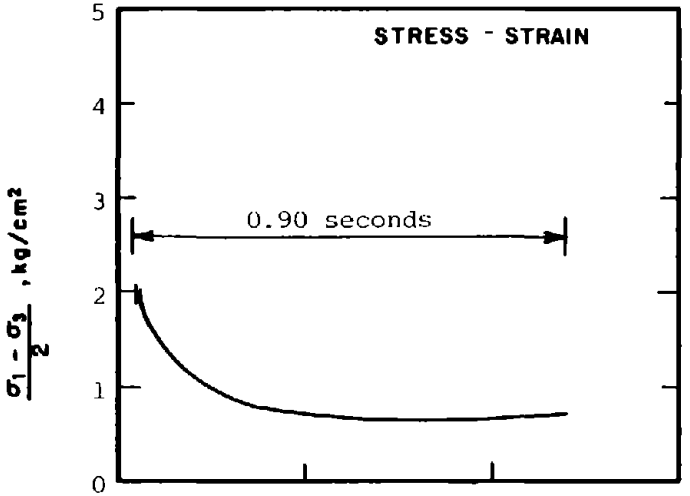

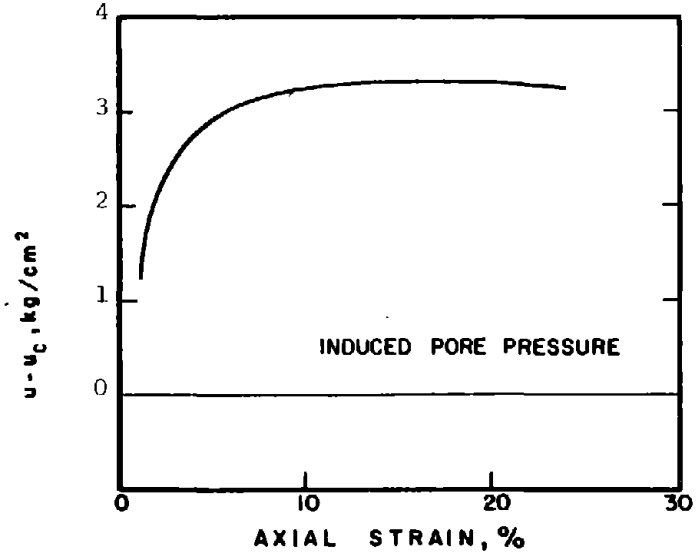

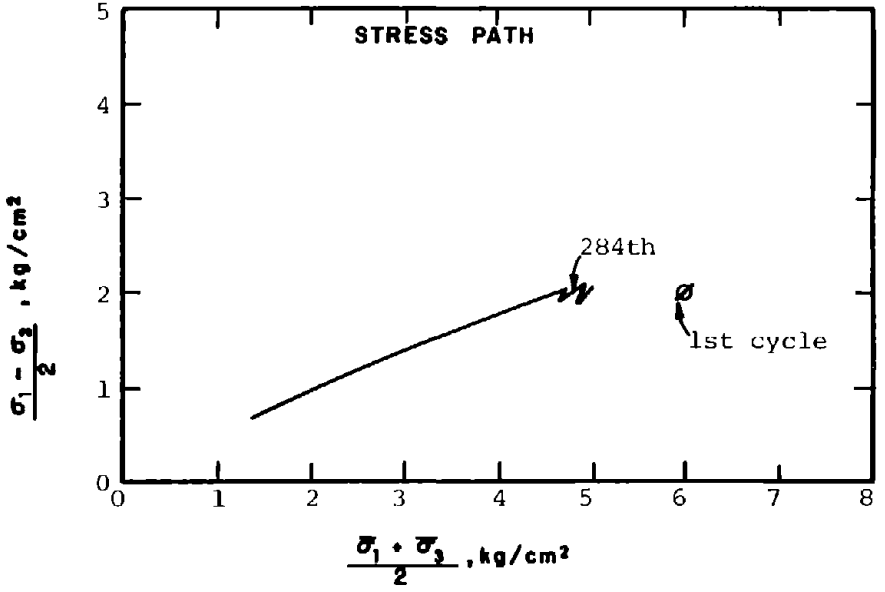

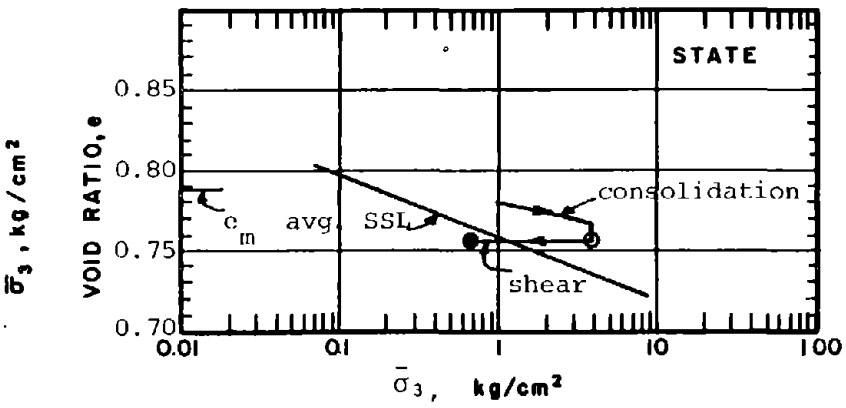

CAR-610

SOIL : Banding Sand #6

STRUCTURE : Compacted Moist

STATE AFTER CONSOLIDATION: $\bar{\sigma}_{3c} = 4.00$ kg/cm^2, $\bar{\sigma}_{1c} = 8.00$ kg/cm^2

$e_c = 0.756$, $\gamma_{dc} = 94.5$ pcf

METHOD OF LOADING: Undrained, Cyclic Axial Compression
Load Control
$(\sigma_1 - \sigma_3)_{cy} = 0.18$ ksc

TESTING DETAILS : Specimen Diameter 3.60 cm
: Specimen Height 5.30 cm
: End Platens: Lubricated, Type 1

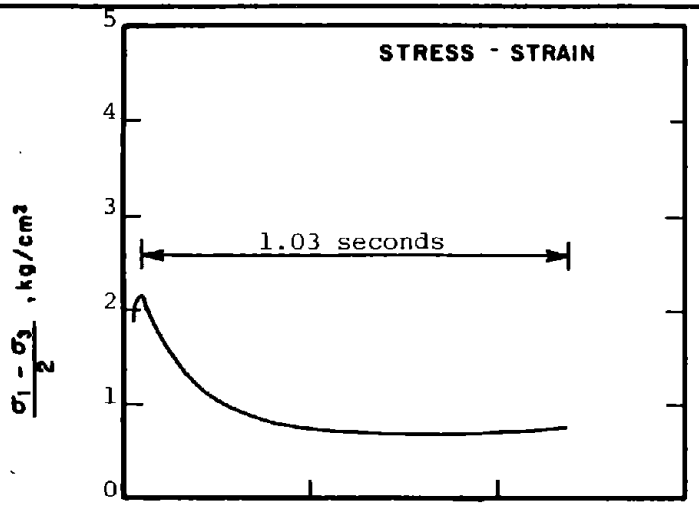

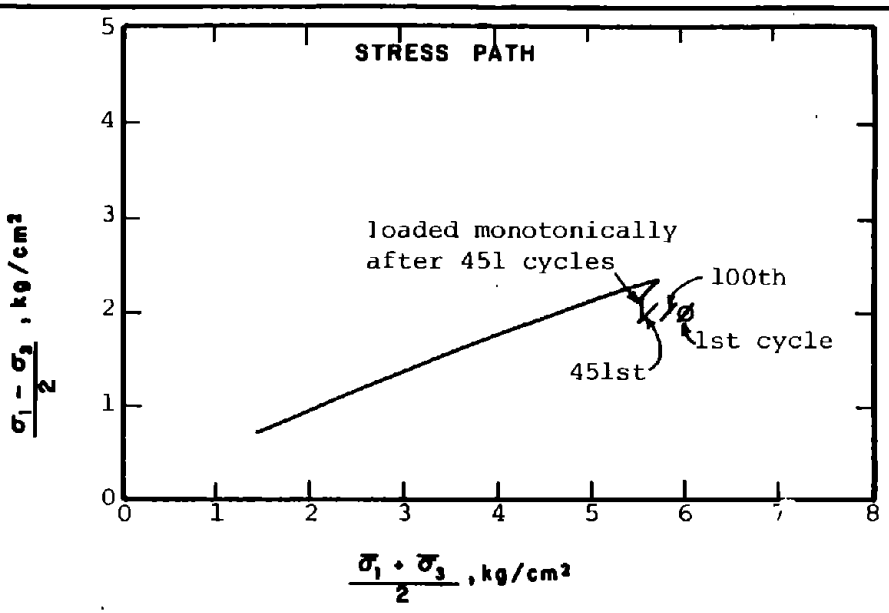

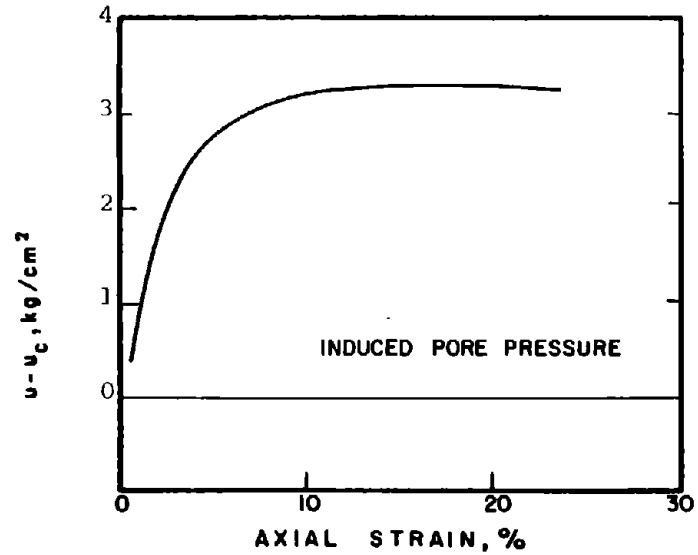

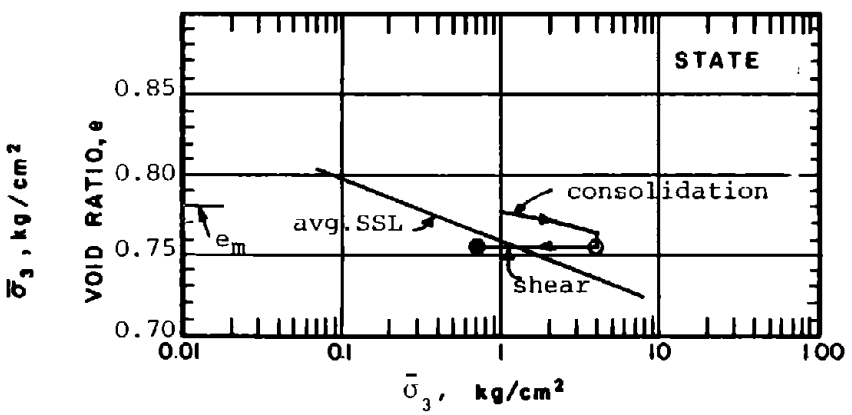

CAR-611

SOIL : Banding Sand #6

STRUCTURE : Compacted Moist

STATE AFTER CONSOLIDATION: $\bar{\sigma}_{3c} = 4.00\ kg/cm^2$, $\bar{\sigma}_{1c} = 8.00\ kg/cm^2$

$e_c = 0.754$, $\gamma_{dc} = 94.6\ pcf$

METHOD OF LOADING: Undrained, Cyclic Axial Compression Load Control

$(\sigma_1 - \sigma_3)_{cy} = 0.22\ ksc$

TESTING DETAILS : Specimen Diameter 3.60 cm

: Specimen Height 5.30 cm

: End Platens: Lubricated, Type 1

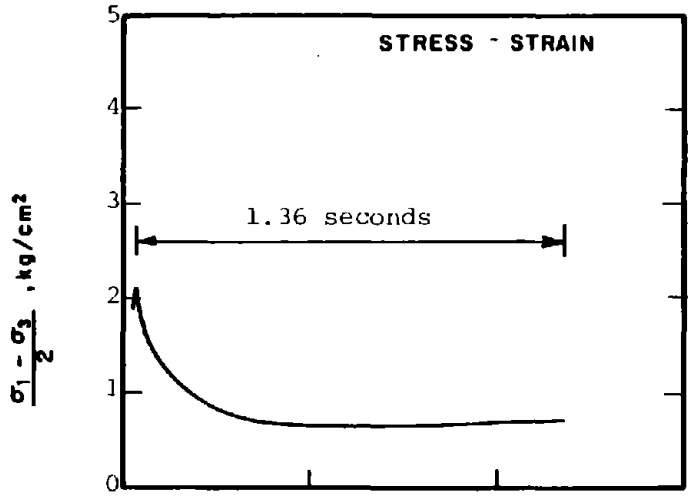

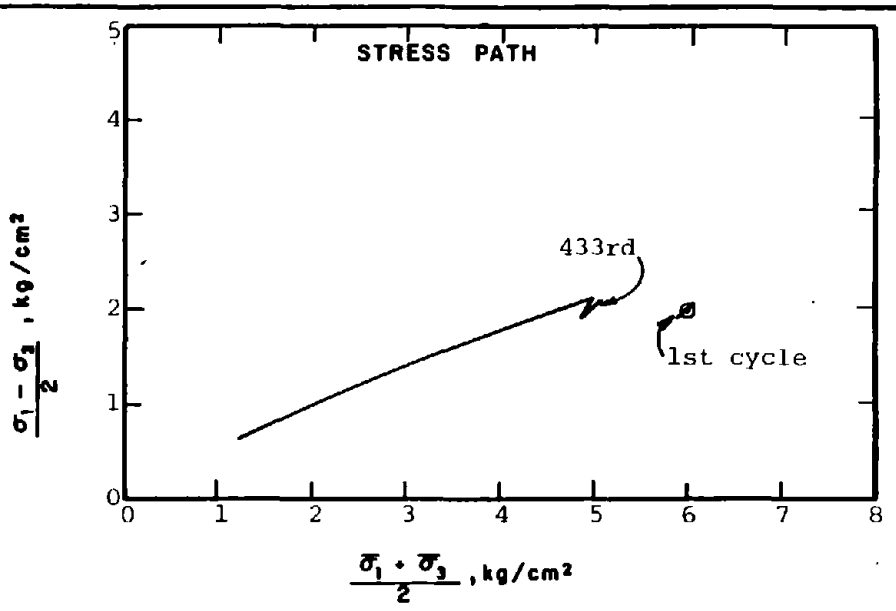

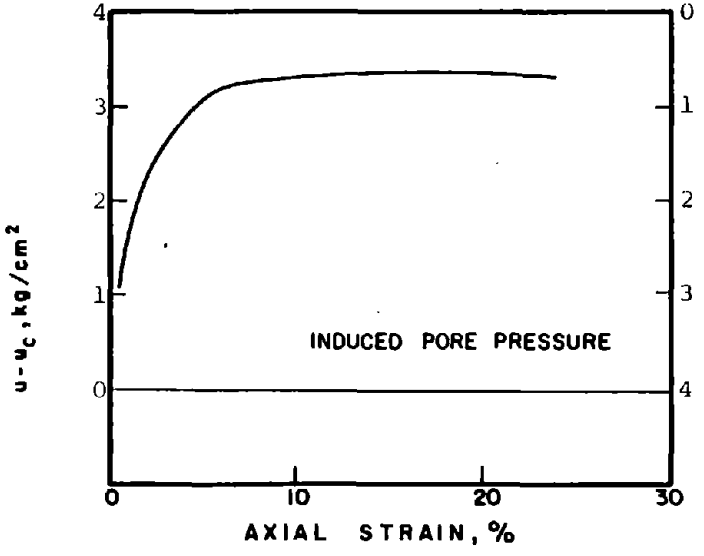

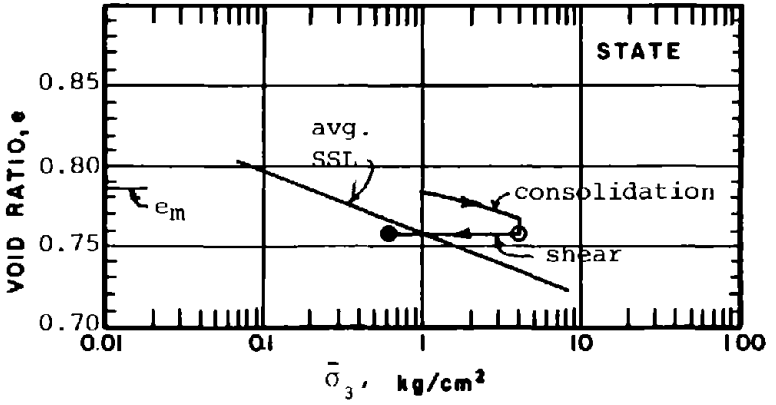

CAR-612

SOIL : Banding Sand #6

STRUCTURE : Compacted Moist

STATE AFTER CONSOLIDATION: $\bar{\sigma}_{3c} = 4.00\ kg/cm^2$, $\bar{\sigma}_{1c} = 8.00\ kg/cm^2$
$e_c = 0.758$, $\gamma_{dc} = 94.4$ pcf

METHOD OF LOADING: Undrained, Cyclic Axial Compression
Load Control
$(\sigma_1 - \sigma_3)_{cy} = 0.22$ ksc

TESTING DETAILS : Specimen Diameter 3.60 cm
: Specimen Height 5.30 cm
: End Platens: Lubricated, Type 1

HLC

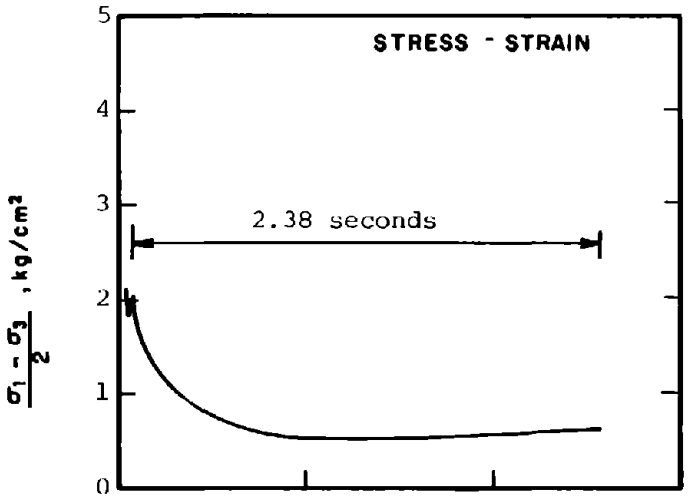

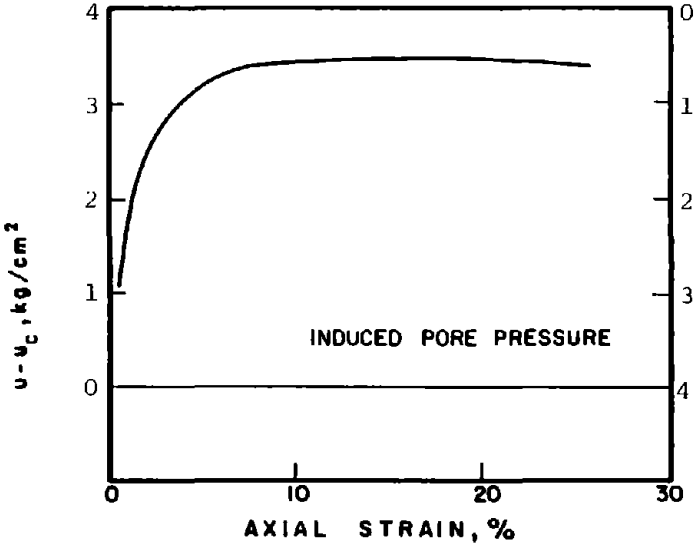

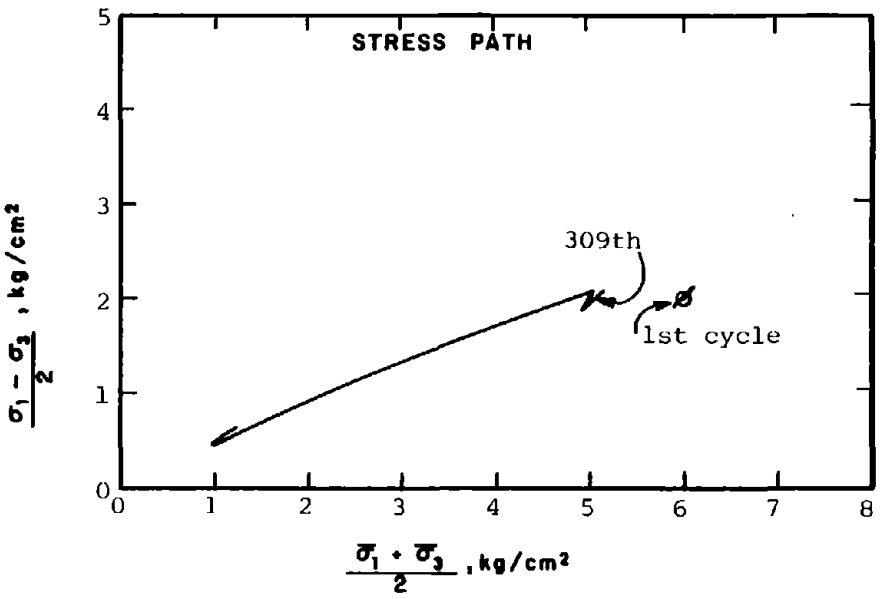

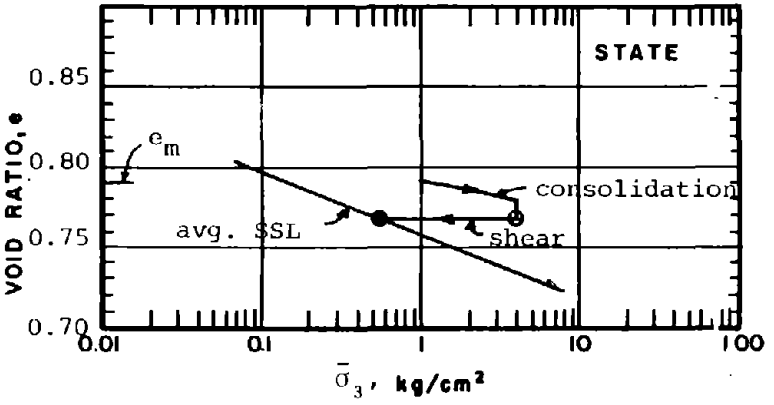

CAR-614

SOIL : Banding Sand #6

STRUCTURE : Compacted Moist

STATE AFTER CONSOLIDATION: $\bar{\sigma}_{3c}$ = 4.00 kg/cm^2, $\bar{\sigma}_{1c}$ = 8.00 kg/cm^2

e_c = 0.768, γ_{dc} = 93.9 pcf

METHOD OF LOADING: Undrained, Cyclic Axial Compression
Load Control
$(\sigma_1 - \sigma_3)_{cy}$ = 0.22 ksc

TESTING DETAILS : Specimen Diameter 3.60 cm
: Specimen Height 5.30 cm
: End Platens: Lubricated, Type 1

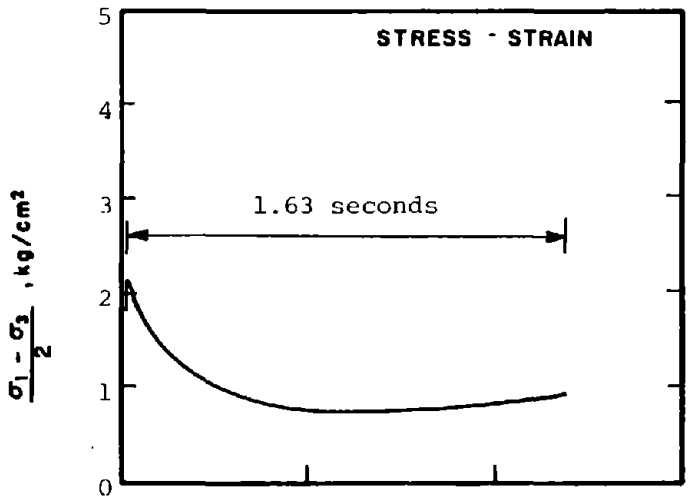

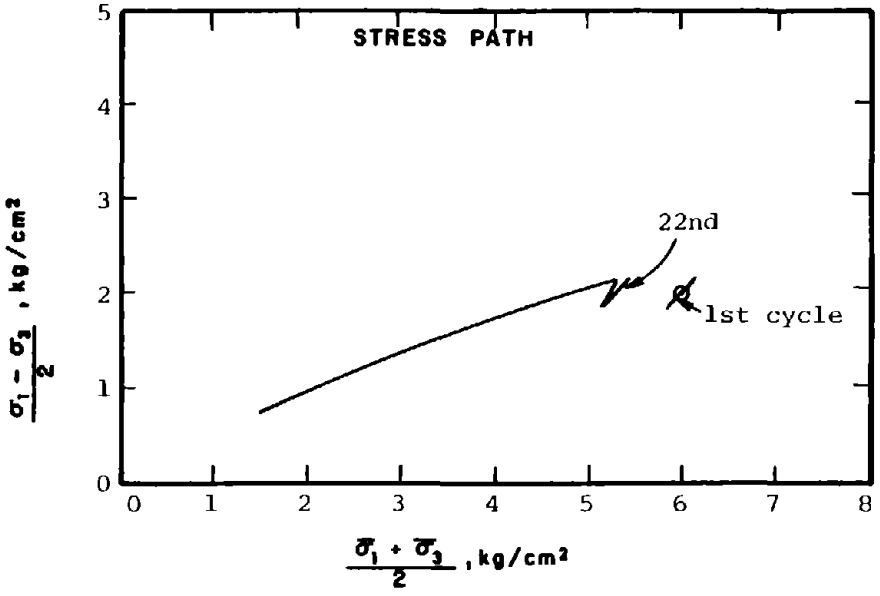

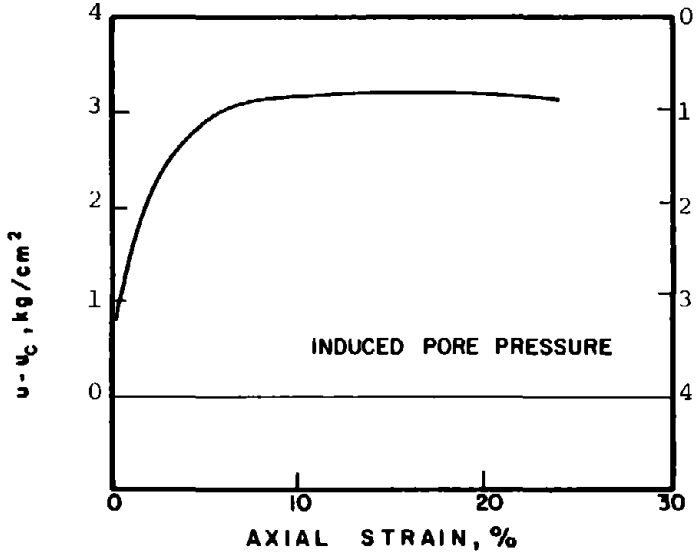

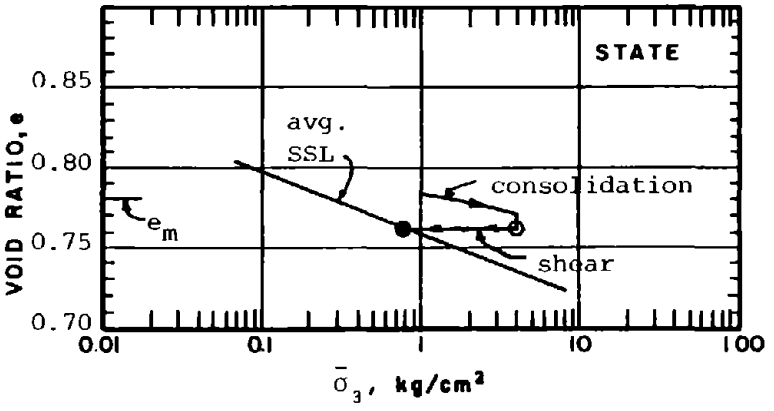

CAR-615

SOIL : Banding Sand #6

STRUCTURE : Compacted Moist

STATE AFTER CONSOLIDATION: $\bar{\sigma}_{3c} = 4.00$ kg/cm^2, $\bar{\sigma}_{1c} = 8.00$ kg/cm^2
$e_c = 0.762$, $\gamma_{dc} = 94.2$ pcf

METHOD OF LOADING: Undrained, Cyclic Axial Compression
Load Control
$(\sigma_1 - \sigma_3)_{cy} = 0.33$ ksc

TESTING DETAILS : Specimen Diameter 3.60 cm
: Specimen Height 5.30 cm
: End Platens: Lubricated, Type 2

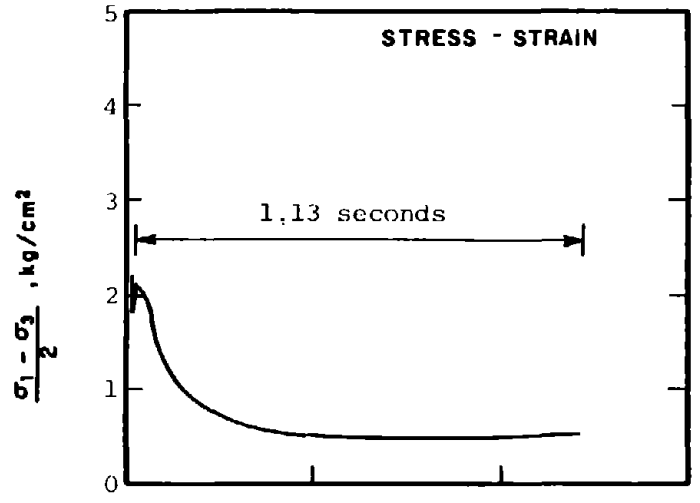

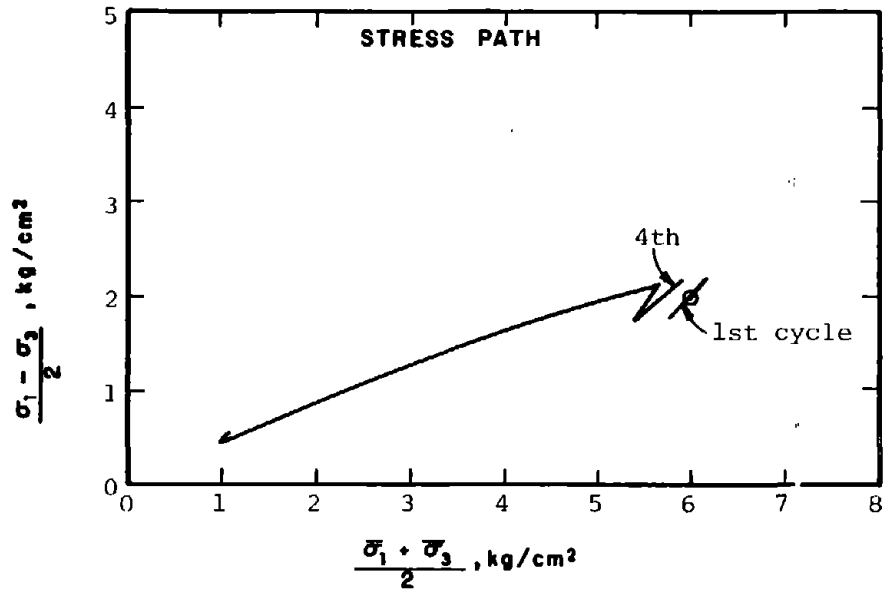

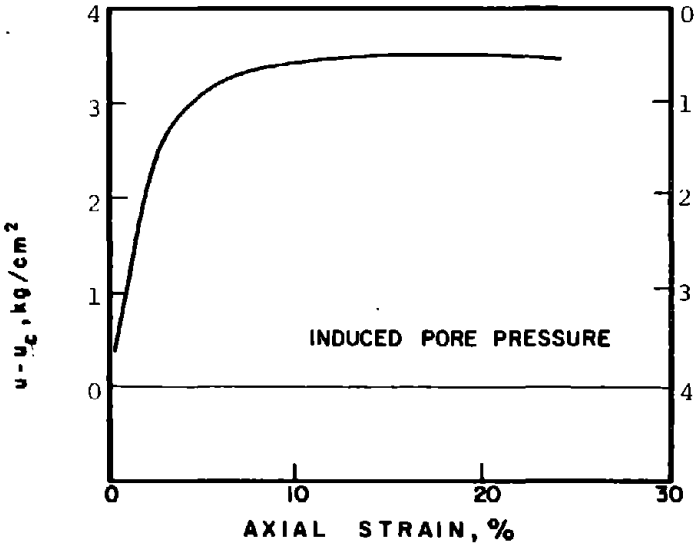

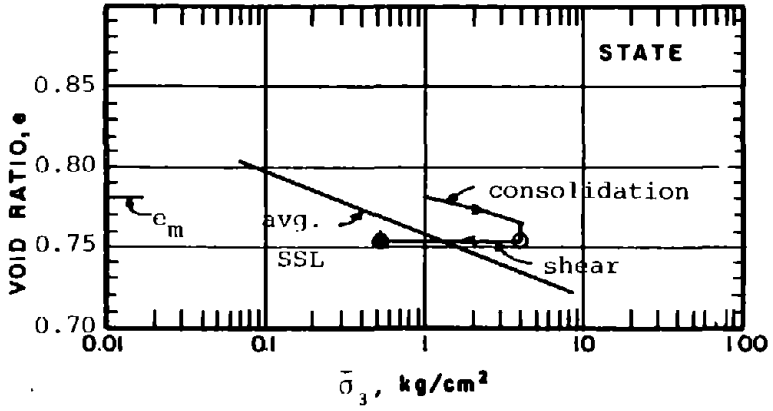

CAR-616

SOIL : Banding Sand #6

STRUCTURE : Compacted Moist

STATE AFTER CONSOLIDATION: $\bar{\sigma}_{3c}$ = 4.00 kg/cm², $\bar{\sigma}_{1c}$ = 8.00 kg/cm²
e_c = 0.753, γ_{dc} = 94.7 pcf

METHOD OF LOADING: Undrained, Cyclic Axial Compression
Load Control
$(\sigma_1 - \sigma_3)_{cy}$ = 0.41 ksc

TESTING DETAILS : Specimen Diameter 3.60 cm
: Specimen Height 5.30 cm
: End Platens: Lubricated, Type 2

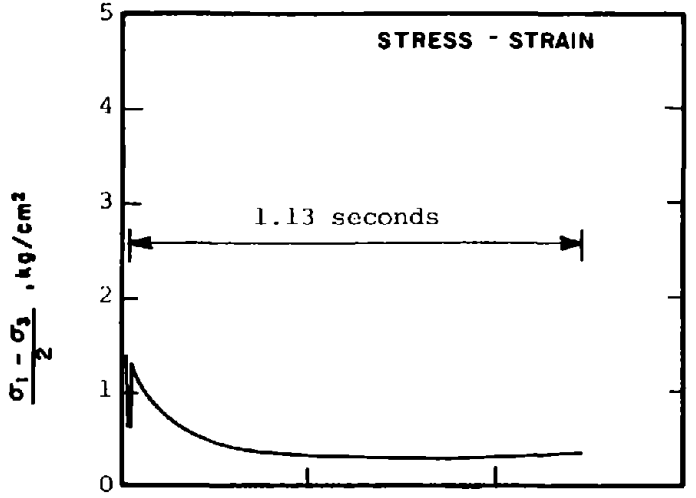

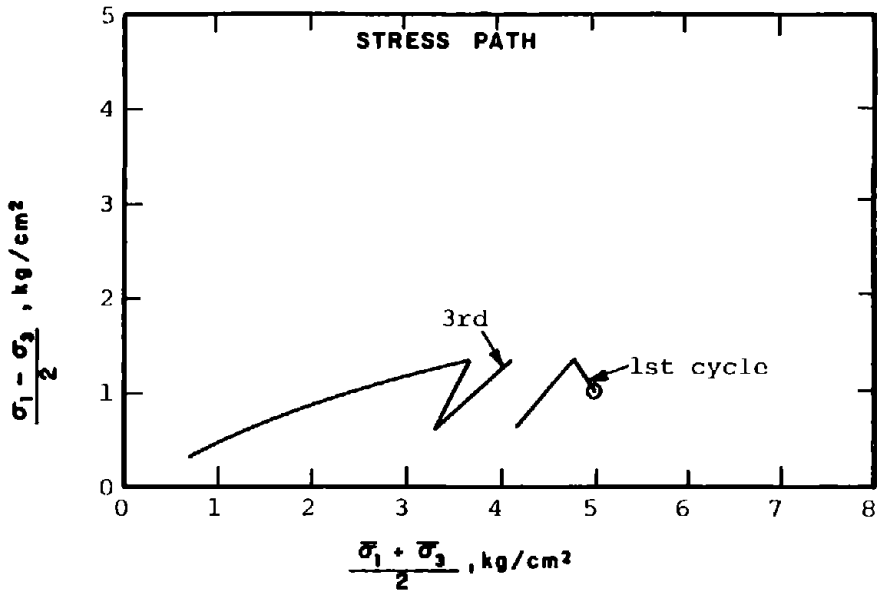

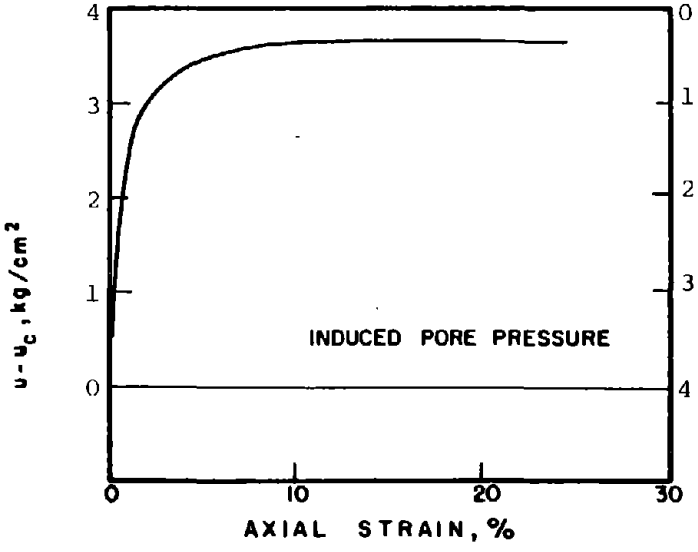

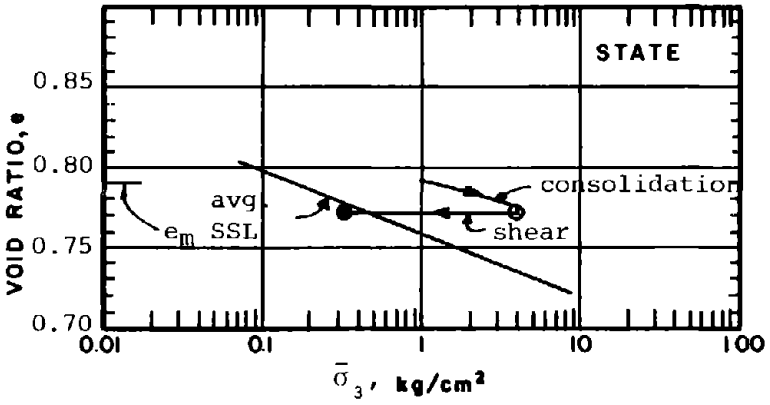

CAR-617

SOIL : Banding Sand #6

STRUCTURE : Compacted Moist

STATE AFTER CONSOLIDATION: $\bar{\sigma}_{3c}$ = 4.00 kg/cm², $\bar{\sigma}_{1c}$ = 6.00 kg/cm²

e_c = 0.771, γ_{dc} = 93.7 pcf

METHOD OF LOADING: Undrained, Cyclic Axial Compression
Load Control
$(\sigma_1 - \sigma_3)_{cy}$ = 0.76 ksc

TESTING DETAILS : Specimen Diameter 3.60 cm
: Specimen Height 5.30 cm
: End Platens: Lubricated, Type 2

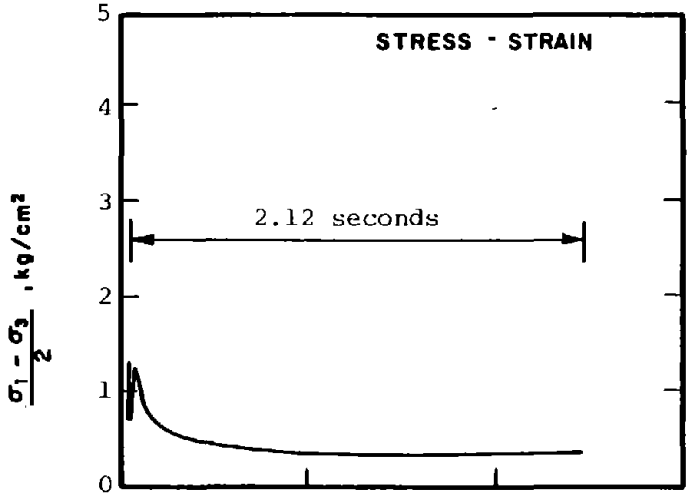

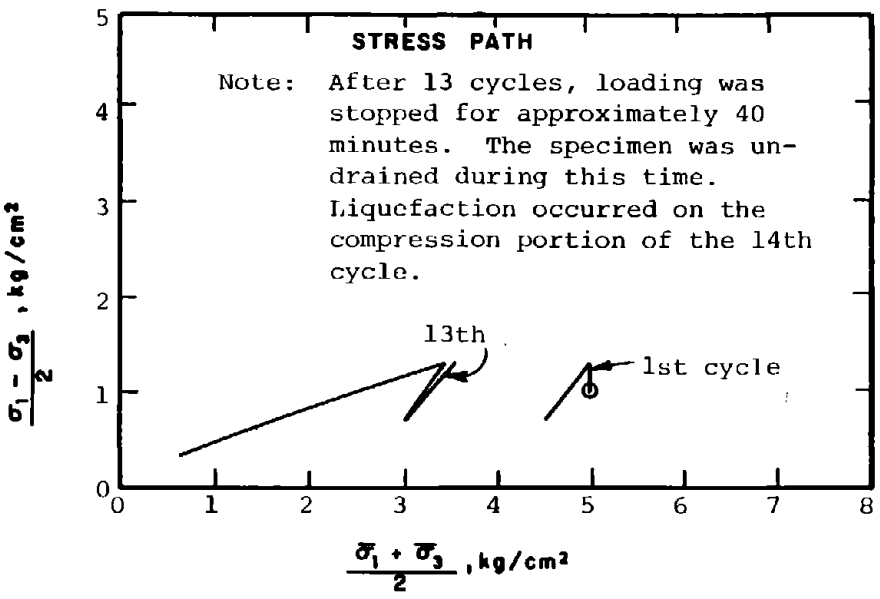

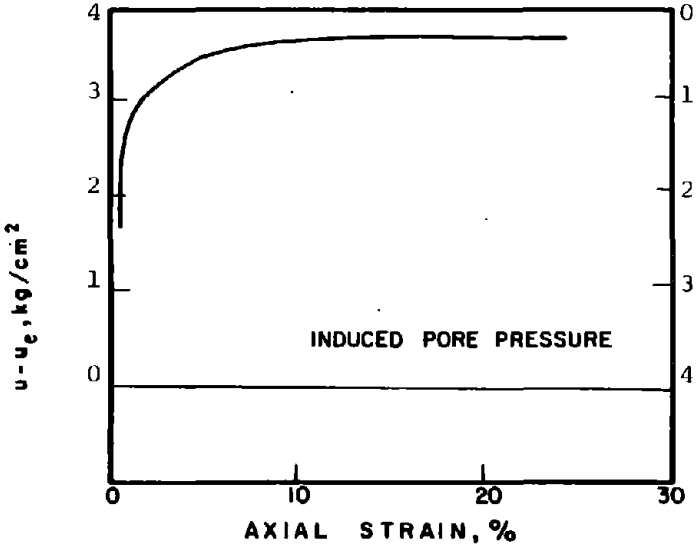

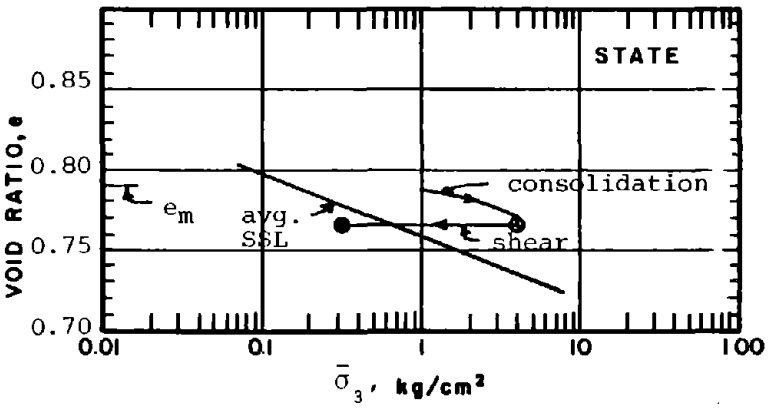

CAR-618

SOIL : Banding Sand #6

STRUCTURE : Compacted Moist

STATE AFTER CONSOLIDATION: $\bar{\sigma}_{3c}$ = 4.00 kg/cm², $\bar{\sigma}_{1c}$ = 6.00 kg/cm²
e_c = 0.766, γ_{dc} = 94.0 pcf

METHOD OF LOADING: Undrained, Cyclic Axial Compression
Load Control
$(\sigma_1 - \sigma_3)_{cy}$ = 0.60 ksc

TESTING DETAILS : Specimen Diameter 3.60 cm
: Specimen Height 5.30 cm
: End Platens: Lubricated, Type 2

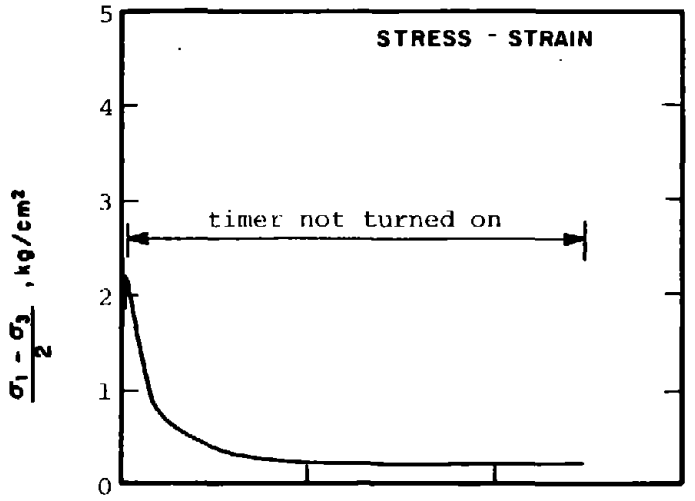

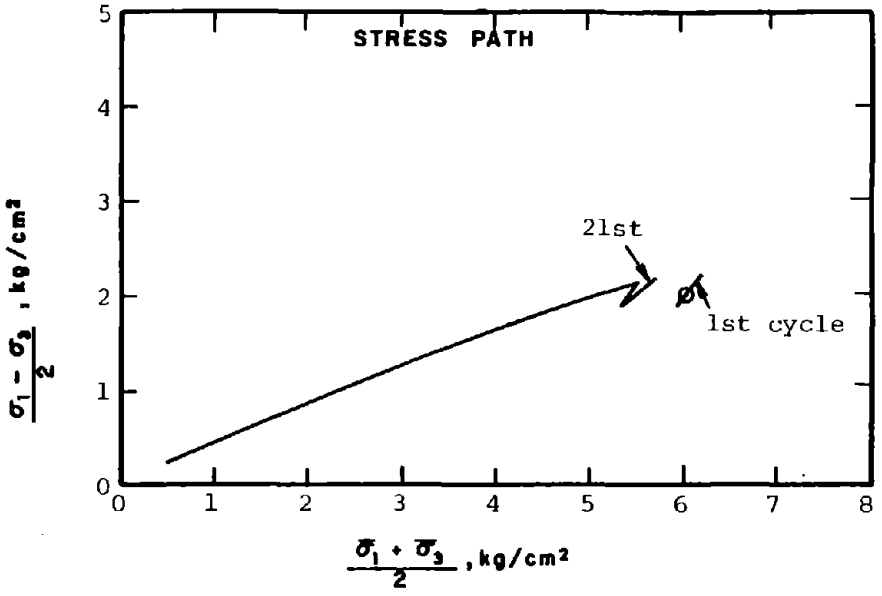

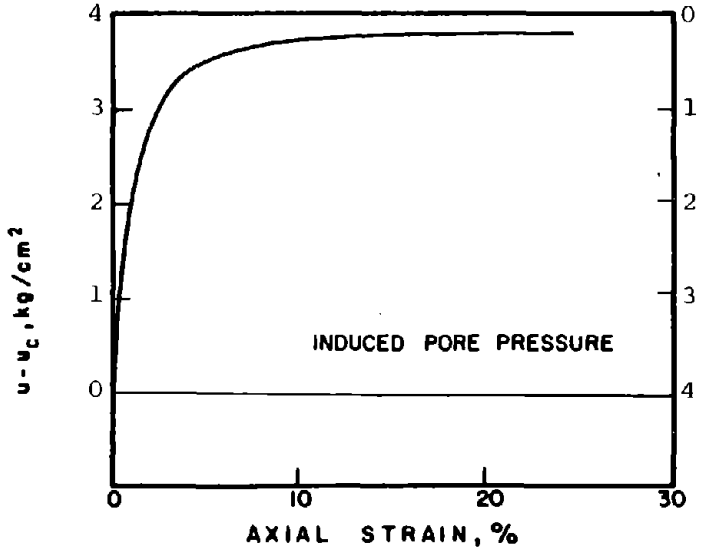

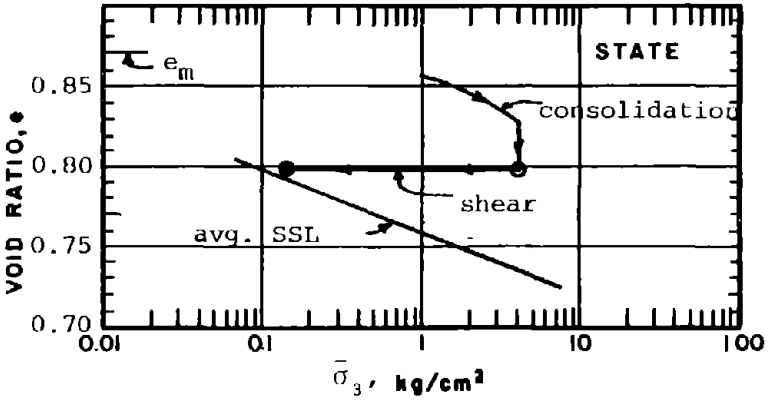

CAR-621

SOIL : Banding Sand #6

STRUCTURE : Compacted Moist

STATE AFTER CONSOLIDATION: $\bar{\sigma}_{3c}$ = 4.00 kg/cm², $\bar{\sigma}_{1c}$ = 8.00 kg/cm²
e_c = 0.799, γ_{dc} = 92.3 pcf

METHOD OF LOADING: Undrained, Cyclic Axial Compression
Load Control
$(\sigma_1 - \sigma_3)_{cy}$ = 0.32 ksc

TESTING DETAILS : Specimen Diameter 3.60 cm
: Specimen Height 5.30 cm
: End Platens: Lubricated, Type 2

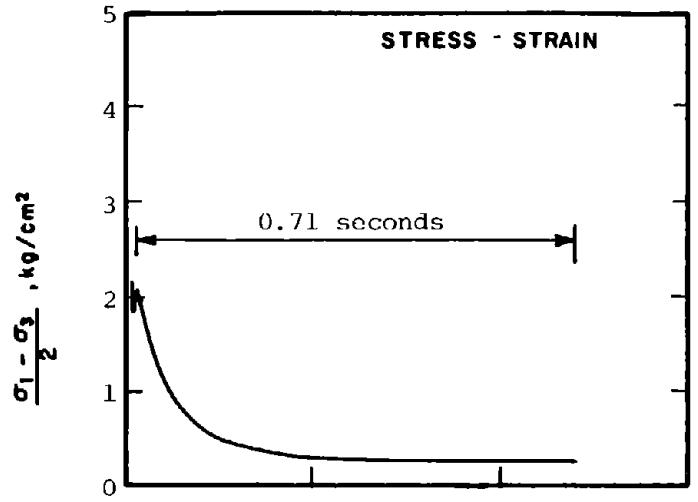

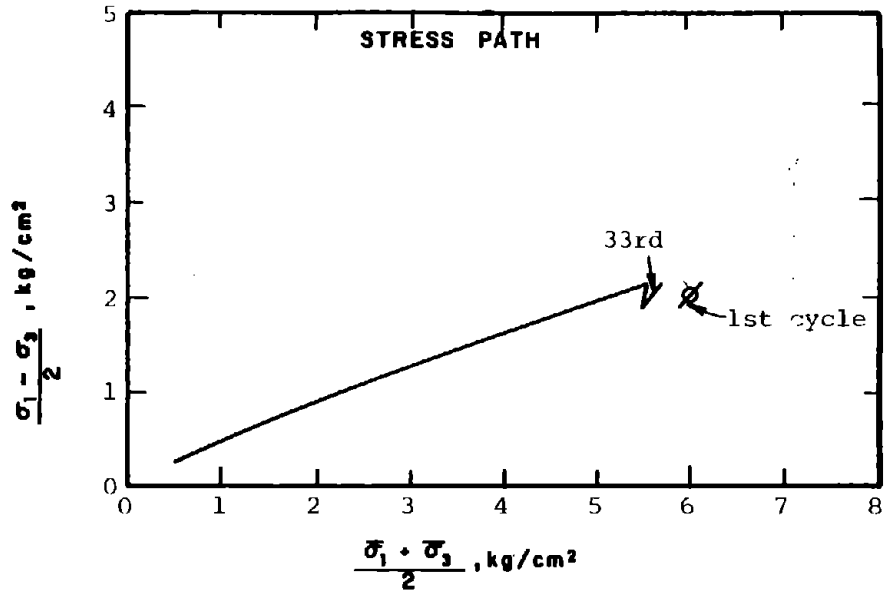

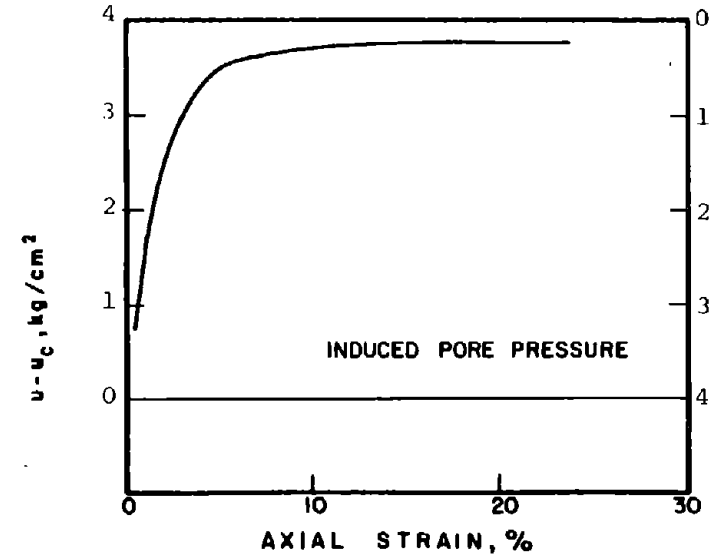

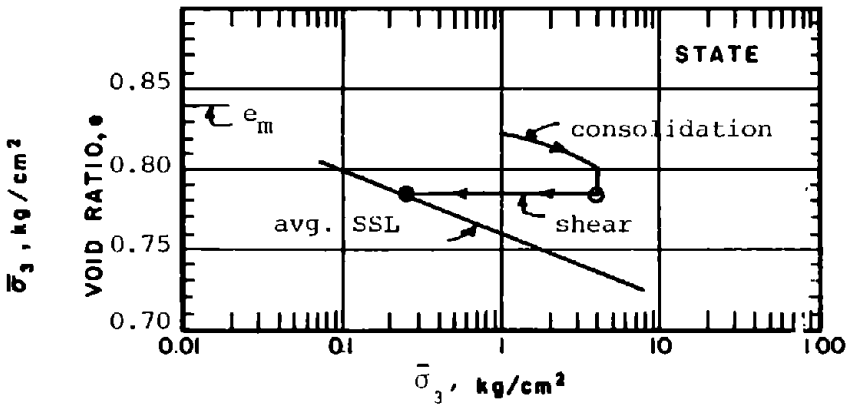

CAR-622

SOIL : Banding Sand #6

STRUCTURE : Compacted Moist

STATE AFTER CONSOLIDATION: $\bar{\sigma}_{3c}$ = 4.00 kg/cm², $\bar{\sigma}_{1c}$ = 8.00 kg/cm²
e_c = 0.782, γ_{dc} = 93.1 pcf

METHOD OF LOADING: Undrained, Cyclic Axial Compression
Load Control
$(\sigma_1 - \sigma_3)_{cy}$ = 0.30 ksc

TESTING DETAILS : Specimen Diameter 3.60 cm
: Specimen Height 5.30 cm
: End Platens: Lubricated, Type 2

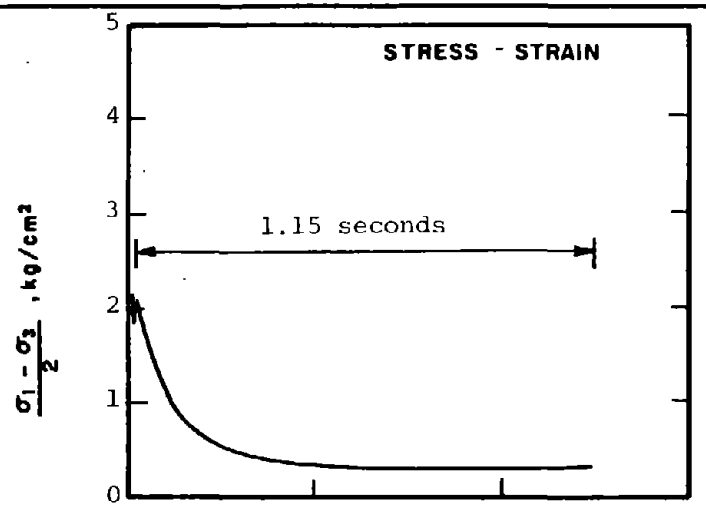

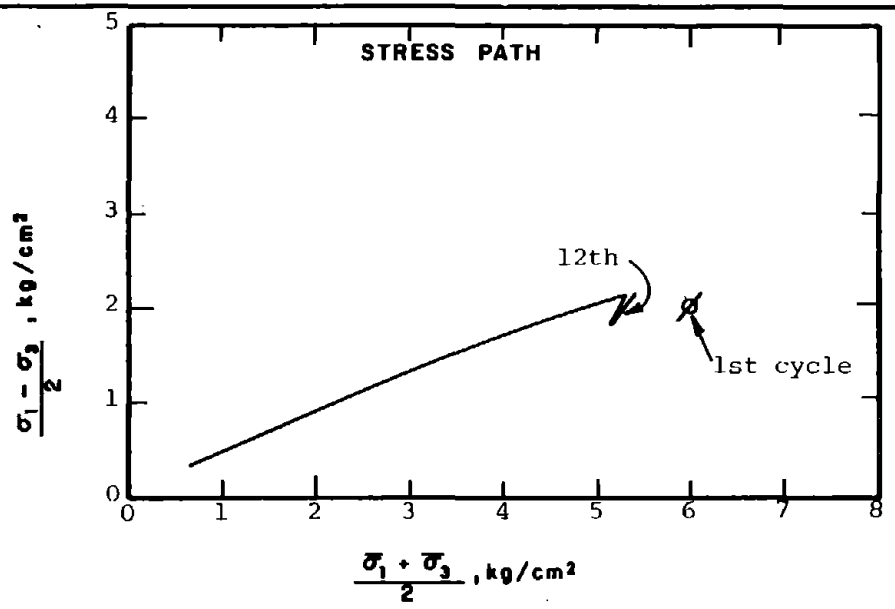

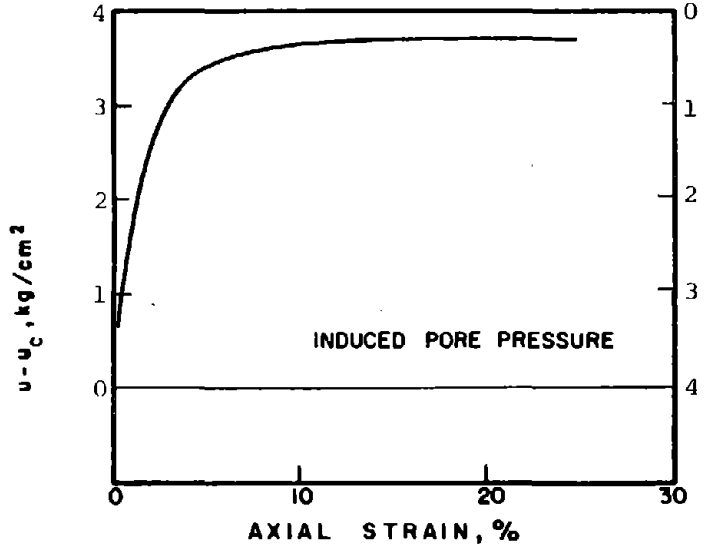

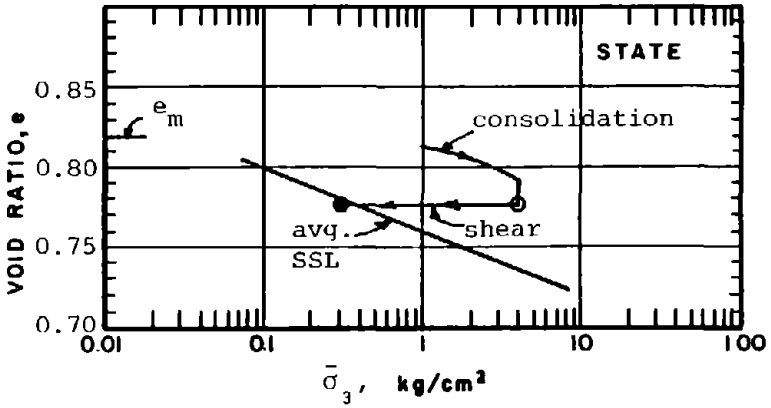

CAR-623

SOIL : Banding Sand #6

STRUCTURE : Compacted Moist

STATE AFTER CONSOLIDATION: $\bar{\sigma}_{3c}$ = 4.00 kg/cm², $\bar{\sigma}_{1c}$ = 8.00 kg/cm²

e_c = 0.775, γ_{dc} = 93.5 pcf

METHOD OF LOADING: Undrained, Cyclic Axial Compression
Load Control
$(\sigma_1 - \sigma_3)_{cy}$ = 0.38 ksc

TESTING DETAILS : Specimen Diameter 3.60 cm
: Specimen Height 5.30 cm
: End Platens: Lubricated, Type 2

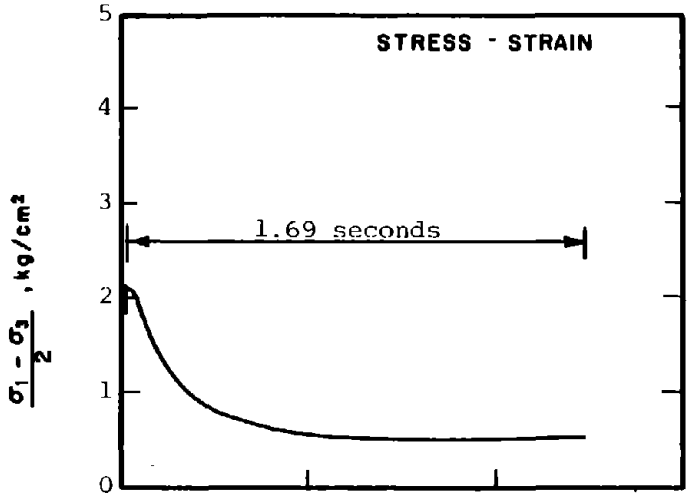

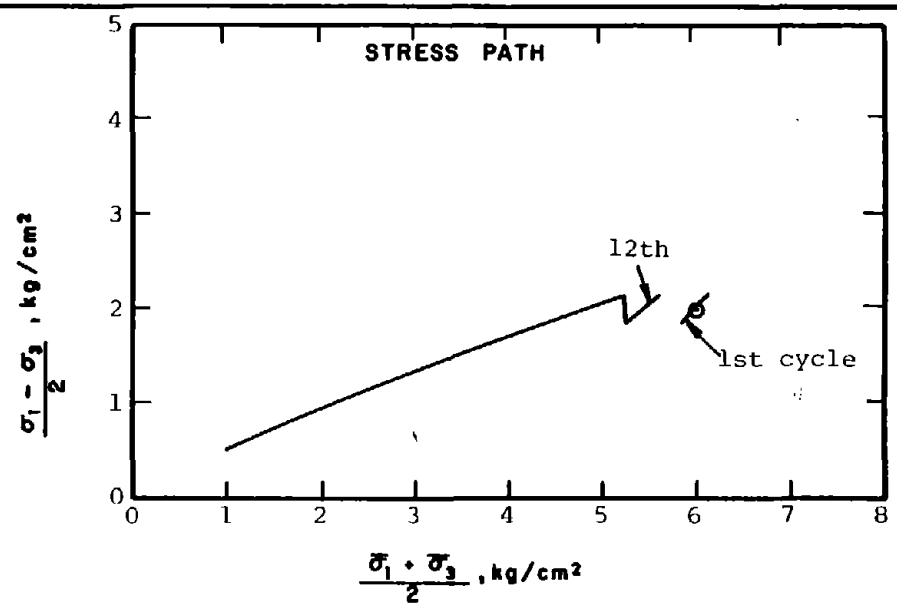

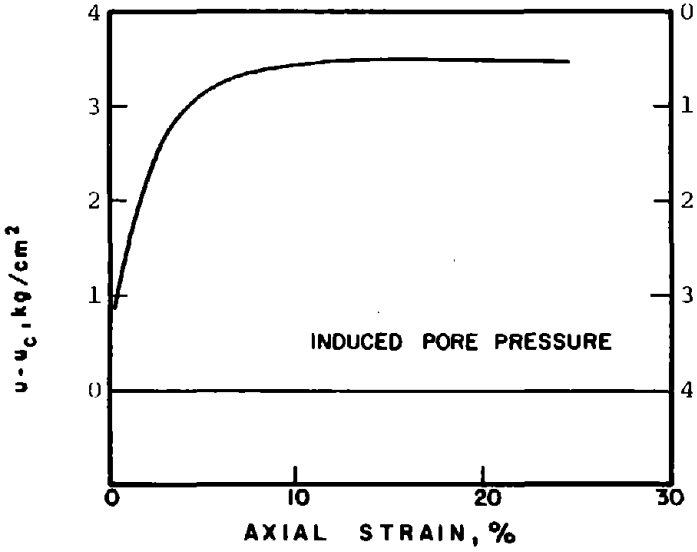

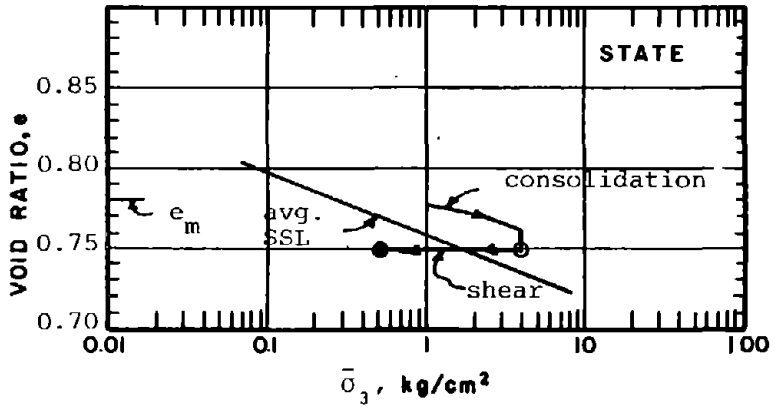

SOIL	: Banding Sand #6	METHOD OF LOADING:	Undrained, Cyclic Axial Compression
STRUCTURE	: Compacted Moist		Load Control
STATE AFTER CONSOLIDATION:	$\bar{\sigma}_{3c}$ = 4.00 kg/cm², $\bar{\sigma}_{1c}$ = 8.00 kg/cm²		$(\sigma_1 - \sigma_3)_{cy}$ = 0.39 ksc
	e_c = 0.749, γ_{dc} = 94.9 pcf	TESTING DETAILS :	Specimen Diameter 3.60 cm
		:	Specimen Height 5.30 cm
		:	End Platens: Lubricated, Type 2

CAR-624

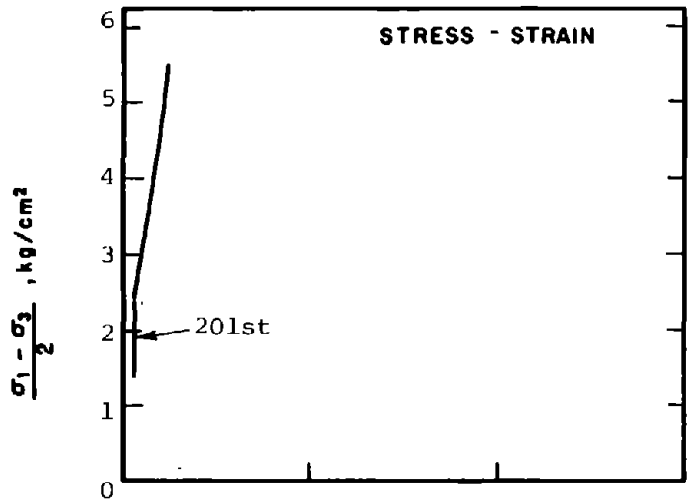

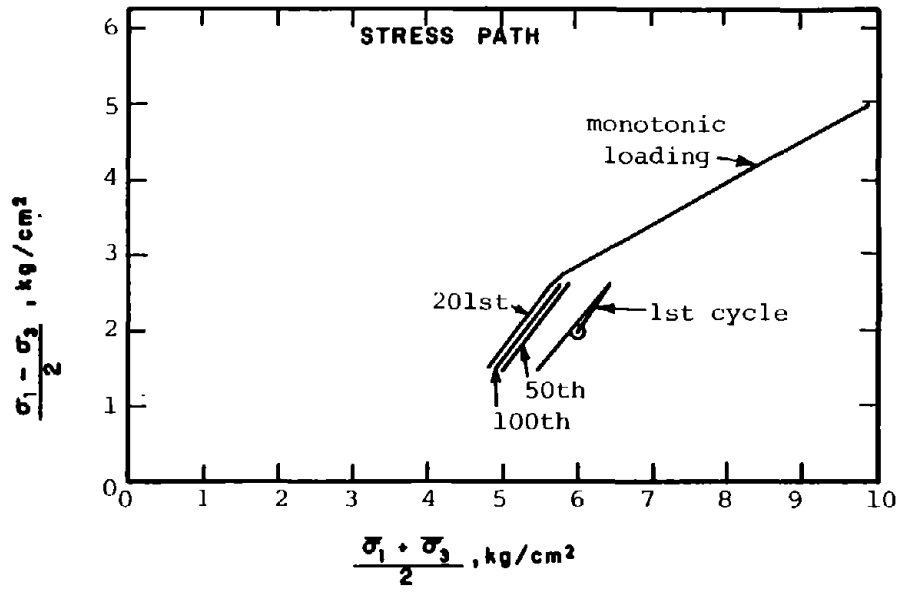

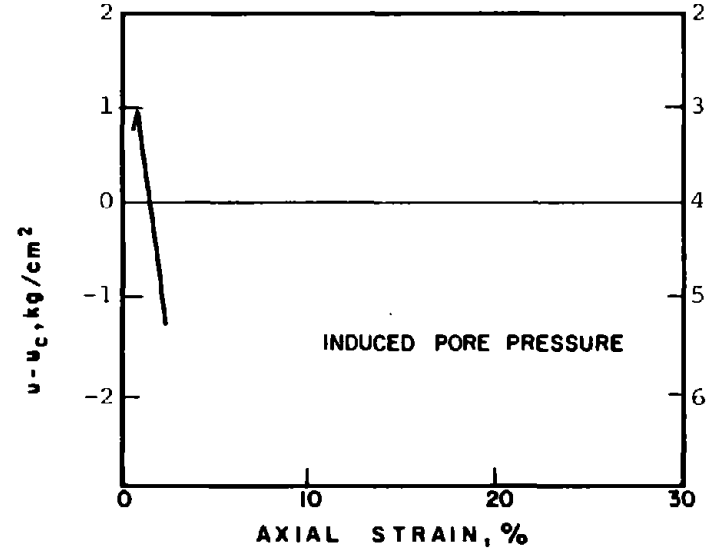

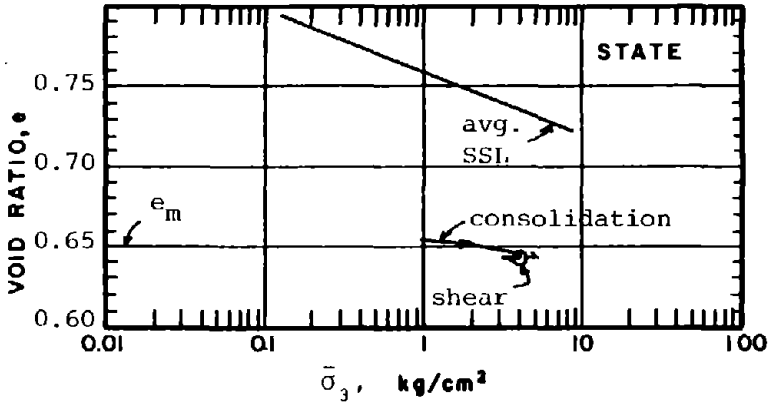

CAR-R-625

SOIL : Banding Sand #6

STRUCTURE : Compacted Moist

STATE AFTER CONSOLIDATION: $\bar{\sigma}_{3c} = 4.00$ kg/cm^2, $\bar{\sigma}_{1c} = 8.00$ kg/cm^2
$e_c = 0.642$, $\gamma_{dc} = 101.1$ pcf

METHOD OF LOADING: Undrained, Cyclic Axial Compression
Load Control
$(\sigma_1 - \sigma_3)_{cy} = 1.20$ ksc

TESTING DETAILS : Specimen Diameter 3.60 cm
: Specimen Height 5.30 cm
: End Platens: Lubricated, Type 2

484

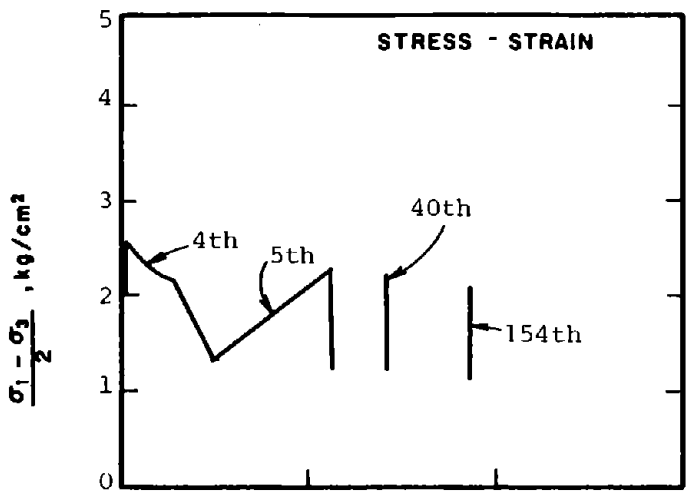

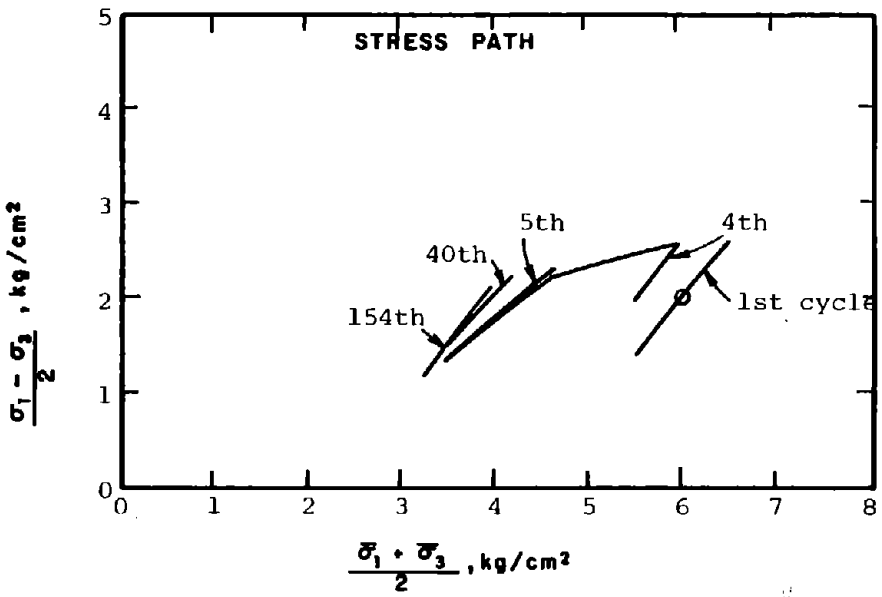

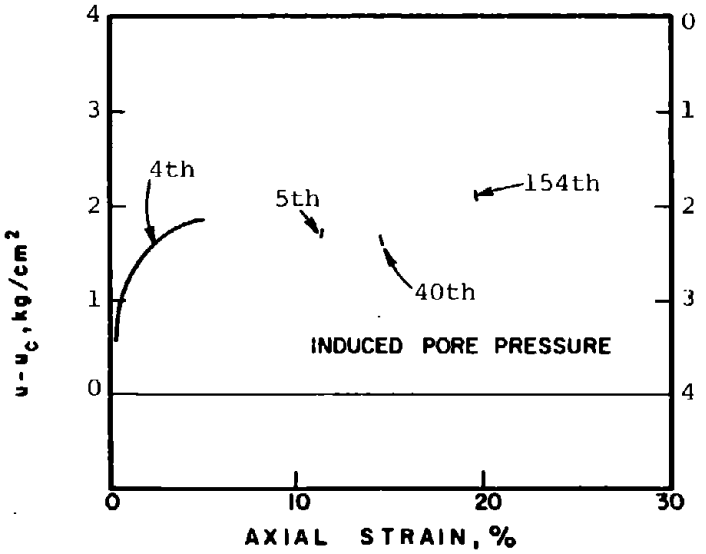

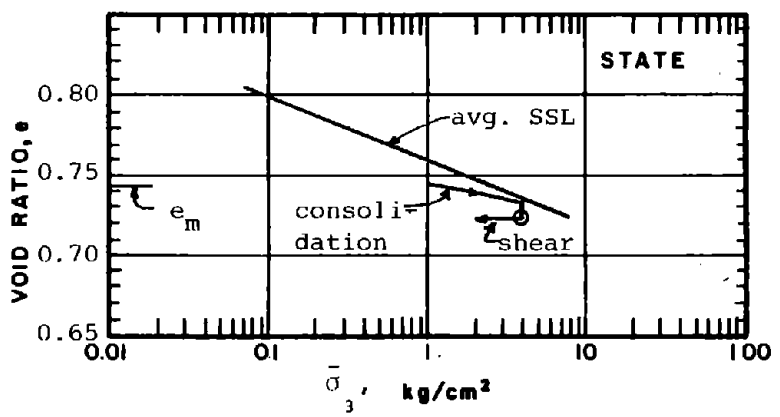

SOIL	: Banding Sand #6	METHOD OF LOADING:	Undrained, Cyclic Axial Compression Load Control $(\sigma_1 - \sigma_3)_{cy}$ = 1.19 ksc
STRUCTURE	: Compacted Moist		
STATE AFTER CONSOLIDATION:	$\bar{\sigma}_{3c}$ = 4.00 kg/cm², $\bar{\sigma}_{1c}$ = 8.00 kg/cm²	TESTING DETAILS	: Specimen Diameter 3.60 cm
	e_c = 0.722, γ_{dc} = 96.4 pcf		: Specimen Height 5.30 cm
			: End Platens: Lubricated, Type 2

CAR-626

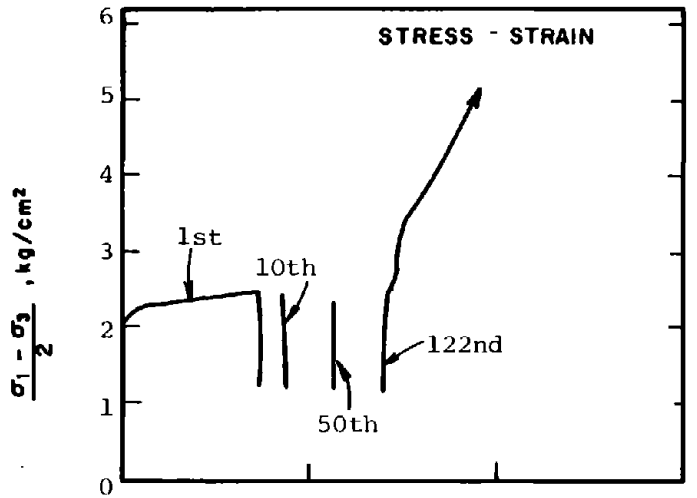

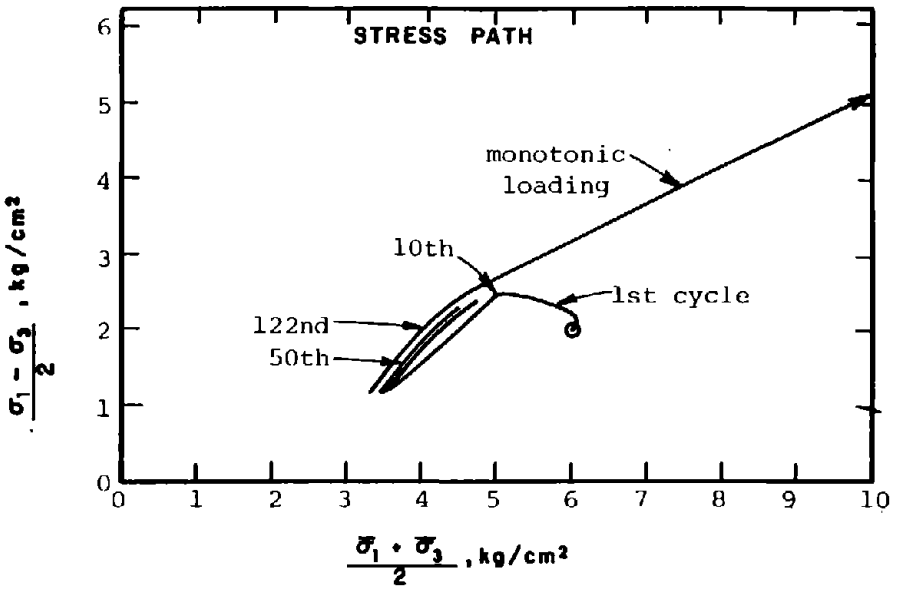

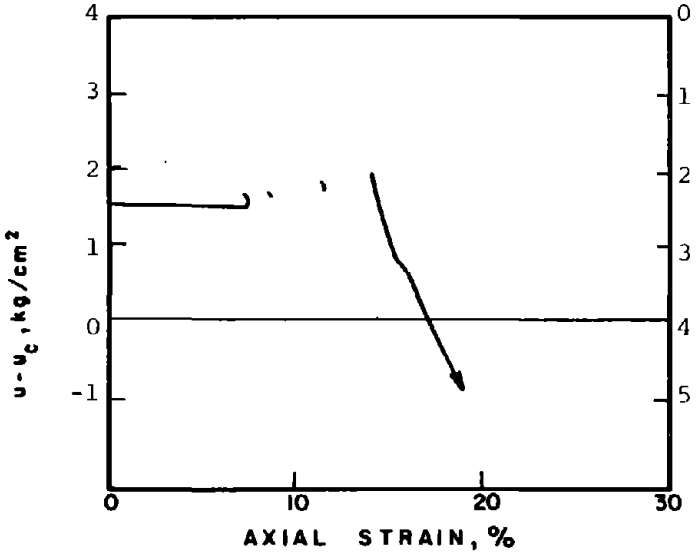

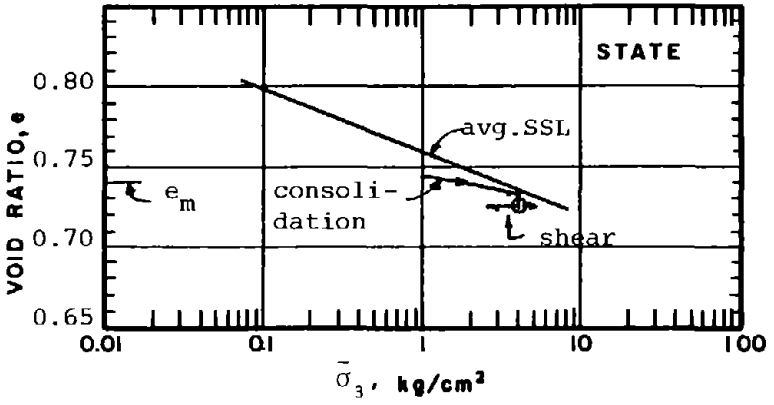

CAR-R-627

SOIL : Banding Sand #6

STRUCTURE : Compacted Moist

STATE AFTER CONSOLIDATION: $\bar{\sigma}_{3c}$ = 4.00 kg/cm², $\bar{\sigma}_{1c}$ = 8.00 kg/cm²
e_c = 0.725, γ_{dc} = 96.2 pcf

METHOD OF LOADING: Undrained, Cyclic Axial Compression
Load Control
$(\sigma_1 - \sigma_3)_{cy}$ = 1.22 ksc

TESTING DETAILS : Specimen Diameter 3.60 cm
: Specimen Height 5.30 cm
: End Platens: Lubricated, Type 2

986

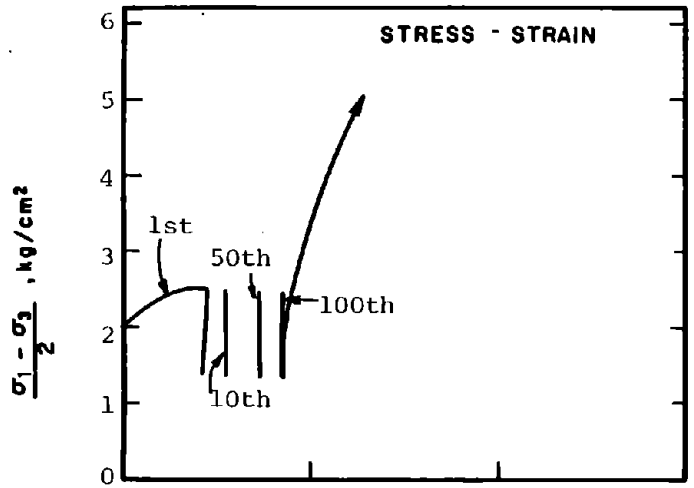

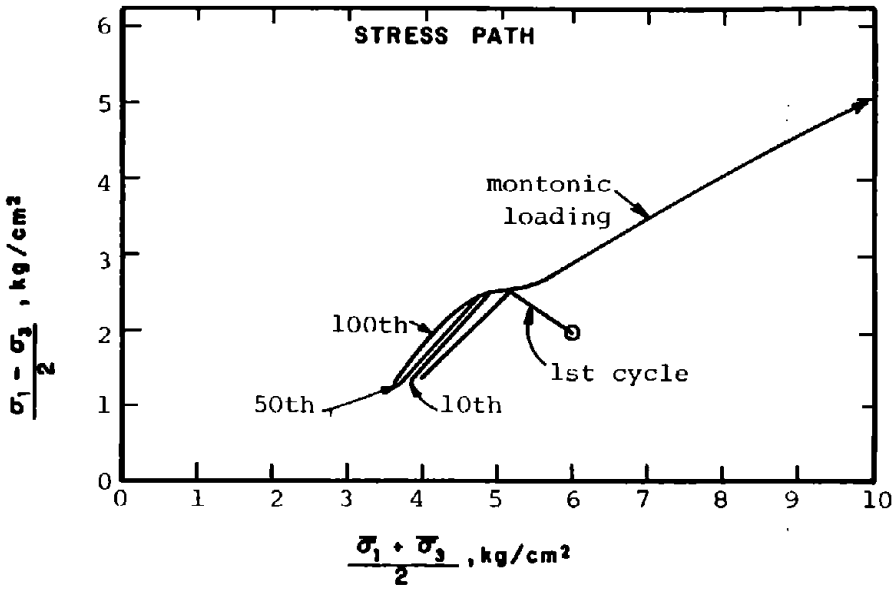

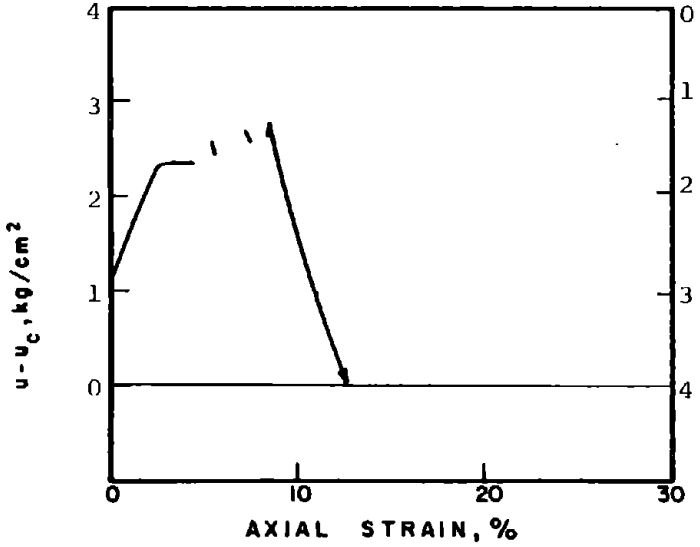

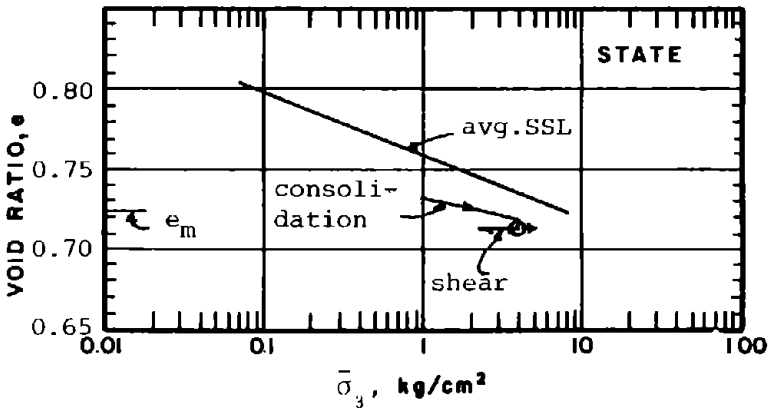

CAR-R-628

SOIL : Banding Sand #6

STRUCTURE : Compacted Moist

STATE AFTER CONSOLIDATION: $\bar{\sigma}_{3c}$ = 4.00 kg/cm², $\bar{\sigma}_{1c}$ = 8.00 kg/cm²
e_c = 0.713, γ_{dc} = 96.9 pcf

METHOD OF LOADING: Undrained, Cyclic Axial Compression
Load Control
$(\sigma_1 - \sigma_3)_{cy}$ = 1.17 ksc

TESTING DETAILS : Specimen Diameter 3.60 cm
: Specimen Height 5.30 cm
: End Platens: Lubricated, Type 2

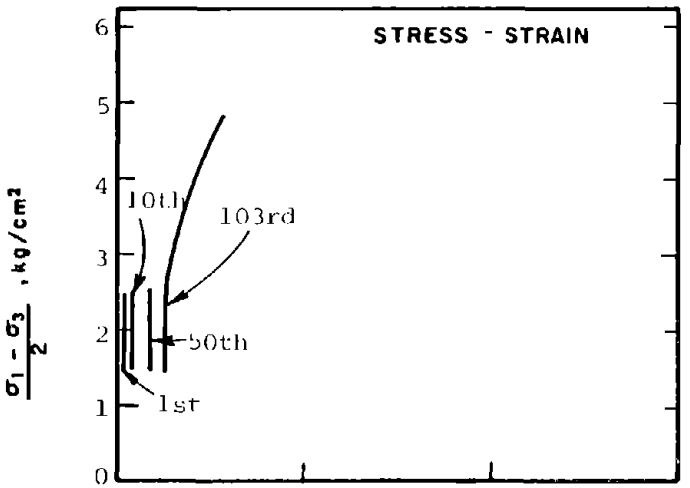

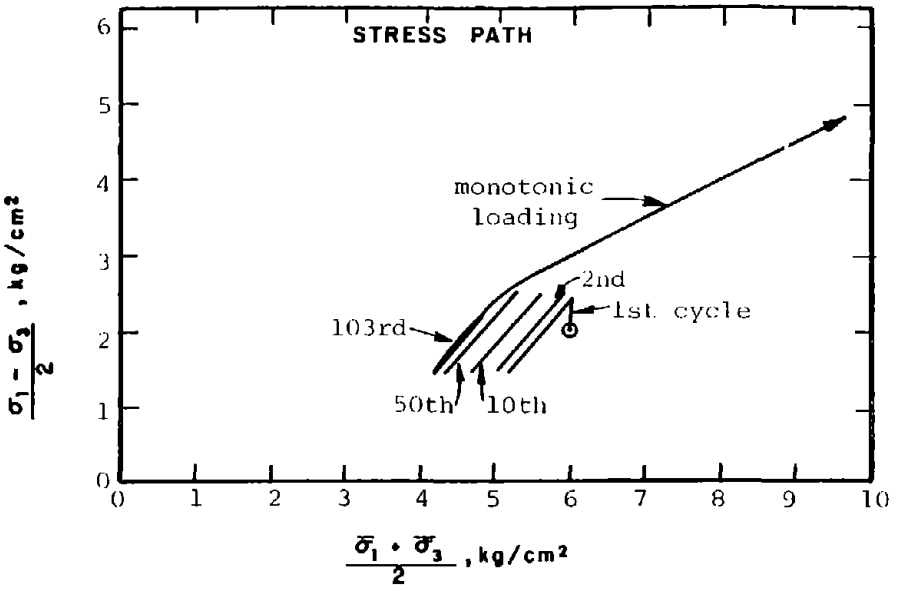

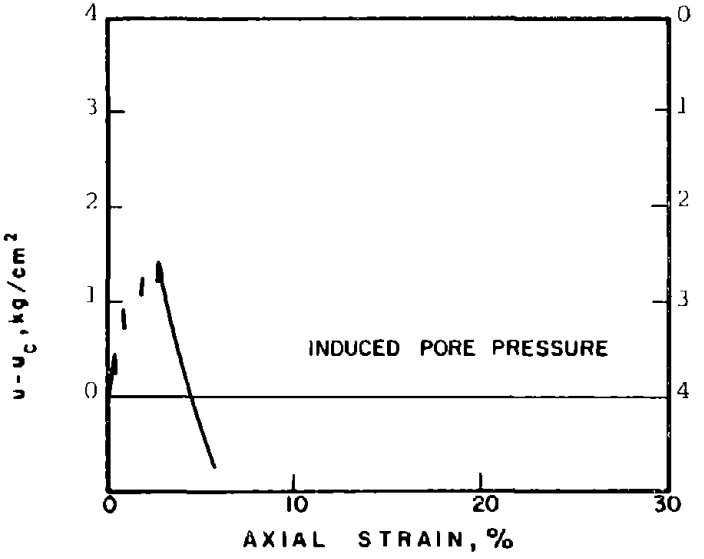

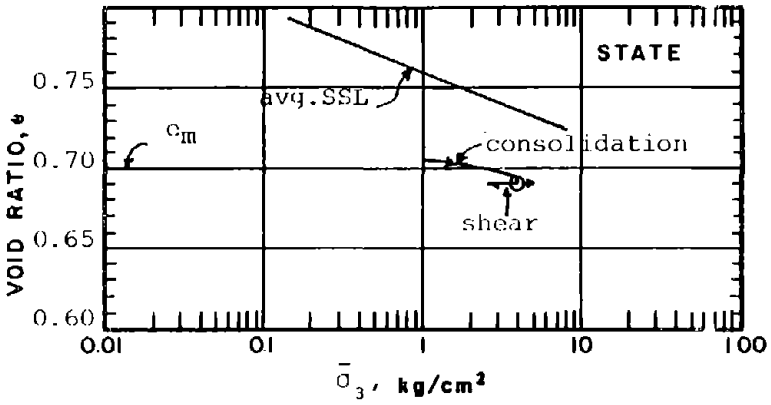

CAR-R-629

SOIL : Banding Sand #6

STRUCTURE : Compacted Moist

STATE AFTER CONSOLIDATION: $\bar{\sigma}_{3c} = 4.00$ kg/cm^2, $\bar{\sigma}_{1c} = 8.00$ kg/cm^2

$e_c = 0.690$, $\gamma_{dc} = 98.2$ pcf

METHOD OF LOADING: Undrained, Cyclic Axial Compression Load Control

$(\sigma_1 - \sigma_3)_{cy} = 1.17$ ksc

TESTING DETAILS : Specimen Diameter 3.60 cm

: Specimen Height 5.30 cm

: End Platens: Lubricated, Type 2

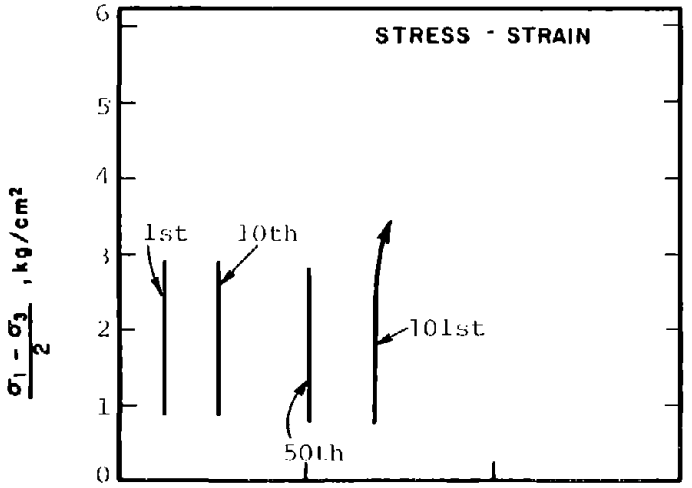

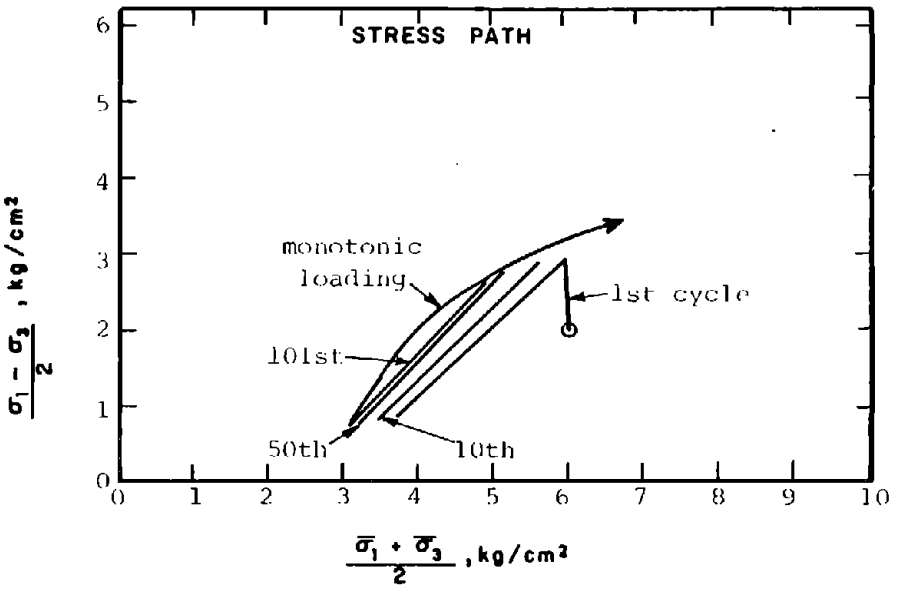

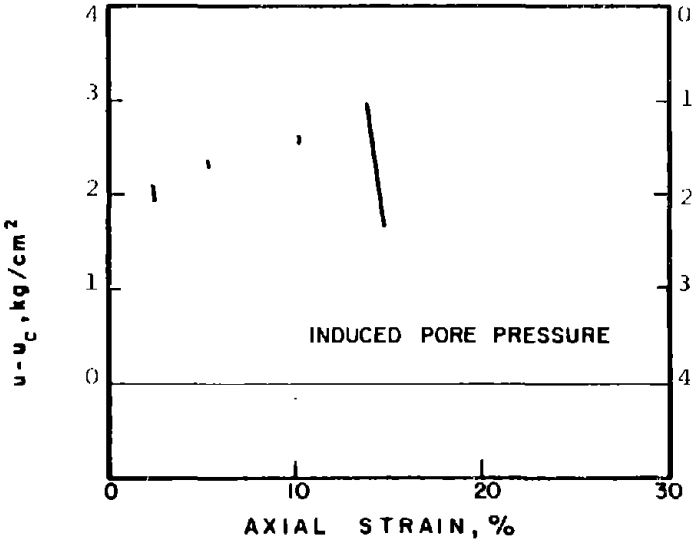

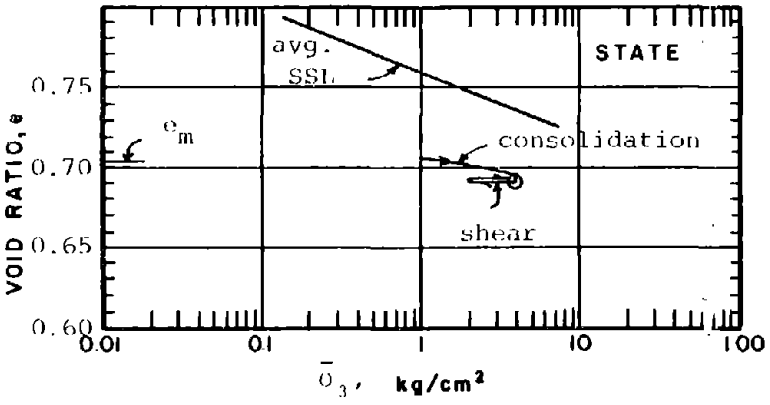

CAR-R-630

SOIL : Banding Sand #6

STRUCTURE : Compacted Moist

STATE AFTER CONSOLIDATION: $\bar{\sigma}_{3c} = 4.00$ kg/cm^2, $\bar{\sigma}_{1c} = 8.00$ kg/cm^2

$e_c = 0.691$, $\gamma_{dc} = 98.2$ pcf

METHOD OF LOADING: Undrained, Cyclic Axial Compression
Load Control
$(\sigma_1 - \sigma_3)_{cy} = 2.18$ ksc

TESTING DETAILS : Specimen Diameter 3.60 cm
: Specimen Height 5.30 cm
: End Platens: Lubricated, Type 2

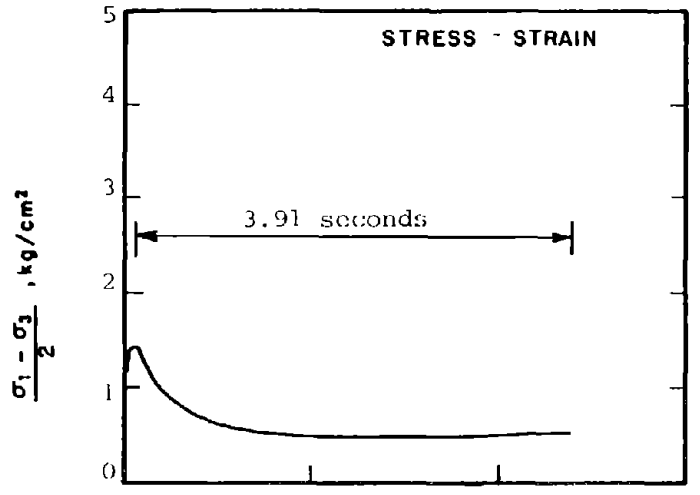

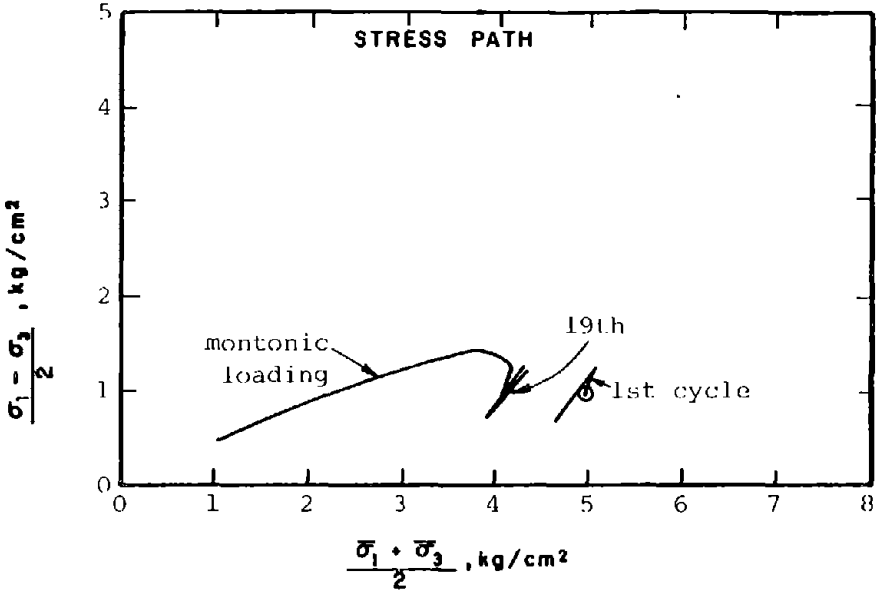

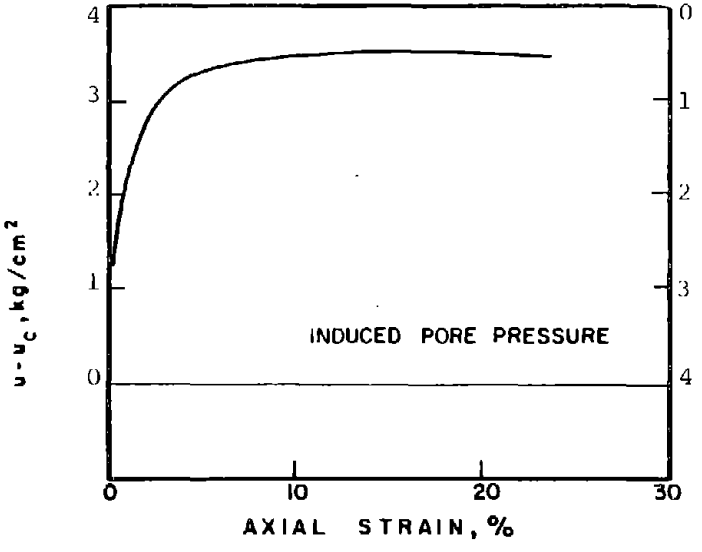

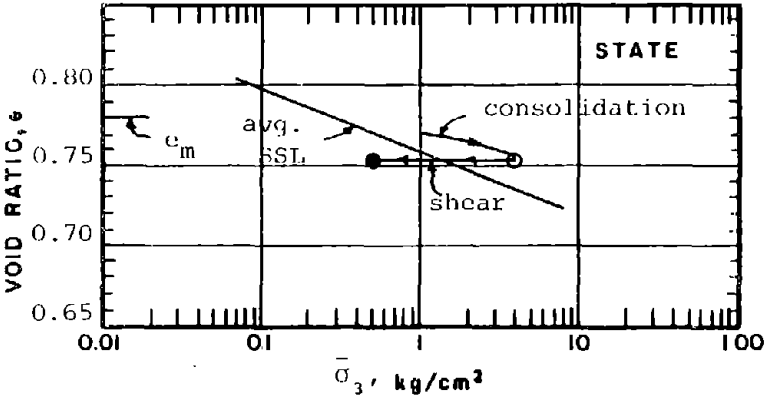

CAR-R-631

SOIL : Banding Sand #6

STRUCTURE : Compacted Moist

STATE AFTER CONSOLIDATION: $\bar{\sigma}_{3c} = 4.00$ kg/cm^2, $\bar{\sigma}_{1c} = 6.00$ kg/cm^2
$e_c = 0.752$, $\gamma_{dc} = 94.7$ pcf

METHOD OF LOADING: Undrained, Cyclic Axial Compression
Load Control
$(\sigma_1 - \sigma_3)_{cy} = 0.59$ ksc

TESTING DETAILS : Specimen Diameter 3.60 cm
: Specimen Height 5.30 cm
: End Platens: Lubricated, Type 2

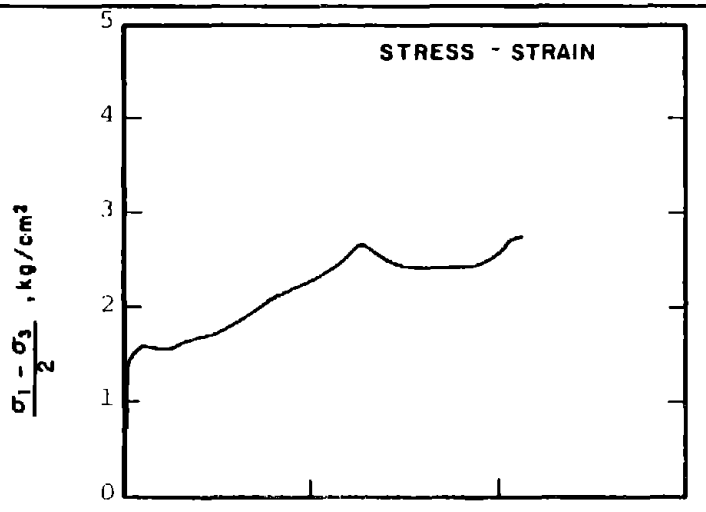

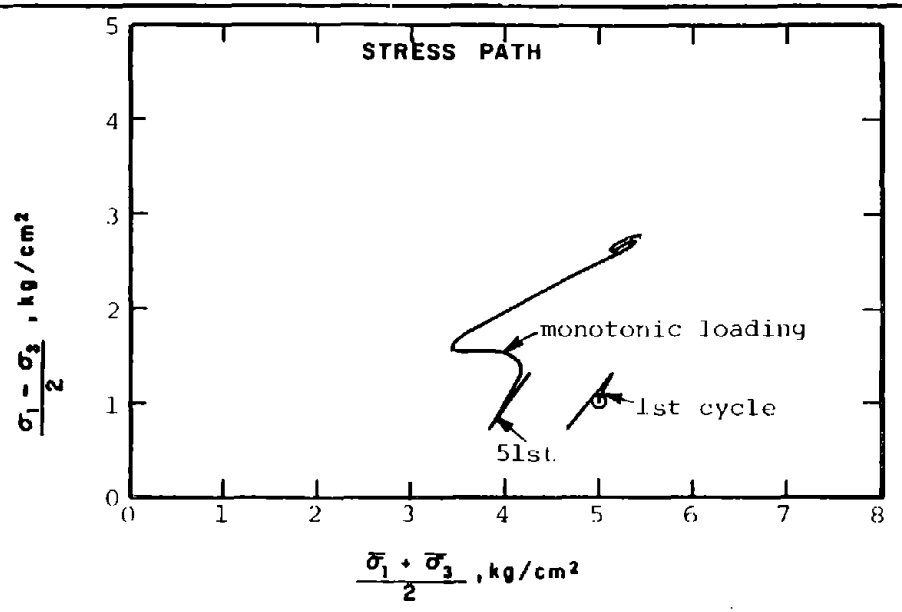

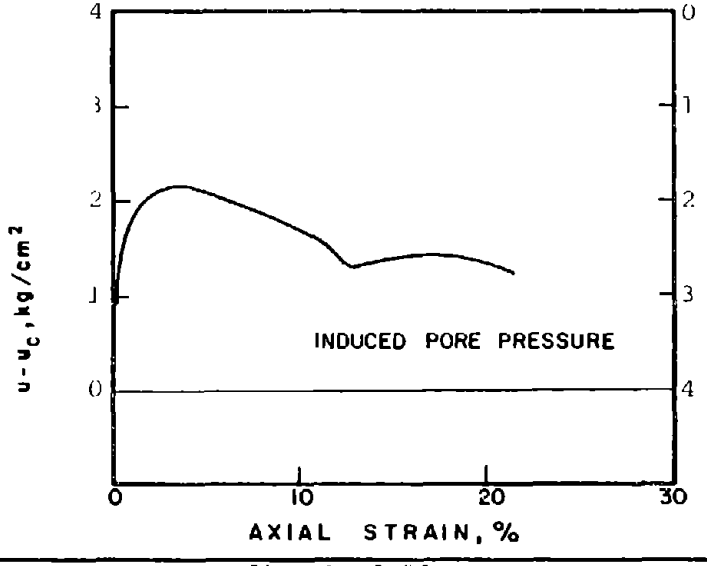

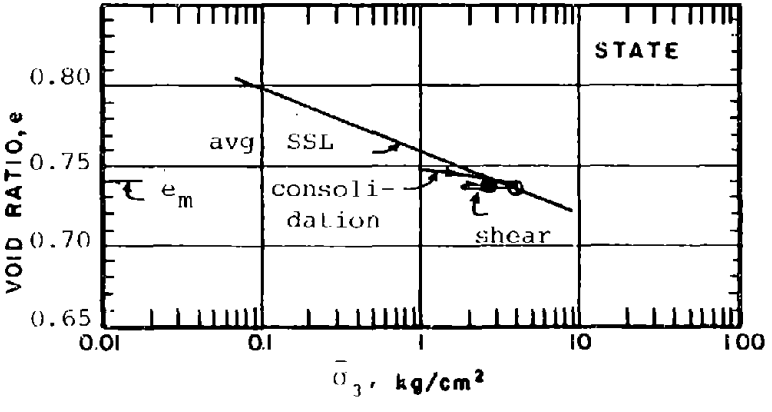

CAR-R-632

SOIL : Banding Sand #6

STRUCTURE : Compacted Moist

STATE AFTER CONSOLIDATION: $\bar{\sigma}_{3c}$ = 4.00 kg/cm², $\bar{\sigma}_{1c}$ = 6.00 kg/cm²
e_c = 0.734, γ_{dc} = 95.7 pcf

METHOD OF LOADING: Undrained, Cyclic Axial Compression
Load Control
$(\sigma_1 - \sigma_3)_{cy}$ = 0.59 ksc

TESTING DETAILS : Specimen Diameter 3.60 cm
: Specimen Height 5.30 cm
: End Platens: Lubricated, Type 2

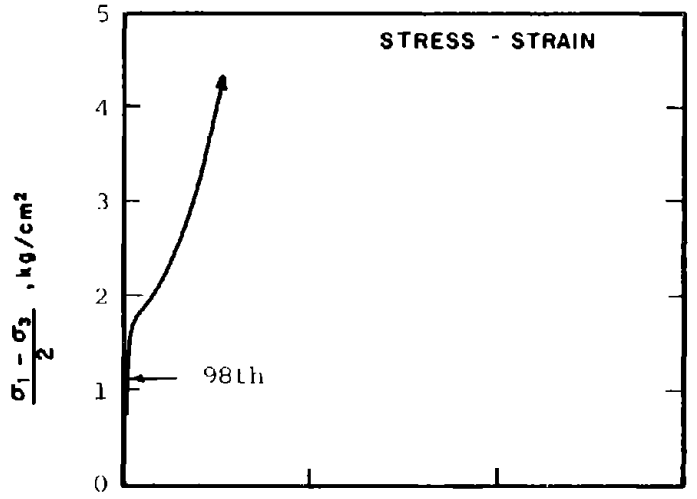

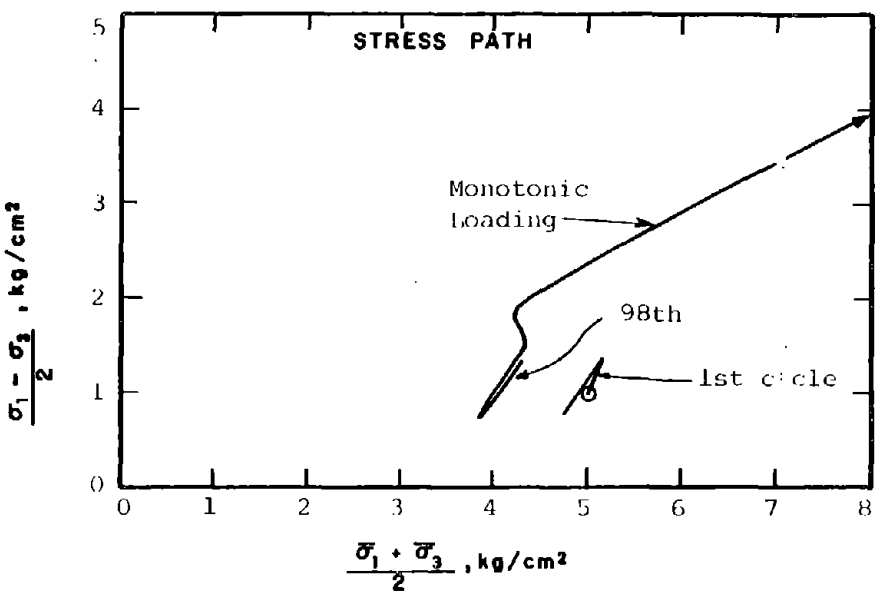

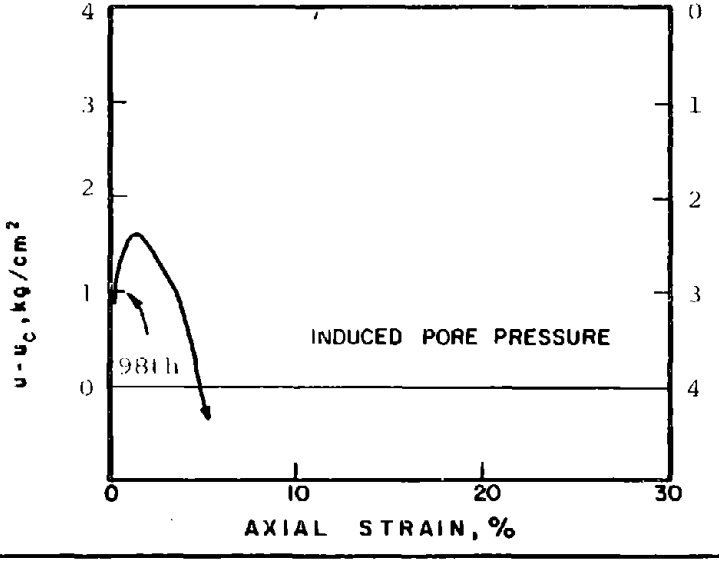

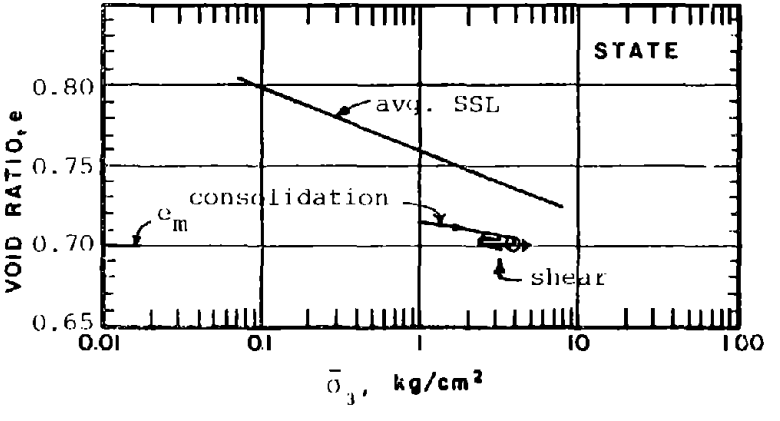

CAR-P-633

SOIL : Banding Sand #6

STRUCTURE : Compacted Moist

STATE AFTER CONSOLIDATION: $\bar{\sigma}_{3c} = 4.00$ kg/cm², $\bar{\sigma}_{1c} = 6.00$ kg/cm²

$e_c = 0.701$, $\gamma_{dc} = 97.6$ pcf

METHOD OF LOADING: Undrained, Cyclic Axial Compression Load Control

$(\sigma_1 - \sigma_3)_{cy} = 0.60$ ksc

TESTING DETAILS : Specimen Diameter 3.60 cm

: Specimen Height 5.30 cm

: End Platens: Lubricated, Type 2

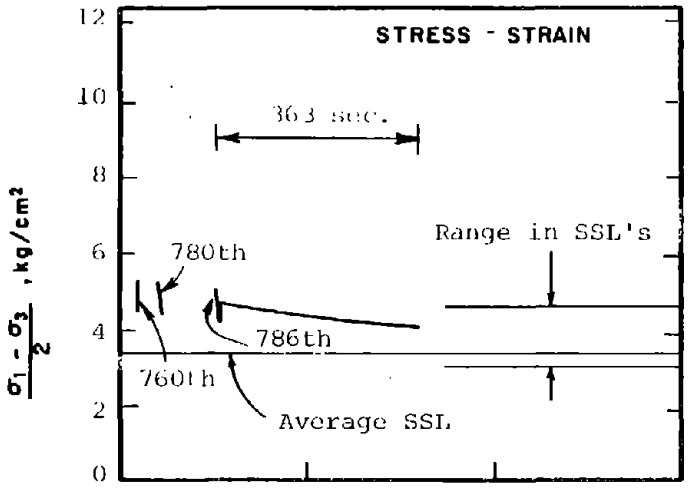

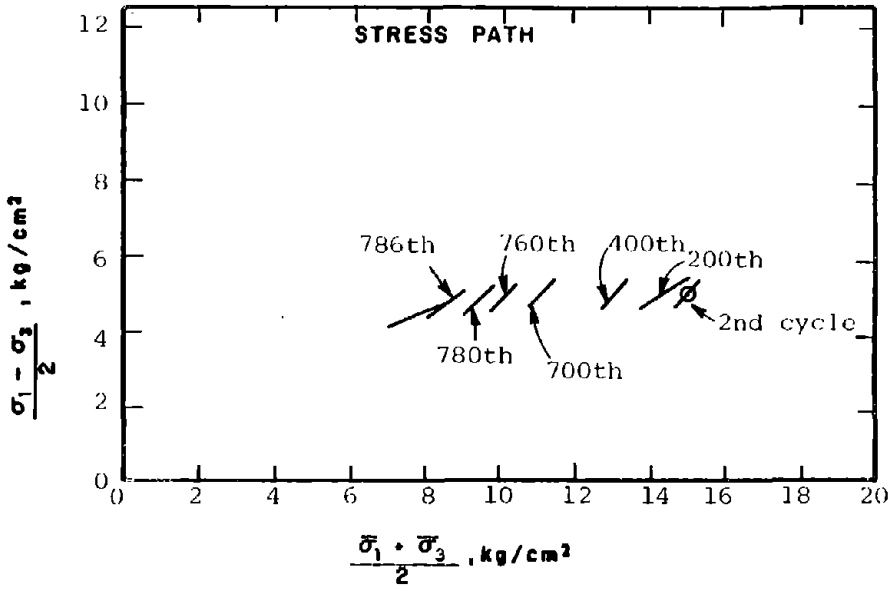

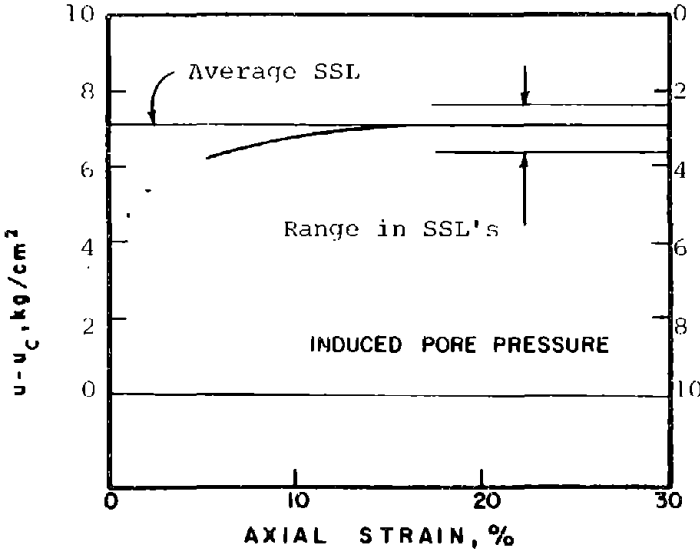

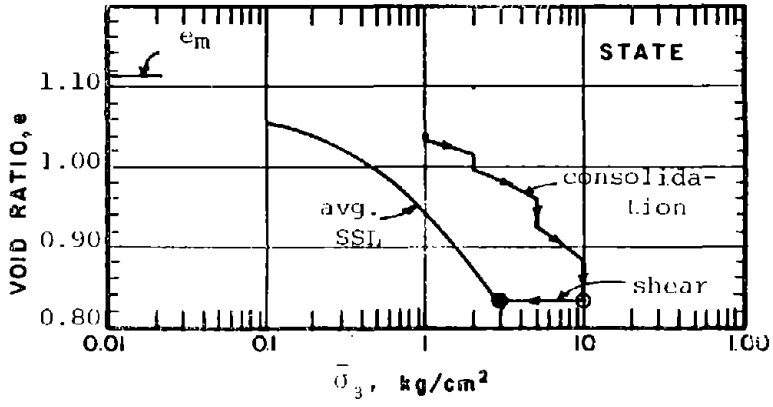

CAR-1001

SOIL : Mine Tailings

STRUCTURE : Compacted Moist

STATE AFTER CONSOLIDATION: $\bar{\sigma}_{3c}$ =10.00 kg/cm², $\bar{\sigma}_{1c}$ =20.00 kg/cm²
e_c =0.831 , γ_{dc} = 91.3 pcf

METHOD OF LOADING: Undrained, Cyclic Axial Compression
Load Control
$(\sigma_1 - \sigma_3)_{cy}$ = 0.83 ksc

TESTING DETAILS : Specimen Diameter 3.60cm
: Specimen Height 5.30cm
: End Platens: Lubricated, Type 2

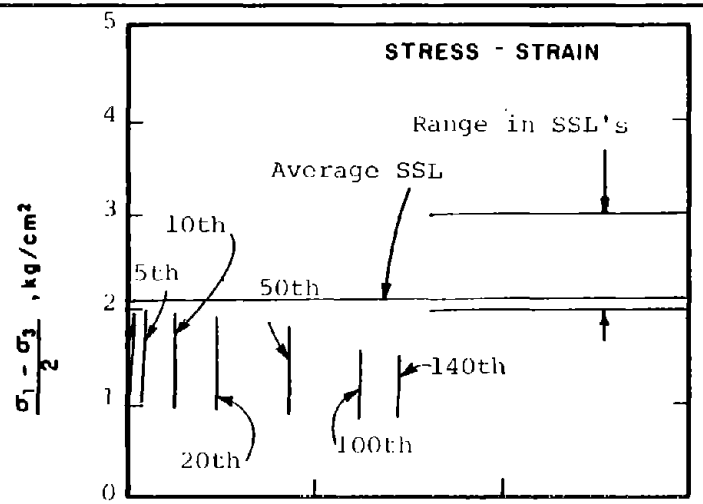

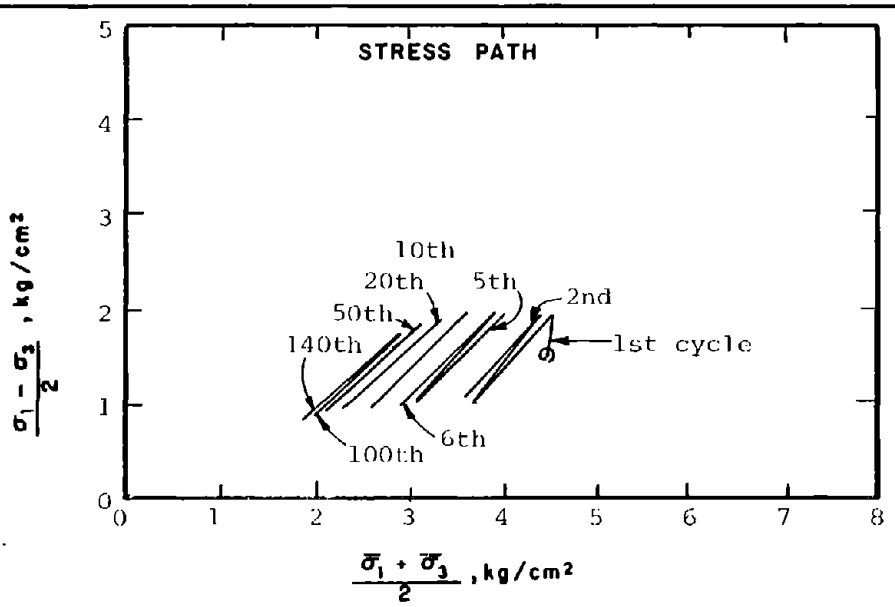

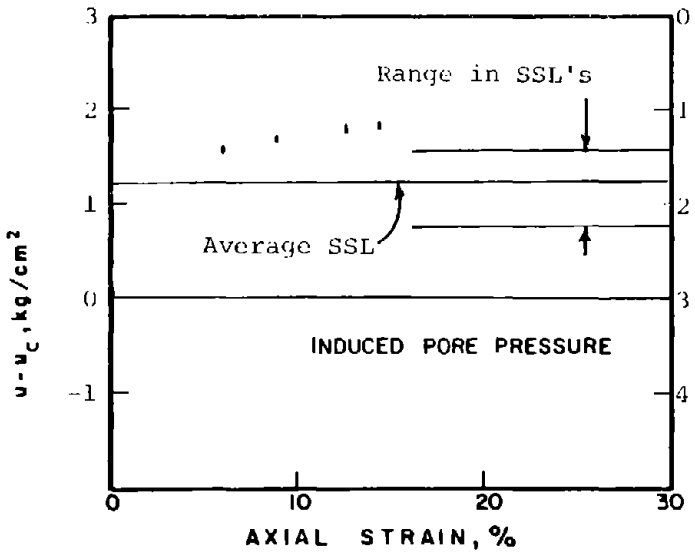

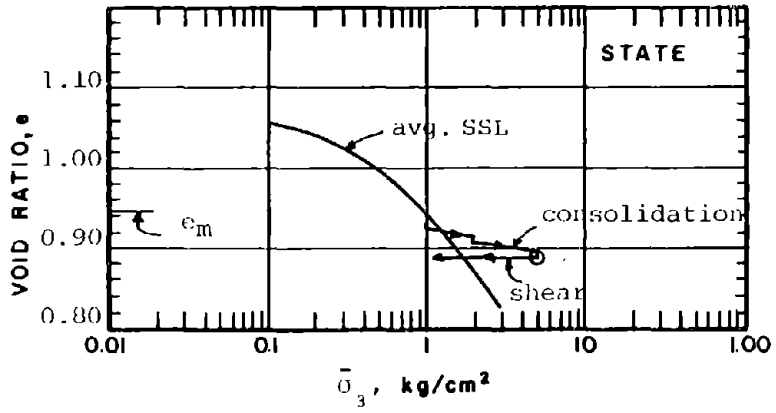

CAR-1002

SOIL : Mine Tailings

STRUCTURE : Compacted Moist

STATE AFTER CONSOLIDATION: $\bar{\sigma}_{3c}$ = 3.00 kg/cm², $\bar{\sigma}_{1c}$ = 6.00 kg/cm²
e_c = 0.887, γ_{dc} = 88.6 pcf

METHOD OF LOADING: Undrained, Cyclic Axial Compression
Load Control
$(\sigma_1 - \sigma_3)_{cy}$ = 0.95 ksc

TESTING DETAILS : Specimen Diameter 3.60 cm
: Specimen Height 5.30 cm
: End Platens: Lubricated, Type 2

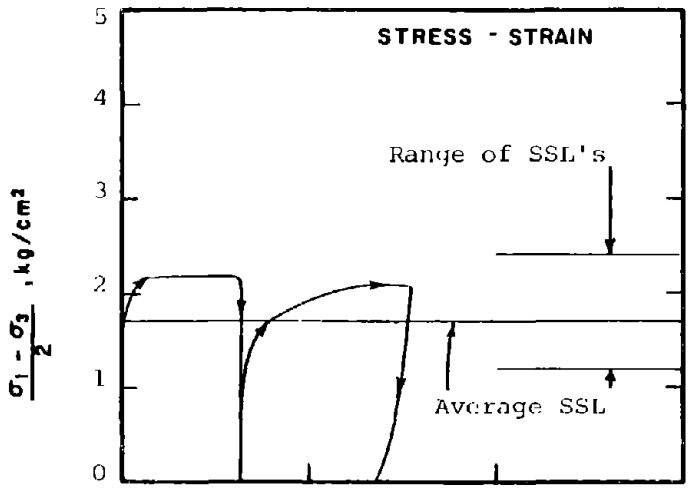

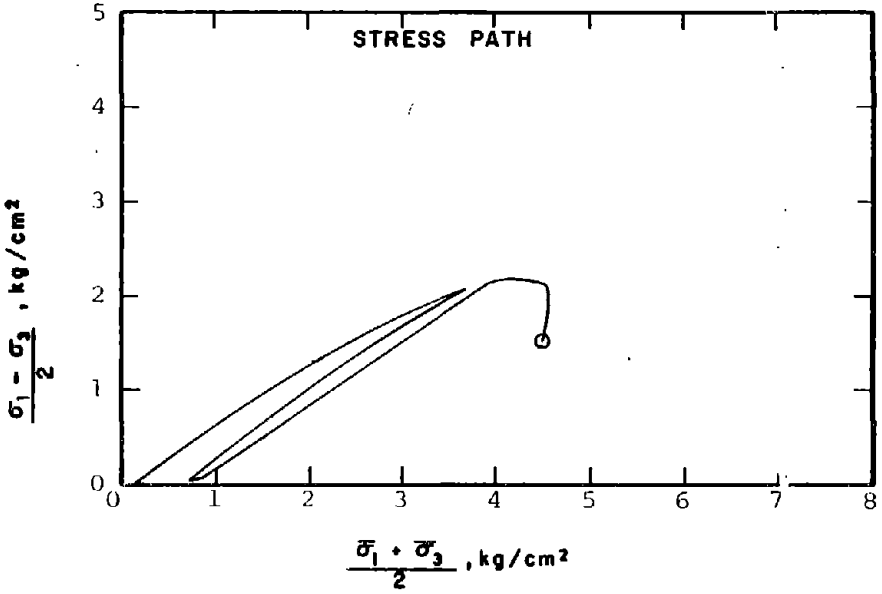

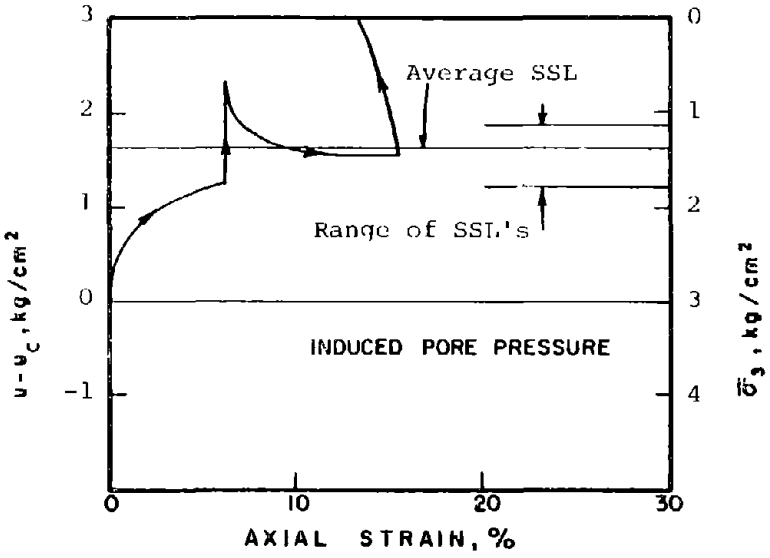

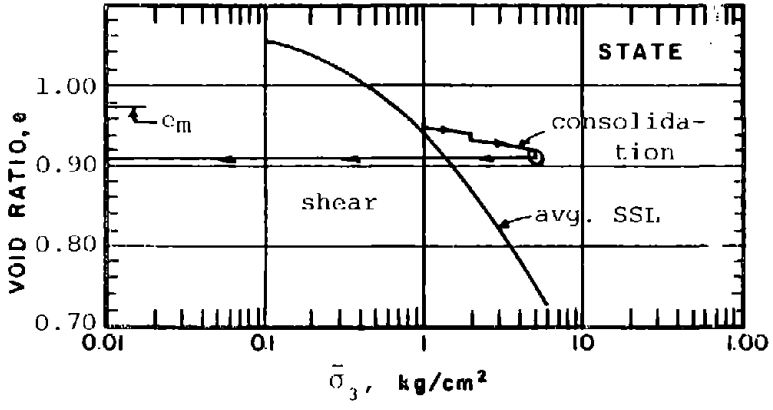

CAR-1003

SOIL : Mine Tailings

STRUCTURE : Compacted Moist

STATE AFTER CONSOLIDATION: $\bar{\sigma}_{3c} = 3.00$ kg/cm², $\bar{\sigma}_{1c} = 6.00$ kg/cm²
$e_c = 0.911$, $\gamma_{dc} = 87.5$ pcf

METHOD OF LOADING: Undrained, Cyclic Axial Compression
Load Control
$(\sigma_1 - \sigma_3)_{cy} = 2.10$ ksc

TESTING DETAILS : Specimen Diameter 3.60 cm
: Specimen Height 5.30 cm
: End Platens: Lubricated, Type 2

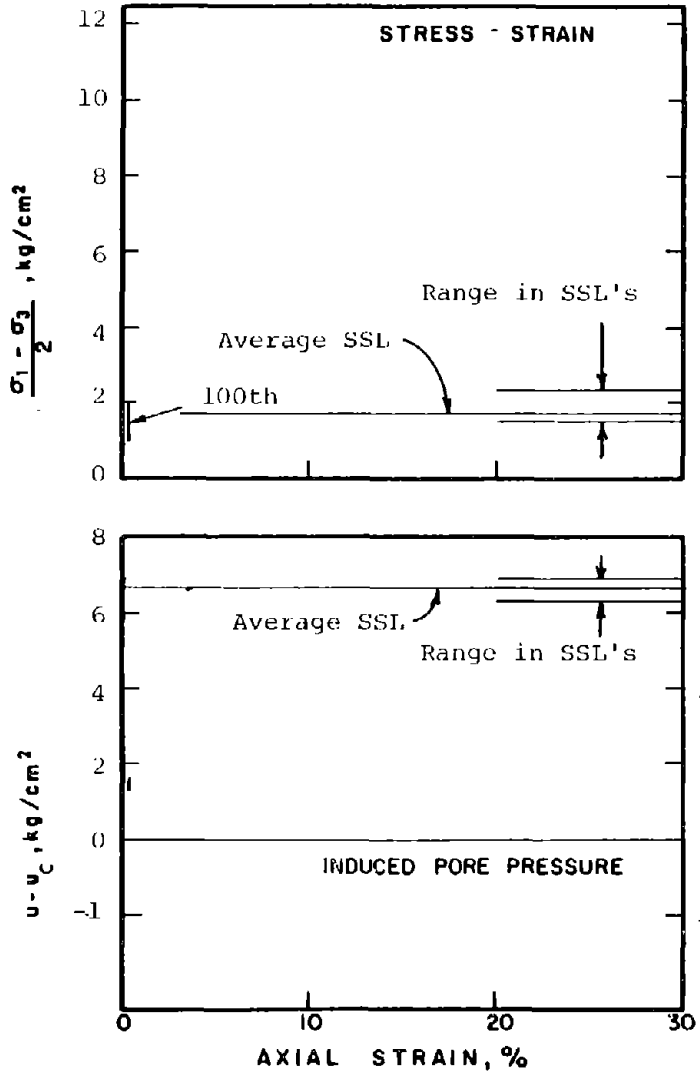

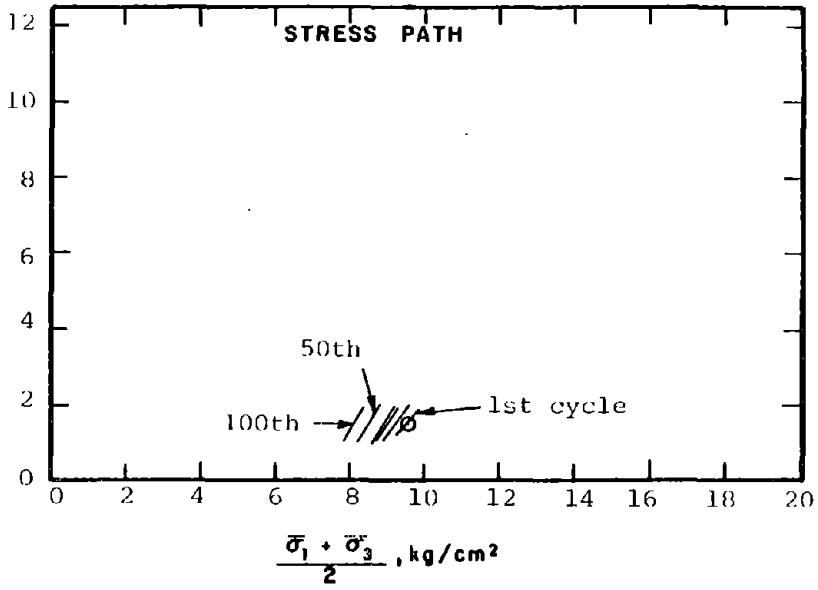

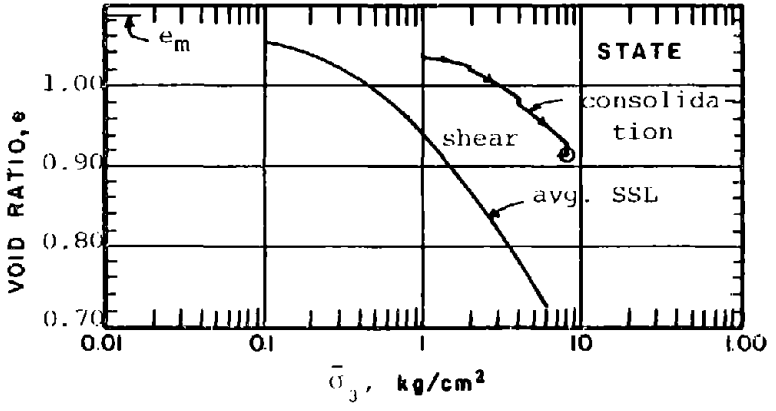

CAR-1004

SOIL : Mine Tailings

STRUCTURE : Compacted Moist

STATE AFTER CONSOLIDATION: $\bar{\sigma}_{3c} = 8.00$ kg/cm², $\bar{\sigma}_{1c} = 11.00$ kg/cm²

$e_c = 0.914$, $\gamma_{dc} = 87.4$ pcf

METHOD OF LOADING: Undrained, Cyclic Axial Compression Load Control

$(\sigma_1 - \sigma_3)_{cy} = 1.00$ ksc

TESTING DETAILS : Specimen Diameter 3.60 cm

: Specimen Height 5.30 cm

: End Platens: Lubricated, Type 2

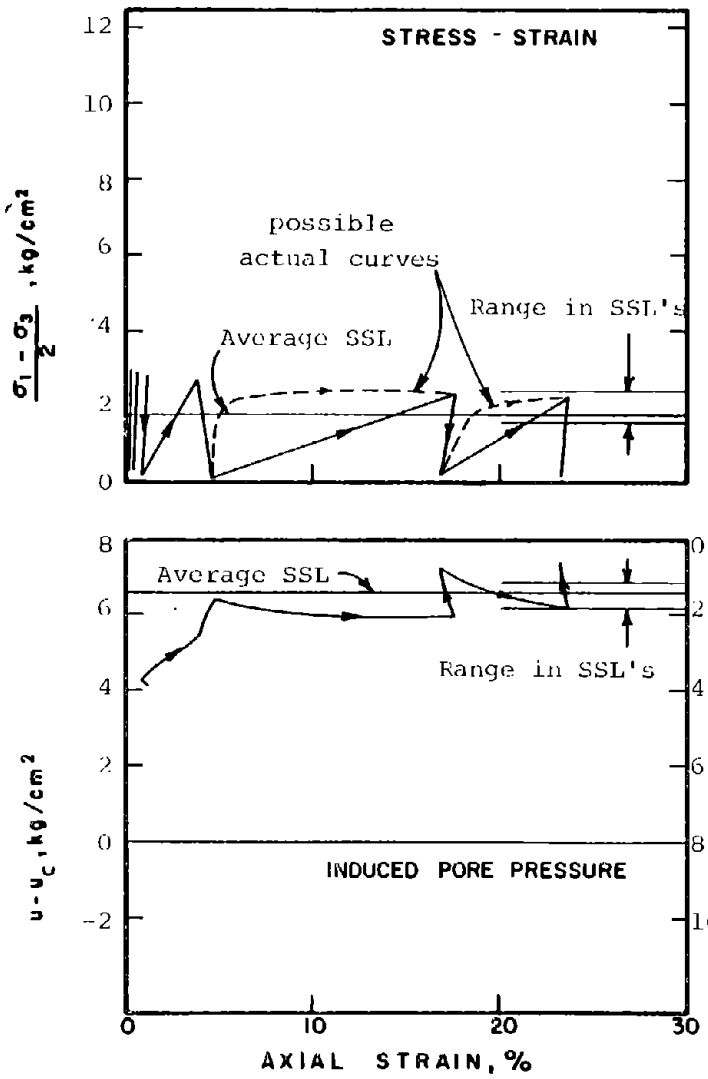

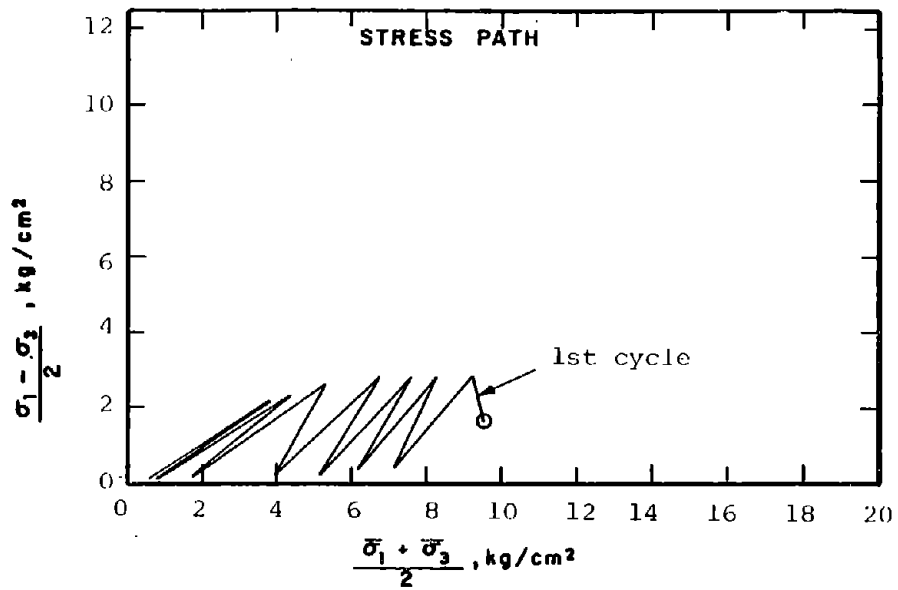

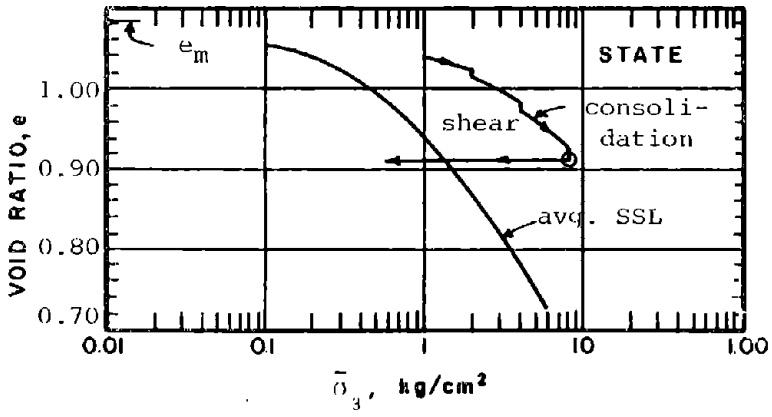

CAR-1005

SOIL : Mine Tailings

STRUCTURE : Compacted Moist

STATE AFTER CONSOLIDATION: $\bar{\sigma}_{3c}$ = 8.00 kg/cm², $\bar{\sigma}_{1c}$ = 11.00kg/cm²

e_c = 0.910, γ_{dc} = 87.6 pcf

METHOD OF LOADING: Undrained, Cyclic Axial Compression
Load Control
$(\sigma_1 - \sigma_3)_{cy}$ = 2.66 ksc

TESTING DETAILS : Specimen Diameter 3.60 cm
: Specimen Height 5.30 cm
: End Platens: Lubricated, Type 2

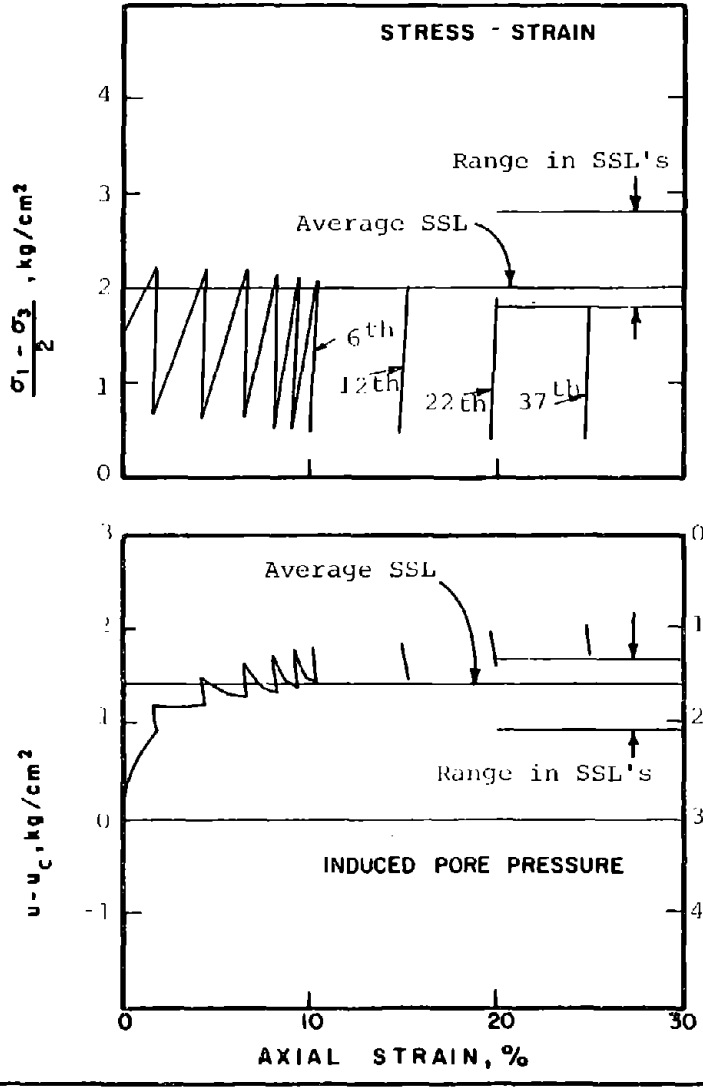

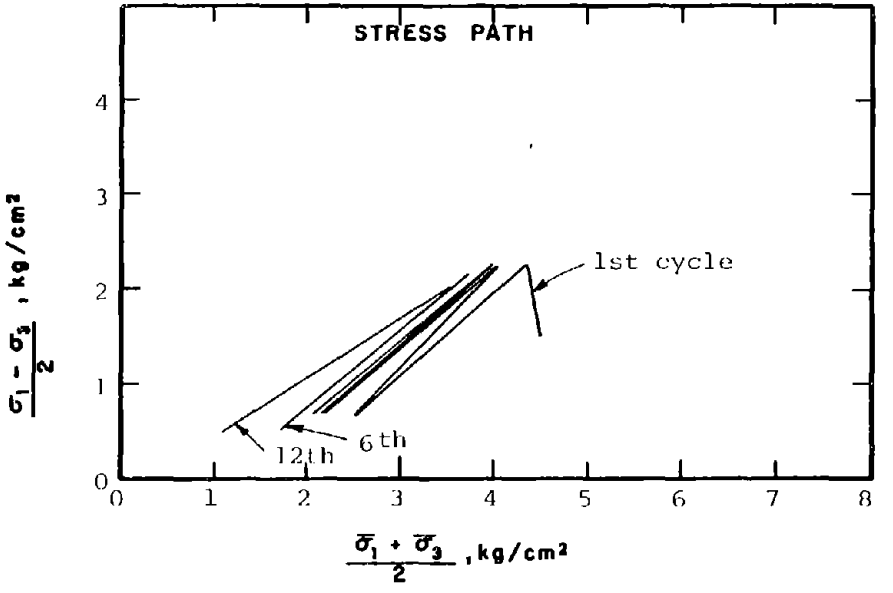

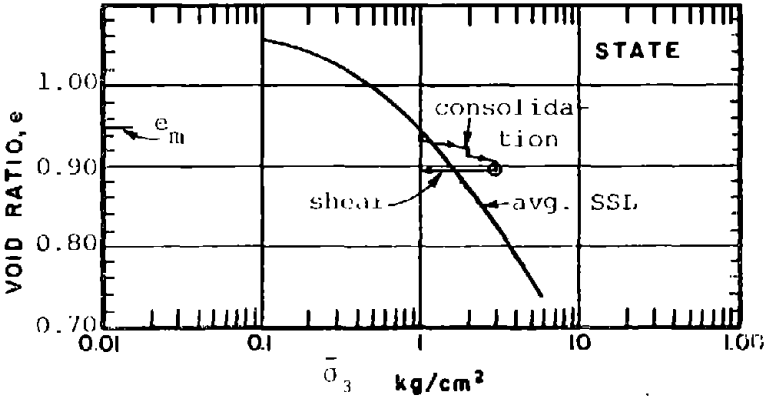

CAR-1006

SOIL : Mine Tailings

STRUCTURE : Compacted Moist

STATE AFTER CONSOLIDATION: $\bar{\sigma}_{3c}$ = 3.00 kg/cm², $\bar{\sigma}_{1c}$ = 6.00 kg/cm²

e_c = 0.895, γ_{dc} = 88.23 pcf

METHOD OF LOADING: Undrained, Cyclic Axial Compression Load Control

$(\sigma_1 - \sigma_3)_{cy}$ = 1.54 ksc

TESTING DETAILS : Specimen Diameter 3.60 cm

: Specimen Height 5.30 cm

: End Platens: Lubricated, Type 2

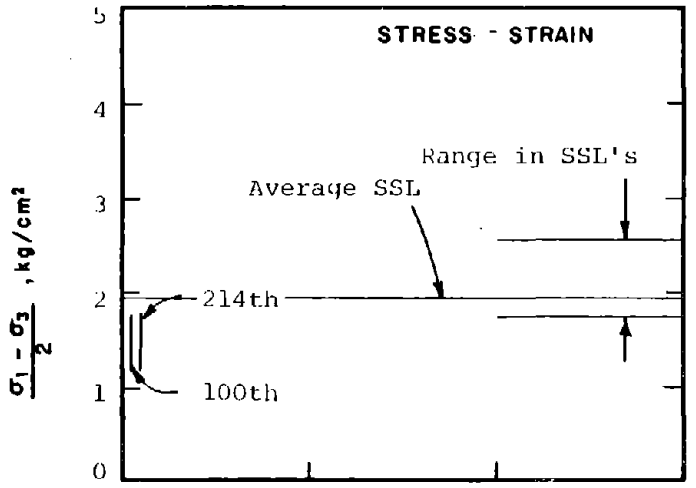

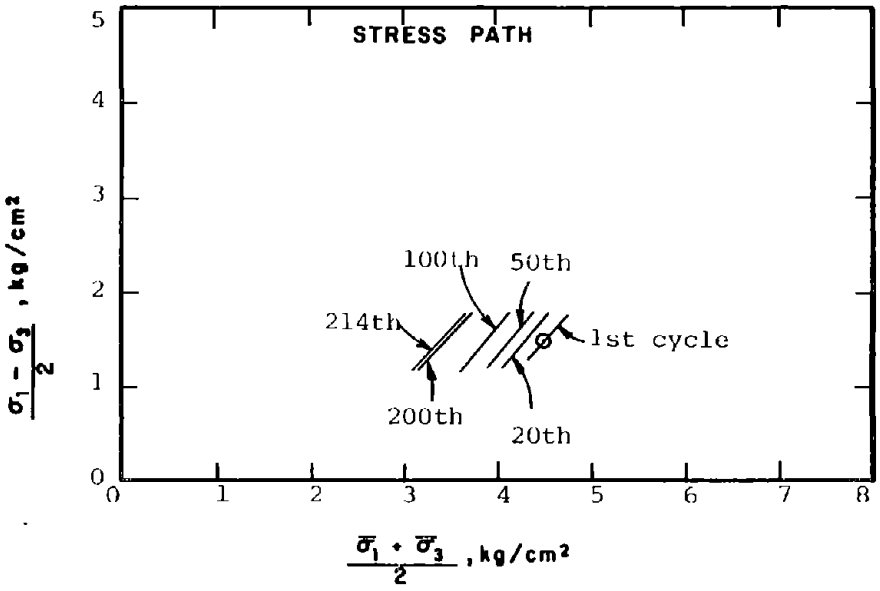

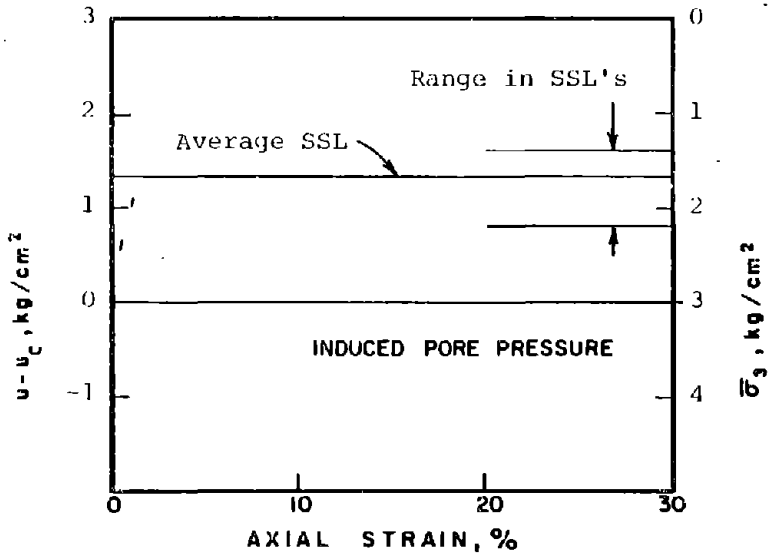

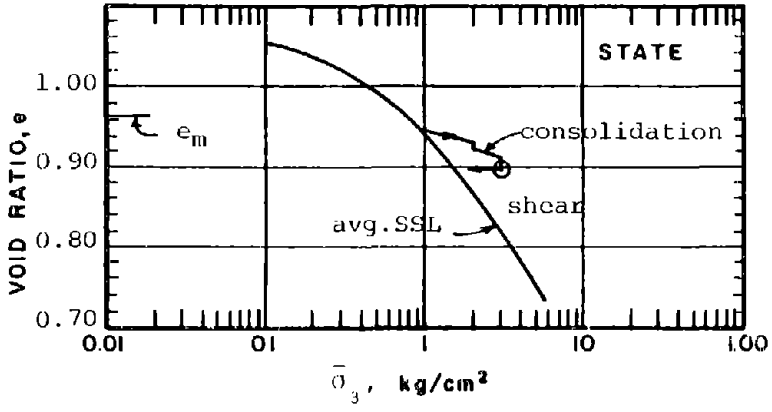

CAR-1007

SOIL : Mine Tailings

STRUCTURE : Compacted Moist

STATE AFTER CONSOLIDATION: $\bar{\sigma}_{3c}$ = 3.00 kg/cm², $\bar{\sigma}_{1c}$ = 6.00 kg/cm²
e_c = 0.899, γ_{dc} = 88.1 pcf

METHOD OF LOADING: Undrained, Cyclic Axial Compression
Load Control
$(\sigma_1 - \sigma_3)_{cy}$ = 0.61 ksc

TESTING DETAILS : Specimen Diameter 3.60 cm
: Specimen Height 5.30 cm
: End Platens: Lubricated, Type 2

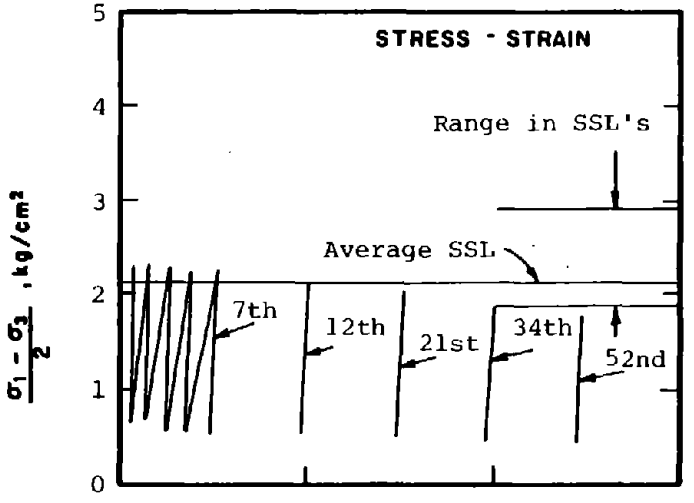

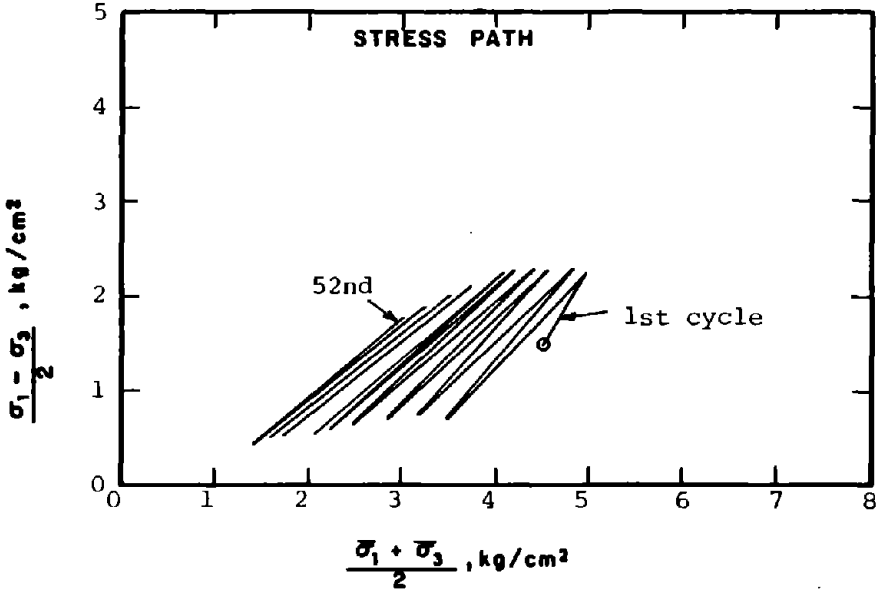

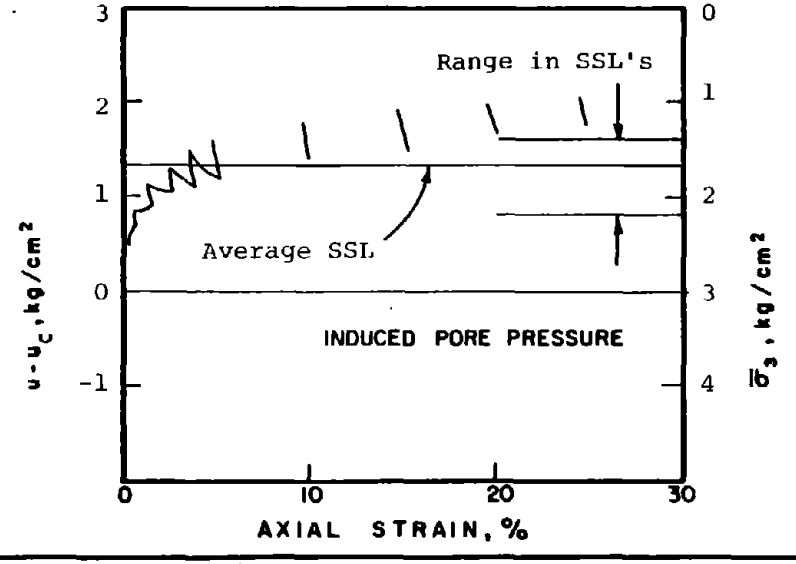

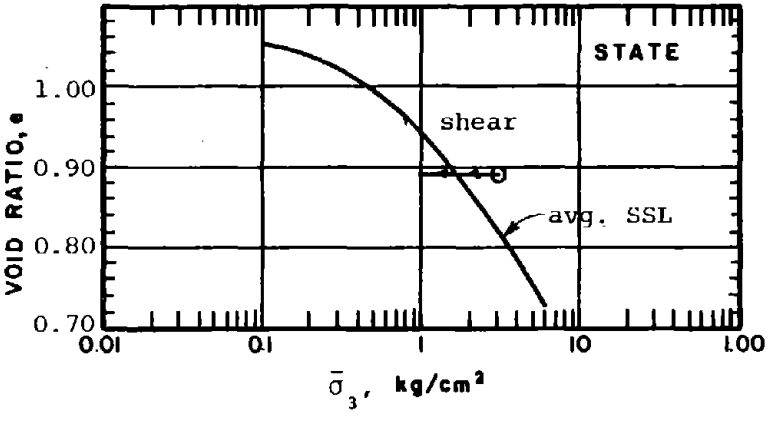

CAR-1007B

SOIL : Mine Tailings

STRUCTURE : Compacted Moist

STATE AFTER CONSOLIDATION: $\bar{\sigma}_{3c}$ = 3.00 kg/cm², $\bar{\sigma}_{1c}$ = 6.00 kg/cm²

e_c = 0.891, γ_{dc} = 88.4 pcf

METHOD OF LOADING: Undrained, Cyclic Axial Compression Load Control

$(\sigma_1 - \sigma_3)_{cy}$ = 1.67 ksc

TESTING DETAILS : Specimen Diameter 3.60 cm

: Specimen Height 5.30 cm

: End Platens: Lubricated, Type 2

APPENDIX B

COMPACTION TEST RESULTS

APPENDIX B

COMPACTION TEST RESULTS

This appendix contains compaction curves for Banding Sand #1, Banding Sand #6, and mine tailings sand. All three curves were determined in accordance with ASTM Procedure D1557-78, Method A.

LIST OF FIGURES

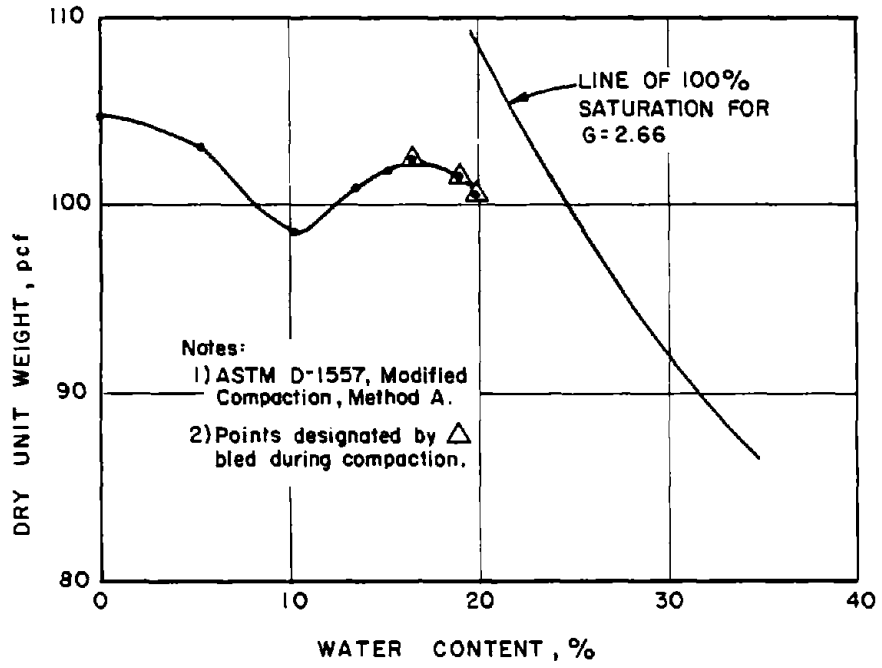

Fig. B-1: Compaction Curve for Banding Sand #1

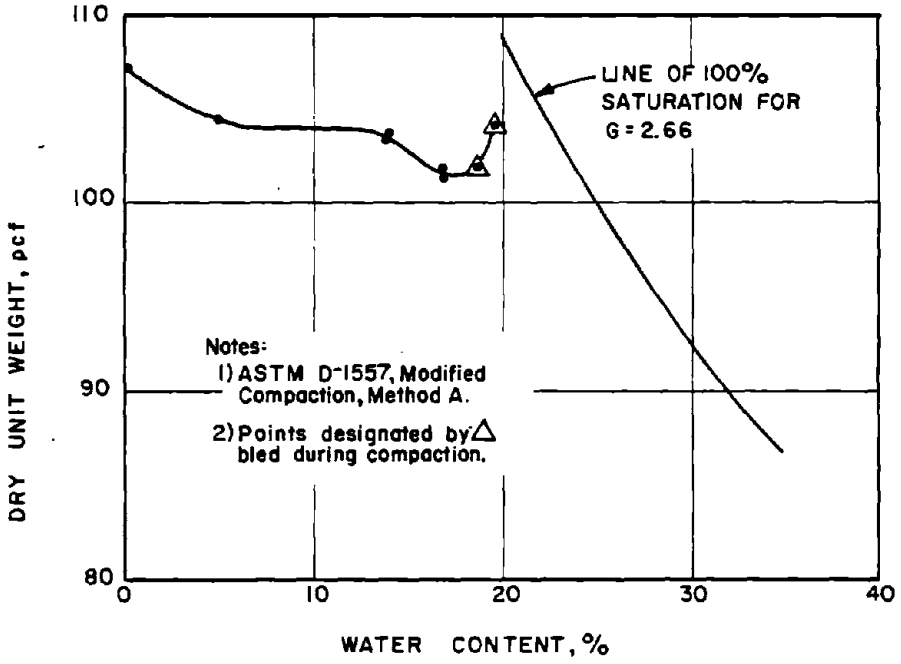

Fig. B-2 Compaction Curve for Banding Sand #6

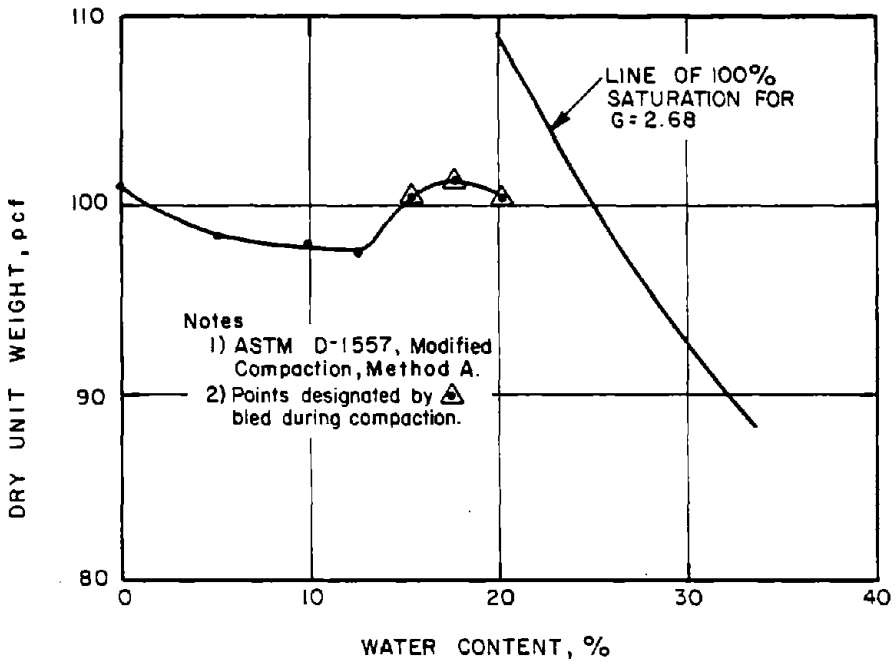

Fig. B-3: Compaction Curve for Mine Tailings Sand.

APPENDIX C

APPARATUS AND PROCEDURES

APPENDIX C

CONTENTS

LIST OF TABLES

LIST OF FIGURES

APPENDIX C

APPARATUS AND PROCEDURES

Triaxial Cell (3.6-cm-diameter specimens)

Triaxial tests were performed in triaxial cells, as illustrated in Fig. C-1. Loads were applied via a 3/8 in. diameter stainless steel piston guided by Thomson Ball Bushings. Loads were measured by a Data Instruments Tyco JP500 load cell connected to a 3/8-in.-diameter piston threaded into the bottom specimen end platen. Specifications for the JP500 are shown in Table C-1. O-ring seals on the top and bottom pistons prevented leakage of cell fluid. Since the load cell piston does not move, this system of measuring the load eliminates the need to correct the deviator load for piston friction as is the case in other loading systems which use external proving rings or load cells to measure the load on the top piston. Full-scale response of the load cell requires very small deformations, and thus the bottom piston friction is negligible.

Pore pressures were measured by Tyco Model AB pore pressure transducers. For tests with a total cell pressure ($u_c + \bar{\sigma}_{3c}$) of 15.00 kg/cm^2 or less, a transducer rated at 200 psi (14.1 ksc) was used, and for tests above this a pressure transducer rated at 500 psi (35.2 kg/cm^2) was used. Specifications for the Model AB Transducers are shown in Table C-1. Volume changes were measured with calibrated burettes graduated to 0.1 cm^3 and estimated to 0.01 cm^3. Axial displacement during rapid deformations was measured by Direct Current Displacement Transducers (DCDT's). Specifications for the DCDT's are shown in Table C-2. Dial extensometers accurate to 0.001 cm were used when the rate of deformation permitted their use. The measurements from the DCDT's and the dial extensometers were compared and found to be equivalent.

Loading Apparatus

Load controlled axial loading was applied by a dead load device in $\bar{R}$, $A\bar{R}$, and $CA\bar{R}$ tests except for six $CA\bar{R}$ tests on mine tailings which were performed using a pneumatic loading device. The dead load apparatus was a modified consolidation test frame. For the static (monotonic) load hanger, there is a 1 to 12 ratio between the load applied to the hanger and the load applied to the specimen. Before placing the triaxial cell in the frame, the system was balanced so that no load would be applied to the top piston. During back pressure saturation, the top piston, which was not threaded into the top cap, was forced upward under the cell pressure and came in contact with the loading yoke. A steel

ball bearing was placed between the piston and the loading yoke. After back pressure saturation weights were added to the load hanger to compensate for the force of the cell pressure acting on the area of the 3/8-in.-diameter piston. This allowed the piston to come into contact with the top cap of the specimen without applying any axial load. During consolidation the piston was kept in contact by adding weights to the hanger to compensate for the increases in cell pressure, and axial dial readings were taken to measure height changes. In order to apply an anisotropic consolidation increment the current area of the sample was calculated and load was added to the hanger so that the desired deviator stress would be applied, as measured by the load cell. For $\bar{R}$ and AR tests, the sample was loaded following consolidation by applying loads to the static load hanger every 60 seconds until a decrease in resistance and rapid deformation occurred or the test was terminated. When a decrease in resistance occurred, the lever arm rotated about its fulcrum as the specimen deformed and the loading yoke dropped in an effort to maintain the load on the sample. Note that as the resistance of the sample decreased, the difference between applied load and specimen resistance produced an acceleration of the dead weights and lever system. Deformation stopped when the static load hanger hit a stop block. The total axial strain of the sample was generally about 35% when the hanger hit the stop block. Typical strip chart records during early application of monotonic loading and during steady state deformation are illustrated in in Fig. C-2.

A second load hanger was used for application of cyclic load. This hanger was suspended beneath the lever arm. The hanger was connected to a Thomson Ball Bushing riding on a horizontally mounted, 3/4-in.-diameter Thomson 60 case hardened stainless steel shaft. Rubber stops were placed so that the center of gravity of the hanger assembly could be moved from a lever ratio of 1 to 5 to a lever ratio of 1 to 10. The cyclic load was applied by moving the hanger assembly back and forth along the horizontal bar. If the hanger is initially at the midpoint of this range (1 to 7.5 lever ratio), then moving it to the 1 to 10 position increases the applied load by 33%. Moving back to the neutral position, the specimen feels the consolidation stresses again. Continuing to move the load to the 1 to 5 position reduces the applied load by 33%. In order to apply the desired cyclic stress, $(\sigma_1-\sigma_3)_{cy}$, the following steps were performed:

1. Calculate the load needed to apply the desired cyclic stress. (moving between 1 to 5 and 1 to 10 lever ratio positions)

2. During anisotropic consolidation, while the cyclic load hanger is fixed at the 1 to 7.5

position, apply loads to the cyclic load hanger up to the amount of weight calculated in 1.

3. Apply any additional anisotropic loads to the static hanger.

After consolidation is completed, the cyclic load hanger is released from the 1 to 7.5 position and moved by hand, first to the 1 to 10 position and then to the 1 to 5 position. Thus the "compression" half of the cycle is applied first, followed by the "extension" half. Cyclic loading was applied a rate of 1 cycle every 4 to 5 seconds (0.25 to 0.20 Hz).

Cycling the load by hand produces a nearly sinusoidal loading, since there is a natural tendency for the operator to slow down the motion of the load hanger as it approaches the end stops. A typical load trace from the strip chart recorder is shown in Fig. C-3. If steady state deformation was induced, the cyclic load hanger was stopped wherever it was when rapid deformation started. Since failures in the Banding sand usually occurred in less than 1 second, it would have been impossible to return the load to the neutral position before the maximum deformation was reached.

The pneumatic loading system used in six of the CAR tests consisted of two air pressure chambers attached to the axial load piston. Cycling of air pressure in the chambers would alternately increase and decrease the axial load on the specimen. Axial loads were measured by the load cell at the base of the specimen, so friction in the pneumatic loader did not effect the load readings.

A conventional strain controlled loading press was used for the limited number of tests performed with strain controlled loading.

Lubricated Ends

Lubricated ends similar to those proposed by Rowe and Barden (1964) were used for all but eight tests. Figure C-4 shows the details of two types of lubricated ends. Initially Type 1 ends consisting of about 0.01 in. of Dow Corning High Vacuum Grease covered with a 0.01 in.-thick rubber membrane were used. After several tests, it was noticed that much of the grease was extruding into the center drainage port. This extrusion caused significant errors in the calculated void ratios of the specimens. After testing of two alternate types of lubricated ends, as discussed in Section 7.2.2, Type 2 ends consisting of a thin smear of grease and a 0.02 in.-thick membrane were used for subsequent tests. Comparison of results of tests using Type 2 with tests using Type 1 showed no difference in specimen stress-strain curves.

Sample Preparation

Specimens were prepared using a moist tamping method. The oven dry sand (Banding Sand or mine tailings) was mixed to 5% water content and compacted inside a membrane held tight to the inside of a split mold by a vacuum. Specimens were compacted in six layers each 0.9 cm thick, using a static weight with a 1/2-in.-diameter foot. The weight varied between 0.30 and 3.0 kg, depending on the target density of the specimen. Each layer of moist sand was placed in the mold using a spoon. The sand was spread out and rodded using a spatula to produce a uniform layer without voids. Next a 1.38-in.-diameter wooden dowel was placed inside the mold, resting on the loosely placed sand. The weight being used for the particular compaction was placed on top of the wooden dowel, causing some densification of the sand. Then approximately 12 tamps of the weight were applied to the surface of the layer, further densifying the sand. The remaining layers were compacted in this same manner, including one additional layer above the intended top of the specimen to allow adequate compaction of the top layer.

After compaction of the last layer, the specimen was trimmed flush with the top of the mold using a spatula. A thin coat of stopcock grease was applied to the sides of the end platens, and the membrane was rolled down over the bottom platen. The top end platen was then placed on the top of the mold, the membrane rolled up around it, and a vacuum applied to the specimen through the bottom drainage port. A plug in the top drainage line prevented loss of the vacuum. A split ring at the top of the compaction mold allowed the specimen to consolidate under the vacuum without jamming the top cap against the mold. In most tests, a full vacuum of 30 in. of Hg (1 kg/cm^2) was applied. In some tests 15 in. Hg or 7.5 in. Hg was used.

Next the mold was removed and the specimen was measured. Diameter was measured to 0.001 cm over the prophylactic membrane. Twice the thickness of the membrane was subtracted from the measured diameter to obtain the actual specimen diameter. The height was measured to 0.005 cm using calibrated calipers. Error in measurement of diameter by ± 0.001 or of height by ± 0.005 results in a maximum error in void ratio of ± 0.001. The dry weight of the specimen was measured to ± 0.01g. Error in measurement of weight by 0.01g results in an error which is negligible compared to the above errors. The void ratio calculated based on the specimen dimensions under the initial vacuum is designated e_i.

A second (and sometimes a third) membrane was (were) then placed around the sample in case the inner membrane was punctured during the sample preparation stage. Rubber O-rings were placed on top and bottom caps to prevent leakage. The top drainage line

was then quickly connected to the base of the cell without significant loss of vacuum. The rest of the cell was then assembled and filled with water. In the early part of the testing program, the top piston had a spherical end which seated itself into the hole in the center of the top cap. Later, in order to ensure that the top cap could not rotate and slide off the specimen when strains became large, a fitting which prevented rotation was placed on the end of the piston. This fitting is shown in Fig. C-1. It does not thread into the top cap. It should be noted that tension loading was not performed.

After placing the cell in the loading device, the vacuum was released in the following way. With the sample valves closed the initial cell pressure (in most cases 1 kg/cm^2) was applied and the vacuum line was removed from the bottom burette. The bottom sample valve was opened and water was allowed to enter from the burette, dissipating the vacuum and forcing any remaining air to the top of the specimen. Then water was circulated from bottom to top of the specimen under a head of several centimeters of water. This was done until no more air bubbles came out the top of the specimen. The specimen was then back pressure saturated.

Back Pressure Saturation

Specimens were back pressure saturated, maintaining the intial effective stress, until a Skempton B-value of 0.95 or greater was attained. A piggyback-type pressure system was used in most tests. In a piggyback system, increasing the back pressure regulator increases the cell pressure by the same amount, thus maintaining the initial difference set between the regulators (the initial effective stress). The back pressure was raised in increments of 1 kg/cm^2, allowing water to enter the specimen and equalize before applying the next increment. Generally a back pressure of at least 4 or 5 kg/cm^2 was necessary to attain a B-value of 0.95 or greater. In some cases back pressures up to 10 kg/cm^2 were necessary. Some tests with B-values less than 0.95 have been reported in the investigation. In some cases, when a specimen had a B-value of say 0.92 or 0.93 at 5 kg/cm^2 back pressure, the back pressure was increased to 6, and the test performed without performing another B-value test. The specimens probably had B-values greater than 0.95 after the back pressure was raised to 6 kg/cm^2. Following back pressure saturation, the specimens were consolidated to the desired effective stresses ($\bar{\sigma}_{1c}$ and $\bar{\sigma}_{3c}$).

Consolidation

Isotropic Consolidation ($\bar{R}$ tests)

Isotropic consolidation was accomplished by increasing the effective minor principal stress $\bar{\sigma}_3$ in increments until the desired stress was attained. The consolidation stress was

doubled each increment. Readings of volume change were taken with time (at 0.1, 0.25, 0.5, 1, 2, 8, 15 minutes etc.) in order to determine the end of primary consolidation. The sample was allowed to consolidate under the last increment until it was well into secondary compression. For the Banding sand almost no volume change occurred after about one minute. The mine tailings required more time and shearing of the sample generally did not take place for at least one hour after application of final condition stress. During consolidation, changes in specimen height were measured using an axial dial.

Anisotropic Consolidation ($A\bar{R}$ and $CA\bar{R}$ tests)

Anisotropic consolidation of the specimens was accomplished by applying an axial load to the specimens using the static and cyclic load hangers, as previously described. The actual load on the specimen was measured by the load cell and shown as a change in millivolt output displayed on a digital multimeter. For all $A\bar{R}$ and $CA\bar{R}$ tests on banding sand, isotropic consolidation to the final $\bar{\sigma}_{3c}$ was performed first, followed by anisotropic consolidation to $\bar{\sigma}_{1c}$. For the $A\bar{R}$ and $CA\bar{R}$ tests on tailings, however, consolidation was done in increments of isotropic/anisotropic consolidation, so that at the end of each isotropic/anisotropic increment the value of $K_c = \bar{\sigma}_{1c}/\bar{\sigma}_{3c}$ was equal to the desired final value. Anisotropic consolidation was performed with the sample valves open and volume and height change measurements were taken with time. Specimens were not sheared until primary consolidation was complete.

Undrained Axial Compression

Monotonic Loading ($\bar{R}$ and $A\bar{R}$ tests)

After consolidation the specimen valves were closed and all but three of the specimens were loaded by load control, one load increment every 60 seconds. A four-channel strip chart recorder was used to obtain a continuous record of load, pore pressure and fine and coarse displacements. A Model TR-444 Strip Chart Recorder, manufactured by Gulton Industries, with two TSC 820 signal conditioners (load and pore pressure) and two TSC-810 signal conditioners (fine and coarse displacements) was used. During the early part of the loading, the recorder was run at a slow speed (0.5 mm/sec), however, when liquefaction was anticipated the speed was increased to 100 mm/sec to record readings during the rapid deformation. The following are the specifications for the TR-444:

Rise time ..... 10 ms maximum, 1% overshoot
Stability ..... 0.5 Div/10° to 40°C

The TSC-820 units provided an excitation voltage of 5.50 VDC for the load cell and pore pressure transducers. A Uni 76 power supply, manufactured by Power Mate Corp. provided a constant 5.50 VDC excitation voltage for the DCDT's. The load cell was calibrated at the beginning of the testing program against the strip chart recorder using proving rings. As can be seen in any of the results of tests on Banding sand, there is a large difference between peak shear stress and steady state shear stress. Recording the deviator load on one channel means that in order to include the peak load and steady state load on the trace, there will be a small resolution (i.e. 4 or 5 divisions out of 50 divisions) of the steady state load. Therefore, in many tests the load was monitored on two channels. On one channel the attenuation was set so that deviator load from 0 to peak would be included. On a second channel the attenuation was selected so that the estimated minimum load (at steady state) would be at least 20 to 30 divisions (out of 50 divisions full scale).

The pore pressure trace calibration depended on the effective stress ($\bar{\sigma}_3$) for each test. For instance, the gain on the signal conditioner was adjusted so that 40 divisions would equal 4 kg/cm^2, etc. This resulted in a pore pressure calibration factor in kg/cm^2/ div.

The DCDT's were also calibrated for each test. The coarse DCDT channel was set such that 1 div = 0.05 cm and the fine DCDT channel was set such that 1 div = 0.01 cm. The number of divisions of displacement on the strip chart recorder was read to 0.1 div. A typical strip chart record is shown in Fig. C-2. The loading system, consisting of lever arms, counter weights, loading yoke and bicycle wheel, has a significant amount of inertia which slows down the deformation of the specimens. Castro's (1969) loading device was a dead load system which had less inertia than the loading device used in this investigation. Comparison of the velocities of deformation generally show faster deformation in Castro's tests.

The two strain controlled $\bar{R}$-tests on Banding Sand #6 were performed in a conventional loading press with a strain rate of about 0.4% per minute. Axial load and pore pressure were measured with electronic transducers which were monitored manually with digital multimeters. Axial deformation was measured with dial extensometers.

The one strain controlled $\bar{R}$-test on mine tailings was also performed in a conventional load press with a strain rate of about 0.7% per minute. Axial load, axial strain, and pore pressure were measured with electronic transducers monitored with the strip chart recorder.

Cyclic Loading ($CA\bar{R}$ Tests)

After consolidation, the sample valves were closed and the specimen was subjected to cyclic loading as described under the section titled "Loading Apparatus." Cycling was continued until either liquefaction occurred or a predetermined criteria for ending cyclic loading was achieved. The onset of liquefaction was evident from the axial dial. When liquefaction was imminent the dial would advance on each compression half cycle by an increasing amount until finally the specimen liquefied and rapid deformation of the specimen occurred. The criterion for stopping application of the cyclic load in tests which were not expected to liquefy was usually a certain number of cycles (i.e., 100 or 200); however, in three tests cyclic loading was continued until a pore pressure buildup corresponding to a reduction in effective minor principal stress ($\bar{\sigma}_{3c}$) from 4.00 to 3.00 kg/cm^2 occurred. Most of the $CA\bar{R}$ tests which did not liquefy were loaded monotonically, after cyclic loading, according to the above described procedure, to determine whether they were dilative or contractive under monotonic loading.

As in the monotonic ($\bar{R}$ and $A\bar{R}$) tests, the outputs from the transducers were recorded on a strip chart recorder throughout the tests. A typical strip chart recorder trace is shown in Fig. C-3. For large differences in peak cyclic load and steady state load, it was necessary to use two channels to record the load, one covering the whole range, the other only the steady state in order to obtain good resolution of the steady state load. When two channels were used for recording the load, only one DCDT (coarse) was used.

None of the cyclic tests involved stress reversal, i.e., cyclic shear stresses were less than the consolidation shear stresses in all cases.

TABLE C-1 - SUMMARY OF TRANSDUCER SPECIFICATIONS

	Load Cell Tyco JP 500	Pressure Transducers		Displacement Transducers	
		Tyco AB200	Tyco AB500	Trans-Tek 201-000	Hewlett-Packard 7DCDT-500
Repeatability, %	0.05	1.00% combined		-	-
Nonlinearity, %	0.10			0.30	0.50
Hysteresis	0.05			0	0
Excitation Voltage, VDC	5.50	5.50	5.50	5.50	5.50
Full-scale Output, mv	168	100	100	2500	3000
Rated Capacity	500 lbs	200 psi	500 psi	± 0.100 in.	± 0.50 in.

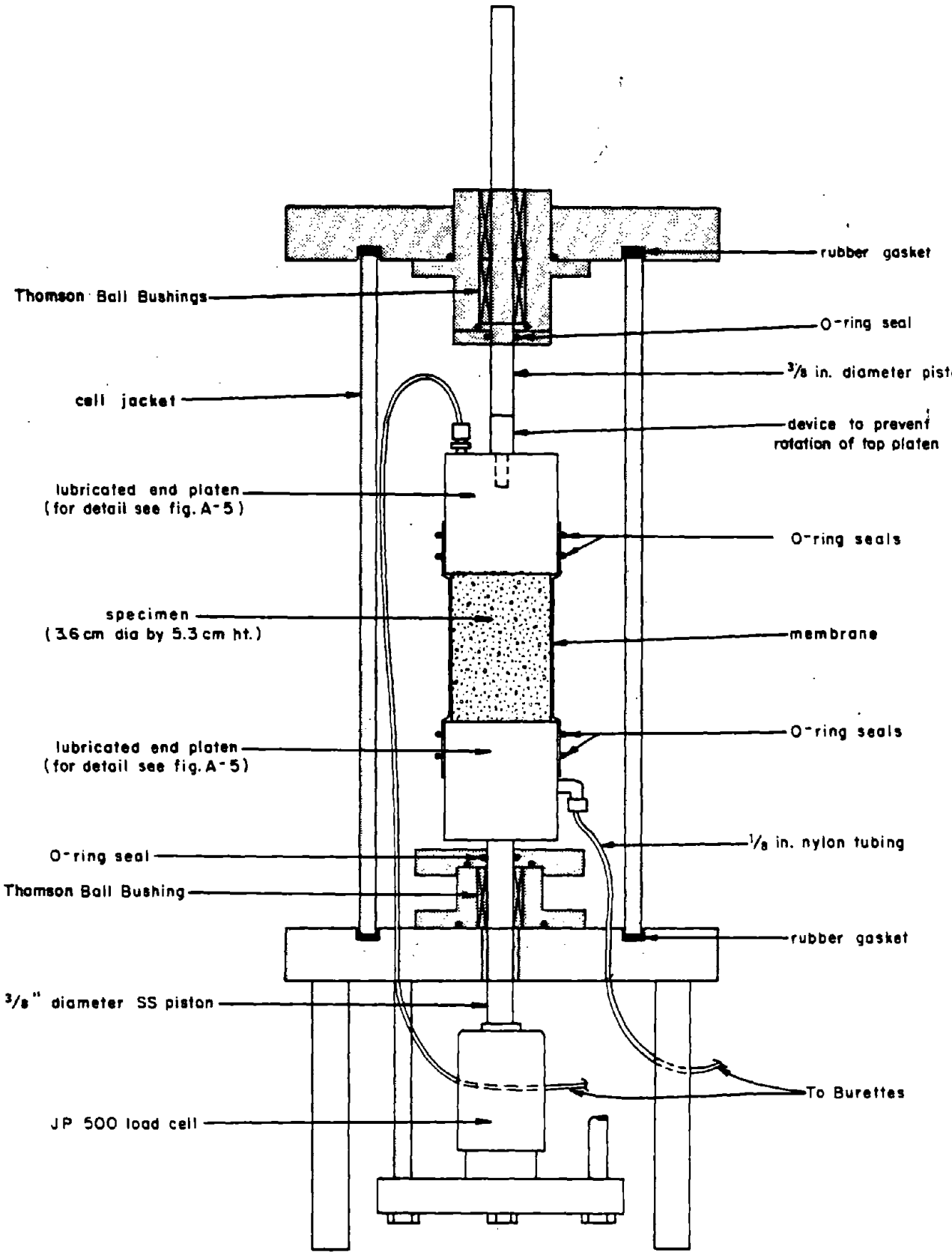

NOT TO SCALE

Fig. C-1 TRIAXIAL CELL (3.6 cm. diameter specimens)

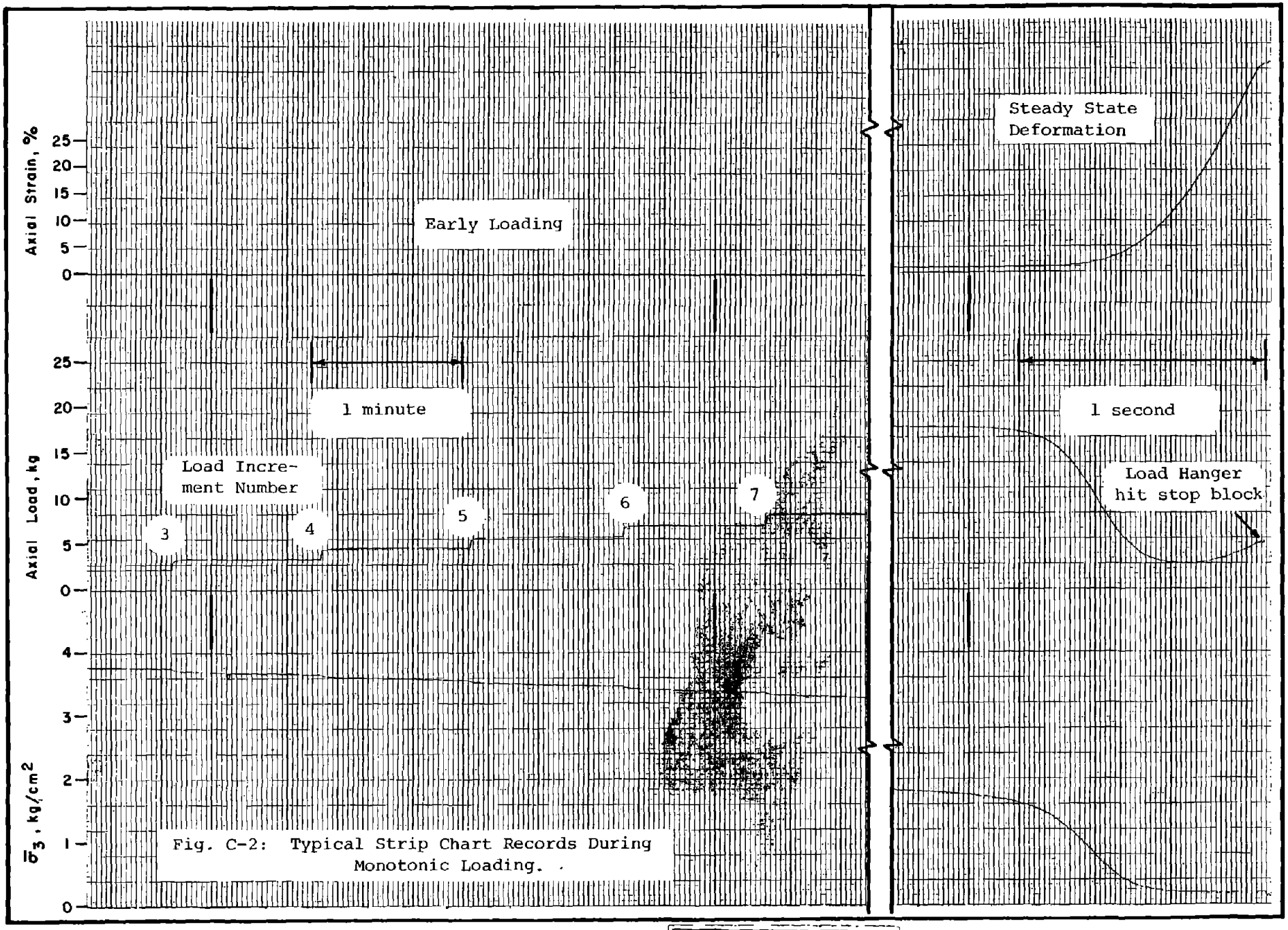

Fig. C-2: Typical Strip Chart Records During Monotonic Loading.

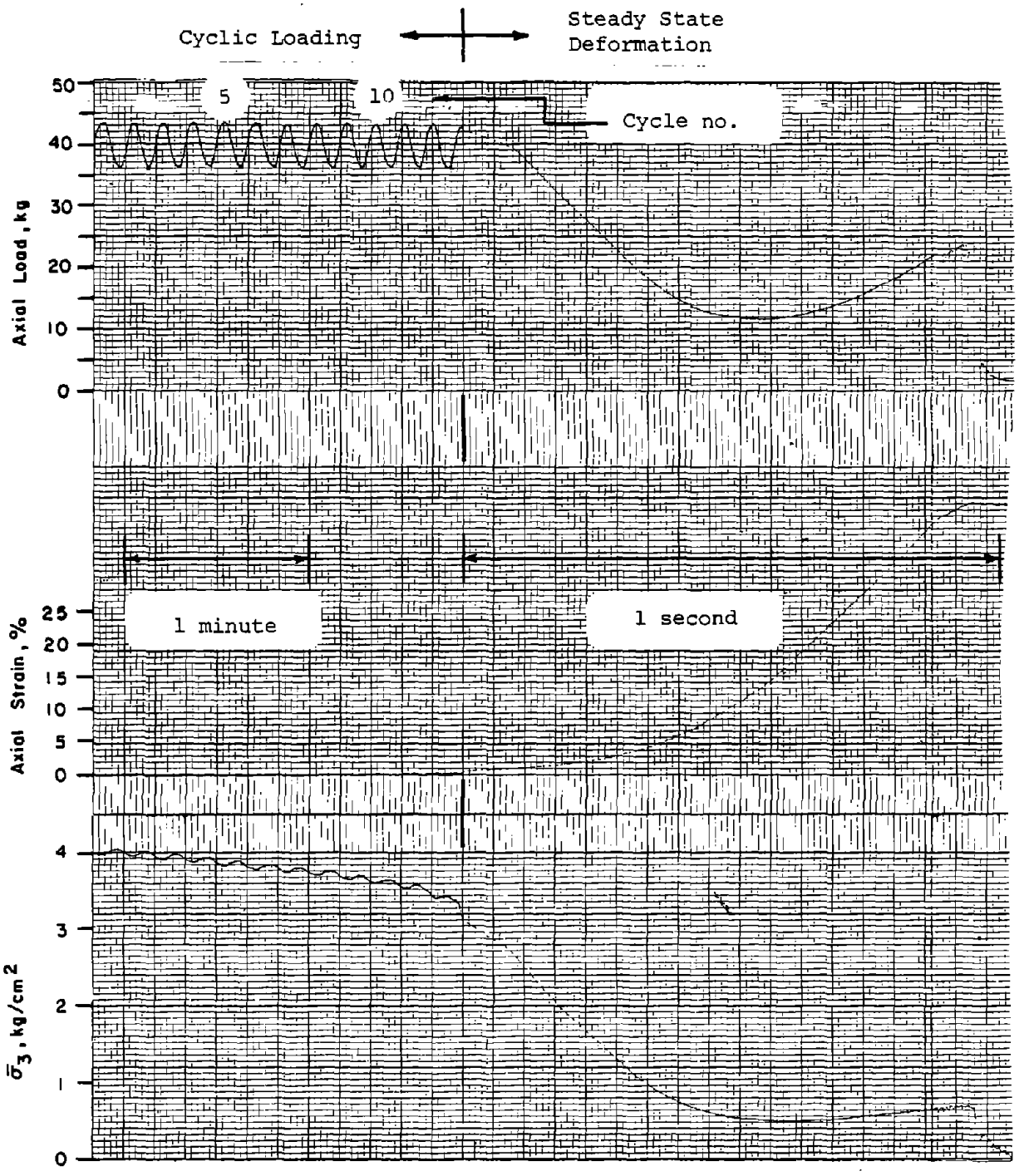

Fig. C-3: Typical Strip Chart Record During Cyclic Loading Leading to Steady State Deformation.

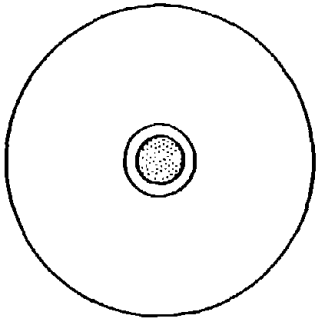

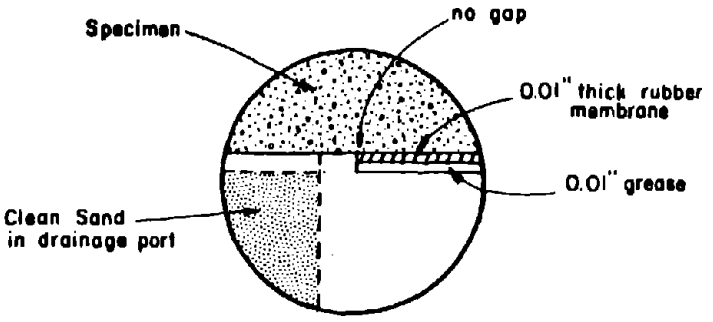

DETAIL A

Lubrication Type 1

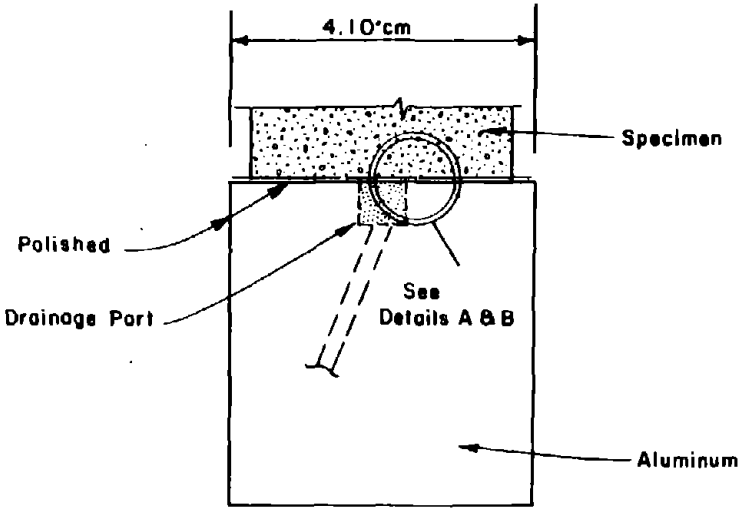

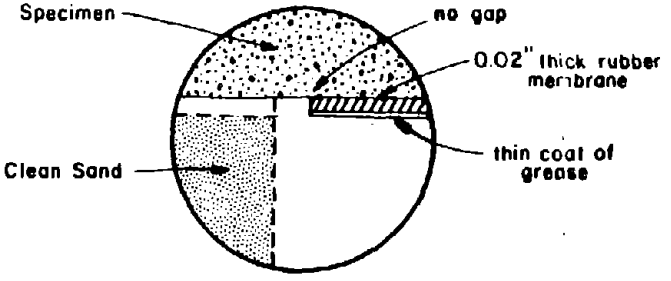

DETAIL B

Lubrication Type 2

NOT TO SCALE

Fig.C-4 Lubricated End Platens

APPENDIX D

INVESTIGATION OF UNIFORMITY OF COMPACTED SPECIMENS

APPENDIX D

INVESTIGATION OF UNIFORMITY OF COMPACTED SPECIMENS

The uniformity of the compacted specimens used for this study were investigated by the following two procedures:

1. Measuring the variations in void ratio within each of two Banding sand specimens compacted in a special mold.

2. Taking X-ray radiographs of two compacted specimens of Banding sand.

The first procedure consisted of compacting two 7.1-cm-diameter, 10.7-cm-high specimens inside a split-compaction mold which was lined with five snuggly-fitting, vertically-stacked rings. The specimen was compacted using the same procedures used for all of the triaxial specimens (see Appendix A). After the entire specimen was compacted, the top was trimmed flush and the split mold was removed. The five rings were separated by sliding a thin, stainless steel plate between each pair of adjoining rings. The soil in each ring was oven dried and weighed and the void ratio for each ring was calculated.

One of the two samples had an average void ratio of 0.802 with a standard deviation of 0.011 among the five sections, while the other had an average void ratio of 0.730 with a standard deviation of 0.008.

The two specimens used for X-ray radiographs were compacted inside 7.3 cm I.D. thin-wall tubes using the same procedures used for compacting the triaxial specimens. The specimens were compacted to average void ratios of 1.00 and 0.79, and photographic copies of the resultant X-ray radiographs are shown in Figs. D-1 and D-2, respectively. The vertical lines in the X-rays are due to the differing thicknesses and orientations of the sections of tube walls which the X-rays must penetrate. In the photographic copies of the X-rays, the lighter tones indicate lower densities (higher void ratios) and vice versa.

The specimen with a void ratio of 1.00 was actually significantly looser than the maximum void ratio of 0.82 determined according to ASTM D2049. This was possible because of "bulking" of the soil at the 5% water content used during compaction. This

very high void ratio was deliberately selected because it was believed that the "bulking" during compaction would produce greater nonuniformity than would be present in any of the test specimens, which were all compacted to lower void ratios. In Fig. D-1, it is seen that there are some variations of density within layers and that there are thin looser zones between layers.

The void ratio of 0.79 for the second specimen is typical of that used in the testing program. In Fig. D-2, it is seen that the density within each layer and in the different layers appears to be relatively uniform. Again thin, looser zones are apparent at the layer boundaries. Because these thin looser zones are oriented horizontally they most probably do not have a significant effect on the test.

From the above results, it is concluded that the triaxial specimens of Banding sand were reasonably uniform within about $\pm$ 0.011 in void ratio, at the end of compaction.

Investigations of uniformity of compacted specimens were not performed for the mine tailings. However, since similar compaction procedures were used, similar uniformity of specimens would be expected.

LIST OF FIGURES

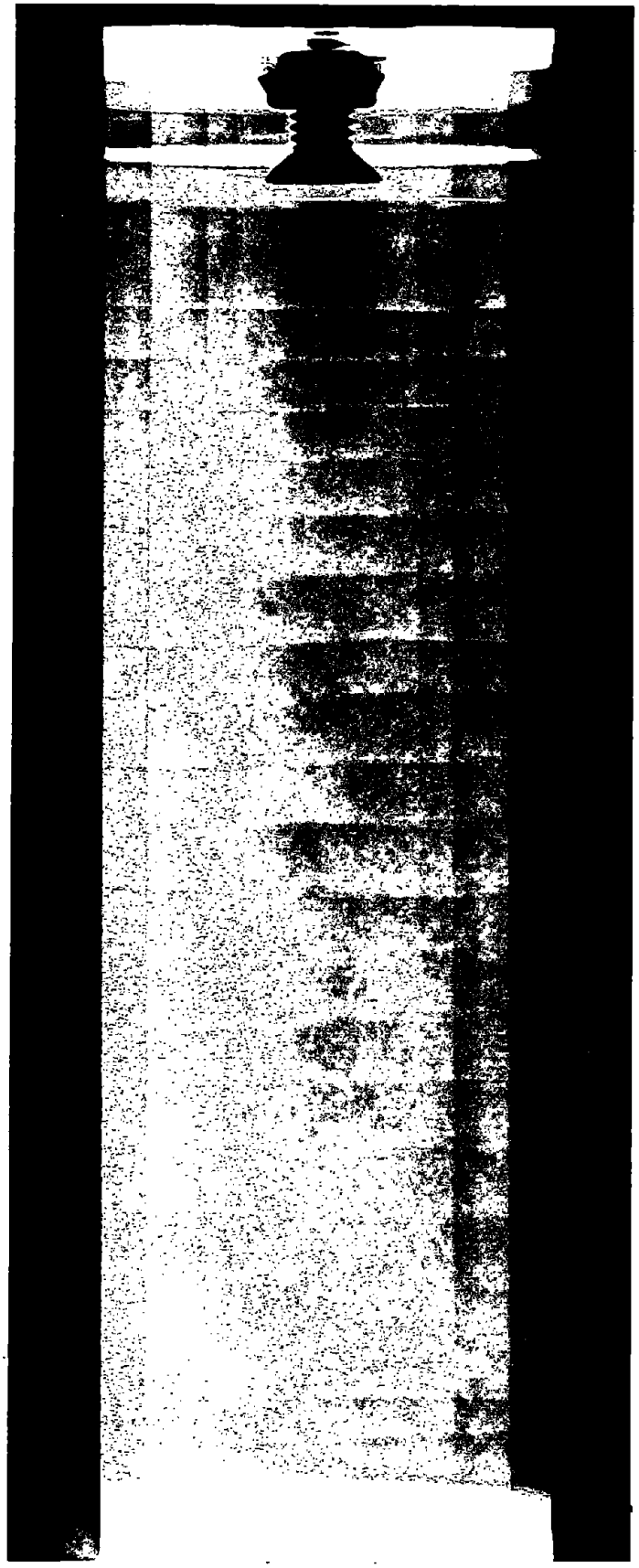

Note: Lighter tones indicate lower densities and vice versa.

Fig. D-1 X-ray Radiograph of Compacted Banding Sand Specimen, $e_{avg} = 1.00$

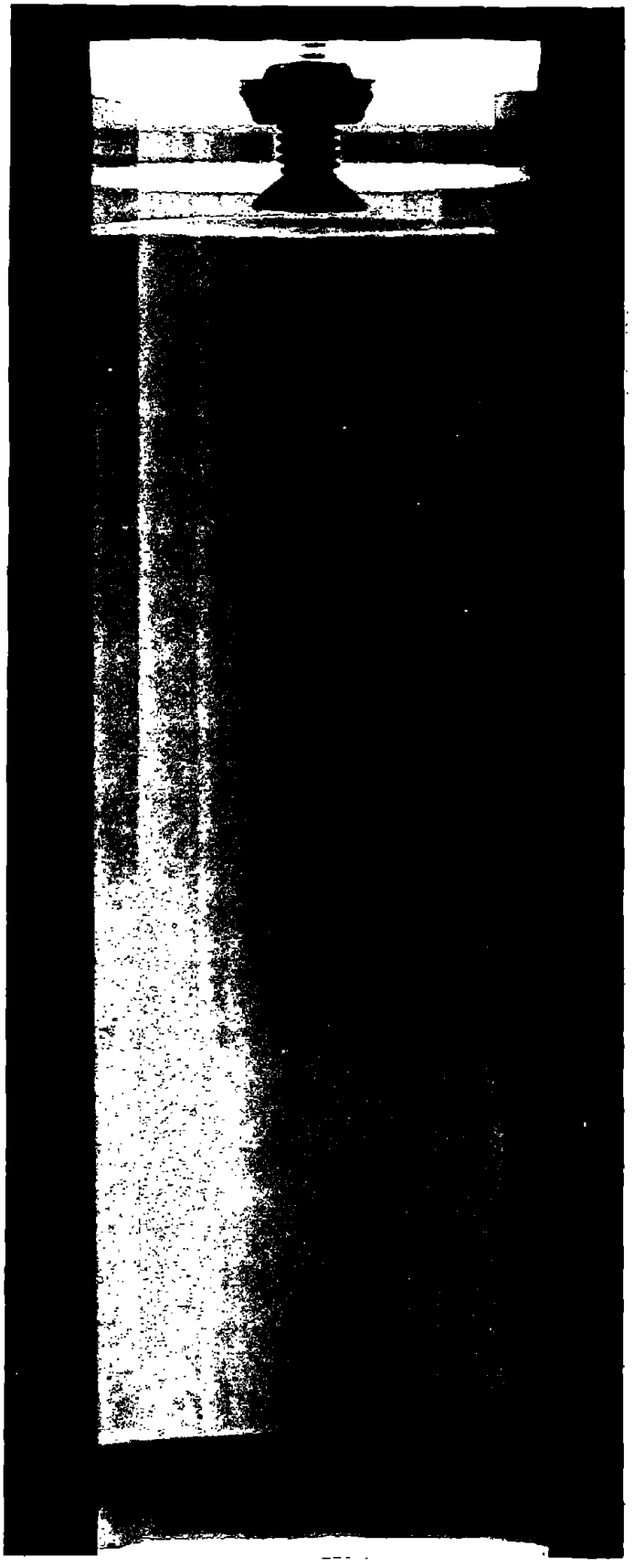

Note: Lighter tones indicate lower densities and vice versa.

Fig. D-2 X-ray Radiograph of Compacted Banding Sand Specimen, $e_{avg} = 0.79$